



Libro de Resúmenes

XIV Reunión Nacional de Óptica

3-5 de julio de 2024, Murcia



ISBN: 978-84-09-66738-3 (ed. digital no comercial)

© de los autores

Noviembre de 2024

Título: XIV Reunión Nacional de Óptica

Subtítulo: Libro de Resúmenes

Editor: Bueno García, Juan Manuel

Diseños logo y portada: Pedro M. Prieto

Fotos portada y contraportada: Antonio Benito, Rafael García Molina

Indice

1	Bienvenida	1
2	Comités	2
3	Sponsors	3
4	Programa Resumido	4
5	Conferencias Plenarias y Mesas Redondas	5
6	Programa V RNO joven (martes 02/07)	13
7	Programa Sesiones Orales Paralelas (miércoles 03/07)	15
8	Programa Sesiones Orales Paralelas (jueves 04/07)	25
9	Programa Sesiones Orales Paralelas (viernes 05/07)	34
10	Programa Sesiones Posters	38
11	Resúmenes/Abstracts – Técnicas de la Imagen	47
12	Resúmenes/Abstracts – Nanofónica	88
13	Resúmenes/Abstracts – Óptica Cuántica y No Lineal	105
14	Resúmenes/Abstracts – Ciencias de la Visión	152
15	Resúmenes/Abstracts – Divulgación Enseñanza e Historia	191
16	Resúmenes/Abstracts – Miscelánea	210
17	Resúmenes/Abstracts Pósters	257
18	Reuniones Comités de SEDOPTICA	394
19	Premios RNO 2024	395
20	Foto de grupo	398
21	Epílogo	399

Bienvenida

Estimados amigos/as y compañeros/as:

Desde 1988, la Reunión Nacional de Óptica (RNO) se ha venido celebrando de forma periódica en algún lugar de nuestra geografía. Sin embargo, la pandemia truncó esa regularidad y, aunque tuvimos la oportunidad de “vernós virtualmente” en el 2021, hace más de 5 años que no hemos podido reunirnos de forma presencial en ese foro, en el que miembros de la Universidad, centros de investigación y empresas compartimos resultados, ideas y conversaciones distendidas.

Con el objetivo de retomar de nuevo esos encuentros trienales, donde “cara a cara” solemos poner en común las investigaciones en Óptica hechas en nuestro país, tengo en placer de comunicaros que la **XIV RNO se celebrará en Murcia entre el 3 y el 5 de julio de 2024**, que estará precedida por la **V RNO Joven**, el 2 de julio.

Con la ayuda del Comité Organizador Local y la Junta de Gobierno de SEDOPTICA estamos iniciando la organización el evento. En particular, la página web estará previsiblemente disponible en unas semanas. Allí podréis encontrar detalles útiles sobre el envío de comunicaciones, fechas importantes y lugares para alojarse, entre otros. También habrá links de utilidad para obtener información sobre la bondades y atractivos tanto de la propia ciudad como de los diferentes enclaves turísticos de la Región de Murcia.

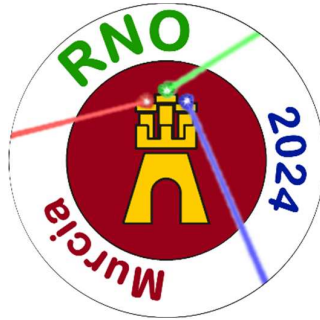
Esperamos que este esperado reencuentro sea del agrado de todos y de todas, y os animamos a participar junto con vuestros/as colegas y estudiantes con excelentes contribuciones científicas.

En nombre del Comité Organizador, ¡recibid un cordial saludo!

Juan M. Bueno
Presidente Comité Organizador RNO 2024
Universidad de Murcia

Luis Plaja
Presidente SEDOPTICA
Universidad de Salamanca





Comités

Presidente

Juan M. Bueno (*Universidad de Murcia*)

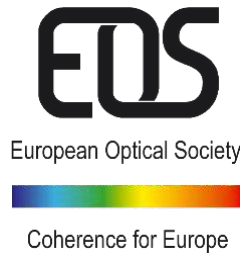
Comité Organizador Local

Alba Paniagua
Antonio Benito
Eloy Villegas
Esther Berrio
Josua Fernández
Pablo Artal
Pedro Prieto

Comité Científico

Mikel Aldaba (*Universidad Politécnica de Cataluña*)
Justo Arines (*Universidad de Santiago*)
Francisco J. Ávila (*Universidad de Zaragoza*)
Alejandro Carballar (*Universidad de Sevilla*)
Olga Conde Portilla (*Universidad de Cantabria*)
Martina Delgado (*Universidad de Valencia*)
Mario García Lechuga (*CSIC, Madrid*)
Ana Isabel Gómez Varela (*Universidad de Santiago*)
Verónica González (*Universidad Complutense de Madrid*)
Carlos Hernández-García (*Universidad de Salamanca*)
M^a Rosa López-Ramírez (*Universidad de Málaga*)
Lluis Marsal Garví (*Universidad Rovira i Virgili*)
Sonia Martín (*Universidad de Alcalá de Henares*)
Rosario Martínez Herrero (*Universidad Complutense de Madrid*)
Manuel Montejo Gámez (*Universidad de Jaén*)
Sara Núñez-Sánchez (*Universidade do Minho*)
Inmaculada Pascual (*Universidad de Alicante*)
Esther Perales Moreno (*Universidad de Alicante*)
Rosa Ana Pérez Herrera (*Universidad Pública de Navarra*)
Ana Rodríguez Aramendia (*Mbryonics Ltd.*)
Diego Romero Abujetas (*Universidad de Castilla - La Mancha*)
Santiago Royo (*Universidad Politécnica de Cataluña*)
Alejandro Turpin (*ICFO, Castelldefels*)
María Viñas Peña (*CSIC, Madrid*)
Rosa Weigand (*Universidad Complutense de Madrid*)

Patrocinadores





XIV Reunión Nacional de Óptica
3-5 de julio de 2024
V Reunión Nacional de Óptica Joven
2 de julio de 2024
Murcia



V RNOj		XIV REUNIÓN NACIONAL DE ÓPTICA		
Facultad de Óptica		Facultad de Economía y Empresa		
Martes, 02/07/2025		Miércoles, 03/07/2024	Jueves, 04/07/2024	Viernes, 05/07/2024
MAÑANA		Desde las 8:00 Inscripción	Desde las 8:30 Inscripción	Desde las 8:30 Inscripción
		9:00-9:30 Salón de actos Inauguración	9:00-9:45 Salón de actos Conferencia plenaria <i>Prof. Austin Roorda</i>	
		9:30-10:15 Salón de actos Conferencia plenaria <i>Prof. Andrew Forbes</i>	9:45-10:30 Salón de actos Conferencia plenaria <i>Dr. Carlos Hernández-García</i>	9:30-11:00 Sesiones paralelas • Ciencias Visión (Sala C2/06) • Cuántica y No Lineal (Sala B2/09) • Divulgación e Historia (Sala B2/07)
		10:15-11:00 Salón de actos Conferencia plenaria <i>Dr. Ana Doblás</i>	10:30-10:45 FOTO DE GRUPO	
		11:00-11:30 Cafetería Pausa / Café	10:45-11:45 Hall / Cafetería Posters (sesión 1) / Café	11:00-11:20 Cafetería Pausa / Café
		11:30-13:30 Sesiones paralelas • Técnicas Imagen (Sala C2/04) • Nanofotónica (Sala C2/06) • Miscelánea (Sala B2/07)	11:45-13:45 Sesiones paralelas • Técnicas Imagen (Sala C2/04) • Ciencias Visión (Sala C2/06) • Cuántica y No Lineal (Sala B2/09) • Miscelánea (Sala B2/07)	11:20-12:00 Sala de grados Entrega de Premios
	13:00-15:00 Comida Reunión Nacional de Óptica Joven	13:30-15:00 Pausa / Comida	13:45-15:15 Pausa / Comida	12:00-13:00 Reuniones Comités • Comités SEDOPTICA • Red FASLIGHT
		15:00-16:00 Sala de grados Mesa redonda <i>Mujer, Óptica y Fotónica</i>	15:15-16:00 Salón de actos Conferencia plenaria <i>Prof. José Benito Vázquez Dorrió</i>	13:00-14:00 Sala de grados Asamblea general SEDOPTICA
		16:00-17:00 Sesiones paralelas • Técnicas Imagen (Sala C2/04) • Cuántica y No Lineal (Sala B2/09) • Miscelánea (Sala B2/07)	16:00-17:30 Sesiones paralelas • Ciencias Visión (Sala C2/06) • Cuántica y No Lineal (Sala B2/09) • Divulgación e Historia (Sala B2/07)	14:00-14:15 Sala de grados Clausura XIV RNO
		17:00-17:30 Cafetería Pausa / Café	17:30-18:30 Hall / Cafetería Posters (sesión 2) / Café	
TARDE	15:00-15:15 Bienvenida			
	15:15-16:45 Speed networking	17:30-18:30 Salones paralelos • Técnicas Imagen (Sala C2/04) • Cuántica y No Lineal (Sala B2/09) • Miscelánea (Sala B2/07)		
	16:45-17:15 Pausa / Café	18:30-19:00 Sala de grados Meeting OPTICA Representative <i>Prof. Susana Marcos</i>		
	17:15-18:45 Carrera profesional en Óptica: Más allá del doctorado			
18:45-19:00 Clausura V RNOj				
NOCHE	20:30 Visita Ayuntamiento Ruta de Tapeo Pint of Science (monólogo)	21:30 Casino de Murcia Recepción de Bienvenida	21:30 Finca Buenavista Cena de Gala	

Conferencias Plenarias y Mesas Redondas




Plenary Talk – Conferencia Plenaria

Wednesday july/3

9:30-10:15 h

(Salón de Actos)

Miércoles 3/julio

<p>Prof. Andrew Forbes School of Physics, University of the Witwatersrand, Johannesburg andrew.forbes@wits.ac.za</p>	
---	---

Seeing through Distortion with Structured Light

Light can be tailored in its many degrees of freedom for so-called structured light. This opens many exciting avenues in seeing smaller in imaging, enhanced precision in manufacturing, and in optical communication and information processing, where the many forms of structured light can be used as an information alphabet. Unfortunately, light gets distorted when passing through noisy channels, negating the benefits of its initial structure. Here I will outline how to find degrees of freedom and forms of structured light that are invariant to noisy channels, and show near distortion-free transport of classical and quantum forms of structured light, even in highly distorted media.

Short bio:

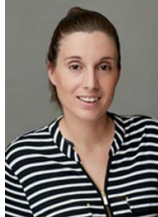
Andrew has at various times in his career found himself as teacher, janitor, secretary, receptionist, web-master, systems engineer, sales rep, manager, director, and sometimes a scientist. Andrew is presently a Distinguished Professor within the School of Physics at the U. Witwatersrand (South Africa) where in 2015 he established a new laboratory for Structured Light. Andrew is active in promoting photonics in Africa, a founding member of the Photonics Initiative of South Africa and Director of South Africa's Quantum Roadmap. He is a Fellow of SPIE, Optica, the South African Institute of Physics (SAIP), and an elected member of the Academy of Science of South Africa. He holds an A-rating by the South African NRF, 4 honorary professorships, is editor-in-chief of the IoP's Journal of Optics and sits on the editorial board of five other international journals. Andrew has won several awards, including the NSTF national award for his contributions to photonics in South Africa, the Georg Forster prize from the Alexander von Humboldt Foundation for outstanding contributions to photonics, the SAIP Gold Medal, the highest award for physics in South Africa, making him the youngest winner to date, the Sang Soo Lee award from Optica and the Korean Optical Society and the TWAS Prize for Physics. Andrew spends his time having fun with the taxpayers' money, exploring structured light in lasers as well as classical and quantum optics.

Plenary Talk – Conferencia Plenaria

Wednesday July/3

10:15-11:00 h (Salón de Actos)

Miércoles 3/julio

<p>Dr. Ana Doblas PI Optical Imaging Research Lab Department of Electrical & Computer Engineering University of Massachusetts Dartmouth adoblas@umassd.edu</p>	
---	---

What is Digital Holographic Microscopy? State of the Art and Applications

Quantitative Phase Imaging (QPI) techniques provide quantitative information about the refractive index variations and thickness of samples, which is not accessible with conventional intensity-based imaging systems. Among the different QPI methods, Digital Holographic Microscopy (DHM) stands out for its high resolution, sensitivity, wide field of view and fast acquisition rate. This talk provides an overview of the basic principles of DHM systems, including a description of the optical designs and the different reconstruction strategies to reconstruct quantitative phase images with high accuracy. hardware and software information. To finish, we will revise the applicability of DHM systems to different applications, including biological and biomedical research studies, characterization of materials, and oceanography sciences.

Short bio:

Ana Doblas received her BS, Ms., and Ph.D. degrees in Physics from the Universitat de València, Spain, in 2010, 2011, and 2015, respectively. After she finished her PhD work, she joined the Optical Coherence Imaging Laboratory under the supervision of Dr A. Oldenburg (Department of Physics and Astronomy, University of North Carolina in Chapel Hill, U.S.A.), where she did her 1-year Postdoc. From 2016 to the summer of 2023, she was in the Department of Electrical and Computer Engineering at the University of Memphis (Memphis, Tennessee, U.S.A.). From 2016 to 2018, she was the Research Assistant Professor at the Computational Imaging Research Laboratory (CIRL). In 2019, she became an Assistant Professor and principal investigator of the Optical Imaging Research Laboratory (OIRL). In 2021, she received the NSF CAREER award for her project titled “Three-dimensional super-resolution light microscopy of thick, unprocessed biological samples.” Since Fall 2023, she has joined UMass Dartmouth, becoming the newest faculty member of the Electrical & Computer Engineering department. Her current research interests are focused on optical engineering, computational optics, and three-dimensional imaging. Her final goal is to advance the fundamental science and engineering in imaging and photonics instrumentation for biological and biomedical applications, transitioning research outcomes to commercial products and systems. Since 2012, she has co-authored of 46 peer-reviewed scientific journals, her work has been presented at over eighty-five international conferences, and she is co-inventor of three US patents.

Mesa Redonda

Wednesday July/3

15:00-16:00 h (Salón de Grados)

Miércoles 3/julio

Dra. Ana Vidu Afloarei

Facultad de Derecho,
Universidad de Deusto
ana.vidu@deusto.es



Acoso en la Academia: una responsabilidad de todos y todas

El acoso en el ámbito laboral es un problema presente desde siempre que, en la actualidad se denuncia más. En la Academia no sólo hemos de prestar atención al acoso sexual de superiores hacia trabajadores, sino que también entra en juego su posible existencia entre docentes y estudiantado. Las Sociedades Científicas agrupan a profesionales de diferentes campos de conocimiento, les ponen en contacto y propician las redes laborales e incluso de amistad. ¿Cómo se debe reaccionar desde una Sociedad Científica ante una denuncia verosímil de acoso? ¿Cuál es el papel que deben jugar? ¿Cuál debería ser la actitud del resto de socios y socias? ¿Debería una persona bajo sospecha verosímil ocupar un papel relevante en una Sociedad Científica? ¿Tienen recursos las Sociedades Científicas para ejercer algún tipo de presión sobre los sospechosos? Estas son las preguntas que nos hacemos en Mujeres en Óptica y Fotónica, y sobre las que pretendemos dialogar con todos y todas vosotras.

Short bio:

Ana Vidu es investigadora postdoctoral Marie Sklodowska-Curie en la Universidad de California-Berkeley, y en la Universidad de Deusto, llevando a cabo el proyecto #UniswithHeart sobre redes y mecanismos de solidaridad para prevenir y responder al acoso sexual en las universidades. Ana es también miembro electo del Comité Ejecutivo de la ESA (Asociación Europea de Sociología) (2021-2024) y co-coordinadora de la Red de Investigación: Women's and Gender Studies. Ana también es miembro de la Red de Investigación de la ESA sobre Sociología del Derecho, así como miembro de la Asociación Internacional de Sociología (ISA) y de la Asociación Americana de Sociología (ASA), entre otras asociaciones, como la Asociación Europea de Mujeres Juristas (EWLA). La Dra. Vidu ha sido asistente editorial de la revista de la ISA, "International Sociology" desde 2015 hasta 2020. Recibió el Premio Extraordinario por su Licenciatura y también por su Máster en Sociología. Su tesis doctoral aportó conocimientos científicos pioneros en España sobre el tratamiento de una de las primeras denuncias contra un profesor por acoso sexual en la Universidad de Barcelona, comparándola con la primera denuncia en la Universidad de California-Berkeley. Fue cofundadora de la "Red solidaria de víctimas de violencia de género en las universidades" (actualmente *MeToo Universidad*). Ana Vidu ha participado en múltiples congresos internacionales, proyectos de investigación competitiva y ha publicado numerosos artículos científicos sobre violencia de género y consentimiento sexual.

-
- Estructura de la mesa redonda:
 - (1) Conferencia (30').
 - (2) Diálogo con la Prof. Millán (ex-presidenta de SEDOPTICA) (15').
 - (3) Turno abierto de palabra para el público (15').

Meeting **OPTICA** Representative

Wednesday July/3

18:30-19:00 h (Salón de Grados)

Miércoles 3/julio

Prof. Susana Marcos

Center for Visual Sciences
The Institute of Optics and Flaum Eye Institute
University of Rochester, Rochester
smarcos2@ur.rochester.edu



How OPTICA can shape your career?

Professional societies provide an excellent framework to a researcher's day to day work, but it is hard to think of a scientific society that better accompanies your career than Optica, nurturing students since their beginning of the journey, young professionals, seasoned academics, and industry. In this presentation, I will review programs from Optica and its Foundation (from Student Chapters and Ambassador program, to funding opportunities), its portfolio of meetings and journals, and corporate engagement activities. I will share bits of my journey at Optica, and other examples of how Optica can share a career in Optics, creating opportunities for growth, boosting the impact of your and creating long-lasting connections.

Short bio:

Susana Marcos is the current David R. Williams Director of the Center for Visual Science, Nicholas George Professor of Optics at the Institute of Optics and Professor of Ophthalmology at the Flaum Eye Institute, University of Rochester, NY, USA. She received a MsC (1992) and PhD (1996) in Physics from the University of Salamanca and was a postdoctoral researcher (1997-2000) at Harvard University, with Fulbright and Human Frontiers Science scholarships. She has been Director and Founder of the Visual Optics and Biophotonics Lab, and Professor of Research at the Institute of Optics, CSIC. She is a pioneer in the development of new techniques for evaluation and treatment in ophthalmology, several of which have been marketed and already contributed to improving the diagnosis and treatment of thousands of patients. She has published >220 highly cited research articles, is the inventor of 27 patent families (14 licensed), co-founder of 2EyesVision, has supervised 25 PhDs and pronounced >300 talks at international conferences. She has served in leadership positions in numerous organizations. At Optica, she has been Chair of the Applications of Visual Science Technical Group, Director at Large (2012-2015), Member of the Awards Committee, Chair of the Tyllier Award and Yves Medal Committee, Editorial Board Member in Biomedical Optics Express and Optica, and guest editor in special issues in Optical journals. Currently, she is Chair of the Optica Publications Council, Member of the Financial Committee and Optica Board Member, and Optica student chapters (CSIC and Rochester) advisor. She is a fellow of multiple societies (including Optica) and has received numerous recognitions, including the Optica Adolph Lomb Medal and the Edwin Land Medal.

Plenary Talk – Conferencia Plenaria

Thursday July/4

9:00-9:45 h

(Salón de Actos)

Jueves 4/julio

Prof. Austin Roorda

Herbert Wertheim School of Optometry and Vision Science
University of California, Berkeley
aroorda@berkeley.edu



Hacking Human Vision

Humans possess an exquisite ability to immediately generate rich and accurate percepts of a viewed scene in color, space, motion and depth. The process is so effortless that we often take it for granted, but like most lines of scientific investigation, the closer you look, the more interesting it gets. An ability to hack the visual system and directly control the factors (optical blur, eye motion, activation of three types of cone photoreceptor cells) that govern the sensory inputs that inform our percepts can offer some insight into this remarkable process. Systems that combine adaptive optics, high-speed tracking, and precise aberration-corrected light delivery to the retina allow us to do just that. I will describe our most recent systems, their capabilities and applications. Specifically, I will focus on experiments that investigate spatial vision [the beneficial role of eye motion for visual acuity] and color vision [how signals from the three cone types are used to generate percepts of color]. I will end with some discussion of how these technologies are being translated for clinical applications.

Short bio:

Austin Roorda received his Ph.D. from the University of Waterloo in 1996 with joint degrees in Vision Science & Physics. Since that time, Dr. Roorda has been pioneering applications of adaptive optics and ophthalmoscopy, including mapping of the human trichromatic cone mosaic while a postdoc at the University of Rochester, designing and building the first adaptive optics scanning laser ophthalmoscope (AOSLO) at the University of Houston, tracking and targeting light delivery to individual cones in the human eye at UC Berkeley, and being part of the first team to use AO imaging to monitor efficacy of a treatment to slow retinal degeneration. Since 2005, he's been at UC Berkeley where he is a member of the Vision Science, Bioengineering and Neuroscience graduate programs. He is a Fellow of the Optical Society of America, the Association for Research in Vision and Ophthalmology and the American Academy of Optometry. Notable awards are the Distinguished Alumni Award from the University of Waterloo School of Optometry (2007), the Glenn A. Fry Award from the American Academy of Optometry (2009), a John S. Guggenheim Fellowship (2014), an Alcon Research Institute Award (2016) a Leverhulme Visiting Professorship at the University of Oxford and the Rank Prize in Optoelectronics (2024).

Plenary Talk – Conferencia Plenaria

Thursday July/4

9:45-10:30 h (Salón de Actos)

Jueves 4/julio

Dr. Carlos Hernández-García

Grupo de Investigación en Aplicaciones del Láser y Fotónica
Unidad de Excelencia en Luz y Materia Estructuradas
Dpto. Física Aplicada, Universidad de Salamanca
carloshergar@usal.es



Attosecond Structured Light

The development of structured ultrafast laser sources is a key ingredient to advance our knowledge about the fundamental dynamics of electronic and spin processes in matter. It is widely recognized the relevance of ultrafast sources structured in their spin angular momentum (associated to the polarization of light) and orbital angular momentum (associated with the transverse phase profile, or vorticity of a light beam) to study chiral systems and magnetic materials in their fundamental temporal and spatial scales. In the last decade, the possibility to generate structured ultrafast laser pulses in the shortest time scales known, as attosecond pulses, has triggered substantial developments in nonlinear optics. In particular, thanks to the highly nonlinear process of high harmonic generation (HHG), where an intense infrared driving beam is up converted into the EUV extreme-ultraviolet (EUV)/soft x-rays, structured attosecond pulses can be nowadays obtained. In this talk we will review several works that have boosted the field of attosecond structured pulses during the last decade. We will focus not only in the ability to tailor the angular momentum properties of EUV/soft x-ray pulses, but also on how through the angular momentum of the infrared driving beam we can harness the spatiotemporal properties of the attosecond pulses being emitted.

Short bio:


Associate Professor at Universidad de Salamanca (Spain). He obtained his PhD in Physics in 2013. After a Marie Skłodowska Curie postdoctoral stay at JILA, University of Colorado at Boulder (USA), he returned to Universidad de Salamanca where he leads the Unit on Structured Light and Matter (LUMES) and the ERC Starting Grant project ATTOSTRUCTURA. His work focuses on the generation and applications of structured laser pulses, with durations in the attosecond timescale. Together with his colleagues and collaborators, he has designed theoretical tools to understand and combine quantum simulations with highly non-linear strong-field processes. Recipient of the Fresnel Prize 2019, the RSEF-BBVA 2019 Prize for young physics researchers, the IUPAP Young Scientist Prize 2021, and the ICO Prize 2023.

Conferencia Plenaria

Thursday july/4

15:15-16:00 h (Salón de Actos)

Jueves 4/julio

<p>Prof. José Benito Vázquez Dorrío Departamento de Física Aplicada, Instituto de Física y Ciencias Aeroespaciales, Universidad de Vigo bvazquez@uvigo.gal</p>	
---	---

Aprender Óptica Haciendo Óptica: Dentro y Fuera del Aula

Aprender Óptica haciendo Óptica es un reto y una necesidad, para acercar y hacer más comprensible este importante campo de la Ciencia y de la Ingeniería, en particular al alumnado de nuestro sistema educativo y en general a la Sociedad. El componente manipulativo y experimental, que permite utilizar todos los sentidos para comprender y establecer relaciones con el mundo natural, se reconoce como una fuente de inspiración, motivación y aprendizaje desde hace mucho tiempo. Es por ello que existen innumerables experiencias ya contrastadas del beneficio del empleo y difusión del aprendizaje activo experimental de la Óptica, teniendo así a nuestra disposición un amplio espectro de recursos para ser empleado por profesorado y alumnado de forma integrada con los contenidos conceptuales a enseñar dentro y fuera del aula. Actividades experimentales bien estructuradas que pueden poner de manifiesto, por ejemplo, los problemas que originaron el conocimiento, la metodología empleada, los avances y las aplicaciones técnicas relacionadas pasadas y recientes, la influencia de los contenidos a nivel social y ambiental, la historia de los contenidos y el aporte de la mujer a los mismos. Es tiempo de que hagamos uso de la información disponible e impulsemos, adaptemos, transformemos y modifiquemos el diseño e implementación de estas potentes herramientas de aprendizaje. En esta ponencia experimental invitada presentaremos nuestra visión y experiencia, así como una panorámica de los recursos disponibles y sugerencias de uso.

Short bio:

José Benito Vázquez Dorrío es catedrático de Física Aplicada en la Universidad de Vigo y su campo de investigación se centra en las aplicaciones metrológicas de la Óptica. Mantiene al mismo tiempo una línea de investigación e innovación en enseñanza y divulgación de la Física desde principios de los noventa relacionada con el diseño, creación y empleo de actividades manipulativas/experimentales fuera y dentro del aula, utilizando diferentes metodologías activas y herramientas, que han dado lugar, a un número 70mpeti de publicaciones, cursos de formación, organización de congresos, conferencias y proyectos de ámbito nacional e internacional en este 70mpeti de Aprender Física Haciendo Física. Es Vicepresidente de la Asociación Hands-on Science y miembro de la “International Council of Associations for Science Education. Es responsable del Grupo de Innovación Docente de Aprendizaje Manipulativo de la Física de la Universidad de Vigo, vocal del Grupo Especializado de Didáctica e Historia de la Física y la Química de las Reales Sociedades Españolas de Física y de Química, y representante de la RSEF en International Day of Light. Recientemente recibió el Premio Enseñanza y Divulgación de la Física (modalidad Enseñanza Universitaria) de la RSEF-Fundación BBVA 2023.

Martes 02/07/2024

V RNO joven



Martes 02/07/2024 – V RNOj

13:00 - 19:00

Facultad de Óptica (salón de actos)

13:00 a 15:00 – Comida conjunta (Cafetería Facultad de Química)

15:00 a 15:15 – Presentación del Área Joven – Bienvenida

15:15 a 16:45 – Speed Networking

Actividad orientada a la creación de grupos de personas basados en su trabajo y hobbies. Se invitará a los participantes a realizar una breve presentación personal de acuerdo con su situación actual y a sus intereses próximos.

16:45 a 17:15 – Pausa / Café (Cafetería Facultad de Bellas Artes)

17:15 a 18:45 – Carrera profesional en Óptica: más allá del doctorado

Mesa redonda que reunirá a distintos perfiles profesionales relacionados con la Óptica, Fotónica, y Optometría. Entre los y las ponentes, se contará con la presencia de 5 investigadores/as de reconocido prestigio tanto a nivel nacional como internacional que nos hablarán de su trayectoria académica/profesional dentro de sus respectivas áreas de especialización, y de sus iniciativas más allá de estas.

18:45 a 19:00 – Cierre / Clausura por parte del Área Joven

Miércoles 03/07/2024
Sesiones Orales Paralelas



Miércoles 03/07/2024

11:30 - 13:30

Sesiones Orales Paralelas (mañana)

Técnicas de la Imagen: **Aula C2/04**

Moderadora: María Viñas-Peña (Instituto de Óptica, CSIC)

Nanofotónica: **Aula C2/06**

Moderadora: Sara Núñez-Sánchez (Universidades do Minho e do Porto)

Miscelánea: **Aula B2/07**

Moderadora: Esther Perales (Universidad de Alicante)

Óptica Cuántica y No Lineal (jueves 4 de julio, sesión de mañana)

Moderadora: María Viñas-Peña (*Instituto de Óptica, CSIC*)

11:30 **Liquid crystals Mueller matrix imaging polarimeters tolerances to experimental errors.** Montes-González I, Estévez I, Canabal-Carbia M, Lizana A, Campos J. *Universidad Autónoma de Barcelona.*

11:45 **Polarization approach on the characterization and optimization of LCoS devices.** Sánchez-Montes AR, Francés J, Márquez A, Nájjar G, Moya A, Sirvent-Verdú JJ, Beléndez A. *Universidad de Alicante.*

12:00 **Polarimetric techniques for the study and classification of biological samples.** Canabal-Carbia M, Estévez I, Rodríguez C, Van Eeckhout A, Montes-González I, González-Arnay E, Luque J, Garnatje T, Campos J, Lizana A. *Universidad Autónoma de Barcelona.*

12:15 **Propagation of polarized pulsed light through fog: modeling and experiments.** Ballesta-García M, Bobi AR, Royo S. *Universidad Politécnica de Cataluña.*

12:30 **Development of an UV polarimetric characterization set-up for the ESA's Aeolus2 mission beam expander pre-development.** Marzoa A, Lizana A, Estévez I, Campos J, Miravet C, Soto I. *Universidad Autónoma de Barcelona.*

12:45 **Holographic sensors for water detection in organic solvent mixtures.** García-Vázquez JC, Ramírez MG, Nieto-Rodríguez B, Lloret T, Ortuño M, Pascual I. *Universidad de Alicante.*

13:00 **Multiplexing-based holographic concentrators for solar applications.** Lloret T, Morales-Vidal M, García-Vázquez JC, Nieto-Rodríguez B, Pascual I. *Universidad de Alicante.*

13:15 **Computational imaging through object sampling with Talbot effect.** Ipus E, Lenz AJM, Martínez-León L, Lancis J, Tajahuerce E. *Universidad Jaime I.*

Nanofotónica (miércoles 3 de julio, sesión de mañana)

Moderadora: Sara Núñez-Sánchez (Universidades do Minho e do Porto)

11:30 **Perfect absorption with spectrally overlapped electric and magnetic lattice resonances.** Cerdán L, Deop-Ruano JR, Álvarez-Serrano JJ, Manjavacas A. *Consejo Superior de Investigaciones Científicas.*

11:45 **Normal incidence excitation of out-of-plane lattice resonances.** Álvarez-Serrano JJ, Deop-Ruano JR, Aglieri V, Toma A, Manjavacas A. *Consejo Superior de Investigaciones Científicas.*

12:00 **Recent activity of the Optics Group (U. Cantabria) in nanophotonics and related areas.** Saiz JM, Moreno F, González F, Ortiz D, Albella P, Franco A, Gutiérrez Y, Santos G, González-Colsa J, Rosales S, Serrera G. *Universidad de Cantabria.*

12:15 **Superchiral light emerging from quasi-bound states in the continuum in Si nanorod dimer metasurfaces.** Castillo B, Pura JL, Liang M, García-Martín A, Gómez-Rivas J, Sánchez-Gil JA. *Consejo Superior de Investigaciones Científicas.*

12:30 **Plasmonic nanostructured biosensor for discriminating glioblastoma tumor from normal tissue.** Franco A, Ortiz D, Velásquez C, García-Milán V, Marcos S, Martín-Laez R, Moreno F, Fernández-Luna JL. *Universidad de Cantabria.*

12:45 **Long-range molecular energy transfer mediated by strong coupling to plasmonic topological edge states.** Buendía A, Giannini V, Sánchez-Gil JA, Barnes WL, Rider M. *C Consejo Superior de Investigaciones Científicas.*

13:00 **Optical sensor based on surface-enhanced Raman scattering coupled to plasmon catalysis applied in the detection of pollutants.** Sánchez-Cortés S, Celis F, Fuenzalida F, Miskovsky P, Jurasekova Z. *Consejo Superior de Investigaciones Científicas.*

13:15 **Aplicaciones de las guías curvas acopladas asimétricas en la plataforma de nitruro de silicio.** Chamorro-Posada P. *Universidad de Valladolid.*

Miscelánea (miércoles 3 de julio, sesión de mañana)

Moderadora: Esther Perales (Universidad de Alicante)

11:30 **Principal components analysis on measurements of spectral reflectance and transmittance of glazing systems for different angles of incidence.** Santafé-Gabarda P, Álvarez J, Campos J, Muñoz A, Barbero-Barrera MM, Ferrero A. *Consejo Superior de Investigaciones Científicas.*

11:45 **Measurement of reflectance and transmittance of glazing systems for different incidence angles.** Álvarez J, Santafé-Gabarda P, Campos J, Barbero M, Muñoz A, Ferrero A. *Consejo Superior de Investigaciones Científicas.*

12:00 **Rationalizing the mechanisms behind the stimulated emission processes in CsPbBr₃ nanocrystals films.** Cerdán L, Milanese S, De Giorgi ML, Anni M, Bodnarchuk MI. *C Consejo Superior de Investigaciones Científicas.*

12:15 **Si photodiode reflectance measurements in the ultraviolet.** Gómez R, Kaan C, Bazkir O, Campos J. *Consejo Superior de Investigaciones Científicas.*

12:30 **Reflectancia de materiales de enfriamiento radiante pasivo.** Campos J, Ferrero A, Gómez M, Pérez G, González-Cruz E. *Consejo Superior de Investigaciones Científicas.*

12:45 **Femtosecond laser ablation in 3D-printed biopolymeric scaffolds to increase cell adhesion for bone tissue regeneration purposes.** Radziunas-Salinas Y, Carnero B, Pita-Vilar M, Aboal-Castro L, Díaz-Gómez LA, Flores-Arias MT. *Universidad de Santiago de Compostela.*

13:00 **Multispectral imaging to train deep learning algorithms for the discrimination of skin cancer lesions: a preliminary study.** Rey-Barroso L, Burgos-Fernández FJ, Royo S, Puig S, Malveyh J, Pellacani G, Lihacova I, Bondarenko A, Vilaseca M. *Universidad Politécnica de Cataluña.*

13:15 **Manufacturing protocols for straight micromixers combining stereolithography and pulsed laser ablation.** Carnero B, Radziunas-Salinas Y, Rodiño-Janeiro BK, Varela S, Flores-Arias MT. *Universidad de Santiago de Compostela.*

Miércoles 03/07/2024

16:00 - 17:00

Sesiones Orales Paralelas (tarde 1)

Técnicas de la Imagen: Aula C2/04

Moderadora: Inmaculada Pascual (Universidad de Alicante)

Óptica Cuántica y No Lineal: Aula B2/09

Moderador: Miguel Soriano (Universidad de las Islas Baleares)

Miscelánea: Aula B2/07

Moderadora: María del Mar Sánchez-López (Universidad Miguel Hernández)

Técnicas de la Imagen (miércoles 3 de julio, sesión de tarde 1)

Moderadora: Inmaculada Pascual (*Universidad de Alicante*)

16:00 **Resolution-enhanced single-pixel fluorescence microscopy.** Ordóñez L, Lenz A, Lancis J, Tajahuerce E. *Universidad Jaime I.*

16:15 **Vector beams for super-resolution depletion microscopy.** Tiana-Alsina J, Toledo-García N, Maluenda D, Martínez-Herrero R, Carnicer A, Martín-Badosa E, Montes-Usategui M. *Universidad de Barcelona.*

16:30 **Parallelized laser-scanned super-resolution depletion microscopy.** Toledo-García N, Cambior-Navarro L, Martín-Badosa E, Montes-Usategui M, Tiana-Alsina J. *Universidad de Barcelona.*

16:45 **Scanning laser microscopy with a 2D detector to enhance resolution and signal in two-photon excitation fluorescence.** Fernández EJ, Bueno JM. *Universidad de Murcia.*

Óptica Cuántica y No Lineal (miércoles 3 de julio, sesión de tarde 1)

Moderador: Miguel Soriano (*Universidad de las Islas Baleares*)

16:00 **Photonic quantum reservoir computing: Role of squeezing.** García-Beni J, Giorgi GL, Soriano MC, Zambrini R. *Universidad de las Islas Baleares.*

16:30 **High-root topological insulator in non-Hermitian photonic ring resonators.** Viedma D, Marques AM, Días RG, Ahufinger V. *Universidad Autónoma de Barcelona.*

16:45 **Vortex quantum droplets described by a variational approximation.** Salgueiro JR, Paredes A, Michinel H. *Universidad de Vigo.*

Miscelánea (miércoles 3 de julio, sesión de tarde 1)

Moderadora: María del Mar Sánchez-López (*Universidad Miguel Hernández*)

16:00 **Compact liquid-crystal anisotropic axicon for the generation of Bessel beams with tunable polarization transformation.** Sánchez-López MM, Moreno I, Jankowski T, Bennis N, Spadlo A, Algorri JF. *Universidad Miguel Hernández.*

16:15 **Pantalla LCoS alineada verticalmente y uso de órdenes superiores en una red blazed.** Nájjar G, Martínez FJ, Pérez A, Moya A, Sánchez AR, Gallego S, Márquez A. *Universidad de Alicante.*

16:30 **Estudio de los parámetros críticos para el comportamiento láser de redes de Bragg inscritas en guías de onda activas.** Sanz A, Vallés JA. *Universidad de Zaragoza.*

16:45 **Análisis de la reproducción colorimétrica en dispositivos Apple.** Larrosa A, Perales E, Vázquez C, Espinosa J, Kirchner E, Njo L. *Universidad de Alicante.*

Miércoles 03/07/2024

17:30 - 18:30

Sesiones Orales Paralelas (tarde 2)

Técnicas de la Imagen: Aula C2/04

Moderador: Bastián Carnero Groba (Universidad de Santiago de Compostela)

Óptica Cuántica y No Lineal: Aula B2/09

Moderador: Luis Plaja (Universidad de Salamanca)

Miscelánea: Aula B2/07

Moderador: Pedro Prieto (Universidad de Murcia)

Técnicas de la Imagen (miércoles 3 de julio, sesión de tarde 2)

Moderador: Bastián Carnero Groba (*Universidad de Santiago de Compostela*)

17:30 **2D Image, 3D LiDAR & 4D radar fusion for autonomous driving.** Subirana A. *Universidad Politécnica de Cataluña.*

17:45 **Measurement of global tortuosity of retinal vessels in fundus images.** Ramírez N, Ralló M, Millán MS. *Universidad Politécnica de Cataluña.*

18:00 **Derivas y distorsiones térmicas en cámaras digitales al realizar medidas con precisión subpíxel.** Baralida M, Ferrer B, Mas D. *Universidad de Alicante.*

18:15 **Characterization of key error sources of imaging devices for measuring luminance.** Sáez A, Ferrero A. *Consejo Superior de Investigaciones Científicas.*

Óptica Cuántica y No Lineal (miércoles 3 de julio, sesión de tarde 2)

Moderador: Luis Plaja (*Universidad de Salamanca*)

17:30 **Nonlinear optical propagation in self-defocusing perovskite materials.** Suárez I, Martínez-Pastor JP, Oszajca MF, Lüchinger NA, Graves B, Agouram S, Milián C, Ferrando A. *Universidad de Valencia.*

17:45 **Clean Temporal Pulses from All-Bulk Multipass Cells.** Segundo Staels VW, Conejero Jarque E, San Roman J. *Universidad de Salamanca.*

18:00 **Improving pulse self-compression in photonic crystal fibers using particle swarm optimization algorithm.** Vaquero A, Galán F, San Román J, Rodríguez Frías MD, Conejero-Jarque E, Méndez C. *Centro de Láseres Pulsados.*

18:15 **Towards an all-fiber source of isolated attosecond pulses driven by high-energy sub-cycle waveforms from soliton dynamics.** Fernández Galán M, Serrano J, Conejero Jarque E, Borrego-Varillas R, Lucchini M, Reduzzi M, Nisoli M, Brahms C, Travers JC, Hernández-García C, San Román J. *Universidad de Salamanca.*

Miscelánea (miércoles 3 de julio, sesión de tarde 2)

Moderador: Pedro Prieto (Universidad de Murcia)

17:30 **Exploring the fluid dynamics of a carotid bifurcation model with low-coherence digital in-line sideband holography.** Errea C, Lobera J, José Torcal-Milla FJ. *Universidad de Zaragoza.*

17:45 **Light Structuring Through Few-mode Optical Fibers Using Singular Value Decomposition of the Transmission Matrix.** Cifuentes A, Varga M, Molina-Terriza G. *Consejo Superior de Investigaciones Científicas – Universidad de País Vasco.*

18:00 **Lateral-shearing interferometric microscopy for applications in biology, material sciences and semiconductors.** Terborg RA, Haegele S, Hussain R, Cusini I, Pruneri V. *Instituto de Ciencias Fotónicas.*

18:15 **Nested opto- and mechanical resonators for an all fiber, frequency encoded, mass balance proposal.** Garrigues-Navarro AI, Delgado-Pinar M, Díez A, Andrés MV. *Universidad de Valencia.*

18:30 **Experimental characterization of the Q-factor of whispering-gallery modes in non-uniform fiber resonators.** Julian-Barriel J, Delgado-Pinar M, Díez A, Andrés MV. *Universidad de Valencia.*

Jueves 04/07/2024
Sesiones Orales Paralelas



Jueves 04/07/2024

11:45 - 13:45

Sesiones Orales Paralelas (mañana)

Técnicas de la Imagen: **Aula C2/04**

Moderadora: Olga Conde (Universidad de Cantabria)

Ciencias de la Visión: **Aula C2/06**

Moderadora: Alba Paniagua (Universidad de Murcia)

Óptica Cuántica y No Lineal: **Aula B2/09**

Moderadora: Crina Cojocarú (Universidad Politécnica de Cataluña)

Miscelánea: **Aula B2/07**

Moderador: Francisco J. Burgos (Universidad Politécnica de Cataluña)

Técnicas de la Imagen (jueves 4 de julio, sesión de mañana)

Moderadora: Olga Conde (*Universidad de Cantabria*)

11:45 **Examination of the composition of incubator solutions employed to preserve unslanted transmission holograms within photohydrogels.** Nieto-Rodríguez B, G-Ramírez M, Morales-Vidal M, García-Vázquez JC, Lloret T, Lucio MI, Bañuls MJ, Maquieira A, Pascual I. *Universidad de Alicante*.

12:00 **HSI assessment of radiochromic films for dosimetric evaluation.** Gutiérrez JA, Mieites V, Fabregat R, Astudillo R, Suárez N, Gutiérrez M, Conde OM. *Universidad de Cantabria*.

12:15 **Enhancing Agricultural Sustainability by means of Canopy Characterization based on RGB and Time-of-Flight Imaging.** Rey-Barroso L, Canals E, Biscamps J, García-Ruiz F, Gil E, Díaz-Doutón F. *Universidad Politécnica de Cataluña*.

12:30 **Identificación de mezclas de tintas históricas mediante técnicas de unmixing espectral.** López-Baldomero AB, Valero EM, Martínez-Domingo MA, Reichert AS, López-Montes A. *Universidad de Granada*.

Ciencias de la Visión (jueves 4 de julio, sesión de mañana)

Moderadora: Alba Paniagua (*Universidad de Murcia*)

11:45 **Vision with diffractive ophthalmic optics.** Clavé L, Faria-Ribeiro M, Millán MS. *Universidad Politécnica de Cataluña*.

12:00 **Numerical analysis of intraocular lenses performance in different eye models.** Habib M, Remón L, Torcal-Milla FJ. *Universidad de Zaragoza*.

12:15 **Image quality of an enhanced monofocal intraocular lens with corneal astigmatism.** Cuéllar F, Azor JA, Pérez-Sanz L, Millán MS, Vega F, Garzón N. *Universidad Politécnica de Cataluña*.

12:30 **Preoperative perceptual glare assessment with multifocal intraocular lenses using a binocular visual simulator.** Varea S, Papadogiannis P, Rodríguez-Lopez V, de Castro A, Sawides L, Gamba E, Marcos S, MacRae S, Sisó-Fuertes I, Dorronsoro C. *2 Eyes Vision, SL*.

12:45 **Applications of adjustable astigmatic devices: Stokes lens concept.** Ferrer-Altobás S, Lin AL, Micó V. *Universidad de Valencia*.

13:00 **Exploring changes in the scleral tissue of myopic eyes using second harmonic generation microscopy.** Bueno JM, Martínez-Ojeda R, Fernández EJ, Feldkaemper M. *Universidad de Murcia*.

13:15 **Night vision disturbances: does the chromaticity of visual stimuli play a role?** Castro-Torres JJ, Casares-López M, Ortiz-Peregrina S, Martino F, Gómez-Robledo L, Jiménez JR. *Universidad de Granada*.

13:30 **Aberración cromática en sistemas ópticos con codificado de frentes de onda con fase trébol.** Olvera JM, Acosta E, Arines J. *Universidad de Santiago de Compostela*.

Óptica Cuántica y No Lineal (jueves 4 de julio, sesión de mañana)

Moderadora: Crina Cojocarú (Universidad Politécnica de Cataluña)

11:45 **VEGA laser: facility status and near future capabilities.** Méndez C, García-García E, Olivar M, Hernández-Palmero I, Pisonero JD, Varela O, Galán-Prado F, Zapatero P, Pisonero J, Vaquero A, Hernández-Pérez JM, L Volpe, Cives AM, Gatti G, Apiñániz J, Henares JL, Pérez-Hernández JA, Arana D, Cebriano T, Álvarez JM, Rodríguez-Frías MD. *Centro de Láseres Pulsados.*

12:15 **Medida de pulsos ultracortos vectoriales con *amplitude swing*.** Barbero C, Alonso B, Sola IJ. *Universidad de Salamanca.*

12:30 **Sistema óptico aplicado a la espectroscopía resuelta en tiempo en el rango de femtosegundo y picosegundo.** Guerras M, López-Quintás I, Sola IJ. *Universidad de Salamanca.*

12:45 **IR Image upconversion to second and third harmonic.** Torregrosa AJ, Rico ML, Capmany J. *Universidad Miguel Hernández.*

13:00 **Experimental study of the effects of optical feedback on the spatial and temporal coherence of the radiation emitted by a semiconductor laser.** Duque-Gijón M, Tiana-Alsina J, Masoller C. *Universidad Politécnica de Cataluña.*

13:15 **Diseño de guías de ondas superficiales optimizadas para sensado y extracción de luz en materiales cristalinos fabricadas mediante escritura directa con láser de femtosegundo.** Arroyo V, López-Quintás I, Vázquez de Aldana JR, Bonduelle M, Martín G, Romero C. *Universidad de Salamanca.*

13:30 **Microscopía de generación de segundo armónico en cristales microestructurados con pulsos de femtosegundo: BBO y Nd:YAG.** Sevilla-Sierra N, Rodríguez-Vázquez de Aldana J, Romero C, Mateos X, López-Quintás I. *Universidad de Salamanca.*

Miscelánea (jueves 4 de julio, sesión de mañana)

Moderador: Francisco J. Burgos (*Universidad Politécnica de Cataluña*)

11:45 **Multimodal sensing and perception for autonomous vehicles.** DeMas-Giménez G, García-Gómez P, Bernal E, Subirana A, Riu J, Royo S. *Universidad Politécnica de Cataluña*.

12:00 **The Gradient-Phase Interferometer for Precise Segment Phasing in the Primary Mirror of the ESO Extremely Large Telescope.** Rodrigo N, Santos P, Royo S, Díaz A, Murga G, González M, Vega B, Teixeira A, Márquez JF, Förster A, Schmid SP, Lévêque S, Gitton P, Dimmler M. *Universidad Politécnica de Cataluña*.

12:15 **Quantum communications space systems: INTA contributions.** Álvarez A. *Instituto Nacional de Técnica Aeroespacial*.

12:30 **Multipoint temperature sensing with time-resolved acousto-optic interaction in optical fibers.** Marrou JP, Cascante J, Delgado M, Díez A, Andrés MV. *Universidad de Valencia*.

12:45 **Measurement of optical fiber diameter changes with nanometer resolution based on forward-stimulated Brillouin scattering.** Álvarez-Ocampo C, Delgado-Pinar M, Díez A, Cruz JL, Andrés MV. *Universidad de Valencia*.

13:00 **Characterisation of the double pulse configuration for the PW class laser system VEGA-3 at CLPU.** García-García E, Olivar M, Hernández-Palmero I, Varela O, Galán F, Pisonero JD, Pisonero J, Vaquero A, Hernández-Pérez JM, Lera R, Gatti G, Rodríguez MD, Méndez C. *Centro de Láseres Pulsados*.

Jueves 04/07/2024

16:00 - 17:30

Sesiones Orales Paralelas (tarde)

Ciencias de la Visión: Aula C2/06

Moderadora: Clara Mestre (Universidad Politécnica de Cataluña)

Óptica Cuántica y No Lineal: Aula B2/09

Moderador: Carlos Hernández-García (Universidad de Salamanca)

Divulgación, Enseñanza e Historia: Aula B2/07

Moderador: Justo Arines (Universidad de Santiago de Compostela)

Ciencias de la Visión (jueves 4 de julio, sesión de tarde)

Moderadora: Clara Mestre (*Universidad Politécnica de Cataluña*)

16:00 **Fast defocus oscillations have a mild effect on contrast sensitivity.** Prieto PM, Pourreza-Ghoushchi V, Mompeán J, Artal P. *Universidad de Murcia*.

16:15 **Developing a protocol to objectively measure oculomotor deficits in amblyopia during naturalistic tasks.** Valentino MT, Teruel M, Mestre C, Argiles M, Pérez-Mañá L, Pujol J. *Universidad Politécnica de Cataluña*.

16:30 **Eye tracking cognitive assessment: Exploring neuropsychological tests.** Goset J, Viñuela V, Mestre VC, Rey L, Aldaba M, Vilaseca M. *Universidad Politécnica de Cataluña*.

16:45 **Use of non-psychoactive cannabinoids: effects of cannabidiol (CBD) on vision and driving.** Ortiz-Peregrina S, Martino F, Casares-López M, Granados-Delgado P, Anera RG. *Universidad de Granada*.

17:00 **Investigating the perception of complex natural stimuli in polychromatic conditions using adaptive optics.** Moreno E, Rodríguez-López V, Dotor-Goytia P, Vinas-Pena M. *Universidad Complutense de Madrid*.

17:15 **Optimization of a color difference database by fuzzy logic.** Arranz D, Huertas R, Latorre-Carmona P, Morillas S. *Universidad de Granada*.

Óptica Cuántica y No Lineal (jueves 4 de julio, sesión de tarde)

Moderador: Carlos Hernández García (*Universidad de Salamanca*)

16:00 **Strong field physics in solids from a Wannier perspective.** Silva REF. *Consejo Superior de Investigaciones Científicas*.

16:30 **Generation of extreme-ultraviolet high-topological charge spatiotemporal optical vortices.** Martín-Hernández R, Gui G, Plaja L, Kapteyn HK, Murnane MM, Liao CT, Porras MA, Hernández-García C. *Universidad de Salamanca*.

16:45 **Tailoring gold plasmonic metasurfaces for efficient harmonic generation.** Cojocarú C, Mukhopadhyay S, Vincenti MA, Hallman L, Scalora M, Vilaseca R, Trull J. *Universidad Politécnica de Cataluña*.

17:00 **Macroscopic simulations of high-order harmonic generation assisted by artificial intelligence.** Serrano J, Pablos-Marín JM, Hernández-García C. *Universidad de Salamanca*.

17:15 **Self-interference of Hermite-Gaussian high-order harmonics simulated through machine learning.** Pablos-Marín JM, Schmidt DD, De las Heras A, Westlake N, Serrano J, Lei Y, Kazansky P, Adams D, Durfee C, Hernández-García C. *Universidad de Salamanca*.

Divulgación, Historia y Enseñanza de la Óptica (jueves 4 de julio, sesión de tarde)

Moderador: Justo Arines (Universidad de Santiago de Compostela)

16:00 **Exploring image formation with lenses and pinholes.** Escofet J, Pérez-Cabré E. *Universidad Politécnica de Cataluña.*

16:15 **Una década de Óptica y Fotónica en las aulas: lecciones aprendidas por el Grupo de Ingeniería Fotónica de la UC.** Conde OM, Quintela A, Quintela MA, Madruga FJ, Mieites V, Fernández-Manteca MG, Gómez-Galdós C, Algorri JF, García B, Pérez A, López-Higuera JM. *Universidad de Cantabria.*

16:30 **3D educational model for understanding refractive errors and optometric protocols.** Arines J, Rendo-González S, García-Porta N. *Universidad de Santiago de Compostela.*

16:45 **Photonets UV: What can a student chapter do to spread the knowledge of the optical sciences?** Salvador-Roger R, Pérez-Safont M, Julián-Barriel J, Ferrer-Altabás S, Garrigues-Navarro AI. *Universidad de Valencia.*

17:00 **Tornem als instituts: a peer-to-peer approach to teen women for promoting STEM careers.** Delgado-Pinar M, García-Martínez P, Planelles S, Tòrtola M, Garro N. *Universidad de Valencia.*

4

Viernes 05/07/2024
Sesiones Orales Paralelas



Viernes 05/07/2024

9:30 - 11:00

Sesiones Orales Paralelas (mañana)

Ciencias de la Visión:

Aula C2/06

Moderador: Mikel Aldaba (Universidad Politécnica de Cataluña)

Óptica Cuántica y No Lineal:

Aula B2/09

Moderador: Ramón Vilaseca (Universidad Politécnica de Cataluña)

Divulgación, Enseñanza e Historia:

Aula B2/07

Moderador: José J. Castro-Torres (Universidad de Granada)

Ciencias de la Visión (viernes 5 de julio)

Moderador: Mikel Aldaba (*Universidad Politécnica de Cataluña*)

9:30 **Imaging through opaque human cataracts enabled by optical wavefront shaping.** Rodríguez I, Paniagua-Díaz AM, Yago I, Marín JM, Artal P. *Universidad de Murcia*.

9:45 **Age related changes of the crystalline lens gradient refractive index.** De Castro A, Martínez-Enríquez E, Ruggeri M, Manns F, Marcos S. *Consejo Superior de Investigaciones Científicas*.

10:00 **Temporal variations in defocus virtually paralyze accommodation.** Dotor-Goytia P, Dorronsoro C, Rodríguez-López V. *Consejo Superior de Investigaciones Científicas*.

10:15 **Do best visual acuity and minimum accommodation coincide in subjective refraction? An objective análisis.** Turull-Mallofré A, García-Guerra CE, Pujol J, Aldaba M. *Universidad Politécnica de Cataluña*.

10:30 **A binocular adaptive optics visual simulator with convergence control.** Sager S, Prieto PM, Artal P. *Universidad de Murcia*.

Óptica Cuántica y No Lineal (viernes 5 de julio)

Moderador: Ramón Vilaseca (*Universidad Politécnica de Cataluña*)

9:30 **Sobre la historia de la dispersión de la luz.** Roldán E. *Universidad de Valencia*. [Premio Ramón Corbalán – Modalidad A]

10:00 **Topological spectroscopy: High Harmonic Generation from Graphene irradiated by structured fields.** Plaja L, García-Cabrera A, Boyero-García R, Zurrón-Cifuentes O, Serrano J, San Román J, Hernández-García C. *Universidad de Salamanca*.

10:15 **Experimental approaches to investigate dynamics and optimize performance in femtosecond laser material processing.** García-Lechuga M, Grojo D, Utéza O, Solís J, Siegel J. *Consejo Superior de Investigaciones Científicas*. [Premio Ramón Corbalán – Modalidad B]

10:45 **Intense and isolated polarization-controlled magnetic fields from structured laser beams to drive nonlinear magnetization dynamics.** Martín-Domene S, Sánchez-Tejerina L, Martín-Hernández R, Hernández-García C. *Universidad de Salamanca*.

Divulgación, Historia y Enseñanza de la Óptica (viernes 5 de julio)

Moderador: José J. Castro-Torres (*Universidad de Granada*)

10:00 **Lluminària: An outreach magazine crafted by students for students.** Fernández-Saiz C, Ghadban-Gimeno N, Pérez-Safont M, Rivero S, Lapeña A, Giménez J, Piles R, Garrigues-Navarro AI, Julián-Barriel J, Salvador R, Casteló-Lurbe D, Delgado-Pinar E, Delgado-Pinar M. *Universidad de Valencia*.

10:15 **Fostering and disseminating optics and photonics with hands-on experiments in high schools.** Doval A, Muñoz-Ramos A, Santiago-Alonso A, Carnero B, Feijoo-Piedrafita DA, Romo-Díez I, Varela-Carballo J, Paz-Martín J, Fernández-Rodicio S, Villa-Ortega V, Radziunas-Salinas Y, Flores-Arias MT. *Universidad de Santiago de Compostela*.

10:30 **La fotografía estereoscópica, la estereopsis y el patrimonio histórico-artístico como herramientas para la innovación docente interdisciplinar y la divulgación.** Castro-Torres JJ. *Universidad de Granada*.

10:45 **El Proyecto Óptica recreativa, del cole a casa y el kit de Fresnel.** Sanz M, Gálvez O, Montoya MM, Pancorbo M, Sánchez-Fernández JP, Tajuelo J, Williard A, García-Arcos C, Rodríguez M, Mártir AI. *Universidad Nacional de Educación a Distancia*.

Sesiones Pósters



Jueves 04/07/2024

Sesión de Posters 1 (mañana)

10:45 - 11:45

Hall Central (planta 0)

Nanofotónica: P1-P6

Técnicas de la Imagen: P7-P26

Miscelánea: P54-P60

Nanofotónica

P1 **Size and temperature characterization of levitating particles.** Martínez Maestro L, Tomás Echavarría JI, Antón-Revilla M, van Oosten D, Weigand R, Hernandez-Rueda J. *Universidad Complutense de Madrid.*

P2 **Bio-inspired nanophotonics: new strategies to confine, transport and harvest light with organic matter.** Núñez-Sánchez S. Universidade do Minho.

P3 **Fabricación y caracterización de celdas de cristal líquido basadas en fotoalineado de colorantes azo.** Adrián Moya A, Calzado EM, Mena EJ, Navarro-Fuster V, Ortuño M, Márquez A, Beléndez A. *Universidad de Alicante.*

P4 **Brewster quasi-bound states in the continuum in silicon nanodisk metasurfaces.** Hidalgo Arteaga L, Sánchez Gil JA. *CSIC.*

P5 **Metasurface design algorithm for near-field polarization control.** Soria-García A, Andres-Porras J, Sanchez-Brea LM, del Hoyo J, Pastor-Villarrubia V, Elshorbagy MH, Alda J. *Universidad Complutense de Madrid.*

P6 **Moderate-refractive-index nanoantennas for QD fluorescence enhancement.** Ramos Uña R, García Cámara B, Barreda Gómez AI. *Universidad Carlos III.*

Técnicas de la Imagen

P7 **Sub-nanometric stitching metrology for ALBA synchrotron X-ray mirrors.** Van Eeckhout A, Sics I, Heinis D, Nicolas J. *CELLS-ALBA.*

P8 **Analysis of the propagation features of a new type of finite energy Airy plasmon polariton.** Pando M, Martínez-Herrero R, Hernández-Rueda J. *Universidad Complutense de Madrid.*

P9 **Determinación de la aberración de fase con aprendizaje profundo.** Flores VH, Estrada JC, Soria-García A, Sánchez-Brea LM, del Hoyo J, Vargas J. *Universidad Complutense de Madrid.*

P10 **Haces no uniforme y totalmente polarizados invariantes en propagación para polarimetría Mueller.** de Sande JCG, Suárez-Bermejo JC, Santarsiero M, Piquero G. *Universidad Politécnica de Madrid.*

P11 **Towards optimized volume holograms for augmented and virtual reality near-eye displays.** Cobos A, Treptow D, Díaz-Doutón F. *Universidad Politécnica de Cataluña.*

P12 **Automatic characterization of morphological structures and their orientation in biomedical images.** Ayala A, Orenes-Miñana G, Standret I, Bueno JM, Fernández EJ. *Universidad de Murcia.*

P13 Topographical characterization of an intraocular lens. A preliminary study based on in-line digital holography. Vila-Andrés R, Martínez-Espert A, Esteve-Taboada JJ, Micó V. *Universidad de Valencia*.

P14 Puesta a punto de un sistema para holografía pulsante en régimen lineal. Mena EJ, Sirvent-Verdú JJ, Sánchez-Montes AR, Nájjar G, Álvarez ML, Gallego S, Márquez A. *Universidad de Alicante*.

P15 Generación de vórtices ópticos en infrarrojo mediante elementos ópticos holográficos. Paredes A, Marín Sáez J, Collados V, Atencia J. *Universidad de Zaragoza*.

P16 Propiedades cromáticas de las lentes sectoriales. Fernández-Núñez S, Gómez-Pedrero JA, Sánchez-Brea LM, Torcal-Milla FJ. *Universidad Complutense de Madrid*.

P17 Developing holographic couplers for see-through application without prisms. Sirvent-Verdú JJ, Bravo JC, Colomina-Martínez J, Mena EJ, Neipp C, Gallego S, Beléndez A. *Universidad de Alicante*.

P18 Calibration of a focus tunable lens under the effect of gravity. Pérez Cabré E, Cuéllar F, Clavé L, Millán MS. *Universidad Politécnica de Cataluña*.

P19 Spatio-temporal characterization of ultrashort light pulses by structured compressed sampling with a single-pixel detector. Ordóñez-Pérez M, Clemente-Pesudo PJ, Ipus E, Mínguez-Vega G, Tajahuerce E. *Universidad Jaime I*.

P20 30 años de Óptica Espacial en el INTA: Una historia de éxito. Belenguer Dávila T, Álvarez Herrero A, González Fernández LM. *Instituto Nacional de Técnica Aeroespacial (INTA)*.

P21 Análisis numérico de lentes difractivas cilíndricas basadas en series de Fourier. Soria-García A, Torcal-Milla FJ, Andrés-Porras J, del Hoyo J, Gómez-Pedrero JA, Sánchez-Brea LM. *Universidad Complutense de Madrid*.

P22 Py_pol + Diffractio: herramienta numérica para el estudio vectorial de la propagación de la luz. Del Hoyo J, Sanchez-Brea LM, Soria-García A, Andrés-Porras J, Elshorbagy MH, Pastor-Villarrubia V, Alda J, Torcal-Milla FJ. *Universidad Complutense de Madrid*.

P23 Reconstruction-less autofocus for single-pixel microscopy. Zapata-Valencia SI, Tobon-Maya H, Willstatter L, Bonora S, Farina A, Lancis J, Tajahuerce E. *Universidad Jaime I*.

P24 Photon statistics and coherence properties of light sources for random illumination microscopy. Pelegrín S, Carrasco J, Bueno JM, Fernández EJ. *Universidad de Murcia*.

P25 Measuring polarization distributions for three wavelengths simultaneously with a color polarimetric camera. Altaweel M, Estévez I, Montes I, Lizana A, Campos J. *Universidad Autónoma de Barcelona*.

P26 **Optical quality check in afocal systems: from the workshop to the clinic.** Urizar MP, Guerrero G, Martín L, Sisó-Fuertes I, Gamba E, Dorronsoro C. *2EyesVision*.

Miscelánea

P54 **Caracterización termo-óptica de materiales urbanos para fachadas, cubiertas y pavimentos.** Herrera L, Pérez G, Rodríguez Marín M, Montero I, Martínez A, Martín-Consuegra F, Alonso C, Frutos B. *CSIC*.

P55 **Polarization based Monte-Carlo simulation for correlating inherent nanoparticles features with its depolarizing response.** Mao y, Van Eeckhout A, Estévez I, Campos J, Lizana A. *Universidad Autónoma de Barcelona*.

P56 **Combination of the indices of polarimetric purity and the polarizance-reflection-transformation observables for modelling depolarizing responses of samples.** Li D, Montes I, Canabal M, Estévez I, Campos J, Lizana A. *Universidad Autónoma de Barcelona*.

P57 **Introduction to meteor spectroscopy within the UMA/SMA Fireball and Meteor Detection Network.** Lozano Fernández AM, Peris Baixauli V, Castellón Serrano A, López-Ramírez MR. *Universidad de Valencia*.

P58 **Efecto de la tonalidad de los pigmentos de absorción en la percepción del graininess.** Perales E, Tejedor-Sierra N, Larrosa A, Espinosa J, Pérez J, Ferrero A. *Universidad de Alicante*.

P59 **Single-step calibration of liquid crystal spatial light modulators with Fresnel zone plates.** Ordóñez L, Ipus E, Mendoza-Yero O. *Universidad Jaime I*.

P60 **SENER Aeroespacial, S.A. Optics and Optomechanical projects.** Marzoa A, Miravet C, Mujica J, Taubman G, Tomàs A, Grañena F, Casamor O, Soto I. *SENER*.

Jueves 04/07/2024
Sesión de Posters 2 (tarde)
17:30 - 18:30

Hall Central (planta 0)

Divulgación, Enseñanza e Historia: P27-P30

Óptica Cuántica y No Lineal: P31-P37

Ciencias de la Visión: P38-P53

Miscelánea: P61-P68

Divulgación, Enseñanza e Historia de la Óptica

P27 **Herramientas de inteligencia artificial generativa aplicadas a la docencia en Fotónica.** Piquero G, Martínez-Matos O, Hernández-Rueda J, Martínez-Maestro L. *Universidad Complutense de Madrid.*

P28 **Prácticas de Óptica Física expuestas en Reels.** Espinosa J, Vázquez C, Mas D, Larrosa A, Chorro E, Perales E, Pérez J, Hernández C, Domenech B, Tejedor N. *Universidad de Alicante.*

P29 **Actividades de divulgación científica del Grupo de Investigación de Óptica de Castellón (GROC-UJI).** Cortés F, Fernández S, Ipus E, Lenz A, Ordoñez L, Ordoñez M, Tobón H, Zapata S, Doñate C, Durán V, Torrent D, Mendoza O, Martínez L, Mínguez G, Tajahuerce E, Lancis J, Climent V. *Universidad Jaime I.*

P30 **Galileo and Saturn's rings in the lab: an experience for undergraduates and Master's students.** Marzoa A, Santiago Vallmitjana. *SENER.*

Óptica Cuántica y No Lineal

P31 **Topological modes in planar structures containing halide perovskites semiconductors.** Da Silva H, Suarez I, Martínez-Pastor JP, Ferrando A. *Universidad de Valencia.*

P32 **Finite element 3D modeling of photonic open microcavities with 2D perovskites.** De María-García S, Sanchis L, Gorji S, Smith WL, Ferrando A, García-March MA, Muñoz-Matutano G. *Universidad Politécnica de Valencia.*

P33 **Abrupt transition to coherent emission in a semiconductor laser with optical feedback.** Duque-Gijón M, Masoller C, Tiana-Alsina J. *Universidad Politécnica de Cataluña.*

P34 **Fabricación de dispositivos fotónicos funcionales mediante escritura directa con láseres de femtosegundo.** Romero C, Arroyo V, Sevilla-Sierra N, López-Quintas I, Vázquez de Aldana JR. *Universidad de Salamanca.*

P35 **PW-class laser spatio-temporal characterization.** Barbero C, García-García E, Méndez C, Rodríguez-Frías MD, López-Ripa M, Sola IJ, Alonso B. *Universidad de Salamanca.*

P36 **Conversión de imágenes del infrarrojo medio en un cristal de CPLN.** Maestre H, Cuenca M, Ortega AE, Torregrosa AJ, Capmany J. *Universidad Miguel Hernández.*

P37 **High efficiency upconversion of IR eye-safe images.** Capmany J, Torregrosa AJ, Hachair X. *Universidad Miguel Hernández.*

Ciencias de la Visión

P38 **Experimental study of just noticeable gaussian noise differences in synthetic flat image patches of different luminance.** Calvo LM, Latorre-Carmona P, Huertas R, Morillas S. *Universidad Politécnica de Valencia.*

P39 **Do alcohol consumption and the presence of interocular differences affect driving performance?** Martino F, Castro-Torres JJ, Casares-López M, Granados-Delgado P, Jiménez del Barco L, Anera RG. *Universidad de Granada.*

P40 **Frequency analysis of interocular corneal astigmatism symmetry in a large sample.** Salvador-Roger R, Albarrán-Diego C, Garzón N, García-Montero N, Muñoz G, Micó V, Esteve-Taboada JJ. *Universidad de Valencia.*

P41 **Objective assessment of fusional vergence amplitude: Feasibility and impact of vision therapy.** Rovira-Gay C, Mestre C, Argiles M, Pérez-Mañá L, Pujol J. *Universidad Politécnica de Cataluña.*

P42 **Smartglasses for see-through visual correction using economical spatial light modulators.** Vázquez V, Paniagua-Díaz AM, Artal P. *Universidad de Murcia.*

P43 **Diseño multi-tórico para corregir el astigmatismo ocular regular con mayor tolerancia a la rotación.** Gargallo D, Martínez-Espert A, Perches S, Collados V, Remón L, Ares J. *Universidad de Zaragoza.*

P44 **Análisis comparativo de la medición de la curvatura corneal entre diferentes instrumentos.** Perales E, Lajarín E, Larrosa A, Espinosa J. *Universidad de Alicante.*

P45 **The influence of disability glare and surround contrast on temporal contrast sensitivity.** Casado P, Collados V, Ávila F, Ares J. *Universidad de Zaragoza.*

P46 **A bibliometric analysis of vision science.** Aldaba M. *Universidad Politécnica de Cataluña.*

P47 **Effect of monocular diffusion or defocus on stereo acuity.** Espinosa E, Farcas IA, Tabernero J, Benito A. *Universidad de Murcia.*

P48 **Digital reading performance in junior students.** Farcas IA, Gil P, Tabernero J, Benito A. *Universidad de Murcia.*

P49 **Análisis de la deformación de lentes de contacto blandas sobre superficies esclero-corneales artificiales.** Gargallo D, Tolón N, Ares J, Macedo-de-Araújo RJ, González-Meijomé JM. *Universidad de Zaragoza.*

P50 **Analysis of the optical performance of intraocular lenses using profilometry.** García C, Miret JJ, Camps VJ, Caballero MT, Gonzalez-Leal JM. *Universidad de Alicante.*

P51 **The influence of visual deterioration induced with Bangerter foils on fine motor skills.** Casares-López M, Granados-Delgado P, Castro-Torres JJ, Anera RG. *Universidad de Granada.*

P52 Accurate estimation of the relative magnification of the retinal images under different corrections. Egea M, Bueno JM, Fernández EJ. *Universidad de Murcia*.

P53 Evaluation of the influence of headrest use and Plusoptix photorefractor holding setup on its precision. Arines J, Rendo-González S, García-Porta N. *Universidad de Santiago de Compostela*.

Miscelánea

P61 Single-arm interferometer for the calibration of liquid crystal spatial light modulators. Ipus E, Ordoñez L, Mendoza-Yero O. *Universidad Jaime I*.

P62 Set-up of a Hartmann test for the characterization of large-area deformable mirrors. Giménez-Aragón S, Royo S. *Universidad Politécnica de Cataluña*.

P63 Portable multispectral imaging for eye fundus evaluation. Bou M, Vilaseca M, Burgos FJ. *Universidad Politécnica de Cataluña*.

P64 SEDOPTICA-MOF: programas para visibilizar a las investigadoras. Tomás MB, Pérez-Herrera RA, Gómez-Varela AI, Santamaria Fernández B, de las Heras A, Granados-Delgado P, Garrigues-Navarro AI, Delgado-Pinar M, González-Fernández V. *Universidad de Alicante*.

P65 Design and construction of an underwater LiDAR system for multimodal imaging. Bobi Olmo AR. *Universidad Politécnica de Cataluña*.

P66 Raman study of different species of lichens after space and Mars like conditions. López-Ramírez MR, Martínez-Frías J, García-Sancho L, Baqué M, de Vera JP, de la Torre Noetzel R. *Universidad de Málaga*.

P67 Theoretical and experimental analyses of a radially polarized beam: Further implications on uniaxial retarder characterization. Contreras M, del Barco O, Bueno JM. *Universidad de Murcia*.

P68 Stimulated teleportation of high-dimensional spatial states with a nonlinear spatial detector. Vallés A, Sephton B, Nape I, Cox MA, Steinlechner F, Konrad T, Torres JP, Roux FS, Forbes A. *Instituto de Ciencias Fotónicas*.

RESÚMENES/ABSTRACTS

Sesiones Orales

Técnicas de la Imagen



Liquid crystals Mueller matrix imaging polarimeters tolerances to experimental errors.

Ivan Montes-Gonzalez, Irene Estévez, Monica Canabal-Carbia, Angel Lizana, Juan Campos

Grup d'Òptica, Physics Department, Universitat Autònoma de Barcelona, Bellaterra, Spain

*E-mail: ivan.montes@uab.cat

1. Introduction.

Polarimeters based on liquid crystal variable retarders (LCVRs) are widely used, because of the variable retardance of these devices, allowing manipulation of the polarization state of a light beam. This can be achieved by applying a low voltage, with the benefit of eliminating the errors caused by moving parts. However, due to the nature of the liquid crystals, a well-known problem in these types of devices is that they have spatial variations in the induced retardance. Another problem is the fast axis dependance on the applied voltage, if these errors are not considered, they will lead to polarimetric measurements different from the ideal [1].

To estimate the real parameters of the components of a polarimeter, an accurate calibration procedure is necessary. However, regardless of the calibration, even if we can accurately estimate the parameters of the polarimeter, the errors can lead to a larger noise amplification in the final measurements. An optimization is normally used to minimize the noise amplification from the irradiance measurements to the polarimetric information, in this work we used the Condition Number (CN), as optimization metric [2]. However, systematic errors due to nonideal elements or orientation errors, are not considered in the optimization process. Considering these facts, in this work we analyze the tolerance of a Mueller matrix imaging polarimeter to the principal errors on LCVRs, in order to improve their performance and accuracy.

2. Numerical analysis

Before experimentally implementing the polarimeter, we performed a numerical analysis of the complete Mueller imaging polarimeter considering the use of LCVRs, in the polarization state generator and analyzer. To analyze the tolerance of the optimization of the polarimeter to these errors, we numerically simulated 100,000 cases of an optimized Mueller matrix polarimeter, including variations of $\pm 3^\circ$ in the fast-axis position and variations of $\pm 6^\circ$ in the induced retardances of the LCVRs. Then we calculated the CN, for each one of the simulated cases of the Polarization State Generator, CN(G), and Polarization State Analyzer, CN(A). The results of the obtained values are shown as histograms in Fig. 1.

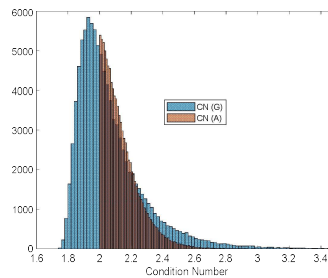


Figure 1 Histogram of the condition numbers obtained during the simulations.

3. Calibration and experimental results

The calibration method used in this paper is based on the widely known Eigenvalue Calibration Method (ECM) proposed by Compain et. al. [3]. The calibration was implemented, measuring the irradiance obtained for a set of calibration samples. With these measured irradiances and following the procedure in [3], we obtained the experimental generated and analyzed polarization states, of the Mueller polarimeter. Using the estimated parameters, we can calculate the 16 elements of the Mueller matrix of a sample. In order to test the performance of the imaging polarimeter we measure the Mueller matrix of air, a linear

polarizer at two different angles and a quarter wave plane oriented at 0° . The Mueller matrix images obtained are shown in Fig. 3, each parameter was normalized by dividing it by the total irradiance in each pixel. In this figure the axes represent the pixels of the image, thus the Mueller matrix elements are shown in groups of 128×128 pixels.

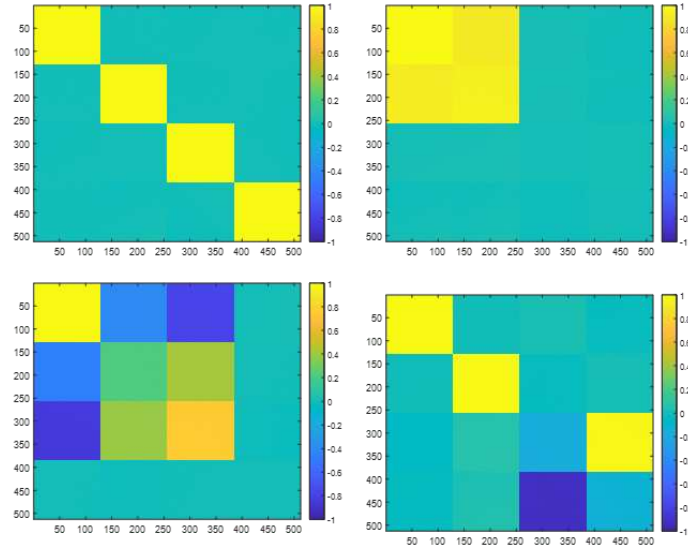


Fig. 2. Mueller images of air (Top left), an horizontal linear polarizer (Top right), a linear polarizer oriented at 120° (Bottom left), and a quarter wave plate oriented at 0° (Bottom right).

4. Conclusions

In this work we showed the tolerances of a Mueller imaging polarimeter to instrumental errors in LCVRs. The results of the numerical simulations showed the tolerance of the optimizations with maximum probabilities of obtaining CNs around 2 for the polarization state generator and analyzer and 99% of the cases have CN values below 2.90. To compensate the retardance and axis position errors, we have used and verified the performance of the ECM. The results show that this method can help to retrieve the complete Mueller matrix of a sample with errors below 5% from the expected values.

References

- [1] I. Montes-González, O. G. Rodríguez-Herrera, M. Avendaño-alejo, and N. C. Bruce, "Effects of typical liquid-crystal retarder errors on optimized Stokes polarimeters," *Appl. Opt.* 61, 10458-10464 (2022)
- [2] J. S. Tyo, "Noise equalization in Stokes parameter images obtained by use of variable-retardance polarimeters," *Opt. Lett.* 25, 1198-1200 (2000) Onestone and P. W. Giggs, "Optical properties of the Giggs photon", *Phys. Rev.* 6, 430-439 (1905).
- [3] E. Compain, S. Poirier, and B. Drevillon, "General and self-consistent method for the calibration of polarization modulators, polarimeters, and Mueller-matrix ellipsometers," *Appl. Opt.* 38, 3490-3502 (1999)

Polarization approach on the characterization and optimization of LCoS devices

Adriana R. Sánchez-Montes^{1,*}, Jorge Francés^{1,2}, Andrés Márquez^{1,2}, Guillem Nájjar^{1,2}, Adrián Moya¹, Joan Josep Sirvent-Verdú¹, Augusto Beléndez^{1,2}

¹*I. U. Física Aplicada a las Ciencias y las Tecnologías, Universidad de Alicante, España.*

²*Dept. de Física, Ing. de Sistemas y Teoría de la Señal, Universidad de Alicante, España.*

*E-mail: adrianaros.sanchez@gcloud.ua.es

1. Theory

Parallel-Aligned Liquid Crystal on Silicon Spatial Light Modulators (PALCoS-SLM) play a vital role in controlling light properties like amplitude, phase, and polarization, finding applications in optical processing, adaptive optics, holographic data, and more.[1] These devices face challenges due to their inherent pixel grid pattern, leading to phenomena such as electric field, crosstalk and diffraction effects. This study explores the impact of voltage signal levels and grey level addressing on retardance modulation across the visible spectrum, aiming to determine optimal voltage parameters for specific wavefront and polarization requirements. We employed the Stokes polarimetry technique[2], consisting of illuminating a circularly polarized unexpanded beam of a supercontinuum laser (SuperK COMPACT, NKT Photonics) onto a commercial SLM display (PLUTO, HOLOEYE), treated for practical purposes as a linear retarder with $8\mu\text{m}$ pixel size. Retardance, flicker, and director orientation were derived from the Stokes parameters using the following equations:

$$\text{sinc}(a) = \frac{\sqrt{S_1^2 + S_2^2 + S_3^2}}{S_0}, \quad \tan(\Gamma) = \frac{\sqrt{S_1^2 + S_2^2}}{S_3}, \quad \text{and} \quad \tan(2\theta) = \frac{S_1}{S_2}, \quad (1)$$

where S_0 , S_1 , S_2 , and S_3 represent the Stokes parameters of the output beam, Γ represents retardance, and θ represents the director angle. Retardance calculations involved inverse trigonometric functions and were constrained to representation, ranging between $\pm 180^\circ$. Values outside this range were evaluated using the unwrapping method outlined in reference [3]. It is important to mention that Eq. (1) is true when the output state of polarization (SOP) corresponds to a right-handed circular (RHC) beam. Figure 1 represents the director orientation depending on the retardance for two wavelengths $\lambda_G = 532\text{nm}$ and $\lambda_R = 633\text{nm}$.

Additionally, we estimated the orientation vector by minimizing the total free energy, incorporating contributions from the Frank-Oseen free-energy density and interaction with the electric field within the liquid crystal (LC):

$$f = \frac{1}{2}K_1(\nabla \cdot \mathbf{n})^2 + \frac{1}{2}K_2(\mathbf{n} \cdot \nabla \times \mathbf{n})^2 + \frac{1}{2}K_3(\mathbf{n} \times \nabla \times \mathbf{n})^2 - \frac{1}{2}\epsilon E \cdot E, \quad (2)$$

here K_1 , K_2 , and K_3 represent the splay, twist, and bend elastic constants. E stands for the electric field inside the LC, and ϵ denotes the dielectric tensor of the LC material. Once the optimal distribution of the LC director is determined, the electrical permittivity ϵ at optical wavelengths is computed and is supplied to the three-dimensional Finite-Difference Time-Domain (FDTD) engine [4] for calculating diffracted light and, consequently, the Stokes parameters as we can see in Figure 2, where the S_0 parameter is shown for the wavelengths we mentioned above λ_G and λ_R .

2. Conclusions

By the development of the methodology detailed in this work, we obtain exciting results such as the average retardance and director orientation depending on the applied voltage and wavelength, as well as the Stokes parameters involved, in order to understand more how the PALCoS works and the behaviour we can expect when designing and using these devices.

3. Figures

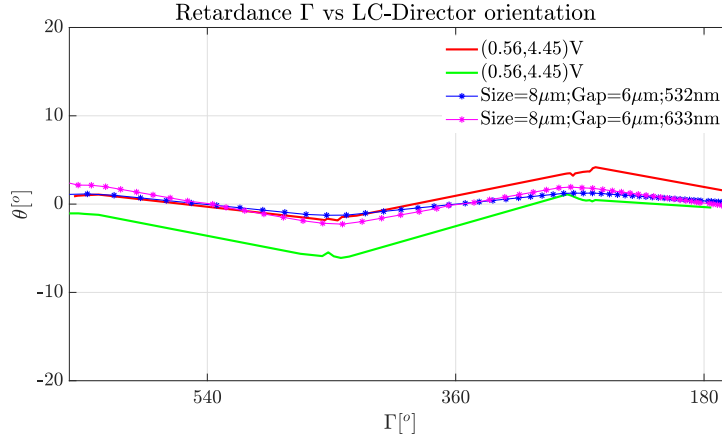


Figure 1: Interpolation for the director orientation for an $8\mu\text{m}$ pixel size. Green line refers to values obtained at $\lambda_G = 532\text{nm}$ while the red line corresponds to the ones at $\lambda_R = 633\text{nm}$, both of them at the binary voltage configurations for PA-LCoS backplane $(0.56, 4.45)$ V. Blue and magenta lines represents the interpolation for the simulation for λ_G and λ_R respectively.

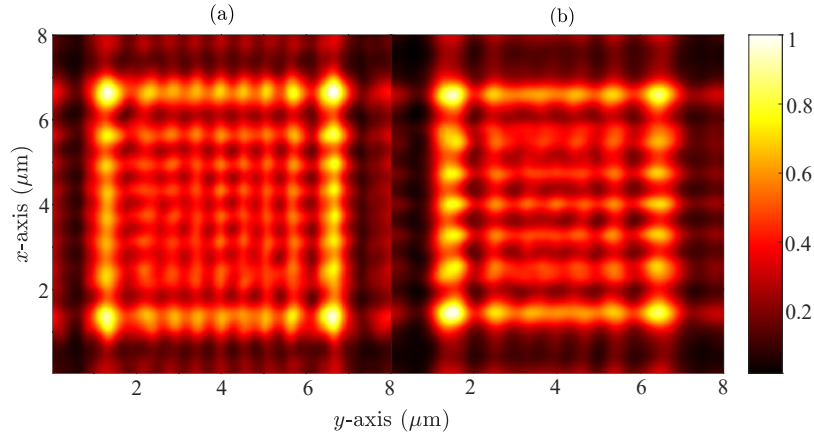


Figure 2: Spatial distribution of the S_0 of the Stokes parameters. Depicted in a plane parallel to the pixel plane, perpendicular to the direction of light propagation (the z -axis), at a distance of $1.5(\lambda)$ from the PA-LCoS device in reflection. (a) λ_G . (b) λ_R

Acknowledgments

The work was funded by the “Generalitat Valenciana” (Spain) (PROMETEO/2021/006), “Ministerio de Ciencia, Innovación y Universidades/AEI” (Spain) (PID2021-123124OB-I00 cofunded by “ERDF/EU”). ARS-M thanks the “Generalitat Valenciana” for the grant GRISOLIAP/2021/106 and JJS-V thanks “Ministerio de Ciencia, Innovación y Universidades/AEI” for the grant FPU22/04316.

References

- [1] G. Lazarev *et al.*, *Opt. Express*, 27(11), 16206-16249 (2019).
- [2] A. Márquez *et al.*, *Opt. Lett.* 45(20), 5732-5735 (2020).
- [3] A. Sánchez-Montes *et al.*, *Proc. SPIE*, 12673(12673A), (2023).
- [4] J. Francés *et al.*, *Materials*, 13(17), (2020).

Polarimetric techniques for the study and classification of biological samples

Mónica Canabal-Carbia^{1*}, Irene Estévez¹, Carla Rodríguez², Albert Van Eeckhout³, Ivan Montes-Gonzalez¹, Emilio González-Arnay⁴, Jordi Luque⁵, Teresa Garnatje⁶, Juan Campos¹ and Angel Lizana¹

¹Grup d'Òptica, Dept. de Física, Universitat Autònoma de Barcelona, 08193, Bellaterra, Spain

²Max Planck Institute for the Science of Light, Erlangen, 91058, Germany

³ALBA Synchrotron Light Source, 08290, Cerdanyola del Valles, Spain

⁴Serv. de Anatomia Humana, Dept. de Ciències Mèdiques Bàsiques, Universitat de La Laguna, 38200, Santa Cruz de Tenerife, Spain

⁵Institute of Agrifood Research and Technology (IRTA), 08348 Cabrils, Spain

⁶Botanical Institute of Barcelona (IBB, CSIC-Ajuntament de Barcelona), 08038 Barcelona, Spain

*E-mail: monica.canabal@uab.cat

1. Introduction

Polarimetry is a widely used optical technique that employs polarized light to inspect and characterize samples. This technique is based on the study of light-matter interaction effects in the polarimetric properties of light. When polarized light interacts with a sample, variations in the sample composition can affect to the polarization state of the incident light. These changes are due to variations in the physical properties of samples, some of which may not be detected at naked eye or by other commonly used optical techniques. Thus, polarimetry offers a non-invasive, non-destructive and fast tool to obtain meaningful information of samples, providing an excellent tool for studying biological samples both biomedical and botanic field.

The polarimetric properties of samples can be classified in three main groups: dichroism, birefringence and depolarization. Dichroism gives information of the capacity of a sample to change the polarization state of incident light, birefringence is related to the change in the retardance induced by the sample and depolarization is related to the capability of a sample to depolarize light. It has been demonstrated that the study of the polarimetric response of a sample can not only increase the visibility of different tissues or components due to different response in these channels, but also the unveiling of structures hidden to other common optical techniques. For instance, biological tissues are collagen rich structures and collagen gives a strong birefringent response; also, orientation and density of tissues provide different polarimetric signals. The amount, distribution, orientation and alignment of fibers in samples are important factors underlying the properties of tissues, affecting also the response in dichroism and depolarization. More important, changes in these characteristics are directly related with many diseases both in biomedical and botanic scenarios. In this sense, the study of polarimetric observables has been used for the detection of different types of cancer, the study of the presence and progression of diverse pathologies both for human and plant samples^{1,2}. Moreover, polarimetric observables are also used for developing automatic classification models, allowing to distinguish between different types of tissue or the detection of healthy pathological areas^{2,3}.

In this work, we present different sets of polarimetric observables and the study of their capabilities in the inspection of different biological samples including the visualization enhancement of different regions, identification of pathologies and the automatic classification of different types of tissue both for animal and plant samples.

2. Mathematical background

To characterize the polarimetric properties in the light-matter interaction process we use the Mueller-Stokes formalism, where the polarimetric state of light is described by a 4-element vector named Stokes vector and the polarimetric properties of samples are encoded the Mueller matrix (M), a 16-element real matrix. The characteristics of samples encoded in M are related to dichroism, birefringence and depolarization. To decode this information, it is necessary to further analyze the matrix performing different decompositions allowing us to separate these channels⁴. In this work, we chose the following representative observables:

- **Dichroism:** diattenuation (D) and polarizance (P) parameters can be directly obtained from M . D gives the dependence of the transmitted light as a function of the incident polarization state, whereas P describes the capability of the system to polarize an incident unpolarized state.
- **Birefringence:** to obtain the birefringence parameters we chose two different decompositions, the Lu-Chipman (R, δ, θ) and the Arrow decomposition ($\varphi, \varphi_0, \varphi_0 \chi, R, \varphi_0, \chi_0, R_0$)⁵.
- **Depolarization:** depolarization properties can be described by the Indices of Polarimetric Purity (IPP)

(\mathbf{P}_1 , \mathbf{P}_2 and \mathbf{P}_3), representing different depolarization sources. The IPP are obtained from the covariance matrix $\mathbf{H}(\mathbf{M})$. Also, the Depolarization index (\mathbf{P}_Δ) and the Spherical Purity Index (\mathbf{P}_s), directly obtained from \mathbf{M} , are inspected. \mathbf{P}_Δ describes the overall depolarization capability of a system, and \mathbf{P}_s estimates the contribution to depolarization of non-dichroic features of the samples.

To obtain the experimental Mueller matrix of a sample, we use a complete Mueller matrix image polarimeter². This set up allows to obtain \mathbf{M} images, where each pixel contains the polarimetric information of the correspondent region in the sample. In addition, we can use different wavelengths in the visible range (470 nm, 530 nm, 590 nm and 625 nm) to inspect the sample taking advantage of the different response of the material depending on the penetration depth of light with the wavelength.

3. Experimental results

In this section we analyze the interest of the polarimetric observables derived from the Mueller matrix to inspect different biological samples.

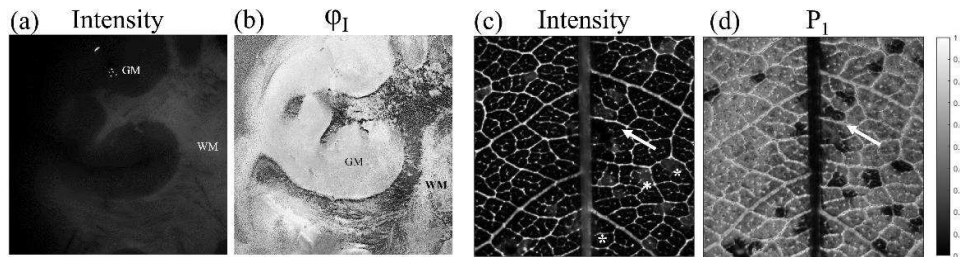


Figure 1 Comparison of intensity (a, c) and polarimetric (b, d) images of the selected samples: *ex-vivo* cow brain (a, b), and pathological *Prunus dulcis* (c, d).

Fig. 1 shows the comparison between intensity (a, c) and polarimetric observables (c, d) images. Figs. (a) and (b) correspond to a coronal section of an *ex-vivo* cow brain, where in the φ_I parameter we can see how the polarimetric observable unveils information inside the white matter (WM) region that was totally hidden in the intensity image. Fig. 1 (c) shows the intensity image of the pathological *Prunus dulcis* sample, where the pathological areas (some of them indicated with the white asterisks) are almost invisible. In the P_I image (d), we demonstrate how the visibility between healthy/pathological tissue is highly increased and some areas affected by the pathologies that not recognized in intensity are.

4. Conclusions

In conclusion, we present polarimetry as an excellent tool to study biological samples. The use of polarimetric methods and analysis lead to a visualization enhancement between different structures inside samples and, even unveil structures hidden to conventional techniques. In particular, we want to highlight the performance of the depolarization related metrics, being especially suitable for the study of highly depolarization materials such as biological samples. This paves the way to applications of polarimetric techniques in the field of biomedicine and botanics.

Acknowledgments

We acknowledge the financial support of Ministerio de Ciencia e Innovación and Fondos FEDER (PID2021-562 126509OB-C21 and PDC2022-133332-C21) and support of Generalitat de Catalunya (2021SGR00138).

References

1. He, C. *et al.* Polarisation optics for biomedical and clinical applications: a review. *Light Sci Appl* **10**, 194 (2021).
2. Rodríguez, C. *et al.* Polarimetric observables for the enhanced visualization of plant diseases. *Sci Rep* **12**, 14743 (2022).
3. Rodríguez, C., *et al.* Optimizing the classification of biological tissues using machine learning models based on polarized data. *J Biophotonics* **16**, (2023).
4. Gil, J. J. & Ossikovski, R. *Polarized Light and the Mueller Matrix Approach*. *Polarized Light and the Mueller Matrix Approach* (2016). doi:10.1201/b19711.
5. Gil, J. J. *et al.* Polarimetric Images of Biological Tissues Based on the Arrow Decomposition of Mueller Matrices. *Photonics* **10**, 669 (2023).

Propagation of polarized pulsed light through fog: modeling and experiments

Maria Ballesta-Garcia^{1*}, Aleix R. Bobi¹, and Santiago Royo^{1,2}

¹*Centre de Desenvolupament de Sensors, Instrumentació i Sistemes, Universitat Politècnica de Catalunya (UPC-CD6), Rambla Sant Nebridi 10, E08222, Terrassa, Spain*

²*Beamagine SL C/Bellesguard 16 E08755 Castellbisbal, Spain*

*E-mail: maria.ballesta.garcia@upc.edu

1. Introduction

Given the unique features of LiDAR imaging systems, their potential for new applications in computer vision, such as autonomous vehicles, outdoor recognition, and surveillance appears very promising. However, there are still uncertainties and challenges in the current technology implementation. One major issue is its performance in adverse weather conditions and scattering media, like fog, where LiDAR's effectiveness is significantly reduced, leading to degraded detection quality [1].

LiDAR operates on a simple principle called time-of-flight (ToF). This method measures the time it takes for light to travel to determine distances. Pulsed ToF is one of the most usual approaches where the time gap between emitting a light pulse and receiving it back after reflecting it on a target allows to calculate the exact distance to the target using the time elapsed between both events. When using a pulsed LiDAR in scattering media (such as fog), the acquired signal reveals not only the target reflection peak at the ToF distance but also the appearance of a fog reflection peak at the beginning of the signal, due to backscattered photons. A significant portion of the energy gets lost within this fog reflection due to light backscattering, occasionally leading to the loss of the target's response. Furthermore, in certain instances, the sensor may become blinded and reach saturation due to the amplitude of the fog reflection peak, hindering the detection of peaks of interest, such as the ones from the target [2].

Based on the successful application of polarimetric properties to improve imaging contrast and depth penetration in tissues, which represent microscopic scattering media, we hypothesized that similar advantages could be achieved in fog conditions, which constitute macroscopic scattering media [3]. However, the diverse range of potential scenarios and applications, coupled with the unpredictable nature of real-world adverse weather conditions, complicates and limits accurate experiments in outdoor environments. Factors such as the properties of the medium (e.g., particle density, distribution, and composition) or the characteristics of the target being observed can significantly influence the outcomes. This underscores the importance of developing algorithms that precisely model the physics of the problem domain, thereby refining the scope of experimental actions. Additionally, the development of controlled experimental setups appears to be the most viable option for exploring this possibility further.

2. Methods

Firstly, we developed a Monte Carlo (MC) model based on the propagation of photon packets through a medium consisting of air and spherical water droplets, with their optical characteristics computed using the Mie Theory [4]. This model facilitates simulation and analysis of various aspects of the system, including assessing different polarization configurations, examining interactions with targets and medium irregularities, considering realistic visibilities based on Koschmieder's law, and predicting acquired signals to aid in electronics design.

For our experiments, we built a small-scale fog chamber filled with artificial fog, providing us control over properties like particle size and transmittance. These setups offer a cost-effective means for validating our models. Subsequently, we employed a simplified version of a polarized LiDAR imaging system, which includes a pulsed 1064 nm fiber laser, an avalanche photodiode (APD) as a detector, and a set of optical components for polarization control. The entire setup is presented in Fig. 1.

3. Results and Conclusions

Some of the obtained results using both methods are shown in the following figures. Fig. 2 corresponds to results for non-polarized light for (a) the model and (b) the experiments. Fig. 3 displays the signals obtained for polarized light for (a) the model and (b) the experiments.



Figure 1 Experimental setup.

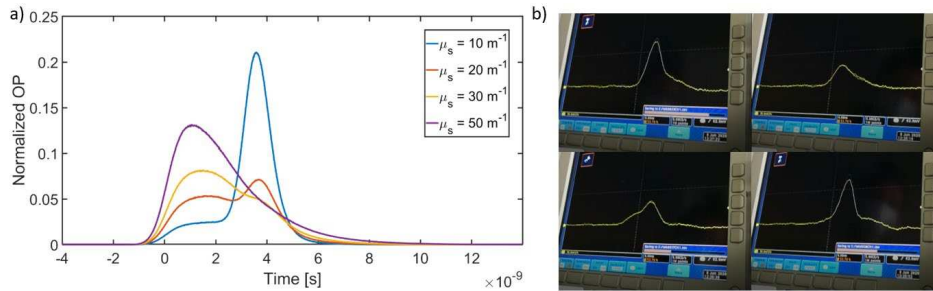


Figure 2 Signal of a non-polarized pulse in the presence of a nearby target, shown for (a) the model and (b) the experiments.

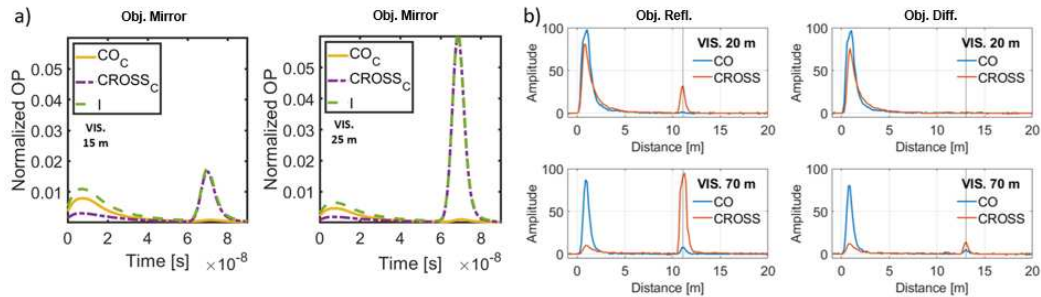


Figure 3 Signal of a circularly polarized pulse in the presence of different targets, shown for (a) the model and (b) the experiments.

Results in Fig. 2 and Fig. 3, which are obtained using similar media characteristics for each pair (a) and (b), demonstrate agreement between them. By utilizing both methods, we showcase the capability of our MC model and experimental setup to simulate the problem of interest, accurately capturing the expected behavior: the appearance of the target reflection and the fog reflection. Additionally, we acquire valuable insights into the signal characteristics, visibility limits, and the behavior of polarization, underscoring its potential advantages in our system.

Acknowledgments

This research was funded by MICINN projects PID2020-119484RB-I00 and TED2021-132338B-I00, and by AGAUR Grant 2021FI_B2 00077, supported by the Secretaria d'Universitats i Recerca de la Generalitat de Catalunya and the Fons Social Europeu (FSE).

References

- [1] S. Royo and M. Ballesta-Garcia. "An overview of lidar imaging systems for autonomous vehicles", *Applied sciences* **9.19**, 4093 (2019).
- [2] M. Kutila, et al. "Automotive LiDAR performance verification in fog and rain", in *21st International Conference on Intelligent Transportation Systems* (2018), 1695–1701.
- [3] M. Ballesta-Garcia, et al. "Analysis of the performance of a polarized LiDAR imager in fog", *Optics express* **30.23**, 41524–41540 (2022).
- [4] J. Ramella-Roman, et al. "Three Monte Carlo programs of polarized light transport into scattering media: part I", *Optics Express* **13.12**, 4420–4438 (2005).

Development of an UV polarimetric characterization set-up for the ESA's Aeolus2 mission beam expander pre-development

Antonio Marzoa^{1,2*}, Angel Lizana³, Irene Estévez³, Juan Campos³, Carlos Miravet⁴ and Isabel Soto⁵

¹*Department of Precision Engineering, SENER Aeroespacial, S.A., C/ Creu Casas i Sicart, 86-87, 08290, Cerdanyola del Vallès, Barcelona, Spain*

²*Department de Física, Universitat Politècnica de Catalunya, C/ d'Esteve Terradas, 7, 088660, Castelldefels, Barcelona, Spain*

³*Department de Física, Universitat Autònoma de Barcelona, Carretera de Bellaterra a la UAB, 08193, Cerdanyola del Vallès, Barcelona, Spain*

⁴*Avionics and Advanced Systems division, SENER Aeroespacial, S.A., C/ de Severo Ochoa, 4, 28760, Tres Cantos, Madrid, Spain*

⁵*Electro-Mechanical Systems Division, SENER Aeroespacial, S.A., Zugatzarte Etorb., 56, 48930, Getxo, Bizkaia, Spain*

*E-mail: antonio.marzoa@aeroespacial.sener

1. Introduction

The European Space Agency (ESA) Earth Explorer mission, Aeolus, was launched into space on August 22nd of 2018 and was retired on April 30th of 2023. This mission had the main goal of recording and monitoring the weather in different parts of the world to provide data that allowed climatic scientists to build complex weather models to help predictions on the environmental behavior in future. To do so, Aeolus used the active Doppler Wind Lidars method, which ensures direct wind profile observations in clear air, but also inside thin and thick clouds, and provides information on vertical distribution of aerosols and clouds. In particular, knowledge derived by Aeolus's observations of Earth's wind fields has led to progress in atmospheric dynamics research and weather forecasting [1].

Aeolus has been reported as one of the most successful ESA's missions so far, and its successor is currently being studied. Aeolus2 mission will continue the work carried out by its ancestor at the same wavelength (355 nm).

SENER Aeroespacial S.A. has won a contract with ESA to design and pre-develop a beam expander for Aeolus2 mission. This contract corresponds to a pre-development of a prototype to analyze the different critical technologies in which the new mission is based.

Some of the requirements of the project are to include very stable mounting of large lenses; low Wave Front Error; optical coatings qualified for high laser energy fluence; and hermetic sealing for a large volume housing to allow pressurisation of the unit and minimise the risk of laser induced contamination. Selected sealing technology should avoid organic materials to minimize contamination issues. In addition, lenses and windows need to be supported by metallic means. This direct contact metal-glass will introduce tensions over the lenses used in the beam expander, which will affect the polarization state through stress-induced birefringence. Since one of the main requirements of the project is to ensure that the output polarization state of the expanded beam is the same as in the input beam, a set-up to characterize the polarization state of the beam is being developed in collaboration with the Optics Group of the Universitat Autònoma de Barcelona (UAB). This contribution describes the development of the set-up at UAB's laboratories and the current state of the project.

2. Theoretical background

The stress induced on the optical surfaces (mainly lenses and windows) by the supports might modify the local refractive index, hence, producing a stress-induced birefringence that will modify the optical path differences (OPD) of the rays when passing through the glass (Figure 1 (a) shows results on a unitary load case simulation of stress-induced birefringence). If the OPD are different to the orthogonal components of the input beam, this will affect the polarization of the output beam, modifying it respect to the entrance polarization state.

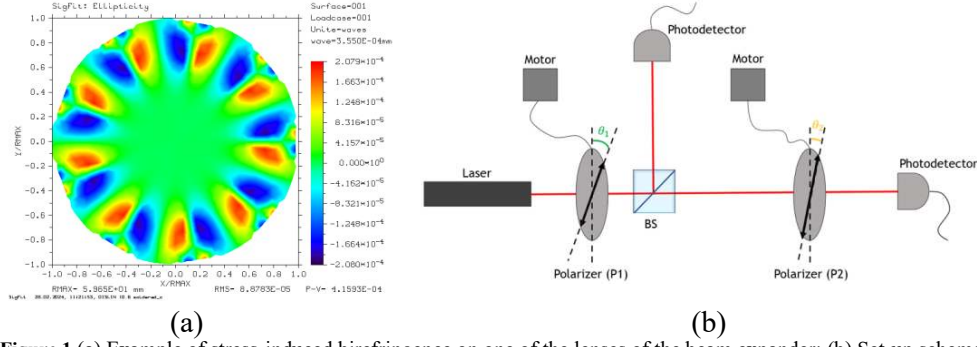


Figure 1 (a) Example of stress-induced birefringence on one of the lenses of the beam expander; (b) Set-up scheme to perform measurements of the polarization state. The beam splitter (BS) enables to monitor the input intensity over time to compensate for possible laser source emission fluctuations. The test sample is placed between polarizers P1 and P2, and the intensity of the output beam is measured. Stokes parameters are derived by adjusting the experimental data to equation (1).

The depolarization ratio, according to ESA's requirement specifications for Aeolus2, is, therefore, defined as the power ratio of the perpendicular polarization (orientated 90° from the incident polarization direction) to the parallel linear polarization (orientated along the incident polarization direction), assuming an incident linear polarization.

An efficient way to perform the measurements required within the project is to use a Malus' law based set-up and adjusting the experimental measurements to a non-ideal polarizer model, which in Stokes formalism may be written as [2]:

$$I_{mi} = \frac{P^2}{2} (S_0 + S_1 \cos(2\gamma) \cos(2\theta) + S_2 \cos(2\gamma) \sin(2\theta)) \quad (1)$$

where S_1 , S_2 , S_3 and S_4 are the four Stokes parameter describing the beam polarization, γ the transmission relation between polarizer axis and θ the rotation angle of the polarizer.

3. Set-up description and preliminary results

A preliminary set-up (see Figure 2(b)), at 633 nm has been developed at UAB's facilities. With such set-up, the accuracy of the method has been tested, providing measurements accuracies of the ellipticity and the Stokes parameters of the output beam for different depolarization cases within the mission requirements.

4. Conclusions

The results obtained at 633 nm provide the information to perform a scaling of the system to 355 nm. With this information we are currently developing the set-up at 355 nm. To map the polarization state over the whole exit pupil of the system, a x-y stage is being designed to place the stressed lens sample that would be used for final characterization.

Acknowledgments

Authors acknowledge their SENER colleagues José Gonzalo Taubmann, Oriol Casamor, Jorge Mujica and Roger Macías for the analysis of the induced birefringence, and Ferran Grañera for fruitful discussions. The authors extend their sincere gratitude to the European Space Agency (ESA) for their invaluable support throughout this research project. UAB team acknowledge the funding received for their laboratory by the Ministerio de Ciencia e Innovación and Fondos FEDER (PID2021-562 126509OB-C21 and PDC2022-133332-C21), Generalitat de Catalunya (2021SGR00138) and Beatriu de Pinós Fellowship (2021-BP-00206).

References

- [1] <https://earth.esa.int/eogateway/missions/aeolus>
- [2] D. H. Goldstein, Polarized Light, *Polarized Light* (CRC Stress, Taylor&Francis Group, 2010).

Holographic sensors for water detection in organic solvent mixtures

José Carlos García-Vázquez^{1,2,*}, Manuel G. Ramírez^{1,2}, Belén Nieto-Rodríguez³, Tomás Lloret López³, Manuel Ortuño^{1,2} and Inmaculada Pascual^{1,3}

¹*I.U. de Física Aplicada a las Ciencias y las Tecnologías, Universidad de Alicante, España*

²*Dept. de Física, Ingeniería de Sistemas y Teorías de la Señal, Universidad de Alicante, España*

³*Dept. de Óptica, Farmacología y Anatomía, Universidad de Alicante, España*

*E-mail: jc.garciavazquez@ua.es

1. Introduction

In recent years, there has been a growing interest in reflection holography, a technique with versatile applications ranging from energy efficiency to sensing various parameters like temperature, humidity, or pressure. This study delves into the evaluation of sensing capabilities for water mixed with other organic solvents utilizing reflection holography [1,2]. Specifically, we employed Biophotopol [3], a water-based photopolymeric material well-known for its high sensitivity to environmental humidity changes, wherein reflection diffraction gratings were incorporated. Our objective revolved around detecting wavelength shifts and alterations in the diffraction efficiency (DE) of these reflection gratings upon immersion in the these mixtures.

To achieve this, we employed different concentrations of water mixed with acetone (C_3H_6O) and tetrahydrofuran (C_4H_8O). These organic solvents were selected due to their low relative polarity (low dielectric constant), thereby mitigating the risk of dissolving Biophotopol components.

2. Methods and results

To perform these experiments, the polymeric sample was completely immersed in the mixtures of organic solvents and water. Table 1 shows the acetone/water and THF/water ratios used.

Acetone (%)	THF (%)	Water (%)
100	100	0
97	97	3
95	95	5
93	93	7
90	90	10

Table 1 Acetone/water and THF/water ratios used for the experiments.

Higher proportions of water have not been used since the reflection gratings disappear from the material in the presence of a higher amount of this component.

Fig. 1 (a) shows the wavelength variation with respect to the time the sample was immersed in THF/water mixtures. In the 100% THF curve a shrinkage of the reflection grating due to the presence of this solvent can be observed. This implies a decrease in the grating period and, therefore, a blue shift in the diffraction wavelength. However, as water begins to be added to the mixture, the evolution of the Bragg wavelength of the diffraction peak changes, redshifting more with respect to its initial value ($\Delta\lambda = 0$). It can be observed that this shift stabilizes over 24 hours of measurements, reaching a maximum wavelength shift value for each mixture. When more than 7% water is added, the wavelength shift occurs abruptly because all Biophotopol components are dissolved in water.

However, this is not an advantage, but a problem. Such a sharp shift means that the water in the mixture is impinging on the interior of the material and erasing the holographic grating structure. This can be seen in

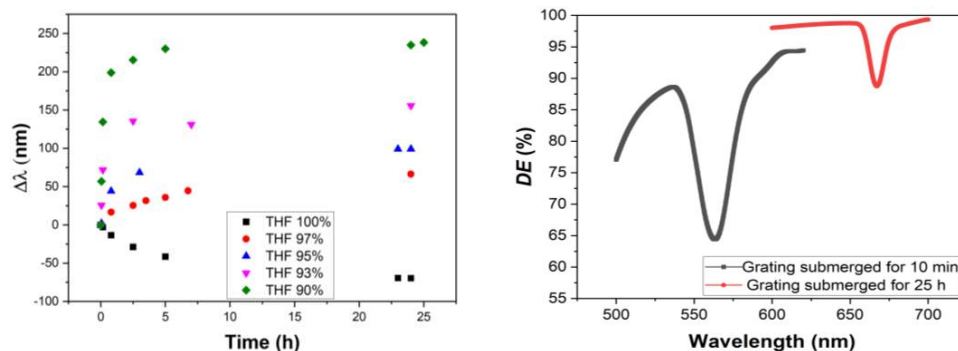


Figure 1. Wavelength shift in THF-water mixtures (a) and decrease in DE in mixtures of 90% THF and 10% water (b).

Fig. 1 (b), which shows the difference in diffraction efficiency of a reflection grating in a 90% THF mixture 10 minutes after the immersion (a) and 25 hours later (b).

With these results, it can be stated that Biophotopol stored reflection gratings are a fast way to determine the presence of very small amounts of water in organic solvent mixtures.

3. Conclusions

These findings unequivocally establish the efficacy of the water sensing method in the presence of organic solvents. The developed system exhibits exceptional sensitivity, capable of detecting substantial variations in diffraction wavelength of reflection gratings in response to small fluctuations in water content. Furthermore, it offers a sample conservation approach, as reflection gratings reach an equilibrium state when submerged in THF and acetone-water mixtures.

Additionally, the ability to obtain the diffraction wavelength of the grating relative to the quantity of water added enables precise control over the optical and physical characteristics of the holograms.

Acknowledgments

This research was funded by MICIU/AEI/10.13039/501100011033 grant PID2019-106601RB-I00; Generalitat Valenciana grants CIDEX/2022/60, IDIFEDER/2021/014, PROMETEO/2021/006; Universidad de Alicante grant UAFPU20-23.

References

- [1] Blyth, J., Millington, R. B., Mayes, A. G., Frears, E. R., & Lowe, C. R. (1996). Holographic Sensor for Water in Solvents. *Analytical Chemistry*, 68(7), 1089-1094. <https://doi.org/10.1021/ac9509115>
- [2] Liu, H., Dai, Y., Mao, D., Geng, Y., & Wang, W. (2016). Modeling swelling and absorption dynamics for holographic sensing in analytes sensitive photopolymer. *Optics Communications*, 368, 95-104. <https://doi.org/10.1016/j.optcom.2016.02.005>
- [3] Ortuño, M., Gallego, S., Neipp, C., Pascual, I., & Beléndez, A. (2012). Biophotopol: A Sustainable Photopolymer for Holographic Data Storage Applications. *Materials*, 5(12), 772-783. <https://doi.org/10.3390/ma5050772>

Multiplexing-based holographic concentrators for solar applications

Tomás Lloret^{1*}, Marta Morales-Vidal^{1,3}, José Carlos García-Vázquez^{2,3}, Belén Nieto-Rodríguez^{1,2}, and Inmaculada Pascual^{1,3}

¹*Departamento de Óptica, Farmacología y Anatomía, Universidad de Alicante, Carretera San Vicente del Raspeig s/n, 03690 San Vicente del Raspeig, Spain*

²*Departamento de Física, Ingeniería de Sistemas y Teoría de la Señal, Universidad de Alicante, Carretera San Vicente del Raspeig s/n, 03690 San Vicente del Raspeig, Spain*

³*Instituto Universitario de Física Aplicada a las Ciencias y las Tecnologías, Universidad de Alicante, Carretera San Vicente del Raspeig s/n, 03690 San Vicente del Raspeig, Spain*

E-mail: tomas.lloret@ua.es

1. Introduction

Nowadays, a significant challenge in advancing photovoltaic technology lies in developing lightweight, cost-effective, and non-tracking systems. Moreover, there is a pressing need to mitigate the impact of harmful wavelengths on photovoltaic cells, particularly those contributing to overheating. Addressing these concerns, volume holographic lenses (HLs) offer a promising solution by selectively controlling solar radiation exposure to photocells, effectively mitigating damage from infrared radiation that tends to heat solar cells without converting solar energy efficiently into electrical energy. Furthermore, holographic solar concentrators leveraging multiplexed HLs offer the additional advantage of eliminating the requirement for solar tracking systems [1]. In this study, we focus on optimizing key fabrication parameters of multiplexed HLs stored in Biophotopol. These parameters encompass material considerations such as optimal dye and monomer concentrations, as well as thickness, alongside optical recording factors including the ideal number of multiplexed HLs, angular separation between peaks, and exposure times [2]. Additionally, we conduct a theoretical investigation into exposure times utilizing the exposure schedule method (ESM) to enhance average diffraction efficiency.

When multiplexing holograms, the primary parameter of interest is the average diffraction efficiency [3]. To compute this, one must initially determine the dynamic range, which quantifies the number of holograms with a diffraction efficiency of 1 (100%) that can be stored within a material of specific thickness. The dynamic range is defined as follows:

$$M\# = \sum_{i=1}^N \eta_i \quad (1)$$

After calculating the dynamic range, which depends on the diffraction efficiency (η) of each hologram and the total number of holograms recorded (N), one can infer the diffraction efficiency at which holograms would be recorded given a certain quantity of stored holograms. To determine the average diffraction efficiency (η_{AVR}), the following mathematical expression is employed:

$$\eta_{AVR} = \left(\frac{M\#}{N} \right)^2 \quad (2)$$

2. Results

The analysis focused on improving the average diffraction efficiency of the HSC based on six multiplexed holographic lenses. The dynamic range was investigated using the ESM to improve and equalize the efficiency and the short-circuit current response of all the multiplexed lenses to optimize their performance as a solar concentrator, as shown in Figure 1.

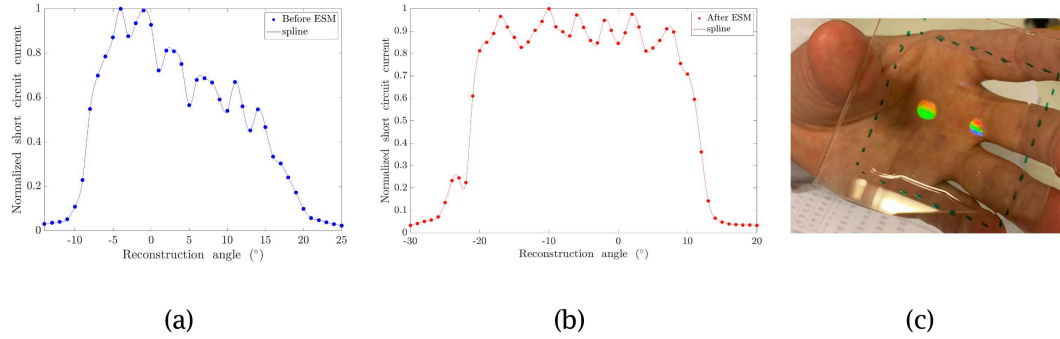


Figure 1 Reconstruction with the solar simulator: (a) Before using ESM, (b) After using ESM, (c) Image of the photopolymer-based holographic concentrator.

3. Conclusions

In this work we have explored ways to improve the performance of existing holographic solar concentrators. Specifically, we have developed a holographic solar concentrator based on six multiplexed holographic lenses recorded in a low-toxicity photopolymer. The goal was to broaden the acceptance angle and improve the diffraction efficiency of existing holographic concentrators. Taking advantage of the ESM, we achieved an average diffraction efficiency of 75% at a reconstruction wavelength of 633 nm. Notably, the acceptance angle, evaluated using a solar simulator, was extended to approximately 40°. Our results verify the usefulness of ESM as an effective tool for optimizing exposure conditions in multiplexed holograms.

Acknowledgments

This research was funded by Universidad de Alicante grant UAFPU20-23; MICIU/AEI/10.13039/501100011033 grant PID2019-106601RB-I00; Generalitat Valenciana grants CIDEX/2022/60, IDIFEDER/2021/014, PROMETEO/2021/006.

References

- [1] E. Alfaro, T. Lloret, J. M. Vilarly, M. Bastidas, M. Morales-Vidal, and I. Pascual, “Photopolymer holographic lenses for solar energy applications: A review,” *Polymers* 16(6) (2024).
- [2] T. Lloret, M. Morales-Vidal, B. Nieto-Rodríguez, J. C. García-Vázquez, A. Beléndez, and I. Pascual, “Building-integrated concentrating photovoltaics based on a low-toxicity photopolymer,” *Journal of Physics: Energy* 6(1), 015017 (2024).
- [3] R. K. Kostuk, *Holography: Principles and Applications* (CRC Press, 2019).

Computational imaging through object sampling with the Talbot effect

Erick Ipus*, Armin J. M. Lenz, Lluís Martínez-León, Jesús Lancis and Enrique Tajahuerce
GROC-UJI, Institute of New Imaging Technologies (INIT), Universitat Jaume I, 12071, Castelló, Spain

*E-mail: ipus@uji.es

1. Introduction

Single-pixel imaging (SPI) techniques are an interesting alternative to conventional imaging methods that do not require the use of pixelated sensors [1]. They work by scanning the scene with a set of structured light patterns encoded by a spatial light modulator (SLM), while the light transmitted or reflected by the objects is detected with a single-pixel photodetector. The SPI approach may be suitable for multidimensional imaging applications, in situations where the amount of light is scarce, or when a high temporal resolution is required [2]. In addition, these imaging techniques are tolerant to light scattering between the object and the sensor. However, the measurement process tends to be slow due to the sequential nature of the acquisition, which is severely limited by the switching rate of the SLM. Several optical setups have been proposed to overcome this limitation by using multiple pixels of a 2D sensor array and implementing the single-pixel imaging technique in parallel [3-5], thus reducing the measurement time. In general, images of the coded masks generated by the SLM are projected onto the sensor array in such a way that multiple coded elements are mapped onto individual pixels of the array.

In this work we propose to use the Talbot effect to perform parallel computational imaging by sampling the object with periodic patterns generated by the Talbot effect. The Talbot effect, also known as self-imaging phenomenon, is observed when a grating is illuminated by a coherent light beam [6]. Under parallel illumination, copies of the grating appear periodically at distances multiple of the Talbot distance. This phenomenon has been widely described and applied to many different fields such as holography, microscopy, wavefront sensing, or lithography [7]. In our approach, we use an SLM to codify a set of 2D binary gratings where each unit cell is a function of the Walsh-Hadamard basis. A sequence of self-images is then projected onto the object, which is located at the Talbot distance. Selected pixels of a 2D sensor array collect the light projected by each unit cell. The image is reconstructed by applying single-pixel imaging reconstruction algorithms in parallel. In this way, we can obtain higher spatial resolution than that provided by a conventional sensor array and shorter measurement times than those permitted by a pure single-pixel camera.

2. Experimental setup

The concept is shown schematically in Fig. 1. The SLM codifies a set of periodic distributions of Walsh-Hadamard patterns. The object is scanned by the sequence of self-images generated at the Talbot distance, Z_t . Light is recorded by selected pixels of the sensor array. The image is reconstructed computationally by using proper algorithms.

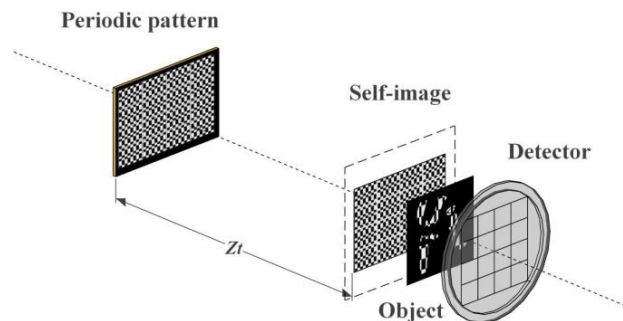


Figure 1 Schematic diagram of the proposed method. The object is scanned by self-images generated by periodic distributions of Hadamard patterns.

In our first experimental verification we use a fiber-coupled solid-state laser with a wavelength of 532 nm as light source and a digital micromirror device (DMD) with a pixel pitch of 13.7 μm as SLM. The binary patterns codified in the DMD are 32 x 32 periodical repetitions of functions of the Walsh-Hadamard basis. Each unit cell of the periodic pattern consists of 16-by-16 micromirrors. The first self-image of the periodic structure is generated at the Talbot distance that corresponds to 180,6 mm. Therefore, the object, a binary transparency codifying a letter, is located at this distance from the image of the DMD. A CMOS camera simulating a low-resolution camera by using binning is placed almost at the same plane, at a short distance from the object, to measure the intensities transmitted for each projected pattern. The measurement and reconstruction processes are performed in blocks. Firstly, for each unit cell of the periodic pattern, the corresponding pixels of the sensor acquire integrated measurements of the intensities transmitted by the object. Next, a small low-resolution image is reconstructed for each cell by inverse Walsh-Hadamard transform. A final image is obtained by stitching the set of small reconstructed images. The method allows us to obtain images with higher spatial resolution than the sensor native resolution.

3. Results

Experimental results are shown in Fig. 2. The object is a binary transparency codifying the letter A. We simulate a low-resolution camera with 32x32 pixels by using a CMOS camera and computational binning. In each unit cell of the periodic patterns, we codify 64 different patterns of the Walsh-Hadamard basis with order 8x8. Fig. 2(a) shows the image of the 2D binary object acquired by the low-resolution camera with uniform illumination. In Fig. 2(b) we present the image obtained by applying our method for parallel single-pixel imaging. We can distinguish clearly the increased spatial resolution and the improved image quality. For comparison, Fig. 2(c) shows the image of the object obtained by using the full spatial resolution of the CMOS camera without binning.

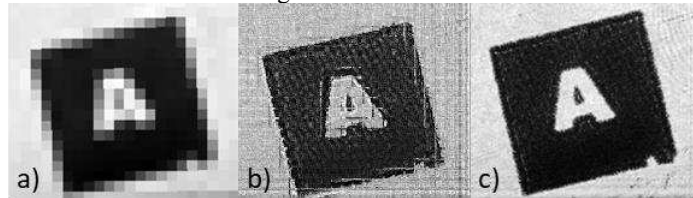


Figure 2 Images obtained with (a) low-resolution camera, (b) low-resolution camera with our parallel SPI technique and, (c) full high-resolution camera.

4. Conclusions

We have presented a new parallel single-pixel imaging technique by combining a DMD and a low-resolution camera. The periodic distributions of Walsh-Hadamard patterns generated in the DMD are projected onto the object by using Talbot effect. Images are reconstructed by applying single-pixel image reconstruction algorithms by blocks. In our experiments, we achieved an enhancement in spatial resolution by a factor of 8 in the final image while maintaining a high frame rate.

References

- [1] M.P. Edgar, G. M. Gibson, and M. J. Padgett, "Principles and prospects for single-pixel imaging," *Nature Photon* 13, 13-20 (2019).
- [2] F. Soldevila, A. J. M. Lenz, A. Ghezzi, A. Farina, C. D'Andrea, and E. Tajahuerce, "Giga-voxel multidimensional fluorescence imaging combining single-pixel detection and data fusion," *Opt. Lett.* 46, 4312-4315 (2021).
- [3] A. Mahalanobis, R. Shilling, R. Murphy, and R. Muike, "Recent results of medium wave infrared compressive sensing," *Appl. Opt.* 53(34), 860-8070 (2014).
- [4] H. Chen, M. Salman Asif, A. C. Sankaranarayanan, and A. Veeraraghavan, "FPA-CS: focal plane array-based compressive imaging in short-wave infrared," in *Proceedings of the IEEE Conference on Computer Vision and Pattern Recognition* (2015), pp. 2358-2366.
- [5] J. P. Dumas, M. A. Lodhi, W. U. Bajwa, and M. C. Pierce, "Computational imaging with a highly parallel image-plane-coded architecture: challenges and solutions," *Opt. Express* 24, 6145-6155 (2016).
- [6] K. Patorski, "The self-imaging phenomenon and its applications", *Progress in Optics* 27, 1-108 (1989).
- [7] Wen, J., Zhang, Y., & Xiao, M. "The Talbot effect: recent advances in classical optics, nonlinear optics, and quantum optics", *Advances in Optics and Photonics* 5, 83-130 (2013).

Resolution-Enhanced Single-Pixel Fluorescence Microscopy

L Ordóñez*, AJM Lenz, J Lancis, E Tajahuerce

GROC-UJI, Institute of New Imaging Technologies (INIT), Universitat Jaume I, 12071, Castelló, Spain

*E-mail: lordonez@uji.es

1. Introduction

Spatial resolution is a critical aspect of imaging, especially in microscopy, determining an instrument's ability to distinguish fine details within a scene [1]. Super resolution structured illumination microscopy (SR-SIM) emerged as a powerful technique to surpass the Abbe diffraction limit barrier [2] utilizing advanced optical methods and interactions between light and sample. While historical advancements like confocal microscopy [4] have contributed to pushing resolution limits, single-pixel imaging (SPI) presents a versatile approach, particularly in addressing issues related to detection optics, wavelength spectra, and phase detection [6]. However, despite SPI's advantages, it encounters limitations by diffraction when spatial frequencies exceed the numerical aperture of the objective lens (NA). In this study, we propose a novel configuration for achieving SR-SIM using SPI method, eliminating the need for spatial resolution detectors or raster-scanning methods.

The SPI technique involves illuminating the scene with structured light patterns while measuring the transmitted, reflected, or emitted fluorescence light with a single-pixel photodetector [7]. By correlating light intensities with projected patterns, image reconstruction becomes possible, finding applications in various fields such as infrared, hyperspectral, and multidimensional imaging. [4]. Our proposed microscope utilizes a digital micromirror device (DMD) to project Walsh-Hadamard patterns (WH), with a photodetector capturing the reflected light intensity from the sample or emitted fluorescence.

SR-SIM, on the other hand, utilizes light-sample interactions to overcome optical resolution limitations by projecting phase-shifted grating patterns through the objective lens to capture a sequence of images with a superposed grating. The application of appropriate phase-shifting algorithms extends spatial frequencies of the sample in the frequency domain. SR-SIM improves image resolution and enhances sectioning capability compared to traditional microscopy approaches [8].

In contrast to conventional imaging sensor techniques, single-pixel microscopy (SPM) offers a unique approach by projecting demagnified light patterns onto the sample. Consequently, the resulting scanning light patterns contain high-frequency components, although constrained NA affecting both sample and light-sample interaction spatial frequencies. Moreover, the NA imposes limitations on the high-frequency components of the fluorescence sample [9]. In our study, we employ a photomultiplier tube (PMT) to measure the fluorescent light intensity resulting from the light-sample interaction. Our proposed method utilizes a combination of Walsh-Hadamard and SR-SIM patterns to achieve super resolution.

2. Experimental setup

The experimental system is illustrated in Figure 1. An LED light source (LS) illuminates the DMD, which projects the combination of WH and SR-SIM light patterns onto the sample. A relay lens system, consisting of two lenses (L1 and L2) with the same focal length ($f=150\text{mm}$), projects the light patterns onto the field diaphragm (FD) of an inverted microscope, placed at the back focal plane of the tube lens (TL1). The input light beam is filtered by a fluorescence cube comprised of an exciting filter (F1), a dichroic mirror (DM) and a barrier filter (F2), before being focused into the sample using a 50x objective lens (OL). The fluorescence light emitted by the sample passes through the fluorescence cube once more, and a second tube lens (TL2) focuses the image into the grating (DG) located at the output plane of the microscope. To enhance the optical sectioning capability to this microscope, a second DMD is employed to codify a grating pattern with 31 lines/mm. The photodetector, measures light intensity, is synchronized with the first DMD through a TTL signal.

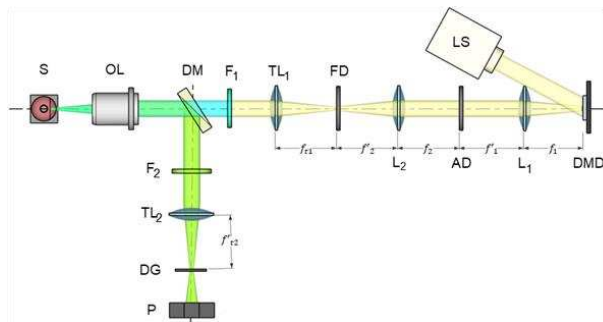


Figure 1 Scheme of the enhance optical sectioning and super-resolution single-pixel microscope.

3. Results

Figure 2 illustrates a biological sample of buccal cells stained with Carbon dots, capturing a fluorescence microscopic view of the sample. Both images' areas correspond to approximately a 9 by 9 μm region. Analysis of the image reveals a line of interest delineating a grayscale intensity profile across the original image. Specifically, this profile is depicted for both cases: SPI in Figure 2a and SPI-SR in Figure 2c. Comparison between the two cases demonstrates the enhanced level of detail achieved with SPI-SR, highlighting its efficacy in resolving finer structures within the sample.

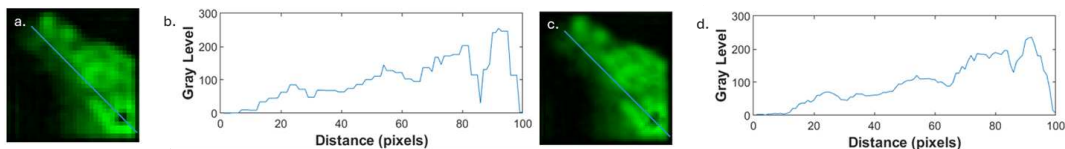


Figure 2 (a) A 64 by 64 fluorescence image of a cell obtained by using SPI microscopy, accompanied by its grayscale intensity profile plotted in (b). In contrast, the proposed SPI-SR method is depicted in (c), with its grayscale intensity profile plotted in (d).

4. Conclusion

In conclusion, combination of fluorescence SPM with SR-SIM offers a competitive solution to surpass diffraction limits in microscopy. Our SPM integrates optical methods based to achieve enhanced resolution without the need for specialized spatial resolution detectors or raster-scanning methods. This highlights SPI as a competitive single-pixel detection method that uses effective and sensitive detectors, along with spatial light modulator devices for structured illumination. Experimental results demonstrate significant improvements in resolving fine details within both high-resolution targets and biological samples for epifluorescence and fluorescence imaging.

References

- [1] J. Mertz, *Introduction to Optical Microscopy* (Cambridge University Press, Cambridge, 2019).
- [2] R. Heintzmann and C. G. Cremer, "Laterally modulated excitation microscopy: improvement of resolution by using a diffraction grating", in *Proceedings of SPIE 3568, Optical Biopsies and microscopic Techniques III* (1999).
- [3] A. D. Elliott, "Confocal microscopy: principles and modern practices", *Current Protocols in Cytometry*, 92(1), e68 (2020).
- [4] M. P. Edgar, et al., "Principles and prospects for single-pixel imaging", *Nature Photonics*, 13, 13-20 (2019).
- [5] G. M. Gibson, S. D. Johnson, and Padgett, M. J., "Single-pixel imaging 12 years on: a review", *Optics Express*, 28(19), 28190-28208 (2020).
- [6] R. Heintzmann, and T. Huser, "Super-resolution structured illumination microscopy". *Chemical Reviews*, 117(23), 13890-13908 (2017).
- [7] K. Guo, et al., "Multilayer fluorescence imaging on a single-pixel detector". *Biomedical Optics Express*, 7, 2425-2431 (2016).

Vector beams for super-resolution depletion microscopy

J. Tiana-Alsina^{1,2*}, N. Toledo-García¹, D. Maluenda^{1,2}, R. Martínez-Herrero³, A. Carnicer¹, E. Martín-Badosa^{1,2} and M. Montes-Usategui^{1,2}

¹Departament de Física Aplicada, Facultat de Física, Universitat de Barcelona, Martí i Franquès 1, 08028 Barcelona, Spain

²Institut de Nanociència i Nanotecnologia (IN2UB), 08028, Barcelona, Spain

³Departamento de Óptica, Facultad de Ciencias Físicas, Universidad Complutense de Madrid, Ciudad Universitaria, 28040, Madrid, Spain

E-mail: jordi.tiana@ub.edu

1. Introduction

In this contribution we aim to introduce the building blocks for a super-resolution optical microscope based on photo switchable fluorophores capable of improving the state-of-the-art fluorescence super-resolution microscopy techniques. Nowadays, cutting-edge super-resolution depletion fluorescence microscopy (STED and its derivatives) needs support from an array of scientific and technological developments, which involve expertise in multiples disciplines, ranging from optical engineering to cellular biology. To find and implement improved vectorial beams for depletion microscopy, two research groups at the Applied Physics Department of the University of Barcelona, with a track record in parallel structured illumination microscopy techniques [1] (Fig. 1a), optical trapping and spatial light modulation [2], as well as an extensive expertise in modelization of paraxial and highly focused vector beams [3] and its generation with SLM technology [4], have joined their expertise to develop a super-resolution depletion microscope.

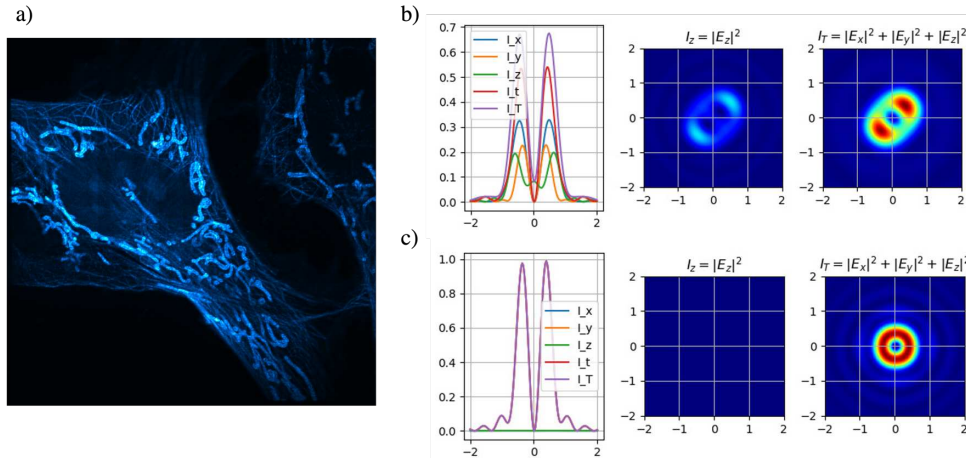


Figure 1. a) Images of mitochondria in huFIB cells synthesized with subtraction microscopy algorithm. Laguerre-Gaussian 01 beam and its profile along the x -axis subject to astigmatic aberrations ($Z=0.1\lambda$) with (b) circular and (c) azimuthal polarization.

The first depletion beams used in STED microscopy were a pair of shifted linearly polarized Gaussian beams leaving a dark region surrounded by high intensity peaks, which resulted in modest resolution improvements [5]. Later, a $0-\pi$ binary phase plate was introduced, enabling 3D confinement of fluorescence emission and larger resolution enhancements [6]. More advanced depletion beams, such as Laguerre-Gauss 01 beams with circular polarization, were then adopted, significantly improving resolution to a few tens of nanometers [7]. The polarization of excitation and depletion beams was identified as crucial for STED performance due to its role in shaping the beams and achieving optimal resolution [8]. However, fluorescence depletion is a highly non-linear process, and the effectiveness of alternative beams needs to be rigorously assessed.

The use of vector beams with non-uniform polarization could enhance resolution and reduce

photodamage. Various types of vector beams, such as radially and azimuthally polarized beams, have shown promising results in producing sharper focus and improved resolution. Current proposals involve complex optical setups and are not usually implemented on an actual microscope setup. The design of vectorial beams will also enable us to investigate more robust solutions against astigmatic aberrations. In Figure 2a and 2b, we present two Laguerre-Gaussian 01 beams with circular and azimuthal polarization, respectively, subjected to astigmatic aberration. For the Zernike term representing primary astigmatism ($Z_2=0.1\lambda$), the azimuthally polarized beam demonstrates greater robustness against aberrations.

2. Methods

A key element of this contribution is the addition, within the microscope layout, of a spatial light modulator (SLM), which will enable the implementation of any beam under study in a single, merged microscope setup. In this contribution we propose a double pass scheme through the SLM, where the two orthogonal polarization components are simultaneously modulated and allowing a full polarization control by manipulating both the amplitude and the phase of the input beam. Moreover, the use of SLMs will enable us to correct for aberrations arising from stigmatism inherent to the optical system, a critical factor in Laguerre-Gauss 01 beams. To design improved beams, we will use a matrix formalism for calculating the Born and Wolf integral as in Keller *et al.* [9]. However here, we will generalize their approach to beams with arbitrary complex amplitude, polarization and topological charge. Preliminary numerical results aiming to improve the characteristics of the depletion beam showed a minor improvement; however, and due to fluorescence depletion being a highly non-linear process, the impact on microscopy fluorescent images could be significantly larger. For example, as shown in [10], only 2% residual light (with respect to the lateral intensity maxima) at the doughnut singularity makes the resulting fluorescence intensity shrink down below 50% of its original value. The improved beams will be then coupled to a microscope to study its performance in STED-like microscopy.

Acknowledgments

This work was supported by grant PDC2022-133351-I00, funded by MCIN/AEI/10.13039/501100011033 and by the European Union NextGenerationEU/PRTR, and by grant PID2022-136796OB-I00, funded by MCIN/AEI/10.13039/501100011033/FEDER, UE.

References

- [1] M. Montes-Ustegui, R. Bola, E. Martín-Badosa, and D. Treptow, PCT/EP2019/067517 (2019).
- [2] I. Verdeny, A. Farré-Flaquer, J. Mas-Soler, C. López-Quesada, E. Martín-Badosa, and M. Montes-Ustegui, M, "Optical trapping: a review of essential concepts," *Opt. Pura Apl.* 44(3), 527-551 (2011).
- [3] D. Maluenda, I. Juvells, R. Martínez-Herrero, and A. Carnicer, "Reconfigurable beams with arbitrary polarization and shape distributions at a given plane," *Opt. Express* 21, 5432-5439 (2013).
- [4] D. Maluenda, R. Martínez-Herrero, I. Juvells, and A. Carnicer, "Synthesis of highly focused fields with circular polarization at any transverse plane," *Opt. Express* 22, 6859-6867 (2014).
- [5] T. A. Klar and S. W. Hell, "Subdiffraction resolution in far-field fluorescence microscopy," *Opt. Lett.* 24, 954-956 (1999).
- [6] T. A. Klar, S. Jakobs, M. Dyba, A. Egner, and S. W. Hell, "Fluorescence microscopy with diffraction resolution barrier broken by stimulated emission," *Proc. Natl. Acad. Sci.* 97, 8206-8210 (2000).
- [7] P. Török and P.R.T. Munro, "The use of Gauss-Laguerre vector beams in STED microscopy," *Opt. Express* 12, 3605-3617 (2004).
- [8] Y. Xue, C. Kuang, S. Li, Z. Gu, and X. Liu, "Sharper fluorescent super-resolution spot generated by azimuthally polarized beam in STED microscopy," *Opt. Express* 20, 17653-17666 (2012).
- [9] J. Keller, A. Schönle, and S. W. Hell, "Efficient fluorescence inhibition patterns for RESOLFT microscopy," *Opt. Express* 15, 3361-3371 (2007).
- [10] Silvia Galiani, Benjamin Harke, Giuseppe Vicidomini, Gabriele Lignani, Fabio Benfenati, Alberto Diaspro, and Paolo Bianchini, "Strategies to maximize the performance of a STED microscope," *Opt. Express* 20, 7362-7374 (2012)

Parallelized laser-scanned super-resolution depletion microscopy

N. Toledo-García^{1*}, L. Cambior-Navarro¹, E. Martín-Badosa^{1,2}, M. Montes-Usategui^{1,2}
and J. Tiana-Alsina^{1,2}

¹*Departament de Física Aplicada, Facultat de Física, Universitat de Barcelona, Martí i Franquès 1,
08028 Barcelona, Spain.*

²*Institut de Nanociència i Nanotecnologia (IN2UB), 08028, Barcelona, Spain.*

*E-mail: nicktoledogarcia@ub.edu

1. Introduction

Advanced optical microscopy techniques play a crucial role in a multitude of applications within the field of life sciences, being fluorescence microscopy an outstanding tool for the study of biological processes that occur at the cellular and molecular levels. However, conventional optical microscopy faces spatial resolution limitations due to the diffraction phenomenon, preventing structures below the subcellular scale (200 nm) from being observed. The development of the first super-resolution microscopy techniques managed to circumvent the diffraction limit only using optical means. These early proposals of super-resolution microscopy such as STED [1] or PALM-STORM [2,3], despite achieving resolutions in the order of nanometers, are poorly suited for use in living cells. While STED microscopes use high-power pulsed lasers that are harmful to living samples, PALM-STORM microscopes are very slow and therefore incompatible with observations of cellular dynamics in real time.

To overcome these limitations, it is necessary to develop super-resolution technologies compatible with the observation of living cells in real time. In the last years, RESOLFT [4] microscopy has emerged as a potential solution, being a derivative of STED microscopy which uses photoactivatable fluorophores and doughnut-shaped illumination beams, allowing the acquisition of super-resolution images (70 nm) with low light intensities. Therefore, RESOLFT is a promising candidate for obtaining high-resolution images of living cells since the illumination requirements minimize cellular damage. However, the current methods of image reconstruction from a point-by-point scan of the sample do not enable the obtention of images at video speed, leading to the necessity of parallelizing the illumination to speed up acquisition. Although proposals to illuminate the sample with a multi-beam configuration have been made, these present implementation problems due to the complexity of the optical system, and there is still no commercially viable device.

We propose the use of acousto-optic holography techniques to parallelize the illumination by generating large arbitrary arrays of switchable Gaussian and doughnut-shaped beams to achieve RESOLFT microscopy at high speeds. Importantly, both Gaussian and Laguerre-Gaussian (doughnut-shaped) beams exhibit minimal distortion after crossing AODs, evidencing the promising potential of acousto-optic holography technology to develop live cell super-resolution imaging [5].

2. Methodology

The microscope we present achieves parallelization of illumination with the use of acousto-optic holography. Its core components are acousto-optic deflectors (AODs), exploited as general spatial light modulators through the computation of tailored RF driving signals obtained with digital holography techniques [6]. In this way, by using 2 AODs (one for each modulation direction), we can generate an array of illuminating beams with an arbitrary distribution, resulting in a programmable array of illumination beams and a fast scanning (up to 150kHz) without the need for any mechanical moving element. Switching between Gaussian and doughnut-shaped (Laguerre-Gaussian) illumination can be achieved employing a multiple path setup that merges all beams, selecting the desired path by triggering different lasers (one for each path) or by polarization means.

Our setup, depicted in Fig. 1a, is composed by two 488nm CW lasers, each one coupled to a single mode fiber, and two optical paths that merge into a common path. One path generates a Laguerre-Gaussian beam using a vortex phase plate (VPP), while the other path maintains the beam as Gaussian.

The two paths are merged into a common path with a beam splitter (BS). The switching between illumination beams is performed by digitally triggering each laser. The common path crosses an AODx, and a telescope conjugates the pivot plane of the AODx into the AODy so that both pivot planes are at the same position. A second telescope introduces another conjugated plane, enabling the generation of the doughnut-shaped beam after the AODs if desired by positioning the VPP in said conjugated plane. A quarter-wave plate (QWP) is employed to ensure circular polarization, then the beam is reflected by a dichroic mirror (DM) into the microscope (Nikon Eclipse TE2000) equipped with a high numerical aperture objective (Nikon CFI PlanApo λ D, oil-immersion, 100x, NA=1.45). Fluorescence is collected by the objective, filtered by the DM and imaged onto the camera.

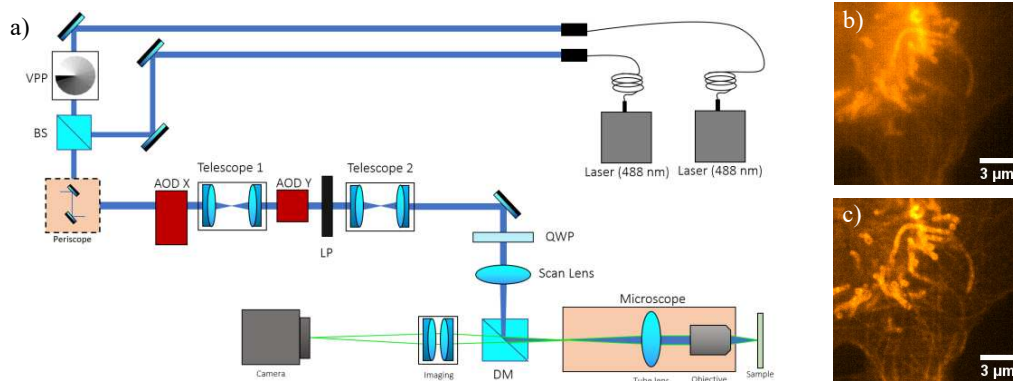


Figure 1 (a) Microscope setup. (b) Epifluorescence image. (c) Subtraction image with virtual pinhole processing and a subtraction factor of 0.65.

Using this microscope setup, we performed the characterization of the illumination beams by raster scanning our illumination across sub-diffraction sized fluorescent beads. Subtraction microscopy is performed with commercial biological samples to test the performance of the microscope, as depicted in Fig. 1b and 1c.

3. Conclusions

In this work we implement a microscope setup the parallelization of Gaussian and Laguerre-Gaussian beams using acousto-optic holography techniques and beam switching via laser triggering. We provide a characterization of the quality of the illuminating beams with different architectures of the setup to ensure the best speed and resolution improvement. Finally, we test the performance of the microscope by imaging commercial biological samples with subtraction microscopy.

Acknowledgments

This work was supported by grant PREP2022-000292, funded by MICIU/AEI/10.13039/501100011033 and ESF+, by grant PDC2022-133351-I00, funded by MCIN/AEI/10.13039/501100011033 and by the European Union NextGenerationEU/PRTR, by grant PID2022-136796OB-I00, funded by MCIN/AEI/10.13039/501100011033/FEDER, UE and grant F2I-PdC-2023-008-600427 funded by Fundació Bosch i Gimpera from Universitat de Barcelona.

References

- [1] S.W. Hell and M. Kroug, *Appl. Phys. B* 60, 495–497 (1995).
- [2] E. Betzig, G. H. Patterson, R. Sougrat, OW Lindwasser, S. Olenych, J. S. Bonifacino, M. W. Davidson, J. Lippincott-Schwartz, and H. F. Hess, *Science* 313, 1642–1645 (2006).
- [3] M. Rust, M. Bates, and X. Zhuang, *Nat. Methods* 3, 793–796 (2006).
- [4] M. Hofmann, C. Eggeling, S. Jakobs, and S.W. Hell, *Proc. Natl. Acad. Sci.* 102, 17565–17569 (2005).
- [5] F. Klingmann, N. Toledo-García, E. Martín-Badosa, M. Montes-Usategui, and J. Tiana-Alsina, submitted to *J. Eur. Opt. Society-Rapid Publ.* (2024).
- [6] M. Montes-Usategui, R. Bola, E. Martín-Badosa, and D. Treptow, *PCT/EP2019/067517* (2019).

Scanning laser microscopy with a 2D detector to enhance resolution and signal in two-photon excitation fluorescence

Enrique J. Fernández* and Juan M. Bueno

*Laboratorio de Óptica, Instituto Universitario de Investigación en Óptica y Nanofísica
Universidad de Murcia, Campus de Espinardo (Ed. 34), 30100 Murcia, Spain*

*E-mail: enriquej@um.es

1. Introduction

Two-photon excitation fluorescence (TPEF) microscopy employs a near infrared focused laser beam that scans across the sample and generates one visible photon [1]. Measurements are digitized from the photodetector signal, typically in a confocal arrangement with a point detector. While various detectors have been utilized, photomultipliers (PMTs) are prevalent due to their affordability, sensitivity, and durability. PMTs convert incident photons into electrical signals at the photocathode surface, allowing photon counting with proper calibration.

The acquisition of images in TPEF microscopy relies on the spatial and temporal characteristics of the scanning pattern. While recent studies have explored the trade-off between acquisition time and image quality through various experimental conditions, such as detector sampling frequency and pixel integration, the technique's performance is limited by the sequential detection operation associated to a single-point detector [2]. This limitation can lead to reduced visualization of details in specimens with high spatial frequency patterns and inaccurate tracking of dynamic processes, rendering the technique less suitable for certain applications. Efforts to integrate cameras into TPEF microscopy have primarily aimed to enhance imaging speed, although their spatially resolved capabilities remain underutilized. In this work, a new quantitative complementary metal-oxide-semiconductor (CMOS) image sensor employing exhibiting ultra-low readout noise was characterized and compared with the performance of a PMT for TPEF microscopy, specifically in the context of biomedical imaging. Resolution and signal quality have been confronted in both modalities.

2. Methods

A modified commercial inverted microscope (Nikon TE2000-U, Tokyo, Japan) was used to record TPEF images. The microscope employed an 800-nm external mode-locked laser source to illuminate the samples. A couple of conjugated galvanometric mirrors were used to perform XY raster scan on the sample. These were synchronized with the PMT or with the camera (ORCA-Quest, Hamamatsu, Japan), depending on the modality of image acquisition. This camera incorporated a back illuminated CMOS sensor (9.4 Mpixels) with ultra-low readout noise, enabling photon counting on every pixel (4.6 μm lateral size). The scanning protocol enabled to select both the size (90, 180, 270 and 360 μm of lateral size) and the number of scanned points (128, 256, 512 and 1024 points per line) on the sample. The exposure of the camera was in operation during the entire raster scan.

3. Results

The non-linear nature of the signal emitted by the sample and subsequently detected by the camera was examined to ensure that potential artifacts were ruled out. To achieve this, a series of images were captured from a cellulose sample using the camera at different power levels (30, 40, 50, 60, 70, and 80 mW at the sample's surface). The scanning protocol of 1024 points/line was employed to capture images sized 180x180 μm^2 . Within these images, regions of interest measuring 25x25 pixels² were selected, encompassing areas of different intensities. Each set of experimental data was then fitted to a power function of the form $y=Ax^B$, with A and B as the free parameters of the curve fitting. The square correlation coefficients of the curve fittings exhibited $R^2>0.99$. The corresponding exponents (parameter B) obtained from the fittings, within a 95% confidence interval, were in the range [1.8, 2.2]. These results confirm the quadratic nature of the fit, indicating that the signal detected by the camera is associated with a TPEF emission.

Figure 1 shows an example of a TPEF image obtained with the camera over a square of 1024^2 pixels with two different scanning protocols, corresponding to 1024 and 128 points/line (as indicated), with identical illumination power. Zoomed versions of a region of interest, limited by a red rectangle, showing structures of high spatial frequencies are presented at the bottom of each panel.

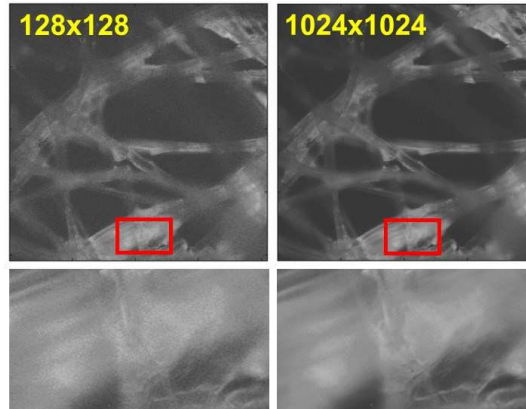


Figure 1 Camera's images from a cellulose sample with zoomed region of interest obtained with different scanning protocol.

In the case of the TPEF images obtained with the PMT, the synchronization of the detector with the raster scanning limits, and significantly changes, the resolution of the images. The evolution of intensity of the signal retrieved under each modality as a function of the scanning protocol differed significantly. Whereas with the camera the trend showed a linear increase of the non-linear signal with the number of scanned points, the data from the PMT images were fitted to a negative potential function, with decreasing energy as the number of points increased.

Images from a cellulose sample at identical locations were acquired with the PMT and the camera to compare their performance. The comparison across images from both detectors exhibited a benefit in resolution of more than 5-fold for the images recorded by the camera.

Moreover, TPEF images from a mice retina were finally retrieved as a proof of concept of the use of the camera for biomedical applications [3]. These images were recorded at different depths resolving morphological details in the order of 2-3 μm .

4. Discussion and conclusions

A new modality of non-linear microscopy combining a 2D sensor with a flying aerial spot scanned over the sample has been presented and characterized. The technique has been confronted with the state-of-the-art modality using a PMT, showing a large benefit in terms of signal and resolution when using the camera. Because of the inherent confocal character of the TPEF, the camera could be employed to acquire images at different depths still maintaining the optical sectioning capability within the sample without loss of quality. The technique has been tested successfully on biological samples.

Acknowledgments

V. Bernardo, Hamamatsu Photonics France, is acknowledged for his valuable help with the camera employed in this study. Supported by grant PID2020-113919RBI00/AEI/10.13039/501100011033.

References

- [1] W. R. Zipfel, R. M. Williams, and W. W. Webb, "Nonlinear magic: multiphoton microscopy in the biosciences," *Nat. Biotechnol.* 21(11), 1369-1377 (2003).
- [2] W. Denk, J. Strickler, and W. Webb, "Two-photon laser scanning fluorescence microscopy," *Science* 248(4951), 73-76 (1990).
- [3] J. M. Bueno, R. Cruz-Castillo, M. Avilés-Trigueros, et al., "Arrangement of the photoreceptor mosaic in a diabetic rat model imaged with multiphoton microscopy," *Biomed. Opt. Express* 11(9), 4901-4914 (2020).

2D Image, 3D LiDAR & 4D radar fusion for autonomous driving

Adrià Subirana^{1*}, Gerard deMas-Giménez¹, Pablo García-Gómez², Eduardo Bernal¹, Jordi Riu¹, Santiago Royo^{1,2}, Josep R. Casas³

¹Center for Sensors, Instruments and Systems Development (UPC-CD6), Universitat Politècnica de Catalunya, Rambla de Sant Nebridi 10, 08222, Terrassa, Spain.

²Beamagine S.L., Carrer de Bellesguard 16, 08755, Castellbisbal, Spain.

³Grup de Processament d'Imatge (UPC-GPI) Universitat Politècnica de Catalunya, C/Jordi Girona 1-3 08034 Barcelona, Spain.

*E-mail: adria.subirana@upc.edu

1. Introduction

Robust detection, localization and tracking of objects is essential for autonomous driving. Computer vision has largely driven development in recent years based on camera sensors, but 3D localization from images is still challenging. LiDAR point clouds provide accurate localization in 3D by measuring distance and even 3D object's shapes, but LiDAR sensors are expensive, data is less semantic, rather sparse and its range is typically limited to 150m. Imaging radars achieve larger ranges up to 300m adding radial velocity (the 4thD) to the objects detected thanks to Doppler Effect. However, the returns are even sparser than LiDAR, and less precise in terms of localization, both for range and beam direction (azimuth and elevation). Cost and limited resolution of range sensors still keep them as promising complementary devices to video processing, evolving forcibly towards fusion strategies [1] that may consider both the 3D localization capabilities of range sensors and the higher spatial resolution of image data.

Fusing range and image data can enhance object detection, localization, and tracking for autonomous driving, and any fusion strategies require registered and synchronized data from range and image sensors. The challenge is to design an interpolation or depth image generation method able to generate a high-resolution depth image from the radar data considering the higher resolution of the registered image data, in order to assign correct range and speed to objects detected in the images, or to perform an easier and most robust detection of such objects. But just super-resolving LiDAR data would also help to better define the 3D scene around. The aim of the proposed project is to start exploring how to obtain such high-resolution depth data interpolation considering registered image data, by preserving the contours of objects found in the image while assigning correct range to the detected objects.

2. Methodology

This project proposes using a two-stage neural network structure for radar-camera pixel depth association for depth completion using LiDAR frames as ground truth, previously tested on the nuScenes dataset [6], in order to test and use it in a custom dataset created in collaboration with Beamagine SL and CD6 at UPC.

Figure 1 shows the scheme of the two-stage architecture used [2]. Network 1 learns N-channel radar-camera pixel depth association (RC-PDA), here illustrated for two radar pixels (marked with white squares) on their neighboring pixels (white boxes). The RC-PDA is converted into a multi-channel enhanced radar (MER), and input to Network 2 which performs image-guided depth completion.

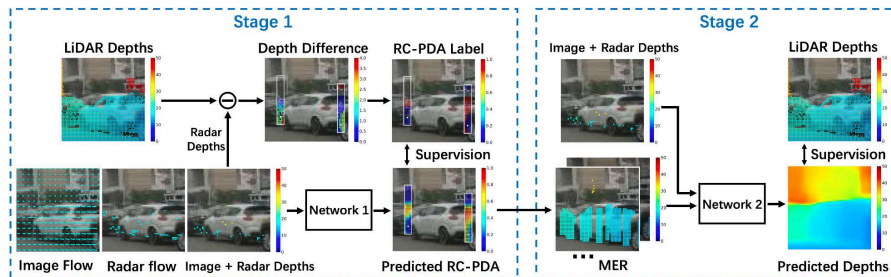


Figure 1 Two Stages Neural Network Structure.

The nuScenes dataset [6] will be exploited for experimentation and reference. Fine-tuning and inference will be carried out over our own datasets. Testing with state of the art metrics should assess the validity of explored solutions proposals. An interpolation method on depth data [2][3] and a 2-branch DL architecture with GCL [4] are proposed as starting points to evolve towards the needs of the project. Previous projects exploring neural architectures on point clouds in automation [5] will contribute experience in state of the art point cloud networks and 3D data annotation.

An example of the kind of outputs this architecture can get from a nuScenes scene is shown in Figure 2. Given an RGB image and the projection of the radar points to the image, the first stage generates the MER, and the second stage generates the depth image.

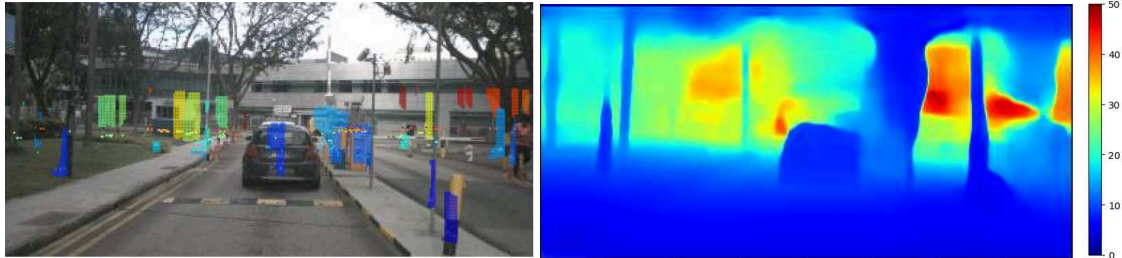


Figure 2 Processed nuScenes scene. (left) RGB image with radar points and maximum MER (first stage output) overlapped. (right) Depth image (second stage output). Colormap in meters.

3. Conclusions

This project addresses the need for robust detection, localization, and tracking of objects in autonomous driving scenarios through the fusion of range and image data. The proposed two-stage neural network structure offers a promising approach, enabling the association of radar and camera pixels for depth completion enhancing the accuracy of object detection and localization. Using the nuScenes data set to test ideas, this project aims to develop and test practical solutions for practical application, aiding in the advancement of autonomous vehicle technology.

Acknowledgments

This work has been possible thanks to projects MISTED PID2020-119484RB-I00 and USEFUL TED2021-132338B-I00 funded by Ministerio de Ciencia e Innovación de España.

References

- [1] V. John and S. Mita, “RVNet: Deep Sensor Fusion of Monocular Camera and Radar for Image-Based Obstacle Detection in Challenging Environments,” in *Image and Video Technology*, Cham, 2019, pp. 351–364. doi: [10.1007/978-3-030-34879-3_27](https://doi.org/10.1007/978-3-030-34879-3_27)
- [2] Y. Long, D. Morris, X. Liu, M. Castro, P. Chakravarty, and P. Narayanan, “Radar-Camera Pixel Depth Association for Depth Completion,” in *2021 IEEE/CVF Conference on Computer Vision and Pattern Recognition (CVPR)*, Jun. 2021, pp. 12502–12511. doi: [10.1109/CVPR46437.2021.01232](https://doi.org/10.1109/CVPR46437.2021.01232)
- [3] P. Biosca, “Depth Estimation for AV Perception with Camera & Radar,” Stage report, July 2023.
- [4] M. Hu *et al.*, “PENet: Towards Precise and Efficient Image Guided Depth Completion,” in *2021 IEEE Int. Conf. on Robotics Automation (ICRA)*, May 2021, doi: [10.1109/ICRA48506.2021.9561035](https://doi.org/10.1109/ICRA48506.2021.9561035)
- [5] Ò. Lorente, J. R. Casas, S. Royo, and I. Caminal, “Pedestrian Detection in 3D Point Clouds using Deep Neural Networks,” *arXiv:2105.01151 [cs]*, May 2021, <http://arxiv.org/abs/2105.01151>
- [6] H. Caesar *et al.*, “nuScenes: A Multimodal Dataset for Autonomous Driving,” in *2020 IEEE/CVF Conference on Computer Vision and Pattern Recognition (CVPR)*, Jun. 2020, pp. 11618–11628. doi: [10.1109/CVPR42600.2020.01164](https://doi.org/10.1109/CVPR42600.2020.01164)

Measurement of global tortuosity of retinal vessels in fundus images

Natalia Ramírez, Miquel Ralló, María S. Millán*

Grupo de Óptica Aplicada y Procesado de Imagen, Universitat Politècnica de Catalunya-BarcelonaTech

*E-mail: m.millan@upc.edu

1. Introduction

Increased retinal vessel tortuosity is a potential biomarker for various serious diseases. To objectively assess this, local tortuosity indices are calculated on individual vessel segments extracted from digital fundus images [1]. These indices, derived from the geometric properties of the vessel segments, are typically evaluated by comparing their results to subjective grading by ophthalmologists [2][3]. To our knowledge, BioImLab is the only publicly available fundus image database containing 30 arteries and 30 veins with ranked tortuosity assessments [2]. In the pursuit of a single index to evaluate the tortuosity of the entire retinal vessel network, researchers have investigated formulas to combine the set of local tortuosity values. These values correspond to a segmentation of the retinal vessel network into individual segments. A comprehensive collection of aggregation formulas can be found in [4]. Some studies have incorporated additional anatomical factor assessments into the aggregation formulas, resulting in a global tortuosity index [5]. Similar to local indices, global tortuosity indices are also compared to ophthalmologists' overall gradings [5].

This work focuses on the objective evaluation and comparison of global tortuosity indices, incorporating the concept of “vessel compositionality”, introduced in [1] and further developed in [2]. This concept involves taking a single vessel segment, dividing it into smaller parts, computing the local tortuosity of each part, and then using an aggregation formula to obtain the global tortuosity of the entire segment. This value is then compared to the local tortuosity calculated for the original, undivided vessel segment. The procedure for dividing the vessel segment determines endpoints, bifurcation points, and crossing points in a first stage. These points are then used to determine the endpoints of the individual parts. This segmentation approach is commonly utilized to divide the retinal vessel network into individual segments, as described in [4].

2. Method and results.

Let $C(t) = (x(t), y(t))$ with $t_0 \leq t \leq t_1$ be a parameterized curve describing the centerline of a single vessel segment. Its chord and length are defined as: $D(C) = \sqrt{(x(t_1) - x(t_0))^2 + (y(t_1) - y(t_0))^2}$ and $L(C) = \int_C 1 ds = \int_{t_0}^{t_1} 1 \cdot \sqrt{x'(t)^2 + y'(t)^2} dt$. Distance factor (DF) is a simple and widely used local tortuosity index. It is defined as the ratio of the segment length to the segment chord, $DF(C) = L(C)/D(C)$. DF equals one when the vessel segment lies on a straight line and is greater than one otherwise. Let $C_i, i = 1, \dots, N$ be a partition of the vessel segment C into N parts. Table 1 contains five global tortuosity indices [4] defined by aggregation formulas that incorporate the DF index.

Mean Tortuosity $DF_M(C) = \frac{\sum_{i=1}^N DF(C_i)}{N}$	Weighted Additivity on Length $DF_{WAL}(C) = \frac{\sum_{i=1}^N L(C_i) \cdot DF(C_i)}{\sum_{i=1}^N L(C_i)}$	Weighted Additivity on Chord $DF_{WAC}(C) = \frac{\sum_{i=1}^N D(C_i) \cdot DF(C_i)}{\sum_{i=1}^N D(C_i)}$
Mean Tortuosity with Weighted Additivity $DF_{MTWAL}(C) = \frac{\sum_{i=1}^N L(C_i) \cdot DF(C_i)}{N \cdot \sum_{i=1}^N L(C_i)}$	Tortuosity Density Global index $DF_{TDG}(C) = \frac{\sum_{i=1}^N DF(C_i)}{N \cdot \sum_{i=1}^N L(C_i)}$	

Table 1. Definitions of global tortuosity indices as proposed in [4].

To illustrate this method with an example, we take three samples from BioImLab database (arteries labelled #1, #8, and #48) to represent mild and severe tortuosity. Table 2 includes their rank order within the 30 arteries of the database. We obtained the centerline, endpoints, bifurcation points, and crossing points of each vessel segment following the image process described in [6]. From them, the vessel segment is divided into a number of parts. Very

small parts, i.e., those with lengths shorter than one vessel calibre half, were excluded. Table 2 contains the values of the five DF -based global tortuosity indices and the local DF tortuosity for each vessel segment. The global $DF_M(C)$, $DF_{WAL}(C)$, $DF_{WAC}(C)$ tortuosity indices give the same order for the artery samples as the local $DF(C)$ index. This order also coincides with the rank order set by the ophthalmologist referred by the database [2]. In contrast, $DF_{MTWAL}(C)$ and $DF_{TDG}(C)$ produce the opposite order, probably due to the larger number of parts of arteries #48 and #8 in comparison with #1.

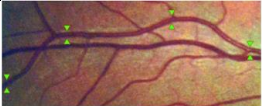
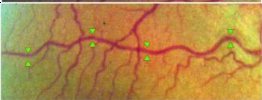
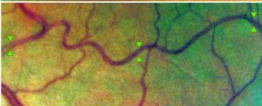
Artery	#	rank	$DF(C)$	$DF_M(C)$	$DF_{WAL}(C)$	$DF_{WAC}(C)$	$DF_{MTWAL}(C)$	$DF_{TDG}(C)$
	1	12	1.0330	1.0135	1.0134	1.0134	0.1013	0.00190
	48	23	1.0824	1.0298	1.0504	1.0485	0.0750	0.00184
	8	30	1.2607	1.1118	1.0558	1.0545	0.0704	0.00179

Table 2. 1st column: BioImLab images of arteries with marks [2]; 2nd column: sample label; 3rd column: rank order within the 30 samples of the database. Dr. Piermarocchi, from the Department of Ophthalmology, University of Padova, Italy, provided the fundus images and the manual tortuosity grading. 4th column: Local DF tortuosity values. Rest of columns: Global tortuosity values (formulas in Table 1).

3. Conclusions

Global tortuosity indices can be objectively evaluated on single vessel segments and compared to local tortuosity values. Preliminary results distinguished those global indices that better aligned ophthalmologists' criteria.

Acknowledgments This work was supported by PID2020PID2020-114582RB-I00/AEI/10.13039/501100011033.

References

- [1] W. E. Hart, M. Goldbaum, B. Côté, P. Kube, and M. R. Nelson, "Measurement and classification of retinal vascular tortuosity," *Int J Med Inform* 53, 239-252 (1999).
- [2] E. Grisan, M. Foracchia, and A. Ruggeri, "A novel method for the automatic grading of retinal vessel tortuosity," *IEEE Trans Med Imaging* 27(3), 310-319 (2008).
<https://bioimlab.dei.unipd.it/Retinal%20Vessel%20Tortuosity.htm>
- [3] L. Ramos, J. Novo, J. Rouco et al. "Retinal vascular tortuosity assessment: inter-intra expert analysis and correlation with computational measurements," *BMC Med Res Methodol* 18, 144 (2018).
- [4] Handayani, T. Nafia, T. Mengko, "Quantification of Global Tortuosity in Retinal Blood Vessels," *Int J Adv Sci Eng Inf Technol* 8, 1358-1365 (2018).
- [5] Á.S. Hervella, L. Ramos, J. Rouco et al. "Explainable artificial intelligence for the automated assessment of the retinal vascular tortuosity," *Med Biol Eng Comput* 62, 865–881 (2024).
- [6] N. Ramírez, M. Ralló and M. S. Millan "Retinal Vessel Local Tortuosity under a Macula-to-Optic Disc Central-Framing Change," *Diagnostics*, 13, 1030 (2023).

Derivas y distorsiones térmicas en cámaras digitales al realizar medidas con precisión subpíxel

María-Baralida Tomás^{1*}, Belén Ferrer¹ y David Mas¹

¹Instituto Universitario de Física Aplicada a las Ciencias y las Tecnologías, Universidad de Alicante, ctra. San Vicente, s.n. 03690 San Vicente del Raspeig, Alicante, España

*E-mail: maria.baralida@ua.es

1. Introducción

En los últimos años cada vez se utilizan más las cámaras digitales en los campos de la física y la ingeniería para el análisis experimental a través de imágenes. Las capacidades de las cámaras junto a técnicas de análisis de imagen que mejoran su resolución en más de dos órdenes de magnitud permiten medir movimientos subpíxel a bajo coste [1]. Sin embargo, cuando se trata de movimientos subpíxel hay que tener en cuenta cualquier inestabilidad de la cámara que pueda afectar a la medida. El calentamiento de la cámara por factores externos, pero, sobre todo, el producido por el calor emitido por los elementos electrónicos de la cámara, puede producir distorsiones y derivas en la imagen que limiten las ventajas de utilizar los métodos super-resolventes, haciendo difícil o incluso inviable la interpretación de los resultados [2]. Este calentamiento del sensor de la cámara afecta a las medidas tomadas incluso controlando la temperatura ambiental del laboratorio [3–5], especialmente cuando más precisas deban ser las medidas.

2. Materiales y métodos

En esta comunicación se pretende caracterizar las distorsiones térmicas de la cámara Basler a2A5328-15um en una medida de larga duración. Para ello se ha grabado una imagen cada 2 minutos durante 17 horas de un objeto estático formado por círculos negros sobre fondo blanco iluminados con dos fuentes de luz e instalando el experimento dentro de una cabina de iluminación tal y como se muestra en la Figura 1. Además, se compara la distorsión térmica producida por la cámara sin y con el uso de disipadores de calor.

Se ha determinado la posición de cada círculo a lo largo del tiempo mediante el cálculo del centroide utilizando el algoritmo *regionprops* de Matlab.

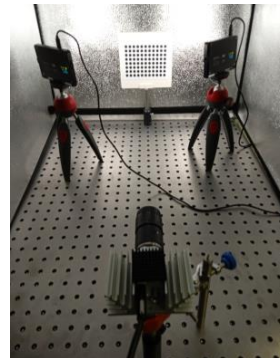


Figura 1. Montaje experimental de la cámara con los disipadores de calor, el objeto y las dos fuentes de luz dentro de una cabina de iluminación.

3. Resultados

El cálculo de la posición del centroide en horizontal y vertical permite entender las distorsiones que ocurren en la cámara digital. Por tanto, en la Figura 2 se muestra la posición media de todos los centroides para los ejes x e y utilizando la cámara con y sin disipador de calor. Se puede observar una deriva bastante grande durante las 2 primeras horas de grabación y una posterior estabilización de la imagen al utilizar los disipadores de calor. Sin utilizar disipadores, la imagen no llega a estabilizar incluso tras 17 horas de grabación.

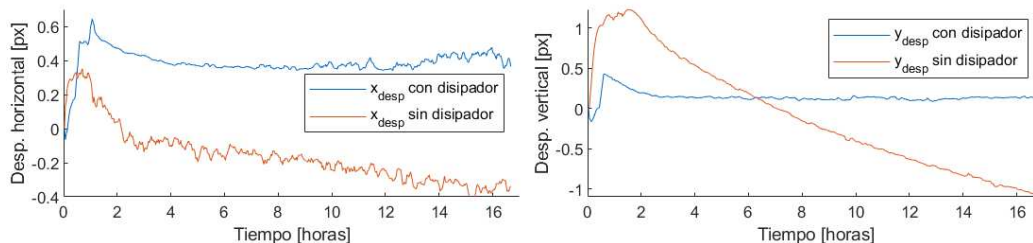


Figura 2. Posición media de los centroides en horizontal y vertical utilizando la cámara con y sin disipadores de calor.

En la Figura 3 se muestra otra perspectiva de los cambios producidos en el sensor de la cámara al calentarse, en donde se evalúan la distorsión y las derivas de los cuatro círculos de las esquinas del objeto grabado. La cruz central muestra el estado inicial del experimento sin distorsión y las esquinas de los polígonos indican las posiciones de los círculos cuando comienza la estabilización de la cámara (a las 2 horas de grabación) y al final del experimento (a las 17 horas). Se puede apreciar que, aunque los disipadores de calor previenen las derivas térmicas, no eliminan por completo la dilatación de la imagen. Sin embargo, sin la utilización de disipadores las derivas son bastante mayores.

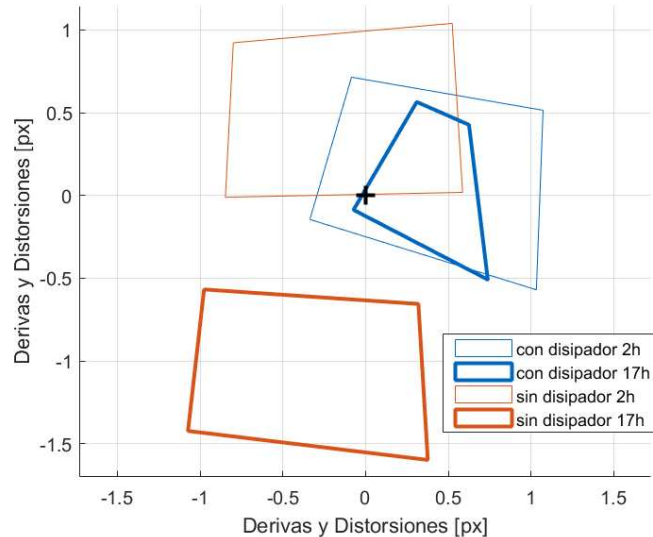


Figura 3. Derivas de la cámara en las cuatro esquinas del objeto en diferentes momentos del experimento. La cruz central muestra el estado inicial del experimento sin distorsión y las esquinas de los polígonos indican las posiciones de los círculos tras 2 horas y 17 horas de grabación utilizando la cámara con y sin disipador de calor.

Los resultados muestran que, aunque la dilatación es prácticamente completa tras las 2 primeras horas de grabación, las derivas continúan hasta el final del experimento. No obstante, el uso de disipadores de calor muestra una mayor estabilidad sin llegar a eliminar por completo las distorsiones y derivas térmicas.

4. Conclusiones

En esta comunicación se muestran las distorsiones y derivas en el sensor de una cámara digital por el calentamiento de los elementos electrónicos de la misma al grabar sin y con disipadores de calor. Los resultados muestran que al inicio de la grabación se producen cambios rápidos obteniendo grandes errores en la medida, pero tras un periodo de aproximadamente 2 horas, las distorsiones en la cámara se reducen de manera notable con el uso de disipadores de calor, aunque siguen ocurriendo deformaciones en el sensor que podrían afectar a la medida.

Agradecimientos

Este trabajo es parte del Proyecto PID2021-126485OB-I00 financiado por el Ministerio de Ciencia e Innovación y cofinanciado por la Unión Europea.

Referencias

- [1] B. Ferrer, M.B. Tomás, M. Wan, J.T. Sheridan, D. Mas, “Comparative analysis of discrete subtraction and cross-correlation for subpixel object tracking”, *Appl. Sci.* **13**(14), 8271 (2023).
- [2] B. Ferrer, M.B. Tomás, D. Mas, “Use of image correlation to measure macroscopic strains by hygric swelling in sandstone rocks”, *Appl. Sci.* **11**(6), 2495 (2021).
- [3] Q. Ma, S. Ma “Experimental investigation of the systematic error on photomechanic methods induced by camera self-heating”, *Opt. Express* **21**(6), 7686–7698 (2013).
- [4] B. Pan, “Thermal error analysis and compensation for digital image/volume correlation”, *Opt. Lasers Eng.* **101**, 1–15 (2018).
- [5] S. Ma, S. Zhou, Q. Ma, “Image distortion of working digital camera induced by environmental temperature and camera self-heating”, *Opt. Lasers Eng.* **115**, 67–73 (2019).

Characterization of key error sources of imaging devices for measuring luminance

Ángela Sáez and Alejandro Ferrero*

Instituto de Óptica “Daza de Valdés”, Agencia Estatal Consejo Superior de Investigaciones Científicas (IO-CSIC), c/ Serrano 144, 28006 Madrid, España

*E-mail: alejandro.ferrero@csic.es

1. Introduction

Nowadays, matrix detectors as CCD or CMOS cameras are very adequate to evaluate radiance spatial distributions of scenes, and are used, in combination with a photopic filter, to evaluate complex outdoor or indoor lighting scenes. These systems, also known as Imaging Luminance Measurement Devices (ILMDs), require to be characterized for providing traceability to optical radiation standards. One of the main sources of error in the measurement is the spectral mismatch of the photopic filter with respect to the spectral luminous efficiency function, $V(\lambda)$, which makes that the luminous responsivity of the detector changes with respect to the spectral distribution of the light sources in the scene. This is a serious issue when the different sources in the scene have different spectral distributions than the light source used for the calibrations. An alternative is to use a multispectral imaging system, which would provide spectral and spatial radiance measurement simultaneously. This more complete measurement allows not only spatial luminance free of spectral mismatch errors to be obtained, but additionally luminance in mesopic or scotopic conditions to be calculated, since the mathematical evaluation for any spectral efficiency function can be implemented from the spectral irradiance and background luminance, and, in addition, the adaptation condition can be estimated from the spatial distribution of radiances. In conclusion, a well calibrated multispectral imaging system can be regarded as a luminance meter for any adaptation condition, able to evaluate complex lighting conditions.

We present in this contribution procedures to characterize error sources typically found in measurements with CCD cameras, specifically the effect of the internal stray light (diffraction or interreflections, also known as ghosts) and smear. As a result of the procedure, empirical models and parameters are obtained, which are needed for the estimation of the measurement uncertainty, and for establishing the proper conditions under which the imaging system can be used for metrological purposes.

The device under study is a monochromatic camera (Q-Imaging Rolera-XR Fast 1394) in combination with a VariSpec liquid crystal tunable filter (LCTF). In order to evaluate the different sources of errors by the proposed procedures, an 8×8 matrix of RGB LEDs (Adafruit NeoPixel 8×8 RGB NeoMatrix, WS2812B-based LEDs) is used as spatially-variable light source.

2. Methodology

The internal stray light is light that is collected at positions of the matrix detector not corresponding with the positions in the object. This can be caused by diffraction or inter-reflection between objective lens and sensor, or by defocused objects. The stray light due to diffraction manifests itself as a halo around the image of the luminous source to be measured, and, for small apertures, it might contain some additional features as stars. In the case of large apertures, this can be characterized by the evaluation of the Point Spread Function (PSF). A procedure was followed to obtain a representative PSF of the system:

1. To turn on simultaneously six LEDs of the LED matrix, arranged as a hexagon and each LED with different intensity level, from the maximum to the minimum. One image, **I**, is obtained (image on the left in Fig. 1).
2. To acquire high-dynamic-range (HDR) images of the LED matrix at this configuration, using different integration times for expanding the measurement range.
3. To turn on the same six LEDs, but now sequentially, and follow the same procedure described in 1 and 2. As a result, six images are obtained.
4. To compose a ground-truth image (**GT**) from the images acquired in 3, representing the real distribution of the radiance on the source, before being affected by the PSF of the camera. This is formed by the sum of the six images after zeroing all pixels out of the emission surface in the image.

- To obtain the PSF model by optimization of empirical parameters, by convolving the **GT** image with the PSF and comparing the difference of this convolution with the **I** image.

Ghost are stray-light artefacts due to regular inter-reflections or other undesired reflections between the sensor and the lens (image in the middle in Fig. 1). To characterize this effect, it is necessary to know the relation between the position, shape and signal of the luminous source to be measured and its ghost, and relate them by an empirical model. For this purpose, this experimental procedure was followed:

- To turn on sequentially sixteen LEDs (four by row).
- To find the (x,y) positions and signals of the luminous source and the ghost for each image.
- To find a model to relate (x,y) positions and signals of the luminous source and the ghost, and its empirical parameters.

Finally, smear is the effect that occurs in CCDs when photoelectrons generated during the **readout time** are leaked and collected as if they had been collected during the **integration time**. This results in a larger signal in the pixels on the transferring columns which are irradiated (vertical image, see image on the right in Fig. 1), larger when the ratio between the **integration time** and the **readout time** is smaller. The experimental procedure followed to characterize this effect is:

- To turn on a LED with three intensities at three different integration times each one. To reduce the noise, the number of repetitions is increased as the integration time decreases, keeping approximately constant the exposure time (integration time by number of repetitions).
- To calculate the difference of a signal per pixel between the irradiated columns (with smear) and the no irradiated columns (no smear).
- To find the empirical model relating the difference calculated in 2, the integration times used in 1, and the sum of the values in the column of the pixel where the image of the source lies. A “leakage” empirical parameter is obtained from the model.

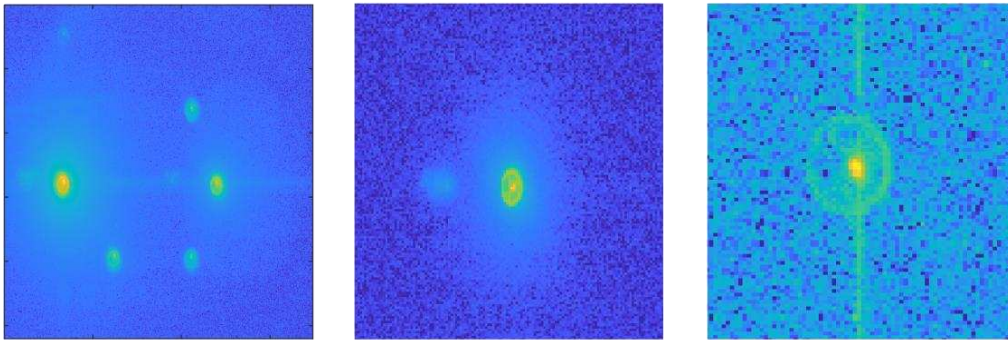


Figure 1 Images from procedures to characterize PSF (left), ghosts (center) and smear (right).

3. Conclusions

A methodology to characterize the internal stray light and smear has been evaluated. The methodology allows empirical parameters to be obtained which can be considered in the estimation of the measurement uncertainty, required to provide traceable luminance measurements with imaging systems.

Acknowledgments

This work was carried out within the joint normative research project 21NRM01 HiDyn which has received funding from the European Partnership on Metrology, co-financed from the European Union’s Horizon Europe Research and Innovation Programme and by the Participating States.

Examination of the composition of incubator solutions employed to preserve unslanted transmission holograms within photohydrogels

Belén Nieto-Rodríguez^{1,2}, Manuel G-Ramírez^{2,3}, Marta Morales-Vidal^{1,3}, José Carlos García-Vázquez^{2,3}, Tomás Lloret¹, María Isabel Lucío⁴, María-José Bañuls⁵, Ángel Maquieira⁵ and Inmaculada Pascual^{1,3}

¹Dept. de Óptica, Farmacología y Anatomía, Universidad de Alicante, Spain

²Dept. de Física, Ingeniería de Sistemas y Teoría de la Señal, Universidad de Alicante, Spain

³I. U. de Física Aplicada a las Ciencias y las Tecnologías, Universidad de Alicante, Spain

⁴I. I. de Investigación de Reconocimiento Molecular y Desarrollo Tecnológico, Univ. Pol. de Valencia, Spain

⁵Dept. de Química, Universidad Politécnica de Valencia, Spain

*E-mail: b.nieto@ua.es

1. Introduction

Holography's recent surge lies in its capacity to store detailed 3D objects in cost-effective photosensitive materials, revolutionizing fields like renewable energy and biodetection¹. With laser tech and optical systems already refined, attention shifts to enhancing holographic materials. Stability becomes paramount, especially in biosensing, where hydrogel matrices prove advantageous as binders². These 3D polymers, adept at retaining water, can be chemically tailored to alter their holographic traits based on environmental cues. This study aims to refine transmission hologram storage in photohydrogels by tweaking the photosensitive solution.

2. Experimental process

The experimental method involved preparing hydrogel matrices with acrylamide (AAm), *N,N'*-methylenebis(acrylamide) (MBA), potassium persulfate (KPS), and *N,N,N',N'*-tetramethylethylenediamine (TEMED) at room temperature. These matrices were then immersed in an incubator solution (IS) for 3 hours, converting them into photohydrogels. The IS comprised AAm, MBA, dimethyl sulfoxide (DMSO), H₂O, triethanolamine (TEA), and yellow eosin (YE). In this work all the compounds in the incubator solution will remain constant for the different IS except for varying quantities of AAm and MBA as detailed in Table 1.

Incubator solution	AAm \pm 1 (mg)	MBA \pm 1 (mg)	$(\chi_{AAm} \pm E_{\chi_{AAm}}) \times 10^2$	$(\chi_{MBA} \pm E_{\chi_{MBA}}) \times 10^3$	$\frac{\chi_{AAm}/\chi_{MBA} \pm E_{\chi_{AAm}/\chi_{MBA}}}{E_{\chi_{AAm}/\chi_{MBA}}}$
IS1	747	367	2.8 \pm 0.3	6.2 \pm 0.7	4.52 \pm 0.10
IS2	747	471	2.8 \pm 0.3	8.0 \pm 0.9	3.50 \pm 0.08
IS3	747	595	2.7 \pm 0.3	10.1 \pm 1.1	2.67 \pm 0.06
IS4	1044	1063	2.2 \pm 0.2	10.3 \pm 1.1	2.14 \pm 0.05
IS5	1660	1063	3.5 \pm 0.4	10.2 \pm 1.0	3.43 \pm 0.07
IS6	2130	1063	4.4 \pm 0.5	10.1 \pm 1.0	4.36 \pm 0.09

Table 1 Different incubator solutions (IS) as a function of AAm and MBA mole fractions.

The third step involved storing volumetric transmission holographic gratings within the photohydrogels through exposure to a 532 nm wavelength laser beam. This process ensured the photomaterial's insensitivity. Utilizing a continuous laser with a 532 nm wavelength, filtered and collimated beams maintained a 1:1 intensity ratio and a 0.35 cm diameter each. These beams were spatially overlaid on the sample at object and reference recording angles of $\theta_o = \theta_r = 18.7^\circ$ relative to normal incidence. For reconstruction, a He-Ne laser, positioned at the theoretical Bragg angle $\theta_c = 22.4^\circ$ measured diffracted and transmitted powers. Following this, a wash step with PBST buffer 10 mM pH 7.4, comprising potassium phosphate dibasic (0.8 mM), potassium phosphate monobasic (2 mM), sodium chloride (137 mM), potassium chloride (2.7 mM), and Tween-20 (0.05% v/v), removed unreacted compounds post-exposure³. Subsequently, during reconstruction after the washing step, the angle of the diffracted beam required modification due to the photohydrogels swelling in the liquid medium.

3. Results

Initially, the diffraction efficiency (DE_B) at a constant radiant exposure (H) of 365 mJ/cm^2 was investigated relative to AAm and MBA concentrations in each IS (Fig. 1a). High-performance outcomes were observed with elevated χ_{AAm}/χ_{MBA} ratios alongside high independent mole fractions. Examining the optimal incubator solution (IS6), transmission gratings within photohydrogels were studied post-wash for different radiant exposures (H). Fig. 1b illustrates increased diffraction yield post-wash for the lowest radiant exposure, contrasting with decreased yields for higher exposures.

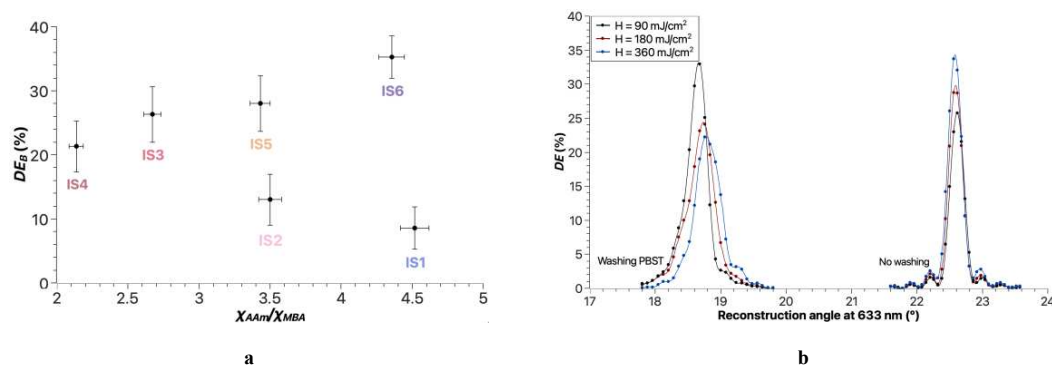


Figure 1 a. Diffraction efficiency as a function of the molar ratio of AAm and MBA for the different incubator solutions. b. Diffraction efficiency as a function of the reconstruction angle at 633 nm for IS6 solution unwashed (right) and after the washing stage (left). The line represented is a guide for the eye.

4. Conclusions

The work carried out unveils significant findings. The highest diffraction efficiency (DE) of 35.3% was achieved with IS6 at a fixed radiant exposure (365 mJ/cm^2). Among IS with identical molar ratios, greater DE correlates with higher AAm and MBA quantities. Pre-wash, higher DE was evident at elevated radiant exposures, diminishing post-wash. Conversely, lower radiant exposures showed enhanced performance after washing. These results underscore the pivotal role of optimized incubation solutions in advancing photohydrogel-based hologram storage, emphasizing the importance of material composition and processing stages in maximizing holographic performance.

Acknowledgments

This research was developed under project PID2019-106601RB-I00, AdBiHol-PID2019-110713RB-I00, and PID2021-1231240B-I00 funded by MICIU/AEI/10.13039/501100011033 and by “ERDF A way of making Europe”; under projects CIDEXG/2022/60, GRISOLIAP/2019/143, PROMETEO/2021/006, PROMETEO/2020/094 and IDIFEDER/2021/014 (co-funded by European Union through the FEDER Program) funded by Generalitat Valenciana, Spain; and under project UAFPU20-23 funded by Universidad de Alicante.

References

- [1] Yetisen, A. K.; Naydenova, I., Da Cruz Vasconcellos, F., Blyth, J., and Lowe, C. R., “Holographic sensors: Three-dimensional analyte-sensitive nanostructures and their applications,” *Chemical Reviews*, 10654–10696 (2014).
- [2] Lucío, M. I.; Cubells-Gómez, A., Maquieira, and Bañuls, M.-J., “Hydrogel-based holographic sensors and biosensors: Past, present, and future,” *Anal. Bioanal. Chem.* 414 (2), 993–1014 (2022).
- [3] Berramdane, K., G. Ramírez, M., Zezza, P., Lucío M. I., M. I., Bañuls, M.-J., Maquieira, Morales-Vidal, M., Beléndez, A., and Pascual, I., “Processing of holographic hydrogels in liquid media: A study by high-performance liquid chromatography and diffraction efficiency,” *Polymers* 14(10) (2022).

HSI assessment of radiochromic films for dosimetric evaluation

José A. Gutiérrez^{1,2}, Verónica Mieites^{1,2}, Rosa Fabregat Borrás³, Rodrigo Astudillo Olalla³, Noelia Suárez Álvarez³, Marina Gutiérrez Ruiz³, Olga M. Conde^{* 1,2,4}

1 Grupo de Ingeniería Fotónica. Universidad Cantabria, Avda. Los Castros S/N, 39006, Cantabria.

2 Instituto de Investigación Sanitaria Valdecilla (IDIVAL), 39011 Santander, Cantabria.

3 Servicio de Oncología Radioterápica. Hospital Universitario Marqués de Valdecilla, Santander.

4 Biomedical Research Networking Center—Bioengineering, Biomaterials, and Nanomedicine (CIBER-BBN), Madrid, España.

*E-mail: olga.conde@unican.es

1. Introduction

Utilizing radiochromic films such as Gafchromic® EBT for film dosimetry is widely adopted in medical physics to perform accurate quality control of the radiation field of the linear electron accelerator as well as for quality assurance of dose distribution in intensity-modulated radiation therapy patient's plans. Employing multichannel dosimetry techniques with radiochromic films has been demonstrated to offer considerable benefits compared to the use of single channel dosimetry methods [1]. This work aims to improve in the current dosimetry estimation methods with the aid of HyperSpectral Imaging (HSI) by considering the complete wavelength-dependent reflectance instead of the conventional three band approaches (red, green, blue).

2. Materials and methods

For the experiment, six calibrated radiochromic films (Gafchromic® EBT3) were irradiated at different doses (487-884 cGy) with a TrueBeam STx (Varian Medical Systems) with 6 MV photon beams without a flattening filter. For irradiation, the films were introduced into a 30x30x30 cm cube-shaped PMMA phantom at different radiation source-surface distances, depths, and field sizes (determined by the accelerator collimation system). To acquire their spectral response, the films were imaged using a custom rotating-mirror-based HSI device (~3nm spectral resolution) [2]. Principal Component Analysis (PCA) was used to combine the 100 wavelengths (448-700 nm) provided by HSI in only three principal components (PCs), for the posterior comparison with the three RGB components commonly used in conventional dosimetry estimation. The RGB reference was captured with a high-resolution scanner (Xerox WorkCentre 7120). Both the RGB reference and HSI-derived PCs were used to find a dosimetry estimate following a multi-linear fit,

$$\hat{d} = ax + by + cz + e \quad (1)$$

where (x, y, z) are the channels used (PC1, PC2, and PC3 for HSI; r, g, and b for RGB), e is the value at the origin and \hat{d} is the estimated dose.

3. Results

The main results are shown in Fig. 1. The films are comprised of a 3-layer structure (28 μm active layer in between two 125 μm matte surface clear polyester bases), which can be viewed in optical coherence tomography (OCT) images (A). The irradiated areas were either 10x10 mm² or 10x30mm², which resulted in a dataset of over 270000 spectra total, given the high spatial resolution provided by the HSI device (B), which is similar to that of the scanner (C). All the spectra (D) showcased significant peaks and valleys that cannot be seen with regular RGB imagery. There was high variance in the data, given the spectra number, therefore the first principal component PC0 explained only the 38% of the variance (E). However, using the first three PCs provided enough separation between doses (F) to correctly estimate the cGy dose with an $R^2 > 0.99$ (H), while for the RGB channels $R^2 = 0.70$ (G).

4. Conclusions

HSI systems are capable of tracking fine spectroscopic changes in the diffuse reflectance of irradiated radiochromic films used for dosimetric evaluation. HSI characterization, when combined with statistical methods for spectral dimension reduction, has demonstrated increased accuracy in dosimetric estimation.

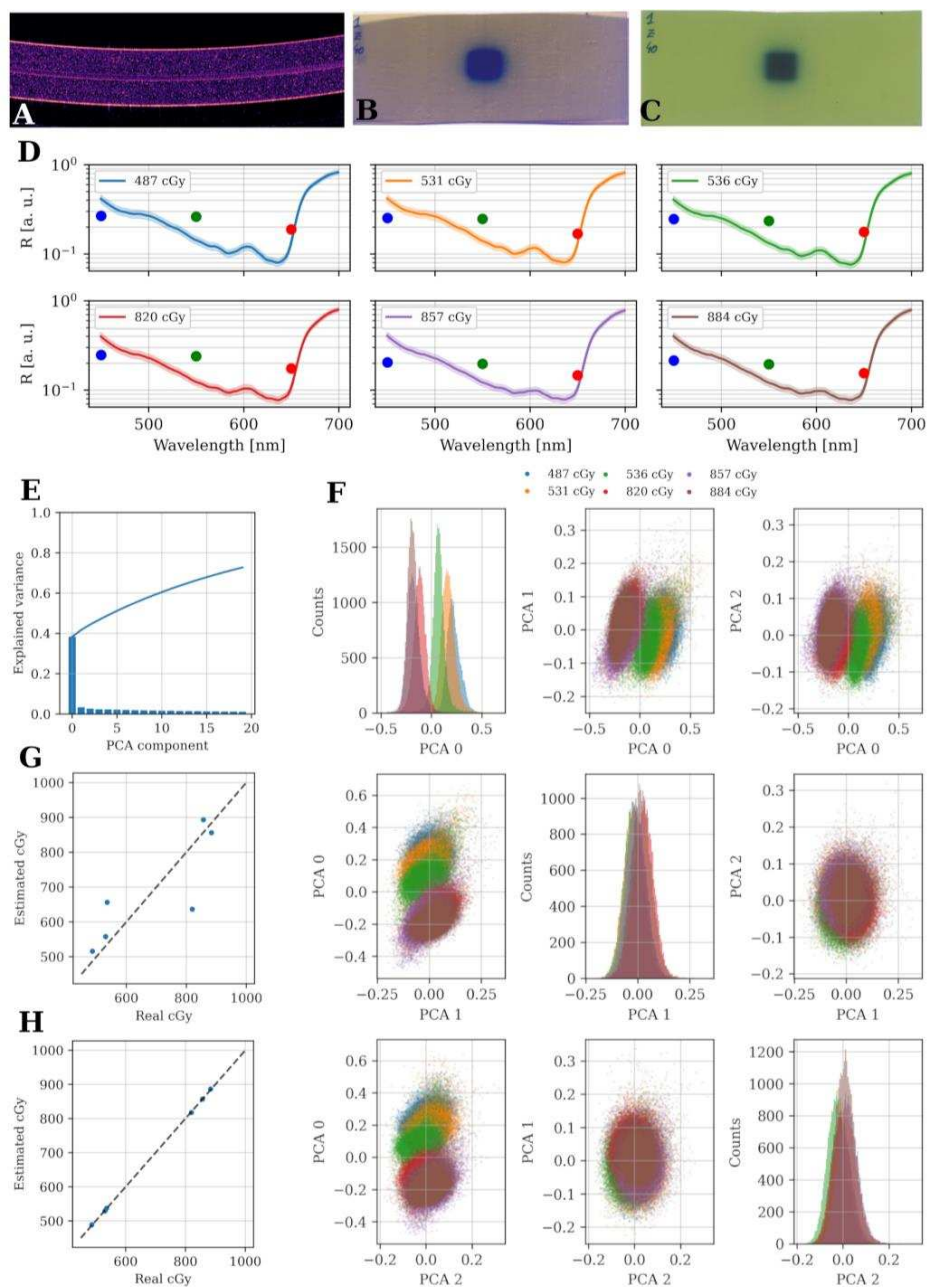


Fig. 1:(A) OCT cross section of one of the films. HSI-derived color reconstruction (B) and scanned (C) image of the same film. (D) HSI spectral average (solid lines) and standard deviation (shaded areas) of the different films. The colors indicate the dose and, the dots, the RGB equivalent obtained with the scanner. (E) Explained variance of each PC and (F) scatter plots and histograms of the first three PCs. The multi-linear fit is shown in (G) for the RGB images ($R^2=0.70$) and (H) for their HSI analogues ($R^2>0.99$).

References

- [1] Micke, M; Lewis, D.F.; Yu X. Multichannel film dosimetry with nonuniformity correction. *Medical Physics* **2011**, 38(5), 2523-2534. <https://doi.org/10.1118/1.3576105>
- [2] Gutiérrez-Gutiérrez, J.A.; Pardo, A.; Real, E.; López-Higuera, J.M.; Conde, O.M. Custom Scanning Hyperspectral Imaging System for Biomedical Applications: Modeling, Benchmarking, and Specifications. *Sensors* **2019**, 19, 1692. <https://doi.org/10.3390/s19071692>

Enhancing Agricultural Sustainability by means of Canopy Characterization based on RGB and Time-of-Flight Imaging

Laura Rey-Barroso^{1*}, Eloi Canals¹, Jordi Biscamps², Fran Garcia-Ruiz², Emilio Gil² and Fernando Díaz-Doutón¹

¹*Centre for Sensors, Instruments and Systems Development, Universitat Politècnica de Catalunya, Rambla Sant Nebridi 10, 08222 Terrassa, Spain*

²*Department of Agro Food Engineering and Biotechnology, Universitat Politècnica de Catalunya, Esteve Terradas, 8, 08860 Castelldefels, Spain*

*E-mail: laura.rey.barroso@upc.edu

1. Introduction

The agricultural sector demands innovative solutions to optimize productivity while minimizing environmental impact through the implementation of more sustainable practices. In these regards, the overdosing derived from continuous and non-selective spraying of Plant Protection Products (PPP, i.e. pesticides) in highly spatially-variable crops (vineyard, olive groves, etc.) poses significant ecological and health risks. It has been demonstrated that it is possible to optimize the PPP spraying process by measuring the structural characteristics of the canopy at each point of the plots [1]. However, manually characterizing the canopy is impractical due to its laborious and costly nature. Accordingly, various technological approaches have emerged for the automation of this task. Satellite and unmanned aerial vehicle (UAV) imagery methods [2] offer extensive coverage but limited spatial resolution, restricting the definition of PPP volume rates to only a few levels per plot. Terrestrial LiDAR provides higher resolution and excellent performance [3], but it is cost-prohibitive for the average farmer. Ultrasound technology [4] presents a more economical option but lacks comprehensive information about canopy density.

Therefore, aiming to minimize those limitations while obtaining a reliable, high-resolution, automatic, and affordable canopy characterization, a prototype of a novel near-canopy sensor has been developed. This sensor combines standard RGB imaging with a low-cost Time-of-Flight (ToF) camera. The sensor was attached to a tractor, capturing real-time, point-wise images in several vineyard plots. Subsequently, through image processing, geolocated maps of crop physical characteristics, such as height and volume of the vines, were obtained and validated through their comparison with a set of manual measurements.

2. Sensor design and calibration

The sensor consists of two standard RGB color cameras (RGB1 and RGB2), providing a 50° x 37.5° field of view (FOV) with high resolution (2064 x 1544 pixels). These cameras are tilted relative to each other by 35°, allowing RGB1 to capture images of the upper part of the plant and RGB2 of the lower part (as schematized in Figure 1). Additionally, it integrates a low-cost ToF camera aligned with RGB1, capable of providing 3D information within a 50° x 19° FOV (160 x 60 pixels) at distances of up to 7.5 m. This camera can withstand ambient illuminance conditions of up to 100 klx (sunny day).

The sensor was installed in a waterproof case with a sealed window and mounted on a tractor at a height of 1.9 m with a 10° downward tilt to scan plants in a row of vegetation, capturing images every second (while the tractor was moving at 6 km/h). A GPS was also installed for geolocating the measurements. Prior to use, distortions produced by the sensor were calibrated. Subsequently, a conversion from image positions to real-world coordinates could be conducted, by calibrating each of the 3 imaging sensors by means of a grid target with known dimensions and relative position to the system.

3. Image processing and canopy characterization

Thanks to the use of RGB cameras, high-resolution images of the plants were obtained. The vegetation was segmented in the images using different vegetation indices (transformations and combinations of the RGB channels). Additionally, the ToF camera allowed distinguishing the row of vines under evaluation from the rest of the scene. If the vine was small, the vegetation extent was determined from RGB2 segmented image (facing downwards); otherwise, the upper limit of the plant was computed from the ToF camera. The distance to the ground was then computed from calibration. The width of the vines could be estimated from the overlapping area of the RGB images from both cameras,

thanks to the mismatch effect caused by their different viewing perspectives, which depends on the distance to the sensor. A correlation function was determined to estimate width based on such disparity. Deep learning algorithms based on convolutional neural networks (CNNs) were developed for estimating vegetation density. These algorithms were trained with RGB images of vines previously classified by 3 experts.

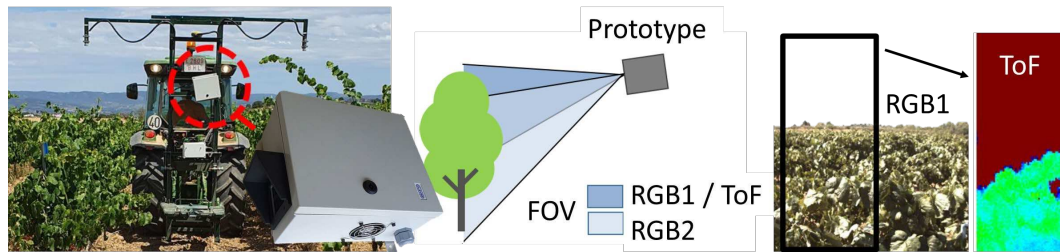


Figure 1 (Left) Sensor mounted on tractor. (Center) FOVs of RGB and ToF cameras. (Right) Images taken with RGB1 and ToF.

4. Results and conclusions

Upon obtaining these canopy structural parameters, geolocated maps with corresponding parameter values were obtained. It was also confirmed that the height and width measurements matched those taken manually in several 10 m length series (with a 2 m sampling) over different rows (Figure 2). Regarding canopy density evaluation, after training the CNN, a validation accuracy of 65% was achieved. A 51% accuracy was observed in the best case when comparing subjective classifications performed by 3 different experts. Finally, it was verified whether point-wise parameters were correlated with satellite-derived parameters.

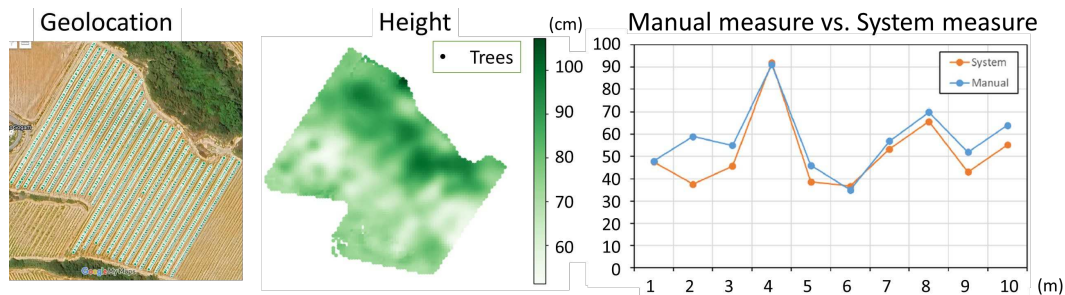


Figure 2 Geolocation of measurements, height values for every geolocated measure and comparison to manual measures (example of height determination over a 10 m series along a row).

Acknowledgments

This work is supported by European Commission's Horizon 2020 research and innovation programme through the project NOVATERRA, grant agreement number 101000554.

References

- [1] J. Campos, M. Gallart, J. Llop, P. Ortega, R. Salcedo and E. Gil, "On-Farm Evaluation of Prescription Map-Based Variable Rate Application of Pesticides in Vineyards", *Agronomy* **10**, 102 (2020).
- [2] A. Sassu, F. Gambella, L. Ghiani, L. Mercenaro, M. Caria, A.L Pazzona, "Advances in Unmanned Aerial System Remote Sensing for Precision Viticulture", *Sensors* **21**, 956 (2021).
- [3] H. Moreno and D. Andújar, "Proximal sensing for geometric characterization of vines: A review of the latest advances", *Comput. Electron. Agric.* **210**, 107901 (2023).
- [4] T. Palleja and A.J. Landers, "Real time canopy density estimation using ultrasonic envelope signals in the orchard and vineyard", *Comput. Electron. Agric.* **115**, 108-117 (2015).

Identificación de mezclas de tintas históricas mediante técnicas de unmixing espectral

Ana B. López-Baldero^{1*}, Eva M. Valero¹, Miguel Á. Martínez-Domingo¹, Anna S. Reichert², Ana López-Montes²

¹*Color Imaging Laboratory, Departamento de Óptica, Facultad de Ciencias, Universidad de Granada, Avda. Fuentenueva s/n, Granada 18071, España*

²*Departamento de Pintura, Facultad de Bellas Artes, Universidad de Granada, Granada 18014, España*

*E-mail: anabelenlb@ugr.es

1. Introducción

La identificación de tintas es esencial para cualquier estudio codicológico, ya que ayuda a la comprensión y contextualización histórica y artística de documentos antiguos. Recetas medievales sugieren que las tintas mixtas desempeñaron un papel importante en el mundo islámico, encontrando mezclas de tintas basadas en carbón y ferrogálicas desde la antigüedad. Sin embargo, detectar y clasificar este tipo de tintas sigue siendo un reto, especialmente si nos limitamos a métodos no invasivos donde la óptica tiene mucho que aportar, con técnicas como el análisis colorimétrico o la espectrofotometría[1].

Entre estos métodos, las imágenes hiperespectrales se están usando cada vez más, ya que permiten una rápida adquisición de datos, abarcando toda la superficie de la obra. Estas cámaras proporcionan el espectro de reflectancia, transmitancia o radiancia en cada píxel de la imagen, cubriendo desde el ultravioleta cercano hasta el infrarrojo de longitud de onda corta.

Aunque estas cámaras se han utilizado previamente para la identificación de tintas modernas en análisis forense[2], sólo se ha encontrado un estudio que aborde la identificación de tintas históricas[3], empleando para ello métricas de comparación espectral.

En este trabajo, se han generado distintas muestras modelo mezclando tintas puras, incluyendo ferrogálica, sepia y basada en carbón, y aplicándolas sobre dos soportes, pergamino y papel de lino y algodón. Se propone el uso de técnicas de unmixing espectral[4,5] para obtener la concentración de cada tinta pura presente en la mezcla y para identificar el soporte utilizado.

2. Material y métodos

2.1 Librería de referencia

A partir de las imágenes hiperespectrales, la librería de referencia se obtuvo promediando los píxeles de tinta pura, lápiz y soporte presentes en documentos históricos reales de diferente origen y en muestras modelo creadas bajo condiciones controladas. Se utilizaron un total de 8 clases, incluyendo tinta ferrogálica, basada en carbón (negro de humo, huesos, uva, marfil, cereza, bistro), sepia, lápiz, pergamino, papel de lino, de algodón y lino, y papel contemporáneo. Algunas tintas fueron elaboradas siguiendo recetas tradicionales, y otras fueron adquiridas de la casa comercial Kremer Pigmente GmbH.

2.2 Muestras

El unmixing espectral se aplicó a seis muestras modelo que se habían obtenido mezclando las tintas ferrogálica, sepia y negro de huesos por parejas en una proporción 1:1, siendo aplicadas sobre pergamino y papel de lino y algodón.

2.3 Captura hiperespectral

La captura espectral se realizó con dos cámaras de la casa comercial Resonon Ltd., acopladas a una plataforma de movimiento lineal: la Pika L (380-1080 nm), y la Pika IR+ (888-1732 nm). Para trabajar con el espectro completo se concatenó la información de ambas, obteniendo todo el rango desde 400 hasta 1700 nm en intervalos de 5 nm mediante interpolación.

2.4 Modelo de unmixing e identificación de tintas

El modelo de unmixing utilizado fue el sustractivo, ya que había proporcionado mejores resultados en estudios previos[4,5]. Para la función de coste de la optimización, se utilizó una métrica combinada de

cGFC y RMSE[5]. Se evaluaron los resultados del unmixing mediante mapas de error (RMSE, cGFC, ΔE_{00}) La identificación de tintas se realizó mediante la evaluación visual de los mapas de concentración obtenidos y el cálculo del porcentaje de píxeles detectados para cada clase.

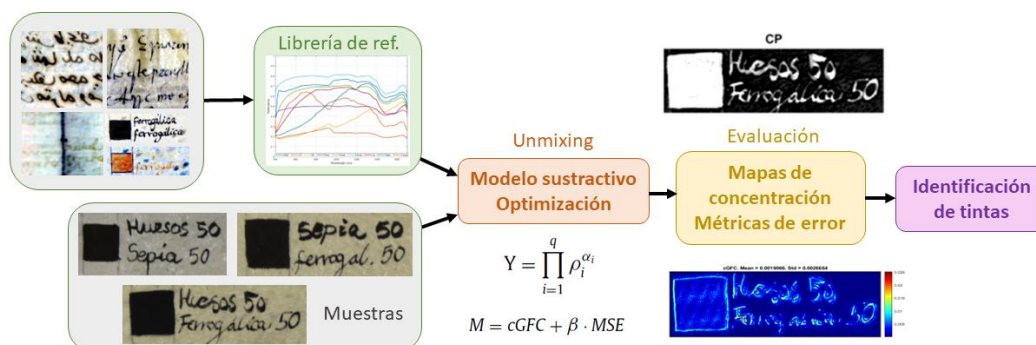


Figura 1. Flujo de trabajo.

3. Resultados

En la Figura 2 se muestran los mapas de concentración obtenidos para una de las muestras estudiadas.

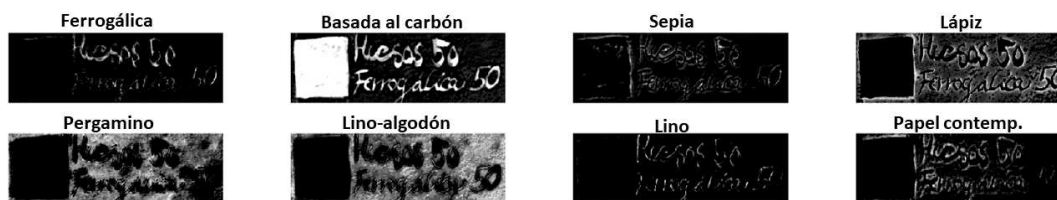


Figura 2. Mapas de concentración para la muestra de ferrogálica y negro de huesos aplicada en pergamino.

Podemos observar que se detecta una mayor cantidad de tinta basada en carbón (negro de humo), tanto en la zona del cuadrado como en los trazos. También encontramos una pequeña cantidad de tinta ferrogálica en los trazos. Una característica que diferencia la tinta ferrogálica de las basadas en carbón es que esta se vuelve casi transparente a partir de los 1000 nm, mientras que las basadas en carbón siguen absorbiendo la mayor parte de la radiación infrarroja. Al mezclar estos dos tipos de tinta, la reflectancia disminuye considerablemente en todas las longitudes de onda, lo que hace que el espectro resultante sea más similar a la tinta basada en carbón, dificultando la detección de ferrogálica. Respecto al soporte, encontramos dificultad para diferenciar entre el pergamino y el papel de lino y algodón.

Agradecimientos

Este trabajo ha sido financiado por MCIN/AEI/10.13039/501100011033 y por FEDER, UE [proyecto PID2021-124446NB-I00], y por el Ministerio de Universidades (España) [FPU2020-05532].

Referencias

- [1] I. Rabin, "Material Studies of Historic Inks: Transition from Carbon to Iron-Gall Inks" in *Traces of ink* (70-78, Brill, 2021).
- [2] A. U. Islam, M. J. Khan, M. Asad, et al., "iVision HHID: Handwritten hyperspectral images dataset for benchmarking hyperspectral imaging-based document forensic analysis" Data in Brief 41, 107964 (2022).
- [3] A. B. López-Baldomero, M. A. Martínez-Domingo, E. M. Valero, et al., "Selection of optimal spectral metrics for classification of inks in historical documents using hyperspectral imaging data", in *Optics for Arts, Architecture, and Archaeology (O3A) IX* (2023), vol. 12620, 99-111.
- [4] F. Grillini, J. B. Thomas and S. George, "Comparison of Imaging Models for Spectral Unmixing in Oil Painting," *Sensors* 21(7), 2471 (2021).
- [5] E. M. Valero, M. A. Martínez-Domingo, A. B. López-Baldomero, et al., "Unmixing and pigment identification using visible and short-wavelength infrared: Reflectance vs logarithm reflectance hyperspaces," *J. Cult. Herit.*, 64, 290-300 (2023).

RESÚMENES/ABSTRACTS

Sesiones Orales

Nanofotónica



Perfect absorption with spectrally overlapped electric and magnetic lattice resonances

Luis Cerdán^{1*}, Juan Ramón Deop-Ruano², Juan José Alvarez-Serrano² and Alejandro Manjavacas²

¹*Instituto de Química-Física Blas Cabrera (IQF-CSIC), Consejo Superior de Investigaciones Científicas, Spain*

²*Instituto de Óptica (IO-CSIC), Consejo Superior de Investigaciones Científicas, Spain*

*E-mail: l.cerdan@csic.es

1. Introduction

When metallic nanostructures are arranged in a periodic array, their localized plasmons can interact coherently to generate collective, strong, and spectrally narrow electromagnetic modes known as lattice resonances (LRs) [1]. However, 2D arrays supporting LR in which only electric or magnetic dipoles are involved can absorb at most half of the incident power [2]. One approach to obtaining perfect absorption consists in spectrally overlapping the LR with a localized mode of the individual constituents of the array with different parity, in what is regarded as a generalized Kerker effect [3]. However, the overlapping wavelength cannot be easily modified, since the spectral position of the localized mode can only be changed by modifying the polarizability of the nanostructures, which, in turn, modifies the properties of the LR. Here, we report a novel approach to attain perfect absorption based on the spectral overlap of two different LR [4]. Our approach relies on the use of a bipartite rectangular array with a unit cell composed of both metallic and dielectric nanostructures. Their proper arrangement leads to the emergence of independent dipolar electric and magnetic LR, which we denote as ED-LR and MD-LR, respectively. We exploit the semi-analytic nature of a coupled dipole model (CDM) to find beforehand the optimal nanostructure disposition and to assess and dissect the optical response of the system.

2. System and model

As depicted in Fig. 1a, we consider a bipartite periodic rectangular array with periods $a_x = 654$ nm and $a_y = 649$ nm. The unit cell contains a nanoparticle (NP) of gold, with diameter $D_1 = 98$ nm, located in the origin ($x_l=0, y_l=0$), and a NP of silicon, with diameter $D_2 = 140$ nm, placed at the center of the unit cell ($x_l=a_x/2, y_l=a_y/2$). We use gold and silicon NPs because the metallic nature of the former results in a strong electric dipole resonance, which can be the source of ED-LRs, whereas the high-refractive-index dielectric nature of silicon produces both electric and magnetic dipole resonances, potentially leading to both ED- and MD-LRs. The array is located in the xy -plane, surrounded by vacuum, and excited at normal incidence by an electromagnetic plane wave polarized along the x -axis. Given that the sizes of the NPs are significantly smaller than both the periods and excitation wavelength λ , we can describe its optical response using the well-established CDM [5]. In it, the optical properties of the LR can be determined from the analysis of the following eigenvalue problem [5]:

$$\begin{pmatrix} \mathbf{p}_i \\ \mathbf{m}_i \end{pmatrix} = \sum_{j=1}^2 \begin{pmatrix} \alpha_i^{EE} \mathbb{I}_{3 \times 3} & 0 \\ 0 & \alpha_i^{MM} \mathbb{I}_{3 \times 3} \end{pmatrix} \begin{pmatrix} \mathcal{G}_{ij}^{EE} & \mathcal{G}_{ij}^{EM} \\ \mathcal{G}_{ij}^{ME} & \mathcal{G}_{ij}^{MM} \end{pmatrix} \begin{pmatrix} \mathbf{p}_j \\ \mathbf{m}_j \end{pmatrix},$$

with \mathbf{p}_i and \mathbf{m}_i being the electric and magnetic dipoles induced in the i -th particle of the unit cell, α_i the corresponding polarizability, and \mathcal{G}_{ij} the different components of the lattice sum (i.e., Fourier transform of the dipole-dipole interaction tensor). This quantity contains all the information regarding the interaction between the elements of the array. In particular, \mathcal{G}_{21}^{EM} describes the electric-magnetic (EM) coupling between the two monopartite arrays.

3. Optical response analysis

Since we aim to independently tune the ED-LR and MD-LR, we must locate the two NPs so that the lattice sum terms \mathcal{G}_{21}^{EM} , accounting for the EM coupling, vanish. This is accomplished by placing one NP at the origin of the unit cell and the other one at its center (Fig. 1b). In addition, for this configuration, \mathcal{G}_{21}^{EE} is

maximized in absolute terms. Thus, the bipartite array should support a single ED-LR resulting from the hybridization of the ED-LRs supported by the two monopartite arrays, and a single MD-LR, solely supported by the silicon monopartite array. Furthermore, under this configuration, the spectral position of the MD-LR and ED-LR should be governed by a_x and a_y , respectively. Thus, by properly choosing a_x and a_y , the two LR can be made to overlap. All these predictions are confirmed in Fig. 1c-d, where we show that, with our array geometrical parameters, we can attain a LR with perfect absorption and a quality factor $Q = 2.4 \times 10^3$. Furthermore, the electric and magnetic dipoles contribute each with half the absorption (Fig. 1c). Finally, each monopartite array absorbs nearly half the incident light, with the silicon one absorbing marginally stronger, as it contributes to both the ED- and MD-LRs (Fig. 1d). Our results provide clear, yet general, guidelines for the rational design of complex 2D arrays capable of sustaining LR with perfect absorption, thus leveraging its potential for applications requiring an efficient absorption of light.

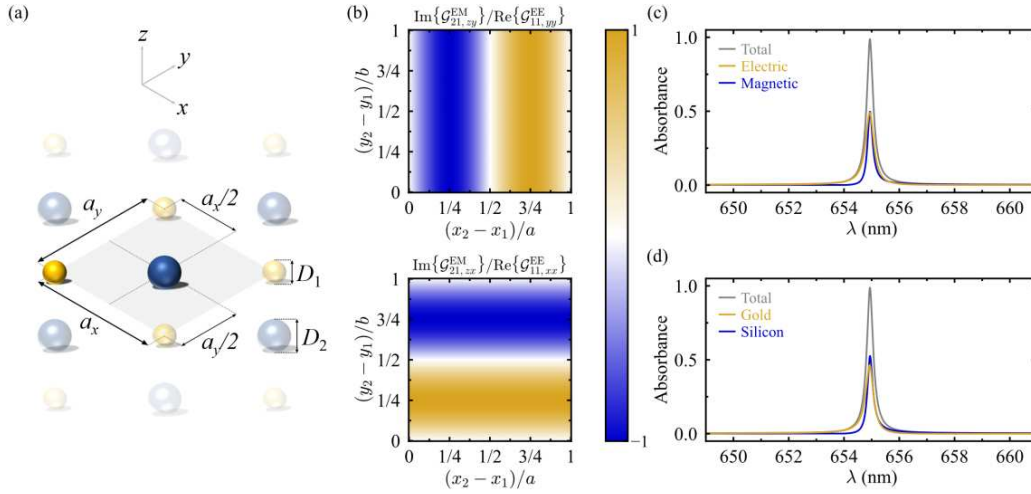


Figure 1: a) Schematics of a bipartite rectangular 2D array built from gold and silicon nanospheres. b) Relevant Electric-Magnetic (EM) coupling terms of the lattice sum \mathcal{G}_{21} , as a function of the relative position of particle 2 with respect to particle 1. c-d) Absorbance spectra for the bipartite array, along with the explicit contributions of electric and magnetic dipoles (c), and the contributions of the gold and the silicon nanoparticles (d).

Acknowledgments

This work was supported by grants PID2022-137569NB-C42 and PID2019-109502GA-I00 funded by MCIN/AEI/10.13039/501100011033/FEDER,EU, and a 2022 Leonardo Grant for Researchers in Physics from the BBVA Foundation. L.C. acknowledges support from a Ramón y Cajal Research Fellowship, Grant RYC2022-038362-I, funded by MCIN/AEI/10.13039/501100011033 and by the European Social Fund Plus (ESF+). J.R.D-R. acknowledges support from a predoctoral fellowship from the MCIN/AEI assigned to Grant no. PID2019-109502GA-I00. J.J.A.S. acknowledges support from an Erasmus Mundus fellowship and a JAEINTRO fellowship from CSIC (JAEINT-23-EX-0157).

References

- [1] V.G. Kravets, A.V. Kabashin, W.L. Barnes, and A.N. Grigorenko, “Plasmonic surface lattice resonances: A review of properties and applications”, *Chem. Rev.* **118**, 912-9591 (2018)
- [2] R. Alaei, M. Albooyeh, and C. Rockstuhl, “Theory of metasurface based perfect absorbers”, *J. Phys.*, **50**, 503002 (2017)
- [3] V. E. Babicheva, and A. B. Evlyukhin, “Resonant Lattice Kerker Effect in Metasurfaces With Electric and Magnetic Optical Responses”, *Laser Photon. Rev.*, **11**, 1700132 (2017)
- [4] L. Cerdán, J. R. Deop-Ruano, J. J. Alvarez-Serrano, and A. Manjavacas, “Perfect Absorption with Independent Electric and Magnetic Lattice Resonances in Metallo-Dielectric Arrays”, *Adv. Opt. Mater.* 2302737 (2024)
- [5] S. Baur, S. Sanders, and A. Manjavacas, “Hybridization of lattice resonances”, *ACS Nano* **12**, 1618-1629 (2018)

Normal Incidence Excitation of Out-of-Plane Lattice Resonances

J.J. Alvarez-Serrano^{1*}, J.R. Deop-Ruano¹, V. Aglieri², A. Toma² and A. Manjavacas¹

¹*Instituto de Óptica “Daza de Valdés” (IO-CSIC), Consejo Superior de Investigaciones Científicas, 28006, Madrid, Spain.*

²*Istituto Italiano di Tecnologia, via Morego 30, 16163, Genova, Italy.*

*juanjose.alvarez@io.cfmac.csic.es

1. Abstract

Two-dimensional periodic arrays of nanostructures support collective modes known as lattice resonances, arising from the coherent interaction between their constituents [1]. In particular, **out-of-plane lattice resonances** correspond to those modes for which the nanoparticles are polarized in the direction orthogonal to the plane of the array, showcasing remarkable optical properties such as minimal losses, extremely high Q-factors and significant field enhancements [2]. Consequently, this type of resonances is ideally suited for applications in nano-lasing and biosensing.

Given their potential, an efficient excitation of out-of-plane lattice resonances holds paramount importance. Previous research efforts have relied on oblique incidence [3], which not only degrades the properties and quality of the resonance, but also introduces experimental complexities. Excitation under normal incidence could address many shortcomings of conventional approaches, though this avenue has been traditionally disregarded in light of the transversality condition of the electromagnetic field.

In our work, we propose a novel methodology to achieve **efficient excitation of out-of-plane lattice resonances in bipartite arrays at normal incidence** [4]. We demonstrate that, by leveraging the electric-magnetic interaction between the constituents of the array, it is possible to attain sharp out-of-plane lattice resonances with exceptional Q-factors (Fig. 1). Unlike traditional studies that solely focused on the dominant electric interaction, our approach also considers the magnetic response of the system, underscoring its criticality for effectively exciting out-of-plane modes. In addition, our study also evaluates the impact of the relative position of the particles within the unit cell and the polarization of the incident field.

Our theoretical analysis relies on a rigorous coupled dipole model, in excellent agreement with full solutions of Maxwell’s Equations. Starting from the study of a bipartite square lattice, composed of metallic nanospheres, our investigation draws conclusions that are general and applicable to more complex array geometries and particle shapes. Moreover, we examine a potential application of our findings, considering the utilization of a nanodisk array integrated with both a substrate and a coating (Fig. 2).

In this context, our investigation introduces a pioneering approach to excite out-of-plane lattice resonances at normal incidence with great efficacy, opening avenues for leveraging their properties across a myriad of applications.

2. Figures

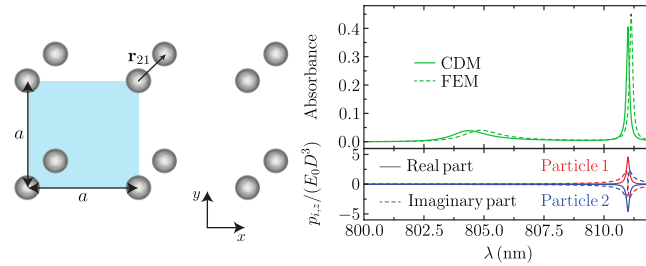


Figure 1: Optical response of a square array of silver nanoparticles, located in the XY plane with relative position $r = (1,1,0)a/4$. For this configuration, the out-of-plane induced dipole presents a resonance at around 811 nm, which coincides with the spectral position where the absorbance displays a sharp lattice resonance. This indicates its out-of-plane nature.

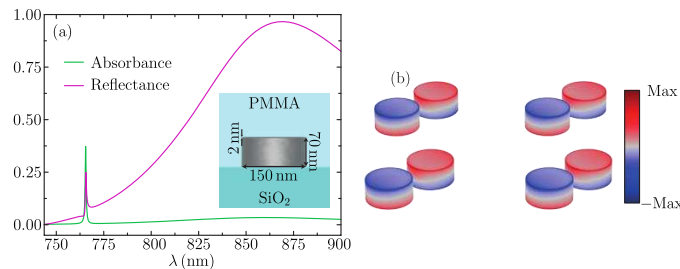


Figure 2: (a) Absorbance and Reflectance spectrum for a square array of silver nanodisks, over a substrate of silica and covered with a PMMA coating. As visible in the figure, an out-of-plane lattice resonance appears around 770 nm. (b) Density of charge induced in the nanodisks.

3. Conclusions

Our study introduces a novel approach for the efficient excitation of out-of-plane lattice resonances at normal incidence in bipartite arrays of metallic nanostructures. Our method leverages the electric-magnetic interaction between the nanostructures, which give rise to sharp resonances with high quality factors, and proves to be a formalism applicable to arrays made of atoms or dielectric nanostructures, as well as complex array geometries and particle shapes.

Acknowledgments

Our investigation was sponsored by a 2022 Leonardo Grant for Researchers in Physics from the BBVA Foundation. We also acknowledge support from the grants PID2022-137569NB-C42 and PID2019-109502GA-I00 funded by MCIN/AEI/10.13039/501100011033 together with a predoctoral fellowship from MCIN/AEI assigned to Grant No. PID2019-109502GA-I00, a JAE-Intro fellowship from CSIC (JAEINT-23-EX-0157) and an Erasmus Mundus fellowship (2018-1456-EUROPHOTONICS-Project 599098-EPP-1-2018-1-FR-EPPKA1-JMD-MOB).

References

- [1] García de Abajo, F. J. Colloquium: “Light scattering by particle and hole arrays”, *Rev. Mod. Phys.* **79**, 1267-1290 (2007).
- [2] L. Zundel, A. Cuartero-González, S. Sanders, A. I. Fernández-Domínguez and A. Manjavacas, “Green tensor analysis of lattice resonances in periodic arrays of nanoparticles”, *ACS Photonics*, **9**, 540-550 (2022).
- [3] Y. Hua, A. K. Fumani and T. W. Odom, “Tunable lattice plasmon resonances in 1D nanogratings”, *ACS Photonics*, **6**, 322-326 (2019).
- [4] J. J. Alvarez-Serrano, J. R. Deop-Ruano, V. Aglieri, A. Toma, and A. Manjavacas, “Normal Incidence Excitation of Out-of-Plane Lattice Resonances in Bipartite Arrays of Metallic Nanostructures”, *ACS Photonics*, **11**, 1, 301–309, (2024).

Recent activity of the Optics Group (U. Cantabria) in nanophotonics and related areas

J.M. Saiz*, F. Moreno, F. González, D. Ortiz, P. Albella, A. Franco, Y. Gutiérrez, G. Santos, J. González-Colsa, S. Rosales, G. Serrera

Departamento de Física Aplicada, Universidad de Cantabria, Av Los Castros, Santander, SPAIN

*E-mail: saizvj@unican.es

1. Objective

In recent years, the UC Optics Group has worked on several lines related to the field of nanophotonics through a series of well-differentiated projects. In this presentation we intend to review this activity, including some of its most representative references.

2. Research Lines

First of all, we must cite the results obtained within the European PHEMTRONICS Project, in which the changes in the properties of the so-called PCMs (Phase Change Materials) have been investigated, materials whose optical properties can be modified in a controlled way through external stimuli, such as the application of electrical fields or thermal stimuli [1]. These materials play an important role in “reconfigurable” photonics, which focuses on the design and development of optical devices whose response can be dynamically adjusted to adapt to different applications or operating conditions. Several reconfigurable optical devices have been designed: dynamic reflective pixels [2], tunable band plasmonic photodetectors [3], metasurfaces with dynamic control of the scattered light [4], and optical switches [5].

Secondly, we must mention the projects in the field of thermoplasmonics. Some nanostructures can, under pulsed illumination, become efficient local heat sources, with high spatial and temporal resolution. The following two problems have been addressed, among others: i) the search for optimal particles, made of biocompatible materials, in terms of size and shape, for their eventual application in photothermal therapies [6], ii) the exploration of directionality in the heat delivery and iii) the study of the heat transfer mechanisms from the small volume in which the dissipation is produced. The latter is especially complex in the pulsed illumination regime, where the interfacial thermal conductance (ITC) acquires special importance [7] and the role of convection and radiation must be re-examined.

Another research topic that deserves attention, is the study of the interaction of light with chiral media, and the possibility of developing chiral sensors based on the generation of plasmonic resonances. In particular, the combination of high refractive index dielectric media (HRID) with metals has been investigated, so that the hot-spots of the electric and magnetic fields in the resonances of both materials amplify the chiro-optical response of a medium. Recently, the anapolar modes of one of these hybrid structures have been investigated, which allow great local confinement of energy, enabling the transfer of the chiral response to the nonlinear regime [8].

The fourth line to highlight is the experimental development of biosensors based on extraordinary optical transmission (EOT), consisting of gold films with nanoholes, which allow analyzing the spectral response of biological material. The EOT is very sensitive to changes in the refractive index of the material in contact with the nanostructure, which serves, for example, to discriminate cancerous and healthy material. The system has been successfully tested in the identification of different cancer cell lines [9], and discrimination of glioblastoma tumor tissue from peritumoral tissue [10]. In addition, the optical system has been useful to identify the cellular actin cortex and the extracellular matrix as key biomarkers in the discrimination of biological material and to study the proliferation and invasiveness dynamics characteristic of cancer cells [11].

Finally, it is worth mentioning other works framed in lines of research complementary to the previous ones. One of them is the development of a low-noise dynamic imaging polarimeter, adapted to a microscope (that is, capable of obtaining Mueller Matrices with micrometric spatial resolution). With this technique, it has been possible to evaluate the effects of treatments on cancer cells by measuring the

circular diattenuation generally located in their membranes. Another recent work consists of the adaptation of a polarimeter for the characterization of layers on surfaces by ellipsometry. Finally, in terms of computational tools, the development of a Monte-Carlo type model of light transport in a dense media, for simulation of diffuse spectral reflectance/transmittance [12], and the development of a chiral model of the discrete dipole approximation, or C-DDA, for the calculation of the light-matter interaction in the chiral case [13].

Acknowledgments

We would like to acknowledge the funding obtained through the H2020 Future and Emerging Technologies projects (899598 – PHEMTRONICS), and the PGC, State Research Agency. (PID2022-139560NB-I00 – MOPHOSYS)

References

- [1] Y. Gutiérrez, (+22 co-authors) “*Interlaboratory study on Sb₂S₃ interplay between structure, dielectric function, and amorphous-to-crystalline phase change for photonics*”, *IScience* **25**, N.6, 104377-104403 (2022)
- [2] G. Santos, F. González, D. Ortiz, J. M. Saiz, M. Losurdo, Y. Gutiérrez, F. Moreno, “*Design of Switchable On/Off Subpixels for Primary Color Generation Based on Molybdenum Oxide Gratings*”, *Physics* **3**, N.3, 655-663, (2021).
- [3] G. Santos, M. Georghe, C. Cobianu, M. Modreanu, M. Losurdo, Y. Gutiérrez, F. Moreno. “*Plasmonic hot-electron reconfigurable photodetector based on phase-change material Sb₂S₃*”. *Opt. Express* **30**, 38953–38965 (2022).
- [4] G. Santos, M. Losurdo, F. Moreno, Y. Gutiérrez, “*Directional scattering switching from an all-dielectric phase change metasurface*”; *Nanomaterials* **13**, N.3, 496-507 (2023)
- [5] D. Pérez-Francés, G. Santos, J. Resl, M. Losurdo, Y. Gutiérrez, F. Moreno. “*Sb₂S₃-based optical switch exploiting the Brewster angle phenomenon*” [Inv]. *Opt. Mater. Express* **13**, 3677–3687 (2023).
- [6] J. González-Colsa, G. Serrera, J. M. Saiz, D. Ortiz, F. González, F. Bresme, F. Moreno, P. Albella,, “*Gold nanodoughnut as an outstanding nanoheater for photothermal applications*”, *Opt. Exp.* **30**, N.1, 125–137 (2022).
- [7] J. González-Colsa, F. Bresme P.Albella, “*Impact of the Interfacial Thermal Conductance on the Thermoplasmonic Response of Metal/Polymer Hybrid Nanoparticles under Nanosecond Pulsed Illumination*”, *J. Phys. Chem C* **127**, 19152–19158 (2023).
- [8] G. Serrera, J. González-Colsa P. Albella, “*Amplified linear and nonlinear chiral sensing assisted by anapole modes in hybrid metasurfaces*”, *ArXiv* (2024)
- [9] A. Franco, V. Vidal, M. Gómez, O. Gutiérrez, M. Martino, F. González, F. Moreno, J.L. Fernández-Luna, “*A label-free optical system with a nanohole array biosensor for discriminating live single cancer cells from normal cells*”, *Nanophotonics* **11**, 315-328 (2022).
- [10] V. García-Milán, A. Franco, M.E. Zvezdanova, S. Marcos, R. Martín-Laez, F. Moreno, C. Velasquez, J.L. Fernández-Luna, “*Discriminating glioblastoma from peritumoral tissue by a nanohole array-based optical and label-free biosensor*”, *Biosensors* **13**, 591 (2023).
- [11] M. Carcelen, V. Vidal, A. Franco, A. M. Gomez, F. Moreno, J. L. Fernandez-Luna, “*Plasmonic Biosensing for Label-Free Detection of Two Hallmarks of Cancer Cells: Cell-Matrix Interaction and Cell Division*”. *Biosensors* **12**, 674 (2022)
- [12] R. Alcaraz de la Osa, I. Iparragirre, D. Ortiz J.M. Saiz, *The extended Kubelka–Munk theory and its application to spectroscopy*, *ChemTexts* **6**, 1-14 (2020)
- [13] S.A Rosales, P.Albella, F. González, Y. Gutiérrez F. Moreno, *CDDA: extension and analysis of the discrete dipole approximation for chiral systems*. *Opt. Exp.* **29**, N.19, 30020-30034 (2021)

Superchiral light emerging from quasi-Bound States in the Continuum in Si nanorod dimer metasurfaces

Jose Luis Pura^{1,2}, Beatriz Castillo López de Larrinzar^{3*}, Minpeng Liang^{4,5}, Antonio García-Martín³, Jaime Gómez-Rivas^{4,5}, and José A. Sánchez-Gil¹

¹*Instituto de Estructura de la Materia (IEM), Consejo Superior de Investigaciones Científicas, Serrano 121, 28006 Madrid, Spain*

²*GdS-Optronlab, Física de la Materia Condensada, Universidad de Valladolid, Paseo de Bel en 19, 47011 Valladolid, Spain.*

³*Instituto de Micro y Nanotecnología IMN-CNM, CSIC, CEI UAM+CSIC, Isaac Newton 8, Tres Cantos, 28760 Madrid, Spain*

⁴*Department of Applied Physics and Science Education and Eindhoven Hendrik Casimir Institute, Eindhoven University of Technology, P.O. Box 513, 5600 MB Eindhoven, The Netherlands.*

⁵*Institute for Complex Molecular Systems-ICMS, Eindhoven University of Technology, P.O. Box 513, 5612 AJ, Eindhoven, The Netherlands, institution, address*

*E-mail: beatriz.castillo@csic

1. Introduction

Bound states in the continuum (BICs) in all-dielectric metasurfaces enhance light-matter interaction at the nanoscale due to their infinite Q factors and strong confinement [1]. Among a variety of phenomena already reported, it has been recently shown that BICs may enhance the chiral response of metasurfaces and chiral emission through chiral q-BICs can be achieved [2]. Therefore, their impact on chiral light has attracted great interest. Objects are considered to present intrinsic chirality when they cannot be superimposed with their mirror image.

In this work, we investigate the emergence of intrinsic and extrinsic optical chirality [3] associated with the excitation of BICs in various metasurfaces made of Si nanorod dimers on a silica substrate, comparing three cases: parallel (neutral), shifted, and slanted dimers, with/without index-matching superstrate. We analyze both the circular dichroism (CD) of the far-field (FF) interaction and the helicity of the near-field (NF) distribution. We show that the best approach to achieve chiral response in FF based on extrinsic chirality is to exploit quasi-BICs appearing in the case of slanted nanorod dimers. By contrast, the helicity density is enhanced in the case of shifted dimers, as it presents intrinsic chirality, with values two orders of magnitude larger than those of circularly polarized plane waves. These so-called superchiral electromagnetic fields - defined as an electromagnetic field whose chirality (helicity density) is higher than that of free-standing monochromatic circularly polarized - concentrated at the nanoscale within the metasurface hold promise of appealing implications in phenomena such as strong-coupling, photoluminescence emission, or other local light-matter interactions.

2. Methodology

The metasurfaces (MSs) are studied by two complementary approaches: quasi-analytic calculation with a coupled electric-magnetic dipole (CEMD) model [4,5], and full numerical calculations through COMSOL Multiphysics. We have presented an analysis of the chiral behavior of BICs supported by MSs based on poly-Si rod pairs in the visible range. We analyzed the circular dichroism (CD) of the far-field (FF) interaction, as well as the helicity of the near-field (NF) distribution for different configurations.

3. Conclusions

Our analysis explored chiral behavior in bound states in the continuum (BICs) on poly-Si metasurfaces, revealing optimal configurations for achieving high circular dichroism (CD) and helicity density. We demonstrated that mixing orthogonal field components leads to quasi-BICs, ideal for extrinsic chirality in

far-field (FF) interactions, while C2 symmetric systems with no mirror planes exhibit intrinsic chirality, enhancing near-field (NF) interactions. By breaking z-axis symmetry, we achieved local intrinsic chirality without compromising BIC properties, offering opportunities for manipulating and enhancing chiral electromagnetic fields at the nanoscale for applications in FF and NF regimes such as filters, polarizers, and chiral light-matter interactions.

References

- [1] D C Marinica, Andrei G. Borisov, and S V Shabanov. Bound States in the Continuum in Photonics. *Phys. Rev. Lett.*, 100(18):183902, May 2008.
- [2] Diego R. Abujetas, Niels van Hoof, Stan ter Huurne, Jaime Gómez Rivas, and José A. Sánchez-Gil. Spectral and temporal evidence of robust photonic bound states in the continuum on terahertz metasurfaces. *Optica*, 6(8):996, Aug 2019
- [3] Jose Luis Pura, Ruhinda Kabonire, Diego R. Abujetas, and José A. Sánchez-Gil. Tailoring Polarization Conversion in Achiral All-Dielectric Metasurfaces by Using Quasi-Bound States in the Continuum. *Nanomaterials*, 12(13):2252, Jun 2022.
- [4] Diego R. Abujetas, Ángela I. Barreda, Fernando Moreno, Juan J. Sáenz, Amelie Litman, Jean-Michel Geffrin, and José A. Sánchez-Gil. Brewster quasi bound states in the continuum in all-dielectric metasurfaces from single magnetic-dipole resonance meta-atoms. *Sci. rep.*, 9(1):16048, Dec 2019
- [5] Beatriz Castillo López de Larrinzar, Norberto Daniel Lanzillotti-Kimura, and Antonio García-Martín. Interaction effects in chiral acoustoplasmonic nanostructures. *Proceedings of SPIE*, Paper Number 12991-32, Submitted 2024
- [6] Jose Luis Pura, Beatriz Castillo López de Larrinzar, Minpeng Liang , Antonio García-Martín, Jaime Gómez-Rivas , and José A. Sánchez-Gil. Superchiral light emerging from quasi-Bound States in the Continuum in Si nanorod dimer metasurfaces. Submitted 2024

Plasmonic nanostructured biosensor for discriminating glioblastoma tumor from normal tissue

Alfredo Franco^{1*}, Dolores Ortiz¹, Carlos Velásquez^{2,4}, Víctor García-Milán², Sara Marcos³, Rubén Martín-Laez², Fernando Moreno¹, José L. Fernández-Luna⁵

¹*Applied Physics Department, University of Cantabria, 39005 Santander, Spain*

²*Neurological Surgery and Spine Unit, Hospital Universitario Marqués de Valdecilla, 39008 Santander, Spain*

³*Pathology Unit, Hospital Universitario Marqués de Valdecilla, 39008 Santander, Spain*

⁴*Anatomy and Cell Biology Department, University of Cantabria, 39005 Santander, Spain*

⁵*Genetics Unit, Hospital Universitario Marqués de Valdecilla, 39008 Santander, Spain*

*E-mail: alfredo.franco@unican.es

The identification of the tumor margins and their distinction from the surrounding parenchyma are key for the surgical treatment of glioblastoma. A simple, fast, and label-free optical technique for discriminating glioblastoma from peritumoral tissue is of great value in clinical settings. We present a plasmonic-based optical technique that potentially could meet these criteria to analyze the tumoral borders in glioblastoma surgeries in real time and in a minimal invasive way. As proof of concept, we use a system (Fig. 1) consisting of an upright optical microscope to measure the spectral response from samples in contact with a plasmonic biosensor [1]. The biosensor consists of nanoholes (diameter: 220 nm) distributed along a gold film (thickness: 60 nm) forming a square array (periodicity: 550 nm).

Changes in the spectral transmission response of the biosensor to the presence on its surface of extracellular matrix from tumor and peritumoral tissue are influenced by the refractive index of the extracellular matrix [2]. The biosensor enables the determination of the extracellular matrix refractive index within the penetration depth of the surface plasmon field in circular regions of 40 microns in diameter. This optical system shows sensitivity and specificity rates around 80% discriminating between glioblastoma tumor and peritumoral tissue [2], such values are in accordance with the performance of this system discriminating normal colon epithelial cells from colorectal cancer cells from surgical specimens [3] and determining the proliferation and invasiveness of cultured cancer cells [4].

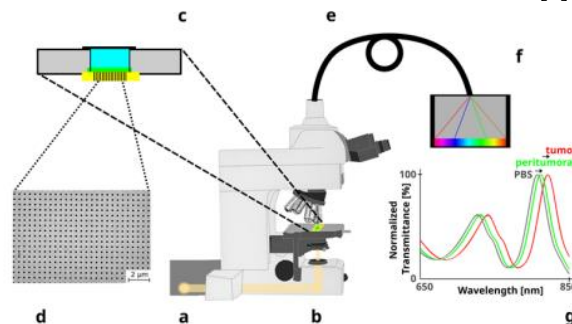


Figure 1 Main parts of the plasmonic biosensor system. (a) Halogen lamp as source of light. (b) Adapted upright microscope. (c) Sample holder with the biosensor (in yellow with vertical lines) at the bottom of a well that is filled with saline buffer during the measurements. (d) Scanning electron micrograph of the nanostructured gold film. (e) Optical fiber.

(f) Spectrophotometer. (g) Representative spectral shift due to optical differences between glioblastoma tumors and peritumoral tissues. As a background reference, the spectrum of phosphate buffered saline (PBS) is also included. [2]

The discriminative capacity of the system was studied in a prospective series of 25 patients with glioblastoma undergoing surgical resection [2]. For each patient, two paired samples were studied ex-vivo (tumoral and peritumoral). In both cases the imprint of extracellular matrix left by the samples on the surface of the nanostructured biosensor was analyzed and compared with histopathology results. Fig. 2 shows an overview of the experimental procedure. The biosensor was able to discriminate tumor from peritumoral tissue in 18 of the 25 cases. The results obtained by the biosensor agreed with the histopathology results in 84% of the cases.

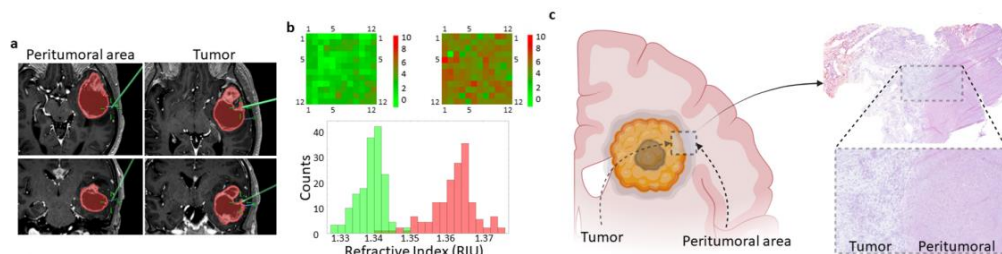


Figure 2 (a) Magnetic resonance images showing the tumor area (red). Green lines pinpoint the specific sites where the tissue samples were taken. (b) Heatmap showing the shift of the plasmon resonance wavelength at each position on the biosensor due to the refractive index of the imprinted extracellular matrix. A representative histogram showing the refractive index values of the imprints left by peritumoral (green) and tumor (red) tissues is shown. (c) Schematic representation of tumor and peritumoral areas of a glioblastoma showing the tumor border and the necrotic tumor core. The right image shows a representative hematoxylin-eosin-stained section revealing the tumor-peritumoral tissue border. [2]

Conclusions

The plasmonic nanostructured optical biosensor has been shown to efficiently discriminate between tumor and peritumoral tissue ex-vivo in patients with glioblastoma. The sensitivity and specificity of the biosensing system were determined to be about 80%, indicating that the biosensor provides a suitable procedure to distinguish glioblastoma from its peritumoral tissue. This is the first step in the road map to transfer the experimental setup to an in-vivo system able to discriminate between both tissues in real time, which would assist decision-making during surgery.

Acknowledgments

This work is supported by the Ministerio de Ciencia e Innovación grant PID2021-128220NB-I00, the Instituto de Salud Carlos III through grant DTS18/00141, co-funded by the European Regional Development Fund/European Social Fund, “A way to make Europe/Investing in your future”, and the Instituto de Investigación Valdecilla (IDIVAL) (APG/03).

References

- [1] A. Franco, D. Otaduy, A.I. Barreda, J.L. Fernández-Luna, S. Merino, F. González, F. Moreno, “Optical inspection of manufactured nanohole arrays to bridge the lab-industry gap”, *Optics & Laser Technology* **116**, 48-57 (2019).
- [2] V. García-Milán, A. Franco, M.E. Zvezdanova, S. Marcos, R. Martín-Laez, F. Moreno, C. Velasquez, J.L. Fernández-Luna, “Discriminating glioblastoma from peritumoral tissue by a nanohole array-based optical and label-free biosensor”, *Biosensors* **13**, 591 (2023).
- [3] A. Franco, V. Vidal, M. Gómez, O. Gutiérrez, M. Martino, F. González, F. Moreno, J.L. Fernández-Luna, “A label-free optical system with a nanohole array biosensor for discriminating live single cancer cells from normal cells”, *Nanophotonics* **11**, 315-328 (2022).
- [4] M. Carcelen, V. Vidal, A. Franco, M. Gómez, F. Moreno, J.L. Fernández-Luna, “Plasmonic biosensing for label-free detection of two hallmarks of cancer cells: cell-matrix interaction and cell division”, *Biosensors* **12**, 674 (2022).

Long-range molecular energy transfer mediated by strong coupling to plasmonic topological edge states

Álvaro Buendía^{1*}, Vincenzo Giannini², Jose Antonio Sánchez-Gil¹, William L. Barnes³ and Marie Rider³

¹*Instituto de Estructurade la Materia (IEM-CSIC), Serrano 121, 28006, Madrid, Spain*

²*Technology Innovation Institute, Masdar City 9639, Abu Dhabi, United Arab Emirates;*

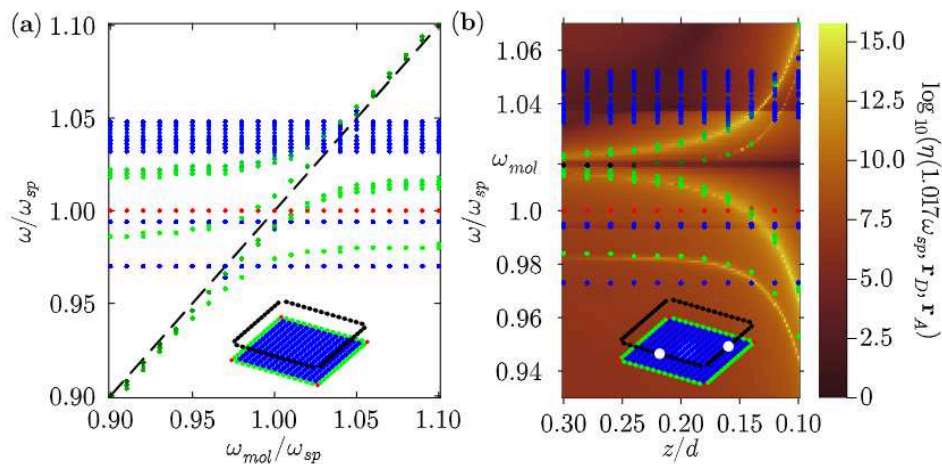
³*Department of Physics and Astronomy, University of Exeter, Stocker Road, Devon, EX4 4QL, UK*

*E-mail: a.buendia@csic.es

1. Abstract

Strong coupling between light and molecular matter is currently attracting interest both in chemistry and physics, in the fast-growing field of molecular polaritonics [1]. The large near-field enhancement of the electric field of plasmonic surfaces and their high tunability make arrays of metallic nanoparticles an interesting platform to achieve and control strong coupling. Two dimensional plasmonic arrays with several nanoparticles per unit cell and crystalline symmetries can host topological edge and corner states. Here we explore the coupling of molecular materials to these edge states using a coupled-dipole framework including long-range interactions. We study both weak and strong coupling regimes and demonstrate that coupling to topological edge states can be employed to enhance highly-directional long-range energy transfer between molecules [2].

2. Figures and tables



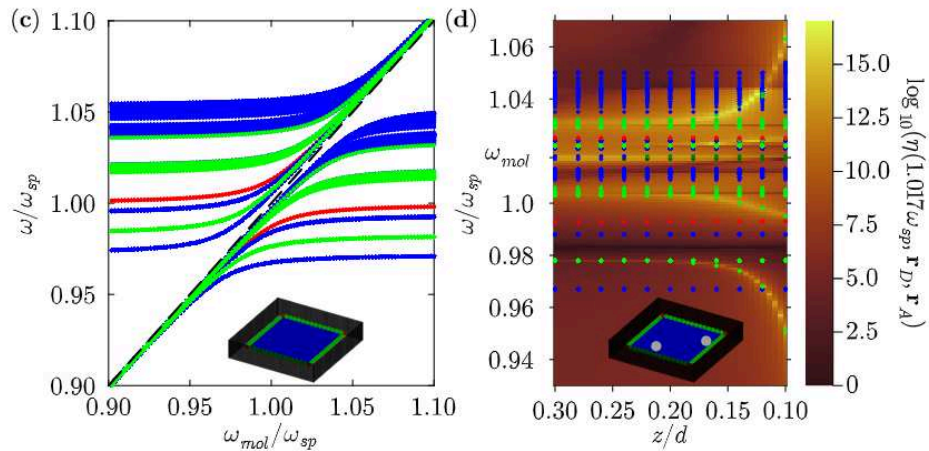


Figure 1 Strong coupling and energy transfer enhancement between molecules and array of plasmonic nanoparticles. Red, green and blue dots represent corner, edge and bulk modes (a) Spectrum of a discrete array of molecules strongly coupled to the plasmonic array of nanoparticles, depending on the molecular resonance frequency (b) Energy transfer between molecules placed over the edge strongly coupled to the plasmonic array, depending on the distance in the z direction (c) Spectrum of molecular continuous medium strongly coupled to plasmonic array of nanoparticles, depending on the molecular resonance frequency. (d) Energy transfer enhancement between molecules placed over the edges in a plasmonic array embedded in the effective medium, depending on the distance in z .

3. Conclusions

Molecular energy transfer in free space is short-ranged, while coupling to photonic modes can substantially extend the distance over which molecules may interact, with promising applications. In this paper we have illustrated how both weak and strong coupling between molecules and the topological edge states of a 2D SSH metallic nanoparticle array can provide energy transfer enhancement using a coupled-dipole model formalism. Using a discrete array and a continuous effective model for the molecular medium, we have shown that coupling to plasmonic edge states leads to dramatic and directional energy transfer enhancement.

Acknowledgments

We thank W. Wardley and F. Herrera for fruitful discussions. V.G. thanks theENSEMBLE3-Centre of Excellence for nanophotonics, advanced materials and novel crystal growth-based technologies, project (GA No. MAB/2020/14) carried out within the International Research Agendas program of the Foundation for Polish Science cofinanced by the European Union under the European Regional Development Fund. A.B. and J.A.S.G. acknowledge financial support from the grants BICPLAN6G (TED2021-131417B-I00) and LIGHTCOMPAS (PID2022-137569NB-C41), funded by MCIU/AEI/10.13039/501100011033, “ERDF A way of making Europe”, and European Union NextGenerationEU/PRTR and from MCIU through predoctoral fellowship PRE2019-090689.

References

- [1] F. Herrera and J. Owrutsky, “Molecular polaritons for controlling chemistry with quantum optics,”*The Journal of chemical physics*, vol. 152, no. 10, p. 100902, 2020
- [2] A. Buendía, et al “ Long-range molecular energy transfer mediated by strong coupling to plasmonic topological edge states”, arXiv:2402:16666

Optical sensor based on surface-enhanced Raman scattering coupled to plasmon catalysis applied in the detection of pollutants

Santiago Sanchez-Cortes¹, Freddy Celis², Francisca Fuenzalida³, Pavol Miskovsky⁴,
Zuzana Jurasekova³

¹*Institute of the Structure of Matter, IEM-CSIC, Serrano 121, 28006 Madrid, Spain*

²*Laboratorio de Procesos Fotónicos y Electroquímicos, Facultad de Ciencias Naturales y Exactas,
Universidad de Playa Ancha, Valparaíso, Chile*

³*Department of Biophysics, Faculty of Science, P. J. Šafárik University, Jesenná 5, 040 01 Košice,
Slovakia*

⁴*SAFTRA Photonics, s.r.o., Moldavská cesta 51, 040 11 Košice, Slovakia*

*E-mail: s.sanchez.cortes@csic.es

The excitation of plasmon modes induces large enhancement of the electric field in the close vicinity of plasmonic nanoparticles that also leads to strong enhancement of the cross section of Raman and fluorescence emissions, as well as the IR absorption leading to the so-called Surface-Enhanced Optical Spectroscopy (SEOS) or plasmon mediated optical spectroscopy. SEOS techniques are the Surface-Enhanced Raman Scattering (SERS), Surface-Enhanced Fluorescence (SEF) and Surface-Enhanced IR Absorption (SEIRA) techniques[1]. Despite the high potentiality of nanostructured platforms in advanced applications dealing with many areas of interest, their application in molecular sensing was not sufficiently exploited so far.

The decay of plasmon excitation generates not only radiations that spectroscopy relies on, but also a considerable number of hot carriers via non-radiative decay[2]. Hot carriers refer to high energy carriers that are not in thermal equilibrium with the lattice. These hot carriers have attracted significant attention due to their potential applications in photodetection, photoelectric energy conversion, and photo-catalysis associated to SERS detection. This effect, called Plasmon Catalysis (PC), can be used in the modification of the chemical structure of adsorbates, what is a novel tendency and an outstanding use of plasmonic materials and their effects in the chemistry, also called Plasmon Chemistry[3]. The chemical effect of nanostructures can be also used for different industrial applications, pollutant remediation and even for energy production.

The chemical processes driven by plasmon catalysis can have a large impact in the SERS detection of pollutants, although this effect was not applied so far in the detection and remediation in pollutants such as pesticides. Plasmon Catalysis combined with SERS detection (PC+SERS) is a relative new and remarkable tool that can be employed to improve the detection of pollutants, thus demonstrating its high potential in molecular detection.

In this work we present the design of optical sensors based on the PC+SERS combination applied in the detection of two important pollutant molecules employed in agriculture: glyphosate and thiocloprid.

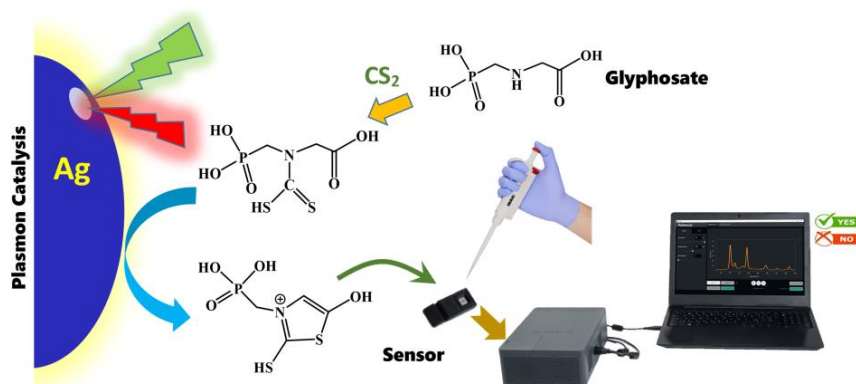
Glyphosate (GPH) is a non-selective post-emergence herbicide used to remove a wide variety of weeds. In the last decade, GPH has been sprayed on more hectares planted with resistant crops as well as applied more intensively. Actually, it is the most widely sprayed pesticide in history. Recent studies have concluded that the consumption of GPH (and its metabolites) can trigger carcinogenic processes in humans. On the other hand, chronic exposure to this herbicide can induce different diseases such as gluten intolerance, diabetes, heart disease, multiple sclerosis, Alzheimer's disease, autism as well as birth defects.

Therefore, the development of an efficient detection system to in-situ detect this important and highly spread pesticide is of high interest. Surface-enhanced Raman scattering (SERS) can intensify Raman emission 10^6 to 10^{11} times by using noble metal nanostructures.[4] Compared to techniques currently used for the sensitive detection of GPH, such as gas chromatography coupled to tandem mass spectrometry and capillary electrophoresis, UV-Vis absorption and fluorescence spectroscopies, the SERS technique has several advantages: no need for sample pre-treatment, fast and cost-effective measurements, and available portable equipments. However, the SERS spectrum of glyphosate is relatively low. Therefore, a new strategy is presented in this work for the selective and sensitive SERS detection of GPH based on a chemical modification of the herbicide into a more active SERS molecule based on the PC+SERS

tandem. Scheme 1 describes the process of modification of GPH into a thiazol molecules which have a stronger response in the presence of plasmon nanoparticles. Plasmon catalysis seems to play an important role in the case of GPH and it was applied for the final detection of the herbicide on plasmonic nanodevices. In particular, the existence of Ag clusters on the surface seems to be the key for the chemical process to take place since the probability of hot carrier transfer is intensified in these adatom structures.

The methodology described in this work was optimized by selecting the most appropriate experimental conditions for the chemical reactions (pH, concentration, reaction time), and the optimal conditions for the plasma catalysis: the plasmonic substrates (nanospheres of Ag and Au; nanostars of Ag and hollow bimetallic Ag/Au nanostars), the excitation laser and the interfacial properties of nanoparticles. Finally, calculations based on Density Functional Theory (DFT) were done in order to obtain the theoretical spectra of GPH and the most important molecules involved in its adsorption and its chemical modification

The main goal of this work was to develop an effective system of GPH optical detection based on portable methods and ensuring a quick, low cost, in-situ and univocal detection of GPH. For this purpose, the application of the technology in a real detection of GPH in the environment (water) was tested and proven by using the portable detection system (Ramascop) and the sensor chips (Pickmol), both developed by the Saftra Photonics Ltd company based on our research.



Scheme 1. Detection of the glyphosate herbicide by a method based on plasmon catalysis and SERS in a nanostructured sensor coupled to a portable Raman device.

Acknowledgments

This work was supported by the Scientific Grant Agency of the Ministry of the Education of Slovak Republic (grant no. APVV-19-0580 by P.M.), by the Ministerio de Ciencia e Innovación (grant no. PID2020-113900RB-I00/AEI/10.13039/501100011033 by S.S.C), by the Operational Programme Integrated Infrastructure funded by European Regional Development Fund (grant ITMS2014+:313011AUW6) and by the financial and in-kind contribution of SAFTRA Photonics Ltd.

References

- [1] R. Aroca, Surface-Enhanced Vibrational Spectroscopy, John Wiley & Sons, Ltd, Chichester, UK, 2006.
- [2] E. Cortés, L. V. Besteiro, A. Alabastri, A. Baldi, G. Tagliabue, A. Demetriadou, P. Narang, Challenges in Plasmonic Catalysis, ACS Nano. 14 (2020) 16202–16219.
- [3] W. Xie, S. Schlücker, Hot electron-induced reduction of small molecules on photorecycling metal surfaces, Nat. Commun. 6 (2015).
- [4] R.F. Aroca, R.A. Alvarez-Puebla, N. Pieczonka, S. Sanchez-Cortes, J.V. Garcia-Ramos, Surface-enhanced Raman scattering on colloidal nanostructures, Adv. Colloid Interface Sci. 116 (2005).

Aplicaciones de las guías curvas acopladas asimétricas en la plataforma de nitruro de silicio

Pedro Chamorro-Posada

Dpto. de Teoría de la Señal y Comunicaciones e Ingeniería Telemática, Universidad de Valladolid, ETSI Telecomunicación, Paseo Belén 15, 47011 Valladolid, Spain

E-mail: pedro.chamorro@uva.es

La plataforma de integración fotónica de nitruro de silicio, basada en los procesos de la tecnología CMOS, es especialmente atractiva para determinadas aplicaciones [1] debido a las propiedades de propagación de las señales ópticas en las guías de nitruro de silicio, en comparación con las de silicio de la plataforma dominante. Así, las pérdidas de propagación intrínsecas, tanto lineales como no lineales, son más pequeñas, el coeficiente termo-óptico es más bajo y la región de transparencia es mucho más amplia cubriendo desde el visible hasta el infrarrojo medio. El principal inconveniente de la plataforma de nitruro de silicio está asociado a un confinamiento del campo óptico más pobre que en el silicio debido al menor contraste del índice de refracción. Esta peculiaridad hace que las pérdidas debidas a la radiación en las secciones curvas sean mayores que en el silicio, lo que en última instancia limita el radio de curvatura mínimo utilizable y, por tanto, la escala de integración de la plataforma.

Las pérdidas por radiación en estructuras de guiado curvas se pueden controlar mediante el empleo de la geometría de guías acopladas asimétricas [2] que se muestra en la Figura 1 de forma esquemática. El guiado de la luz tiene lugar en la guía interior de la figura, de ancho w y alto h , mientras que la guía exterior, separada una distancia s de la anterior, y de ancho w_e y con la misma altura, tiene por objeto el control de las pérdidas del modo principal, responsable del transporte de la señal óptica en la estructura, asociadas a la curvatura.

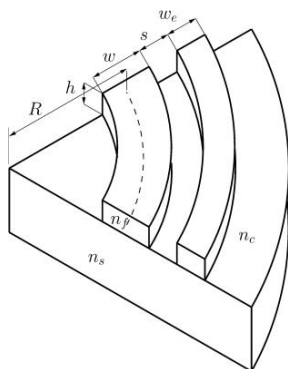


Figura 1 Geometría de guías curvas acopladas empleada en el estudio.

Las propiedades de propagación en la estructura de guiado de la figura se explican mejor partiendo de la geometría recta, en el límite $R \rightarrow \infty$. Si representamos el índice eficaz de los modos propagados en la estructura en función de los parámetros w_e y s , obtenemos una serie de hojas correspondientes a los distintos modos soportados [2]. Para cada valor de w_e y s , el modo principal corresponde al de aquella hoja con el índice eficaz de valor más próximo al del único modo de guía interior aislada (sin la guía acoplada exterior) en el caso recto. El modo principal proporciona el mejor confinamiento en la guía entre todos los modos propagados para w_e y s fijos. Al curvar la geometría, como se muestra en la figura, los modos guiados se transforman en casi-modos con índices eficaces complejos donde la parte imaginaria describe el efecto de las pérdidas por radiación. Por otro lado, los contornos que definen el valor del índice eficaz en el plano (w_e, s) sufren una deformación en función del valor de R finito. La curvatura tiene el efecto, además, de añadir pérdidas de propagación en el modo principal que dependen, a su vez, de los valores de w_e y s .

En la presentación se relacionarán los resultados más relevantes relativos a las aplicaciones de la geometría mostrada en la Figura 1. Un diseño juicioso de estas estructuras permite una reducción

sustancial de las pérdidas de radiación por las curvaturas y la consiguiente disminución de las huellas de los dispositivos de microresonadores o de las interconexiones dentro de los circuitos integrados fotónicos en la plataforma de nitruro de silicio [3,4]. Las guías curvas acopladas asimétricas estudiadas en este trabajo son muy versátiles en el diseño de nuevos dispositivos, al tiempo que no requieren de procesos especiales en su fabricación, fuera de los pasos estándar definidos en la plataforma. Al permitir un ajuste de la atenuación diferencial para las polarizaciones TE y TM, proporcionan un mecanismo para la implementación de polarizadores integrados de banda ancha ultra-compactos, totalmente dieléctricos, con una alta relación de extinción de polarización y bajas pérdidas de inserción [5,6]. La geometría propuesta también se puede utilizar para realizar biosensores sin marcadores basados en microestructuras resonantes en anillo con un rendimiento mejorado [7]. La mayoría de estas aplicaciones requieren de un tratamiento adicional de las pérdidas en las discontinuidades entre las secciones de guía rectas y curvas. Para ello, se puede utilizar la técnica de desplazamiento lateral [8]. Sin embargo, este método define transiciones abruptas que requerirían resoluciones más allá del alcance de las técnicas de fabricación estándar para una realización precisa. Un diseño alternativo estudiado recientemente se basa en secciones curvas de Euler parciales [9,10], combinando secciones con variación lineal de su curvatura (clotoides) y guías de ondas acopladas asimétricas de curvatura constante del tipo mostrado en la Figura 1 [11].

Agradecimientos

Este trabajo de investigación ha sido financiado por el Ministerio de Ciencia e Innovación (MCIIN), proyecto PID2020-119418GB-I00, la Unión Europea a través del programa Next Generation EU, proyecto PRTRC17.II, y por la Consejería de Educación de la Junta de Castilla y León a través del proyecto QCA YLE.

Bibliografía

- [1] T. Sharma, J. Wang, B.K. Kaushik, Z. Cheng, R. Kumar, Z. Wei, and X. Li, “Review of Recent Progress on Silicon Nitride-Based Photonic Integrated Circuits,” *IEEE Access* **8**, 195436-195446 (2020).
- [2] P. Chamorro-Posada, “Radiation in bent asymmetric coupled waveguides,” *Appl. Opt.* **58**, 4450-4457 (2019).
- [3] P. Chamorro-Posada, “Q-enhanced racetrack microresonators,” *Optics Commun.* **387**, 70-78 (2017).
- [4] P. Chamorro-Posada, and R. Baños, “Design and Characterization of Q-enhanced Silicon Nitride Racetrack Micro-Resonators,” *J. Lightw. Technol.* **39**, 2917-2923 (2021).
- [5] P. Chamorro-Posada, “Asymmetric Concentric Microring Resonator Label-Free Biosensors,” *Photonics* **9**, 9010027 (2022).
- [6] P. Chamorro-Posada, “Ultracompact integrated polarizers using bent asymmetric coupled waveguides,” *Opt. Lett.* **44**, 2040-2043 (2019).
- [7] P. Chamorro-Posada, “Design and characterization of silicon nitride ultracompact integrated polarizers using bent asymmetric coupled waveguides,” *Opt. Lett.* **46**, 609-612 (2021).
- [8] T. Kitoh, N. Takato, M. Yasu, and M. Kawachi, “Bending Loss Reduction in Silica-Based Waveguides by Using Lateral Offsets,” *J. Lightwave Technol.* **13**, 555–562 (1995).
- [9] T. Fujisawa, S. Makino, T. Sato, and K. Saitoh, “Low-loss, compact, and fabrication-tolerant Si-wire 90° waveguide bend using clothoid and normal curves for large scale photonic integrated circuits,” *Opt. Express* **25**, 9150–9159 (2017).
- [10] F. Vogelbacher, S. Nevlacsil, M. Sagmeister, J. Kraft, K. Unterrainer, and R. Hainberger, “Analysis of silicon nitride partial Euler waveguide bends,” *Opt. Express* **27**, 31394–31406 (2019).
- [11] P. Chamorro-Posada, “Silicon Nitride Bent Asymmetric Coupled Waveguides with Partial Euler Bends,” *Photonics* **11**, 218 (2024).

RESÚMENES/ABSTRACTS

Sesiones Orales

**Óptica Cuántica
y No Lineal**



Photonic Quantum Reservoir Computing: Role of Squeezing

Jorge García-Beni¹, Gian Luca Giorgi¹, Miguel C. Soriano¹, and Roberta Zambrini¹

¹*Instituto de Física Interdisciplinar y Sistemas Complejos (IFISC, UIB-CSIC), Campus Universitat de les Illes Balears E-07122, Palma de Mallorca, Spain.*

*E-mail: miguel@ifisc.uib-csic.es

1. Introduction

Photonic quantum reservoir computing is an interdisciplinary field that brings together concepts from quantum computing and simulations, photonics, and reservoir computing. By integrating these disciplines, the principles of quantum mechanics can be harnessed to process information in a highly parallel and efficient manner. This field was initiated by the proposal to extend the reservoir computing paradigm to the quantum regime [1] and later extended to the photonic domain [2,3]. Reservoir computing (RC) is a supervised machine learning approach tailored for time series processing, often based on artificial recurrent neural networks, that can be implemented in software or directly on a physical substrate. In particular, photonic implementations of RC allowed for ultra-fast demonstrators for spoken digits recognition or time series prediction [4]. The interest in expanding RC to the quantum regime is driven by the potential to exploit several key advantages: high expressivity, scalability, high-speed processing, room-temperature operation, and low power consumption. The parallel processing capabilities inherent in quantum photonic systems have the potential to surpass the efficiency of classical computers.

Squeezing is recognized as a valuable quantum resource in various applications, including metrology, cryptography, and computing, particularly in multimode settings where it is closely related to entanglement. This contribution explores the role of squeezing in photonic quantum reservoir computing for time-series processing [5]. We investigate a loop-based photonic architecture for RC and examine the impact of squeezing on the reservoir, employing a Hamiltonian system featuring both active and passive coupling terms. Notably, our results show that squeezing can have either detrimental or beneficial effects, depending on the signal-to-noise ratio of the implementation. We demonstrate that multimode squeezing enhances the performance in benchmark temporal tasks. The underlying mechanism behind this improvement stems from the increased robustness of the reservoir to readout noise, which is amplified by squeezing.

2. Description of the system and numerical results

Figure 1 a) and b) illustrate our suggested implementation of photonic quantum reservoir computing where the use of multimode light for the reservoir allows for a powerful solution to continuous monitoring [6].

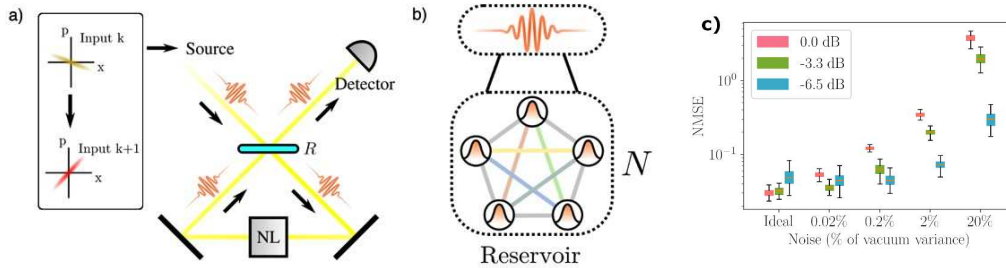


Figure 1 (a) Schematic representation of a photonic quantum reservoir computer based on a frequency comb generated by short light pulses. The external information input is encoded in the angle of squeezing of each optical pulse. The optical setup consists of a nonlinear element within a feedback loop and a homodyne detector. (b) The reservoir comprises multiple frequency modes that are coupled, forming a complex quantum network. (c) Boxplot of the NMSE for the chaotic time-series forecasting task as a function of the intensity of the added readout noise relative to the vacuum variance. Different colours show different values of the squeezing generated by the non-linear cavity. Each box contains values from 100 independent realizations. In all cases, the reservoir had $N = 12$ modes.

The task we consider is the forecasting of the so-called Santa Fe chaotic time series [6]. At each time step, we want the reservoir to predict the next step in the series, so the target function is $y(s_k) = s_{k+1}$. We use the normalized mean-square error (NMSE) as the performance metric that we want to minimise

during training. In Fig. 1 c) the NMSE is shown as a function of the noise intensity (including the ideal noiseless case) for different values of the generated cavity squeezing (different colours). The squeezing seems detrimental to the performance in ideal and very low noise conditions (noise intensities around and below 0.02% of vacuum noise). However, as the noise increases, the robustness of the reservoir is determined by the amount of squeezing produced by the cavity.

3. Conclusions

We demonstrate the performance-enhancing potential of quantum squeezing in an active cavity applied to a vacuum state quantum memory (loop pulse) to mitigate noise in realistic scenarios. This establishes squeezing as a valuable quantum resource for accessing an enlarged space of quantum correlations and entanglement, and for enhancing performance in relevant benchmark tasks, whether predictive or requiring memory. Although tuning the beam splitter (BS) reflectivity also improves memory retention, as shown in [6], our results demonstrate that increasing cavity squeezing is a preferred method for enhancing reservoir robustness under adverse noise conditions. Notably, state-of-the-art frequency multiplexed quantum networks [7,8] represent a powerful platform for near-term experimental implementations of photonic quantum reservoir computing. Our findings serve as a guide for experimental design, laying the foundations for continuous variable implementations in realistic noisy scenarios and exploiting quantum resources.

Acknowledgments

We acknowledge the Spanish State Research Agency, through the María de Maeztu project CEX2021-001164-M funded by the MCIN/AEI/10.13039/501100011033, through the QUARESC project PID2019-109094GB-C21 and -C22/ AEI / 10.13039/501100011033 and through the COQUSY project PID2022-140506NB-C21 and -C22 funded by MCIN/AEI/10.13039/501100011033, MINECO through the QUANTUM SPAIN project, and EU through the RTRP - NextGenerationEU within the framework of the Digital Spain 2025 Agenda. J.G-B. is funded by the Conselleria d'Educació, Universitat i Recerca of the Government of the Balearic Islands with grant code FPI/036/2020. G.L.G. is funded by the Spanish MEFP/MiU and co-funded by the University of the Balearic Islands through the Beatriz Galindo program (BG20/00085). The CSIC Interdisciplinary Thematic Platform (PTI) on Quantum Technologies in Spain is also acknowledged.

References

- [1] K. Fujii and K. Nakajima, “Harnessing Disordered-Ensemble Quantum Dynamics for Machine Learning”, *Phys. Rev. App.* **8**, 024030 (2017).
- [2] S. Ghosh, A. Opala, M. Matuszewski, T. Paterek, and T. C. Liew, “Quantum Reservoir Processing”, *npj Quantum Inf.* **5**, 35 (2019).
- [3] J. Nokkala, R. Martínez-Peña, G. L. Giorgi, V. Parigi, M. C. Soriano, and R. Zambrini, “Gaussian states of continuous-variable quantum systems provide universal and Versatile Reservoir Computing”, *Commun. Phys.* **4**, 53 (2021).
- [4] D. Brunner, M. C. Soriano, and G. V. der Sande, Eds., *Photonic Reservoir Computing: Optical Recurrent Neural Networks*. Berlin, De Gruyter (2019).
- [5] J. García-Beni, G. L. Giorgi, M. C. Soriano, and R. Zambrini, “Squeezing as a resource for time series processing in quantum reservoir computing”, *Opt. Express* **32**, 6733-6747 (2024).
- [6] J. García-Beni, G. L. Giorgi, M. C. Soriano, and R. Zambrini, “Scalable photonic platform for real-time quantum reservoir computing”, *Phys. Rev. App.* **20**, 014051 (2023).
- [7] Y. Cai, J. Roslund, G. Ferrini, F. Arzani, X. Xu, C. Fabre, and N. Treps, “Multimode Entanglement in Reconfigurable Graph States Using Optical Frequency Combs”, *Nat. Commun.* **8**, 15645 (2017).
- [8] T. Kouadou, F. Sansavini, M. Ansquer, J. Henaff, N. Treps, V. Parigi, “Spectrally shaped and pulse-by-pulse multiplexed multimode squeezed states of light”, *APL Photonics* **1**, 086113 (2023).

High-root topological insulator in non-Hermitian photonic ring resonators

David Viedma^{1*}, Anselmo M. Marques², Ricardo G. Dias² and Verónica Ahufinger¹

¹*Departament de Física, Universitat Autònoma de Barcelona, E-08193 Bellaterra, Spain*

²*Department of Physics & i3N, University of Aveiro, 3810-193 Aveiro, Portugal*

*E-mail: david.viedma@uab.cat

The field of Topological Insulators (TIs) has been the focus of extensive research in recent years. TIs exhibit a stark contrast between protected conducting states on the surface and an insulating bulk, and have been implemented in multiple different platforms. In the search for new types of TIs, the concept of square-root TIs ($\sqrt{\text{TI}}$ s) was developed [1]. $\sqrt{\text{TI}}$ s are related to a parent system, from which they inherit their topological properties, through a squaring procedure on their Hamiltonian. Interestingly, however, $\sqrt{\text{TI}}$ s display additional novel properties, such as the appearance of more band gaps that can host protected states.

A direct generalization of $\sqrt{\text{TI}}$ s consists of applying successive root operations on a Hamiltonian, such that root TIs of order $2n$ are found [2]. However, true generalizations to any order n have been elusive until now, only appearing in the context of Floquet systems [3] by dividing the driving period into separate parts associated with different Hamiltonians. Here, we showcase a method to generate any general root of a TI through the usage of unidirectional coupling loops that link the sites of the partner lattice [4]. Although the method is general, we use the Su-Schrieffer-Heeger model for benchmarking, as it is one of the simplest models displaying nontrivial topology. In particular, here we focus on the implementation of its cubic root model, $\sqrt[3]{\text{SSH}}$, whose distribution of couplings we sketch in the bottom part of Fig. 1(a).

We propose to use a lattice of optical ring resonators to implement the root systems. The coupling between resonators can be engineered through the appropriate design of antiresonant link rings, which allow to implement both real and imaginary fluxes in the system [5]. To achieve the necessary coupling asymmetry, a split distribution of gain and loss is used: The upper half of the optical path displays gain that is characterized by a parameter h , and the lower half has an equivalent amount of loss. For a given mode circulation, this induces a bias in the coupling, which will be enhanced in one direction and suppressed in the other such that $t^\pm = te^{\pm h}$. If h is large enough, a regime close to unidirectionality is reached and the root system can be implemented to a great degree of approximation. Half of a unit cell is depicted in the top part of Fig. 1(a).

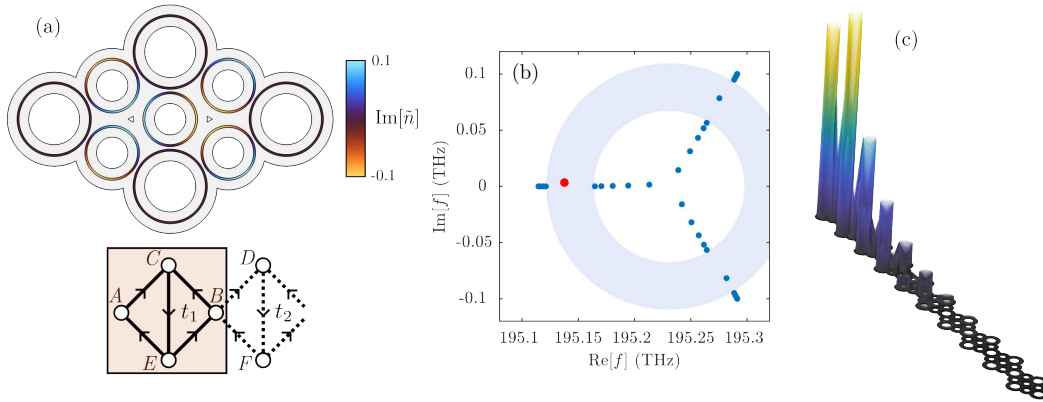


Figure 1 (a) Top: Half of the unit cell of the $\sqrt[3]{\text{SSH}}$ model in the ring resonator implementation. Link rings have split gain and loss structure to induce the coupling asymmetry $t_{1,2}^\pm = t_{1,2}e^{\pm h}$. Bottom: Coupling sketch of the $\sqrt[3]{\text{SSH}}$ model. The highlighted shaded part corresponds to the top part. (b) Complex frequency spectrum of the simulated $\sqrt[3]{\text{SSH}}$ model. The shaded region corresponds to the ring gap, which hosts 3 edge states. (c) Electric field amplitudes in the full $\sqrt[3]{\text{SSH}}$ chain for the edge state highlighted in red in (b).

We simulate a chain of 7 unit cells of the $\sqrt[3]{\text{SSH}}$ model in the proposed ring system, where the relative distance between rings is alternated between $d_1 = 0.33 \mu\text{m}$ and $d_2 = 0.3 \mu\text{m}$ to achieve a staggered distribution of couplings. In Fig. 1(b) we plot the spectrum of eigenfrequencies, which shows a characteristic 3-fold splitting along the complex plane. This is due to the generalized chiral symmetry that accompanies n-partite systems [6]. Additionally, one can define a novel type of gap along the complex plane in this system, i.e. a *ring gap* wherein 3 edge states are found [4], which is shaded in blue in the figure. We show the electric field distribution of one of these edges in Fig. 1(c), where the localization around the end of the chain is readily observed. The ideas presented here can be applied to higher-order roots of the same system, see Ref. [4], or to other TIs of interest.

Acknowledgments

D.V. and V.A. acknowledge financial support from the Spanish State Research Agency AEI (contract No. PID2020-118153GB-I00/AEI/10.13039/501100011033) and Generalitat de Catalunya (Contract No. SGR2021-00138). A.M.M. and R.G.D. developed their work within the scope of Portuguese Institute for Nanostructures, Nanomodelling and Nanofabrication (i3N) Projects No. UIDB/50025/2020, No. UIDP/50025/2020, and No. LA/P/0037/2020, financed by national funds through the Fundação para a Ciência e Tecnologia (FCT) and the Ministério da Educação e Ciência (MEC) of Portugal. A.M.M. acknowledges financial support from i3N through the work Contract No. CDL-CTTRI-46-SGRH/2022.

References

- [1] J. Arkininstall, M. H. Teimourpour, L. Feng, R. El-Ganainy and H. Schomerus, “Topological tight-binding models from nontrivial square roots,” *Phys. Rev. B* **95**, 165109 (2017).
- [2] A. M. Marques, L. Madail and R. G. Dias, “One-dimensional 2n-root topological insulators and superconductors,” *Phys. Rev. B* **103**, 235425 (2021).
- [3] L. Zhou, R. W. Bomantara, and S. Wu, “qth-root non-Hermitian Floquet topological insulators,” *SciPost Phys.* **13**, 015 (2022).
- [4] D. Viedma, A. M. Marques, R. G. Dias and V. Ahufinger, “Topological n-root Su–Schrieffer–Heeger model in a non-Hermitian photonic ring system,” *Nanophotonics* **13**, 51, (2024).
- [5] S. Longhi, D. Gatti and G. Valle, “Robust light transport in non-Hermitian photonic lattices,” *Sci Rep* **5**, 13376 (2015).
- [6] A. M. Marques and R. G. Dias, “Generalized Lieb’s theorem for noninteracting non-Hermitian n-partite tight-binding lattices,” *Phys. Rev. B* **106**, 205146 (2022).

Vortex quantum droplets described by a variational approximation

José R. Salgueiro*, Ángel Paredes, and Humberto Michinel

*Instituto de Física y Ciencias Aeroespaciales (IFCAE), Universidade de Vigo,
Campus As Lagoas, s/n, 32004 Ourense*

*E-mail: jrs@uvigo.gal

1. Introduction

Quantum droplets are a novel state of matter created on a Bose-Einstein Condensate (BEC) when self-attraction effects are balanced by quantum effects. In three dimensional BECs dynamics is described by the Gross Pitaevskii equation after adding the two body interactions as well as a quartic self-repulsive effect. For an effective 2D confinement (pancake-like BEC), the description of lossless states for the BEC mixture comes given by the equation [1],

$$i \frac{\partial \Psi}{\partial t} = -\nabla^2 \Psi + |\Psi|^2 \log(|\Psi|^2) \Psi \quad (1)$$

where Ψ is the mean field wavefunction of the droplet and t the time. We are interested in solutions to this equation in the form of vortices i. e. rotating systems characterized by an angular momentum.

2. Stationary states

The stationary states resulting from considering a wavefunction with a phase variation around the origin $\Psi(r) = \exp(-i\mu t) \exp(il\theta) \psi(r)$, being μ the chemical potential, l the angular momentum and (r, θ) the polar system of coordinates have been computed numerically. In Fig. 1(a) there are some examples corresponding to different values of the angular momentum and chemical potential. The solutions present a ring-like shape whose radius is larger for larger l and vanish at the origin, except but for the case $l=0$ which is a disc with a maximum at the origin. There is a critical value of the chemical potential μ_{cr} (non-dependent from the angular momentum) at which the norm diverges to infinity. Solutions approaching this value show an increasing width and a top-flat shape and their amplitude also tends to a constant saturation value. For smaller values, the states are bell-shaped presenting a lower amplitude. The shape of the eigenstates resembles those from the cubic-quintic medium [2] since both media share the characteristic of turning the interaction from attractive into repulsive as the norm overpasses a threshold. The top-flat shape states correspond to the droplet regime as the system is in such a way characterized by liquid-like properties.

3. Variational method

Using two conserved quantities as the number of atoms (norm), N , and the Hamiltonian, H it is possible to build a quantity $\Omega = H - \mu N$, easy to be identified with the Landau's grand potential, from which approximate solutions can be derived by minimization. The election of a suitable ansatz relies in the 1D case for which a kink function describes quite accurately the shape of the wavefunction at the droplet surface. In such a way the following ansatz function is chosen,

$$\Psi(r) = e^{-i\mu t} e^{il\theta} \psi_{cr} f(r - R_{int}) f(R_{ext} - r) \quad (2)$$

$$f(r) = [(1 + \tanh(\kappa r))^{1/2}] / 2, \quad (3)$$

where R_{int} and R_{ext} are the internal and external radii respectively and κ a parameter describing the function width which can be obtained from the variational approach applied to the 1D case. Minimization of the grand potential allows to deduce an analytical expression to relate both quantities together with the angular momentum $R_{int} = l^2 R_{ext} / (l^2 + \kappa R_{ext} / 2)$. This allows to compare the shape of the variational solution to the numerical one resulting an excellent agreement between both for the quantum droplet regime (top-flat

states). Besides, it remains quite good for those bell-shaped solutions which are not far away from the droplet phase, going increasingly worse as the value of R_{ext} decreases. In Fig. 1(b) there are some plots of solutions corresponding to different chemical potential values and for two different values of the angular momentum ($l=3$ and $l=10$) confirming the results described above.

On the other hand the minimization of the grand potential also provides a solution for the chemical potential in terms of the external radius R_{ext} ,

$$\mu = \mu_{cr} + \frac{\kappa}{2R_{ext}} + \frac{l^2}{R_{ext}^2} \quad (4)$$

which also allows to express R_{ext} in terms of μ . A comparison between these results and the numerical ones are excellent, particularly in the quantum droplet regime. The method also provides an expression of the norm N in terms of the chemical potential with an analogous good agreement with the numerically obtained values.

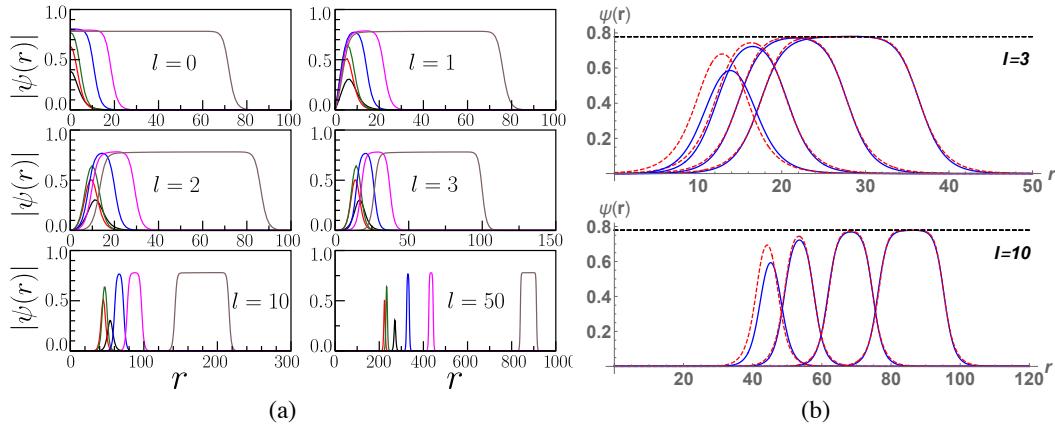


Figure 1 (a) Different examples of numerically calculated stationary states for angular momenta ranging from zero to large values. (b) Comparison between variationally and numerically calculated states for $l=3$ and $l=10$.

4. Conclusions

A variational method has been proposed and successfully used to obtain the vortex-like stationary states of a quantum droplet system, and to describe the main characteristics of the droplet wavefunctions as for instance the internal and external radii or the chemical potential. A comparison to numerical results shows an excellent agreement particularly for the droplet regime but also quite good for further away regimes.

Acknowledgments

This work has been supported by the project PID2020-118613GB-I00, granted by MCIN/AEI/10.13039/501100011033/. Also we thank the Xunta de Galicia for the support through the grant ED431B 2021/22.

References

- [1] Y. Li, Z. Chen, Z. Luo, C. Huang, H. Tan, W. Pang, B. A. Malomed, “Two-dimensional vortex quantum droplets”, *Phys. Rev. A* **98** (6), 063602 (2018).
- [2] H. Michinel, J. R. Salgueiro, M. J. Paz-Alonso, “Square vortex solitons with large angular momentum”, *Phys. Rev. E* **70** (6), 066605 (2004).
- [3] A. Paredes, J. R. Salgueiro, H. Michinel, “On vortex and dark solitons in the cubic-quintic nonlinear Schrödinger equation”, *Physica D: Nonlinear Phenomena* **437**, 133340 (2022).

Nonlinear optical propagation in self-defocusing perovskite materials

I. Suárez¹, J.P. Martínez-Pastor², M. F. Oszajca⁴, N.A. Lüchinger⁴, B. Graves⁴, S. Agouram⁵, C. Milián³, and A. Ferrando²

¹*Escuela Técnica Superior de Ingeniería, Universidad de Valencia, Avenida de la Universidad s/n 46100 Burjassot, Valencia, Spain*

²*UMDO+, Institut de Ciència dels Materials, Universitat de València, C/ Catedrático J. Beltrán, 2, Paterna 46980, Spain*

³*Institut Universitari de Matemàtica Pura i Aplicada, Universitat Politècnica de València, 46022 València, Spain*

⁴*Avantama AG, Laubisrütistrasse 50, 8712 Stafa, Switzerland*

⁵*Departament de Física Aplicada i Electromagnetisme, Universitat de València, C/ Dr Moliner 50, E-46100 València, Spain*

*E-mail: albert.ferrando@uv.es

1. Introduction

Lead-free metal halide perovskites (LFP) have emerged as a promising family of semiconductors to develop a new green technology for optoelectronics [1]. This manuscript demonstrates that Cs₂SnI₆ (a vacancy ordered double perovskite) nanocrystals (NCs) present an extraordinary self-defocusing response not yet observed up to now [2].

2. Beam propagation in a self-defocusing perovskite material

We performed a complete set of experiments to characterize the propagation of an optical beam in a nonlinear optical medium constituted by a solution of Cs₂SnI₆ perovskite NCs in liquid toluene inside a thin cuvette [2]. The intensity of the input beam was regulated by controlling the diameter of the beam spot at the input side of the cuvette. The shape of the exit beam was measured right at the output side of the cuvette. A complete series of measurements of the output shape of the beam were performed at increasing intensities. Equivalent series were realized for different perovskite NC concentrations as well. In all cases, the composite medium showed an extremely high self-defocusing nonlinearity. However, standard methods of measuring the effective nonlinearity, like z-can methods, failed since they did not describe the propagation of the beam properly. Thus, we had to resort to the complete simulation of the nonlinear propagation of the beam inside the cuvette. This required to find the effective nonlinear response of the medium phenomenologically by comparing simulations with different nonlinear models to experimental results. We demonstrated that a quasi-monochromatic beam propagation of an optical field ϕ in this nonlinear medium could be phenomenologically described by a nonlinear-like Schrödinger equation hosting a very untypical self-defocusing inhomogeneous nonlinearity profile given by

$$\Delta n_{\text{NL}}(|\phi|^2) = -\Delta n_0 \left(\frac{|\phi|^2}{|\phi|^2 + a_{\text{co}}(C, I_{\text{peak}})} \right) \left(\frac{|\phi|^2 - a_{\text{th}}(C, I_{\text{peak}})}{|\phi|^2 + a_{\text{co}}(C, I_{\text{peak}})} \right) e^{-r^2/w^2}$$

where C and I_{peak} are the NC concentration and the peak intensity right at the input of the cuvette, respectively. These parameters were changed in different experiments and simulations. Using this nonlinear index profile we were able to achieve an excellent agreement between numerical simulations and experimental results. In Fig.1 we show the calculated negative nonlinear profile for

different typical propagations. In the left column, low C profiles (bottom, low I_{peak} ; top, high I_{peak}). Right column, the same but for a high C above a threshold value. For proper values of C and I_{peak} , the nonlinear modulation Δn_{NL} can reach at some points exceptional high negative values of the order of -0.02 at the operating length of 1064 nm.

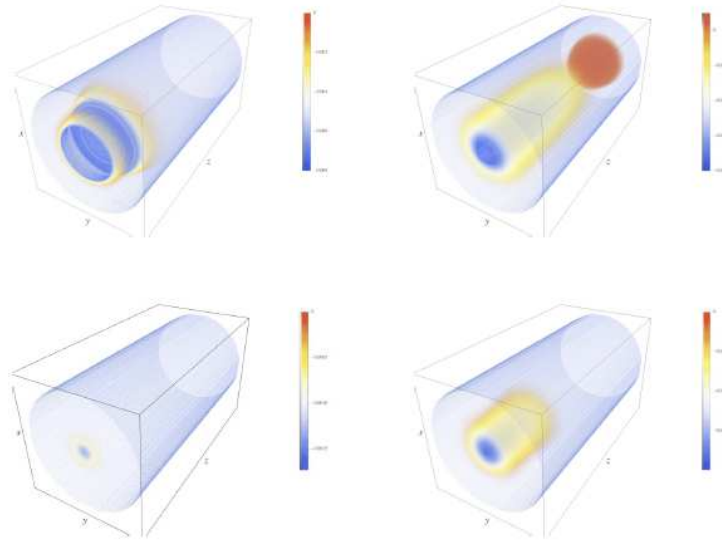


Figure 1 Nonlinear index profile for different propagation regimes in terms of C and I_{peak} . Blue color correspond to higher negative index regions.

3. Conclusions

We have found that Cs_2SnI_6 perovskite NCs in liquid toluene behave as an exceptional negative nonlinear material in a spectral region where most nonlinear materials have positive nonlinear response. This opens the way to use it in guiding devices to achieve negative nonlinearities for pulses in the region of normal dispersion, an unique property able to create a panoply of new effects.

Acknowledgments

This project has received funding from the European Union’s Horizon 2020 research and innovation programme under grant agreement No 62656 (project DROP-IT) and by the Spanish MINECO through projects no. TEC2017-86102-C2-1-R and PID2020-120484RB-I00, and by Generalitat Valenciana PROMETEO/2021/082.

References

- [1] A. Ferrando, J. P. Martínez Pastor, and I. Suárez, “Toward Metal Halide Perovskite Nonlinear Photonics”, *J. Phys. Chem. Lett.*, **9** (18), 5612-5623 (2018).
- [2] I. Suárez, J. P. Martínez-Pastor, M. F. Oszejca, N. A. Lüchinger, B. Graves, S. Agouram, C. Milián and A. Ferrando, “Ecofriendly Perovskites with Giant Self-Defocusing Optical Response”. *Advanced Optical Materials*, **11** (2), 2202120 (2022).

Clean Temporal Pulses from All-Bulk Multipass Cells

Víctor Wilfried Segundo Staels^{1*}, Enrique Conejero Jarque^{1,2} and Julio San Roman^{1,2}

¹*Grupo de Investigación en Aplicaciones del Láser y Fotónica, Departamento de Física Aplicada, Universidad de Salamanca, E-37008, Salamanca, Spain.*

²*Unidad de Excelencia en Luz y Materia Estructurada, Universidad de Salamanca, E-37008, Salamanca, Spain.*

*E-mail: vwsstaels@usa.es

The generation of intense ultrashort pulses with clean temporal profiles is an increasingly stronger necessity to drive progress in fundamental science and ultrafast applications. There are different post-compression schemes proposed to achieve such objective, all based on broadening the pulse spectra through different nonlinear propagation setups and a further spectral phase compensation stage, if needed [1,2]. In this work we focus on the multipass cell (MPC) post-compression scheme [3], which is essentially based on a cavity formed by two mirrors, with some medium inside, allowing for the semi-free-space nonlinear propagation of pulses. This setup enables high output pulse energies and excellent spatial quality, making it an ideal platform for our purpose. Our goal lies in numerically optimizing pulse propagation within all-bulk multipass cells to obtain short and clean pulses i.e. well-shaped temporal pulse profiles without side structures.

1. All-Bulk Multipass Cell Post-Compression Scheme for Clean Temporal Pulse Generation

Since the first proposal of the MPC post-compression technique, MPCs have been used to explore the generation of pulses with better features in pulse energy, average power, and/or spatial and temporal quality [4,5]. In order to improve the temporal quality of the output pulses, the Enhanced Frequency Chirp Regime (EFCR) has proven to be very useful in MPCs filled with gases [6–8]. The EFCR consists of attaining a regime in which the dispersion and the nonlinear interactions (mainly the self-phase modulation (SPM) effect) are both relevant in the propagation. In the EFCR, the spectrum broadens with much less amplitude modulations than if it is broadened only by SPM, enabling the generation of clean pulses with very small secondary structures in the temporal profile, as long as a proper spectral phase correction is applied. Our aim in this contribution is to find the parameters to achieve the EFCR regime in a MPC filled with a bulk medium.

For our numerical study we use a standard Gaussian pulse with 220 μJ and 150 fs pulse duration centred at 800 nm, propagating in a 40 cm long multipass cell, with two convex mirrors with 7.3 m radius of curvature and two fused silica glasses placed beside the mirrors. To properly propagate in the EFCR, we are forced to meet certain requirements tied to the typical propagation lengths, $L_{\text{NL}} < L < L_{\text{D}}$, L_{NL} being the nonlinear distance, L the total amount of glass through which the pulse propagates and L_{D} the dispersion distance. L_{NL} and L_{D} indicate the distance at which the SPM or the dispersion of the system affect the pulse, respectively, and their definition can be found elsewhere [9]. Additionally, we must ensure that the thicknesses of the glasses used in the MPC are smaller than the collapse length to avoid the appearance of strong self-focusing processes. A good configuration to achieve these proposals, for our particular MPC described above, consists of using as nonlinear media two 500 μm thick fused silica glasses placed at the mirrors and a total propagation of 40 round trips.

As can be observed in Fig. 1, we are able to achieve a quite flat spectrum on axis at the end of the propagation, which would lead to a pulse with a Fourier Limit of 20.7 fs at full width at half maximum (FWHM) with secondary structures below the 0.3% of the peak intensity. As seen in figure 1, during the initial round trips, the pulse undergoes an intense spectral broadening, but it is strongly modulated. This is caused mainly by the dominance of SPM over other effects such as dispersion. As the pulse continues its propagation, the spectral broadening stabilizes due the decrease in peak intensity, which is attributable mainly to linear dispersion. Moreover, the interplay between linear dispersion and nonlinear effects fills the spectral valleys, further contributing to the improvement of the spectral flatness.

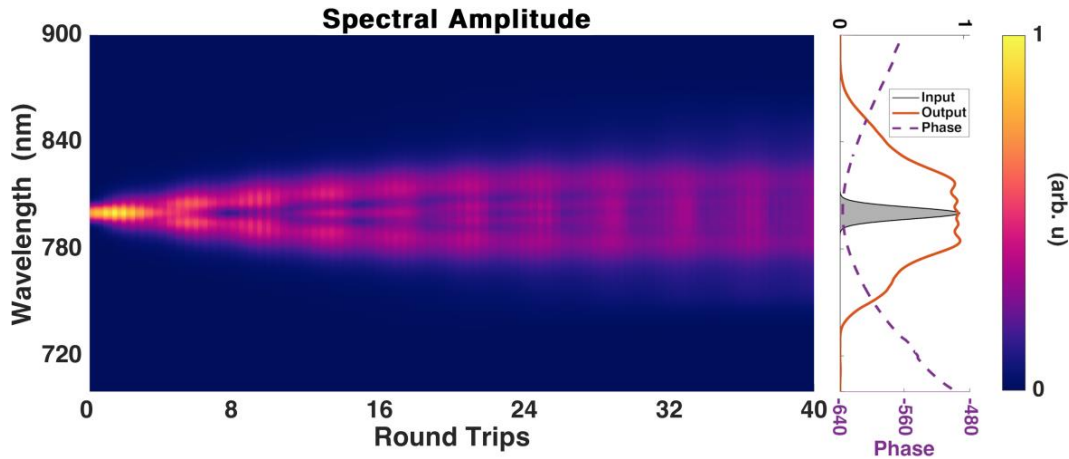


Figure 1 Evolution of the spectral amplitude of the pulse when propagated through the cavity. The right-side figure represents the output spectral amplitude at the output of the cavity compared with the input spectra together with the output phase.

2. Conclusions

By means of numerical simulations, we demonstrate that it is possible to achieve the enhanced frequency chirp regime in an all-bulk MPC configuration. By carefully selecting the size of the glass and the number of roundtrips achieved, we obtain a quite flat spectrum on-axis at the end of the propagation, being compatible with clean and short temporal pulse profiles. These findings represent a significant step forward in the quest to obtain clean ultrashort optical pulses, with promising implications for applications in attoscience and ultrafast optics.

Acknowledgments

This work was supported by grants PID2022-142340NB-I00 and PRE2020-092181, funded by the Spanish Ministry of Science and Innovation.

References

- [1] T. Nagy, P. Simon, and L. Veisz, *Advances in Physics: X* **6**, 1845795 (2021).
- [2] E. A. Khazanov, *Quantum Electron.* **52**, 208 (2022).
- [3] J. Schulte, T. Sartorius, J. Weitenberg, A. Vernaleken, and P. Russbueldt, *Opt. Lett.* **41**, 4511 (2016).
- [4] A.-L. Viotti, M. Seidel, E. Escoto, S. Rajhans, W. P. Leemans, I. Hartl, and C. M. Heyl, *Optica* **9**, 197 (2022).
- [5] M. Hanna, F. Guichard, N. Daher, Q. Bournet, X. Délen, and P. Georges, *Laser & Photonics Reviews* **15**, 2100220 (2021).
- [6] M. Benner, M. Karst, C. Amaya Mendez, H. Stark, and J. Limpert, *J. Opt. Soc. Am. B* **40**, 301 (2023).
- [7] M. Karst, M. Benner, P. Gierschke, H. Stark, and J. Limpert, *Opt. Lett.* **48**, 5899 (2023).
- [8] V. W. S. Staels, E. C. Jarque, D. Carlson, M. Hemmer, H. C. Kapteyn, M. M. Murnane, and J. S. Roman, *Opt. Express, OE* **31**, 18898 (2023).
- [9] G. P. Agrawal, *Nonlinear Fiber Optics*, Fifth edition (Elsevier/Academic Press, 2013).

Improving pulse self-compression in photonic crystal fibers using particle swarm optimization algorithm

Ana Vaquero^{1*}, Fabio Galán¹, Julio San Román^{2,3}, MD Rodríguez Frías^{1,4}, Enrique Conejero Jarque^{2,3} and Cruz Méndez^{1,3}

¹ *Centro de Láseres Pulsados (CLPU), Salamanca, Spain*

² *Grupo de Investigación en Aplicaciones del Láser y Fotónica, Universidad de Salamanca 37008 Salamanca, Spain*

³ *Unidad de Excelencia en Luz y Materia Estructuradas, Universidad de Salamanca 37008 Salamanca, Spain*

⁴ *Universidad de Alcalá E-28801, Madrid, Spain*

*E-mail: avaquero@clpu.es

1. Introduction

Few-cycle pulses are used for a wide variety of applications in many different disciplines. This kind of pulses are commonly generated through post-compression processes or soliton self-compression [1]. However, efficient compression is limited by the difficulty of compensating for certain terms of the acquired spectral phase [2] or the challenge of tuning the specific dynamics needed for self-compression [3]. On the other hand, Machine Learning methods have arisen as advanced techniques to deal with experimental data in order to provide new ways for researchers to effectively handle non easily predictable situations. In this work we explore the potential benefits of modifying the spectral phase of the input pulse before initiating the compression process, pre-compensating some of those remnant phase terms, thus enhancing final compression. In particular, we theoretically optimize self-compression in a hollow core photonic crystal fiber (HC-PCF) by searching for the best initial phase for the input pulses with the optimization algorithm called Particle Swarm Optimization algorithm (PSO) [4].

2. Methodology and results

This study has been carried out by means of simulations and computational methods. Pulse propagation inside the HC-PCF can be described by the Generalized Nonlinear Schrödinger equation for the pulse envelope [5]. The linear and nonlinear responses are given by the properties of the Kagome HC-PCF and the filling gas (argon in our case). For the optimization part we use the PSO algorithm [4] which, inspired by social animal's behavior, tries to iteratively get closer and closer to the solution of a given problem. In this case, the goal is to find the initial phase that minimizes the output pulse duration. Therefore, we build a function that has as input parameters the four terms that determine the input spectral phase and gives as an output the full width at half maximum (FWHM) temporal duration of the pulse obtained after the propagation through the fiber. To maintain similar nonlinear effects, we fix the initial peak power to be the same regardless of the initial phase considered.

To test this method, we propagate 800 nm wavelength gaussian pulses of different durations in a 50 cm long HC-PCF, with 15 μm core radius and filled with one bar of Argon gas at 20°C. For these fiber parameters the zero dispersion wavelength is 350 nm, the pulses propagate in the anomalous dispersion regime of the fiber, allowing for self-compression to occur. Figure 1 shows results obtained for the three different input pulse durations (50 fs, top row, 30 fs middle row and 20 fs bottom row). In the left column we show the intensity (solid blue line) and phase (dashed line) of the input pulse suggested by the PSO accompanied by the non-chirped input pulse (red solid line). The second and third columns show the output pulse and phase obtained when using the non-chirped input pulse and the pulse suggested by the PSO, respectively. The last column compares the spectra obtained with both input pulses; the red (blue) spectrum corresponds to the non-chirped (PSO-optimized) input pulse. As we see, for 50 fs the improvement in

compression is very small, but nonetheless relevant for these two-cycle ultrashort durations. For 30 fs a more noticeable change is achieved, improving compression by 35% (from 8.7 fs to 5.7 fs). Finally, for 20 fs the final duration is reduced by 62% compared to the propagation with flat phase. For pulses longer than 60 fs this procedure does not work as the initial spectral width is so narrow that the spectral phase tailoring does not change the propagation that much.

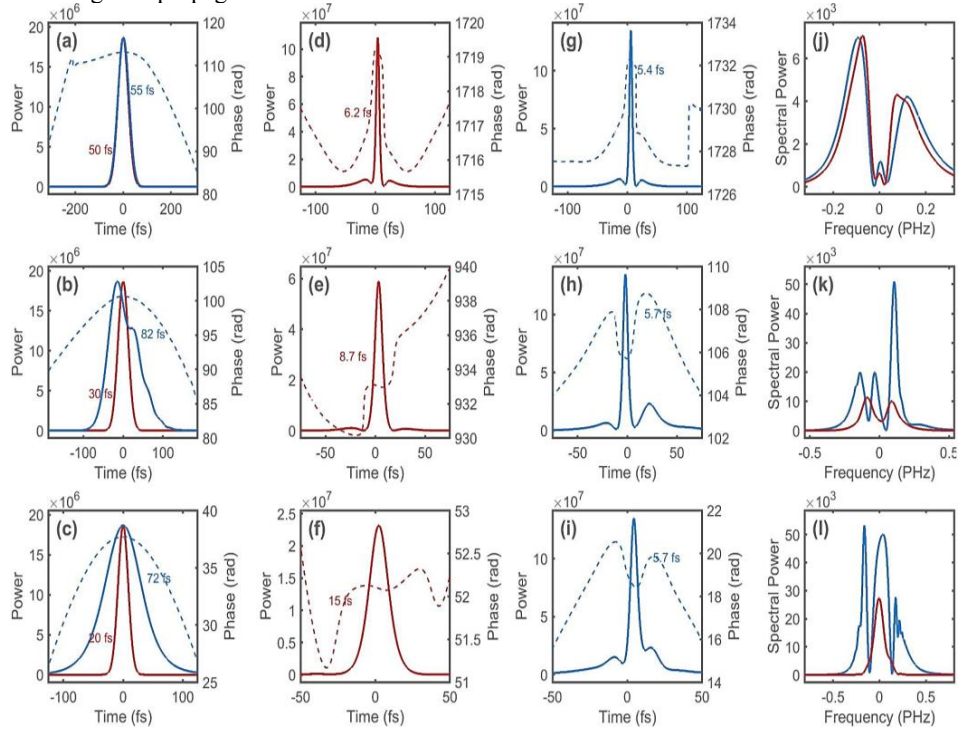


Figure 1 50 fs, 30 fs and 20 fs pulse self-compression in a HC-PCF. (a, b, and c) Input temporal profiles for pulses with flat phase (in red) and optimum phase (in blue). (d-i) Output temporal profiles. (j, k and l) Output spectrums.

3. Conclusions

We have demonstrated that the PSO method can be used to find the optimum phase that leads to the minimum pulse duration at the end of a photonic crystal fiber. This technique has proven to be useful for pulses shorter than 60 fs if we maintain a similar peak power before and after shaping. Results show that the shorter the initial pulses are, the greater enhancement of compression can be achieved with respect to a flat phase input pulse.

Acknowledgments

J.S.R. and E.C. acknowledge funding from Ministerio de Ciencia e Innovación (PID2022-142340NB-I00).

References

- [1] J. C. Travers, W. Chang, J. Nold, N. Y. Joly and P. St. J. Russell, "Ultrafast nonlinear optics in gas-filled hollow-core photonic crystal fibers [Invited]", *J. Opt. Soc. Am. B* 12, vol. 28, A11–A26, (2011).
- [2] F. Silva et al. "Strategies for achieving intense single-cycle pulses with in-line post-compression setups", *Optics Letters*, vol. 43, 2, 337-340 (2018).
- [3] John C. Travers, "Optical solitons in hollow-core fibers", *Opt. Commun.*, vol. 555, 130191, (2024).
- [4] J. Kennedy and R. Eberhart, "Particle swarm optimization" in *Proceedings of ICNN'95 - International Conference on Neural Networks* vol. 4, 1942-1948 (1995).
- [5] G.P. Agrawal, *Nonlinear Fiber Optics* (Academic Press, 3rd Edition, 2001).

Towards an all-fiber source of isolated attosecond pulses driven by high-energy sub-cycle waveforms from soliton dynamics

Marina Fernández Galán^{1,2,*}, Javier Serrano^{1,2}, Enrique Conejero Jarque^{1,2}, Rocío Borrego-Varillas³, Matteo Lucchini^{3,4}, Maurizio Reduzzi⁴, Mauro Nisoli^{3,4}, Christian Brahm⁵, John C. Travers⁵, Carlos Hernández-García^{1,2}, and Julio San Roman^{1,2}

¹Grupo de Investigación en Aplicaciones del Láser y Fotónica, Universidad de Salamanca, 37008 Salamanca, Spain

²Unidad de Excelencia en Luz y Materia Estructuradas, Universidad de Salamanca, 37008 Salamanca, Spain

³Institute for Photonics and Nanotechnologies, Consiglio Nazionale delle Ricerche, 20133 Milano, Italy

⁴Department of Physics, Politecnico di Milano, Piazza Leonardo da Vinci 32, 20133 Milano, Italy

⁵School of Engineering and Physical Sciences, Heriot-Watt University, EH14 4AS Edinburgh, United Kingdom

*E-mail: marinafergal@usal.es

1. Introduction

High-order harmonic generation (HHG) constitutes a well-established table-top source of coherent extreme ultraviolet (EUV) and soft X-ray radiation, which is typically emitted as attosecond pulse trains. This unique light source has become indispensable for probing ultrafast dynamics in the atomic scale [1], and many applications increasingly demand the isolation of a single attosecond pulse from the train. For this purpose, different gating techniques have been developed to confine the HHG process to a single event [2], but these often result in efficiency losses or require additional spectral selection of the HHG spectrum. In this work, we theoretically demonstrate a novel scheme for the compact and robust generation of EUV isolated attosecond pulses (IAPs) from HHG driven by infrared (IR) sub-cycle fields [3]. The latter are generated in a single stage by soliton self-compression in a gas-filled hollow capillary fiber (HCF) [4], which enables pulse compression to durations much shorter than those supported by chirped mirrors and overcomes the complexity of the alternative parametric waveform synthesizers [5].

2. Results and discussion

The proposed setup is shown in Fig. 1(a). Starting from a standard IR pulse (30 fs at 800 nm), a sub-cycle transient is generated by self-compression in an Ar-filled HCF (3 m long, 100 μm core radius). In the simulations, we kept the fiber in a decreasing pressure configuration both to enhance the compression and to deliver the resulting pulses directly to the vacuum HHG beamline [6]. We performed systematic scans of input pulse energy, carrier-envelope phase (CEP) and gas pressure to produce different IR fields at the fiber output. These waveforms were then focused onto a low density gas jet where we computed single-atom HHG emissions by solving the full 3D time-dependent Schrödinger equation (3D-TDSE).

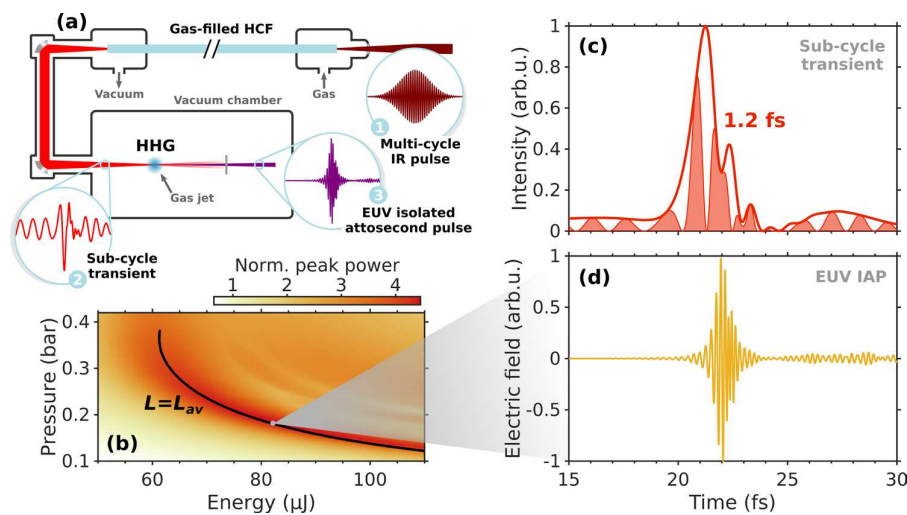


Figure 1. (a) Conceptual setup comprising an in-vacuum HHG beamline driven by the self-compressed IR pulses from a gas-filled HCF with decreasing pressure. (b) Ratio of output to input peak power of the generated pulses from the Ar-filled fiber as a function of initial energy and gas pressure. The contour $L = L_{av}$ runs along the optimal region for high-quality sub-cycle compression. (c) Example of an IR self-compressed pulse and (d) its HHG emission in the form of a clean IAP.

Our results demonstrate that clean IAPs are directly emitted (without additional gating techniques) for a broad set of the IR pulses which undergo the strongest self-compressions in the fiber well down to the sub-cycle regime. Most noticeably, the pump energy and gas pressure which lead to optimal sub-cycle compression, and thus to IAP emission, can be identified in a general manner by matching the HCF length to a characteristic self-compression length ($L = L_{av}$), as shown by the black curve in Fig. 1(b). Thus, this provides a universal guideline towards robust IAP generation for any fiber configuration.

Following this result, we have investigated a simplification of the conceptual setup in Fig.1(a) by removing the focusing stage and driving HHG directly at the fiber output. This requires the generation of millijoule-level sub-cycle pulses with enough intensity so as to efficiently drive the HHG process at the fiber end. By further inspection of soliton scaling laws [4], we verified that the most effective way to upscale the self-compression process to high-energy pulses is to also increase the pump central wavelength by moving towards the mid-IR. This would be of additional interest both for extending the HHG cutoff, and because the stronger anomalous response of HCFs at longer wavelengths ensures the compactness of the setup. As a proof of concept of an all-fiber IAP source, Fig. 2(a) shows the CEP-dependent temporal profiles of the HHG emissions directly computed at the end of a He-filled HCF (1.45 m long, 175 μm core radius), where an input 35 fs, 2 mJ pulse at 1600 nm was compressed to a sub-cycle duration of 2.2 fs. Remarkably, owing to the sub-cycle confinement of the HHG process, the isolation of a single attosecond pulse is preserved for most of the driver CEPs (see Figs. 2(a) and 2(b)), in contrast to the great CEP-sensitivity exhibited by typical HHG experiments with few- to single-cycle driving fields.

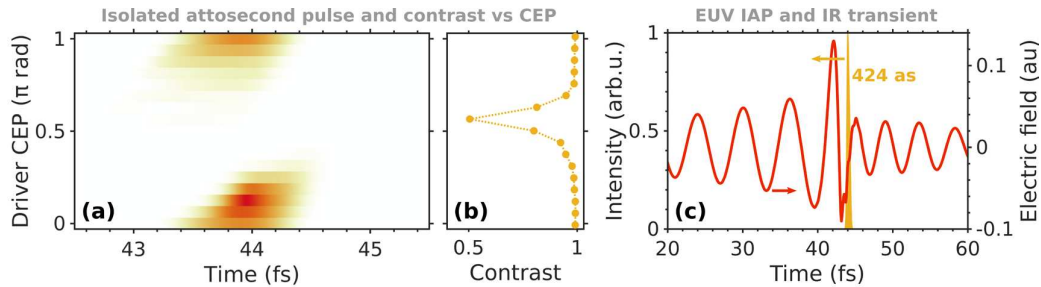


Figure 2. (a) Temporal profile of the single-atom HHG emissions from the He-filled HCF as a function of the CEP of the self-compressed sub-cycle driver (1.3 mJ and 2.2 fs at 1600 nm). (b) Corresponding ratio of energy within the main attosecond pulse to the overall energy in the EUV. (c) Example of IAP generated by the driving waveform with CEP = $3\pi/8$.

3. Conclusions

Altogether, our results demonstrate that IAPs can be directly generated from HHG driven by self-compressed sub-cycle waveforms from gas-filled HCFs. The proposed setup is highly tunable, CEP-robust and compact, opening the way towards a new generation of table-top attosecond EUV sources.

Acknowledgements. This project has received funding from Ministerio de Ciencia e Innovación (PID2022-142340NB-I00) and from the European Research Council under the European Union’s Horizon 2020 Research and Innovation Program (Grant Agreements 851201 and 951224). M.F.G. acknowledges support from Ministerio de Universidades (Grant FPU21/02916). The authors acknowledge RES resources provided by BSC in MareNostrum 4, SCAYLE in Caléndula, and Finisstrae III in CESGA to RES-FI-2022-3-0041 and RES-FI-2023-3-0045.

References

- [1] R. Borrego-Varillas et al, “Attosecond spectroscopy for the investigation of ultrafast dynamics in atomic, molecular and solid-state physics,” *Rep. Prog. Phys.* **85**, 066401 (2022).
- [2] M. Chini et al, “The generation, characterization and applications of broadband isolated attosecond pulses,” *Nat. Photonics* **8**, 178-186 (2014).
- [3] M.F. Galán et al, “Robust isolated attosecond pulse generation with self-compressed sub-cycle drivers from hollow capillary fibers,” *ACS Photonics* **11**, 1673-1683 (2024).
- [4] J.C. Travers et al, “High-energy pulse self-compression and ultraviolet generation through soliton dynamics in hollow capillary fibers,” *Nat. Photonics* **13**, 547-554 (2019).
- [5] G.M. Rossi et al, “Sub-cycle millijoule-level parametric waveform synthesizer for attosecond science,” *Nat. Photonics* **14**, 629-635 (2020).
- [6] M.F. Galán et al, “Optimization of pulse self-compression in hollow capillary fibers using decreasing pressure gradients,” *Opt. Express* **30**, 6755-6767 (2022).

VEGA laser: facility status and near future capabilities

C.Méndez^{1,4}, E. García-García^{1,4}, M. Olivar¹, I. Hernández-Palmero^{1,4}, J.D. Pisonero¹, O. Varela¹, F. Galán-Prado¹, P. Zapatero¹, Javier Pisonero¹, A. Vaquero¹, J.M. Hernández-Pérez¹, L. Volpe^{1,2}, A.M. Cives¹, G. Gatti¹, J. Apiñániz¹, J.L. Henares¹, J.A. Pérez-Hernández¹, D.Arana¹, T. Cebriano¹, J.M. Álvarez¹ and MD Rodríguez Frías¹

¹Centro de Láseres Pulsados (CLPU), Salamanca, Spain

²Universidad Politécnica de Madrid, Madrid, Spain

³Universidad de Alcalá, E-28801, Madrid, Spain

⁴Unidad de Excelencia en Luz y Materia Estructuradas, Universidad de Salamanca, Spain

*E-mail: cmendez@clpu.es

1. Introduction

Due to the enforcement of laser-plasma acceleration research, novel methods for accelerating particles using high-power laser drivers are swiftly developing. Over the last decade, substantial advancements have been achieved in laser performances such as repetition rate, average and peak power, propagation and beam pointing quality as well as laser facility management and operation [1]. VEGA system is an open-to-users Petawatt research facility belonging to the Spanish Pulsed Laser Centre (CLPU) [2]. The Ti:Sapphire Chirped Pulse Amplification (CPA)-based laser chain offers three common front-end outputs called VEGA 1,2,3 with up to 20 TW, 200 TW and 1 PW peak power respectively.

2. Facility beamlines reorganization and operational results

A controllable injection method is crucial for generating high-quality laser-driven electron beams and x-rays. Self-injection represents the most direct approach, yielding high currents and peak energies, but this approximation is vulnerable to fluctuations both in laser parameters and target properties. Some recent works [3] are devoted to enhancing the control of electron self-injection in the nonlinear cavity regime using two co-propagating laser pulses. Taking this into account, from the initial laser configuration, the center has evolved towards a more complex pump-probe scheme including the possibility for using uncompressed VEGA-3 synchronized with VEGA-2 output, a delay line for better than 10 fs beamline-pair jitter synchronization in interaction chambers and a double pulse setup installed into the main VEGA-3 amplifier that generates two collinear beams with different energy and controllable time delay. The new whole beamline scheme characteristics [4] are shown in Table.1. All this reorganization includes low temporal drift between outputs, below 20 fs during the system warming-up time, and a double pulse setup with different operational energy balances for better experimental convenience.

Performance	VEGA 1	VEGA 2	VEGA 3	Double pulse setup		Uncompressed VEGA3
				VEGA 3_1	VEGA 3_2	
Beam diameter FWHM	35 mm	110 mm	220 mm	220 mm	220 mm	110 mm
Energy after compressor	0.5 J	5 J	30 J	121/21 - 10J/2.5J - 8J/3J-7.5J/5J		40 J
Compressor efficiency	70%	70%	74%	74%		
Pulse duration	25 fs, 1.8 % rms	25 fs, 1.8 % rms	30 fs, 1.8 % rms	30 fs, 1.8% rms for both		700 ps, 1.8 % rms
Peak power	15 TW	150 TW	1 PW			0.05 TW
Repetition rate	10 Hz	10 Hz	1 Hz	1 Hz		1 Hz
Central wavelength and spectral bandwidth	800 nm / 70 nm	800 nm / 70 nm	800 / 70 nm	800 / 70 nm	800 / 70 nm	800 / 70 nm
Energy stability (10 minutes)	0.78% rms	0.78% rms	0.6 % rms	0.78% rms	0.78% rms	0.6 % rms
Beam pointing stability (over 500 shots)	3 μrad	3 μrad	5 μrad	5 μrad	5 μrad	5 μrad
Strehl ratio	0.7	0.7	0.8	0.8	0.8	0.8
Beam pointing stability (over 500 shots)	3 μrad	3 μrad	5 μrad	5 μrad	5 μrad	5 μrad
	Possible pump-probe combinations					
	VEGA 2	VEGA 3	VEGA 3_1	VEGA 3_2	VEGA 2	Uncompressed VEGA3
Temporal jitter	< 15 fs		< 10 fs		< 15 fs	
Adjustable delay	0-30 ns (1 fs resolution)		0-1ns (0.5 fs resolution)		0-20 ns (1 fs resolution)	

Table 1. VEGA beamlines characteristics overview

Additionally, facility operational results all over last years of user available time, such as the ones shown in Figure 2 for VEGA-3, are here presented in terms of operative hours, shots per day and per experimental

campaign. Figure 2 shows an improvement in warming-up time as the facility is becoming more operational as well as the possibility of giving energy steps on demand for every experiment. It is also an example of information management usage in order to track critical equipment exposed to degradation, such as compressor diffraction gratings.

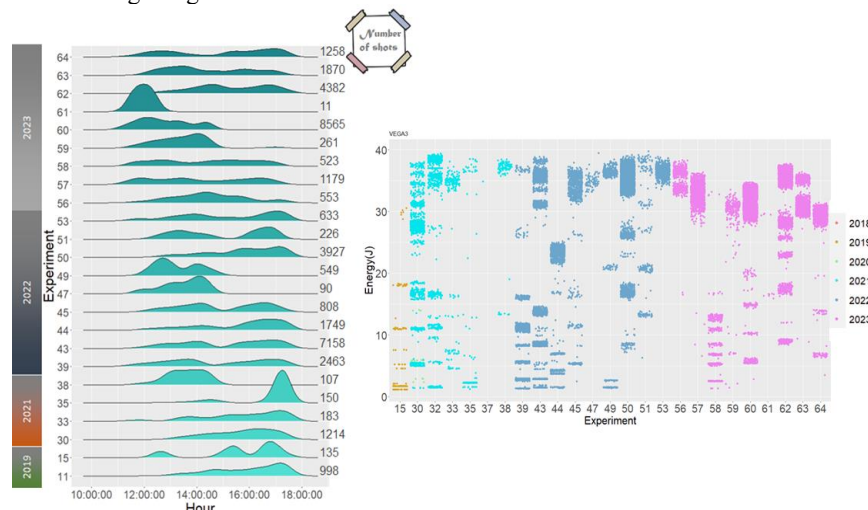


Figure 2. VEGA-3 2019-2023 operational results in terms of hours and shots for different experiments

3. Conclusions and near future developments

The experience developed all over these years [5] [6] has situated CLPU infrastructure within the European high intensity laser community. To reinforce this, an initial proposal of VEGA integration possibilities as secondary site for the Eupraxia [7] European project, using the framework of AREX-2 facility upgrade [8] that is actually ongoing, has been launched. The scheme includes several paths to get 1 PW @ 20 Hz in the actual laser bay as a first step for a future 1 PW @ 100 Hz system with an additional front-end synchronized with the actual one and installed in AREX-2 new facility.

Acknowledgments

We acknowledge the Spanish MCIN through ICTS Equipment Project No. ICTS-2020-04-CLPU-17, FEDER, UE. We also acknowledge all the areas of the CLPU for their support.

References

- [1] Z. Li, Y. Leng, y R. Li, «Further Development of the Short-Pulse Petawatt Laser: Trends, Technologies, and Bottlenecks», *Laser Photonics Rev.*, vol. 17, n.º 1, p. 2100705, ene. 2023, doi: 10.1002/lpor.202100705.
- [2] «Centro de Láseres Pulsados». [En línea]. Disponible en: www.clpu.es
- [3] Z. M. Chitgar, P. Gibbon, J. Böker, A. Lehrach, M. Büscher, «Electron self-injection threshold for the tandem-pulse laser wakefield accelerator», *Phys. Plasmas*, vol. 27, n.º 2, p. 023106, feb. 2020, doi: 10.1063/1.5117503.
- [4] C. Mendez *et al.*, «VEGA laser facility beamlines management for pump-probe experiments», en *Fourth International Conference on Applications of Optics and Photonics*, M. F. P. Martins Costa, Ed., Lisbon, Portugal: SPIE, oct. 2019, p. 151. doi: 10.1117/12.2527481.
- [5] L. Volpe *et al.*, «Generation of high energy laser-driven electron and proton sources with the 200 TW VEGA-2 at the Centro de Láseres Pulsados», *High Power Laser Sci. Eng.*, vol. 7, p. e25, 2019, doi: 10.1017/hpl.2019.10.
- [6] M. Ehret *et al.*, «Ion acceleration by an ultrashort laser pulse interacting with a near-critical-density gas jet». arXiv, 17 de diciembre de 2020. Accedido: 30 de abril de 2024. [En línea]. Disponible en: <https://arxiv.org/abs/2012.09455>
- [7] «EuPRAXIA Design Study Project: “European Plasma Research Accelerator with excellence in Applications”». [En línea]. Disponible en: <https://www.eupraxia-project.eu/home.html>
- [8] «Construcción y equipamiento del área experimental 2. Convocatoria de planes estratégicos ICTS 2021». [En línea]. Disponible en: <https://www.clpu.es/arex2/>

Medida de pulsos ultracortos vectoriales con *amplitude swing*

Cristian Barbero^{1*}, Benjamín Alonso^{1,2} and Íñigo J. Sola^{1,2}

¹Grupo de Investigación en Aplicaciones del Láser y Fotónica, Universidad de Salamanca, Salamanca, E-37008, España

²Unidad de Excelencia en Luz y Materia Estructuradas (LUMES), Universidad de Salamanca

*E-mail: cristianbp@usal.es

1. Introducción

El interés científico y tecnológico en los pulsos láser ultracortos (sub-ps) lleva en constante crecimiento desde que se generaron por primera vez mediante la técnica *mode-locking*, junto a un aumento en su complejidad. Los pulsos en los que el estado de polarización varía temporalmente (y, equivalentemente, con la frecuencia), se conocen como pulsos vectoriales, y tienen aplicaciones en múltiples campos, como ciencia de materiales, biotecnología o *attofísica*. Por ello, se requieren técnicas de caracterización de dichos pulsos capaces de adaptarse a diversas condiciones experimentales. Recientemente, se ha desarrollado la técnica *amplitude swing* (*a-swing*) [1] para la medida temporal de pulsos escalares (aquellos en los que el estado de polarización no depende del tiempo). Ésta presenta un montaje en línea, compacto y versátil (Fig. 1B), fácilmente adaptable a distintas duraciones y *chirps*, anchos de banda y regiones espectrales [2], además de ser robusto frente al ruido [3].

En este trabajo se demuestra la capacidad de *a-swing* de caracterizar pulsos vectoriales, en los que el estado de polarización evoluciona con el tiempo y con la frecuencia, a partir de una sola traza [4]. Primeramente, se estudia analítica y numéricamente cómo se codifica la información del pulso en dicha traza, identificando los distintos términos que contribuyen a la misma. En este tipo de técnicas, denominadas espectrográficas, la información no se puede extraer analíticamente, por lo que es necesario un algoritmo iterativo. Aprovechando el estudio analítico previo, desarrollamos una estrategia de reconstrucción que consta de varias etapas de optimización mediante el algoritmo de Levenberg-Marquardt (si bien se podría usar cualquier otro). Inicialmente, se prueba esta estrategia reconstruyendo distintos pulsos vectoriales simulados y, posteriormente, se aplica a medidas experimentales.

2. Montaje experimental y resultados

Para generar experimentalmente los pulsos vectoriales, se propaga un pulso linealmente polarizado (duración límite Fourier ~ 60 fs) a través de una placa retardadora (cuyos ejes neutros están orientados a un ángulo θ_g) (Fig. 1A). El pulso de entrada se caracteriza mediante una técnica escalar y la placa retardadora se calibra de manera precisa, por ejemplo, mediante interferometría espectral. Por tanto, los pulsos vectoriales generados son conocidos y se pueden comparar con los pulsos reconstruidos mediante *a-swing*, validando así dichas reconstrucciones.

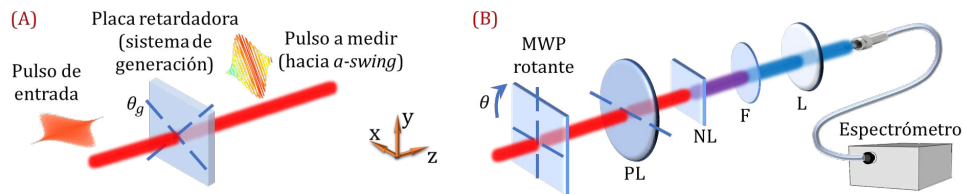


Figura 1. (A) Sistema de generación de pulsos vectoriales, que consiste en una placa retardadora; (B) implementación de *a-swing* para medir los pulsos vectoriales generados previamente: lámina retardadora de orden múltiple lineal (PL), cristal no lineal (NL), filtro (F), lente (L) y fibra acoplada a espectrómetro.

Para medir los pulsos vectoriales así generados, se utiliza la implementación convencional de *a-swing* (Fig. 1B). El pulso vectorial a medir se propaga a través de una lámina retardadora de orden múltiple (MWP) giratoria, donde se generan dos réplicas, temporalmente retardadas, de cada componente del pulso. La amplitud relativa de estas cuatro réplicas estará modulada por θ , la orientación del eje rápido de la MWP respecto al eje horizontal. Estas réplicas se proyectan en la misma dirección utilizando un polarizador lineal, y el pulso resultante genera una señal no lineal (segundo armónico en este caso), cuyo espectro es medido para cada ángulo θ , obteniendo así una traza 2D de *a-swing*.

Se han generado y medido pulsos vectoriales a partir de diversos pulsos escalares de entrada y láminas retardadoras. Como ejemplo, en la Fig. 2 se muestra la reconstrucción de un pulso vectorial que se ha generado de manera que sus componentes apenas se superponen temporalmente. En todos los casos estudiados, los pulsos reconstruidos concuerdan altamente con los simulados, probando la capacidad de *a-swing* para caracterizar el estado de polarización de un pulso vectorial, que es dependiente del tiempo. Además, las ventajas que presenta *a-swing* en el caso escalar se mantienen, puesto que el montaje es el mismo: fácil de alinear, con elementos típicos en cualquier laboratorio de óptica, fácilmente adaptable para medir en un rango amplio de zonas espectrales y duraciones temporales, y robustez frente a ruido.

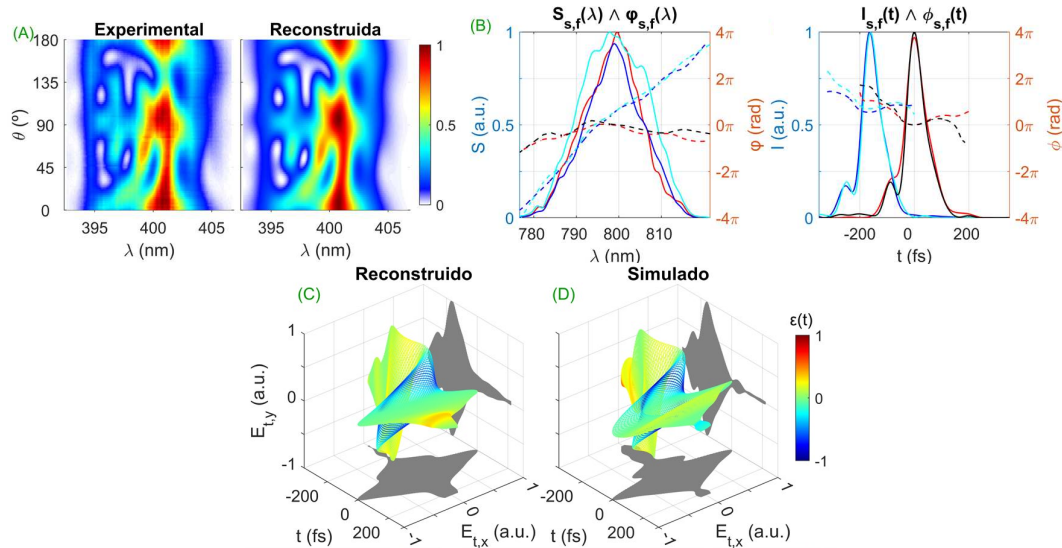


Figura 2. (A) Trazas experimental y reconstruida; (B) espectros experimentales y fases reconstruidas y simuladas en el dominio espectral (izquierda) y temporal (derecha) de dos componentes del pulso; pulso vectorial reconstruido (C) y simulado (D) en el dominio temporal. En (B): rojo: E_x reconstruido; azul: E_y reconstruido; negro: E_x simulado; cian: E_y simulado. Los espectros horizontal y vertical simulados son iguales. El color en (C, D) indica la elipticidad, siendo -1 y +1 polarización circular levógira y dextrógira, respectivamente, y 0 polarización lineal.

3. Conclusiones

En conclusión, se han caracterizado pulsos ultracortos vectoriales, cuya polarización varía a lo largo del tiempo, con la técnica *a-swing*. Una sola traza contiene la información necesaria para reconstruir un pulso vectorial, que ha sido extraída mediante una nueva estrategia de reconstrucción. Esperamos que contribuya al desarrollo del campo de los pulsos vectoriales ultracortos y sus múltiples aplicaciones.

Agradecimientos

Junta de Castilla y León y fondos FEDER (SA136-P20), MINECO (EQC2018-004117-P), y Ministerio de Ciencia e Innovación (PID2020-119818GB-I00). C. B. agradece a la Junta de Castilla y León y al Fondo Social Europeo Plus por el contrato predoctoral.

Referencias

- [1] B. Alonso, W. Holgado, and Í. J. Sola, "Compact in-line temporal measurement of laser pulses with amplitude swing," *Opt. Express* **28**, 15625-15640 (2020).
- [2] M. López-Ripa, Í. J. Sola, B. Alonso, "Amplitude swing ultrashort pulse characterization across visible to near-infrared," *Optics & Laser Technology* **164**, 109492 (2023).
- [3] Í. J. Sola, B. Alonso, "Robustness and capabilities of ultrashort laser pulses characterization with amplitude swing," *Sci. Rep.* **10**, 18364 (2020).
- [4] C. Barbero, B. Alonso, and Í. J. Sola, "Characterization of ultrashort vector pulses from a single amplitude swing measurement," *Opt. Express* **32**, 10862-10873 (2024)

Sistema óptico aplicado a la espectroscopía resuelta en tiempo en el rango de femtosegundo y picosegundo

Mario Guerras^{1*}, Ignacio López-Quintás^{1,2} and Iñigo J. Sola^{1,2}

¹Grupo de Aplicaciones del Láser y Fotónica (ALF), Universidad de Salamanca, España

²Unidad de Excelencia en Luz y Materia Estructurada (LUMES), Universidad de Salamanca, España

*E-mail: mguerras@usal.es

1. Introducción

Existen diversos procesos ultrarrápidos (transiciones de fase en semiconductores, fotofragmentación molecular, generación de fonones en sólidos, fluorescencia ultrarrápida, etc.) [1] cuya caracterización temporal plantea un desafío tecnológico. El reto consiste en alcanzar una resolución temporal más allá del nanosegundo, que es lo que típicamente se alcanza mediante dispositivos electrónicos. Para ello se recurre a una fuente láser que emite pulsos cuya duración temporal se encuentra en el rango subpicosegundo. En particular, existe un reciente interés en realizar espectroscopía resuelta en tiempo de la emisión de fluorescencia que generan ciertos materiales, de forma que, estudiando la evolución temporal de la señal, se obtenga información de sus propiedades ópticas en diferentes situaciones.

El presente trabajo se basa en una técnica conocida como “conmutador óptico” o “puerta óptica” [2] que permite caracterizar procesos ultrarrápidos. En esta técnica también se basan variantes como Frequency Resolved Optical Switching (FROSt) [3] y Plasma Induced FROSt (PI-FROSt) [4]. En estos métodos, un primer pulso se encarga de inducir cambios transitorios en las propiedades ópticas de un medio, actuando como “puerta óptica”. Un segundo pulso genera la señal que se desea medir y se propaga por el medio modificado por el primer pulso a distintos tiempos de retardo, sufriendo cambios en su propagación. De esta forma se analiza la evolución temporal de la señal, ya que la modificación inducida por el primer pulso, provoca un cambio abrupto en el medio por el que se propaga el segundo pulso, actuando como un “conmutador óptico” con resolución temporal suficiente como para estudiar la dinámica de la señal problema.

En este trabajo se presenta el diseño e implementación de un sistema dedicado al estudio de dinámicas ultrarrápidas en el rango de femtosegundos y picosegundos basado en este tipo de “conmutador óptico”. De esta manera, se valida el funcionamiento temporal de la técnica con pulsos ultracortos, con la intención de aplicarlo a la espectroscopía resuelta en tiempo.

2. Montaje experimental

Nuestro montaje experimental (Fig. 1) utiliza dos réplicas de un pulso proveniente de una fuente láser pulsada de Ti:zafiro, cuya longitud de onda central es 798 nm y que emite pulsos de 60 fs con una tasa de repetición de 5 kHz. En la figura 1, el camino óptico 1 incluye una etapa de retardo motorizada que ofrece un control preciso del retardo entre haces, permitiendo obtener medidas con gran resolución temporal. Este primer haz es el que actúa como “conmutador óptico”. Por otra parte, el haz láser del camino 2 se encarga de generar la señal que se desea medir. En este sistema, el principal reto reside en la recolección de la señal debido a su baja intensidad y gran divergencia.

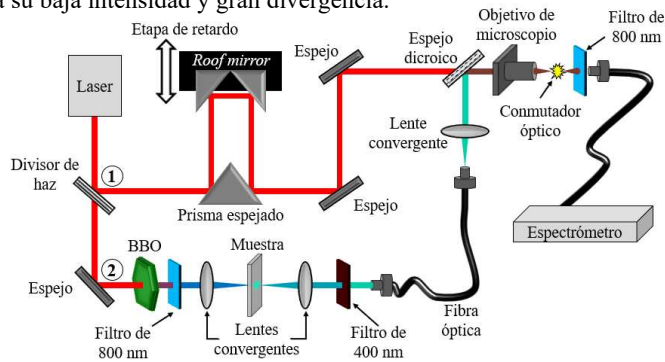


Figura 1. Montaje experimental empleado.

3. Resultados

Las medidas que se obtienen con esta técnica son trazas bidimensionales que presentan la evolución de la señal en función del retardo entre los dos pulsos (Fig. 2). La señal empleada en este trabajo es el segundo armónico de nuestro haz láser (centrado en 400 nm), que se emplea como prueba de concepto para verificar el funcionamiento del sistema. En la figura 2 se diferencian claramente dos zonas, una en la que se tiene máxima intensidad y otra en la que es mínima. Las posiciones previas al retardo cero no muestran cambios, pero una vez se alcanza esta posición, el “conmutador óptico” comienza a actuar y se aprecia una disminución de la intensidad de la señal. Tras el análisis de estas medidas, se está trabajando en un modelo numérico para la reconstrucción de la señal (Fig. 3), obteniendo así la información del pulso tanto en el dominio temporal como espectral.

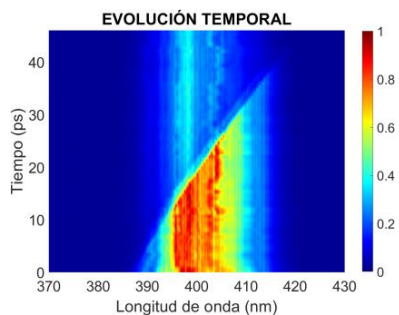


Figura 2. Medida obtenida.

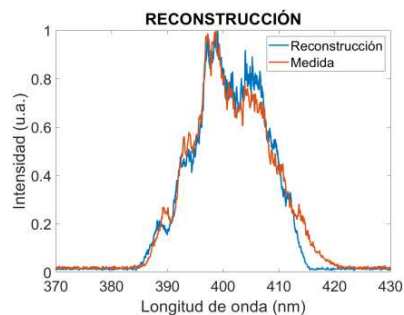


Figura 3. Resultados tras la reconstrucción.

4. Conclusiones

En este proyecto se diseña y construye un sistema para realizar medidas de espectroscopía resuelta en tiempo con una precisión de hasta 7 fs aproximadamente. Para validar el sistema, se verifica el correcto funcionamiento con medidas de una señal de segundo armónico. Se comprueba la robustez del sistema aplicando diferentes condiciones a la señal a medir, principalmente cambiando su duración temporal y comprobándose así que se modifica la inclinación de la transición entre las dos zonas de la señal. Por otra parte, también se modifica la intensidad del pulso que actúa como “conmutador óptico”, afectando a la diferencia de intensidad que se alcanza entre las dos regiones. Una vez validada su operación en el dominio temporal, el siguiente paso es adaptar el sistema al estudio de muestras fluorescentes.

Agradecimientos

Se agradece el apoyo al Programa Investigo, Plan de Recuperación, Transformación y Resiliencia (UE 2021/241). Proyecto financiado por el Servicio Público de Empleo Estatal y la Unión Europea-NextGenerationEU. Proyecto PID2022-142340NB-I00 financiado por MCIN y AEI.

Referencias

- [1] Shank, Charles V. "Investigation of ultrafast phenomena in the femtosecond time domain." *Science* 233.4770 (1986): 1276-1280.
- [2] Itakura, Ryuji, et al. "Frequency-resolved optical gating for characterization of VUV pulses using ultrafast plasma mirror switching." *Optics express* 23.9 (2015): 10914-10924.
- [3] Leblanc, A., et al. "Phase-matching-free pulse retrieval based on transient absorption in solids." *Optics express* 27.20 (2019): 28998-29015.
- [4] Bhalavi, Rishabh Kumar, et al. "Phase-matching-free ultrashort laser pulse characterization from a transient plasma lens." *Optics Letters* 49.5 (2024): 1321-1324.

IR Image Upconversion to Second and Third Harmonic

Adrián J. Torregrosa^{1*}, María Luisa Rico² and Juan Capmany¹

¹*Instituto de Investigación en Ingeniería de Elche I3E, Universidad Miguel Hernández, Avda. de la Universidad s/n, 03202 Elche (Alicante).*

²*Departamento de Tecnología Informática y Computación, Universidad de Alicante, Ctra. San Vicente s/n, 03690 San Vicente del Raspeig (Alicante)*

*E-mail: ajtorregrosa@umh.es

1. Introduction

Infrared (IR) imaging is of great interest in identification, detection, and diagnosis applications in fields such as biomedicine, security, and surveillance. For this purpose, the nonlinear wavelength conversion of images is proposed as a simple technique that allows for translating an image from any band of the IR spectrum to the visible region for real-time visualization with CCD/CMOS silicon sensors by taking advantage of their resolution and efficiency capabilities at a reduced cost. The upconverted image results from the sum frequency mixing (SFM) that takes place in a nonlinear medium between an intense wave acting as a pump and the image resulting from IR illumination with an auxiliary laser at the targeted wavelength. In this work, we present an alternative system based on the generation of the second and third harmonics inside the cavity of a pulsed solid-state laser using passive Q-switching with intracavity peak power levels of the order of kW. For this purpose, a leakage of the generated power is released out used as illumination. Then, the resulting image is coupled back into the cavity through polarization for conversion. Additionally, the system does not require synchronization control for the visualization of objects located several meters away since the pulse duration is between 0.4 and a few microseconds. The proposed system eliminates the need for the auxiliary laser required in conventional image conversion techniques using SFM, resulting simpler, more compact, and portable systems.

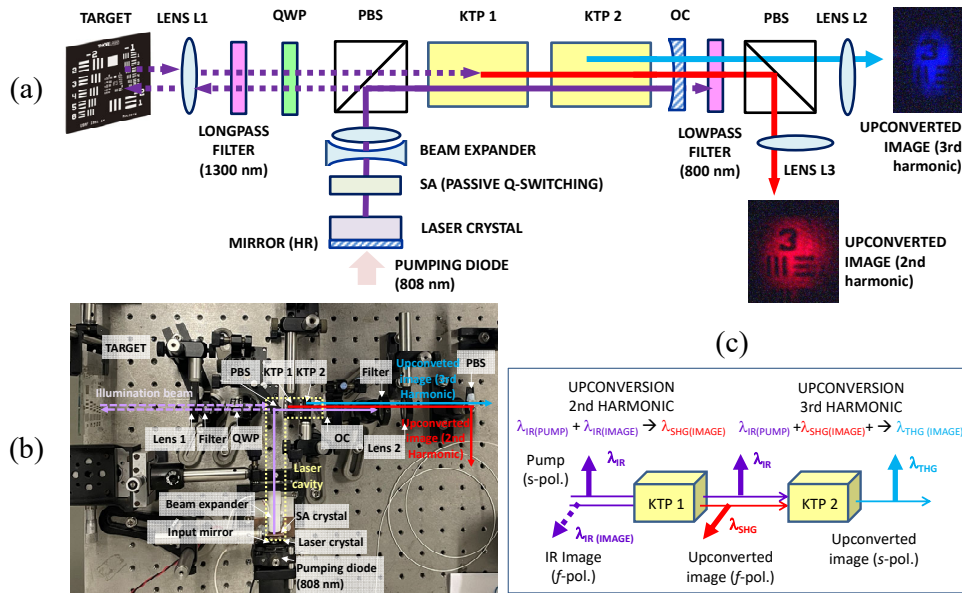


Figure 1. Experimental setup: a) Schematic. b) Experimental arrangement c) Detail of the image upconversion cascading.

2. Experimental configuration and results.

The proposed system is based on an $\text{Nd}^{3+}:\text{YVO}_4$ laser ($3 \times 3 \times 4 \text{ mm}^3$ with Nd^{3+} concentration of 1 at.%), pumped with a laser diode at 808 nm, and oriented so that the polarization of the laser oscillation is perpendicular to the plane contained in Fig. 1 (pol. s) at 1342 nm. The laser operates in a pulsed mode by passive Q-Switching (PQS) with a $\text{V}^{3+}:\text{YAG}$ saturable absorber (SA) with an initial transmittance of 95%. The laser cavity follows a linear configuration folded at a right angle by a polarizing beam splitter (PBS), as shown in Figs. 1.a) and 1.b). The cavity is ended by a flat input mirror, which is deposited on the face

of the laser crystal (HR at 1342 nm and HT at 808 nm on its outer face) and by a flat-concave output mirror OC (HR at 1342 nm with a radius of curvature of 3 m). Through the PBS (transmittance of 0.16% for *pol. s*), a small fraction of the intracavity power is released out to act as an illumination beam [3]. The resulting image at 1342 nm is coupled back into the cavity by polarization (*pol. p*) after the double-pass through a quarter wave plate (QWP). Then, the image is upconverted to the second and third harmonic in two nonlinear crystals of KTP placed inside the laser cavity, by the cascading of two SFM processes, by type II birefringence phase matching (BPM). Fig. 1.c) shows details of the polarization components (*s, f*) of the interacting waves: $1342\text{ nm } (s) + 1342\text{ nm } (f) \rightarrow 671\text{ nm } (f)$, and $1342\text{ nm } (s) + 671\text{ nm } (f) \rightarrow 447\text{ nm } (s)$, where the wave at 1342 nm (*s*) corresponds to the laser oscillation acting as a pump of the concatenated process. In this way, the IR image at 1342 nm (*f*) is upconverted to the second harmonic in the first KTP crystal ($\theta=60^\circ$ and $\phi=0$ cut), and subsequently, the resulting image is upconverted to the third harmonic in the second KTP crystal ($\theta=78^\circ$ and $\phi=0$ cut). The inclusion of a beam expander aims to keep the gaussian-profile laser mode collimated in the laser crystal and in the SA, with a small size of $\sim 100\ \mu\text{m}$ in diameter, in order to reduce the oscillation threshold and to increase the efficiency of the pulsed laser [4]. This configuration also helps to minimize the thermal effect and provides a performance with high intracavity peak power levels. On the opposite side, the beam is also collimated and presents 1 mm diameter in the nonlinear crystals in order not to compromise image resolution. The temporal behaviour is plotted as an example in Figs. 2.a) and 2.b) when the laser crystal is pumped with 3 W, showing a 400 ns pulse duration and a 90 kHz repetition frequency, respectively. Figures 2.c) and 2.d) show the upconverted images to the second and third harmonic when illuminating the group 3 – element 4 (11.3 lp/mm resolution) of an USAF-1951 resolution target.

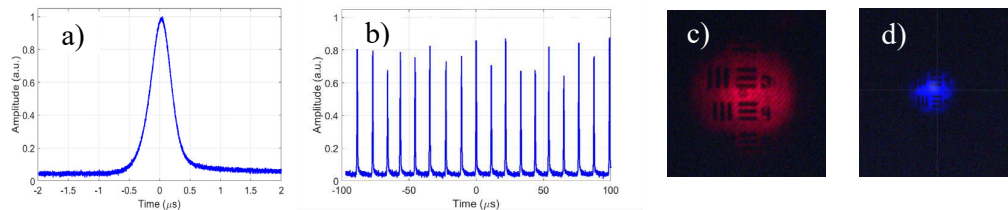


Figure 2. System operation with 3 W pumping at 808 nm: a) y b) Temporal behaviour of the 1342 nm PQS laser (400 ns duration and 90 kHz frequency). Examples of upconverted images: c) Second harmonic (671 nm), d) Third harmonic (447 nm).

3. Conclusion

This work proposes and demonstrates the potential of self-illuminated image conversion systems based on the use of a Q-Switched solid-state laser. The system consists of a $\text{Nd}^{3+}:\text{YVO}_4$ laser pumped by a few-watt commercial diode at 808 nm and a saturable absorber of $\text{V}^{3+}:\text{YAG}$, providing peak intracavity powers above kW with repetition frequencies exceeding 100 kHz. The achieved power levels allow for the cascading of intracavity sum frequency mixing processes in two KTP crystals to translate the original image from 1342 nm to 671 nm, and subsequently, to 447 nm, with good resolution and efficiencies which reach the sensor saturation threshold. Pulse durations fall within the range of 0.4-1.2 μs , facilitating visualization at several meters distance without requiring control electronics for synchronization. The system also presents the advantage of not needing an auxiliary illumination laser, thereby enabling integration and miniaturization for the implementation of compact and portable systems. Furthermore, the appropriate selection of the laser crystal to ensure compatibility of the second and third harmonics with the silicon gap extends visualization with conventional CMOS sensors into the near mid-infrared region.

Acknowledgments

This work has been funded by the following projects: PID2020-117658RB-I00 del MICIU/AEI/10.13039/501100011033 and FEDER (European Union Next Generation EU/PRTR).

References

- [1] J. E. Midwinter, "Parametric Infrared Image Converters," *IEEE J. Quantum Electron.* 4(11), 716–720 (1968).
- [2] C. Pedersen, E. Karamehmedović, J. S. Dam, and P. Tidemand-Lichtenberg, "Enhanced 2D-image upconversion using solid-state lasers," *Opt. Express* 17(23), 20885–20890 (2009).
- [3] A.J. Torregrosa, H. Maestre, M.L. Rico, J. Capmany, "Compact self-illuminated image upconversion system based on intracavity second-harmonic generation", *Opt. Lett.* 43 (20), 5050-5053 (2018).
- [4] J.J. Degnan, "Optimization of Passively Q-Switched Lasers", *IEEE J. Quantum Electron.* 31(11), 1890-1901 (1995).

Experimental study of the effects of optical feedback on the spatial and temporal coherence of the radiation emitted by a semiconductor laser

María Duque Gijón*, Cristina Masoller¹ and Jordi Tiana-Alsina²

¹ Departament de Física, Universitat Politècnica de Catalunya, Rambla Sant Nebridi 22, 08222 Terrassa, Spain

² Department de Física Aplicada, Facultat de Física, Universitat de Barcelona, Martí i Franques 1, 08028 Barcelona, Spain

*E-mail: maria.duque.gijon@upc.edu

1. Abstract

Optical feedback can reduce the linewidth of a semiconductor laser by several orders of magnitude, but it can also cause line broadening (the so-called coherence collapse). While these effects are well understood, the influence of feedback on spatial coherence has received less attention. We propose a technique based on speckle analysis to discriminate feedback effects on spatial and temporal coherence. Speckle is a granular, noisy spatial structure produced by the interference of coherent waves. The contrast of the speckles decreases when the laser is under optical feedback or current modulation, which cause a chaotic output[1]. To discriminate the effects of the excitation of temporal and spatial modes, we perform experiments with an edge-emitting laser (AlGaInP MQW - Thorlabs HL6501MG, 653 nm when $T=18^\circ\text{C}$ and 41.95 mA): we compare the contrast of speckle images recorded with a CMOS camera (IDS UI-1222LE-M, pixel size $5.3\ \mu\text{m}$ with a resolution of 1280×1024 (h \times v) pixels) using either a multimode (MM) or a single-mode (SM) fiber and an optical diffuser (OD), and we also compare the optical spectra after light propagates in the MM or SM fiber. In the regime of coherence collapse we find that: 1) the spectra measured using the MM or SM fiber are the same and 2) the speckle contrast (SC) measured using the MM fiber is significantly lower than that measured using the SM fiber. This difference is interpreted as due to the destabilization of spatial modes which lower the spatial coherence of the laser light and reduce the SC when the MM fiber is used, but which are filtered out by the SM fiber and therefore, the SC measured with the SM fiber is not reduced [2].

Three experiments were performed using either i) a MM fiber, ii) a MM fiber and an optical difussor and iii) a SM fiber and a difussor (see Fig. 1). The detection system allows us to measure the optical spectrum at the end of the MM or SM fiber, or the speckle image generated after propagation in the fiber and dispersion by the difussor. The spectra and the speckle contrast (the standard deviation of the values of the pixels over the average value, $SC = \sigma I / \langle I \rangle$), calculated in a circle of radius 200 pixels in the center of the image) are shown in Fig. 1. With the MM fiber, as expected, low SC is in general correlated with a broad spectrum. However, for some pump currents, this correlation does not hold. This could be due to switching between two regimes: stable emission and chaotic emission. It could be also due to the emission of a single temporal mode but several spatial modes. Ongoing experiments are aimed at distinguishing these effects. With the SM fiber, in contrast, the SC remains high after the laser turns on, despite the broadening of the spectrum. We interpret this as due to the filtering of the spatial modes done by the SM fiber: in the coherence collapse regime optical feedback excites temporal and spatial modes that would lower the SC value, but the spatial modes are filtered out by the SM fiber. This technique is generic and can be used to inspect spatial and temporal coherence under other operating conditions (e.g., optical injection, current modulation) that can induce a chaotic output.

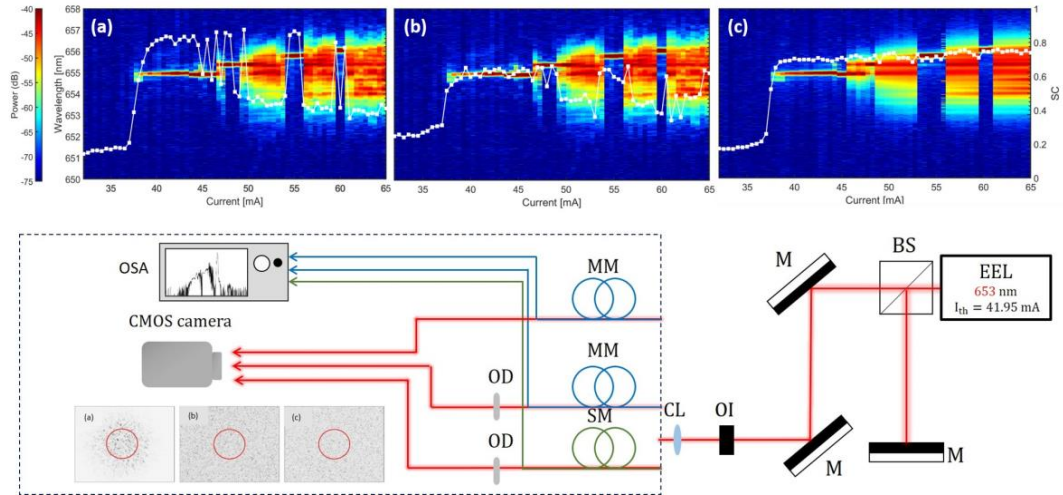


Figure 1. Top: SC (white) and optical spectra (color code) recorded with the laser with feedback (15% threshold reduction) by using the MM fiber (a), the MM fiber + OD (b) and the SM fiber + OD (c). Bottom: Experimental setup.

Acknowledgements

Ministerio de Ciencia, Innovación y Universidades (PID2021-123994NB-C21); Institució Catalana de Recerca i Estudis Avançats (Academia); Agència de Gestió d’Ajuts Universitaris i de Recerca (AGAUR, FI scholarship).

References

- [1] M. Duque-Gijón, C. Masoller, and J. Tiana-Alsina, “Abrupt transition from low-coherence to high-coherence radiation in a semiconductor laser with optical feedback,” *Opt. Express* 31, 3857–3864 (2023).
- [2] M. Duque-Gijón, C. Masoller, and J. Tiana-Alsina, “Experimental study of spatial and temporal coherence in a laser diode with optical feedback,” *Opt. Express* 31, 21954–21961 (2023)

Diseño de guías de ondas superficiales optimizadas para sensado y extracción de luz en materiales cristalinos fabricadas mediante escritura directa con láser de femtosegundo

Victor Arroyo^{1,2*}, Ignacio Lopez-Quintas^{1,2}, Javier R. Vázquez de Aldana^{1,2}, Myriam Bonduelle³, Guillermo Martín³ and Carolina Romero^{1,2}

¹Aplicaciones del Láser y Fotónica, Universidad de Salamanca, Spain

²Unidad de Excelencia en Luz y Materia Estructurada (LUMES), Universidad de Salamanca, Spain

³Université Grenoble Alpes/CNRS, IPAG, Grenoble, France

*E-mail: varroyo@usal.es

1. Introducción

Se ha demostrado que el uso de láseres de pulsos de femtosegundos es muy útil para la fabricación de dispositivos fotónicos integrados en materiales dieléctricos. Esta técnica de fabricación proporciona ventajas sobre otros métodos tradicionales, como por ejemplo la litografía. Entre estas ventajas, podemos mencionar el hecho de que se trata de un proceso en un solo paso y que proporciona la capacidad de realizar estructuras tridimensionales con geometría arbitraria [1]. El desarrollo de esta técnica ha permitido la fabricación de circuitos fotónicos complejos, que pueden emplearse en distintas ramas científicas, como es el caso de la astrofotónica, la biomedicina o la detección óptica.

Para realizar el proceso de fabricación de las estructuras, se focalizan los pulsos láser ultracortos en el interior del material, de esta manera se induce una modificación de su índice de refracción, de forma controlada y siguiendo la geometría deseada.

2. Diseño y resultados

En este trabajo se presenta el diseño y la fabricación de diferentes tipos de estructuras utilizando pulsos láser ultracortos. Presentamos varios diseños que combinan guías de ondas superficiales, basadas en *depressed-index cladding* [2,3], y micro-antenas superficiales fabricadas sobre las guías de onda. El objetivo de las guías de onda superficiales es aumentar el área de interacción de la luz confinada en el interior del dispositivo con la superficie, manteniendo un perfil de propagación monomodo de manera controlada, de esta forma la estructura puede interactuar con el entorno y detectar los pequeños cambios que se produzcan en la zona adyacente.

Por un lado, presentaremos guías de onda superficiales, las cuales se estrechan a medida que nos desplazamos a lo largo del cristal, esto nos permitirá tener una entrada suficientemente amplia como para que el haz se acople sin problemas en la guía, mientras que, al irse reduciendo el tamaño de la guía, conseguimos que el haz quede confinado de tal manera que tengamos un haz monomodo y controlado, manteniendo el contacto con la superficie, tal y como se puede observar en Fig. 1.

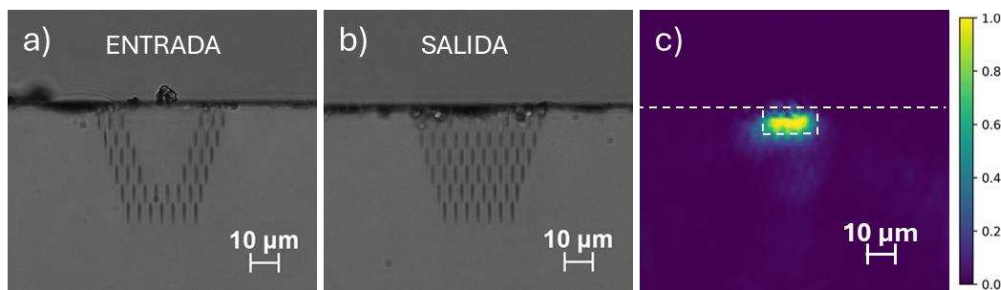


Figure 1 En a) y b), imágenes de microscopía óptica de las secciones de entrada y salida de una guía de onda superficial con estructura hexagonal. En c) imagen del modo confinado a la salida de la guía de onda.

Por otro lado, presentaremos guías de onda superficiales rectas a las cuales les hemos añadido micro-antenas en la superficie mediante ablación. El uso de las micro-antenas potencia la capacidad de las guías superficiales de extraer luz, estas se inscriben con orientación perpendicular a la guía de ondas, tal y como se puede observar en Fig. 2.

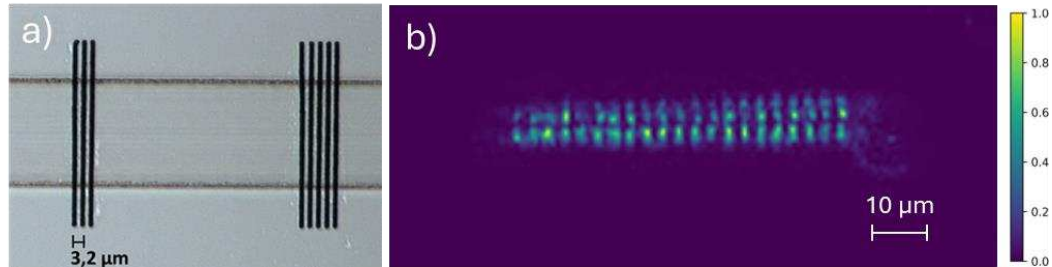


Figure 2 En a) imagen de microscopía óptica de algunas antenas inscritas en la sobre la guía de onda. En b) imagen de la luz extraída de la guía por medio de una antena de 21 *grooves*.

Este tipo de estructuras combinadas presentan un gran potencial para su integración en sensores ópticos activos de alta eficiencia [4]. Aunque la fabricación se ha demostrado en Nd:YAG y LiNbO₃, es posible extender esta configuración a cualquier otro cristal transparente.

Agradecimientos

Este trabajo es parte de la ayuda PID2020-119818GB-I00 y PRE2021-101131, financiado por MCIN/AEI/10.13039/501100011033 y por el FSE+.

Referencias

- [1] Osellame, R., Maselli, V., Vazquez, R. M., Ramponi, R., & Cerullo, G. (2007). Integration of optical waveguides and microfluidic channels both fabricated by femtosecond laser irradiation. *Applied physics letters*, 90(23).
- [2] Okhrimchuk, A., Mezentsev, V., Shestakov, A., & Bennion, I. (2012). Low loss depressed cladding waveguide inscribed in YAG: Nd single crystal by femtosecond laser pulses. *Optics express*, 20(4), 3832-3843.
- [3] Amandine Baillard, Pavel Loiko, Carolina Romero, Víctor Arroyo, Javier Rodríguez Vázquez de Aldana, Michaël Fromager, Abdelmjid Benayad, Alain Braud, Patrice Camy, and Xavier Mateos, "Orange surface waveguide laser in Pr:LiYF₄ produced by a femtosecond laser writing," *Opt. Lett.* 48, 6212-6215 (2023).
- [4] Li, G., Li, H., Gong, R., Tan, Y., de Aldana, J. R. V., Sun, Y., & Chen, F. (2017). Intracavity biosensor based on the Nd: YAG waveguide laser: tumor cells and dextrose solutions. *Photonics Research*, 5(6), 728-732.

Microscopía de generación de segundo armónico en cristales microestructurados con pulsos de femtosegundo: BBO y Nd:YAG

Nuria Sevilla-Sierra^{1,2*}, Javier Rodríguez Vázquez de Aldana^{1,2}, Carolina Romero^{1,2},
Xavier Mateos³, Ignacio Lopez-Quintas^{1,2}

¹ Grupo de Investigación en Aplicaciones del Láser y Fotónica, Universidad de Salamanca (USAL),
Pl. La Merced SN 37008 Salamanca, Spain

² Unidad de Excelencia en Luz y Materia Estructurada (LUMES), Universidad de Salamanca, Spain

³ Física i Cristal·lografia de Materials (FiCMA), Universitat Rovira i Virgili (URV),
43007 Tarragona, Spain

*E-mail: nsevillasierra@usal.es

1. Introducción

La generación de segundo armónico (SHG por sus siglas en inglés, *Second Harmonic Generation*) es un proceso óptico paramétrico no lineal que implica la creación de un fotón de frecuencia 2ω destruyendo al mismo tiempo dos fotones de frecuencia ω [1]. Esto sólo puede darse en materiales no centrosimétricos con susceptibilidad de segundo orden $\chi^{(2)}$ no nula, como puedan ser cristales anisótropos o tejidos biológicos con microestructura fibrilar. El campo de segundo armónico depende cuadráticamente del campo fundamental ω , lo que implica que la eficiencia del proceso aumenta con la intensidad de la radiación fundamental. Los láseres de pulsos ultracortos son, por lo tanto, la fuente más apropiada para generar señal 2ω detectable. La microscopía de segundo armónico (SHM, por sus siglas en inglés) es una técnica basada en escanear la muestra con un láser de pulsos ultracortos altamente focalizado, al mismo tiempo que se mide la señal de segundo armónico generada en cada posición de escaneo. Dado que la principal interacción no lineal láser-materia está muy restringida al volumen focal las medidas son intrínsecamente confocales y por ello permiten un preciso seccionado tridimensional. La técnica SHM puede revelar mucha información morfológica y estructural en la microescala, propiedades no lineales y composición química de la muestra [2].

2. Materiales y métodos

Los pulsos láser de femtosegundo pueden nano- y microestructurar sólidos transparentes, modificando localmente y con gran precisión espacial su índice de refracción. En este trabajo se ha investigado la respuesta no lineal de dos cristales previamente microestructurados mediante láser: un cristal no centrosimétrico (β -BaB₂O₄, BBO) y uno centrosimétrico (Nd:YAG). Se utilizó un sistema láser de femtosegundos (láser de escritura) para irradiar la muestra, produciendo micromodificaciones dentro del volumen del cristal, haciendo diferentes grupos de irradiaciones tanto en el BBO como en el Nd:YAG. Las medidas SHM fueron realizadas con un microscopio de fabricación propia que utiliza un oscilador de Ti:Zafiro como fuente de iluminación. Los pulsos generados en este oscilador tienen una duración de 120 fs, están centrados en 795 nm y se emiten con una tasa de repetición de 80 MHz. En este estudio se obtuvieron mapas de segundo armónico escaneando la muestra gracias a un sistema motorizado que permite mover la muestra de forma que el punto focal se vea desplazado a lo largo de las líneas inscritas mediante láser, lo que resulta en variaciones espaciales de la intensidad de señal de segundo armónico generada, que pueden ser medidas y asignadas con precisión a su punto XYZ de generación.

3. Resultados

El BBO es uno de los cristales no lineales más ampliamente utilizados debido a su alta no linealidad óptica, su gran rango de transparencia y su robustez física. Además, permite establecer ajuste de fase (*phase-matching*) en una amplia ventana espectral, asegurando así una conversión eficiente [3]. En este trabajo se ha demostrado que, bajo ciertas condiciones, el proceso de SHG en las líneas de daño creadas por irradiación con pulsos ultracortos exhibe un aumento local en condiciones de polarización en desajuste de fase para la zona no irradiada (figura 1). Este fenómeno se atribuye en este trabajo a una modificación de la susceptibilidad no lineal y a procesos de *phase-matching*.

El segundo cristal estudiado, Nd:YAG, tiene una estructura centrosimétrica. Se confirmó en este

trabajo la generación de señal de segundo armónico en las líneas de daño y se analizó en detalle en función de los parámetros de irradiación de las micromodificaciones inscritas. Se encontró que la señal de segundo armónico aumenta al aumentar la energía del pulso de escritura y al disminuir la velocidad de desplazamiento del láser de escritura (ya que aumenta la superposición de pulsos). También se observó que la polarización del láser de medida tiene un efecto significativo en la intensidad de la señal SH. En este caso, la polarización del láser de medida más eficiente a la hora de generar señal de segundo armónico es la perpendicular a la interfaz, ya que es la orientación del campo la que revela más eficazmente la anisotropía inducida por el daño (figura 1).

Las micromodificaciones inducidas en la estructura del YAG por el láser de escritura explican estos efectos, que incluyen la modificación local del estado cristalino y la transformación de fase que ocurre en las líneas procesadas [4, 5].

4. Conclusiones

Los fenómenos no lineales observados permiten validar la microscopía de segundo armónico como una técnica útil para conseguir imágenes tridimensionales y de diagnóstico de microestructuras fabricadas mediante pulsos láser ultracortos, como puedan ser guías de onda o *microgratings*, de utilidad en dispositivos fotónicos. Aunque la técnica ya ha sido ampliamente utilizada en materiales no lineales, los resultados obtenidos abren la posibilidad de fabricar dispositivos fotónicos integrados en materiales centrosimétricos en los que inicialmente no se espera tener una respuesta no lineal.

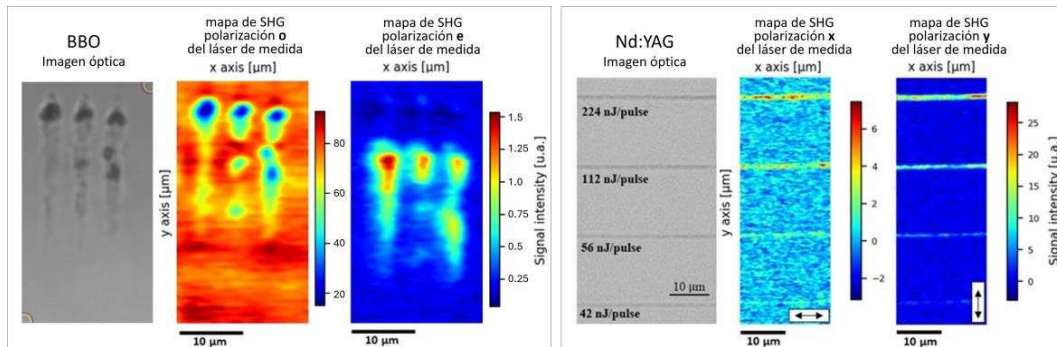


Figura 1 Mapas de segundo armónico obtenidos y sus correspondientes imágenes ópticas.

Agradecimientos

N. Sevilla-Sierra agradece a la Consejería de Educación de la Junta de Castilla y León, así como al Fondo Social Europeo Plus (FSE+) por su financiación. También agradecen los autores a los proyectos de la Consejería de Educación de la Junta de Castilla y León (SA136P20); Ministerio de Ciencia, Innovación y Universidades (PID2020-119818); y al proyecto PID2022-141499OB-10, financiado por MICIU/AEI/10.13039/501100011033/ y por FEDER/UE.

Referencias

- [1] R. W. Boyd, AL Gaeta, and E. Giese. *Nonlinear optics* (Springer, 2008).
- [2] V. Parodi et al. "Nonlinear optical microscopy: From fundamentals to applications in live bioimaging". *Frontiers in bioengineering and biotechnology*, **8**:585363 (2020).
- [3] D. N. Nikogosyan. "Beta barium borate (BBO) a review of its properties and applications". *Applied Physics A*, 52:359–368 (1991).
- [4] S. S. Fedotov, L. N. Butvina, and A. G. Okhrimchuk. "Plastic deformation as nature of femtosecond laser writing in YAG crystal". *Scientific Reports*, **10**(1):19385 (2020).
- [5] T.O. Lipateva et al. "Direct laser writing in YAG single crystal: Evolution from amorphization to nanograting formation and phase transformation". *J of Alloys and Compounds*, **942**:169081, (2023).

Strong field physics in solids from a Wannier perspective

Rui E. F. Silva^{1*}

¹*Instituto de Ciencia de Materiales de Madrid (ICMM), Consejo Superior de Investigaciones Científicas (CSIC), Sor Juana Inés de la Cruz 3, 28049 Madrid, Spain*

²*Department, institution, address*

*E-mail: ruiefdasilva@gmail.com

1. Format description

The recent discovery of high harmonic generation in solids [1], merging the fields of strong field and condensed matter physics, opened the door for the direct observation of Bloch oscillations [1], all-optical reconstruction of the band structure [2] and direct observation of the influence of the Berry curvature in the optical response [3]. In this work, we will focus on 2D materials, focusing on the fingerprint of excitons in the high harmonic spectrum [4]. Furthermore, we discuss how nonlinear optical response can be used to track the magic angle in twisted bilayer graphene [5]. Last, we will show how the use of Wannier orbitals can be useful in the calculation of the nonlinear optical response of solids [6], in particular, the development of a real-time, real-space, approach for the light-matter interaction problem in crystals.

References

- [1] S. Ghimire *et al*, *Nature Physics* **7** (2011) 138.
- [2] G. Vampa *et al*, *Phys. Rev. Lett.* **115** (2015) 193603.
- [3] H. Liu *et al*, *Nature Physics* **13** (2017) 262.
- [4] E. B. Molinero *et al*, *arXiv* (2023) 2307.16647.
- [5] E. B. Molinero *et al*, *Optica* **11** (2024) 171.
- [6] R. E. F. Silva, F. Martín, M. Ivanov, *Phys. Rev. B* **100** (2019) 195201.

Generation of extreme-ultraviolet high-topological charge spatiotemporal optical vortices

Rodrigo Martín-Hernández^{1,2,*}, Guan Gui³, Luis Plaja^{1,2}, Henry K. Kapteyn³, Margaret M. Murnane³, Chen-Ting Liao³, Miguel A. Porras⁴ and Carlos Hernández-García^{1,2}

¹Grupo de Investigación en Aplicaciones del Láser y Fotónica, Departamento de Física Aplicada, Universidad de Salamanca, 37008, Salamanca, Spain

²Unidad de Excelencia en Luz y Materia Estructuradas (LUMES), Universidad de Salamanca, Salamanca, Spain

³JILA and Department of Physics, University of Colorado and NIST, Boulder, CO 80309, United States of America

⁴Grupo de Sistemas Complejos, ETSIME, Universidad Politécnica de Madrid, Ríos Rosas 21, 28003 Madrid, Spain

*E-mail: rodrighomh@usal.es

1. Introduction

The interest in the spatiotemporally tailored of light beams has increased exponentially due to their applications in diverse fields. Particularly, a novel family of optical vortices, known as spatiotemporal optical vortices (STOVs), have deserved a substantial attention. Unlike longitudinal vortices, which have a twisted phase profile in the transverse spatial plane, STOVs present a spiral phase profile in the spatiotemporal plane. STOVs are identified by a topological charge defined by the number of 2π -phase jumps, and have been extensively studied and generated in the near infrared (IR) and the visible, where they can be obtained with standard optical elements [1]. Recently, perturbative second order harmonic STOV generation was observed resulting in the driving STOV's topological charge doubling [2, 3]. As optical elements are inefficient at short wavelengths, high-frequency STOVs are still to be observed.

In this work, we study high-order harmonic generation (HHG) non-linear process to convert low topological charge near-IR STOVs into high-frequency high-topological charge STOVs in the extreme-ultraviolet (EUV). Analogously, HHG has been demonstrated an excellent strategy for obtaining standard vortices with high topological charges [4]. A recent theoretical work paved the way towards the generation of high-frequency STOVs through HHG [5]. In this contribution we demonstrate that HHG with focused STOVs show interesting possibilities depending on the target's position, as they are not propagation eigenmodes [6]. In Fig. 1a schematic representation of the process is given. A near-IR, low topological charge (n_0) elliptical STOV (Fig. 1a), is focused into a gas target where the HHG process takes place. At the gas-jet, the q -th harmonic-order near-field is upconverted into an elliptical STOV with $n_q = qn_0$ topological charge (Fig. 1b). Due to STOV's propagation dynamics, the elliptical EUV STOV evolves into a lobulated spatiotemporal distribution with n_q 2π -phase jumps (Fig. 1c). To recover a high-frequency, high-topological charge harmonic elliptical STOV, refocusing the far-field harmonic is required to exchange the temporal and spectral features (Fig. 1 d) [7].

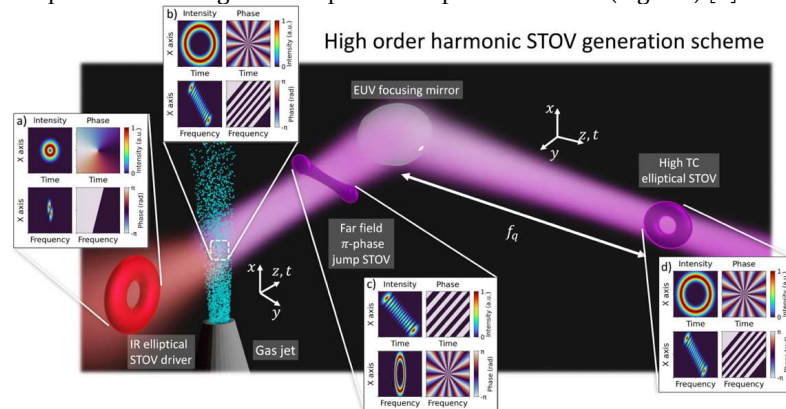


Figure 1. Schematic representation of the HHG process driven by a near-IR elliptical STOV. The insets show (a) the spatio-temporal and spatio-spectral intensity and phase profiles for the driving IR beam; (b) the 13th harmonic order near-field distribution at the gas jet; (c) its far-field propagation, and (d) refocusing leading to EUV high topological charge elliptical STOV.

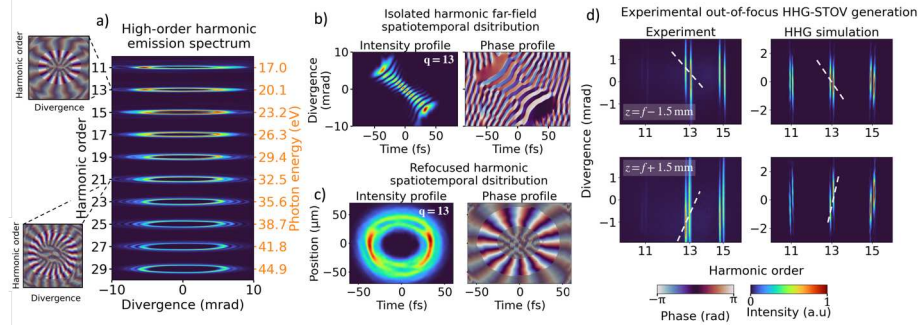


Figure 2. High-order harmonic generation results driven by a STOV (HHG-STOV). In panel a) the simulated far-field spectrum showing an elliptical spatio-spectral distribution driven by a single charged elliptical STOV. b) The spatiotemporal intensity and phase distribution of the far field 13th harmonic order and its refocusing with a 20 cm focal length mirror in c). d) On the left, experimental results of HHG driven by a single charged STOV before $z = f - 1.5 \text{ mm}$ and after $z = f + 1.5 \text{ mm}$. On the right, the simulated counterpart, showing a great agreement. The dashed lines remark the line connecting the double striped maximum intensity points.

2. Results

In Fig. 2a we present the calculated high-order harmonic far-field spectra using 800 nm driving wavelength and a single charged STOV focused into a hydrogen gas target. The driving STOV topological charge is upconverted in the near-field, and its far-field propagation results in spatio-spectral optical vortices (SSOV), with the harmonics exhibiting elliptical intensity distributions. The phase distributions for 13th and 21st harmonic orders (see insets) clearly show $n_q - 2\pi$ phase jumps. Fig. 2b corresponds with the spatiotemporal intensity (left) and phase (right) far-field distribution for the 13th harmonic order, presenting $n_q + 1$ lobes. This lobulated far-field harmonic distribution, thanks to the STOV propagation dynamics, can be converted into an elliptical distribution through refocusing, for example, with an EUV focusing mirror. In Fig. 2c the 13th harmonic is refocused assuming a $f=20$ cm focal length mirror, resulting in an elliptical intensity distribution and a twisted phase profile with 13 2π phase jumps. Thus, the topological scaling law for the refocused STOVs is $n_q = qn_0$.

In Fig 2d we present the first experimental results of high harmonic STOVs driven by a near-IR elliptical STOV. The experiments are performed in a Xenon gas-jet with STOV laser pulses of 800 nm central wavelength, ~ 60 fs pulse duration and ~ 0.35 mJ pulse energy. An imaging spectrometer is used to characterize the far-field emission. The target is placed before ($z = f - 1.5 \text{ mm}$) and after ($z = f + 1.5 \text{ mm}$) the driving STOV focus. The displacement of the gas-jet respect to the STOV focus results on a non-perfect elliptical driving STOV, leading to a striped harmonic distribution. Interestingly, the slope of the line connecting the center of each harmonic stripes shows a sign swap dependent on the location respect to the driving STOV focus, arising from the driving STOV warping as it travels and goes through its focus. Next to the experimental results, the corresponding HHG simulations are presented, in a hydrogen gas-jet, predicting the experimental intensity stripes and the slope swapping in the out-of-focus configuration. The excellent agreement between theory and experiment allows us to confirm the generation, for the first time, of high-order STOVs in the EUV.

Acknowledgments

We acknowledge financial support from the European Research Council (ERC) under the European Union's Horizon 2020 research and innovation program (Grant Agreement No. 851201). This project has also received funding from the Spanish Ministerio de Ciencia, Innovación y Universidades (PID2022-142340NB-I00). Partially supported by the Spanish Ministry of Science and Innovation, Gobierno de España, under Contract No. PID2021-122711NB-C21.

References

- [1] Andy Chong, Chenhao Wan, Jian Chen, and Qiwen Zhan "Generation of spatiotemporal optical vortices with controllable transverse orbital angular momentum" Nat. Phot., 14(6):350–354, 2020.
- [2] Gui, G., Brooks, N.J., Kapteyn, H.C. et al. Second-harmonic generation and the conservation of spatiotemporal orbital angular momentum of light. Nat. Photon. 15, 608–613 (2021).
- [3] S. W. Hancock, S. Zahedpour, and H. M. Milchberg, "Second-harmonic generation of spatiotemporal optical vortices and conservation of orbital angular momentum," Optica 8, 594-597 (2021)
- [4] Carlos Hernández-García, Antonio Picón, Julio San Román, and Luis Plaja "Attosecond extreme ultraviolet vortices from high-order harmonic generation" Phys. Rev. Lett., 111:083602, 2013.
- [5] Fang, Y., Lu, S., & Liu, Y. (2021). Controlling photon transverse orbital angular momentum in high harmonic generation. Physical Review Letters, 127(27), 273901.
- [6] Porras, M. A., & Jolly, S. W. (2024). Procedure for imparting transverse orbital angular momentum by focusing spatiotemporally coupled ultrashort pulses. Physical Review A, 109(3), 033514.
- [7] Rodrigo Martín-Hernández, Guan Gui, Luis Plaja, Henry K. Kapteyn, Margaret M. Murnane, Miguel A. Porras, Chen-Ting Liao and Carlos Hernández-García. In preparation.

Tailoring gold plasmonic metasurfaces for efficient harmonic generation

C. Cojocaru^{1*}, S. Mukhopadhyay¹, M. A. Vincenti², K. Hallman³, M. Scalora⁴, R. Vilaseca¹ and J. Trull¹

¹ *Department of Physics, Universitat Politècnica de Catalunya, Rambla Sant Nebridi 22, 08222 Terrassa (Barcelona), Spain*

² *Department of Information Engineering – University of Brescia, Via Branze 38, 25123 Brescia, Italy*

³ *PeopleTec, Inc. 4901-I Corporate Dr., Huntsville, AL 35805, USA*

⁴ *Aviation and Missile Center, US Army CCDC, Redstone Arsenal, AL 35898-5000, USA*

*E-mail: crina.maria.cojocaru@upc.edu

In the last few decades, both experimental and theoretical nonlinear optics (NLO), have focused on illuminating thick materials under phase matching conditions in the low absorption spectral range, to maximize the bulk nonlinear (NL) interaction and achieve very high NL efficiencies. The NL polarization term plugged into the Maxwell's equations, primarily consists of the electric-dipole/bulk contribution ($\chi^{(2)}$) while other contributions coming from the surface or magnetic effects, are usually many order of magnitude smaller and thus neglected. However, as the material thickness is reduced down to nanometer size, the bulk nonlinearity reduces drastically producing second (SH) and third harmonic (TH) signals with efficiencies of the order of 10^{-7} - 10^{-13} , thus becoming comparable to surface nonlinearity, electric quadrupole and magnetic sources [1]. In this scenario, optical nanomaterials have emerged as a very promising platform to capture new and unique aspects of light localization and light-matter interaction at the nanoscale. The rapid development in nano-fabrication techniques lead to precision designs of subwavelength optical metamaterials (nanospheres, gratings, pillars etc.). But soon it became clear that classical NLO theories rely on approximations that cannot fully explain metals/metallic nanostructures, the observed effects and an effort is needed to fully describe the behavior of light propagation and interaction at the nanoscale and in particular in metasurfaces.

Here we propose a novel approach to face this problem that considers in first place the nontrivial problem of how the strategic materials used in the photonics nanostructure fabrication (i.e. metals, semiconductors, or conductive oxides) respond to linear and NL excitation by ultrashort laser pulses in different spectral range. These studies, performed on layers a few nanometers thick, remove the usual approximations and identify new mechanisms that may trigger the interaction, and must be consistently accounted for in the theoretical models in order to understand the physics involved. Recently we have studied, both experimentally and theoretically, the behavior of different materials and gained new understanding about the basic physical mechanisms responsible for their optical response. Our theoretical approach is based on a Maxwell Hydrodynamic model that accounts for competing surface, magnetic, and bulk nonlinearities arising from both free (conduction) and bound (valence) electrons and preserves linear and NL material dispersions, nonlocal effects, and the influence of hot electrons [2].

Our recent studies on SH and TH generation from 20 nm and 70 nm-thick gold nano layers allowed us to extract its basic physical intrinsic properties [4]. However, the NL efficiency from nanolayers are extremely low. An important enhancement can be envisaged by tailoring and enhancing the NL optical properties of metals in specifically designed metasurfaces by taking profit of plasmonic resonances responsible for the strong spatial confinement of electromagnetic field near the surface of the metal. The properties of the nanostructures are determined by the geometrical (shape, size, and sharpness) and physical parameters (dielectric functions at a given wavelength) of both the metal and the surrounding dielectric materials. A strong plasmonic interaction can significantly enhance light-matter interaction, and generate very large surface nonlinearities [3,5], giving rise to HHG conditions under relatively low input laser intensities. This enables the manipulation of optical fields with unprecedented spatial (far beyond the diffraction limit) and time resolutions.

Fig.1 shows several of the considered configurations and demonstrates the E-field localization within two kinds of SP surface plasmonic localization (E-field is confined around the corner of a 2-D grating [5], E-field is confined inside a nanohole). Our very recent results from the 2D nanograting show that under the right excitation conditions we can achieve between three and five orders of magnitude enhancement factor in the SH and TH harmonic generation (Fig 1(a)). Although a more sophisticated quasi-3D

structure consisting of nanoholes in gold, provides more tunability and shaping of the plasmonic resonance, however the NL enhancement is much lower. Fig-1(b) shows the narrow plasmonic resonance centered around 790 nm, both measured and simulated using Finite Difference Time Domain, the depth and position of which depends on the period of the hole pattern, the diameter and depth of the hole and thickness of the gold layer deposited on top. Under the resonant illumination conditions as in ref 5, the nanoholes show a TH enhancement factor of ~ 100 (Fig-1(c)).

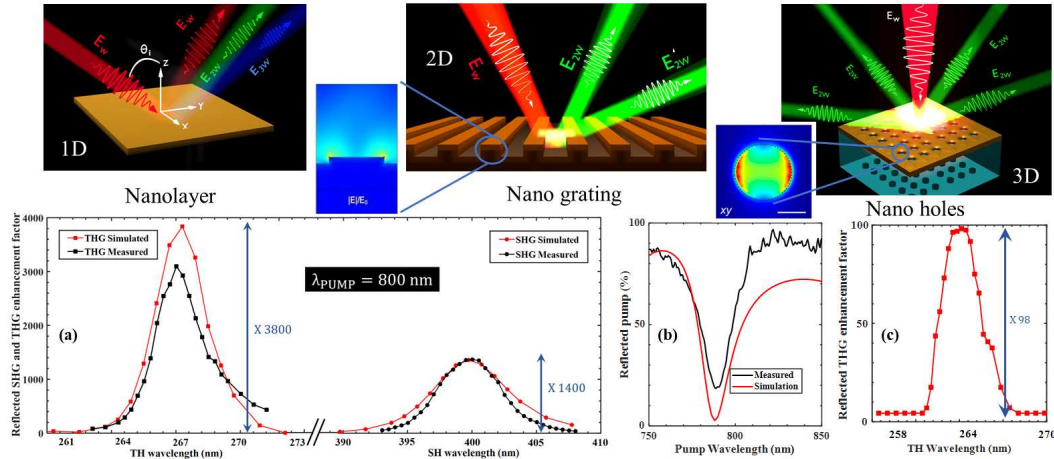


Fig 1. Examples of 1D, 2D and 3D nanostructures, light confinement and enhancement in nonlinear interaction [4-5]

Plasmon induced NL generation can be directional or diffused, the periodicity of the structures may enable constructive interference of the generated SH/TH in certain directions, producing diffraction orders, proving experimental retrieval of the total generated SH/TH to be challenging. A 2D grating will diffract in the plane of incidence while the diffraction from a 3D structure is more complicated (Fig-1). Our sophisticated detection system and precision calibration enables us to detect and quantify SH/TH efficiencies, and corroborate our theoretical and experimental observations of shape, spectral width, and maximum amplitude of the spectral response.

Apart from Au, successful detection of SH from few nm thick aluminum also unraveled remarkable consequences of resonant absorption, a critical role that bound electrons play in light-matter interactions across the optical spectrum. Precise engineering of metasurface geometry and modern fabrication methods promise very well-tailored plasmonic structures and is the way to produce compact higher frequency light sources embedded with nonlinear components beam-deflecting, metalenses, metaholograms, orbital-angular-momentum (OAM) beams etc [3].

Acknowledgments

SM, JT, and CC acknowledge Spanish Agencia, Estatal de Investigación (project no. PID2019-105089GB-I00/AEI/10.13039/501100011033) and US Army Research Laboratory Cooperative Agreement N° W911NF-22-2-0236 issued by US ARMY ACC-APG-RTP.

References

- [1] J. A. Armstrong, N. Bloembergen, J. Ducuing et al, Phys. Rev. 127, 1918 (1962)
- [2] M. Scalora, M. A. Vincenti, D. de Ceglia, et al, Phys. Rev. A 82, 043828 (2010)
- [3] San Kim, Tae-In Jeong, Jongkyoon Park, et al, Nanophotonics, 11 (11), 2393-2431 (2022).
- [4] L. Rodriguez-Suñé, J. Trull, C. Cojocaru, et al, Optics Express 29, 8581 (2021).
- [5] S. Mukhopadhyay, L. Rodriguez-Suné, C. Cojocaru, et al, APL Photonics 8, 046108 (2023).

Macroscopic simulations of high-order harmonic generation assisted by artificial intelligence

Javier Serrano^{1,2*}, José Miguel Pablos-Marín^{1,2} and Carlos Hernández-García^{1,2}

¹Grupo de Investigación en Aplicaciones del Láser y Fotónica, Departamento de Física Aplicada, Universidad de Salamanca, Pl. Merced s/n 37008 Salamanca, Spain

²Unidad de Excelencia en Luz y Materia Estructuradas (LUMES), Universidad de Salamanca, Pl. Merced s/n 37008 Salamanca, Spain

*E-mail: fjaviorsr@usal.es

1. Abstract

High harmonic generation (HHG) is an extremely non-linear process that allows to convert laser light from the infrared domain into much higher frequencies (extreme UV or even soft x-rays), in the form of pulses as short of tens of attoseconds [1] (see Fig. 1). Such ultrashort pulses suppose a unique light source for the exploration of Nature at the spatial and temporal limits of human knowledge. However, macroscopic HHG simulations are computationally very expensive. The exact solution requires to couple the laser-driven wavepacket dynamics given by the three-dimensional time-dependent Schrödinger equation (3D-TDSE) with the Maxwell equations to account for macroscopic propagation. That's beyond current computational capabilities, so it's required to rely on approximations like the Strong Field Approximation (SFA) [2] at the microscopic level, or the discrete dipole approximation at the macroscopic level [3]. Nowadays, artificial intelligence is emerging as a powerful tool in Physics, and more specifically in ultrafast science [4, 5]. In our work, we show that using neural networks (NNs) trained with exact 3D-TDSE calculations, it's possible to drastically speed up macroscopic HHG simulations (5 to 6 orders of magnitude), allowing to get accurate results, and revealing hidden signatures neglected in the standard approximations.

2. Training of our neural networks

We have created and trained two NNs using Keras and TensorFlow to accurately predict the single-atom HHG emission. Our NNs take the amplitude and spatial phase of the infrared laser pulse on each atom and predict the real and imaginary parts of the generated spectrum. To achieve more accurate results, we train our networks to predict the higher-order harmonics (above 12th), since the lower ones are usually filtered in experiments.

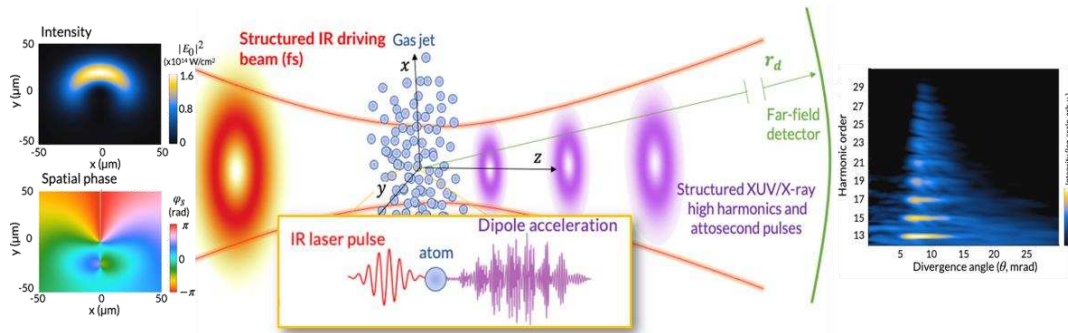


Figure 1 HHG from an ultrafast and ultraintense structured IR driving beam focused on a gas jet. The highly non-linear interaction between the driving beam and the gas on each atom, and the coherent addition of the emitted high-order harmonics, result on structured XUV/X-ray attosecond pulses in the far field. In the example shown in the figure, a structured driving field composed of two vortex beams of different topological charge is used to generate harmonic vortices.

The network that predicts the real part of the spectrum is trained in steps of 500 epochs, with a dataset of 40.000 3D-TDSE calculations, and an increasing batch size of 2^m (with $m = 3, 4, 5 \dots 9$). The second NN is built with the same configuration and the already trained parameter values from the first one (transfer learning), and we only allow to vary the weights of the last two dense layers during its training. That way, following the same training methodology, the second NN only requires 50 epochs per step to reach the same accuracy level as the first one (MSE $\sim 10^{-6}$).

Calculation	Resources	Required time
Regular single-atom simulation	1 CPU core	~70 minutes
Regular single-atom simulation	1 processor (24 CPU cores)	~5 minutes
AI-assisted single-atom simulation	1 CPU core	~0.1 seconds
AI-assisted single-atom simulation	1 processor (24 CPU cores)	~0.01 seconds
Regular macroscopic simulation	1 CPU core	~13 years (estimated)
Regular macroscopic simulation	4 processors (96 CPU cores)	~3 months (estimated)
AI-assisted macroscopic simulation	1 CPU core	~1 hour
AI-assisted macroscopic simulation	4 processors (96 CPU cores)	~1 minute

Table 1 Comparison of performance between regular simulations and simulations assisted by artificial intelligence (AI). Macroscopic simulation times are considered for $\sim 10^5$ atoms. The reduction of the parallel performance in respect to the ideal case is mainly due to the automatic reduction of the CPU frequency when multiple cores of a single processor are active and the integration of individual HHG emissions in the common far-field detector.

3. Results

We have integrated our NNs in the highly parallelized framework that we have created, and we use to run HHG simulations. This framework allows to parallelize (OpenMP and MPI) the calculation of the HHG emission in individual atoms, either using the full 3D-TDSE or multiple instances of our neural networks. This way, we achieve an efficient use of computing resources in powerful computing clusters or even supercomputers.

We have validated our method with simulations that compute HHG from structured driving beams in low density gas jets [6] (see Fig. 1). Our results demonstrate that machine learning applied to HHG allows not only to speed-up the simulations (see Table 1), but also to reveal hidden signatures in the HHG process that are neglected in the standard approximations, paving the way for the exploration of new physics at the nanometer and attosecond spatiotemporal scales.

Acknowledgments

This project has received funding from the European Research Council (ERC) under the European Union’s Horizon 2020 research and innovation program (Grant Agreement No. 851201) and from Ministerio de Ciencia de Innovación y Universidades (PID2022-142340NB-I00). The authors thankfully acknowledge RES resources provided by BSC in MareNostrum 4, SCAYLE in Caléndula and CESGA in FinisTerra III (FI-2022-3-0041, FI-2023-3-0045).

References

- [1] T. Popmintchev, et al. “Bright coherent ultrahigh harmonics in the keV x-ray regime from mid-infrared femtosecond lasers” *Science* 336, 1287–1291 (2012)
- [2] M. Lewenstein, et al. “Theory of high-harmonic generation by low-frequency laser fields” *Phys. Rev. A* 49, 2117 (1994)
- [3] C. Hernández-García et al. “High-order harmonic propagation in gases within the discrete dipole approximation” *Phys. Rev. A* 82, 033432 (2010)
- [4] A. Sánchez-González et al. “Accurate prediction of X-ray pulse properties from a free-electron laser using machine learning” *Nat. Commun.* 8, 15461 (2017)
- [5] C. Brunner et al. “Deep learning in attosecond metrology” *Opt. Express* 30, 15669–15684 (2022)
- [6] J.M. Pablos-Marín, J. Serrano, and C. Hernández-García, “Simulating macroscopic high-order harmonic generation driven by structured laser beams using artificial intelligence” *Comput. Phys. Commun.* 291, 108823 (2023)

Self-interference of Hermite-Gaussian high-order harmonics simulated through machine learning

José Miguel Pablos-Marín^{1,2,*}, David D. Schmidt³, Alba de las Heras^{1,2}, Nathaniel Westlake³, Javier Serrano^{1,2}, Yuhao Lei⁴, Peter Kazansky⁴, Daniel Adams³, Charles Durfee³ and Carlos Hernández-García^{1,2}

¹*Grupo de Investigación en Aplicaciones del Láser y Fotónica, Departamento de Física Aplicada, Universidad de Salamanca, Pl. Merced s/n 37008 Salamanca, Spain*

²*Unidad de Excelencia en Luz y Materia Estructuradas (LUMES), Universidad de Salamanca, Pl. Merced s/n 37008 Salamanca, Spain*

³*Department of Physics, Colorado School of Mines, 1523 Illinois Street, Golden, CO 80401, USA*

⁴*Optoelectronics Research Centre, University of Southampton, Southampton SO17 1BJ, UK*

*E-mail: jmpablosm@usal.es

1. High Harmonic Generation driven by Hermite-Gaussian beams

High Harmonic Generation (HHG) is a highly non-linear non-perturbative process where high frequencies are generated, usually reaching the extreme-ultraviolet (XUV) or soft X-ray regime, and producing the shortest pulses ever created [1] (see Fig. 1a). This process requires an intense laser pulse, usually in the infrared region and with duration of tens of femtoseconds, which is focused onto a gas target. The intense field ionizes the atoms in the gas, whose electronic wavepacket is accelerated by the laser field, and finally recombines with the ion. As a result, high-energy photons are released, in the form of high-order harmonics of the driving laser frequency [2].

Structured laser beams are often used to study HHG process due to the high control they offer in the phase matching conditions and their suitability to spatially modulate the generated HHG spectra in phase and intensity. Some examples include the generation of XUV vortex beams [3], XUV vector beams [4], or low-divergence XUV harmonics from necklace-driving beams [5].

In this work we study HHG driven by Hermite-Gauss (HG) beams. Up to now, most works of HHG driven by structured light have been studied in terms of Laguerre-Gauss beams, which are typically used to represent vortex or vector beams. However, apart from the interest to drive HHG with pure HG modes, both vortex and vector beams can be mathematically represented as a superposition of HG beams, so understanding the HHG emission coming from these driving beams is essential. We perform theoretical simulations using a macroscopic HHG method based on artificial intelligence [6], which are compared against experimental results. We demonstrate that HHG driven by HG beams allows for self-interference between the high-order harmonics produced [7]. This is because, in contrast to vector and vortex beams, the HG mode is not translated into the generated harmonic beam. The two-lobe scenario given by the $HG_{0,1}$ (or $HG_{1,0}$) mode lead to two well defined point sources that propagate as independent coherent XUV beams, interfering in the far-field. This interference is highly dependent to the divergence of the HG beam, being almost non-existing if HHG is produced before the focus, and particularly significant in the near-focus and post-focus configurations (see Fig. 1b).

2. Experimental and simulation results

Fig. 1b shows the far-field harmonic emission from harmonic 15th to 31st for different positions of the gas jet with respect to the focus position of the $HG_{0,1}$ mode. From the experimental point of view, HG beams were produced by passing vector beams through a linear polarizer, isolating a single $HG_{0,1}$ mode. By changing the generation plane for HHG, the self-interference effect is observed. The HHG signal is then passed through thin Al filters gathered onto an XUV camera. Theoretically, the simulations are performed with the methodology described in [6], an AI-based macroscopic HHG model, where the single-atom dipole acceleration is obtained through the time-dependent Schrödinger equation enhanced by machine learning. The simulations were performed with an ideal $HG_{0,1}$ beam at different gas jet positions following the experimental approach.

The excellent agreement between the prediction and the experimental result allows us to validate the AI-based model, and to demonstrate the existence of the interference pattern. Thanks to additional simulations that make use of the Thin Slab Model [8], we demonstrate that the interference pattern results from the quantum dipole phase of the harmonics.

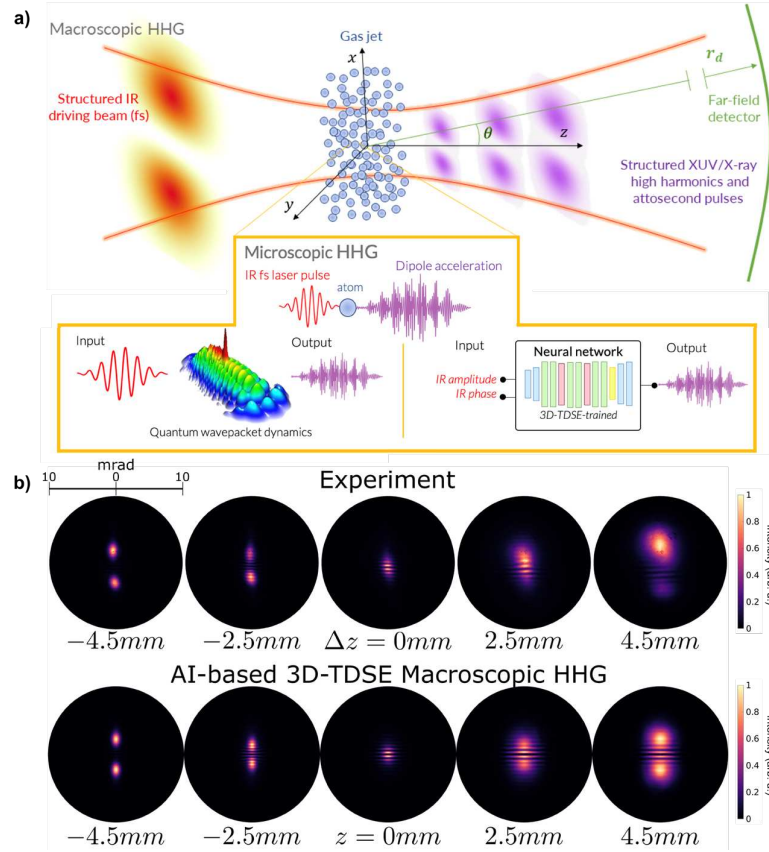


Figure 1 a) HHG from an ultrafast and ultraintense structured IR, HG driving beam focused on a gas jet. The highly non-linear interaction between the driving beam and the gas on each atom, and the coherent addition of the emitted high-order harmonics, result on structured XUV/X-ray attosecond pulses in the far field. b) Experimental far-field HHG emission (from harmonic 15th to 31st) driven by an HG_{0,1} at different gas jet positions from the beam focus (Δz), along with the theoretical HG_{0,1} HHG simulations performed using an AI-based model [6].

Acknowledgments

This project has received funding from the European Research Council (ERC) under the European Union’s Horizon 2020 research and innovation program (Grant Agreement No. 851201) and from Ministerio de Ciencia de Innovación y Universidades (PID2022-142340NB-I00). The authors thankfully acknowledge RES resources provided by BSC in MareNostrum 4, SCAYLE in Caléndula and CESGA in FinisTerra III (FI-2022-3-0041, FI-2023-3-0045).

References

- [1] T. Popmintchev, et al. *Science* 336, 1287–1291 (2012)
- [2] M. Lewenstein, et al. *Phys. Rev. A* 49, 2117 (1994)
- [3] C. Hernández-García et al. *Phys. Rev. Lett.* 11,1 083602, (2013)
- [4] C. Hernández-García, et al. *Optica* 4, 520-526 (2017)
- [5] L. Rego, et al. *Science Advances* 8, eabj7380 (2022)
- [6] J. M. Pablos-Marín et al. *Comput. Phys. Commun.* 291C, 108823 (2023)
- [7] D. D. Schmidt, J. M. Pablos-Marín, et al. in preparation.
- [8] C. Hernández-García, et al. *New Journal of Physics* 17, 093029 (2015)

Sobre la historia de la dispersión de la luz

Eugenio Roldán¹

¹*Department d'Òptica i d'Optometria i Ciències de la Visió, Dr. Moliner 50, 46100-Burjassot, Spain*

E-mail: eugenio.roldan@uv.es

Los fenómenos ópticos de reflexión, refracción, interferencia, difracción y birrefringencia, no requieren de conocimiento alguno sobre la estructura submicroscópica de la materia para su correcta descripción, solo se ha de asignar un determinado índice de refracción al medio. De hecho, la teoría ondulatoria de la luz, formulada por Fresnel hacia 1820, la teoría del éter elástico, fue capaz de dar una brillante explicación de todos esos fenómenos. La dispersión, sin embargo, sí que iba a requerir de una teoría de la materia y de su interacción con la luz para poder ser comprendida.

Ciertamente, ya Newton había propuesto una “teoría” de la dispersión, pero basada en supuestos falsos y contraria a los hechos experimentales; de hecho, hasta la década de 1820 no hubo ningún avance relevante relativo a la dispersión. Aunque Cauchy formularía una teoría de la dispersión, a principios de la década de 1830, que podía explicar la dispersión normal (i.e., cuando el índice de refracción es mayor para frecuencias mayores), esa teoría no podía dar mucho de sí al no contemplar el papel de la materia.

En 1862, P. Leroux descubre la dispersión anómala, en vapor de yodo; es entonces cuando empieza a ser posible elaborar una teoría de la dispersión de la luz. Al principio, esa teoría se formularía dentro del marco de la teoría del éter elástico: W. Sellmeier supuso, en 1871, que las partículas materiales vibrarían armónicamente, alrededor de sus posiciones de equilibrio, con ciertas frecuencias propias, y que las oscilaciones del éter (las ondas luminosas) forzarían su oscilación que, a su vez, generaría una oscilación de la misma frecuencia en el éter, aunque desfasada con respecto a la oscilación primaria. La interferencia entre las oscilaciones primaria y secundaria explicaría la dispersión, puesto que el desfase entre ambas depende de la frecuencia. Esta teoría original de Sellmeier (vislumbrada con anterioridad, aunque no publicada, por Maxwell), sería refinada y bien formulada por H. Helmholtz en 1875 y, posteriormente, desarrollada por otros autores.

La paulatina imposición de la teoría electromagnética de la luz de Maxwell, llevaría a la reformulación de la teoría de Sellmeier-Helmholtz. En 1893, en su último trabajo publicado en vida, el gran Helmholtz llevaría a cabo un intento de *maxwellizar* su vieja teoría, un trabajo que resultó ser muy influyente. Pero es, sin duda, el trabajo de H.A. Lorentz (de 1878 y, especialmente, su reelaboración de 1892), el más relevante para la formulación de una teoría electromagnética de la dispersión óptica. También resultaron relevantes las aportaciones de P. Drude. A principios del siglo XX, la teoría clásica del índice de refracción está, pues, completamente formulada.

Sin embargo, la investigación cuantitativa revelaría que, aunque la teoría de Lorentz proporcionaba resultados razonables para los gases moleculares, no ocurría lo mismo con los gases atómicos, para los que los resultados experimentales sugerían que solo un electrón por cada 50000 átomos vibraría a la frecuencia espectral. Esto llevó a problemas conceptuales que solo podrían resolverse con el uso de la teoría cuántica. Es más, la aparición del modelo atómico de Bohr (1913), que tan exitoso resultó en la interpretación de los resultados espectroscópicos, parecía totalmente incompatible con la teoría clásica de Lorentz, lo cual ahondaba el estado de crisis de esta última.

Los intentos por formular una teoría híbrida, dentro del marco de la teoría cuántica antigua (Sommerfeld, Debye), resultaron infructuosos. Pero R. Ladenburg encontró una manera de relacionar la fórmula de Sellmeier-Helmholtz con la teoría cuántica que permitía reinterpretar los resultados experimentales, aproximación al problema que H. Kramers utilizó para obtener una versión cuántica de la fórmula de Sellmeier-Helmholtz que es, básicamente, correcta. Posteriormente, la formulación de la mecánica cuántica permitiría obtener el resultado de Kramers a partir de primeros principios (Dirac, Schrödinger), con lo que el largo viaje de la fórmula de Sellmeier-Helmholtz llega a su fin, al poder ser completamente deducida e interpretada en el marco de la nueva teoría cuántica.

Trabajo financiado por el Ministerio de Ciencia, Innovación y Universidades-Agencia Estatal de Investigación, y fondos FEDER de la Unión Europea (proyecto FIS2017-89988-P), y por la Direcció General de Ciència i Investigació de la Generalitat Valenciana (proyecto CIAICO/2021/ 276).

[1] E. Roldán, “Pre-historia de la óptica cuántica: historia de la dispersión de la luz”, *Rev. Esp. Fís.* **37**(4), 21–32 (2023).

Topological spectroscopy: High Harmonic Generation from Graphene irradiated by structured fields.

Luis Plaja*, Ana García-Cabrera, Roberto Boyero-García, Óscar Zurrón-Cifuentes, Javier Serrano, Julio San Román and Carlos Hernández-García

Grupo de Investigación en Aplicaciones del Láser y Fotónica, Unidad de Excelencia en Luz y Materia Estructuradas (LUMES), Universidad de Salamanca, E-37008, Salamanca, Spain

E-mail: lplaja@usal.es

High-order harmonic spectroscopy is a powerful technique used to probe ultrafast dynamics in matter with exceptional temporal resolution. High-harmonic generation (HHG) is an extreme non-linear process in which intense laser pulses are focused onto a target material, typically a gas or solid, causing the material to emit high-energy photons in the form of harmonics of the driving laser frequency. What sets HHG apart is its ability to generate harmonics with energies extending into the extreme ultraviolet (XUV) or even soft X-ray regime. High-order harmonic spectroscopy provides information of the electron dynamics under the driving field interaction, on timescales as short as attoseconds (10^{-18} seconds).

1. High-order harmonic spectroscopy

Recent advancements in high-order harmonic generation (HHG) have revealed an unprecedented complexity in the dynamics of electrons in crystals. Traditionally confined to atomic, molecular gases, and plasmas, HHG's exploration expanded a decade ago with its demonstration in solids [1]. Solids, containing higher electron densities, offer enhanced efficiency and their symmetry properties are mapped to the harmonic field [2]. Concurrently, HHG has emerged as a new playground for producing structured high-frequency harmonic radiation [3,4], exploiting the coupling of spin and angular momentum of structured light with the target symmetries.

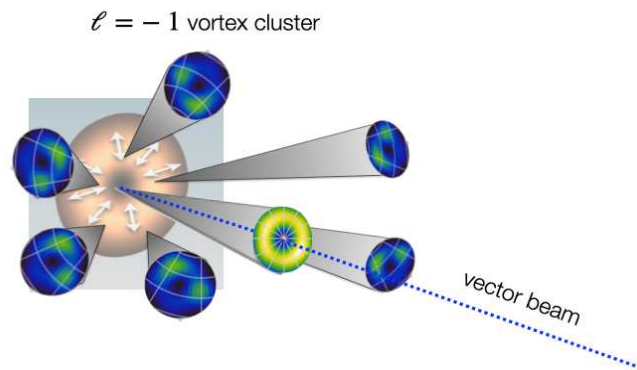


Figure 1 Scheme of the multivortex geometry of the harmonic field driven by a radial vector beam in graphene.

Low-dimensional crystals, with their atomic-scale widths, provide a pristine environment for such investigations, minimizing propagation effects. This contribution explores the characteristics of HHG from graphene under radial vector beam illumination. We unveil how graphene's nonlinear anisotropy, consequence of its crystalline nature, interacts with the azimuthally variant polarization of the driver beam, yielding a complex, structured harmonic field. Our interpretation identifies a central vector beam overlaid with a topological background structured as a cluster of vortices (see Fig. 1).

We demonstrate that the complex structure of the harmonic field provides space-resolved information of the target's non-linear response. Based on these ideas, we propose a method to retrieve such local properties of the target response by identifying well defined topological structures in the harmonic field [5]. Indeed, the position and sizes of the cluster of vortices is shown to be directly linked with the spatial Fourier components of the target response. Understanding and harnessing these topological aspects open new avenues for exploring non-linear matter dynamics processes with unprecedented spatial and temporal resolution.

2. Conclusions

We explore the process of high-harmonic generation from crystalline solids, attending to the spatial structure of the harmonic field. By spotting the characteristic topological features of the harmonic field, we propose an extension of traditional spectroscopic approaches that provides spatially resolved information about the target response.

Acknowledgments

We acknowledge economic support from the Spanish Ministerio de Ciencia, Innovación y Universidades (PID2022-142340NB-I00). This project has also received funding from the European Research Council (ERC) under the European Union's Horizon 2020 research and innovation program (Grant Agreement No. 851201). A.G.-C. acknowledges support from Ministerio de Educación, Cultura y Deporte (FPU18/03348).

References

- [1] S. Ghimire, D.A. Reis, "High-harmonic generation from solids". *Nature Phys* **15**, 10–16 (2019)
- [2] O. Zurrón-Cifuentes, R. Boyero-García, C. Hernández-García, A. Picón, and L. Plaja, "Optical anisotropy of non-perturbative high-order harmonic generation in gapless graphene," *Opt. Exp.* **27**, 7776–7786 (2019).
- [3] C. Hernández-García, A. Turpin, J. San Román, I.J. Sola, "Extreme ultraviolet vector beams driven by infrared lasers," *Optica* **4**, 520 (2017).
- [4] N. Yoshikawa, T. Tamaya, and K. Tanaka, "High-harmonic generation in graphene enhanced by elliptically polarized light excitation," *Science* **356**, 736–738 (2017).
- [5] A. García-Cabrera, R. Boyero-García, Ó. Zurrón-Cifuentes, *et al.* "Topological high-harmonic spectroscopy" *Commun Phys* **7**, 28 (2024).

Experimental approaches to investigate dynamics and optimize performance in femtosecond laser material processing

Mario Garcia-Lechuga^{1*}, David Grojo², Olivier Utéza², Javier Solis¹ and Jan Siegel¹

¹*Laser Processing Group, Instituto de Optica Daza de Valdes (IO), CSIC, 28006 Madrid, Spain*

²*Aix Marseille Université, CNRS, LP3, UMR7341, 13288 Marseille, France*

*E-mail: mario.garcia.lechuga@csic.es

Femtosecond lasers are widely used in material processing, serving as a micromachining strategy with applications in microelectronics, photonics or plasmonics. Furthermore, the extreme nonlinear and thermodynamic conditions experienced by the material during femtosecond laser processing make it an area of great interest from a fundamental perspective. However, these conditions lead to complex problems involving the interplay of various processes. In this work, we present different experimental approaches that allow for a better understanding of the fundamentals involved in modifying the surface, as well as the resulting consequences on machining performance.

First, we present the results obtained using time-resolved microscopy [1]. This pump-and-probe technique enables the visualization of electron excitation dynamics with femtosecond time resolution, aiding in determining the relative roles of different excitation mechanisms (multiphoton versus impact ionization). We also examine in different materials, irreversible transformation dynamics, such as ablation, as well as studying the sub-ablative regimes as melting and resolidification [2].

Second, we present a comprehensive study on the role of laser wavelength, covering the range from UV to MIR (258 nm to 4 μm), in superficial modifications of dielectrics and silicon. Firstly, we focus on understanding and controlling spatial resolution aspects, challenging the applicability of the concept of nonlinear resolution commonly used in multiphoton microscopy to femtosecond laser transformations [3]. Secondly, we investigate laser-induced in-depth modifications by tuning the wavelength, as crater topographies in dielectrics [4] and amorphization depth in silicon [5]. Those studies reveal counterintuitive quasi-invariance of material responses, despite strongly varying nonlinear interaction processes. These findings are supported by basic numerical calculations, which include the balance between different excitation mechanisms (multiphoton, tunneling, and avalanche) and various thermodynamic considerations (dissociation energy, melting threshold, etc.) [4,5].

Acknowledgments

This work has been partially supported by grant HyperSolar (TED2021 -130894B-C22) funded by MICIU/AEI/ 10.13039/501100011033 and by the “European Union NextGenerationEU/PRTR, by grant ULS_PSB (PID2020-112770RB-C21) funded by MICIU/AEI/ 10.13039/501100011033, and by CSIC through the call for internationalization i-LINK 2022 (project I LINK22056).

References

- [1] M. Garcia-Lechuga, M., Solis, J., Siegel, J. (2023). Probing Matter by Light. In: Stoian, R., Bonse, J. (eds) Ultrafast Laser Nanostructuring. Springer Series in Optical Sciences, vol 239. Springer.
- [2] M. Garcia-Lechuga, “Time-resolved imaging techniques applied to femtosecond laser material processing” *Optica Pura y Aplicada*. 54 (2), 1-10, (2021)
- [3] M. Garcia-Lechuga, O. Utéza, N. Sanner, and D. Grojo, “Evidencing the nonlinearity independence of resolution in femtosecond laser ablation” *Opt. Lett.* 45, 952 (2020).
- [4] M. Garcia-Lechuga, O. Utéza, N. Sanner, and D. Grojo, “Wavelength-Independent Performance of Femtosecond Laser Dielectric Ablation Spanning Over Three Octaves” *Phys. Rev. Appl.* 19, 044047 (2023).
- [5] M. Garcia-Lechuga, N. Casquero, J. Siegel, J. Solis, R. Clady, A. Wang, O. Utéza, and D. Grojo, “Amorphization and ablation of crystalline silicon using ultrafast lasers: dependencies on the pulse duration and irradiation wavelength”. *Laser Photonics Rev* (2024, submitted).

Intense and isolated polarization-controlled magnetic fields from structured laser beams to drive nonlinear magnetization dynamics

Sergio Martín-Domene^{1,2*}, Luis Sánchez-Tejerina³,
Rodrigo Martín-Hernández^{1,2}, and Carlos Hernández-García^{1,2}

¹Grupo de Investigación en Aplicaciones del Láser y Fotónica, Departamento de Física Aplicada, Universidad de Salamanca, E-37008, Salamanca, Spain

²Unidad de Excelencia en Luz y Materia Estructuradas (LUMES), Universidad de Salamanca, Salamanca, Spain

³Departamento de Electricidad y Electrónica, Universidad de Valladolid, 47011, Valladolid, Spain

*E-mail: sergiomardom@usal.es

1. Introduction

The ability to spatially separate the electric (E-field) and magnetic (B-field) fields of a light beam enables the inspection of laser-matter interactions driven solely by optical B-fields, covering studies in magnetic spectroscopy, force microscopy, or ultrafast magnetization dynamics, among others. However, B-field excitations are typically orders of magnitude weaker than E-field ones, thus not only isolated, but also intense B-fields are required. Several studies have already demonstrated the isolation of intense, linearly polarized B-fields using structured light beams [1-3]. However, this feature excludes applications in which the control over its polarization state is crucial, such as to drive nonlinear magnetization dynamics in ferromagnets using a circularly polarized B-field [4].

The solution of Maxwell equations for a spatially isolated circularly polarized B-field requires an exceedingly challenging E-field structure—a vortex beam linearly polarized along the longitudinal propagation direction—which is out of the scope with the current laser technology. To circumvent this drawback, we propose the use of several moderately intense azimuthally polarized vector beams tightly focused (see Fig. 1) to generate isolated circularly polarized B-fields up to tens of Tesla [5].

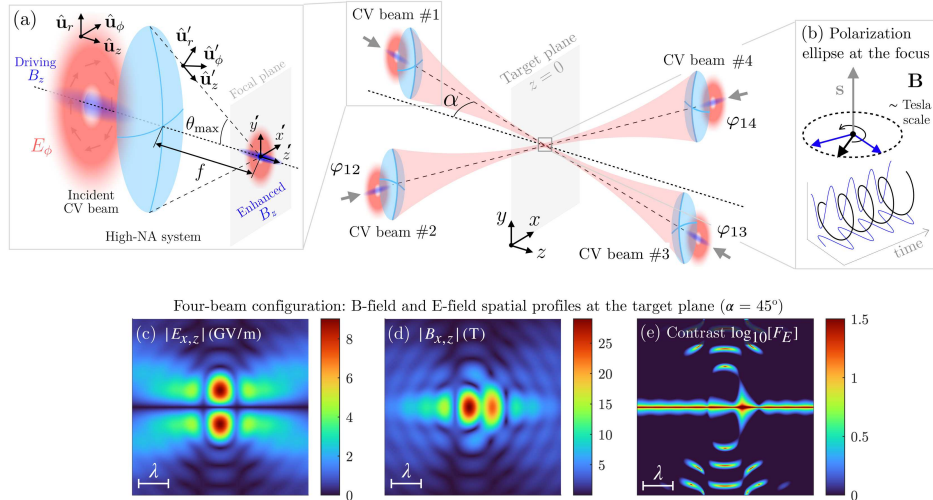


Figure 1 Optimum setup of four azimuthally polarized beams propagating in orthogonal directions for the generation of intense and isolated polarization-controlled B-fields. (a) Tight-focusing scheme for a single incident azimuthal vector beam (B_r component not shown). (b) Conceptual picture of the circularly polarized B-field achieved at the focus and its associated polarization ellipse. (c)-(e) Total fields and contrast characterized within the target xy -plane at an observation angle of 45° .

When each consecutive beam is dephased by $\pi/2$ the two orthogonal total components B_x and B_z having the same spatial distribution are also dephased by $\pi/2$ (y -components vanish), thus the resulting circular polarization state is homogeneous.

2. Results

First, our theoretical findings, based on the Richards-Wolf vectorial diffraction theory [6] out of the paraxial regime, highlight a significant enhancement in the amplitude of the longitudinal B-field (B_z) carried by an azimuthally polarized vector beam under tight-focusing conditions, dominating over the associated

radial B-field component (B_r). For the optimal focusing conditions this factor increases from $B_z/B_r \sim 10^{-6}$ for a standard paraxial azimuthally polarized beam to $B_z/B_r \sim 1.75$ in the tight-focusing regime. Second, by implementing a multiple-beam configuration, we achieve precise sub-wavelength control over the polarization state and amplitude of the spatially isolated B-field from a feasible experimental setup point of view, with particular attention on circular polarization. The optimum configuration consists of four driving beams propagating orthogonally, being dephased each consecutive beam by $\pi/2$ with respect to the previous one. A homogeneous circularly polarized B-field is achieved at the target plane when the observation angle is 45° , Figs. 1(c) and 1(d). In addition, this approach also provides further spatial isolation of the B-field, characterized through the contrast $F_E = c|B|/|E|$, Fig. 1(e). Moreover, the polarization state of the B-field can be tuned by modifying the amplitude ratio between opposite-pair beams, ranging from linear to circular through elliptical, and keeping the isolation with respect to the associated E-field.

3. Conclusions

Our theoretical study demonstrates the generation of intense and isolated polarization-controlled B-fields using tightly focused structured laser vector beams with azimuthal polarization. We prove that the non-paraxial regime allows for a substantial enhancement of the magnetic longitudinal component carried by an azimuthally polarized laser beam. Such B-field, being linearly polarized and placed at the E-field singularity, can reach tens of Tesla, starting from a moderately intense driving beam (focused intensity of $\sim 10^{12}$ W/cm²). The implementation of a multiple-beam configuration allows for a precise control of the B-field polarization state, allowing to reach isolated circularly polarized B-fields at the target plane. The setting of the amplitudes and dephases of the driver lasers allows a sub-wavelength control of the intense and isolated B-field spatial distribution achieved at the focus of the system.

The range potential applications of the presented work is wide within various scientific and technological scenarios. We highlight applications in probing ultrafast non-linear dynamics in ferromagnetic layers. Additionally, our findings usher the possibility to control the magnetization response in a sub-wavelength scale, increasing the potential spatial resolution of optically controlled magnetization. If translated to the ultrafast regime, these B-fields pulses may boost applications in femtosecond and attosecond science.

Acknowledgments

We acknowledge funding from the European Research Council (ERC) under the European Union's Horizon 2020 research and innovation program (Grant Agreement No. 851201), and from Ministerio de Ciencia e Innovación (PID2022-142340NB-I00).

References

- [1] M. Blanco, F. Cambroner, M. T. Flores-Arias, E. Conejero Jarque, L. Plaja, and C. Hernández-García, "Ultrafast Femtosecond Magnetic Nanoprobes Induced by Azimuthally Polarized Laser Beams", *ACS Photonics* **6**, 38–42 (2019).
- [2] S. Sederberg, F. Kong, and P. B. Corkum, "Tesla-Scale Terahertz Magnetic Impulses", *Phys. Rev. X* **10**, 11063 (2020)
- [3] R. Martín-Hernández, L. Grünwald, L. Sanchez-Tejerina, E. Conejero Jarque, L. Plaja, Carlos Hernández-García, and S. Mai, "Optical magnetic field enhancement using ultrafast azimuthally polarized laser beams and tailored metallic nanoantennas", <https://arxiv.org/abs/2401.08726> Photonic Research, in press (2024). Selected as Editor's Pick.
- [4] L. Sánchez-Tejerina, R. Martín-Hernández, R. Yanes, L. Plaja, L. López-Díaz, and C. Hernández-García, "All-optical nonlinear chiral ultrafast magnetization dynamics driven by circularly polarized magnetic fields", *High Power Laser Science and Engineering* **11**, e82 (2023).
- [5] S. Martín-Domene, L. Sánchez-Tejerina, R. Martín-Hernández, and C. Hernández-García, "Generation of intense, polarization-controlled magnetic fields with non-paraxial structured laser beams", <https://arxiv.org/abs/2401.07649>
- [6] B. Richards and E. Wolf, "Electromagnetic diffraction in optical systems, ii. structure of the image field in an aplanatic system", *Proceedings of the Royal Society of London. Series A. Mathematical and Physical Sciences* **253**, 358–379 (1959).

RESÚMENES/ABSTRACTS

Sesiones Orales

Ciencias de la Visión



Vision with diffractive ophthalmic optics

Laura Clavé^{1,2*}, Miguel Faria³ and María S. Millán¹

1. Departament d'Òptica i Optometria, Universitat Politècnica de Catalunya-BarcelonaTech, Spain

2. Consorci Sanitari del Maresme, Hospital de Mataró, Carretera de Cirera 230, 08304 Mataró, Spain

3. Physics Center of Minho and Porto Universities, University of Minho, 4710-057 Braga, Portugal

E-mail: laura.clave@upc.edu

1. Introduction

Diffractive profiles [1] have been successfully incorporated into ophthalmic optics to correct presbyopia by forming multiple coaxial images. Optical theory predicts that the power and energy efficiency of diffraction orders are both strongly wavelength-dependent, with the exception of the null power of the zero order, which exhibits no wavelength dependence. This is relevant in human vision, which typically operates under polychromatic illumination. We aim to evaluate the changes in spatio-chromatic vision that may affect individuals with diffractive multifocal lenses.

The power variation with wavelength causes longitudinal chromatic aberration (LCA). For diffractive lenses operating with the first diffraction order and higher, LCA is the opposite sign of that of refractive lenses. LCA and the wavelength dependence of the energy efficiency distribution among diffraction orders have been proved experimentally with multifocal diffractive intraocular lenses on optical bench [2], but their effects on vision are often masked by the influence of other factors.

In this study, we use a diffractive contact lens (CL) to compare, for each subject, their own visual acuity (VA) under white (W), red (R), green (G), and blue (B) illuminations, in far and near vision, in two conditions: with and without a diffractive CL.

2. Material and method

We used a hybrid refractive-diffractive bifocal CL (Rigid Gas Permeable Pilkington Diffrax®)[3], which operates with the 0th-order for distance vision and the 1st-order for near vision. The energy efficiency is 40.5% in these two orders for a 550nm wavelength. VA was assessed in one eye of nine presbyopic phakic subjects aged 51-64 years (mean 56.5 years) in two conditions: with and without diffractive CL. When CL was not used, spectacle lens (SL) was utilized to provide the necessary correction or addition. High-contrast Landolt rings optotype charts illuminated sequentially with W light and three narrowband colour lights – G (530 nm), R (625 nm), and B (455 nm) – were used to measure VA in logMAR scale at far and near distances. A mathematical simulation illustrates the behaviour of the diffractive CL and helps the physical interpretation of the clinical results [4].

3. Results

Figure 1 shows the computational simulation of the normalized irradiance distribution of the axial point of the point spread function (PSF) produced by the combination of the diffractive CL with a human eye. In the far focus, the R peak reaches the highest intensity and the B peak the lowest. The opposite happens in the near focus. The positive LCA induced by the ocular media (+1.08 D) remains unaffected in the far focus (0th-order), but drops to less than a half (+0.47 D) in the near focus (1st-order). For the nine presbyopic eyes, Figure 2 shows the far and near average VA differences obtained under R, G, and B illuminations relative to W light (labelled as R-W, G-W and B-W) in the two observation conditions. In far vision, the VA under B light is significantly worse than VA under R and G lights in both SL and CL conditions. The same trend is observed with SL correction in near vision. However, the introduction of the 1st-order of the diffractive CL in near vision makes the AV under R light worsen notoriously and the AV under B light improve.

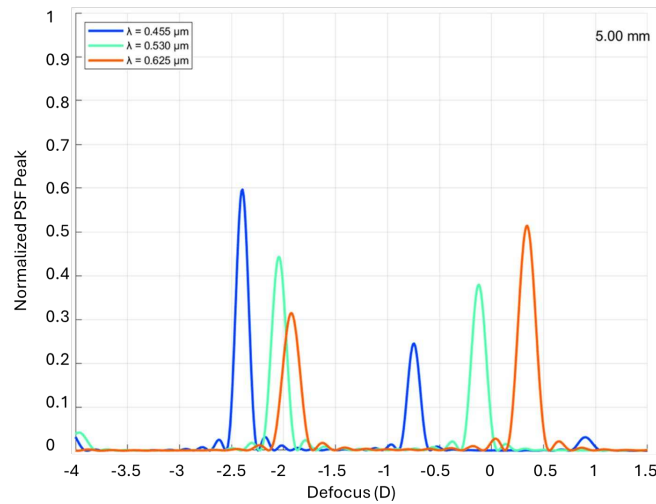


Fig. 1: Numerical simulation for a diffractive CL (Diffrax®) combined with an eye. R (625 nm), G (530 nm), and B (455 nm) normalized intensities of the axial point of the PSF versus defocus (D), with 0.0 D adjusted to the 550nm-far focus. Pupil 5.0 mm.

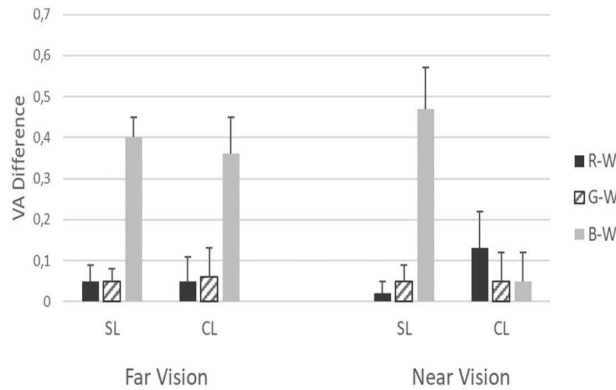


Fig. 2: Far and near VA differences (logMAR) obtained under R, G, B lights compared to W light in two observation conditions: with diffractive contact lens (CL) and with spectacle lens correction (SL). Bars represent mean values and segments standard deviations. A positive value means that VA under certain (R,G, B) illumination is worse than under W light.

4. Conclusion

Diffractive optics, used to create multiple coaxial foci in presbyopia-correcting ophthalmic lenses, can introduce changes in spatio-chromatic vision. Depending on the diffraction orders used for far and near vision, a VA asymmetry arises when illuminating under R and B light. The reported changes produced by a removable diffractive CL in presbyopics are consistent with the simulation.

Acknowledgments. (PID2020-114582RB-I00/AEI/10.13039/501100011033).

References

- [1] D. A. Buralli, G. M. Morris, and J. R. Rogers, "Optical performance of holographic kinoforms," *Appl. Opt.* **28**(5), 976-983 (1989).
- [2] M. S. Millan and F. Vega, "Extended depth of focus intraocular lens: chromatic performance," *Biomed. Opt. Express* **8**(9), 4294-4309 (2017).
- [3] D. A. Atchison and L. N. Thibos, "Diffractive properties of the Diffrax bifocal contact lens," *Ophthalm. Physiol. Opt.* **13**(2), 186-188 (1993).
- [4] L. Clavé, M. Faria-Ribeiro, and M. S. Millan, "Chromatic changes in vision with diffractive ophthalmic optics," *Opt. Express* **32**, 10348-10361 (2024).

Numerical analysis of intraocular lenses performance in different eye models

Mohammed Habib, Laura Remon^{1,*}, and Francisco José Torcal-Milla²

Departamento de Física Aplicada, Universidad de Zaragoza, Zaragoza, Spain

¹*Applied mechanics and bioengineering. Aragon Institute for Engineering Research (I3A), (Zaragoza)*

²*Laser Optical Technologies Group. Aragon Institute for Engineering Research (I3A), (Zaragoza)*

*E-mail: lauremar@unizar.es

1. Introduction

Cataract surgery, one of the most commonly performed surgical procedures worldwide, involves the removal of the cloudy crystalline lens and replacement with an artificial intraocular lens (IOL) to restore visual function. With advancements in surgical techniques and lens technology, the selection of an appropriate IOL has become increasingly crucial for achieving optimal visual outcomes and patient satisfaction. Various types of IOLs are available on the market, such as toric IOLs to correct pre-existing corneal astigmatism, multifocal and accommodative IOLs to simultaneously provide good distance and near vision, and aspheric IOLs to provide a better optical quality than the traditional IOLs with spherical optical design [1]. In recent years, computational modelling techniques have emerged as valuable tools for evaluating the optical performance of IOLs and predicting their visual outcomes in different clinical scenarios. For numerical simulations, ray tracing programs are used to evaluate the impact of IOL design parameters on the optical quality [1]. Depending on the complexity of the simulation, more realistic results can be obtained using theoretical [2] eye models such as Atchison [3], Gullstrand-Legrand [2], Liou-Brennan [4], and Navarro [5].

The aim of this study is to accomplish a comprehensive analysis of the optical properties offered by different aspheric IOLs and to compare their optical performance in different theoretical eye models. OSLO EDU (Edition 2001–2012, Revision 6.6.0 –Lambda Research Corporation) design software was employed to evaluate their behavior.

2. Material and methods

Eye Models

In this study, three theoretical eye models were employed: Atchison [3], Gullstrand-Legrand [2], and Navarro [5]. These three models feature two corneal surfaces, a pupil, and different types of lenses. However, the ocular parameters for the different models vary, and the greatest differences are found in the corneal asphericity (Q) value, which directly affects the model's spherical aberration (SA). The corneas of the Atchison, Gullstrand-Legrand, and Navarro eye models have fourth-order Zernike standard spherical aberrations of +0.24 μm , +0.31 μm , and +0.14 μm , respectively, for a 6.00 mm entrance pupil diameter (5.51 mm iris diameter). The crystalline lens was replaced by the different IOLs for the simulations.

Intraocular lens design and numerical simulations

The IOLs models with a refractive power of +21.00 D were designed with a refractive index $n=1.408$ at the design wavelength $\lambda_0 = 546 \text{ nm}$. Two types of aspherical IOLs, with an anterior conical equi-convex surface (0.0 shape factor), were designed in each eye model. The aspheric surfaces used to model the different IOLs take the form of a rotationally symmetric conic cross-section. Lens A was an IOL with negative fourth-order Zernike SA to totally compensate for the fourth-order Zernike positive SA of the eye models corneas. Lens B was designed as an IOL that does not add any fourth-order Zernike SA to the eye, taking into account the convergent light beam that comes from the different considered cornea. Table 1 shows the asphericity values of each IOL. For each IOL design, the vitreous chamber depth was set in order to get the point of maximum Modulation Transfer Function (MTF) value at 100 cycles/mm for a 3.00 mm pupil diameter.

Once each IOL was designed in its corresponding eye model, its optical performance was evaluated using OSLO in the Navarro eye model. The through frequency MTF curves with a 3.00 mm pupil diameter were calculated in accordance with the ISO 11979-9 Standard [6].

Table 1 Asphericity values (Q) of each IOL and eye model calculated for a 6.00 mm entrance pupil diameter.

	Atchison	Gullstrand-Legend	Navarro
Lens A	-11.641	-20.103	-8.224
Lens B	-4.719	-4.974	-4.998

3. Results

The results of the MTFs computed for the different IOLs evaluated in the Navarro eye model are shown in Figure 1. The MTF value at 100 cycles/mm with a 3.00 mm diameter aperture is shown in Figure 1 (left column) following the procedure described in the ISO [6]. The through frequency MTF curves for each designed IOL in each eye model is shown in Figure 1 (right column). The MTF value for the lens B is higher than those for lens A in all considered cases. As can be seen, for lens B, the behavior between them is very similar. However, for lens A, the MTF values depend on the SA of the cornea.

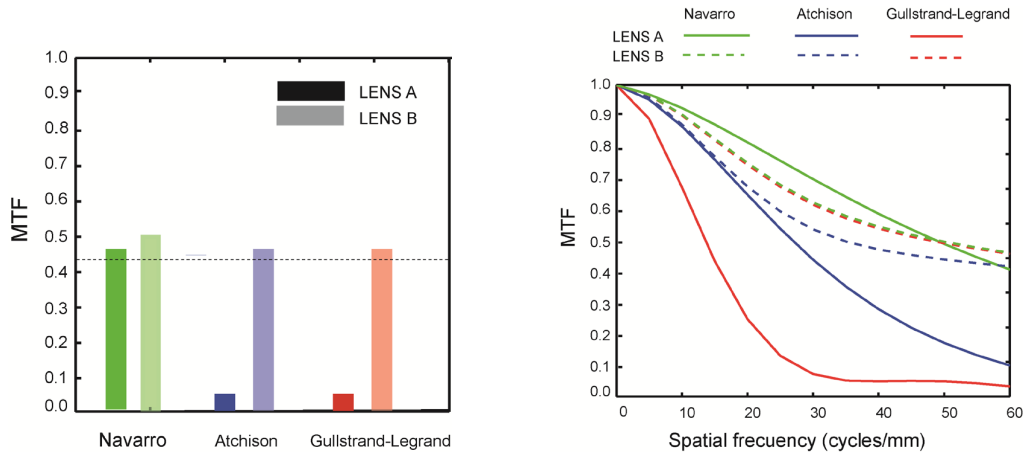


Figure 1 MTFs computed for each designed IOLs in each eye model evaluated in the Navarro eye model. Left: MTF at 100 cycles/mm with a 3.00 mm diameter aperture. The horizontal dashed line represents the value of MTF 0.43 specified in the ISO [6]. Right: Through frequency MTF curves with a 3.00 mm diameter aperture. Continuous lines represent lens A and discontinues lines represent lens B (see more details in the text).

4. Conclusions

The results show that, the performance of lens B, IOL that does not add any fourth-order Zernike SA to the eye, is less affected by the choice of theoretical eye model used to evaluate the optical performance compared to lens A (IOL with negative SA to totally compensate the positive SA of the eye models corneas). For lens A, the MTF values depend on the SA of the cornea under consideration.

Acknowledgments

This work has been funded by TOL (E44_23R) and AMB group (T24-17R), Gobierno de Aragón.

References

- [1] J. Pérez-Gracia, A. Varea, J. Ares, J.A. Vallés, and L. Remón, “Evaluation of the optical performance for aspheric intraocular lenses in relation with tilt and decenter errors”, *PLoS One* **15**(5), e0232546 (2020).
- [2] S. Norrby, P. Piers, C. Campbell, and M. van der Mooren, “Model eyes for evaluation of intraocular lenses”, *Appl. Opt.* **46**(26), 6595–605 (2007).
- [3] D.A. Atchison, “Optical models for human myopic eyes”, *Vision Res.* **46**(14), 2236-2250 (2006).
- [4] H.-L. Liou and N. A. Brennan, “Anatomically accurate, finite model eye for optical modeling”, *J. Opt. Soc. Amer. A, Opt. Image Sci.*, **14**(8), 1684–1695 (1997).
- [5] I. Escudero-Sanz y R. Navarro, Off-axis aberrations of a wide-angle schematic eye model *J. Opt. Soc. Am. A.* **16**(8), 1881–1891 (1999).
- [6] *Ophthalmic Implants—Intraocular Lenses—Part 2: Optical Properties and Test Methods*, Standard ISO 11979-2:2014 (2014).

Image quality of an enhanced monofocal intraocular lens with corneal astigmatism

Fátima Cuéllar^{1*}, Juan Antonio Azor¹, Lidia Pérez-Sanz², María S. Millán¹, Fidel Vega¹ and Nuria Garzón²

¹*Group of Applied Optics and Image Processing, Department of Optics and Optometry, Universitat Politècnica de Catalunya, BarcelonaTech, Spain.*

²*Optometry and Vision Department, Faculty of Optics and Optometry, Complutense University of Madrid, Spain.*

*E-mail: fatima.cuellar@upc.edu

1. Purpose

This work studies the impact of corneal astigmatism on the quality of the image formed by a (non-toric) enhanced monofocal intraocular lens (EM-IOL) (EM Isopure, BVI Medical, Belgium) immersed in a model eye on optical bench. A comparison with a standard monofocal lens of the same material and platform (Micropure, BVI Medical, Belgium) is provided.

2. Methods

A model eye implemented on optical bench was used to study the optical quality of the IOLs in vitro. The model eye's design closely resembles a natural, physiological eye [1]. The setup was further equipped with an adaptive optics (AO) system composed of a deformable mirror combined in loop with a Hartmann-Shack wavefront sensor, allowing for precise control over low and high order aberrations [2, 3]. Specifically, corneal astigmatism was induced with the AO system. The modulation transfer function (MTF) in the X and Y transversal directions was computed from the line spread function of a four-slit test. The area under the MTF (MTFa) was obtained integrating the MTF function from 0 to 50 cycles/mm (50 cycles/mm was equivalent to 15 cycles/deg in the object space of the model eye). The MTFa metric has proved to be a preclinical predictor of postoperative visual acuity (VA) [4]. The effect of increasing corneal regular positive astigmatism (from 0.0 D to + 1.75 D, in 0.25 D steps) on the optical performance of the lenses was assessed for 2.0-, 3.0-, and 4.5-mm pupil diameters at the IOL plane. Astigmatism was introduced keeping the image of the X line in focus at the retinal plane (0.0 D defocus) while the image of the Y line was myopically shifted according to the severity of the induced astigmatism.

3. Results

Figure 1 shows the $(MTFa)_X$ and $(MTFa)_Y$ versus induced corneal astigmatism separately for the three pupils [5]. Due to the direction of the cylinder induced by the AO system, the image of the X line remains in focus at the retinal plane and as a consequence, the $(MTFa)_X$ values (blue symbols) kept constant for both IOLs. In contrast, the $(MTFa)_Y$ values (orange symbols) decreased with the increased astigmatism. Pupil dependence can be also reported. The results of the monofocal standard Micropure (Fig. 1A) are quite close to those of EM Isopure (Fig. 1B) with 2.0- and 3.0-mm pupils: there is a reduction of the $(MTFa)_Y$, and thus of the optical quality in the Y axis that began with the lowest amount of astigmatism (0.25 D) and worsened with the aberration severity. These results suggest a similar trend in the VA loss and, consequently, a limited tolerance to corneal astigmatism for patients implanted with either the EM-Isopure or the monofocal Micropure, as long as the pupil diameter remains equal or lower than 3.0 mm. For 4.5-mm pupil, EM Isopure showed worse optical image quality (in both X and Y directions) than monofocal Micropure even in absence of corneal astigmatism. When corneal astigmatism was induced with a 4.5-mm pupil, image quality with EM Isopure reduced slowly. For induced astigmatism 0.75 D and greater, both IOL performances were quite similar.

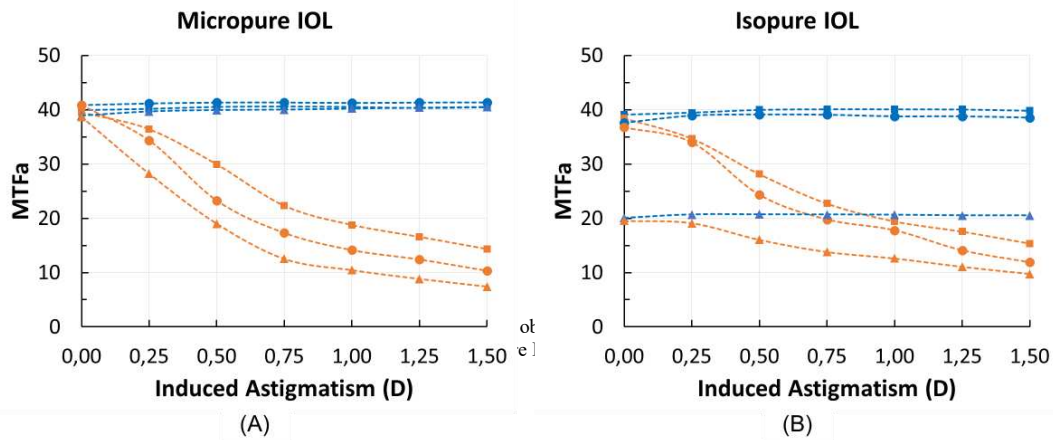


Figure 1 (MTF_x)_x (blue symbols) and (MTF_y)_y (orange symbols) obtained at the retinal plane (0.0 D defocus) of the model eye versus the induced corneal astigmatism. (A) monofocal Micropure IOL, (B) EM Isopure IOL. Results were obtained with (■, ●): 2.0- (▲, △): 4.5- mm pupils at the IOL plane. Dotted blue and orange lines are drawn to guide the eye.

4. Conclusions

The reduction of optical quality of the (non-toric) EM Isopure IOL in presence of corneal astigmatism is similar to that of a reference monofocal Micropure IOL when tested in a model eye with pupils up to 3.0 mm. These results anticipate similar trends in VA outcomes and therefore, in the tolerance to residual astigmatism of patients implanted with EM Isopure compared to those implanted with monofocal Micropure IOL. Further clinical data are necessary for comparison and, in particular, to determine the role of patient's pupillary dynamics on the visual outcomes of the EM Isopure.

Acknowledgments

Spanish Agencia Estatal de Investigación (PID2020-114582RB-I00/AEI/ 10.13039/501100011033). Fátima Cuéllar acknowledges a pre-doctoral contract (PRE2021-100674)

References

- [1] S. Norrby, P. Piers, C. Campbell and M. van der Mooren, "Model eyes for evaluation of intraocular lenses," *Appl. Opt.* **46**, 6595-6605 (2007).
- [2] L. Zheleznyak, M. Kim, S. MacRae and G. Yoon, "Impact of corneal aberrations on through-focus image quality of presbyopia-correcting intraocular lenses using an adaptive optics bench system," *J. Cataract Surg.* **38**, 1724-1733 (2012).
- [3] J. A. Azor, F. Vega, J. Armengol, M. S. Millan, "Astigmatism-induced image degradation in a model eye with a monofocal intraocular lens," *Opt. Pura Apl.* **57**(1) 51168 (2004).
- [4] A. Alarcon, C. Canovas and Rosen R, "Preclinical metrics to predict through-focus visual acuity for pseudophakic patients.," *Biomed. Opt. Express* **7**, 1877-1888 (2016).
- [5] L. Pérez-Sanz, F. Vega, J.A. Azor, F. Cuéllar, M. S. Millan, N. Garzón, "Tolerance to residual astigmatism of an isofocal intraocular lens," *Graefes Arch. Clin. Exp. Ophthalmol.* **262**, 1169–1180 (2024).

Preoperative perceptual glare assessment with multifocal intraocular lenses using a binocular visual simulator

A. Varea*^{1,2}, P. Papadogiannis¹, V. Rodriguez - Lopez², A. de Castro², L. Sawides², E. Gamba¹, S. Marcos^{2,3}, S. MacRae⁴, I. Sisó-Fuertes¹, C. Dorronsoro^{1,2}

¹2EyesVision SL

² Institute of Optics, Spanish National Research Council (IO-CSIC), Madrid, Spain

³ Center for Visual Science, The Institute of Optics, Flaum Eye Institute, University of Rochester

⁴ Department of Ophthalmology, Department of Visual Science, University of Rochester, Rochester, New York, New York, United States

*E-mail: avarea@2eyesvision.com

1. Introduction

The study aims to assess and quantify glare (including halo, starburst, and streaks of light) associated with trifocal, Extended Depth of Focus (EDOF), and bifocal Intraocular Lenses (IOLs). These lenses were simulated using SimVis Gekko (2EyesVision, Madrid, Spain) [1], a commercial binocular visual simulator. The primary objectives were to compare the glare size based on psychophysical measurements with computer simulations, and to evaluate visual symptoms using a shortened version of the AIOLIS questionnaire [2].

2. Methods

Ten healthy subjects between 27 and 51 years old participated in the study. A visual simulator (SimVisGekko) was used to simulate 10 IOLs: 3 trifocals (Synergy-J&J, PanOptix-Alcon, FineVision-BVI), 3 EDOF (Vivity-Alcon, Symphony-J&J, Isopure-BVI), 3 generic bifocals (+1.50, +3.00 and +4.50 D near addition) and a plano monofocal. The perceived glare size was measured using a modified version of the Halo Software V1.0 (University of Granada) [3] with a central LED, and then a reduced version of the AIOLIS questionnaire was conducted to assess the visual symptoms of glare for each patient. Finally, computer simulations using Fourier Optics were used to predict theoretically the glare size of the monofocal and bifocal IOLs (a 3mm pupil and a diameter that encircles 66% of the PSF image intensity were used) with and without wavefront aberrations. The average size of perceived glare was calculated for each IOL in arcminutes. Friedman test was conducted to compare the perceived glare sizes between the different IOLs and Spearman test was conducted to assess the correlation between perceived glare sizes and the responses from the AIOLIS questionnaire. Finally, the computational glare size results (with and without aberration) were compared with the experimental glare size for a plano monofocal and the 3 generic bifocals IOLs.

3. Results

Figure 1 shows the perceived glare size for each IOL. The glare size measured for the group of trifocals, bifocals and EDOFs was 7.2' (SD=0.54), 8.0' (SD=2.91) and 4.4' (SD=0.83), respectively. The biggest glare was produced by the +4.50D-bifocal (11') and the smallest by the plano monofocal (2.9'). However, amongst the multifocal IOLs simulated, the smallest glare size was produced by the EDOF-Isopure (3.6'). Also, in the bifocals group, higher near addition provided larger glare size (from 5.2' to 11', for +1,50D to +4.50D of addition). There was statistically significant difference ($Q=75.33$, $p<0.05$) in the glare size across IOLs, but no statistically significant differences within groups in the trifocals ($Q=2.6$, $p>0.05$) and EDOFs ($Q=8.6$, $p>0.05$). Additionally, the questionnaire results showed disturbances that were highly correlated with the glare size results ($r_s >0.97$) showing that the larger the glare, the more disturbing effect was perceived by the subject.

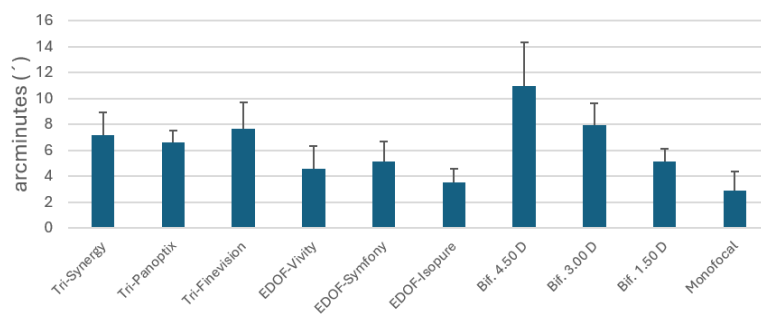


Figure 1 Perceived glare size in arcminutes for each IOL. Error bars represent standard deviation.

The computational results were compared with the experimental results for a monofocal and the 3 generic bifocals (with +1.50, +3.00 and +4.50 D of near addition); a mean difference of 1.2' and a maximum difference of 2.3' for the glare size were observed. Therefore, the computational results predicted the experimental results ($R^2=0.99$, mean difference $\sim 1'$) and indicated a minor effect of wavefront aberrations in normal subjects (Figure 2).

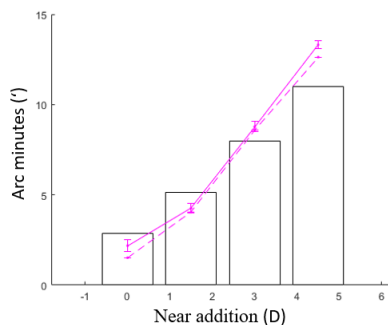


Figure 2. Comparison of the experimental glare size results (bars) with the computational results with and without aberrations (solid and dotted line, respectively) for a plano monofocal and the 3 generic bifocals IOLs (+1.50, +3.00 and +4.50 D near addition).

4. Conclusions

SimVis Gekko demonstrated high sensitivity in revealing variations in photic phenomena across different multifocal intraocular lenses (IOLs) prior to surgery. The magnitude of glare perceived through the visual simulator, exhibited a direct correlation with reported symptoms and simulation outcomes. Notably, bifocals and trifocal IOLs produced greater glare than EDOF lenses. Among the multifocal options, the +4.50 D bifocal lens resulted in the most pronounced glare, while EDOF lenses provided the least glare after monofocal correction. Also, responses from the AIOLIS questionnaire showed a linear correlation with experimental glare size, suggesting that increased glare was associated with greater visual disturbance. Finally, computational simulations can predict the experimental results and wavefront aberrations had a minor impact on glare size in normal subjects prior to IOL implantation.

Acknowledgments

Comunidad de Madrid - Doctorado Industrial (IND2023/BMD-27723) to AV; Ministerio de Ciencia e Innovación, Ayudas a proyectos de colaboración público-privada (CPP2021-008388) to AdC, CD, VR, PP; Torres Quevedo (PTQ2021-011963) to ISF and Ramon y Cajal (RYC2021-033355I) to LS.

References

- [1] Sawides L, de Castro A, Lago CM, Barcala X, Zaytouny A, Marcos S, et al. SimVis simulations of multifocal IOL designs based on public-literature data. En: Babington J, Fuchs U, Mazuray L, editores. Optical Design and Engineering VIII. SPIE; 2021.
- [2] Hays RD, MacRae S, Holladay J, Tarver ME, Lum F, Stark W, et al. Development of a patient-reported outcome measure to assess symptoms associated with cataract surgery and intraocular lens implants. *Ophthalmology* [Internet]. 2023;130(7):715–25. Available at: <http://dx.doi.org/10.1016/j.ophtha.2023.02.026>.
- [3] Castro JJ, Jiménez JR, Ortiz C, Alarcón A, Anera RG. New testing software for quantifying discrimination capacity in subjects with ocular pathologies. *J Biomed Opt* [Internet]. 2011;16(1):015001. Available at: <http://dx.doi.org/10.1117/1.3526702>.

Applications of adjustable astigmatic devices: Stokes lens concept

Sara Ferrer-Altabás*, Ana Lin Lin¹ and Vicente Micó¹

¹ *Department of Optics and Optometry and Vision Sciences, Faculty of Physics, University of Valencia, Street Doctor Moliner, 50, 46100 Burjassot, Valencia (Spain)*

*E-mail: Sara.Ferrer@uv.es

1. Introduction and objective

The versatility of variable optical devices has been demonstrated to be highly applicable in a multitude of fields. Regarding variable astigmatic optics, the concept has already a long history. In fact, one of the first variable optical devices presented was precisely the astigmatic Stokes lens in 1849 [1]. The invention comprised two cylindrical lenses of equal dioptric power but opposite signs that can rotate relative one each other. The two cylindrical lenses, in terms of astigmatic power, act as a vector in a double angle space. Consequently, the astigmatism generated from the combination can vary from zero to twice the value of the individual cylindrical lenses, depending on the relative angle. [1]

Over the years, other methods for variable optical design have been proposed [2], but this contribution will focus on the applications of the Stokes lens concept and its related versions. It is especially interesting to mention Foley and Campbell's generalization of the Stokes design that considered the use of two identical sphero-cylindrical lenses for pure astigmatic power generation.[3]

Several different applications of astigmatism-adjustable devices have been emerging, most of them related with ocular astigmatism from different points of view. Here, we will classify the applications in two main groups: measurement (quantification) and compensation (improving image quality). Concerning measurement, the initial application was for measuring astigmatism in patients[1], a use for which its potential has been validated [4] as well as for measuring ophthalmic optics [5] (see section 2.1). In the second group, most of the applications aimed to compensate astigmatism in the observer's eye or generated by oblique incidence, so it can be suitable for eye fundus observation or ocular aberrations characterization[6]. Similarly, the incorporation of the Stokes lens in eyepieces enhances the image quality perceived by astigmatic patients, making it an ideal solution that eliminates the need for additional compensation. [7]. In addition, this method can be implemented in optical systems where due to other reasons undesired astigmatism arises, and thus correct it without drastic changes of the optical setup. [8]

Our aim is to show some of these applications of the Stokes lens concept for both measurement and compensation of astigmatism in some fields where the presence of astigmatism is quite normal.

2. Developed applications.

2.1. Measuring astigmatism in ophthalmic lenses

Included in the first group mentioned above, the use of a Stokes lens comprising two cylinders of $\pm 1,75D$ in a Risley prism mount extracted from a manual focimeter Topcon LM-8© and implemented again in the same apparatus and location, was employed for the dioptric power measurement of ophthalmic lenses. [5] Images showing such application are shown in Fig. 1. A similar device was used for measuring astigmatism in human eyes during subjective refractive procedures.[4]

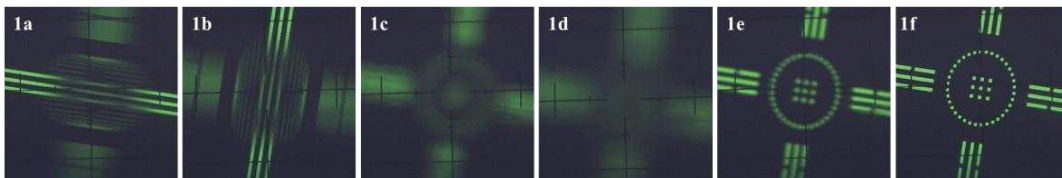


Figure 1 Visual examples of each step of the measuring process in a lens of $+0,25D$ ($-1,25D \times 70^\circ$). More info ref. [5]

2.2. Compensating astigmatism in eyepieces.

Stokes lenses have also been adapted to eyepieces for different purposes. In particular, Arines and Acosta [7] used the Foley and Cambell generalization in a microscope eyepiece and we introduce here Stokes' initial concept application to a manual focimeter (Topcon LM-8©). The Stokes lens described in section 2.1 was externally introduced close to the eyepiece of the focimeter for generating astigmatic

power capable of compensating the user's astigmatism. Visual examples of the generated astigmatism over the eyepiece reticle are shown in Fig. 2.

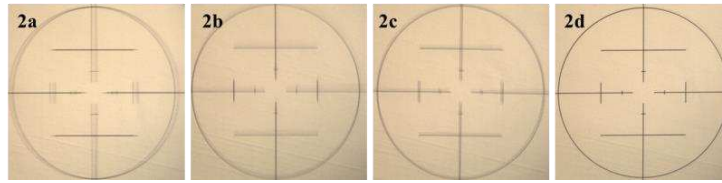


Figure 2 Visual examples of astigmatism produced over the eyepiece reticle using white light. In 2a and 2b there is uncompensated 3,00D astigmatism in horizontal and vertical orientations, in 2c the astigmatism is equal in both orientations (Sturm's interval midpoint). Image 2d shows the reticle free of astigmatism.

2.3. Compensating internal astigmatism in a microscope

Our final application relates with the use of a Stokes lens in a conventional microscope to compensate unwanted astigmatism that can rise due to different reasons. For instance, the authors presented a method of coherent sensing in microscopy by converting a regular microscope into a holographic one through the inclusion of a module that requires of a non-conventional use of a beam-splitter cube which in turns introduces a non-negligible amount astigmatism in the final image. The Stokes lens provides a low-cost solution improving final image quality and phase recovery (Fig.3) free of astigmatism. [8]

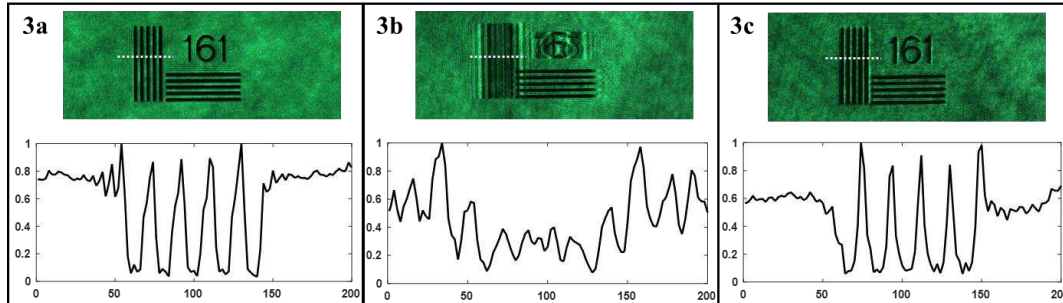


Figure 3 .Images of the reticle and recovered phase from: 3a, conventional use of the microscope; 3b, simulation of unwanted astigmatism by introducing a 0,125D cylinder trial lens; and 3c, using the Stokes lens correction.

Acknowledgments

This research has been granted by the Grant PID2020-120056GB-C21 funded by MCIN/AEI/10.13039/501100011033 and Grant FPU21/00985.

References

- [1] G. G. Stokes, "On a Mode of Measuring the Astigmatism of a Defective Eye," in *Math. Phys. Pap. vol.2* (Cambridge University Press, 1883).
- [2] C. E. Campbell, "Conditions under which two-element variable power lenses can be created Part 1 Theoretical analysis," *J. Opt. Soc. Am. A* **28**, 2148 (2011).
- [3] J. P. Foley and C. E. Campbell, "An optical device with variable astigmatic power," *Optom. Vis. Sci.* **76**, 664–667 (1999).
- [4] J. R. Albero-Moreno et al., "Subjective refraction using power vectors by updating a conventional phoropter with a Stokes lens for continuous astigmatic power generation," *Ophthalmic Physiol. Opt.* **43**, 1029–1039 (2023).
- [5] S. Ferrer-Altabás et al., "Vectofocimetry: Dioptric power measurement in manual focimeters using power vectors," *Opt. Lasers Eng.* **146**, 106703 (2021).
- [6] S. Ferrer-Altabás et al., "Astigmatic Stokes lens revisited," *Opt. Express* **30**, 8974 (2022).
- [7] J. Arines and E. Acosta, "Adaptive astigmatism-correcting device for eyepieces," *Optom. Vis. Sci.* **88**, 1524–1528 (2011).
- [8] J. A. Picazo-Bueno et al., "Single-shot slightly off-axis digital holographic microscopy with add-on module based on beamsplitter cube," *Opt. Express* **27**, 5655–5669 (2019).

Exploring changes in the scleral tissue of myopic eyes using second harmonic generation microscopy

Juan M. Bueno*, Rosa Martínez-Ojeda, Enrique J. Fernández and Marita Feldkaemper[‡]

Laboratorio de Óptica, Universidad de Murcia, 30100 Murcia, Spain

[‡]Institute for Ophthalmic Research, Section of Neurobiology of Eye, 72076 Tübingen, Germany

*E-mail: bueno@um.es

1. Introduction

The outer layer of the sclera is a dense connective tissue mainly composed of collagen fibers [1]. Its main function is protecting the eye from external injury. Due to its high collagen content, this ocular element can be explored with second harmonic generation (SHG) microscopy [2]. This is a nonlinear imaging technique where, in the absence of absorption, two infrared photons interact with a non-centrosymmetrical structure (such as collagen-based tissues). As a result, light at exactly half of the excitation wavelength is emitted. SHG signals are generated not only from collagen (due to its significant second-order nonlinear susceptibility) but also from biological tissues containing myosin [2-4]. Although SHG microscopy has been successfully used to image scleral collagen [5,6], those analyses were mainly descriptive.

Myopia results from a mismatch between the eye's optical power and its axial length. The progression of this ocular condition is associated with abnormal eye growth which leads to structural and morphological changes [7]. The shape and size of a myopic eye are partly determined by the resistance of the sclera. Different experiments based on histological analyses have reported that the scleral collagen arrangement could be affected. Scleral thinning was also shown to occur during myopia development [8]. However, these previous works are mainly qualitative, and in some cases findings do not agree to each other.

There is a lack of studies dealing with quantitative analyses of the sclera under different experimental conditions. Moreover, since SHG microscopy allows visualizing collagen-based tissues without the use of markers and fixation procedures, this technique is especially suitable for imaging scleral tissues. In that sense, here we propose the use of SHG microscopy to further analyze the changes suffered by the sclera of myopic eyes. In particular, SHG images from scleral tissues were acquired to objectively quantify possible changes in collagen organization as a function of different amounts of induced deprivation myopia in chicks.

2. Methods

A custom backscattered SHG microscope [4] was used to image the collagen fibers of unstained scleral punches from areas close to the optic nerve head. Samples of both control and deprived eyes were used in the experiment. Myopia was induced by placing a translucent plastic diffuser in one of the chickens' eyes for 7 days. Contralateral eyes had normal vision and served as control.

Two SHG imaging modalities were used: Tomographic (XZ or YZ), and regular XY microscopy images. The former allowed direct estimation of the scleral thickness. The latter permitted the visualization of the fibers and were used to perform spatially resolved analyses. The Structural Dispersion (SD), computed through the Radon Transform [9], was used as an objective assessment of the level of organization of the collagen network.

3. Results

After one week of diffuser wearing, the eyes developed myopia of -4.7 ± 2.7 D on average. As typically found, fellow control eyes exposed to normal vision remained slightly hyperopic (2.5 ± 0.6 D). There was a statistically significant linear relationship between individual final refraction and axial length after deprivation. That is, larger (lower) myopia values correspond to longer (shorter) ocular lengths. In addition, changes in axial length (ΔAL) and baseline refraction (ΔRx) were also linearly correlated.

From each tomographic SHG image the intensity profile along the depth location was computed and the scleral thickness calculated. Averaged thickness values ranged between 50 and 70 μm , but there was no correlation between this parameter and neither the final refraction nor the axial length.

Figure 1 shows two examples of SHG images of scleral tissues corresponding to eyes with low and

high myopia. Scleral collagen fibers provided strong SHG signal for analysis and individual fibers were easily observable within the images. The insets show the corresponding SD values computed through the procedure explained in Methods.

SD was computed for all specimens and results show a relationship between the final ocular refraction and SD, which ranged from a random distribution ($SD < 20^\circ$) to a well-organized aligned organization ($SD > 40^\circ$). In addition, this parameter was closely related to the axial length increment.

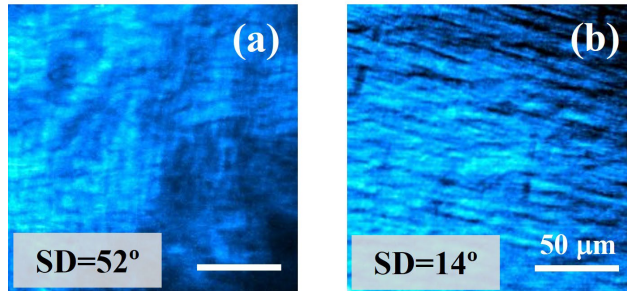


Figure 1 SHG images for after-deprivation chicken scleras with low (a) and high (b) myopia values. Insets indicate the SD values computed using the Radon Transform algorithm.

4. Discussion and conclusions

In the present study, SHG microscopy has been used to image unstained scleral punches in both control and myopic chicken eyes. This imaging technique provided a high-resolution visualization of individual scleral collagen fibers. A significant decrease in fiber SD was associated to a higher myopic refraction, what demonstrates the existence of a remodeling process of the scleral collagen associated to myopia progression. This technique allows quantifying alterations during myopia induction, providing a useful tool for a better understanding of the emmetropization processes.

Acknowledgments

Supported by grant PID2020-113919RBI00/AEI/10.13039/501100011033.

References

- [1] F. W. Keeley, J. D. Morin, and S. Vesely, "Characterization of collagen from normal human sclera," *Exp. Eye Res.* 39(5), 533-542 (1984).
- [2] J. M. Bueno, F. J. Ávila, and P. Artal, "Second harmonic generation microscopy: a tool for quantitative analysis of tissues," in *Microscopy and Analysis*, S. G. Stanciu, ed. (IntechOpen, 2016).
- [3] P. J. Campagnola, H. A. Clark, W. A. Mohler, A. Lewis, and L. M. Loew, "Second-harmonic imaging microscopy of living cells," *J. Biomed. Opt.* 6(3), 277–286 (2001).
- [4] J. M. Bueno, R. M. Martínez-Ojeda, M. Pérez-Zabalza, L. García-Mendivil, M. C. Asensio, L. Ordovás, and E. Pueyo, "Analysis of age-related changes in the left ventricular myocardium with multiphoton microscopy," *Biomed. Opt. Express* 15(5), 3251-3264 (2024).
- [5] M. Han, G. Giese, and J. Bille, "Second harmonic generation imaging of collagen fibrils in cornea and sclera," *Opt. Express* 13(15), 5791-5797 (2005).
- [6] S.-W. Teng, H.-Y. Tan, J.-L. Peng, H.-H. Lin, K. H. Kim, W. Lo, Y. Sun, W.-C. Lin, S.-J. Lin, S.-H. Jee, P. T. C. So, and C.-Y. Dong, "Multiphoton autofluorescence and second-harmonic generation imaging of the ex vivo porcine eye," *Invest. Ophthalmol. Vis. Sci.* 47(3), 1216-1224 (2006).
- [7] D. Troilo and J. Wallman, "The regulation of eye growth and refractive state: an experimental study of emmetropization," *Vision Res.* 31(7-8), 1237-1250 (1991).
- [8] N. A. McBrien and A. Gentle, "Role of the sclera in the development and pathological complications of myopia," *Prog. Retin. Eye Res.* 22(3), 307-338 (2003).
- [9] Y. Mega, M. Robitaille, R. Zareian, J. McLean, J. Ruberti, C. DiMarzio, "Quantification of lamellar orientation in corneal collagen using second harmonic generation images," *Opt. Lett.* 37(16), 3312-3314 (2012).

Night vision disturbances: does the chromaticity of visual stimuli play a role?

José Juan Castro Torres^{1*}, Miriam Casares López¹, Sonia Ortiz Peregrina¹, Francesco Martino¹, Luis Gómez Robledo¹ and José Ramón Jiménez¹

¹*Department of Optics, University of Granada., Avenida de Fuentenueva, s/n 18071 Granada*

*E-mail: jjcastro@ugr.es

1. Introduction

Night vision disturbances are a common complaint in clinical practice, for example, in some patients after refractive surgery or in patients with certain ocular pathologies, who usually indicate the perception of halos or glare [1]. Such visual disturbances must be assessed in order to characterize patient's visual performance. For that, visual tests that use stimuli devoid of tone (achromatic) are usually used to assess the extent of these visual disturbances [2]. However, the visual stimuli and light sources present in everyday life may present different chromaticities, so it is of interest to analyze whether the chromaticity of the stimuli has any influence on these visual disturbances.

The aim of this work is to assess the influence of the chromaticity of visual stimuli on night vision disturbances. For that, we analyzed visual discrimination and intraocular straylight under low illumination using achromatic and chromatic luminous stimuli (red, green, and blue).

2. Methods

A total of 27 subjects participated in the study and gave their informed consent. The study was approved by the Human Research Ethics Committee of the University of Granada (1256/CEIH/2020). The inclusion criteria were decimal best-corrected visual acuity of 1.0 (decimal notation) or higher and no pathological conditions that could affect visual performance. Night visual disturbances were assessed by means of visual discrimination capacity (halo perception) under low-lighting conditions and intraocular straylight. Discrimination capacity was evaluated using the Halo test, a test that consists of presenting stimuli around a central stimulus of higher luminance that the subject has to perceive [2]. This test provides the visual disturbance index (VDI, the higher the VDI, the stronger the halos and night vision disturbances perceived) as well as a graph of results showing the number of detected and undetected stimuli around the central one, providing a shape of the visual disturbance perceived by the subject. Intraocular straylight (log(s)) was evaluated using the C-Quant device (C-Quant, Oculus GmbH, Wetzlar, Germany), which uses the psychophysical compensation comparison method and has been extensively validated [3].

Both the Halo test and the straylight measurements were performed for achromatic stimuli (white light) and for stimuli of different chromaticity (red, green and blue). In the case of the Halo test, this was achieved by changing the color settings of the stimuli in the computer to electrical driving levels of (255, 0, 0), (0, 255, 0) and (0, 0, 255) for the red, green and blue stimuli, respectively, as well as adjusting different levels of luminance, and in the case of the straylight measurement, using different dichroic filters.

3. Results and discussion

Fig. 1 shows the graphical results of the Halo test under different chromatic conditions for a participant with a low halo perception for achromatic stimuli. Although it can be seen that for the red and green chromatic stimuli the perception of halos was maintained, for the blue stimuli the halo became considerably larger, with hardly any stimuli perceived. We observed this trend both for the maximum luminance of the central stimuli presented on the screen, as well as maintaining the luminance level for all chromaticity conditions. Table 1 shows mean values for the monocular VDI under the different experimental conditions (different chromaticity and two levels of stimuli luminance). We found significant differences in the VDI under both luminance conditions (maximum luminance of the central stimulus, L_{max} , and maintaining equal luminance of the central stimulus, $L_{constant}$) ($p < 0.01$), in such a

way that for the low luminance conditions the VDI and the pupil size were significantly higher, showing a greater influence of halos. Pairwise comparisons showed that the VDI for the blue stimulus was significantly higher ($p < 0.001$) compared to the other chromatic stimuli in both luminance conditions.

Intraocular straylight, $\log(s)$, was significantly lower for the achromatic stimulus compared to the three chromatic stimuli ($p < 0.001$) (Table 1), and no significant differences were found between the red and green filters ($p > 0.05$). Intraocular straylight wearing the blue filter was significantly higher than that of the achromatic, red, and green stimuli ($p < 0.001$), which indicates the blue filter produces a greater degree of intraocular straylight.

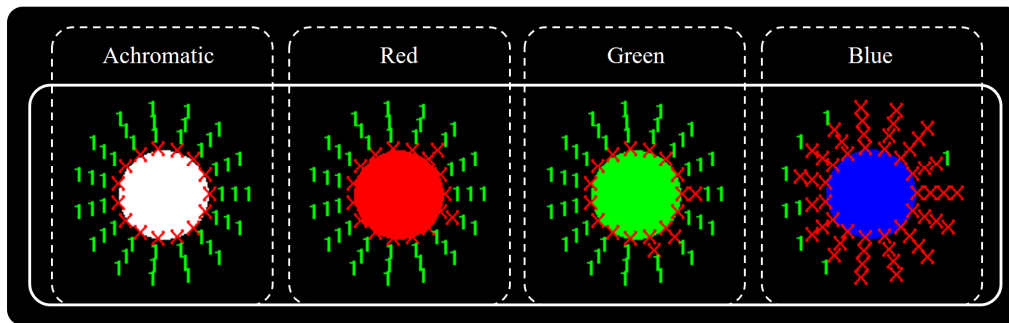


Figure 1 Graphical results of the Halo test using different achromatic and chromatic stimuli for one subject under the maximum luminance condition (maximum luminance of the central stimulus achieved by the test monitor).

	Achromatic (white light)	Red	Green	Blue
VDI (Lmax)	0.20 ± 0.09	0.18 ± 0.08	0.21 ± 0.12	0.69 ± 0.21
VDI (Lconstant)	0.33 ± 0.17	0.25 ± 0.12	0.34 ± 0.18	0.69 ± 0.21
Straylight	0.86 ± 0.12	1.07 ± 0.17	1.04 ± 0.22	1.24 ± 0.19

Table 1 Mean monocular VDI for the two luminance conditions and mean straylight value under the different chromatic conditions (achromatic, red, green and blue).

4. Conclusions

Night vision disturbances perceived by young subjects depend on the chromaticity of the light stimuli that generate them, wherein visual impairment is greater for the blue stimuli, both in conditions of maximum luminance of the stimuli and maintaining the same level of luminance. A similar trend occurs with straylight, which increased significantly for blue stimuli, demonstrating a major contribution of shorter wavelengths, thus resulting in a stronger luminous veil over the retina and, therefore, more glare. Our findings could be of greater relevance in driving, as driver vision may be affected by the type of headlights of oncoming cars, but may also be of interest in drivers who have undergone some type of refractive surgery or who have some type of ocular pathology.

Acknowledgments

Grants A-FQM-532-UGR20, funded by FEDER, and PID2020-115184RB-I00, funded by MCIN/AEI/10.13039/501100011033.

References

- [1] E. S. Rosen, "Night vision disturbance". *J Cataract Refrac Surg.* **31**, 247-249 (2005).
- [2] J. J. Castro, F. Martino, M. Casares-López, S. Ortiz-Peregrina and C. Ortiz, "Visual performance after the deterioration of retinal image quality: induced forward scattering using Bangerter foils and fog filters", *Biomed Opt Express.* **12**(5): 2902–2918 (2021).
- [3] T. van den Berg, L. Franssen and J. E. Coppens, "Straylight in the human eye: testing objectivity and optical character of the psychophysical measurement". *Ophthalmic Physiol Opt.* **29**, 345-350 (2009).

Aberración cromática en sistemas ópticos con codificado de frentes de onda con fase trébol

Juan Miguel Olvera¹, Eva Acosta² and Justo Arines³

¹Universidad Politécnica de Puebla, México

²Facultad de Física, Universidad de Santiago de Compostela, 15782, España

^{3,1}Facultad de Óptica y Óptica, iMATUS, Universidad de Santiago de Compostela, 15782, España

*E-mail: justo.arines@usc.es

1. Introducción

La profundidad de campo limitada de los sistemas ópticos convencionales dificulta la obtención de imágenes claras de objetos a distintas distancias en una sola toma manteniendo la apertura del sistema óptico. Para abordar esta limitación Dowski y Cathey [1] proponen la técnica conocida como codificado de frente de onda (WFC, por sus siglas en inglés). WFC se basa en la modificación controlada de la fase óptica del sistema, junto con procesamiento digital de imágenes, para extender la profundidad de campo sin sacrificar la resolución de la imagen. Este método supone colocar en el plano de la pupila de salida una lámina de fase cúbica de la forma $\alpha(x^3 + y^3)$, lo que produce una imagen borrosa casi invariante al desenfoque. En otras palabras, este elemento óptico modifica el sistema de imagen de tal manera que la PSF del sistema y OTF son invariantes al desenfoque. Las imágenes borrosas, también llamadas intermedias, se restauran digitalmente mediante un filtro de deconvolución único para la profundidad de campo deseada, que es proporcionada por la fuerza de la lámina α . Aunque la fase cúbica ha demostrado su eficacia en múltiples aplicaciones en campos como la microscopía, imagen térmica y la endoscopia entre muchas otras, la aparición de oscilaciones en la OTF hace que aparezcan artefactos en las imágenes procesadas que son difíciles de eliminar. Recientemente, fases con dependencia azimutal del tipo $f(r)\cos(3\theta)$ [2] han demostrado su eficacia no sólo ante la atenuación de artefactos sino también en lo que corresponde a la minimización de ruido.

El efecto de la aberración cromática en sistemas que utilizan WFC tanto con fase cúbica como con fase tipo trébol no ha sido estudiado experimentalmente. En este trabajo exploramos la capacidad de las láminas en la forma trébol para compensar la aberración cromática.

2. Montaje Experimental

Las imágenes de un test USAF 1951 iluminado con tres LEDs de longitudes de onda central R=630nm, G=555nm y B=460nm se adquieren en distintos planos alrededor del plano focal correspondiente al LED verde, de una lente biconvexa de 50 mm de focal y 2.5 cm de diámetro (Thorlabs LB4096-B). La lámina de WFC se fabricó mediante tallado de precisión con punta de diamante de una de sus superficies siguiendo la expresión $\phi(r, \theta) = Ar^3 \sin(3\theta)$, siendo A el pico valle de la topografía y r el radio normalizado a la unidad. La lámina fabricada se montó en un diafragma de 5mm de diámetro y se situó delante de la lente. y ha sido fabricada mediante tallado de precisión a diamante en PMMA. El interferograma de la fase (@633nm) y las aberraciones que induce en el sistema para distintos radios de apertura se muestran en la figura 1 [2]. Se tomaron un conjunto de imágenes del test, colocado en el foco objeto de la lente biconvexa, y fuera de foco las cantidades de (-0.5, 0, 0.5, 1) mm. Un sistema 4f permitió conjugar la lámina de WFC con el objetivo de una cámara monocromo Hamamatsu ORCA R2 usada para registrar las imágenes. Los resultados sin y con lámina WFC + postprocesado se muestran en la figura 2.

Generamos digitalmente las OTFs para cada longitud de onda para el plano focal objeto encontrado para $\lambda=555\text{nm}$ y las utilizamos para decodificar todas las imágenes intermedias obtenidas para las diferentes distancias objeto. Para la decodificación empleamos el filtro de Wiener construido con la OTF.

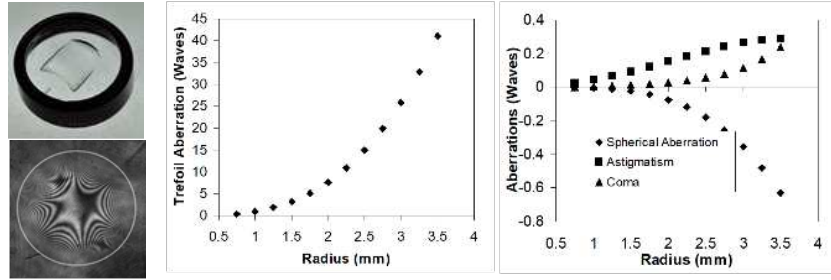


Figura 1 Lámina trébol para WFC y caracterización óptica

3. Resultados

En la figura 2 se muestran las imágenes del test en distintos planos situados a una distancia Δ del plano focal encontrado para $\lambda=555\text{nm}$. La aberración esférica que induce la lámina sólo produce una traslación de la profundidad del foco [3], y la aberración de coma no afecta a la calidad de imagen, ya que estas láminas también pueden usarse para corregir astigmatismo, coma y aberraciones de orden superior [2]. Se puede observar que la aberración cromática longitudinal se corrige con gran profundidad de foco aunque la transversal se mantiene en cierta medida.

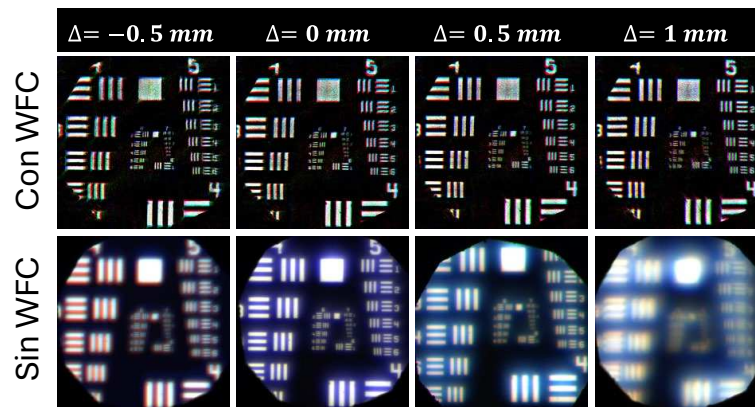


Figura 2 Imágenes a distintas distancias del plano focal con WFC (fila superior) y sin WFC (fila inferior)

4. Conclusiones

WFC con elementos de fase en forma de aberración tipo trébol corrigen la aberración cromática longitudinal de sistemas ópticos sin compensación alguna de aberración cromática, lo que implica un abaratamiento de los costes de los mismos.

Agradecimientos

Este trabajo ha sido subvencionado por Ministerio de Ciencia e Innovación PID2020-115909RB-I00.

Referencias

- [1] E. R. Dowski and W. T. Cathey, "Extended depth of field through wave-front coding," *Appl. Opt.* **34**, 1859-1866 (1995).
- [2] J. Arines, R. O. Hernandez, S. Sinzinger, A. Grewe, and E. Acosta, "Wavefront-coding technique for inexpensive and robust retinal imaging," *Opt. Lett.* **39**, 3986-3988 (2014).
- [3] Y. Shi, S. Chen, V. Nhu Le, Z. Fan, W. Zhang, "Performance analysis of wavefront coding system with spherical aberration by using ray aberration approach", *Optik*, **130**, 1266-1271(2017).

XIV Reunión Nacional de Óptica, Murcia (2)3-5 Julio 2024

Fast defocus oscillations have a mild effect on contrast sensitivity

Pedro M. Prieto, Vahid Pourreza Ghoushchi, Juan Mompeán, Pablo Artal

Laboratorio de Óptica, Universidad de Murcia, Edificio CiOyN, Campus de Espinardo, Murcia (Spain)

*E-mail: pegrito@um.es

1. Introduction

The temporal properties of the visual system regarding aspects such as fastest perceptible flicker or minimum presentation time for image recognition, among others, have been thoroughly explored in the literature. However, most studies approach the topic from the point of view of information processing and hardly, if at all, consider the fact that the retinal image quality is not stable over time. In natural conditions, the fluctuations in accommodation have been found to typically vary the focus of the eye in the range of ± 0.5 D for temporal frequencies up to 2–5 Hz but can have non-zero components even for oscillations above 10 Hz [1]. Additionally, tunable lenses, increasingly used for visual applications such as presbyopia correctors [2], visual simulators [3, 4], and virtual/augmented reality systems, can induce fast and sometimes periodic defocus variations with a wide range of amplitudes.

In this context, the aim of this study is to analyze the effect on contrast sensitivity of sinusoidal defocus fluctuations with temporal frequencies in the range between 5 and 25 Hz and peak-to-valley (PtoV) values up to 3 D, induced with a tunable lens.

2. Methods

The experimental apparatus was based on an open-view Hartmann-Shack sensor [5, 6], with the addition of a tunable lens in front of the right eye. Measurements of contrast threshold at 12 cpd were taken on 5 young emmetropic subjects (age = 26.6 ± 4.0 years, mean spherical equivalent = -0.15 ± 0.24 D, cylinder below -0.25 D in all cases). None of them had any visual problem and their accommodation was not paralyzed. The target was a 1-deg Gabor patch located at 3 m, viewed monocularly through a tunable lens (Optotune EL-16-40-TC-VIS-20D) inducing sinusoidal defocus oscillations around 0 D at 5 Hz, 15 Hz, and 25 Hz, and PtoV defocus of 0.15 D, 0.25 D, 0.5 D, 0.75 D, 1 D, 1.5 D, 2 D, and 3 D. For each combination, contrast threshold was measured with a forced-choice protocol comprising 5 contrast values presented 10 times each. The total number of trials were divided into 10 series, each one with a fixed temporal frequency (in a random order) and randomized in defocus PtoV and contrast. Each Gabor patch was tilted 10 deg from the vertical in a random direction, which the subject had to guess, and was presented at most for 2 seconds but an earlier answer by the subject triggered the next presentation.

Trying to model the behavior of contrast threshold for defocus oscillations in terms of average blur in a hypothetical integration time, we calculated the modulation transfer function (MTF) associated to the mean blurred point spread function (PSF) calculated by averaging instantaneous defocused PSFs over intervals of different length. From there, we calculated the modulation loss as the ratio between the diffraction-limited MTF at 12 cpd and blurred MTF at the same spatial frequency. Although there is not a straightforward numerical relationship between contrast sensitivity and MTF, a certain modulation loss could be expected to produce a similar increase in contrast threshold.

3. Results

Fig. 1 shows the mean contrast threshold as a function of defocus PtoV for each temporal frequency studied. Error bars represent standard deviation across subjects. Although there is some intersubject variability, contrast threshold appears to be surprisingly resilient to fast defocus oscillations around 0 D. Even for 2 D of PtoV (meaning an oscillation between -1 D and $+1$ D), there is hardly a degradation in contrast sensitivity. Only the largest and fastest fluctuation (25 Hz, 3 D of PtoV) can be seen to start producing a noticeable increase in threshold.

Fig. 2 shows the results of MTF loss simulation for two potential integration times, 0.005 and 0.01 sec. Qualitative comparison with Fig. 1 suggests that the eye's integration time for defocus may be around or below 1 hundredth of a second.

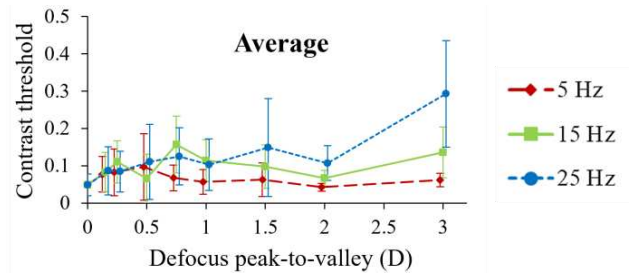


Figure 1 Mean contrast threshold at 12 cpd for defocus oscillations of varying PtoV and temporal frequency. Error bars represent standard deviation. Slight shifts in horizontal direction have been introduced for visibility reasons.

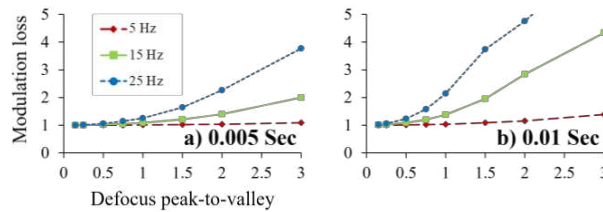


Figure 2 Simulated modulation loss (diffraction-limited MTF over blurred MTF) at 12 cpd, obtained by averaging the blurring caused by defocus oscillations across 0.005 sec (a) or 0.01 sec (b).

4. Conclusions

Visual function in terms of contrast threshold was found to be surprisingly immune to fast defocus oscillations in the range between 5 and 25 Hz. Qualitative comparison of the experimental results with a simulation of modulation loss as a function of integration time suggests that the eye only requires the image to be in focus for a very short integration time, around or below a hundredth of a second, to perform the task. This finding may have some implications in present and future uses of tunable lenses for visual applications.

Acknowledgments

The authors acknowledge the following sources of funding: Horizon 2020 Framework Programme (675137); Fundación Séneca (19897/GERM/15); Agencia Estatal de Investigación (PID2019-105684RB-I00/AEI/10.13039/501100011033).

References

- [1] A. W. Lohmann, D. P. Paris, *Appl. Opt.* 4(4), 393–397 (1965).
- [2] J. Mompeán, J. L. Aragón, P. Artal, *Sci. Rep.* 10(1), 20293 (2020).
- [3] S. R. Soomro, S. Sager, A. M. Paniagua-Díaz, P. M. Prieto, P. Artal, *Biomed. Opt. Express* 15(2), 608-623 (2024).
- [4] C. Dorronsoro, E. Gamba, L. Sawides, S. Marcos, V. Akondi, and Y. Marrakchi, *Biomed. Opt. Express*, 9(12), 6302-6317 (2018).
- [5] E. Chirre, P. M. Prieto, P. Artal, *Biomed. Opt. Express* 6(10), 4200-4211 (2015).
- [6] V. P. Ghouschi, J. Mompeán, P. M. Prieto, P. Artal, *Biomed. Opt. Express* 12(6), 3282-3295 (2021).

Developing a protocol to objectively measure oculomotor deficits in amblyopia during naturalistic tasks

Maite Valentino*, Marta Teruel, Clara Mestre, Marc Argiles, Luis Pérez-Mañá, Jaume Pujol
*Centre for Sensors, Instruments and Systems Development (CD6), Universitat Politècnica de Catalunya,
Rambla Sant Nebridi, 10, 08222 Terrassa, Barcelona, Spain*

*E-mail: maria.teresa.valentino@upc.edu

1. Introduction

Amblyopia affects up to 2-4% of the population and is characterized by a usually unilateral loss of vision due to abnormal visual development in early childhood [1]. While decreased visual acuity is its clinical hallmark, other visuospatial functions such as contrast sensitivity, stereopsis, and ocular movements are also compromised. In search for a proper assessment of amblyopia, these dysfunctions are gaining increasing significance, as some of them can be measured objectively, such as eye movements. Conventional eye movements studies in amblyopia have typically been conducted in controlled laboratory settings using remote eye-trackers and presenting visual stimuli on a monitor. However, no studies to date have objectively measured eye movements in individuals with amblyopia while they perform tasks resembling everyday life activities. Therefore, the main objective of this study was to develop and validate a protocol to assess oculomotor performance in children with amblyopia during the performance of naturalistic tasks.

2. Materials and methods

The instrument used in this project was the binocular wearable Pupil Core (Pupil Labs, Berlin, Germany) eye-tracker. Its familiar goggle-shape is convenient to be used with children and its configuration allows free and confident movement of the subjects while doing naturalistic tasks. To determine the specific requirements for conducting the measurements, two essential aspects were identified: the specific tasks that the child would perform and the optimal calibration procedure of the Pupil Core for each of these tasks.

The chosen tasks of the protocol should be capable of measuring the different parameters related to amblyopic eye movement deficits: increased saccadic latencies and reduced saccadic amplitudes, low pursuit gain (eye velocity/target velocity) and intrusive saccades, fixation instability, and impaired vergence coordination [2,3]. Two types of naturalistic tasks were distinguished, those where the child has free movement and can explore the environment (gross motor skills encompassing orientation, mobility, and balance) and eye-hand coordination tasks (fine motor skills which include both bimanual and unimanual dexterity) where the child remains static or seated. A series of fine and gross motor tasks were designed to be achievable and appropriate for measuring each oculomotor parameter as allowed by the Pupil Core specifications and configuration. It was also important to consider the age range intended for this protocol (3 to 12 years old) to choose suitable tasks for children's cognitive ability. Considering the different calibration procedures described in the Pupil Core technical documentation [4], the most suitable method for each task was designed.

In this pilot study to determine the optimal methodology, the experimental protocol was validated in a group of 10 adults (mean \pm SD age of 28.3 ± 3.3 years) without amblyopia.

3. Results

The most proper tasks for measuring each oculomotor parameter, as well as the calibration method for each of them, were identified. The parameters that were evaluated in the established protocol were: saccadic amplitude, peak velocity, main sequence (ratio between amplitude and peak velocity), latency, and accuracy; vergence amplitude, velocity, and latency; smooth pursuit velocity, position, and saccadic intrusions; and fixation frequency, duration, and stability. The final protocol's battery of tasks was: visual search game, reaching and colouring dots, following with the eye a sinusoidal and an ellipse pattern, painting on a sinusoidal and an ellipse pattern, target aiming game, maintaining fixation on a point while balancing on one foot, and walking along a specific path while stepping on marked points. The results obtained from some of them are shown below as an example.

The visual search game consisted of finding the character wearing a specific sock. The participants made an average number of 9.7 ± 7.4 saccades until they found the corresponding character, where the large standard deviation represents the variability in the search ability of participants. The need to return to look at the sock was 1.3 ± 1.1 times. Fig. 1A shows the performance obtained for one participant. Fig. 1B represents the main sequence of all participants, where the expected values were obtained [5]. With the painting on a sinusoidal pattern task, the smooth pursuit movement was evaluated by studying how many intrusive saccades participants made and their amplitude. On average, 7.1 ± 5.8 intrusive saccades with amplitudes of 1.66 ± 0.65 deg were made. The wide variability of results reflects the difference in how participants performed the task. Some participants performed the task more slowly and exhibited no or few saccades, while others performed the test quickly and executed saccadic movements instead of smooth pursuit. Finally, in the fixation task while balancing on one foot, the fixation stability was assessed by calculating the Bivariate Contour Ellipse Area (BCEA) [6], with average values of 3.17 ± 1.67 deg².

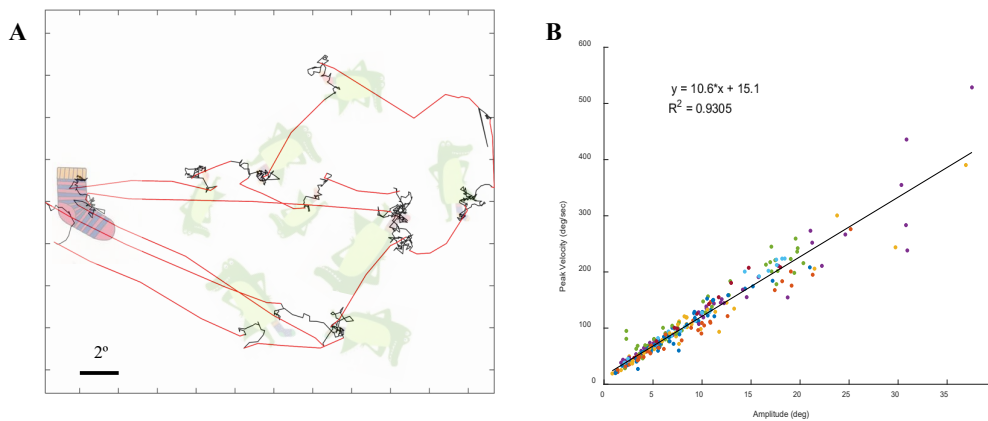


Figure 1 Results obtained with the visual search game. (A) Example of a patient's performance showing saccades in red and fixations in black. (B) Main sequence of the total number of saccades performed by the participants during the task, where the colours of the dots represent different patients.

4. Conclusions

The protocol developed and validated in this study has proven to be effective to assess oculomotor performance during the performance of different naturalistic tasks that involve abilities usually impaired in amblyopia. Future research will focus on testing this protocol in children with amblyopia and typically developing children to identify potential oculomotor differences. As a result, this project takes a pioneering approach by investigating how the oculomotor deficits of amblyopia could manifest in real-world functional activities, offering a more ecologically valid assessment of their visual function.

Acknowledgments

This publication is part of the project PID2020-112527RB-I00 and TED2021-130409B-C54, funded by MCIN/AEI/10.13039/501100011033 and the European Union through the “NextGenerationEU”/PRTR.

References

- [1] J. R. Polling, S. E. Loudon, and C. C. W. Klaver, “Prevalence of Amblyopia and Refractive Errors in an Unscreened Population of Children”, *Optometry and Vision Science* **89**(11), 44–49 (2012).
- [2] Y. Fan, L. Li, P. Chu, Q. Wu, Y. Wang, W. Cao, and N. Li, “Clinical analysis of eye movement-based data in the medical diagnosis of amblyopia”, *Methods* **213**, 26–32 (2023).
- [3] A. L. Webber, “The functional impact of amblyopia” *Clinical and Experimental Optometry* **101**(4), 443–450 (2018).
- [4] Pupil Labs, “Pupil Core Documentation”, <https://docs.pupil-labs.com>.
- [5] A. T. Bahill, M. R. Clark, and L. Stark, “The main sequence, a tool for studying human eye movements”, *Mathematical Biosciences* **24**(3), 191–204 (1975).
- [6] R. Steinman, “Effect of Target Size, Luminance, and Color on Monocular Fixation”, *Journal of The Optical Society of America* **55**(9), 1158-1164 (1965).

Eye Tracking Cognitive Assessment: Exploring Neuropsychological Tests

Joan Goset^{1*}, Valldeflors Viñuela¹, Clara Mestre¹, Laura Rey¹, Mikel Aldaba¹, Meritxell Vilaseca¹

¹ Center for Sensors, Instruments and Systems Development, Universitat Politècnica de Catalunya, Terrassa (Barcelona), Spain

*E-mail: joan.goset@upc.edu

1. Introduction

Due to the complex interactions between different parts of the central nervous system involved in vision and oculomotor control, eye movements can be affected by cognitive impairment [1]. Despite the significant prevalence of cognitive impairment, its diagnosis is still a challenge. In particular, neuropsychologists traditionally use tests that include a series of tasks and questions to evaluate cognition, such as the Montreal Cognitive Assessment (MoCA), the Stroop test and the Trail Making Test (TMT). Nevertheless, the former tests involve long clinical measurement times and none of them allow the diagnosis in a timely manner. As a consequence, new approaches are still needed to diagnose neurological diseases earlier. In this sense, considering that eye movements are affected in cognitive impairment, new tools based on eye tracking technology could play a role on this [2].

In this framework, the TMT measures cognitive functions such as planning, organizing and decision making [6]. The test consists of two parts: in Part A, the subject is instructed to connect, in ascending order, a set of 25 numbers (from 1 to 25) randomly distributed as quick as possible using a pencil. Part B introduces a greater cognitive challenge: the page includes both numbers and letters. The task is to connect them in an alternating sequence (1-A-2-B-3-C and so forth). In this work we investigated the relationship between the traditional outcomes of the TMT and those from a computer-based implementation of the test using eye tracking, from which objective parameters related to the quality of the visual task can be retrieved.

2. Methods

Participants were positioned 60 cm away from a 17" LCD monitor and stabilized with a chinrest. Eye movements were recorded while performing the TMT displayed on the monitor using a desktop-mounted EyeLink 1000 Plus (SR Research) eye tracker. Stimuli presentations were generated using Matlab and the Psychophysics Toolbox library. Saccades and fixations were identified and quantified following Nyström and Holmqvist algorithms [3]. Additionally, the Bivariate Contour Ellipse Area (BCEA) [4] and the main sequence fit function parameters V_{max} and C [5] were computed (Fig. 1).

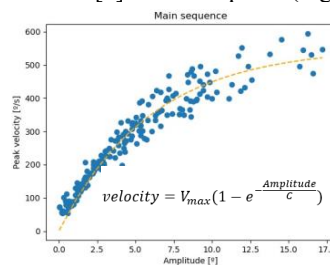


Figure 1 Peak velocity as a function of amplitude of saccades (blue dots) exhibited during the performance of the TMT by a representative participant. A commonly used exponential equation to describe the main sequence was fitted (orange dotted line) and both V_{max} (maximum saccade velocity) and C parameters were calculated for each participant according to the equation shown.

3. Results

Five healthy participants (4 females, 1 male) with mean \pm SD age of 53 ± 2 years participated in the study. Figure 2 depicts various saccade and fixation parameters observed among participants in relation to their test completion times (the longer the completion time, the worse the result). Prolonged test durations exhibited a slight reduction in fixations per second (Figure 2A), alongside with extended fixation durations (Figure 2B) and an increased fixation instability as measured by BCEA (Figure 2C). These associations were visible comparing TMT's parts A and B, suggesting more cognitive demand in part B. Moreover, the

saccades mean amplitude showed a relation with test duration (Figure 2D), indicating larger eye movements in longer tests. Differences between part A and part B support this trend, with slightly higher amplitudes in part B. Conversely, little to no relation between the parameters of the main sequence fit function (Figure 2E and F) and completion time was found, although part B showed an increased saccade velocity.

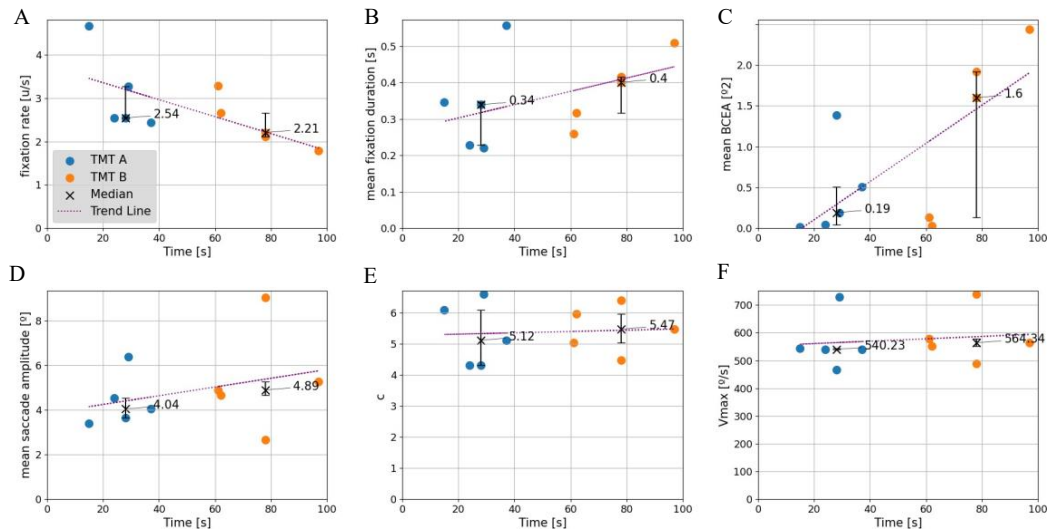


Figure 2 Fixation rate (A), mean fixation duration (B), mean BCEA (C), mean saccade amplitude (D), parameter C (E) and maximum saccade velocity (V_{max}) (F) exhibited by participants in parts A (blue) and B (orange) of the TMT as a function of the time spent on the test. Medians and interquartile ranges across participants are also depicted on each plot.

4. Conclusions

Results suggested a relationship between task completion time and eye movement parameters retrieved from the eye tracker recordings, indicating that the mental effort involved affected eye movements. Part B, as opposed to part A, required more time reflecting the higher cognitive effort while also depicting differences among all movement parameters between the two parts. Additionally, all parameters except for the fit function, showed a relation with time within each part, reflecting an additional cognitive load and resulting in the prolonged completion times for both separate test parts. While the results obtained focus on broad variations and lack statistical consideration due to the sample size, the aim of this study was to address current TMT shortcomings by proposing further eye movement analyses. Future research will include a larger sample size and the study of additional eye movement parameters during the TMT.

Acknowledgments

This publication is part of the project TED2021-130409B-C54, funded by MCIN/AEI/10.13039/501100011033 and the European Union “NextGenerationEU”/PRTR. With the support of Ajuntament de Terrassa and Diputació de Barcelona.

References

- [1] L. Tao, Q. Wang, D. Liu, J. Wang, Z. Zhu, and L. Feng, "Eye tracking metrics to screen and assess cognitive impairment in patients with neurological disorders," *Neurol Sci* **41**(7), 1697–1704 (2020).
- [2] J. Beltrán, M. S. García-Vázquez, J. Benois-Pineau, L. M. Gutierrez-Robledo, and J.-F. Dartigues, "Computational Techniques for Eye Movements Analysis towards Supporting Early Diagnosis of Alzheimer’s Disease: A Review," *Computational and Mathematical Methods in Medicine* **2018**, 1–13 (2018).
- [3] M. Nyström and K. Holmqvist, "An adaptive algorithm for fixation, saccade, and glissade detection in eyetracking data," *Behavior Research Methods* **42**(1), 188–204 (2010).
- [4] D. C. Niehorster, R. Zemblyš, T. Beelders, and K. Holmqvist, "Characterizing gaze position signals and synthesizing noise during fixations in eye-tracking data," *Behavior Research Methods* **52**(6), 2515–2534 (2020).
- [5] R. J. Leigh and D. S. Zee, *The Neurology of Eye Movements*, 5th ed. (Oxford University Press, 2015).

Use of non-psychoactive cannabinoids: effects of cannabidiol (CBD) on vision and driving

Sonia Ortiz Peregrina^{1*}, Francesco Martino¹, Miriam Casares-López¹, Pilar Granados-Delgado¹, Rosario G Anera¹

¹*Departamento de Óptica. Universidad de Granada. Edificio Mecenas, Campus de Fuentenueva sn, 18071. Granada (España)*

*E-mail: soniaortiz@ugr.es

1. Introduction

Cannabis is composed of a variety of cannabinoids, primarily Δ^9 -tetrahydrocannabinol (THC) and cannabidiol (CBD). THC is associated with psychoactive effects and CBD is known for its calming and sedative properties [1]. Interest in and use of isolated CBD has recently increased significantly, with surveys in countries such as France, the UK and the USA showing usage rates between 10% and 26% [2].

For cannabis containing THC, there is evidence of negative effects on vision, including visual acuity, contrast sensitivity and stereopsis. At the same time, there has been a reduction in the ability of people to drive after using this drug, altering aspects such as the ability to keep the car within its lane [3, 4].

Despite the popularity of CBD, there is very limited information available on its possible effects on driving, with no significant changes found. In the case of vision, a fundamental sensory mechanism for this task, there is no information showing possible changes from CBD.

This raises concerns that CBD may cause drowsiness, and other effects such as visual changes that could pose a risk to driving. Therefore, the aim of this study was to analyze the effect of CBD consumption on visual function and its possible relationship with changes in driving performance.

2. Methods

This study was a randomized, double-blind, placebo-controlled trial that involved twenty healthy young adults (mean age 24.8 ± 6.3 ; 75% male) who were occasional users of CBD and/or cannabis, and held valid driving licenses. The study assessed visual aspects relevant for driving such as static and dynamic visual acuity, stereoacuity, contrast sensitivity, and motion detection. All these tests were carried out binocularly, as this is the natural state for driving. In addition, driving assessments were performed using a driving simulator. The simulator was used to obtain various variables such as average speed, distance travelled out of lane and Overall Driving Performance Score (ODPS). The ODPS is computed as a general metric based on several individual metrics obtained as a result of the driving exercise. A positive ODPS value indicates better than average driving for the sample as a whole, while a negative value would indicate the opposite.

Participants attended three experimental conditions in a randomized order: placebo, a session after vaporized CBD at 15% and another session after vaporized CBD at 30%. In each session, the visual and driving tests were performed to compare the sessions after CBD consumption (CBD 15% and 30%) with the placebo session (CBD 0%).

3. Results

Visual function remained largely unchanged, with no statistically significant change after vaporizing CBD (15% or 30%) with respect to the placebo condition (Table 1).

Additionally, comparisons between experimental conditions showed no significant changes in driving performance after vaporizing CBD at 15% or 30% compared to the placebo condition. Figure 1 shows the results for ODPS and number of crashes. As shown, these parameters even improved slightly on average in some of the sessions after CBD consumption. However, the Friedman test showed no statistically significant differences were found ($p=0.951$ and $p=0.642$).

Visual tests	Placebo (CBD 0%)	CBD 15%	CBD 30%	χ^2 (p-value)
Static visual acuity (decimal notation)	1.25 ± 0.16	1.23 ± 0.13	1.28 ± 0.12	1.507 (0.471)
Dynamic visual acuity (decimal notation)	0.68 ± 0.12	0.69 ± 0.11	0.68 ± 0.08	0.197 (0.906)
Stereoacuity (arcmin 5,5 m)	63.50 ± 62.85	64.00 ± 64.67	79.50 ± 59.07	5.265 (0.072)
Mean contrast sensitivity	148.90 ± 18.00	144.50 ± 21.50	137.99 ± 23.92	1.595 (0.450)
Dot motion detection	0.86 ± 0.11	0.86 ± 0.12	0.85 ± 0.09	2.303 (0.316)

Table 1 Comparisons between sessions for visual parameters

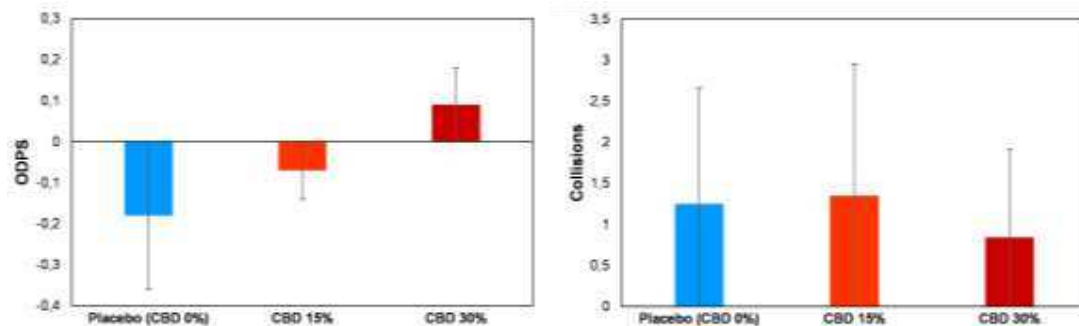


Figure 1 Results for Overall Driving Performance Score (ODPS) and number of collisions for the three experimental conditions (placebo - CBD 0%, CBD 15% and CBD 30%).

4. Conclusions

The results suggest that the doses of cannabidiol used did not affect simulated driving performance and visual function, the main sensory system employed in this task. CBD seems to be a safer substance than THC for visually-dependent tasks.

Acknowledgments

Research Projects PID2020-115184RB-I00, funded by MCIN/ AEI/10.13039/501100011033. FEDER/Junta de Andalucía-Consejería de Transformación Económica, Industria, Conocimiento y Universidades (C-EXP-194-UGR23)

We also thank Dräger Hispania S.A.U. (Madrid, Spain) and LABOGRAN (Granada, Spain) for providing the drug analyzer and "Los niños de la Puri S.L." (Granada, Spain) for sharing information on common usage patterns in the population.

References

- [1] Radwan MM, ElSohly MA, El-Alfy AT, et al. Isolation and Pharmacological Evaluation of Minor Cannabinoids from High-Potency Cannabis sativa. *J Nat Prod.* 2015;78(6):1271. doi:10.1021/ACS.JNATPROD.5B00065
- [2] Grand View Research. Cannabidiol Market Growth Analysis Report, 2021-2028.; 2021. <https://www.grandviewresearch.com/industry-analysis/cannabidiol-cbd-market> Grotenhermen.
- [3] Ortiz-Peregrina S, Ortiz C, Casares-López M, Jiménez JR, Anera RG. Effects of cannabis on visual function and self-perceived visual quality. *Sci Rep.* 2021;11:1655. doi:10.1038/s41598-021-81070-5
- [4] Ortiz-Peregrina S, Ortiz C, Castro-Torres JJ, Jiménez JR, Anera RG. Effects of Smoking Cannabis on Visual Function and Driving Performance. A Driving-Simulator Based Study. *Int J Environ Res Public Health.* 2020;17:9033. doi:10.3390/ijerph17239033

Investigating the perception of complex natural stimuli in polychromatic conditions using Adaptive Optics

Elena Moreno, Víctor Rodríguez-Lopez, Paulina Dotor-Goytia, and María Vinas-Pena*

¹*Institute of Optics. Spanish National Research Council (CSIC). Serrano, 121, Madrid (Spain)*

*E-mail: maria.vinas@csic.es

1. Introduction

Visual information plays a fundamental role in the emmetropization process, a tightly coordinated process that relies heavily on the integration of environmental and genetic factors, encoding a multifaceted signaling cascade that spans all ocular tissues and involves multiple signaling pathways that convert visual stimuli into molecular signals that control eye growth[1, 2]. A decisive factor is that the retina detects optical defocus, using different optical cues, and generates sign specific molecular signals[3] that stimulate (hyperopic) or inhibit (myopic) eye growth, where the specific cues detection processes are not fully understood. An important challenge in understanding how the response to these optical signals of opposite sign is processed is that the optical cues that modulate eye growth are rarely well-defined homogenous patches of light or dark but are typically a mixture of large- and small-scale structures that interact with the dynamics of visual function (i.e., accommodation, neural adaptation). Besides the known optical cues that activate different molecular mechanisms (sign-dependent/independent mechanisms, brightness & circadian rhythm, chromatic cues, and peripheral defocus), the perception of contrast has emerged as a possible cue for emmetropization[4] because optical defocus leads to a proportional degradation of contrast at the luminance edges of the images projected onto the retina, whereby the retina would use the contrast of the luminance edges to determine the focal plane and color contrast to identify the sign of defocus. In addition, natural images (i.e., scenes that are naturally present in our world such as forests, facades, roads, etc.), have a characteristic frequency spectrum that is slightly different for outdoors and indoors scenarios, which has been reported to be a potential cue for myopia progression. In addition to this, blur detection mechanisms of the visual system are modified after prolonged exposure to a degraded stimulus (i.e. myopic retinal blur)[5]. The role of native aberrations in blur discrimination is increased in myopes, with early-onset myopes being more susceptible to this mechanism, suggesting potential differences in neural sensitivity to blur, and therefore in defocus detection, which may be enhanced by chromatic blur[6], and in altered cone spectral sensitivity, which correlates with myopic progression.

Adaptive Optics (AO) based systems allow to explore the limits of spatial vision imposed by the ocular optics[7] and to bypass them to study the neural adaptation processes in the brain. They typically consist of a wavefront sensor (to measure the eye's aberrations), an AO element[8] that modifies the wavefront, and a psychophysical channel to test visual function and neural adaptation. Polychromatic AO simulation[8] operating at multiple wavelengths, with complementary AO elements for blur manipulation, allows vision to be simulated under very realistic conditions, testing the visual response to different optical cues in combination with relevant ocular characteristics (i.e., aberrations, accommodation, neural adaptation). The aim of this study is to investigate the perception of combined optical cues and its dependence on refractive error using an AO-based polychromatic visual simulator.

2. Methods

Measurements were performed in a custom-made multichannel polychromatic AO system[3], where a supercontinuum-laser (450-670nm) illuminated a Digital Micromirror Device (DMD). For each wavelength, the subject focused the stimuli using a Badal-optometer (3 repetitions/wavelength) in natural conditions (free accommodation & natural aberrations). Measurements were performed in 4 young subjects (2 emmetropes, 2 myopes >3D of spherical equivalent) for 6 isoluminant wavelengths (450, 480, 500, 550, 633, 670 nm) randomly presented and 3 different stimuli: binary black-and-white sunburst, natural indoor, and natural outdoor stimuli. LCA was estimated from 2nd-order polynomial fittings of chromatic-defocus curves[6]. An artificial pupil (5 mm) ensured similar conditions across subjects.

3. Results & Discussion

Measured chromatic difference of focus (CDF: 450-670 nm) varied for the different stimuli used and refractive profile of the subjects participating in the study. As shown in figure 1, CDF varied for the different

stimuli and refractive profiles. CDF for the sunburst and outdoor stimulus was higher for myopes ($2.71 \pm 0.12D$ and $1.96 \pm 0.14D$, respectively) than for emmetropes ($1.52 \pm 0.03D$ and $1.41 \pm 0.11D$, respectively), across subjects. Those differences disappeared when using the indoor stimulus (myopes $2.18 \pm 0.12D$ vs. emmetropes $1.99 \pm 0.26D$).

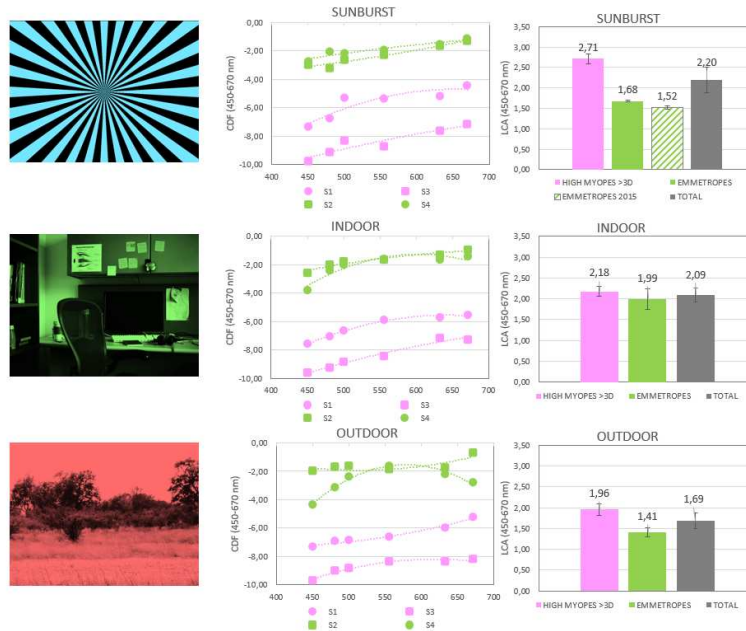


Figure 1: Chromatic difference of focus curves (central column) and LCA (450 - 670 nm) (right column) when using a binary B&W sunburst (upper row), and a natural image stimuli depicting an indoor (mid row) and outdoor (lower row) scenery. Pink elements correspond to myopic subjects (>3 D), while green correspond to emmetropes. Dash green bar corresponds to results obtained in a previous study in similar experimental conditions in emmetropic subjects [6].

4. Conclusions

In this study we report that perceived LCA is higher in myopic than in emmetropic eyes, suggesting that chromatic features may have an influence on the underlying stimulus detection mechanisms that lead to the development of myopia. Investigating blur sensitivity to different optical cues and different visual features (mono- and chromatic aberrations, accommodation, neural adaptation, and blur discrimination) will shed light on cause-effect relationships in eye growth and refractive error development.

Acknowledgments

This research has received funding from the Optica Foundation under the Optica Women Scholars (2022) program to EM; La Caixa Foundation LCF/TR/CI22/52660002 to VRL and PD; Spanish Research Agency grant CPP2021-008388D to VRL; Spanish National Research Agency (Spanish Government) under the Ramón y Cajal (RYC2021-034218-I), the Consolidacion2022 (CNS2022-135326), and the PID2022 (PID2022-139840OA-I00) programs to MV.

References

- [1] J. A. Summers, F. Schaeffel, S. Marcos *et al.*, "Functional integration of eye tissues and refractive eye development: Mechanisms and pathways," *Exp Eye Res*, 209, 108693 (2021).
- [2] J. Wallman, and J. Winawer, "Homeostasis of eye growth and the question of myopia," *Neuron*, 43(4), 447-68 (2004).
- [3] T. V. Tkatchenko, D. Troilo, A. Benavente-Perez *et al.*, "Gene expression in response to optical defocus of opposite signs reveals bidirectional mechanism of visually guided eye growth," *PLoS Biol*, 16(10), e2006021 (2018).
- [4] F. J. Rucker, "The role of luminance and chromatic cues in emmetropisation," *Ophthalmic Physiol Opt*, 33(3), 196-214 (2013).
- [5] M. Vinas, L. Sawides, P. de Gracia *et al.*, "Perceptual adaptation to the correction of natural astigmatism," *PLoS ONE*, 7(9), e46361 (2012).
- [6] M. Vinas, C. Dorronsoro, D. Cortes *et al.*, "Longitudinal chromatic aberration of the human eye in the visible and near infrared from wavefront sensing, double-pass and psychophysics," *Biomed Opt Express*, 6(3), 948-62 (2015).
- [7] S. Marcos, P. Artal, D. A. Atchison *et al.*, "Adaptive optics visual simulators: a review of recent optical designs and applications [Invited]," *Biomed Opt Express*, 13(12), 6508-6532 (2022).
- [8] M. Vinas, C. Benedi-Garcia, S. Aissati *et al.*, "Visual simulators replicate vision with multifocal lenses," *Sci Rep*, 9(1), 1539 (2019).

Optimization of a color difference database by fuzzy logic

Daniel Arranz¹, Rafael Huertas^{2*}, Pedro Latorre-Carmona³ and Samuel Morillas⁴

¹*Escuela de Ing. Informática, Universidad de Valladolid, P.º de Belén, 15, 47011 Valladolid (España).*

²*Dpto. de Óptica, Universidad de Granada, Avda. de Fuentenueva s/n, 18071, Granada (España).*

³*Dpto. de Ingeniería Informática, Universidad de Burgos, Avda. Cantabria s/n, 09006. Burgos (España).*

⁴*Instituto Universitario de Matemática Pura y Aplicada, Universidad Politécnica de Valencia, Camino de Vera s/n, 46022, Valencia (España).*

*E-mail: ahuertas@ugr.es

1. Introduction

In the field of color differences, databases are essential, both for the development of new color difference formulas and checking their performance. Each of the data in these databases is formed by the color coordinates of a pair of color stimuli and the perceived color difference between them (ΔV), which is measured through psychophysical experiments, and is the average of a considerable number of observers and/or several repetitions. Thus, producing these databases is both time and resources consuming.

With the color coordinates of each of the stimuli in the pair, a color difference between them can be computed using different mathematical formulas, which can be just the Euclidean distance or other more sophisticated formulas. The calculated color difference is generally called ΔE , and it is desirable that ΔV and ΔE be as similar as possible throughout the entire database.

The measurement of agreement between perceived and calculated color differences constitutes another field of study within Colorimetry. Different statistical measures have been proposed, and today the STRESS index[1] is one of the most used due to its best properties. Please, note that the lowest the STRESS index the better agreement between ΔV and ΔE .

As we have mentioned, the consistency of databases is important for their reliability. We consider an inconsistency when two data, which must be close in color space, and whose distance between the colors of the pair is similar, have very different perceived differences. We need a metric to measure these distances, the closeness of the two data in color space and the distance between the two pairs of each data. To study the consistency of the database we will use fuzzy logic techniques, as described in the following previous works[2, 3], where two fuzzy logic rules are proposed, called *Fuzzy Rule 1* (FR1) and *Fuzzy Rule 2* (FR2) in this work. For application of the fuzzy rules is necessary that ΔV and ΔE are on the same scale, so a normalization of ΔV is carried out. With these rules, a degree of consistency, between 0 and 1, is calculated for each data in the database. Finally, to optimize the database, all data with a degree of inconsistency greater than a threshold value is removed.

The objective of this work is to analyze the effects of the different parameters and variables involved in the definition of this consistency analysis method.

2. Method

We will use the COMData[4] database to illustrate the study carried out, since it is one of the most extensive databases (3813 data), used and known in the field of colorimetry. We will perform all calculations in the CIELAB color space, using as metrics the Euclidean distance in this space, called ΔE_{ab} , and the metric provided by the CIEDE2000 color difference formula, called ΔE_{00} . These same two color difference formulas, ΔE_{ab} and ΔE_{00} will be used to analyze the agreement (using the STRESS index) with the ΔV values from the original and optimized database. In this study, we analyze the influence of normalizing the ΔV values with the F_1 or F_3 factors, used in the STRESS[1] assessment. We also analyze the result of the application of the FR1, FR2 rules and its combination.

3. Results and conclusions

Figure 1 shows STRESS against threshold, after the application of the fuzzy rules 1, 2 and their combination, ΔE_{ab} for the optimization and F_1 or F_3 for the normalization of ΔV . In general, the combination of both fuzzy rules removes a higher number of data and obtains lower STRESS values, being therefore more efficient. This result also applies if ΔE_{00} is used for the optimization. In terms of the normalization of ΔV , F_1 obtains slightly lower STRESS values, at the expense of a higher number of removed data.

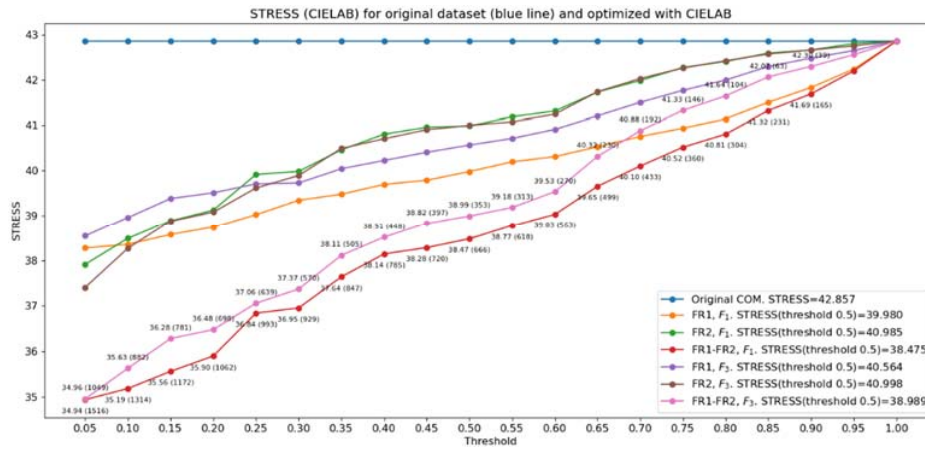


Figure 1 STRESS against threshold after FR1, FR2 and their combination using CIELAB for the optimization, and F_1 or F_3 for the normalization of ΔV . The number of removed data appears in parenthesis.

Figure 2 shows STRESS against threshold, optimizing the database using the combination of the fuzzy rules 1 and 2, the F_3 normalization, and the ΔE_{ab} or ΔE_{00} metrics. Before and after optimization, STRESS has been computed for both the CIELAB and the CIEDE2000 formulae.

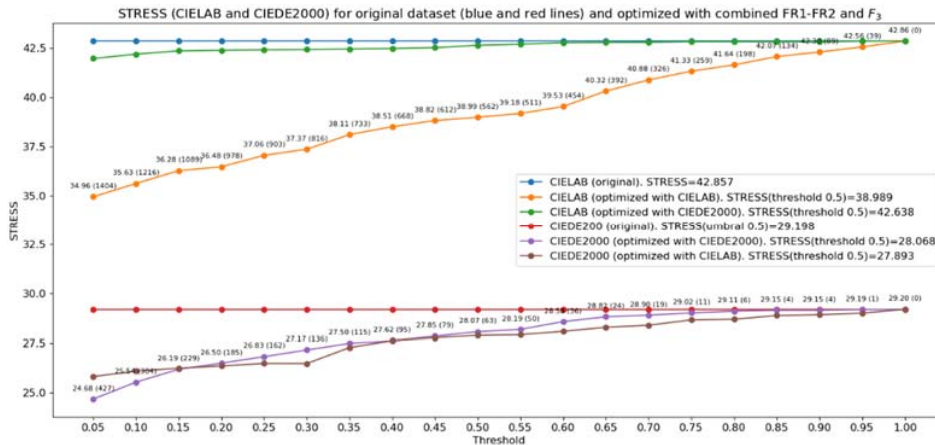


Figure 2 STRESS against threshold for the fuzzy after FR1, FR2 and their combination, F_3 for the normalization and CIELAB and CIEDE2000 for the optimization. The number of removed data appears in parenthesis.

As conclusion, the color difference formula used for database optimization affects the results. It also affects, to a lesser extent, the normalization factor of visual differences, being F_1 which achieves lower STRESS values, at the cost of removing more data, while F_3 obtains similar STRESS values.

Acknowledgments

This research was funded by Generalitat Valenciana under grant CIAICO/2022-051 IMaLeVICS and Spanish Ministry of Science under grant PID2022-140189OB-C21.

References

- [1] P. A. Garcia, R. Huertas, M. Melgosa, and G. Cui, "Measurement of the relationship between perceived and computed color differences," *JOSA A* **24**, 1823-1829 (2007).
- [2] S. Morillas, L. Gómez-Robledo, R. Huertas, and M. Melgosa, "Fuzzy analysis for detection of inconsistent data in experimental datasets employed at the development of the CIEDE2000 colour-difference formula," *Journal of Modern Optics* **56**, 1447-1456 (2009).
- [3] S. Morillas, L. Gómez-Robledo, R. Huertas, and M. Melgosa, "Method to determine the degrees of consistency in experimental datasets of perceptual color differences," *JOSA A* **33**, 2289-2296 (2016).
- [4] M. Melgosa, R. Huertas, and R. S. Berns, "Performance of recent advanced color-difference formulas using the standardized residual sum of squares index," *JOSA A* **25**, 1828-1834 (2008).

Imaging through opaque human cataracts enabled by optical wavefront shaping

Irene Rodríguez^{1*}, Alba M. Paniagua-Díaz¹, Inés Yago², Jose María Marín² & Pablo Artal¹

¹Laboratorio de Óptica, Campus de Espinardo, University of Murcia, Murcia (Spain)

²Oftalmología, Hospital Universitario “Virgen de La Arrixaca”, El Palmar, Murcia (Spain)

*E-mail: irene.r.f@um.es

1. Introduction

Cataracts are an ocular pathology that impairs vision due to elevated intraocular light scattering in the crystalline lens. Controlling the propagation of light through scattering media is a challenge of interest in different fields and there is substantial effort put into overcoming this issue. In recent years Wavefront Shaping (WS) techniques appeared as an excellent tool to control the propagation of light through scattering materials[1]. WS is based on the coherent control of the wavefront incident on a scattering medium, using a spatial light modulator for the local manipulation of the phase and/or amplitude of the wavefront. Recently, wavefront shaping techniques have been suggested for the optical (non-surgical) correction of scattering in artificial cataractous lenses in a non-invasive double-pass configuration[2], where the Point Spread Function (PSF) of the incident light was optimized. In this work we perform wavefront shaping optimizations on human cataractous crystalline lenses for the first time, forming extended images through highly opaque cataractous crystalline lenses.

2. Experimental Setup

A schematic diagram for the wavefront shaping approach is shown in Fig. 1a. A 532-nm laser is expanded and sent to a Spatial Light Modulator (SLM) to shape the wavefront in phase. The shaped wavefront is then sent to an electronic XY Fast Steering Mirror (FSM) through a 4f system that optically conjugates the plane of the SLM on the surface of the FSM. This beam is finally sent to the artificial eye through an extra 4f system, conjugating the plane on the FSM and SLM with the pupil plane of the artificial eye. The artificial eye is formed by an excised human crystalline lens (Fig. 1a inset) with a developed cataract and a camera acting as a retina, for simplicity. The crystalline lens used for this experiment had a very mature cataract, as shown by its imaging capabilities. In Fig. 1b we show the USAF test target used to form an image through the cataractous lens and Fig.1c shows the actual image, where a clear contrast loss can be appreciated.

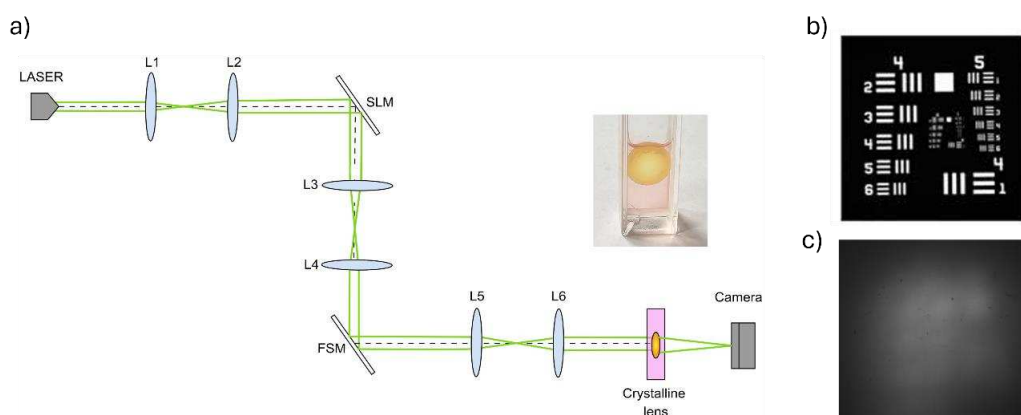


Figure 1. a) Schematic of the experimental setup used for imaging through cataracts, consisting of three 4f systems conjugating the exit of the laser with the SLM, FSM and pupil plane of the artificial eye, formed by a real human cataractous lens and a camera. b) USAF test target used as object for imaging through the cataractous lens, where panel c) shows the actual image.

3. Results

We demonstrated the possibility to improve the PSF through real cataractous crystalline lenses for the first time, where the original noisy and spread PSF of the cataractous lens (Fig.2a) becomes a sharp peak with a signal-to-noise ratio of 72 (Fig.2b). After the PSF was optimized, a letters pattern was displayed by the FSM by scanning the PSF over the cataractous lens. In Fig.2c we show the letters pattern drawn with the non-optimized cataractous PSF, whereas panel d) shows the pattern drawn with the optimized one. As can be observed from the figure, the PSF optimization marks the difference between distinguishing letters or not, that is, the difference between being able to read or form an image or not.

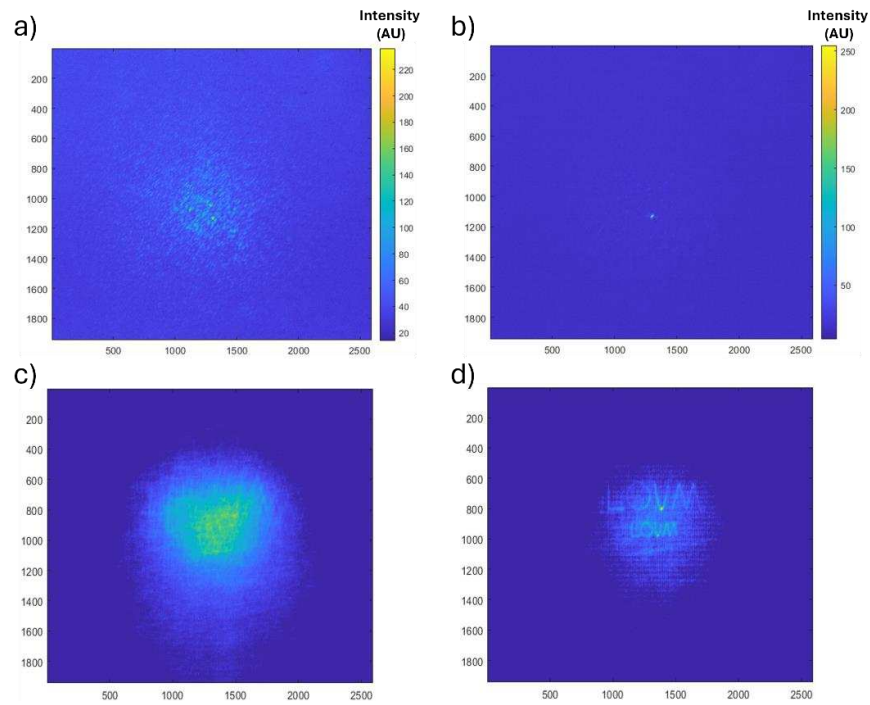


Figure 2. In panel a and b we show the cataractous lens PSF before and after the wavefront optimization, respectively. Panels c and d show the image display with the non-optimized and optimized PSFs.

4. Conclusions

In this work we demonstrate the potential of wavefront shaping for correcting the PSF through a human cataractous crystalline lens, with a significant signal-to-noise ratio. This enables the formation of images that become readable only after the wavefront optimization, being blurry otherwise.

This opens new possibilities for the all-optical correction of cataracts, paving the way for potential smart glasses based on spatial light modulators for the wavefront correction.

References

- [1] Vellekoop, I. M., & Mosk, A. P. *Optics letters*, **32**(16), 2309 (2007).
- [2] Paniagua-Díaz, A. M. *et al. Optics Express*, **29**(25), 42208 (2021).

Age related changes of the crystalline lens gradient refractive index

Alberto de Castro^{1*}, Eduardo Martinez-Enriquez¹,
Marco Ruggeri², Fabrice Manns² and Susana Marcos^{1,3}

¹Instituto de Óptica Daza de Valdés, CSIC. Serrano 121, 28006, Madrid, Spain

²Bascom Palmer Eye Institute, University of Miami School of Medicine, FL, United States

³Flaum Eye Institute, University of Rochester, NY, USA

*E-mail: a.decastro@csic.es

1. Introduction

The crystalline lens of the human eye is a biconic lens with a gradient index of refraction that is known to peak near the center of the lens and decrease towards the surfaces. It contributes with about one third of the optical power of the human eye and, to some extent, compensates some of the corneal aberrations in the young eye [1]. The gradient index of refraction changes with age [2-5] and is known to be the origin of age-related changes in the lens spherical aberration [4].

In the last decades, several methods have been proposed to study the crystalline lens gradient refractive index. These can be broadly grouped in methods that employ a calibration curve to calculate the refractive index from a measured magnitude [2,5], and methods that adjust the parameters of a model to match the computed results with the experimental data [4,6]. We proposed imaging the in vitro crystalline lens with Optical Coherence Tomography (OCT) in two orientations to measure with precision the external geometry and optimizing the variables of a gradient index model to match the measured optical path and other experimental data [4].

In collaboration with the Ophthalmic and Biophysics Center of the Bascom Palmer Eye Institute, we have imaged isolated crystalline lenses with an OCT combined with a ray tracing system to measure the power and the spherical aberration [7]. In this work we will optimize the variables of an age-dependent model to find the best fit to the full dataset and compare the results with previous findings where the gradient index of each lens was individually reconstructed.

2. Methods

Crystalline lenses from 52 donors were measured at the Ramayamma International Eye Bank (L. V. Prasad Eye Institute, Hyderabad, India) while immersed in a chamber filled with a saline solution used as preservation media (BSS). The full crystalline lens was imaged with Optical Coherence Tomography (central wavelength 880 nm, axial resolution 7.4 microns) in two orientations to measure the external geometry of the anterior and posterior surface, its central thickness and its central average refractive index using the deformation produced in the cuvette by the lens itself.

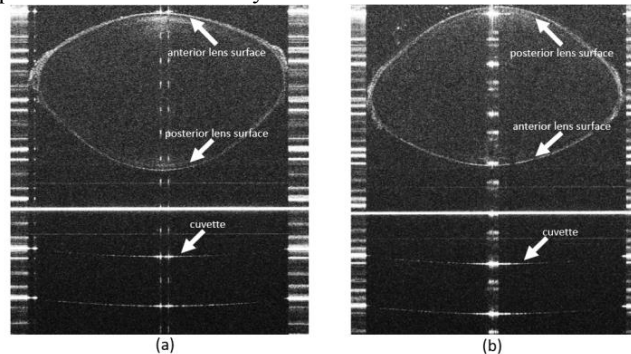


Figure 1 In vitro crystalline lens imaged with the OCT system (a) with the anterior surface facing the OCT beam where the image of the posterior lens surface and the cuvette appear distorted they are imaged through the crystalline lens and (b) with the posterior surface facing the OCT beam.

The OCT beam was also used as light-source in a Laser Ray Tracing system and the position of rays in a 6-mm pupil diameter was detected with a CCD camera below the preservation chamber at 14 positions. The ray direction was reconstructed to calculate the power and spherical aberration of each

individual crystalline lens.

Two age-dependent refractive index models were proposed to test their ability to explain the experimental data: a linear age-dependent homogeneous refractive index, and a power-law gradient index model with fixed surface and nucleus refractive indices and two age-dependent power exponents to model the decay in the axial and meridional directions. The models were used to calculate the average refractive index, optical power and the spherical aberration of all the crystalline lenses and their variables were optimized to minimize a merit function computing the mean square error of the differences between the experimental and simulated data.

3. Results and conclusions

The measured lens geometry and optical properties were consistent with the fully accommodated crystalline lens due to the fact that the lenses were isolated from the ocular globe before the measurement. The homogeneous refractive index model that best explained the experimental data was a constant value of 1.414. The resulting gradient index model was a constant axial exponential decay value of 2.33 and an age-dependent meridional decay, $2.9+0.059*\text{age}$. The simulated data with the power law model fitted better the experimental findings than the data simulated with the homogeneous model in terms of focal length (mean square error of 15.36 vs 11.04 mm) and spherical aberration (0.91 vs 2.34 μm).

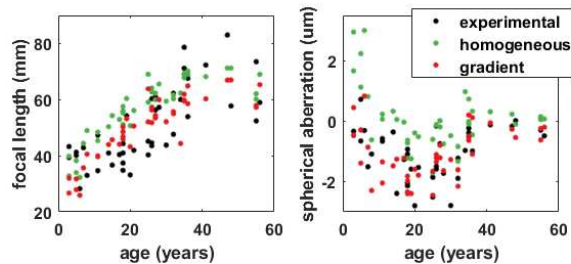


Figure 2 Experimental and simulated with the homogeneous and gradient index model focal length and spherical aberration. The fit to experimental data is better with the gradient model.

When different models were optimized separately for two age groups (below and above an age of 20 years) the conclusions remained unchanged and the best gradient model was a relatively constant exponent in the axial direction and an increasing exponent in the meridional exponent. This behavior can clarify some of the findings presented in the literature [4,5] and the role of the gradient index in the ageing process of the human eye.

Acknowledgments

PID2020-115191RB-I00, RYC2022-038195-I, Becas Leonardo 2023 Fundación BBVA, NIH P30EY 001319; R01 EY035009; P30 EY001319-46, Unrestricted Funds Research to Prevent Blindness, NY.

References

- [1] P. Artal, A. Guirao, E. Berrio, and D. R. Williams, "Compensation of Corneal Aberrations by the Internal Optics in the Human Eye", *J Vis* **1**, 1 (2001).
- [2] S. Kasthurirangan, E. L. Markwell, D. A. Atchison, and J. M. Pope, "In Vivo Study of Changes in Refractive Index Distribution in the Human Crystalline Lens with Age and Accommodation", *Invest Ophthalmol Vis Sci* **49**, 2531 (2008).
- [3] A. de Castro, D. Siedlecki, D. Borja, S.Uhlhorn, J.M.Parel, F. Manns, and S. Marcos, "Age-Dependent Variation of the Gradient Index Profile in Human Crystalline Lenses", *J Mod Opt* **58**, 1781 (2011).
- [4] J. Birkenfeld, A. de Castro, and S. Marcos, "Contribution of Shape and Gradient Refractive Index to the Spherical Aberration of Isolated Human Lenses", *Invest Ophthalmol Vis Sci* **55**, 2599 (2014).
- [5] B. Pierscionek, M. Bahrami, M. Hoshino, K. Uesugi, J. Regini, and N. Yagi, "The Eye Lens: Age-Related Trends and Individual Variations in Refractive Index and Shape Parameters", *Oncotarget* **6**, 30532 (2015).
- [6] D. Vazquez, E. Acosta, G. Smith, and L. Garner, "Tomographic Method for Measurement of the Gradient Refractive Index of the Crystalline Lens. II. The Rotationally Symmetrical Lens", *J Opt Soc Am A* **23**, 2551 (2006).
- [7] M. Ruggeri et al., "System for On- and off-Axis Volumetric OCT Imaging and Ray Tracing Aberrometry of the Crystalline Lens", *Biomed. Opt. Express* **9**, 3834 (2018).

Temporal variations in defocus virtually paralyze accommodation

Paulina Dotor-Goytia¹, Carlos Dorransoro^{1,2}, and Victor Rodriguez-Lopez^{1*}

¹*Institute of Optics, Spanish National Research Council (IO-CSIC), Madrid, Spain*

²*EyesVision SL, Madrid, Spain*

*E-mail: victor.rl@io.cfmac.csic.es

1. Introduction

Direct Subjective Refraction (DSR) is a novel method for evaluating the optical prescription of the eye. It uses rapid and periodic temporal changes in defocus to produce a flicker perception that is minimal at best focus. DSR has been shown to be faster and more accurate than the traditional subjective refractive method [1]. It has also been reported that the method somehow deactivates the accommodative response: the quick temporal change in defocus seems to prevent from accommodation. However, this discovery was made indirectly: the final refraction found with myopic and hyperopic starting points was similar (the correlation between them was very high ($r = 0.90$, $p < .05$)) and the result with free and paralyzed accommodation was highly correlated ($r = 0.99$, $p < .05$) [1]. The purpose of this study was to measure the accommodative dynamics of the eye during the DSR method.

2. Methods

DSR uses a tunable lens projected into the pupil's eye to induce periodic defocus changes of 0.25 D at a frequency of 15 Hz. In Experiment 1, participants minimize flicker perception on a bichromatic (red/blue) stimulus by adjusting the mean optical power of the defocus wave. The residual refractive error is determined by the position of the minimum perceived flicker. For comparison, in Experiment 2, a blur minimization (BM) task was performed using a monochromatic (black/white) version of the stimulus. Participants were asked to focus the target by changing the optical power of the tunable lens. In addition, in Experiment 3 subjects performed DSR and BM tasks but using a line of letters (white on black) stimulus. Accommodation and pupil size were measured during the experiments using a PlusOptix Power Refractor II. Accommodation was free in all the experiments.

For all the experiments, participants performed ten alternating repetitions with their right eye, with five myopic (+1.50 D) and five hyperopic defocus (-1.50 D, which could be accommodated) starting points around their prescription. Staircases with coarse (± 0.25 D) and fine (± 0.10 D) steps were used. Microfluctuations of accommodation were excluded by removing temporal accommodative changes greater than 0.6 Hz [2]. Negative accommodative responses/speeds represent activation of accommodation, whereas positive responses represent relaxation. The standard deviation (repeatability) across repetitions was compared.

Four young subjects (29 ± 1 years) with good visual acuity ($\log\text{MAR} < -0.1$) and no visual function abnormalities participated. They wore their optical correction with spectacles during measurements to ensure that all assessments were performed under emmetropic conditions. Subjects had no accommodative problems, checked with the amplitude of accommodation test (push-up method) and accommodative flippers of ± 2.00 D.

3. Results

Figures 1A and 1B show the result for Experiment 1 (DSR) and Experiment 2 (BM) for one subject. It can be observed that, for DSR task, accommodation is not activated neither in hyperopic (odd) or myopic (even) repetitions (Fig. 1A). However, for BM task, in hyperopic repetitions accommodation is activated, but it is not in myopic repetitions (even repetitions).

Figures 1C and 1D show the analysis of the dynamics of accommodation averaged across subjects. In Experiment 1 (DSR), the accommodative response (Fig. 1C) is not significant and not statistically different for myopic and hyperopic repetitions ($p > .05$). In Experiment 2 (BM), accommodation is activated in hyperopic repetitions, and is statistically different for myopic and hyperopic repetitions

($p < .05$). In Experiment 3, with letters, accommodation is activated in both DSR and BM tasks and there is a statistical difference between myopic and hyperopic starting points. Similar results were found for accommodative speed (Fig. 1D). In Experiment 1 (DSR) accommodation speed is not significant and does not differ between repetitions ($p < .05$). In Experiment 2 (BM) and Experiment 3 (for both tasks) there is a difference between hyperopic (negative speed) and myopic (positive speed; $p > .05$).

In addition, the DSR method shows greater repeatability than BM for both with circular stimuli (± 0.12 vs. ± 0.42 D) and with letters (± 0.18 vs. ± 0.34 D). Specifically, the DSR method shows greater repeatability with circular stimuli than with letters (± 0.12 vs. ± 0.18 D).

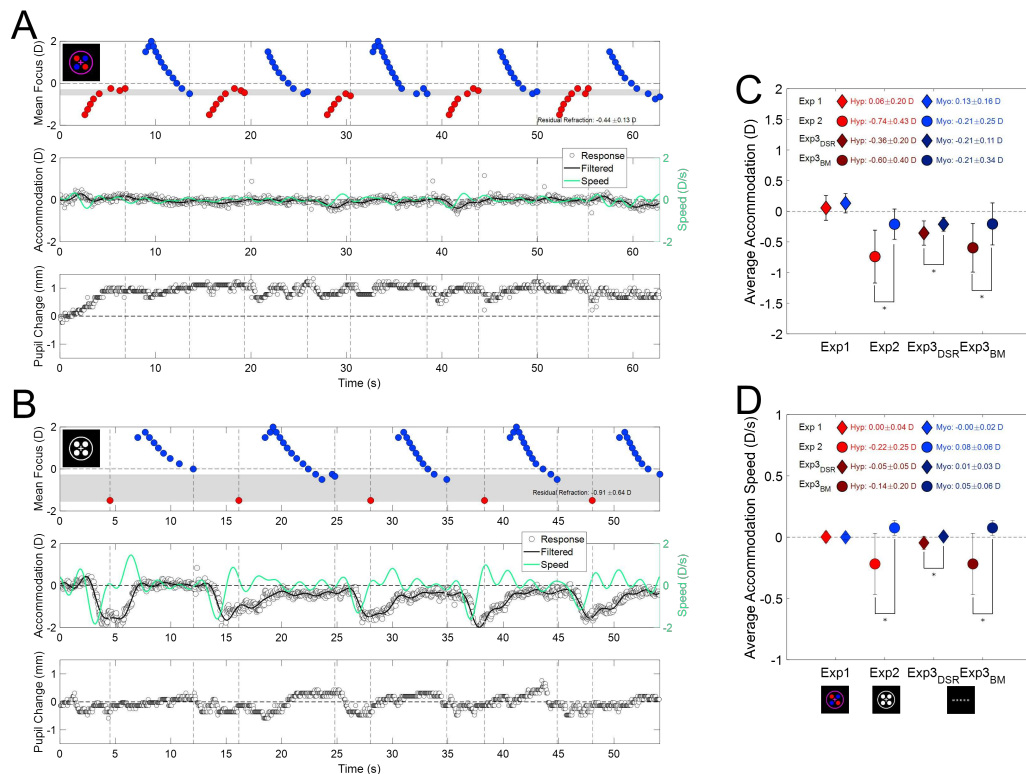


Figure 1. A. and B. show the accommodative response for one participant and Experiment 1 (A, DSR) and Experiment 2 (B, BM). Upper subplots display the mean defocus across ten repetitions (delimited by vertical dotted lines); middle subplots the accommodative response and speed; and lower subplots pupil size changes. C. Shows the average accommodation response for all experiments. D. Shows the average accommodative speed for all experiments.

4. Conclusions

The temporal defocus wave of the DSR virtually eliminates the accommodative response during refractive error measurement. This result explains the increased precision of the DSR task compared to BM and may lead to refractive error measurements that do not require fogging or cycloplegia.

Acknowledgments

Spanish Science Agency PID2022-139840OA-I00 to P.D., La Caixa Foundation LCF/TR/CI22/52660002 to V.R.L. and P.D., La Caixa Foundation LCF/BQ/DR19/11740032 to V.R.L.; and Spanish Research Agency grant CPP2021-008388D to VRL and CD.

References

- [1] Rodriguez-Lopez V, Hernandez-Poyatos A, Dorronsoro C. Defocus flicker of chromatic stimuli deactivates accommodation. *Biomed Opt Express*. 2023;14(7):3671-3688. doi: 10.1364/BOE.486466.
- [2] Charman WN, Heron G. Microfluctuations in accommodation: an update on their characteristics and possible role. *Ophthalmic Physiol Opt*. 2015;35(5):476-99. doi: 10.1111/opo.12234.

Do best visual acuity and minimum accommodation coincide in subjective refraction? An objective analysis

Aina Turull-Mallofré*, Carlos Enrique García-Guerra, Jaume Pujol and Mikel Aldaba

Centre for Sensors, Instruments and Systems Development, Universitat Politècnica de Catalunya, Rambla Sant Nebridi 10, 08222 Terrassa, Barcelona, Spain.

*E-mail: aina.turull@upc.edu

1. Introduction

Many optometry manuals emphasize the importance of good control of accommodation during refraction procedures. In this regard, the goal when assessing subjective refraction (SR) is to achieve the best visual acuity (VA) with the minimum accommodation [1,2]. Theoretically, this will ensure good control of accommodation and will prevent hypercorrection or undercorrection and asthenopia. With the rising interest in new objective and automated technologies for refraction, the behavior of VA and accommodation might be key in their development. The purpose of this work is to study objectively whether there is concurrence between the best VA and minimum accommodation in the SR.

2. Methods

Monocular SR was performed on 68 young adults (mean age \pm standard deviation (SD) 22.69 ± 3.02 years and mean spherical equivalent -1.34 ± 1.73 D). The measurement setup comprised a motorized phoropter coupled to an aberrometer. The aberrometer was a custom-developed Hartmann-Shack [3] used to measure dynamically the refractive state of the eye (M), computed from the measured Zernike coefficients using least square fitting, with a frequency of 10 Hz during the entire test. All subjects were tested for the left eye while measuring M in the occluded right eye. Amplitude of accommodation of each eye was previously tested to discard any anomalies or differences in accommodation between the two eyes.

The steps for the SR assessment were based on the conventional procedure [2]. First, objective refraction was measured with a commercial autorefractor, and the value was used as a starting point for the next step. Second, a first sphere check was carried out starting with a +2.00 D fogging over the objective refraction to control accommodation and followed by a reduction of the spherical power in steps of 0.25 D until achieving the best VA. Then, astigmatism was corrected using the Jackson Cross Cylinder (JCC). Afterward, a second sphere check was performed starting with a +1.00 D fogging and followed by reducing the spherical power in 0.25 D-steps until the best VA was resolved and the subject reported the least blur possible. Right after obtaining the SR value, an extra negative 1.00 D was added in 0.25 D-steps in front of the eye to activate the accommodation. This addition allowed us to examine how the accommodation responded after the SR point (i.e., whether it changed to an activated state according to the stimuli or it followed the trend before the SR point).

To study the accommodative response during the whole test, the median of M was computed for each 0.25 D-step of the process. Relative accommodation was computed as the difference between the measured M at the point of minimum accommodation (PMA) and at each change of lens. For the purpose of this study, only the accommodative response from the second sphere check and the addition of the extra negative diopter were studied, obtaining a plot similar to Fig. 1. In the plot, key points of the analysis appear highlighted: the SR (represented as a circle), the PMA (represented as an inverted triangle) and the point where the best VA is resolved for the first time (represented as a triangle).

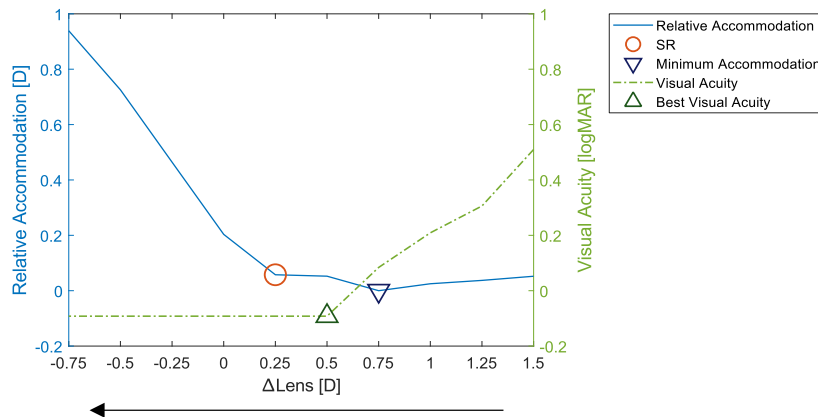


Figure 1 Example plot for one subject of the relative accommodation (left y axis) and VA (right y axis) during the second sphere check and the addition of an extra negative diopter. Δ Lens (x axis) represents the sphere offset respect to the objective refraction. Key points of the analysis are highlighted: SR (circle), PMA (inverted triangle) and first time of resolving the best VA (triangle). The arrow shows the direction of the plot according to the SR assessment process.

3. Results

In the point of SR, the mean VA \pm SD was -0.05 ± 0.06 logMAR and the mean relative accommodation \pm SD was 0.15 ± 0.13 D. In the point of minimum accommodation (PMA), the mean VA \pm SD was 0.13 ± 0.16 logMAR, and this point coincided with SR in 13.2% of the subjects. The mean difference in spherical power in the phoropter between the PMA and SR was 0.47 ± 0.45 D. Regarding the first time when the subjects resolved their best VA, this occurred before the point of SR in 24 out of 68 subjects, who needed a mean difference of spherical power of -0.26 ± 0.07 D to report the least blur possible, and thus the SR. Furthermore, only 6 out of 68 subjects (8.82%) resolved their best VA for the first time at the same point that achieved the PMA and SR.

4. Conclusions

The results show that accommodation in the SR point was slightly activated compared to the PMA and that the SR concurred at the same point as the PMA in only few of the participants. Spherical power in PMA was more positive than SR in most cases and the VA was worse than in the SR point, suggesting that most subjects were still fogged at that point of the examination. The PMA, SR, and best VA coincided in very few cases. Moreover, some subjects were able to resolve their best VA before reaching the SR although with poor resolution, and needed a slightly more negative refraction to improve the quality of the retinal image. This demonstrates the importance of the subjective condition of the test in which small changes in defocus can improve considerably the visual experience of the subject. The findings of this study may be of interest for the development of new technologies for refraction that rely on the accommodative response.

Acknowledgments

This publication is part of the project PID2020-112527RB-I00, funded by MCIN/AEI/10.13039/501100011033. The first author gratefully acknowledges the Universitat Politècnica de Catalunya and Banco Santander for the financial support of her predoctoral grant FPI-UPC.

References

- [1] M. Rosenfield, N. Logan, and K. Edwards, *Optometry: Science Techniques and Clinical Management*, 2nd ed. (Butterworth Heinemann Elsevier, 2009).
- [2] W. J. Benjamin, *Borish's Clinical Refraction*, 2nd ed. (Elsevier, 2006).
- [3] C. E. García-Guerra, J. A. Martínez-Roda, J. C. Ondategui-Parra, A. Turull-Mallofré, M. Aldaba, and M. Vilaseca, "System for Objective Assessment of the Accommodation Response During Subjective Refraction," *Transl. Vis. Sci. Technol.* **12**(5), 22 (2023).

A binocular adaptive optics visual simulator with convergence control

Santiago Sager^{1,2}, Pedro Prieto¹ and Pablo Artal¹

Laboratorio de Óptica, Universidad de Murcia, Campus de Espinardo, 30100 Murcia, Spain¹

Voptica SL, Parque Científico de Murcia, 30100 Murcia, Spain²

Abstract: A binocular visual adaptive optics simulator with automatic convergence control and real time aberration measurement and correction for both eyes simultaneously is presented.

1. Introduction

The first limit of vision is imposed by the retinal image quality, which is affected by the ocular aberrations. Adaptive optics simulators are of great interest in the field of visual science due to their ability to fully measure and correct said aberrations, and more generally allowing to manipulate the wavefront of a displayed stimulus. However, current commercially available instruments are monocular and binocular testing can only be performed with laboratory prototypes. Among this last group, current instruments either do not have convergence control [1] or present a limited version that requires manual adjustment [2] and therefore makes them impractical to use in a clinical setting.

In this work we have developed an instrument capable of measuring both eyes in real time, and of correcting two independent stimulus screens allowing for stereoscopic tests to be performed. This is done through a single optical path to make the device more compact, separating them with a periscope that incorporates the convergence control synchronized with a pupil camera for pupil tracking. Finally, we added an intensity modulator to create the artificial pupils and a tunable lens to increase the range of phase modulation.

2. Methods

The new binocular device has been adapted from a commercial monocular version (VAO, Voptica SL, Murcia, Spain). A schematic of the device can be seen in Fig. 1a).

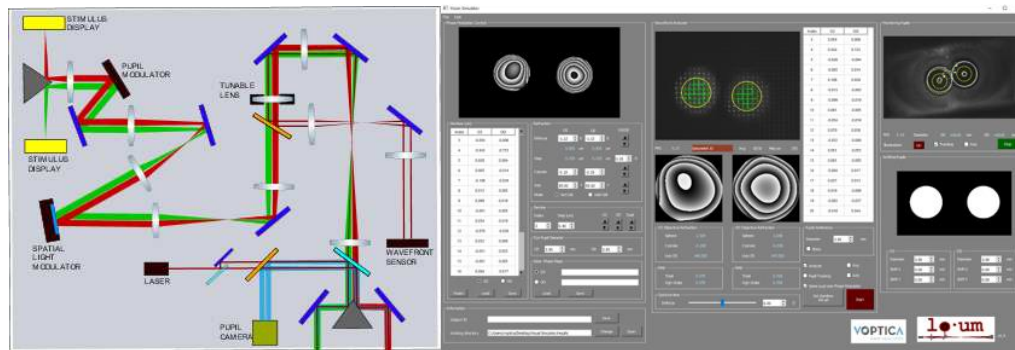


Figure 1: a) Schematic of the binocular visual optics simulator prototype. b) Software interface of the system.

The correction section of the prototype presents two HD microdisplays that show an independent stimulus for each eye and therefore allow to perform stereoscopic and other psychophysics tests. The screens are conjoined into a single optical path projected onto an intensity modulator that creates and controls the size and position of the artificial pupils created. This is conjugated with a spatial light modulator in the form of a liquid crystal on silicon (LCoS) screen that will perform aberration correction and general wavefront manipulation. A tunable lens in the same pupil plane will introduce defocus necessary to increase the correction range of the device.

Finally, the periscope will separate the beams for both eyes. This periscope includes a stepper motor to displace the prism, which in turn would displace the beam over the convergence mirrors and therefore control the distance between artificial pupils. The convergence mirrors in turn have independent servomotors that will control the angle introduced, allowing to introduce convergence due to different object distances or to control single eye convergence to study different pathologies such as phorias. A mechanical model can be seen in Fig. 2a), while the actual implementation is shown in Fig. 2b).

On the measurement section of the prototype we can see the near infrared measurement laser entering through the periscope, and returning using the same optical path of the stimulus screens until after the tunable lens in order to use it to increase the measurement range in addition to the correction range. A dichroic mirror redirects the beam into the

Hartmann-Shack (HS) sensor path, in which both pupils are processed using a GPU-based algorithm [3] for real time measurement of the optical aberrations. A pupil camera performs pupil tracking and measurement of interpupillary distance, which is synchronized with the convergence system for a correct angle rotation.

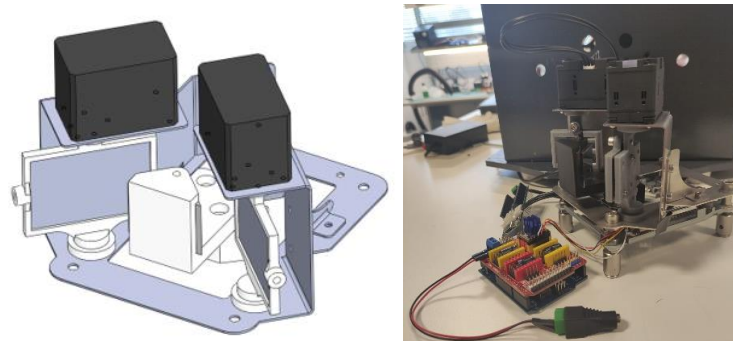


Figure 2: a) Convergence system model. b) Implementation of the convergence system.

The system has been completed with a fully integrated software as seen in Fig. 1b). This allows for a fast control and synchronization between measurement and correction, as well as full customization of pupil size and choice of aberration correction.

3. Results

The overall function of the system was tested by measuring the defocus curve for a subject with paralyzed accommodation under different monocular conditions. Both eyes had best corrected refraction, but a spherical aberration (SA) of $-0.5\mu\text{m}$ was added to the right eye. Then the defocus curve was measured monocularly for each eye, and binocularly with and without the corresponding induced convergence.

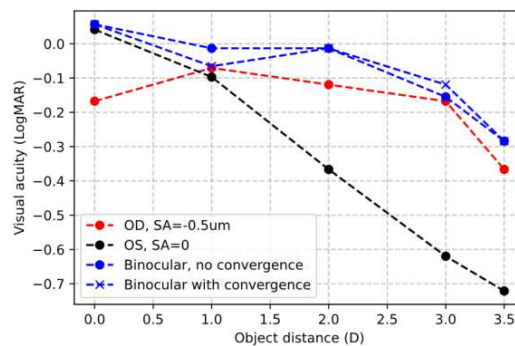


Figure 3: Monocular defocus curve for the left (black) and right (red) eyes, and binocular defocus curves (blue) with (circles) and without (crosses) the convergence corresponding to the simulated distance.

This preliminary test shows that in this scenario the introduction of convergence does not seem to result in a significant different with respect to the traditional method. This however will have to be further studied to determine if it is dependent on the patient or the type of correction applied.

In conclusion, we present a functional binocular adaptive optics system with convergence control and the capability of real time measurement and correction of optical aberrations in both eyes. This device will result in more thorough clinical studies of the impact of higher order aberrations in binocular vision in a comprehensive manner.

4. References

- [1] Enrique J. Fernández, Pedro M. Prieto, and Pablo Artal, "Binocular adaptive optics visual simulator," *Opt. Lett.* 2019; 34, 2628-2630. doi.org/10.1364/OL.34.002628
- [2] Jiakai Lyu, Cherlyn J. Ng, Seung Pil Bang, Geunyoung Yoon; "Binocular accommodative response with extended depth of focus under controlled convergences". *Journal of Vision* 2021;21(8):21. doi.org/10.1167/jov.21.8.21
- [3] Juan Mompeán, Juan L. Aragón, Pedro M. Prieto, Pablo Artal; "GPU-based Processing of Hartmann-Shack Images for Accurate and High-Speed Ocular Wavefront Sensing". *Future Generation Computer Systems* 2018. doi.org/10.1016/j.future.2018.09.010

RESÚMENES/ABSTRACTS

Sesiones Orales

**Divulgación,
Enseñanza e Historia**



Exploring image formation with lenses and pinholes

Jaume Escofet* and Elisabet Pérez-Cabré

¹Department of Optics & Optometry, Universitat Politècnica de Catalunya, Violinista Vellsolà 37, 08222 Terrassa (Barcelona)

*E-mail: jaume.escofet@upc.edu

1. Introduction

Image formation through lenses, mirrors or pinholes is generally a difficult concept to be fully understood by students, both in secondary schools and at the university level [1-3]. While there are texts [4,5] containing conceptual questions to help in grasping this concept, there are limited resources analyzing the experimental visualization of images formed by positive lenses and pinholes. In agreement with Galili's assertion [2], a camera obscura can serve as a valuable instructional tool since it permits not only to contrast the features of images obtained by both lenses and pinholes, but also to analyze multiple characteristics of the image formation process. Additionally, a camera obscura enables the blocking of stray light, thereby enhancing the observation of the formed image, especially when pinholes are used. While images are commonly projected on a screen, another interesting approach is achieved when aerial images are formed after removing the screen from the optical system [4,6].

This paper presents a versatile and inexpensive sliding box, which can function as either a pinhole or a lens camera. It facilitates the analysis of image visualization by the observer, whether a screen is present at the image plane or removed to obtain an aerial image. In all the analyzed situations, the observer can be replaced by a photographic camera (or a mobile camera) to record all the experimental images and to make their comparison easier. Several image features are analyzed by using this box to ensure a comprehensive understanding of the concept of image formation.

2. Versatile and inexpensive camera obscura

The designed sliding box consists of two parallelepiped bodies according to the diagram and the dimensions specified in Figure 1(a). The first body has a circular opening on its entrance side to accommodate a lens or a pinhole, while the exit side remains open. The second, larger body, with both entrance and exit sides open, allows the first body to slide inside it. At the end of this second body, a translucent diffusing screen can be placed. Figure 1(b) shows the elements used in the image formation.

The proposed sliding box can be made of plywood or foamcore to ensure lightweight. It is crucial that the interior is well-insulated from the external light, and the two parts of the camera can slide easily within each other. An additional box made of the same materials or cardboard is useful for blocking stray light, particularly when dim images are obtained from a pinhole. All materials are readily available and inexpensive.

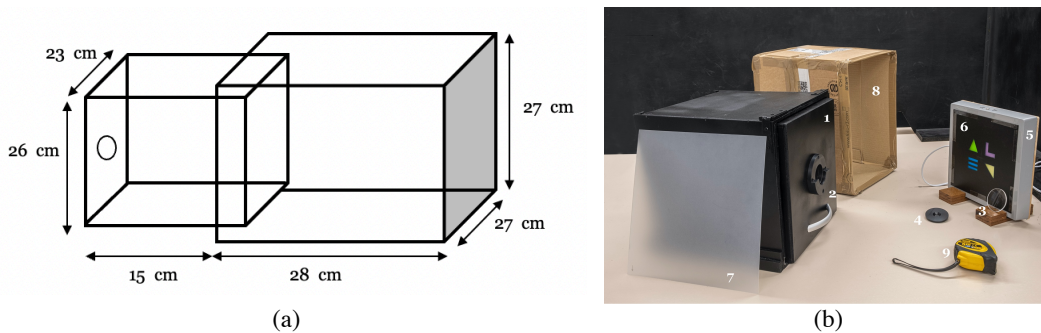


Figure 1 (a) Diagram of the sliding box. (b) Elements: 1: Sliding box, 2: Lens and pinhole holder, 3: Lens, 4: Mounted pinhole, 5: Flat LED luminaire, 6: Object, 7: Diffuser screen, 8: Cardboard box to block stray light and 9: Measuring tape.

3. Image formation analysis

This work analyzes and compares the image formation process for both, lenses and pinholes. Aspects such as observation of the projected image on a screen or aerial images, defocusing, field of depth, and angular field, among others, are considered. For instance, we briefly highlight the main features of aerial images and defocusing compared to the best projected image obtained in the camera obscura.

Figures 2(a)-(d) depict the formation of the image of a real object O by a lens L . The schematic diagram in Figure 2(a) illustrates a simple ray tracing to justify the projection of the real image onto a screen S placed in the best focus position. Figure 2(b) displays the corresponding experimental image captured in the camera obscura. By simply removing the screen, the on-axis image viewed by observer 2 varies significantly due to the system's limited field of view (Figure 2(c)). Figure 2(d) shows the defocused image projected on a screen that has been moved from the best focusing plane.

Similar experiments are conducted using a pinhole P instead of a lens (Fig. 2(e)). Analogous diagrams and pictures are provided for this case. Since distances among the elements of the optical system remain constant, the image projected on the screen using a pinhole (Fig. 2(f)) closely resembles the image obtained by the lens (Fig. 2(b)), both having a similar size. However, it is noteworthy the most significant differences between both optical systems: unlike the lens, the pinhole system does not allow visualization of aerial images when the screen is removed (Fig. 2(g)), as the rays never intersect to form any image. Another significant difference is that the pinhole is more resistant to defocusing than the lens, as it can be noticed from Figure 2(h).

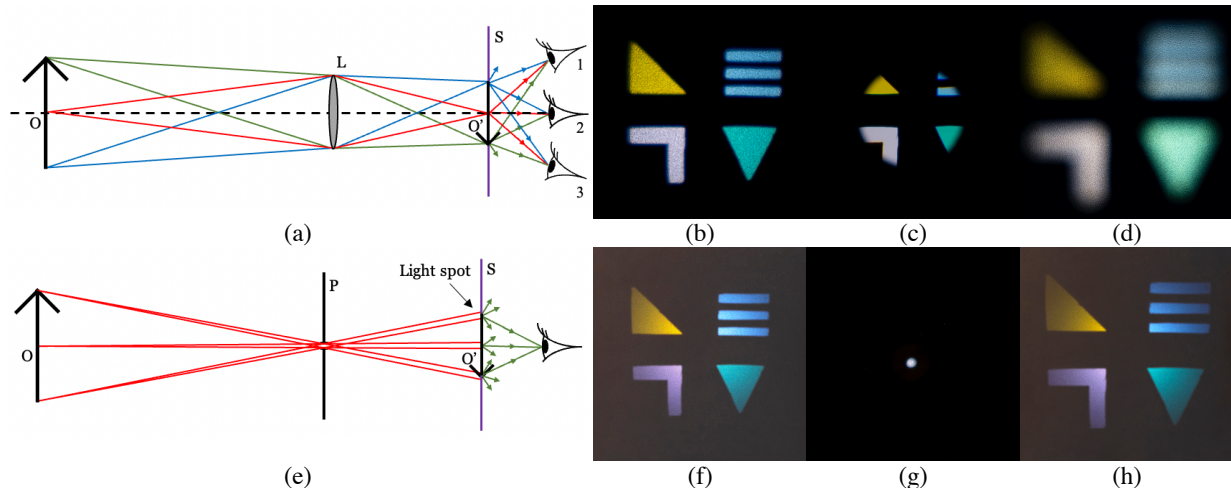


Figure 2 Image formed by a 200mm focal length lens: (a) ray tracing, (b) image on a screen at 300mm from the lens, (c) aerial light distribution when the screen is removed and (d) defocused image at 370mm from the lens. Image obtained with a 1mm diameter pinhole: (e) ray tracing, (f) image on a screen at 300mm from the pinhole, (g) aerial light distribution when the screen is removed and (h) image obtain on the screen at 370mm from the pinhole.

The aforementioned features along with other relevant characteristics will be analyzed in more detail in the complete contribution.

References

- [1] F. Goldberg and L.C. McDermott, *Am. J. Phys.* 55(2), 1987.
- [2] I. Galili, *Int. J. Sci. Educ.* 18(7), 847-868. 1996.
- [3] M. Ronen and B-S. Eylon, *Phys. Educ.* 28, 52-59. 1993.
- [4] F. Goldberg, S. Bendall and I. Galili, *Phys. Teach*, 29, 221-224, 1991.
- [5] P. G. Hewitt, *Conceptual Physics 9th ed.* Addison Wesley, 2002.
- [6] J. Escofet and E. Pérez-Cabr e, *Hands-on Science. Celebrating Science and Sci. Educ.*, 143-150, 2023.

Una década de Óptica y Fotónica en las aulas: lecciones aprendidas por el Grupo de Ingeniería Fotónica de la UC

Olga M. Conde^{* 1,2,3}, Antonio Quintela^{1,2,3}, M. Angeles Quintela^{1,2,3}, Francisco J. Madruga^{1,2,3}, Verónica Mieites^{1,2}, M. Gabriela Fernández-Manteca^{1,2}, Celia Gómez-Galdós^{1,2}, J. Francisco Algorri^{1,2,3}, Borja García^{1,2}, Andrea Pérez¹, José M. López-Higuera^{1,2,3}

¹Grupo de Ingeniería Fotónica. Universidad Cantabria, Avda. Los Castros S/N, 39006, Cantabria.

²Instituto de Investigación Sanitaria Valdecilla (IDIVAL), 39011 Santander, Cantabria.

³Biomedical Research Networking Center—Bioengineering, Biomaterials, and Nanomedicine (CIBER-BBN), Madrid, España.

*E-mail: olga.conde@unican.es

1. Introducción

En esta contribución se hará un balance de la actividad de divulgación realizada por el GIF (Grupo de Ingeniería Fotónica) de la UC (Universidad de Cantabria) en centros de educación primaria y secundaria en los últimos 10 años. Esta actividad, adherida a diferentes programas de divulgación como “#GIFenColes”, “Ciencia en marcha”, “Ciencia circular” o la gymkhana “Fotónica o ¿qué puedes hacer con la luz?” ha permitido identificar un perfil de la audiencia y de los centros que solicitan las actividades. Esto ha hecho diseñar un nuevo itinerario, vertebrado a partir del proyecto “La Fotónica se mueve por Cantabria” cuyo objetivo primordial es trasladar la divulgación de la Óptica y la Fotónica a entornos distantes, rurales y distribuidos por toda Cantabria, para incrementar el impacto social de la divulgación y llegar a aquellas comunidades educativas con un perfil socioeconómico más comprometido y vulnerable.

2. Metodología

Para ello, la actividad consiste en ofertar 6 talleres simultáneos a un mismo centro educativo. La actividad se gamifica mediante la realización de kahoot’s y pruebas en formato gymkhana. Los talleres se centran en explicar brevemente fenómenos básicos de la luz realizando experimentos significativos involucrando, en cada caso, a la audiencia de educación primaria y secundaria. Los talleres se adaptan diferentes niveles educativos, desde educación primaria y secundaria, e incluso educación infantil. El material empleado en los talleres es diverso, desde objetos de la vida diaria a piezas diseñadas e impresas 3D, pasando por instrumentación de laboratorio y elementos de kits comerciales como el “Photonics Explorer Kit” [1] o el “Tech Light Lab - Optics Science Kit” [2]. Cada taller se programa para grupos de 15 personas, grupos que van rotando de taller en taller hasta completar la experiencia. Los talleres ofertados son los siguientes:

1. “Saliendo del laberinto para conocer internet” (Reflexión): la reflexión total interna guía la luz en las fibras ópticas, esencial para la transmisión de información en internet. En este taller, exploraremos cómo la luz se propaga sin pérdida de intensidad a lo largo de las fibras y cómo redirigirla con elementos ópticos. Los participantes experimentarán visualmente cómo los cambios en la dirección de la luz permiten el envío y recepción de información.
2. “Generando el arco iris” (Difracción): la difracción es como separar la luz en “trocitos”. Se muestran patrones de difracción con láseres de diferentes colores y agujeros de diferentes tamaños. También se explica que la luz blanca está compuesta de colores y se puede dividir usando rendijas de difracción. Además, se explora cómo la difracción cambia en objetos como pelos, CDs grabados e incluso alas de mariposas.
3. “El juego del ojo negro” (Polarización): la polarización de la luz revela sus secretos al atravesar materiales que la modifican. En este taller, se exploran conceptos fundamentales y se experimenta con filtros polarizadores. Estos filtros bloquean selectivamente ciertas direcciones de vibración de la luz. Además, se explican aplicaciones prácticas en fotografía, óptica de instrumentos científicos y cine 3D. Los participantes usan gafas 3D y se enfrentan a un compañero. Cuando un alumno guiña un ojo, el filtro polarizador bloquea la luz de ese ojo, alternando entre verlo normal y negro. Así, se comprende cómo la polarización afecta nuestra percepción visual y la tecnología moderna.
1. “Adivina el color de las cosas” (Color): la percepción del color depende de la luz que lo ilumina. La luz

- está formada por fotones, y hay fotones de todos los colores excepto blanco y negro. El blanco es la suma de todos los colores, mientras que el negro es la ausencia de fotones. Los objetos reflejan o absorben fotones según su color. Por ejemplo, una camiseta azul iluminada sólo con luz roja parece negra, y una camiseta blanca bajo luz azul se ve azul. En un experimento, se colocan hojas de diferentes colores en una mesa y se ilumina con una tira LED de distintos colores. Los participantes identifican las hojas según la luz. Además, se muestra un libro con dibujos pintados en cian, magenta o amarillo, demostrando cómo la luz afecta lo que vemos.
2. “Mi bebida es una linterna” (Fluorescencia): comenzando con un juego para identificar “el color más peligroso” dentro del rango visible, se transmite la relación entre color, frecuencia y energía. Con esta información se explica la fluorescencia con analogías sencillas basadas en un ascensor, las “salidas de fin de semana”, etc. Ya en un plano más práctico, se plantean experimentos hands-on para que descubran el contenido de botellas sólo con el empleo de luz de una determinada frecuencia (bebidas refrescantes, aceites y su adulteración, etc.). Finalmente se introduce el concepto de nanopartículas fluorescentes para apoyo a cirugía empleando un material de bajo coste diseñado al efecto.
 3. “El color del calor” (Termografía): pretende transmitir lo que es una imagen térmica con pequeños experimentos y se explicarán conceptos básicos como emisividad, transmisividad y finalmente se explica una aplicación que responde a una sencilla pregunta. Cuándo me subo a un avión, ¿Cómo se sabe que el fuselaje no tiene defectos que puedan producir descompresión durante el vuelo?, ¿qué el timón y los estabilizadores no se van a partir en el aire? Las personas que comprueban que todo esto está en perfectas condiciones de uso se llaman inspectores de ensayos no destructivos y en este taller se pretende que los alumnos se adentren en este mundo sobre todo conociendo los ensayos no destructivos basados en termografía infrarroja.

3. Resultados

Hasta la actualidad, se han visitado 17 centros educativos llegando a una comunidad de 1400 niños y niñas de educación infantil, primaria y secundaria. Desde un punto de vista pedagógico, se considera que el rango de edad más adecuado sería el tercer ciclo de primaria (10-11 años) y educación secundaria (12-15), incluyendo también bachillerato. Aunque la atención más espontánea es la de los cursos intermedios de educación primaria. Es de destacar el aprendizaje realizado por los investigadores a la hora de adaptar su discurso a diferentes edades y capacidades, ampliando el registro de divulgación y promoviendo el desarrollo de diferentes perspectivas para explicar los conceptos físicos asociados a la experiencia.

4. Conclusiones

A lo largo de los años se ha ido viendo la evolución de la comunidad educativa, las relaciones entre los asistentes, el cómo afrontan los talleres, etc. Estas valoraciones han permitido diseñar un nuevo formato que recoja audiencias más diversas y menos expuestas a la divulgación científica con condicionantes tan variados como distancia a la capital, la motivación familiar, el contexto socioeconómico, etc. En la ponencia se expondrán los datos y conclusiones globales de la campaña asociada al proyecto “La fotónica se mueve por Cantabria” y que está en plena ejecución.

Agradecimientos

Los autores agradecen al Unidad de Cultura Científica y de la Innovación (UCC+I), Vicerrectorado de Investigación y Política Científica, de la Universidad de Cantabria la financiación adjudicada con código 04.50.00 dentro de la convocatoria de “Ayudas para la realización de actividades de divulgación científica en la Universidad de Cantabria” en el año 2024.

Referencias

- [1] A. Chalyan, T. De Pauw, N. Debaes, and H. Thienpont, "10 years of Photonics Explorer Kit and the future," in Seventeenth Conference on Education and Training in Optics and Photonics: ETOP 2023, Technical Digest Series (Optica Publishing Group, 2023), paper 1272324.
- [2] Tech Light Lab - Optics Science Kit. [En línea]. [Accedido: 03-may-2024] Disponible en: <https://www.boreal.com/store/product/13150785/tech-light-lab-optics-science-kit>.

3D educational model for understanding refractive errors and optometric protocols

Justo Arines^{1,2}, Sofia Rendo-Gonzalez¹, Nery Garcia-Porta^{1,2*}

¹Department of Applied Physics, Universidade de Santiago de Compostela, 15782, Santiago de Compostela, A Coruña, Spain.

²iMATUS (Instituto de Materiales Universidad de Santiago de Compostela), 15782, Santiago de Compostela, A Coruña, Spain.

*E-mail: nerly.garcia.porta@usc.es

1. Introduction

Through images is much easier to understand difficult concepts. In the field of vision, seeing the different retinal images generated by myopia, hyperopia, astigmatism, or presbyopia will help optometry students to understand the different refractive errors and the answers provided by patients during the ocular examination. Also, seeing the blurry images projected into the retina under the effect of different refractive errors, will help the general public to understand the reasons why they see (or not see) clear images. Different setups have been suggested in the literature to show the retinal images provided by eyes with different refractive errors, and even to show the way in which different optotypes are seeing by patients during the subjective refraction process [1, 2]. The most used educational kit consists of a group of spherical lenses (convergent and divergent), which are placed on a table over a cardboard with a schematic eye drawn (see figure 1). A light source provides a group of light rays that impinges on a lens that acts as the refractive elements of the eye (cornea and crystalline lens). Depending on the refractive power of the lens, the setup simulates an emmetropic, myopic, or hyperopic eye. Then, to correct the refractive errors simulated, a corrective lens is placed as shown in Fig. 1, where lens 2 presents too much refractive power to generate a myopic eye, and lens 5 is a divergent lens that corrects the excess of refractive power of the eye, bringing the image plane to the retina of the schematic eye. The main limitations of this setup are: 1) human eyes have two refractive elements (cornea and crystalline lens) while this schematic eye uses just one lens, 2) the setup operates in two dimensions, which does not allow showing the effects of the astigmatism in the retinal image.

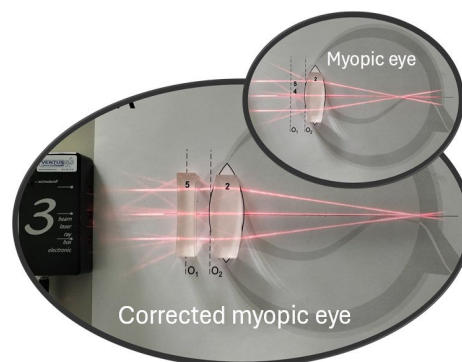


Figure 1 Educational kit (myopic eye). Lens L2 - refractive elements of the eye; lens L5 - corrective lens.

In the present work we present a new set up and method for explaining the different refractive errors and their effects on the retinal image, overcoming the limitations of current 2D educational kits.

2. Demonstrator set up

We used the webapp Tinkercad (<https://www.tinkercad.com/>) to develop a 3D design of the demonstrator. This is a simple software easy to operate. We defined the distinct parts of the project considering that they will be 3D printed with an extrusion printer. The 3D design was downloaded to an .stl file to be introduced in a slicing software for creation of the *gcode* file, which was loaded in the 3D printer. Figure 2a shows the 3D setup developed in Tinkercad. As it shows, the demonstrator has: 1) a

space in the front of the eye for placing a standard 65mm ophthalmic lens, which will act as a cornea; 2) a holder with three slots for holding apertures and trial lenses ; 3) a space at the back of the eye that allows holding a screen, which will act as a retina; 3) an area in front of the artificial eye simulating a spectacle, to hold the correcting lenses. The demonstrator includes different apertures with different shapes: a) two circular pupils, one with 20 mm and another one with 10 mm; b) two slits, one with 3mm and another one with 1mm; c) one mask with holes arranged in a circular shape.

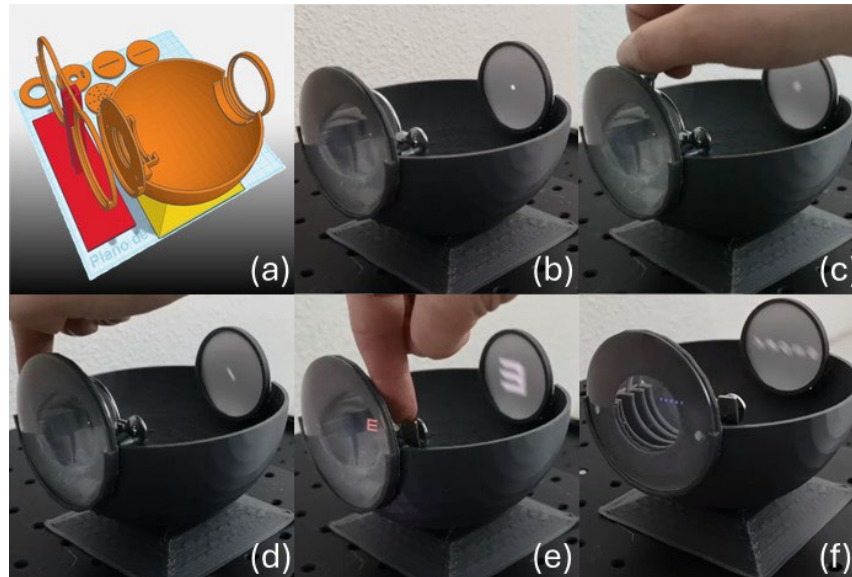


Figure 2 Tinkercad 3D design.

In figure 2b we present examples to explain the effect of defocus and in fig. 2c to 2f the effect of astigmatism on the retinal image. In these examples we used: 1) a +6.00 sph ophthalmic lens of 65mm diameter acting as cornea; 2) a trial lens of +6.00 sph to act as crystalline lens in combination with a trial lens of +2.25 sph or -3.00 cyl to simulate defocus or astigmatism respectively. We used the CC-100 LCD screen (TOPCON healthcare) at 60 cm of the eye to obtain a retinal image easy to visualize. Different combinations of lenses can be used depending on the simulated refractive error and object distance.

3. Conclusions

We developed a 3D demonstrator for explaining the optics of the eye, allowing easy visualization of the effect of the different refractive errors on the retinal image. The demonstrator has two refractive elements, being the cornea and crystalline lens, contributing to a better understanding of the eye. The different pupils and apertures allow for the demonstration of the effect of the pupil size on the quality of the retinal image and the gain in depth of focus; the understanding of what are the impact diagrams... We think that the proposed demonstrator can be useful in teaching and outreach activities overcoming the limitations presented by traditional 2D educational kits.

Acknowledgments

This work was supported by Ministerio de Ciencia e Innovación and FEDER, grant No. PID2020-115909RB-I00, and by Xunta de Galicia grant No. ED431B 2023/07. Nery Garcia-Porta is supported financially by a Maria Zambrano contract at USC under the grants call for the requalification of the Spanish university system 2021-2023, funded by the European Union—NextGenerationEU

References

- [1] A. Gargallo, J. Arines, “Webcams as a tool for teaching in Optometry training”. *Journal of Physics: Conference Series* **605**(1), 012039 (2015).
- [2] M. Rodríguez López, “¿Cómo ve el paciente durante el proceso de refracción subjetiva?” Trabajo de fin de grado, Universidade de Santiago de Compostela, Curso 2021-2022.

Photonets UV: What can a student chapter do to spread the knowledge of the optical sciences?

Raquel Salvador-Roger^{1,2*}, Marc Pérez-Safont^{2,3}, Juan Julián-Barriel^{2,3}, Sara Ferrer-Altabás^{1,2} and Anna I. Garrigues-Navarro^{2,3}

¹*Opto-Electronic Image Processing Group (GPOEI), Universitat de València, Burjassot, Spain*

²*Photonets UV, Student Chapter, Facultat de Física, Universitat de València, Dr. Moliner 50, 46100 Burjassot, Spain*

³*Laboratory of Fiber Optics, ICMUV, Burjassot, Spain*

*E-mail: photonets@uv.es
raquel.salvador@uv.es

Photonets was born three years ago, when some PhD, Masters and undergraduate students from Universitat de València(UV) started this adventure and managed to get involved in the Optica (formerly OSA) Student Chapter initiative. Over time, the team has been renewed and now is more interdisciplinary and more gender-balanced than ever, reaching 52% of women within its 28 members. This is a relevant fact since the main source of members is the UV physics degree, in which this representation does not reach 30%.

Although time has passed, our ideas keep the same. Our primary objectives include coordinating outreach events and generating content related to Optics and Photonics. Additionally, we aim to provide career advancement prospects and recreational options for our members. Recognizing the challenges faced by women in STEM fields, particularly in Optics and Photonics, we strive to promote the visibility of women in science and encourage the participation of new female members in our chapter and its activities.

In order to achieve these purposes, one of the main activities of the chapter from the beginning has been conducting outreach talks in schools and high schools, aimed at fostering a passion for science among young minds.

Since the beginning, we have had the opportunity to participate in relevant science outreach events. For example, we have participated in the last four editions of the *Fira-Concurs Experimenta* and in the European Researchers' Night, both organized by the UV, where we introduce the public to basic optical phenomena through simple experiments and home-made demonstrations (see Figure 1). Furthermore, we are in charge of the closing show every year.

Last year we also organized *¿Hay algún doctor en la sala?*, a PhD students' round table with the purpose of informing undergraduate and master's students about the daily life in the early stages of a scientific career.

This year, a new section in the chapter has been launched: *Lluminària*, the Photonets dissemination magazine. Created by students for students, this magazine features scientific outreach articles written by undergraduate, master's, and doctoral students, catering to learners from the early stages to undergraduate level. We launched the first seven articles by November and are now aiming to publish more by the end of the academic year. In addition, last November we were able to enjoy the visit of Miguel Alonso, Editor-in-Chief of Optics Letters. The opportunity to present this project to him and his encouragement to continue with the work was very much appreciated.

Our chapter is closely connected with other student chapters and we constantly participate in common activities. For instance, the I Mediterranean Meeting of Young Researchers in Optics was organized together with the OCAS Student Chapter and was a successful event. It was a three-day workshop where international and national experts were invited as speakers and students from all levels were welcome to participate with their own contributions (Figure 2). We also participated in the event known as "A la llum

de València", where we collaborated with OCAS and Physics League to create a two-day program with a scientific show and a science fair in the Botanical Garden of Valencia.

In the coming years, we aspire to expand our presence a little more by organizing and participating in outreach initiatives, visiting primary and secondary schools throughout the Comunitat Valenciana. Additionally, we aim to provide our members with an array of engaging and beneficial activities. Connect with us via @photonets_uv on Instagram and X, or reach out via email at photonets@uv.es.



Figure 1 Our stand at the *Fira-Concurs Experimenta 2024*.



Figure 2 Attendees to the I Mediterranean Meeting of Young Researchers in Optics.

ACKNOWLEDGEMENTS:

We thank Optica (formerly OSA) for their financial support.

“*Tornem als instituts*”: a peer-to-peer approach to teen women for promoting STEM careers

Martina Delgado-Pinar^{1*}, Pascuala García-Martínez², Susana Planelles³, Mariam Tòrtola⁴ and Núria Garro^{1*}

¹*Department de Física Aplicada i Electromagnetisme – ICMUV, Universitat de València*

²*Department d'Òptica, Universitat de València*

³*Department d'Astronomia i Astrofísica, Universitat de València*

⁴*Department de Física Teòrica-IFIC, Universitat de València*

*E-mail: martina.delgado@uv.es, nuria.garro@uv.es

1. Motivation of the activity

Tornem als instituts is an activity to commemorate the International Day of Women and Girls in Science on 11th February that has been organized by *Comissió d'Igualtat* of the Faculty of Physics of the *Universitat de València* since the academic year 2022-2023. Now, after two editions, we can review its impact on undergraduate students of the Faculty of Physics and High School students.

We were inspired by the initiative “11th February” which has run in Spain at a national level and consists of young or senior female researchers visiting secondary schools to show the students their daily work and experiences as a woman in STEM. The objective is to provide female referents to students, since it is well known that the lack of them inhibits young girls from addressing their studies to STEM careers [1, 2]. This activity has achieved a huge success and nowadays it is celebrated at most primary and secondary schools in Spain [3]. In our case, we have introduced a new vector to make this activity more engaging: the age of participants. There are studies showing that the impact of peers beliefs or references are substantial factors to be taken into account, especially during adolescence [4-6]. The Faculty of Physics holds an activity, “*Entre iguals*”, where older students mentor the newcomers to the Faculty, with excellent results. With this in mind, we addressed our students, especially girls, and requested them to “go back to High School” on the 11th February. In this way, the secondary school students would receive the visit of a young student who, not so long ago, was one of their peers. In addition, all the undergraduate participants were assigned a mentor among the senior researchers of the Faculty, giving them some training and concepts about how the academic system, as an organizational system as many others, presents gender discriminations that should be avoided, and make them aware about the problem to solve.

2. Development of the activity and impact

The activity consists of a university student giving an informative talk at their original secondary school. The call is open to both men and women students of any of the degrees taught at the Faculty, although we prioritise that women take a leading role while male students could offer support, such as helping in the preparation of the talks or experimental demonstrations, accompanying, etc. In a few schools, there have only been male volunteers, so they took the leading role with the aim of promoting scientific vocations among young people.

As mentioned before the activity begins with a tutorial for the undergraduate students where they are given basic notions about the existence of gender inequality in STEM careers, its causes, effects, and ways to deal with it. With these tools, students can respond effectively and with data to the questions they may receive in the institutes on the subject.

In figures, “*Tornem als instituts*” has been very well received by students and secondary schools’ teachers. In the first two editions, a total of 45 students, 40 women and 5 men, signed up for the activity, and 34 schools spread all around the three Valencian provinces were visited. The format of the activities is flexible in order to adapt to the preferences of the speakers and the needs of the centres, with a

predominance of talks with experimental demonstrations that allow for the participation of the attendees. In this sense, we should mention the collaboration of the Faculty of Physics, which lent the experimental kits of *Col·lecció de Demostracions* to the students [7]. The estimated number of students receiving these talks is around 3,500.

Finally, the participants from the Faculty of Physics are given a questionnaire to evaluate the activity which, together with a final discussion and sharing meeting, constitute the project's self-evaluation and improvement activities.



Figure 1 Pictures of different talks. From left to right: IES La Morería (Mislata, València), IES Penyagolosa (Castelló de la Plana, Castelló), IES Francesc Tàrraga (Vila-Real, Castelló)

3. Conclusions

As a summary, *Tornem als instituts* is an activity where the age factor is taken into account to enhance the impact of this kind of events, due to the proximity in age between the speaker and the students. As secondary advantages, it also trains undergraduate students in gender issues and, finally, it encourages interaction and networking among the faculty's own female professors.

Acknowledgments and funding

The authors acknowledge the Faculty of Physics and Dr. Chantal Ferrer (coordinator of the *Col·lecció de Demostracions*) for lending the material for experimental demonstrations and Unitat d'Igualtat de la Universitat de València for its financial support.
He

References

- [1] Bian *et al.*, "Gender stereotypes about intellectual ability emerge early and influence children's interests," *Science*, **355**, 389-391 (2017). DOI:10.1126/science.aah6524
- [2] Riegler-Crumb C. and Morton K., "Gendered Expectations: Examining How Peers Shape Female Students' Intent to Pursue STEM Fields". *Front Psychol.*, **15**, 329 (2017) DOI: 10.3389/fpsyg.2017.00329
- [3] <https://11defebrero.org/>, last access 5/5/2024
- [4] Feng Hu, "Do girl peers improve your academic performance?," *Economics Letters*, **137**, 54-58 (2015), DOI:10.1016/j.econlet.2015.10.025.
- [5] Ostroff C. and Atwater LE., "Does whom you work with matter? Effects of referent group gender and age composition on managers' compensation," *J Appl Psychol.*, **88**(4), 725-740 (2003) DOI: 10.1037/0021-9010.88.4.725.
- [6] Wu, S. J., & Cai, X., "Adding Up Peer Beliefs: Experimental and Field Evidence on the Effect of Peer Influence on Math Performance," *Psychological Science*, **34**(8), 851-862 (2023) <https://doi.org/10.1177/09567976231180881>
- [7] <https://www.uv.es/uvweb/fisica/ca/col-leccio-demostracions-fisica-aula/cataleg-demos-1286053686292.html>, last access 5/5/2024

Lluminària: An outreach magazine crafted by students for students.

Carolina Fernández-Saiz^{1,2*}, Nadia Ghadban-Gimeno², Marc Pérez-Safont^{2,3}, Salvador Rivero², Ángel Lapeña², Jorge Giménez², Rubén Piles², Anna I. Garrigues-Navarro^{2,3}, Juan Julián-Barriel^{2,3*}, Raquel Salvador^{2,4}, David Casteló-Lurbe², Estefania Delgado-Pinar⁵, Martina Delgado-Pinar²

¹ *Departament de Física Aplicada i Electromagnetisme - Universitat de València, Burjassot, Spain*

² *Laboratory of Fiber Optics, ICMUV, Burjassot, Spain*

² *Photonets UV, Student Chapter, Facultat de Física, Universitat de València, Dr. Moliner 50, 46100 Burjassot, Spain*

³ *Laboratory of Fiber Optics, Departament de Física Aplicada i Electromagnetisme - ICMUV, Universitat de València, Burjassot, Spain*

⁴ *Opto-Electronic Image Processing Group (GPOEI), Universitat de València, Burjassot, Spain*

⁵ *Departament de Química Inorgànica – ICMol, Universitat de València Burjassot, Spain*

*E-mail: lluminaria@uv.es and carolina.fernandez-saiz@uv.es

"Lluminària" is a dissemination project that began in 2023, an idea of the members of the Optica (formerly OSA) student chapter PHOTONETS-UV. Students proposed to produce rigorous, peer-reviewed by senior researchers, informative texts. It consists of a collection of scientific dissemination articles spanning various realms of physics, including optics, classical dynamics, quantum physics, among others. Except for the correction of articles, which is carried out by different supervising researchers, all the content, accessibility and dissemination of the journal is done by undergraduate, graduate students and PhD researchers.. Our target readership ranges from the general public to university students, encompassing both undergraduate and bachelor levels. Therefore, each article is crafted with an adequate language and scientific level, minimizing technical jargon to make complex concepts understandable to a broad audience. They are categorized by difficulty level, allowing readers to navigate based on their curiosity and comprehension. Moreover, to maximize accessibility, articles are presented in both Catalan and Spanish languages, ensuring broader engagement and dissemination of knowledge. Moreover, there is scarce scientific dissemination in catalan, thus this project also aims to reinforce the use of this language in this context.

In November 2023, we had the privilege of hosting a visit from Miguel Alonso, Editor-in-Chief of Optics Letters. During his visit, we had the opportunity to showcase our work to him, and he generously offered us guidance and encouragement to propel the project forward. Consequently, on November 30th we officially launched the magazine (Figure 1), an event where more than 88 people took part, interested in the first seven published articles. The topics were varied: articles dedicated the Nobel prizes 2023 of Chemistry and Physics, for Physics undergraduate students, an explanation of the conservation of energy to understand planetary motions, an article to get an idea of what doses of radiation are dangerous, both adapted to high school level, as well as less known topics such as the so-called "invisibility cloaks" and whispering gallery modes, for the last courses of the Grade in Physics.



Figure 1. Team at the presentation of the first issue of Lluminària.

This project is open to any undergrad and postgrad student of the Degree in Physics at the Universitat de València in a first place, but also to any other undergrad student of grades related to Physics, Optics and Photonics willing to participate as authors of the articles of their interest. The working group developing the project is divided into several teams: from initial organization to the design of website (Figure 2), articles and images for the future in-paper magazine. However, all teams are multidisciplinary and responsible for various tasks. Typically, numerous ideas for new articles are proposed, and those willing or able to write them take charge of this aspect. Several additional articles and various sections are currently in preparation and will be gradually compiled to create a comprehensive and diverse magazine for printing. Initially, the first articles have been centered around concepts elucidated by students, but we aim to broaden our scope to include sections such as explaining the functionality of everyday objects, simplifying research work for children, contributions from senior researchers offering, in an adequate level, a sneak-peek of their work to primary school students and even special features for commemorative occasions, as it was done for the Nobel Prizes 2023.

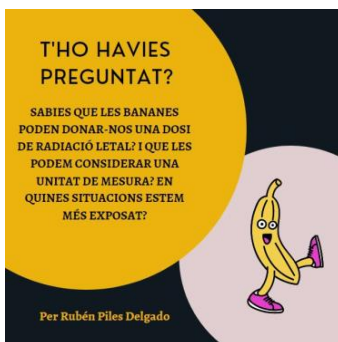


Figure 2. Example of an article's advertising for social media.

To sum up, this initiative aims to allow participating students to acquire cross-cutting competencies related to cultivating scientific culture, specialized writing, and the dissemination of scientific content and provides experience in team management. Furthermore, it seeks to produce educational resources that complement classroom instruction, thereby promoting and disseminating the study of physics among younger students.

As said, we make a call to any undergrad or postgrad student willing to participate as an author; you can contact us at lluminaria@uv.es and follow us at our social networks (X and Instagram) !

Acknowledgements:

We thank the Vicerectorat de Formació Permanent (Universitat de València) grant number PIII-2736653, OPTICA (formerly OSA) and JIQ-RSEQ for their financial support.

Additional Information:

You can access all our articles and news at: [Lluminària, una Revista de Photonets](#)

Fostering and disseminating optics and photonics with hands-on experiments in high schools

Alejandro Doval^{1,2*}, Alicia Muñoz-Ramos¹, Antía Santiago-Alonso^{1,2}, Bastián Carnero^{1,2}, Daniel A. Feijoo-Piedrafita¹, Irene Romo-Díez¹, Javier Varela-Carballo^{1,2}, José Paz-Martín¹, Sabela Fernández-Rodicio¹, Verónica Villa-Ortega¹, Yago Radziunas-Salinas^{1,2} and María Teresa Flores-Arias^{1,2}

¹Dissemination Group and Students Association LUZADA, USC-OPTICA Student Chapter and Santiago USC Young Minds Section, Universidade de Santiago de Compostela, E-15782 Santiago de Compostela, Spain.

²Instituto de Materiales (iMATUS), Universidade de Santiago de Compostela, E-15782 Santiago de Compostela, Spain.

*E-mail: alejandrodoval.casas@usc.es

1. Introduction

The Dissemination Group and Students Association LUZADA, USCOPTICA Student Chapter, and Santiago USC YM Section pursue to actively disseminate physics, optics and photonics throughout Galicia. With more than 10 years of expertise in the field of science fostering, we participate every year in different outreach events with the purpose of approaching Optics to the general public. One of our major events encompasses the performance of interactive workshops in high schools. These are carried out with the idea of motivating students into scientific disciplines, broadening their minds and inspiring them to follow a scientific career. In addition, as our members comprise Degree, Master and PhD Physics students we try to provide them a view of what research is.

2. Our workshops: An opportunity to approach optics interactively

Our hands-on workshops are composed of 4 different experiences where different optical phenomena are explained in an insightful way, relating them to the daily life of the students. They are divided in four different groups around the classroom and 4 stations with the experiments are built. Students follow a circular tour around the experiments, each one lasting for about 15 minutes.

A small compendium of our experiments can be seen in Figure 1, 2 and 3. In Fig. 1 a) a methacrylate piece allows to show the idea of refraction and Snell Law, introducing the concept of waveguiding and its relationship with optical communications. Once the students understand what total reflection is and how to send information by means of light, different experiments with commercial optical fibres are performed. Ideas such as light absorption and signal losses are explained comparing the propagation of white light obtained from a smartphone flashlight in the waveguides.



Figure 1. Performing experiments related to optical communications and polarization. a) plastic piece employed for refraction experiments, b) students using lineal polarizers and c) set of elements for the polarization experience

Fig. 1 b,c) shows the experience based on the concept of polarization and its application to material stress detection. Students are taught that light is polarized employing different elements, comprising springs so they could differentiate among lineal, circular, and elliptical polarizations, lineal polarizers to introduce the Malus Law and plastic forks to study the concept of photoelasticity. In addition, explanations of the physics behind daily life elements related to the topic are given, including polarized glasses, 3D cinema

glasses and the screens of smartphones or computers.

Fig. 2 depicts the elements of a third experience, introducing optical phenomena that can lead to a confusion for students, comprising the difference between fluorescence - phosphorescence and refraction - diffraction. For the former pair, the concept of fluorescence is introduced employing olive oils with different chlorophyll concentrations. For the second case, prisms are used to show the concept of material dispersion, whereas diffracting gratings are employed to approach the concept of diffraction pattern.

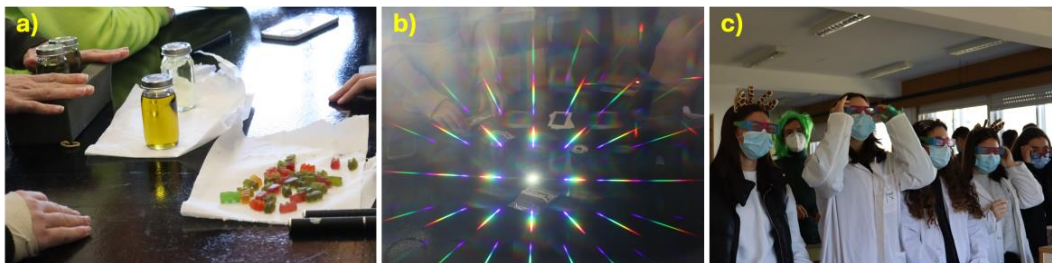


Figure 2. Experiments explaining optical phenomena. a) different elements to address the concept of fluorescence, b) circular diffraction pattern illuminated with a smartphone flashlight and c) glasses with diffraction pattern

Finally, a fourth experiment introducing the human eye is carried out. During this experience, the operation of the human eye is taught, explaining their main parts and most common illnesses (myopia hypermetropia) employing divergent and convergent lenses (Fig. 3a). Besides, to fully understand these concepts, students are shown a home-made 3D-printed eye (Fig. 3b), enabling them to check the different layers of the eye as well as the principles behind astigmatism.

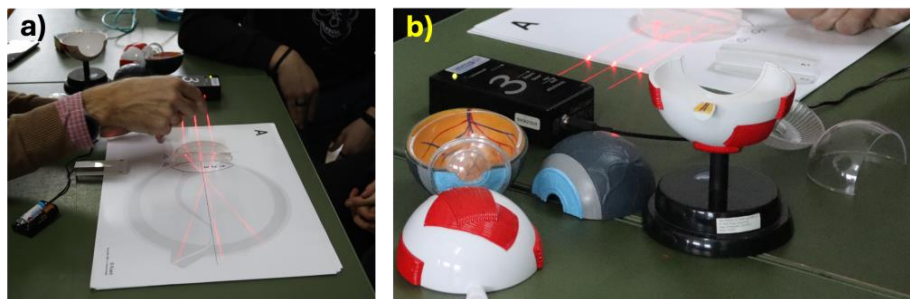


Figure 3. Introducing the human eye with a) set of convergent and divergent lenses and 3-ray laser and b) 3D-printed human eye

3. Conclusions

Our spreading knowledge team has been approaching the field of optics and photonics in an interactive manner since its birth, proving that it is possible to perform simple experiments to teach students. It is worth mentioning that many elements composing our experiences are homemade and easy to achieve, showing that science fostering can be done in an inexpensive way. In the following years, we would like to expand our horizons, incorporating new experiments with the purpose of addressing pivotal concepts in optics related to colour or interference.

Acknowledgments

We would like to acknowledge the European Physical Society, OPTICA and Universidade de Santiago de Compostela for their commitment to financially support our activities.

La fotografía estereoscópica, la estereopsis y el patrimonio histórico-artístico como herramientas para la innovación docente interdisciplinar y la divulgación

José Juan Castro Torres^{1*}

¹*Departamento de Óptica, Universidad de Granada., Avenida de Fuentenueva, s/n 18071 Granada*

*E-mail: jjcastro@ugr.es

1. Introducción

Desde la implantación del Espacio Europeo de Educación Superior (EEES) las actividades de innovación docente en la Universidad han cobrado especial relevancia con el objetivo de mejorar el proceso de enseñanza-aprendizaje, complementando el desarrollo y adquisición de competencias específicas en la materia en la que se forma el alumnado, pero también con el objetivo de trabajar competencias transversales que les ayuden a aportar soluciones en su proceso de formación y que les serán de utilidad en el futuro ejercicio de su profesión, sin olvidar el hecho de que las clases magistrales siguen siendo la base sobre la que se construye una enseñanza universitaria de calidad. En el caso de titulaciones con un alto contenido en Óptica, como el Grado en Óptica y Optometría (GOO), existen diferentes asignaturas y materias que pueden ser objeto de innovación docente de carácter interdisciplinar y permitir interacción con disciplinas muy diferentes. Un marco incomparable para desarrollar actividades de este tipo es el patrimonio histórico-artístico. En este trabajo se describe un proyecto de innovación docente interdisciplinar en la Universidad de Granada (UGR), en el que está implicada la titulación GOO, así como diversas actividades de divulgación centradas en fotografía estereoscópica y visión binocular (estereopsis), pero también en el patrimonio histórico-artístico de la ciudad de Granada.

2. El proyecto

El proyecto llevaba por título «Interdisciplinariedad y trabajo cooperativo en los nuevos títulos de grado: el estudio de la arquitectura, el derecho y la historia del arte a través de la fotografía tridimensional» [1] y obtuvo financiación dentro del «Programa de Innovación y Buenas Prácticas Docentes» de la Universidad de Granada. Se desarrolló a lo largo de un total de cuatro cursos académicos (desde 2013-2014 hasta 2016-2017). Inicialmente hubo cuatro áreas implicadas en el proyecto, correspondientes a cuatro titulaciones de la UGR (óptica y optometría, arquitectura, historia del arte y derecho), incorporándose algunas titulaciones más en cursos posteriores. Una forma de conectar todas ellas y que hubiera interacción entre los alumnos (a través del trabajo colaborativo entre ellos) fue combinar el patrimonio histórico-artístico de la ciudad de Granada con la fotografía estereoscópica, que a su vez está relacionada con la visión estereoscópica, necesaria para obtener una percepción en profundidad de las estereomágenes. La idea era que desde el punto de vista de cada asignatura se pudiera realizar un trabajo interdisciplinar entre los alumnos de cada grupo que permitiera el estudio del rico patrimonio histórico-artístico y arquitectónico de la ciudad de Granada.

La Fig. 1 muestra una infografía que describe la actividad principal del proyecto. Se partió de asignaturas de diferentes titulaciones que participaron en el proyecto y en las que al menos un profesor se encargaba de tutorizar a los alumnos voluntarios de su asignatura. Se crearon diferentes grupos interdisciplinares de alumnos (cada grupo tutorizado por un profesor). Cada grupo interdisciplinar (GI) estaba compuesto por 1-3 alumnos de cada asignatura, de forma que todas las titulaciones estuvieran representadas en el grupo (8-12 alumnos por grupo). La actividad principal consistió en visitar un monumento del patrimonio histórico-artístico de la ciudad de Granada. A cada grupo interdisciplinar se le asignó un monumento, que debía visitar. Previamente a la visita, los alumnos de cada grupo tuvieron una reunión inicial en la que se conocieron y planificaron la visita, estudiando el monumento a través de referencias bibliográficas y preparando diferentes aspectos desde la perspectiva de su asignatura. Durante la visita, cada alumno debía explicar al resto de los alumnos del grupo los aspectos del monumento relacionados con su asignatura. Así, por ejemplo, los alumnos de Arquitectura se centraron en los aspectos arquitectónicos y decorativos del monumento, el conjunto urbano y algunos alumnos realizaron dibujos o bocetos de los mismos. Los alumnos de Historia o Historia del Arte se centraron más en los aspectos relacionados con los

antecedentes históricos y los estilos artísticos del monumento. Los estudiantes de Derecho analizaron el monumento en función de su relevancia desde el punto de vista histórico-jurídico o de la administración de justicia en épocas anteriores, y también se interesaron por estudiar las familias de la nobleza que vivieron en el edificio o monumento, o si albergaban algún archivo histórico. Por su parte, los alumnos del Grado en Óptica y Optometría participaron a través de dos asignaturas, «Instrumentación Óptica» y «Fundamentos de la Visión Binocular», cubriendo en el GI los conocimientos de la cámara fotográfica, estereofotografía y visión estereoscópica. Durante la visita estos alumnos realizaban estereofotografías y, en determinados momentos de la visita, explicaban de forma divulgativa al resto de alumnos del grupo los fundamentos de la visión estereoscópica, así como la metodología en la realización de las fotografías estereoscópicas y cómo las procesaban para obtener los anaglifes. Posteriormente a la visita los alumnos debían trabajar colaborativamente en la realización de un dossier de la visita y, en su caso, presentarlo en clase. Además, a raíz del desarrollo de este proyecto de innovación se realizaron actividades de divulgación mediante la organización de exposiciones, congresos y participación en eventos como la Noche Europea de los Investigadores [2].

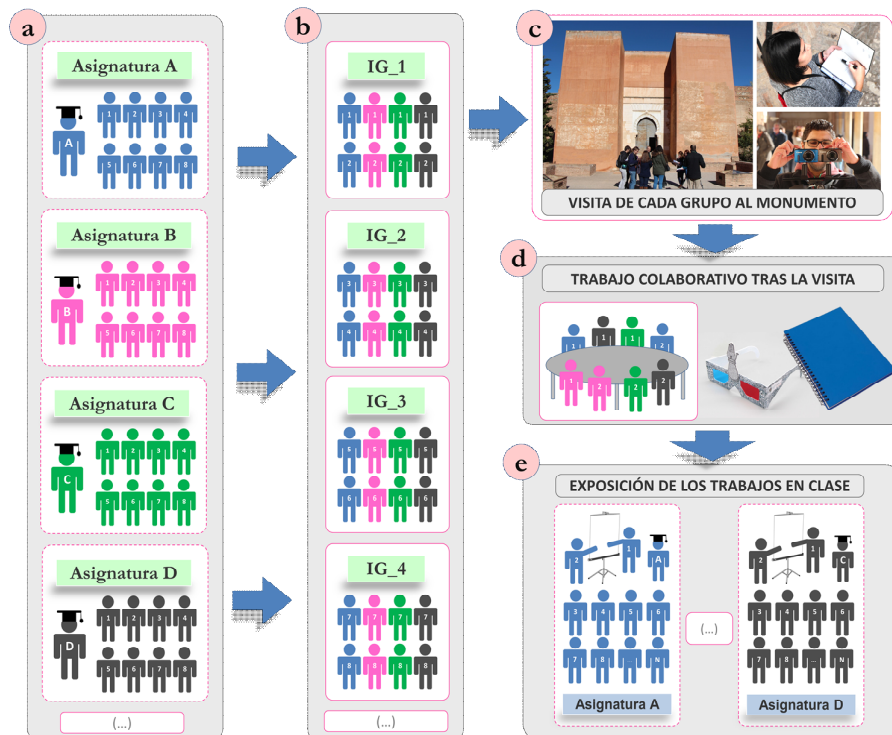


Figura 1. Infografía que describe la actividad principal del proyecto interdisciplinar.

3. Conclusiones

Las acciones de innovación docente interdisciplinar son bien acogidas por alumnos y profesores y mejoran el proceso de enseñanza y aprendizaje, además de potenciar en el alumnado la adquisición de competencias específicas de su disciplina pero también otras competencias de carácter transversal.

References

- [1] J. J. Castro-Torres, et al., *Innovación docente interdisciplinar en la universidad: estudio de la Arquitectura, el Derecho y la Historia del Arte del patrimonio histórico-artístico de la ciudad de Granada a través de la fotografía estereoscópica* (Universidad de Granada, Granada, 2018) [<http://hdl.handle.net/10481/53864>].
- [2] J. J. Castro-Torres, Enrique Hita, Miriam Casares-López, Francesco Martino, and Sonia Ortiz-Peregrina, “Anaglyphs and stereoscopic vision in interdisciplinary education and outreach: the historical-artistic heritage of two Spanish cities seen through stereophotographs”, *Proc. SPIE* **11480**, Optics Education and Outreach VI, 114800E (2020); <https://doi.org/10.1117/12.2567205>.

El Proyecto “Óptica recreativa, del cole a casa” y el kit de Fresnel

Mikel Sanz^{1*}, Óscar Gálvez¹, M^a del Mar Montoya¹, Manuel Pancorbo¹, Juan Pedro Sánchez-Fernández¹, Javier Tajuelo¹, Amalia Williard¹, Carlos García-Arcos¹, Mariana Rodríguez¹ y Ana Isabel Mártir¹

¹Dpto. de Física Interdisciplinar, Facultad de Ciencias. UNED, Las Rozas (Madrid)

*E-mail: mikelsanz@ccia.uned.es

1. Kit de Fresnel, un proyecto de divulgación novedoso en el campo de la Óptica

En el año 2022 se inició el proyecto de divulgación científica “*Óptica recreativa, del cole a casa*”, dirigido fundamentalmente a escolares de 8 a 15 años, proyecto que continúa vigente en la actualidad, tercer año de ejecución, y ha sido financiado en sus tres ediciones por la FECYT (Refs.: FCT-21-17443, FCT-22-18081 y FCT-23-18954). [1,2]

El proyecto pretende, fundamentalmente, promover las vocaciones científicas entre los escolares y el público familiar, fomentando su interés por la ciencia mediante el contacto directo con el método y la práctica investigadora a través de la realización de talleres prácticos lúdicos y divertidos. El formato elegido sigue la metodología y estructura de un proyecto previo de los mismos autores (*Ciencia electromagnética, del cole a casa*), según el cual se plantean dos tipos de actividades diferentes. Por un lado, se imparte una charla-taller con contenidos de óptica básica (física elemental relacionada con la luz, los colores y la visión), adaptada al nivel de los escolares, quienes manipulan los materiales experimentales ofrecidos y participan en los experimentos. Por otro lado, se propone una segunda actividad diseñada para que los propios escolares actúen como “pequeños divulgadores” en otro público que normalmente no es destinatario de actividades de divulgación: su propia familia y entorno doméstico. Se proporciona una caja, llamada *Kit de Fresnel*, cuidadosamente preparada con materiales de bajo coste, junto a sus manuales explicativos, para poder realizar un conjunto de experimentos de óptica básica (contiene todo el material necesario para llevar a cabo 34 experiencias de óptica).



Figure 1 Detalle del kit de Fresnel.

Cada año de ejecución del proyecto se han elaborado entre 150 y 200 unidades del kit de Fresnel, para que cada clase visitada recibiera 4 o 5 unidades y que los estudiantes pudieran tomar uno prestado durante un breve periodo de tiempo y realizaran todos los experimentos en su ambiente familiar, llevando a cabo un pequeño trabajo científico en el cual anotaban los resultados e implementaban las sugerencias que se indican en el manual.

Para incentivar la participación de los escolares en la actividad divulgativa propuesta en sus entornos familiares, se propone a los estudiantes participar en un concurso de vídeos, en el que han de grabarse realizando alguna de las experiencias. Entre los vídeos presentados se eligen los mejores, a los que se les

entregan varios premios en un pequeño acto público al que asisten los escolares premiados, junto a sus familias y docentes.

2. Conclusiones

En las ediciones de 2022 y 2023 fueron visitados cerca de una veintena de centros educativos, realizándose del orden de 60 talleres, llegando la actividad a unos 20 escolares por taller. La actividad está teniendo una excelente acogida en todos los centros educativos que se han visitado hasta el momento, así como en reuniones diversas (jornadas de divulgación, ferias de la Ciencia, etc.).

El Proyecto Kit de Fresnel ha recibido un galardón en la VII edición de los premios UNED-Santander de Investigación, Transferencia y Divulgación 2023, dentro de la modalidad "Mejor trabajo de divulgación".

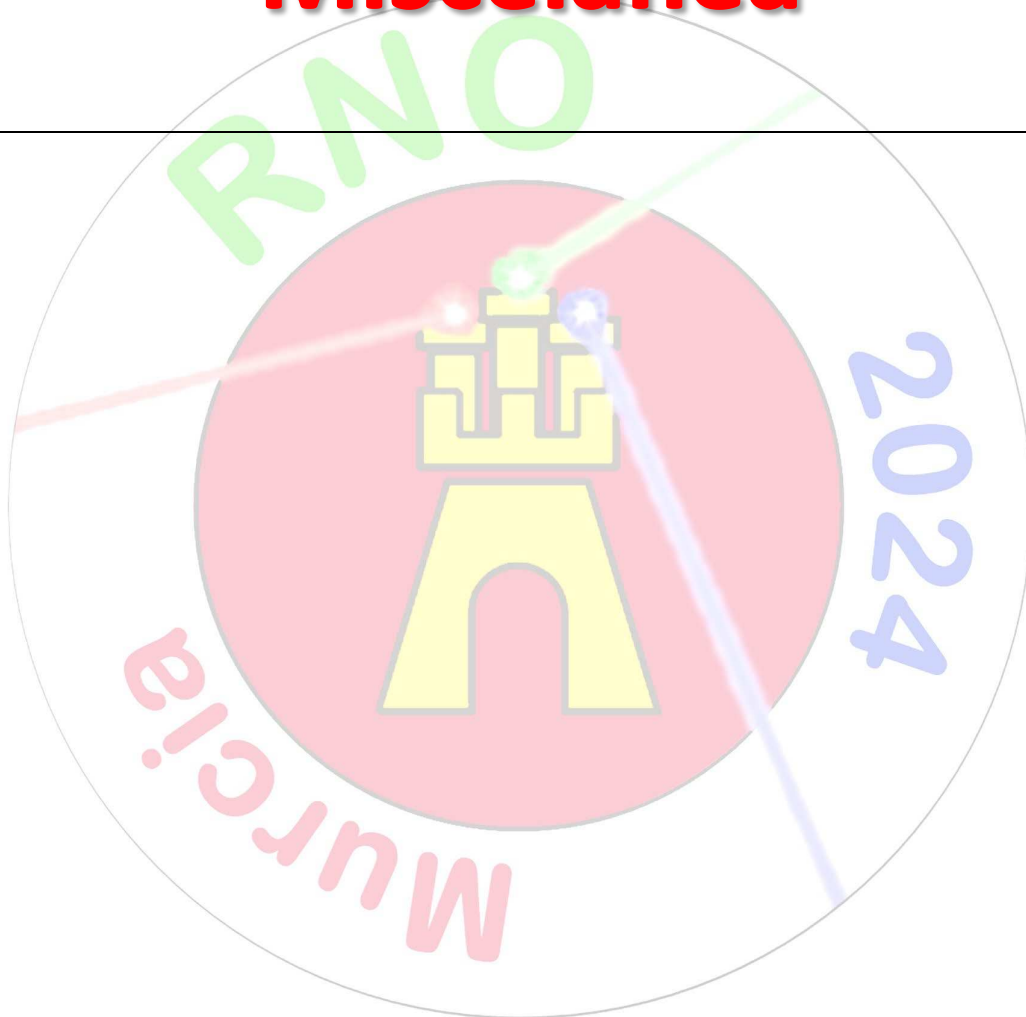
Referencias

- [1] <https://www.divulgateca.es/Proyecto-destacado.aspx?Id=1655>
- [2] <https://blogs.uned.es/innovacion/kit-de-faraday-y-kit-de-fresnel/>

RESÚMENES/ABSTRACTS

Sesiones Orales

Miscelánea



Principal components analysis on measurements of spectral reflectance and transmittance of glazing systems for different angles of incidence

Pablo Santafé-Gabarda¹, Jorge Álvarez¹, Joaquín Campos¹, Adolfo Muñoz², M. Mar Barbero-Barrera³, and Alejandro Ferrero^{1*}

¹*Instituto de Óptica “Daza de Valdés”, Consejo Superior de Investigaciones Científicas (CSIC), c/ Serrano 144, 28006 Madrid*

²*Tecnologías de la Información y de la Comunicación, Universidad de Zaragoza, I3A, C/ Mariano Esquillor s/n, 50018 Zaragoza*

³*Department of Construction and Technology in Architecture. Escuela Técnica Superior de Arquitectura. Universidad Politécnica de Madrid (UPM). Avenida Juan de Herrera, 4. 28040 Madrid*

*E-mail: alejandro.ferrero@csic.es

1. Introduction

Principal components analysis (PCA) is a powerful mathematical technique to identify different contributions to the variations observed in multidimensional data. In this work, we test the adequacy of this technique to evaluate measurements of spectral reflectance and transmittance of glazing systems considering different angles of incidence. The objective is to use this technique not only to separate the variation from angular and spectral variables, and to find simplified empirical models, but also to be able to identify systematic errors, which might be spectrally or angularly correlated.

2. Method

PCA is generally applied for analysing the variance of a multidimensional variable, or a set of variables, $F = \{F_1, F_2, \dots, F_N\}$ [1]. According to this formalism, each F_i can be expressed as a linear combination of the eigenvectors, $e_{i,j}$, and the eigenspectra, A_j , of its diagonalised covariance matrix:

$$F_i = \langle F_i \rangle + \sum_{j=1}^N e_{i,j} A_j, \quad (1)$$

where $\langle F_i \rangle$ is the median of all the realizations of F_i and N is the number of principal components. In our practical case, this variable corresponds to spectral reflectance and transmittance measurements for different angles of incidence, θ , where each wavelength, λ , represents a different realization of the variable. This approach is similar to that thoroughly described in [2]. Thus, Eq. (1) can be rewritten as:

$$R(\lambda, \theta) = M(\theta) + \sum_{j=1}^N e_j(\theta) A_j(\lambda) \quad (2)$$

where $M(\theta)$ is the median of the values of the spectral reflectance/transmittance measurement, $R(\lambda, \theta)$, at a given θ . The eigenvectors $e_j(\theta)$ convey the coefficients of the transformation from the base of the original correlated spectra to a new base of uncorrelated spectra, formed by the eigenspectra $A_j(\lambda)$, and they can be regarded as the weight of each eigenspectra (components) in $R(\lambda, \theta)$. The variance of the different eigenspectra is given by the eigenvalues of each component.

3. Preliminary results

The described PCA formalism has been applied to measurements of spectral reflectance and transmittance, from 380 nm to 2500 nm, at different angles of incidence from 0° to 70° of different glazing samples [3]. An application example for one of those glazing samples is shown in Fig. 1. The upper plots present the data of reflectance measurements, while the lower plots those of transmittance. In these plots only the three components with the higher contributions to the variance of the measurement (higher eigenvalues) are represented, whose accumulated variance constitutes more than 95% of the total.

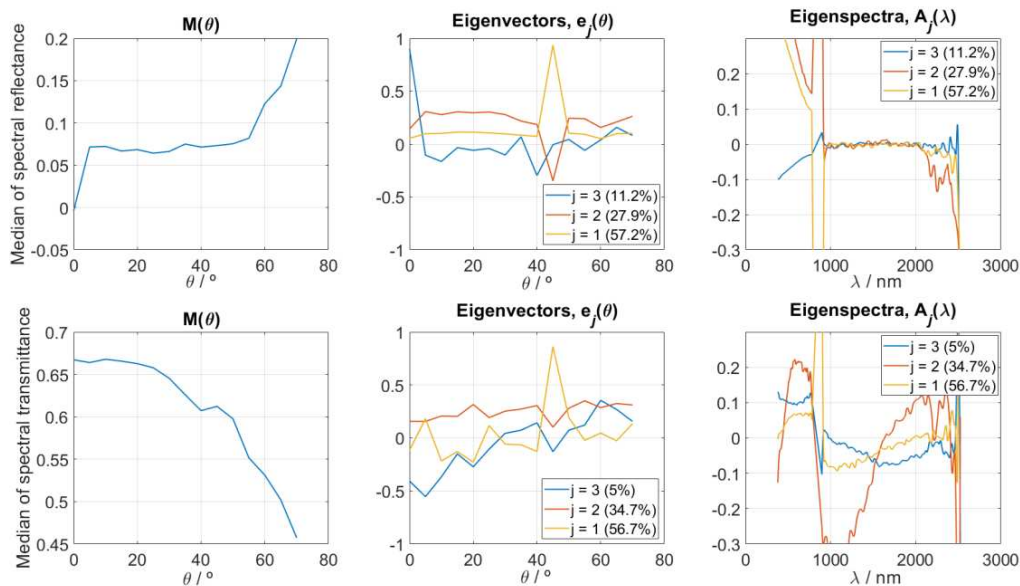


Figure 1 Median (left), eigenvectors (middle) and eigenspectra (right) of reflectance (top) and transmittance (bottom) measurements. Relative contribution to the total variance of each component is in the legend of the middle and right plots.

4. Discussion and conclusions

The PCA approach allows the variation of the spectral distribution with the incidence angle to be evaluated systematically. Illustrative examples are the systematic errors, e. g., the reflectance measurement at $\theta = 0^\circ$, which provides a wrong spectral measurement due to occlusion. This wrong spectrum is identified as the third eigenspectrum of the reflectance measurements ($j=3$, 11.2% of total variance) since its corresponding eigenvector values almost 1 only at $\theta = 0^\circ$ (middle top in Fig. 1). The other two eigenspectra of the reflectance measurements seem to be related to some measurement issue at $\theta = 45^\circ$, as it is revealed by the abrupt peaks in the plot of their corresponding eigenvectors at that geometry. This peak is also observed in the first eigenvector ($j=1$, 56.7% of total variance) of the transmittance measurements (middle bottom in Fig. 1), whose eigenspectrum shows a similar issue as the former eigenspectra of the reflectance measurements in the overlap of the visible and the near-infrared spectral ranges (see right top and bottom plots in Fig. 1).

In a first step, this method will be used for identifying systematic errors or filtering noises (uncorrelated errors) in the measurements. In a second step, the method will be applied to the filtered and corrected data, allowing the empirical study of the angular dependence of the spectral optical properties of the evaluated glazing materials. This, in turn, will allow the development of simplified models for characterizing the angular and spectral reflectance/transmittance of this kind of materials.

Acknowledgments

This contribution is part of the project TED2021-129661B-C21, funded by MCIN/AEI/10.13039/501100011033 and the European Union “NextGenerationEU”/PRTR.

References

- [1] J. M. López-Alonso, J. Alda and E. Bernabéu, “Principal-component characterization of noise for infrared images”, *Applied Optics* **41**(2), 320-331 (2002).
- [2] A. Ferrero, J. Campos, A. M. Rabal, A. Pons, M. L. Hernanz and A. Corróns, “Principal components analysis on the spectral bidirectional reflectance distribution function of ceramic colour standards”, *Optics Express* **19**(20), 19199–19211 (2011).
- [3] J. Álvarez, P. Santafé-Gabarda, J. Campos, M. Barbero, A. Muñoz and A. Ferrero, “Measurement of reflectance and transmittance of glazing systems for different incidence angles”, XIV Reunión Nacional de Óptica, (Murcia, (2)3–5 July 2024).

Measurement of reflectance and transmittance of glazing systems for different incidence angles

Jorge Álvarez¹, Pablo Santafé-Gabarda¹, Joaquín Campos¹, Mar Barbero², Adolfo Muñoz³ and Alejandro Ferrero^{1*}

¹*Instituto de Óptica “Daza de Valdés”, Consejo Superior de Investigaciones Científicas (CSIC), c/ Serrano 144, 28006 Madrid*

²*Dpto. Construcción y Tecnología, Universidad Politécnica, Avda. Juan de Herrera 4, 28040 Madrid*

³*Tecnologías de la Información y de la Comunicación, Universidad de Zaragoza, I3A, c/ Mariano Esquillor s/n, 50018 Zaragoza*

*E-mail: alejandro.ferrero@csic.es

1. Introduction

Lighting together with heating and cooling are the most energy consumers in the use stage of buildings. This consumption can be considerably reduced by optimizing façades and glazing systems, selecting adequate materials through the evaluation of the transmittance and reflectance properties (angular, spatial and spectral distributions) of the surfaces, and using these properties in dynamic simulation of buildings. Connecting the present state of the art in reflectance and transmittance measurements to the present simulation softwares could improve energy efficiency in buildings.

The spectral reflectance and transmittance of different glazing systems, from 380 nm to 2500 nm, have been measured at different incidence angles (from 0° to 70°). The measurement procedure and some preliminary results are presented in this contribution. The methodological issues will be discussed briefly.

2. Description of the measuring procedure

The measurements have been performed in the goniospectrophotometer installed in the *Instituto de Óptica “Daza de Valdés”* of the Spanish National Research Council (IO-CSIC), which is well-described in the literature [1, 2]. This system has been modified according to the needs of the measurements presented in this work. A diagram of the present measurement setup is shown in Fig. 1.

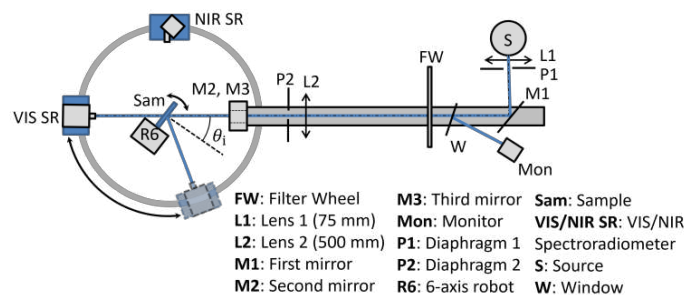


Figure 1 - Goniospectrophotometer.

The glazing samples are irradiated with a broadband uniform beam. The 6-axes robot arm orientates the samples at different angles (θ_i) from the irradiation beam. The regular transmitted flux or specular reflected flux, as applicable, is collected by a spectroradiometer. The measurement setup includes two spectroradiometers: one operating in the visible (VIS) range from 380 nm to 780 nm and another one in the near-infrared (NIR) range from 900 nm to 2500 nm. Each spectroradiometer is mounted on an independent movable platform that can rotate around the sample.

3. Description of glazing samples

A set of samples belonging to two different types of glass families were used in this study. On the one hand, monolithic samples of equal thickness (6 mm) that have surface treatments on one side using magnetron sputtering of low-emissive solar control thin films have been measured. On the other hand,

the so-called Insulating Glass Units (IGU) have been measured, composed of two parallel sheets of glass separated by a hermetically sealed chamber filled in this case with 90% Ar gas, although other inert gas can be used. All the IGU have the same thickness: 6 mm and 4 mm for the sheets, being the thickest glass the one that has the solar treatment in contact with the inert gas, separated by a 16 mm chamber.

4. Preliminary results

As examples, results for a monolithic glazing sample and for an IGU are shown in Fig. 2 and Fig.3.

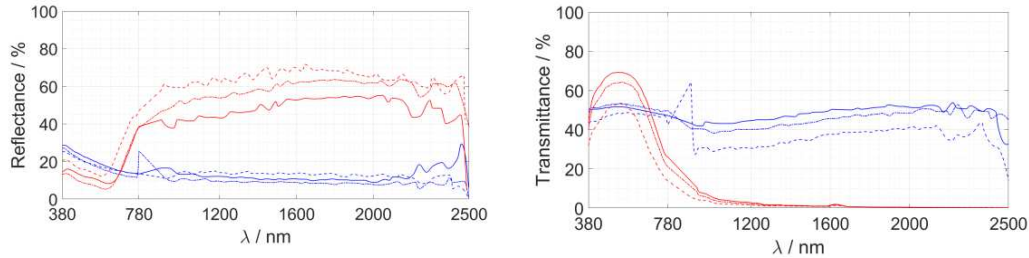


Figure 2 - Spectral transmittance (left) and spectral reflectance (right) of a monolithic glazing sample (blue curves) and an IGU (red curves) at $\theta_i = 5^\circ$ (solid line), $\theta_i = 30^\circ$ (dashed-dotted line) and $\theta_i = 60^\circ$ (dashed line)

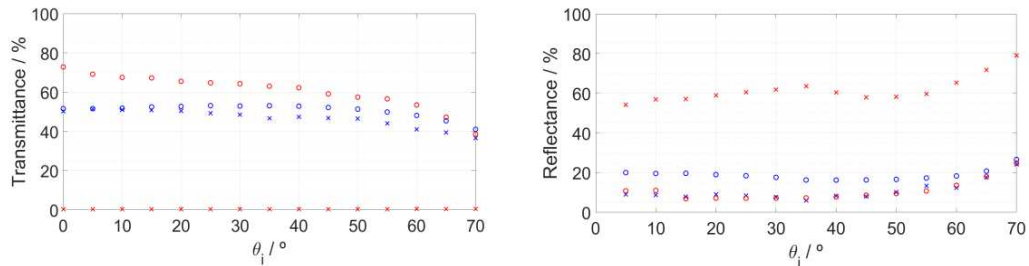


Figure 3 – Transmittance (left) and reflectance (right) at different incidence angles. The circle markers depict a wavelength of 550 nm while the cross markers depict a wavelength of 1998 nm. The blue markers correspond to a monolithic sample and the red ones to an IGU.

5. Discussion and future work

The measurements of transmittance at large incidence angles show an additional complexity due to the step effect generated by the refraction of the beam through the glazing sample, which is aggravated in thicker samples. Besides, in measurements of both reflectance and transmittance also at large incidence angles the second and higher orders reflected or transmitted beams are completely separated spatially from the main reflected or transmitted beam. Thus, for those large incidence angles, they are not being collected by the spectroradiometer. This effect will be analyzed and quantified in future measurements, and a procedure will be developed for its characterization.

This work aims at a deep characterization of relevant glazing materials and systems for efficient buildings, by measuring their reflectance and transmittance in different conditions. The results will be made publicly available in order to support the simulation softwares for designing of efficient buildings.

Acknowledgments

This contribution is part of the project TED2021-129661B-C21, funded by MCIN/AEI/10.13039/501100011033 and the European Union “NextGenerationEU”/PRTR.

References

- [1] A. M. Rabal, A. Ferrero, J. Campos, J. L. Fontecha, A. Pons, A. M. Rubio, and A. Corróns, “Automatic gonio-spectrophotometer for the absolute measurement of the spectral BRDF at in- and out-of-plane and retroreflection geometries”, *Metrologia*, **49** 3, 213–223 (2012).
- [2] B. Bernad, A. Ferrero, A. Pons, M. L. Hernanz and J. Campos, “Upgrade of goniospectrophotometer GEFE for near-field scattering and fluorescence radiance measurements”, in *Measuring, Modeling, and Reproducing Material Appearance 2015*, **9398**, 93980E.

Rationalizing the mechanisms behind the stimulated emission processes in CsPbBr₃ nanocrystals films

Luis Cerdán^{1,*}, Stefania Milanese², Maria Luisa De Giorgi², Marco Anni², Maryna I. Bodnarchuk^{3,4}

¹*Instituto de Química-Física (IQF-CSIC), Consejo Superior de Investigaciones Científicas, Spain*

²*Dipartimento di Matematica e Fisica “Ennio De Giorgi”, Università del Salento, Italy*

³*Institute of Inorganic Chemistry, ETH Zürich, Switzerland*

⁴*Laboratory for Thin Films and Photovoltaics, Empa - Swiss Federal Laboratories for Materials Science and Technology, Switzerland*

*E-mail: l.cerdan@csic.es

1. Introduction

CsPbBr₃ lead halide perovskite nanocrystals (NC) stand out as excellent candidates to implement light-emitting devices thanks to their excellent photoluminescence quantum yields, their facile and low-cost production, and their processing versatility [1,2]. Elucidating their stimulated emission mechanisms is fundamental to address their possible limitations and to achieve much more efficient perovskite lasers. CsPbBr₃ NCs thin films, and most perovskites for that matter, display very distinctive Amplified Spontaneous Emission (ASE) spectral signatures: the ASE band is usually significantly shifted from the fluorescence one, and, in addition, the former seems to suddenly emerge from, and coexist with, the latter (Fig. 1a). These characteristic features have led to a debate on which is the mechanism behind the ASE band shift. Some reports claim that the fluorescence band is generated by single excitons, while the ASE band has a biexcitonic origin, and is shifted due to the binding energy [1]. Some other reports defend that both the fluorescence and ASE bands are generated by localized single excitons, and the shifts owe to reabsorption effects [3]. In this communication, we try to settle this debate and address these questions through experimental ASE measurements, combined with numerical simulations and thorough analysis of the optical gain. Our study shows that the ASE behaviour in CsPbBr₃ NCs thin films stems from four distinctive processes [4]: reabsorption, excited state absorption (ESA), excitation of differently polarized waveguide modes, and coexistence of short- and long-lived localized single excitons.

2. Samples and methodology

The NCs were synthesized by adapting the procedure described in Ref. [5], using didodecyldimethyl ammonium bromide (DDAB) as capping ligand. The films were deposited by spin coating the NCs colloidal solution on fused silica substrates. ASE measurements were performed by exciting the samples with a Nitrogen laser (3 ns pulses at 337 nm, with a repetition rate of 10 Hz). The pump beam was focused onto the sample surface in a rectangular stripe of 4.5 mm length and 80 μm width (inset of Fig. 1a).

The ASE properties of the films were evaluated by means of Variable Pump Intensity (VPI) measurements, where the photoluminescence (PL) emission is acquired as a function of the pump excitation density. To retrieve the optical gain properties, we used a newly reported analytical method (dubbed VPI 2) that accounts for both ASE (1st term in Eq. (1)) and excess fluorescence (2nd term in Eq. (1)) [4]:

$$I_{pL}(\lambda) = \frac{A_1(\lambda)}{\gamma(\lambda)\Delta n - \alpha(\lambda)} \left(e^{(\gamma(\lambda)\Delta n - \alpha(\lambda))L} - 1 \right) + \frac{A_2(\lambda)}{\alpha(\lambda)} \left(1 - e^{-\alpha(\lambda)L} \right) \quad (1)$$

$$\Delta n(I_p) = \Delta n_0 \frac{I_p/I_{p,1}^s + (I_p/I_{p,2}^s)^m}{1 + I_p/I_{p,1}^s + (I_p/I_{p,2}^s)^n} \quad (2)$$

where γ and α are the gross gain and losses, respectively, Δn (Eq. (2)) is the population inversion, A_i are proportionality factors, and $I_{p,i}^s$ are saturation intensities that, together with m and n ($m > n$), determine when the population inversion grows and saturates.

3. Results

VPI 2 allows to obtain a very accurate fit of the emission spectrum above the ASE threshold (Fig. 1a), evidencing that the acquired spectrum is the combination of a strong fluorescence background and a

distinctive ASE band. The same holds true for the experimental pump fluence dependence of the emission intensity at the ASE peak wavelength (Fig. 1b). Indeed, below ASE threshold (dashed vertical line) the PL signal is dominated by a background fluorescence contribution that grows linearly with the pump fluence. It is only when approaching threshold that a strong purely ASE signal becomes dominant. This fact rationalizes why the ASE band seems to suddenly emerge from, and coexist with, the fluorescence band. Fig. 1c shows the fitted α and γ spectra, and the quantity $A_i(\lambda)/\lambda^4$, which is proportional to the stimulated emission cross-section. As can be clearly seen, these results point to the presence of reabsorption (due to overlap of α and $A_i(\lambda)/\lambda^4$), and a very strong ESA band almost overlapping with the fluorescence window, as evidenced by the negative values in γ . These two effects combined explain why the ASE band is shifted with respect to the fluorescence one. The origin of the background fluorescence signal can be understood attending to the timescales of the pumping and relaxation processes. CsPbBr₃ NCs display a multiexponential fluorescent decay, with a short lifetime component (sub-nanoseconds) ascribed to a short-range energy migration of localized excitons, and a long lifetime component (tens to hundreds of nanoseconds) due localized excitons delayed by the activation of a long-range diffusion process. As the pump pulse duration to study ASE in this work (~3 ns) is larger than the lifetime of the short-lived localized excitons, the PL signal generated by these should contribute mostly with ASE. In contrast, the long-lived excitons, with a lifetime much longer than the pulse width, cannot participate in the ASE process, and only provide a fluorescence signal. As this signal accounts for a large percentage of the total emission, the acquired PL spectra displays a huge contribution of excess background fluorescence. Finally, there are other minoritarian processes contributing to the excess fluorescence, like the excitation of two waveguide polarization modes, and time-domain effects related to the pulsed excitation.

In conclusion, the results in this work establish guidelines to analyse the optical gain in perovskite samples, help in understanding the photophysics behind their ASE signatures, and provide insights to boost their lasing efficiency.

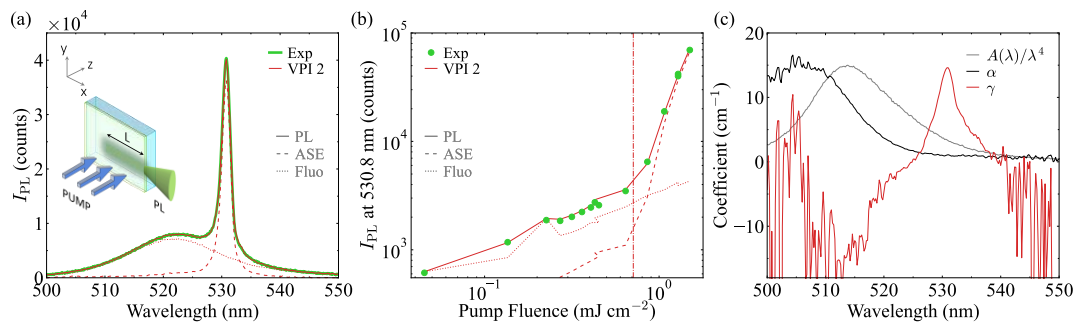


Figure 1: a) Experimental PL spectrum (solid green line) above threshold, and best fit of VPI 2 (solid red line). The dashed and dotted red lines show the contributions of pure ASE and background fluorescence, respectively. Inset: Schematics of the experimental configuration to measure ASE. b) Experimental PL intensity at peak wavelength vs. pump fluence (green points) and best fit of VPI 2. Same colours and line styles code than in a). c) Losses coefficient α (black line) and gross gain γ spectra (red line) obtained from VPI 2, stimulated emission cross section spectrum $A_i(\lambda)/\lambda^4$ in arbitrary units (gray line).

References

- [1] Y. Wang, X. Li, J. Song, L. Xiao, H. Zeng, H. Sun, “All-Inorganic Colloidal Perovskite Quantum Dots: A New Class of Lasing Materials with Favorable Characteristics” *Adv. Mater.* **27**, 44 7101 (2015)
- [2] S. Yakunin, L. Protesescu, F. Krieg, M. I. Bodnarchuk, G. Nedelcu, M. Humer, G. De Luca, M. Fiebig, W. Heiss, M. V. Kovalenko, “Low-threshold amplified spontaneous emission and lasing from colloidal nanocrystals of caesium lead halide perovskites” *Nat. Commun.* **6**, 1 8056 (2015)
- [3] J. Navarro-Arenas, I. Suárez, V. S. Chirvony, A. F. Gualdrón-Reyes, I. Mora-Seró, J. Martínez- Pastor, “Single-Exciton Amplified Spontaneous Emission in Thin Films of CsPbX₃ (X = Br, I) Perovskite Nanocrystals” *J. Phys. Chem. Lett.* **10**, 20 6389 (2019)
- [4] S. Milanese, M. L. De Giorgi, M. Anni, M. Bodnarchuk, and L. Cerdán, “Rationalizing the Amplified Spontaneous Emission Mechanism in CsPbBr₃ Perovskite Nanocrystals Films by means of Optical Gain Measurements”, *submitted*
- [5] Q. A. Akkerman, T. P. T. Nguyen, S. C. Boehme, F. Montanarella, D. N. Dirin, P. Wechsler, F. Beiglböck, G. Rainò, R. Erni, C. Katan, J. Even, M. V. Kovalenko, “Controlling the nucleation and growth kinetics of lead halide perovskite quantum dots,” *Science* **377**, 6613 (2022)

Si Photodiode Reflectance Measurements in the Ultraviolet

Authors: Rubén Gómez^{1*}, Cagri Kaan Akkan², Ozcan Bazkir², Joaquín Campos¹

¹ Instituto de Óptica, Consejo Superior de Investigaciones Científicas (CSIC), C. de Serrano 144, 28047 Madrid, Spain.

² National Metrology Institute (UME), TÜBİTAK Gebze Yerleşkesi, 41470 Türkiye.

*E-mail: ruben.gomez@io.cfmac.csic.es

1. Introduction

The spectral responsivity of a photodiode is determined from its reflectance $\rho(\lambda)$ and internal quantum efficiency $\varepsilon(\lambda)$ by the equation

$$R(\lambda) = [1 - \rho(\lambda)] \cdot \varepsilon(\lambda) \lambda / k \quad (1)$$

Recently, an inversion layer Si photodiode with an internal quantum efficiency that differs from unity by a few p.p.m. and with a low reflectance in the visible spectral range has been developed (chipS-CALe photodiode), thus achieving an absolute radiometer in that spectral range [1]. The follow up project “S-CALe Up” (EPM 22IEM06) attempts to extend the validity of this absolute radiometer to the entire Si photodiode response range.

In this work, the measurements of reflectance performed between 250 nm and 1000 nm by project partners CSIC and UME on previously produced chipS-CALe photodiodes, which had only been studied in the visible range, will be presented, as well as the comparison of the results obtained by the institutes and the methodologies used for the acquisition of the measurements.

2. Methodology

Setup scheme used by UME for reflectance measurements is shown in Fig. 1. Light coming out of the monochromator goes through a chopper and then through a Glan-Laser alpha-BBO polarizer, coated for the range from 210 nm to 450 nm to improve transmittance. To check the polarization states *S* or *P*, a polarization beam splitter and a photodiode that receives the radiation reflected by the beam splitter are used, so that the maximum signal of the photodiode corresponds to the *S* state while the minimum corresponds to the *P* state. After setting the polarizer position the beam splitter is removed from the optical path.

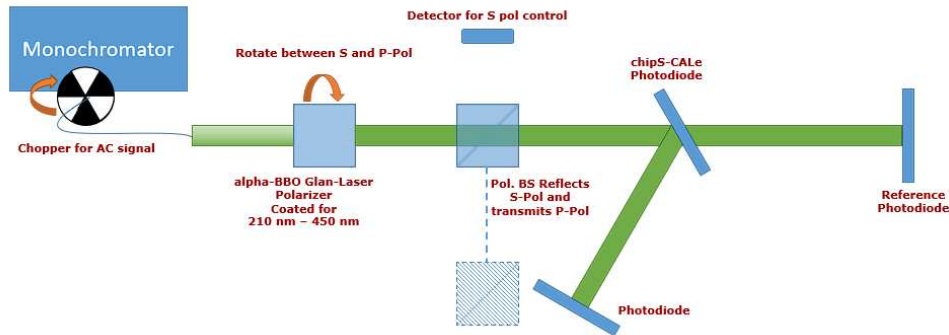


Figure 1. Scheme of the reflection measurement setup of TÜBİTAK.

Incident light is measured with the reference photodiode, while reflected radiation is measured with the photodiode in the lower part of the diagram. The chipS-CALe photodetector, whose reflectance is to be measured, is rotated to four different angles (7° , 15° , 30° and 45°) with respect to the incident beam.

As for the measurements performed in CSIC-Institute of Optics, a Lambda 900 spectrophotometer from PerkinElmer is used along with its Universal Reflectance Accessory (URA). The chipS-CALe photodetector is placed on the sample port, facing down to the incoming beam whose polarization state may be set to unpolarized, *S* or *P*. Measurements for angles of 8° , 15° , 30° and 45° were done.

3. Results

Reflectance results for P -polarized and S -polarized light are represented in graphs of Fig. 2, along with the unpolarized light measured by CSIC.

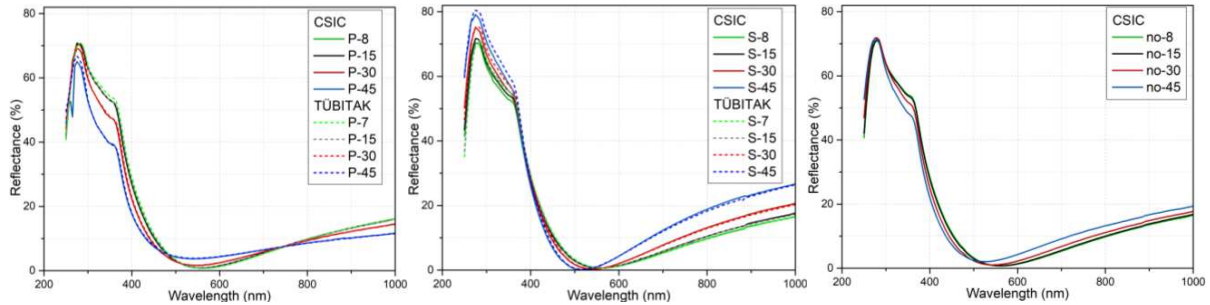


Figure 2. Spectral reflectance for P -polarized, S -polarized and unpolarized light at different incidence angles.

To compare measurements done in both laboratories, the ratio between the CSIC values and TUBITAK values are shown in Fig. 3 for common incidence angles and polarization states.

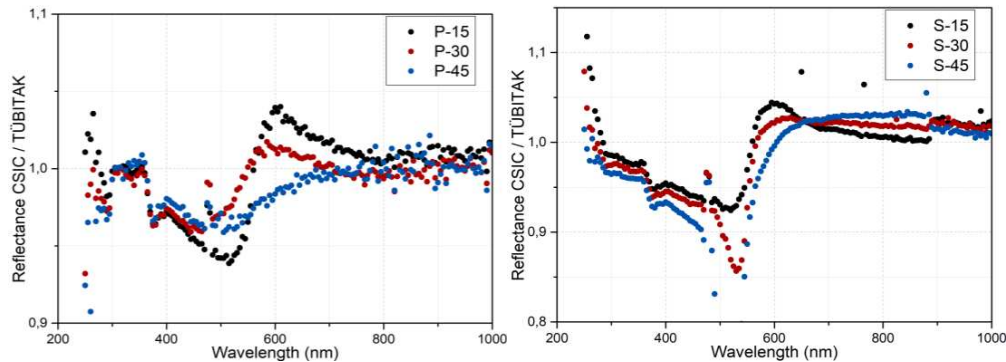


Figure 3. Comparison between CSIC and TUBITAK measurements for P -polarized and S -polarized light.

4. Conclusions

Measurements from TUBITAK and CSIC agree reasonably well considering the measurement uncertainty of each of them, except in the region from 400 nm to 600 nm, where the reflectance reaches a very low value, causing the relative difference to be greatly increased. However, in that region the differences are also within the measurement uncertainty of the laboratories. It is not expected that the difference is due to the fact that the same sample was not measured in both laboratories, so there must be some systematic error that will have to be clarified. In this sense, it is noteworthy that the measurements for P -polarization differ more than those for S -polarization, with no major reflectance differences.

Lastly, unlike the region of visible light (and specially the green-yellow region, 500 nm - 600 nm), where the reflectance is very low, this parameter is very high in the UV, so the efficiency of the photodetector in that area will be insufficient. A new multilayer scheme will have to be studied in order to reduce the reflectance of the photodiode.

Acknowledgments

This work has been carried within the project 22IEM06 S-CALe Up, funded by the EPM, co-financed from the European Union's Research and Innovation Programme Horizon Europe and by the Participating States.

References

- [1] O. Koybasi et al., *High Performance Predictable Quantum Efficient Detector Based on Induced-Junction Photodiodes Passivated with SiO₂/SiNx*, Sensors, 21(23), 7807.

Reflectancia de materiales de enfriamiento radiante pasivo

Joaquín Campos^{1*}, Alejandro Ferrero¹, Miguel Gómez¹, Gloria Pérez² y Eduardo González-Cruz²

¹Instituto de Óptica “Daza de Valdés”, CSIC, C/. Serrano, 144, 28006 Madrid

²Instituto de Ciencias de la Construcción “Eduardo Torroja”, CSIC, C/. Serrano Galvache, 4, 28033, Madrid

*E-mail: joaquin.campos@csic.es

1. Introducción

El enfriamiento radiante es un proceso pasivo producido por la diferencia de temperatura entre los objetos en la superficie de la Tierra (≈ 300 K) y el espacio exterior (≈ 3 K). Para que se produzca enfriamiento radiante diurno, la ganancia de calor debido a la absorción solar y atmosférica, así como a la convección y conducción, deben ser menores que el flujo radiado por la superficie. Por tanto, la caracterización de estos materiales requiere la medida de la reflectancia en el intervalo solar, (300 – 2500) nm, y la medida de su emitancia en el rango de 10 μ m.

Este proceso de enfriamiento es particularmente útil para disipar calor (independientemente de las condiciones climáticas) en: procesos industriales, plantas de energía y centros de datos o edificios (responsables del 40% del consumo energético y del 36% de las emisiones de gases de efecto invernadero en la UE, aproximadamente).

En este trabajo se presenta la medida de la reflectancia de tres materiales usados en enfriamiento radiante pasivo que han sido seleccionados en el proyecto 21GRD03 PaRaMetriC, de la convocatoria 2021 del programa Partenariado Europeo en Metrología. Estos materiales se conocen como GEN 4 (fabricado por 3M), Spacecool (fabricado por Space Cool Inc.) y V98RF (fabricado por Cooling Photonics).

2. Medidas realizadas

Se ha medido la reflectancia 0° :d, incluyendo la componente especular, de dos muestras de cada uno de los materiales anteriores en el intervalo espectral de (300, 2450) nm. Las medidas se han realizado tanto usando un espectrofotómetro de alta gama con su accesorio de esfera integradora (Lambda 1050 de PerkinElmer con esfera de 60 mm de diámetro), como con un espectrofotómetro portátil que consta de una esfera integradora de 50 mm de diámetro de la marca Ocean Insight y dos espectrómetros de fibra óptica de la marca Stellarnet: Dwarf-Star para el rango espectral (900-1700) nm y Black Comet para el rango (200-1080) nm. En este equipo se utiliza una lámpara halógena de alta potencia HL-2000 de Ocean Insight y fibras ópticas con un diámetro de 600 μ m para irradiar la muestra situada en el puerto de entrada de la esfera. Este equipo se usa en medidas de campo de materiales instalados en edificios. También se ha medido la función de distribución de reflectancia bidireccional (BRDF) de las mismas muestras para estudiar la distribución espectral y angular de la radiación reflejada.

Algunos resultados obtenidos se muestran en las figuras siguientes. En la figura 1 se muestra la medida de reflectancia 0° :d. para los materiales GEN4 y SpaceCool. En la izquierda se muestra el resultado de la medida realizada con el espectrofotómetro de alta gama (IO), mientras que en la parte derecha se muestra la diferencia entre el equipo portátil (IETCC) y el anterior. Se observa que las muestras tienen una muy alta reflectancia y que las diferencias entre los dos equipos dependen tanto de la muestra como de la longitud de onda.

En la figura 2 se muestra el valor promedio espectral de la BRDF en función del ángulo de observación de las muestras medidas. Cada trazo corresponde a un ángulo de incidencia diferente. Se observa en la Fig. 2 que el material GEN 4 presenta una distribución angular más próxima a la de un difusor perfecto, reflejando en todas las direcciones, mientras que el material Spacecool presenta una componente de reflectancia especular muy importante. Posiblemente esto hace que la diferencia entre métodos de medida sea mayor para la muestra Spacecool. Los resultados para V98RF son similares a los de Spacecool.

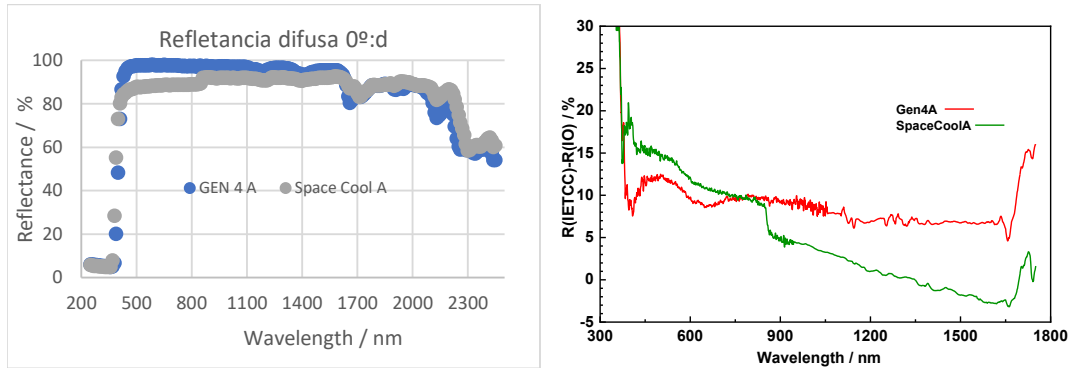


Figura 1. Refletancia difusa espectral de los materiales estudiados

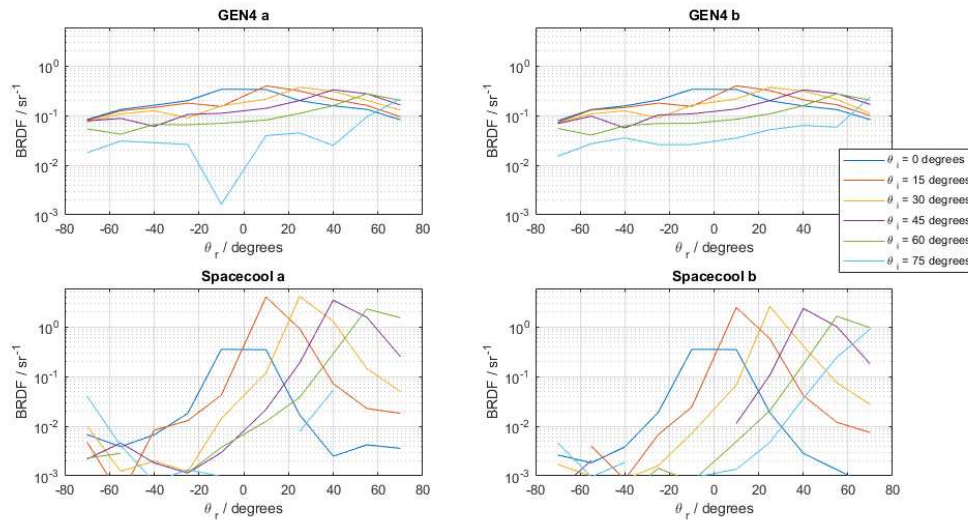


Figura 2. Valores promedio espectrales de BRDF de algunas muestras medidas

3. Conclusiones

Los materiales estudiados presentan una alta reflectancia en el intervalo espectral de 450 nm a 1600 nm aproximadamente, por lo que reflejan la mayor parte del espectro solar y tienen un comportamiento espectral muy similar en todo el rango estudiado. Los valores de reflectancia medidos con el equipo portátil difieren de los medidos en el espectrofotómetro de alta gama en hasta aproximadamente 15 %, por lo que debe haber un error sistemático en el método de medida que debe ser estudiado y corregido.

La principal diferencia entre los materiales está en la distribución angular de la radiación reflejada. Uno lo hace de forma más difusa, enviando radiación en todas direcciones, mientras que los otros lo hacen en forma más direccional, debido a su estructura de multicapas. Esto puede ser relevante cuando se consideran aspectos de confort tanto visual como térmico en su uso en fachadas de edificios.

Agradecimientos

Este trabajo se ha desarrollado en el proyecto 21GRD03, PaRaMetric, de la convocatoria 2021 del programa “European Partnership in Metrology”, financiado por la Unión Europea, dentro del programa marco de investigación e innovación *Horizonte Europa*, y los estados participantes en el partenariado.

Femtosecond laser ablation in 3D-printed biopolymeric scaffolds to increase cell adhesion for bone tissue regeneration purposes

Yago Radziunas-Salinas^{1,3}, Bastián Carnero^{1,3}, María Pita-Vilar^{2,3}, Lucía Aboal-Castro^{2,3}, Luis Antonio Díaz-Gómez^{2,3} and María Teresa Flores-Arias^{1,3*}

¹ Photonics4Life Research Group, Applied Physics Department, Facultade de Física and Facultade de Óptica e Optometría, Universidade de Santiago de Compostela, Campus Vida, E15782 Santiago de Compostela, Spain.

² Department of Pharmacology, Pharmacy, and Pharmaceutical Technology, I+D Farma (GI-1645), Facultade de Farmacia, and Health Research Institute of Santiago de Compostela (IDIS), Universidade de Santiago de Compostela, E15782 Santiago de Compostela, Spain

³ Instituto de Materiales (iMATUS), Universidade de Santiago de Compostela, E15782 Santiago de Compostela, Spain.

*E-mail: maite.flores@usc.es

1. Introduction

With the aim of improving the effectiveness of medical treatments, tissue engineering emerges as a discipline combining new devices and methods to regenerate and repair both tissues and organs. Bones are strongly benefited from these technologies, especially in the case of severe fractures, as they lose their self-regeneration capability. To address this issue, biopolymers are starting to be proposed in the form of shape-variable 3D implants called scaffolds. These biocompatible platforms have the potential to attach cells from the patient onto them and to be implanted in the affected area, triggering its regeneration. Nonetheless, one of the biggest challenges in the field is to enhance cell adhesion over these biopolymers and consequently, to accelerate the regeneration process in terms of cell growth. For its part, laser microtexturing has showcased its potential in many fields, enabling the superficial patterning of materials with different composition, size and shape. Femtosecond Pulsed Laser Ablation (fs PLA) allows performing a high-precision micropatterning with minimal debris and thermal stress [1]. These characteristics are of great interest for polymers, provided their tendency to melt and scatter the material [2] under long pulse duration technologies, such as picosecond or nanosecond ablation [3].

In this work, photonics technologies and tissue engineering are combined through a two-step process comprising the design and printing of layer-by-layer 3D biopolymeric scaffolds along with the change of their morphology employing fs PLA. Its final goal is to evaluate whether an improvement in terms of cell adhesion arises due to the micropattern performed on the surfaces from the scaffold.

2. Materials and Methods

The manufacture of the micropatterned scaffolds is composed of two processes, as depicted in Fig. 1 a). First, the 3D printing of the layer-by-layer scaffold via Fused Deposition Modelling (FDM), where 400 μm width Polycaprolactone (PCL) fibres were deposit to print each layer.

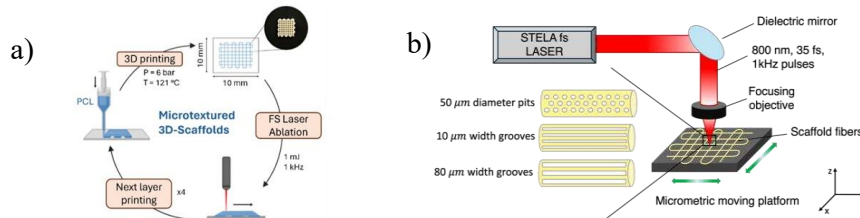


Figure 1 Methods followed to design the micropatterned scaffold. a) global processes and b) fs PLA mechanism

Once the layer was printed, its fibres were micropatterned employing fs PLA. For this purpose, the STELA femtosecond laser from the Laser Laboratory for Acceleration and Applications (L2A2) facilities from University of Santiago de Compostela was used. The main characteristics of the pulses comprise a pulse duration of 35 fs, an energy of 1 mJ, a repetition rate of 1 kHz, a central wavelength in the infrared regime of 800 nm with a bandwidth of 75 nm.

Finally, once all the layers were ablated, an *in vitro* cell culture was performed. Stem cells were attached on their surface under dynamic conditions and a differentiation assay from stem cells to osteoblasts was performed. Fluorescence confocal microscopy allowed to analyse cell adhesion after a drying process.

3. Results and discussion

An analysis of the ablation profile on the biopolymer was carried out employing different optical techniques. With microcomputed tomography (Micro-CT) was possible to verify the effect of the femtosecond microtexturing on the PCL fibres surface, as depicted in Fig. 2. Three different micropatterns were evaluated, including micropits of 50 μm diameters (Fig. 2a) and grooves in two energetic regimes, with 10 and 80 μm width (Fig. 2 b,c). In the three scenarios, Micro-CT confirms the non-destructive effects of fs PLA in polymeric samples as PCL, yielding to neat outcomes, without redeposit nor debris on the surfaces. Furthermore, the ablation pattern keeps unalterable among the layers, showing that FDM do not alter the texturization performed in the prior layers. Finally, the grooves ablation profiles are dependent to the beam laser energy: higher energies (80 μm grooves) manifest a gaussian profile compared to lower energies (10 μm grooves), exhibiting a rectangular profile.

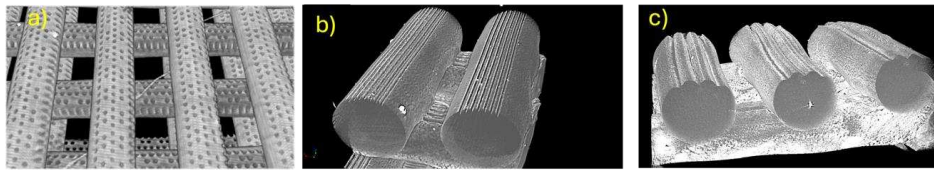


Figure 2 Micro-CT reconstructions of the microtextured scaffolds. a) micropits, b) 10 μm and c) 80 μm grooves

Once the scaffolds were ablated, an evaluation of their attachment efficacy was done. Fig. 4 shows the cell adhesion difference according to the pattern when comparing plain control scaffolds (Fig. 3a) with micropitted (Fig. 3b) and microgrooved (Fig. 3c,d) samples. In the former case, cells attach randomly on the fibre whereas in the patterned samples they tend to attach on the pits and along the grooves.

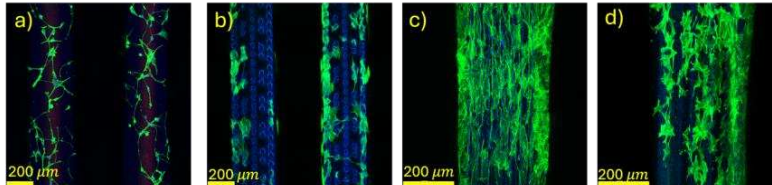


Figure 3 Stem cell differentiation assay on a) plain, b) micropitted, c) 10 μm grooved and d) 80 μm grooves scaffolds

4. Conclusions

The current work presents the effects of cell adhesion on PCL scaffolds after modifying their morphological properties with fs PLA compared to plain scaffolds. Ablation patterns are clean, avoiding PCL melting and the appearance of stress on the material. The improvements in cell attachment and growth are noteworthy in the microtextured samples. In the micropitted scaffolds, cells tend to attach on the pits, adapting their shape to the geometry of the pattern. In the case of grooves, there is a notable shift in the orientation of preosteoblastic cells towards the direction of ablation, resulting in an enhanced cell density. These findings stress the importance of micropatterns in influencing cell adhesion and proliferation when their sizes are alike to the cell dimensional range.

Acknowledgements

Work supported by contracts: ED431B 2023/07 Xunta de Galicia and RTI2018-097063-B-I00 AEI. B. Carnero acknowledges GAIN/Xunta de Galicia for contract 11-IN606D-2021-2604925. Y. Radziunas-Salinas acknowledges Ministerio de Ciencia, Innovación y Universidades for contract FPU22/01231.

References

1. S. Koo, S.M. Santoni, B.Z. Gao et al. "Laser-assisted biofabrication in tissue engineering and regenerative medicine" *Journal of Materials Research* vol. 32, 1 (2017): 128-142
2. M. Aymérich, M.T. Flores-Arias, C. Molpeceres et al. "Comparison among Microchannels fabricated by Nano, Pico and Femtosecond-laser technologies for Microfluidic Applications" *FiO 2017*
3. S. Ravi-Kumar, B. Lies, H. Lyu, H. Qin, *Procedia Manufacturing*, **34**, 316-327 (2019)

Multispectral imaging to train deep learning algorithms for the discrimination of skin cancer lesions: a preliminary study

Laura Rey-Barroso^{1*}, Francisco J. Burgos-Fernández¹, Santiago Royo¹, Susana Puig², Josep Malvehy², Giovanni Pellacani³, Ilze Lihacova⁴, Andrey Bondarenko⁵ and Meritxell Vilaseca¹

¹*Centre for Sensors, Instruments and Systems Development, Technical University of Catalonia, Rambla Sant Nebridi 10, 08222 Terrassa, Spain*

²*Dermatology Service of the Clinic Hospital of Barcelona, C. Villarroel 170, 08036 Barcelona, Spain*

³*Università di Modena e Reggio Emilia, Via del Pozzo 71, 41124 Modena, Italy*

⁴*Institute of Atomic Physics and Spectroscopy, University of Latvia, 1004 Riga, Latvia*

⁵*Faculty of Computer Science and Information Technology, Riga Technical University, 1048 Riga, Latvia*

*E-mail: laura.rey.barroso@upc.edu

1. Introduction

An estimated 60,000 people succumb to skin cancer annually, predominantly from melanoma. Diagnosis primarily involves visual inspection, but around half of lesions pose diagnostic challenges, necessitating surgical biopsy. To address this, non-invasive detection methods such as Computer-Aided Diagnosis (CAD) utilizing deep learning (DL) are gaining prominence. Most DL algorithms are based on convolutional neural networks (CNNs) to automate lesion classification, including pre-processing and feature extraction. CNNs can be trained to classify skin lesions with datasets of diverse nature. The majority of works use high quality medical RGB images [1], like the ones provided by large data repositories such as ISIC (with 71,023 dermoscopic images), PH2, DermQuest, DermIS, HAM10000, etc. There are far fewer studies utilizing multispectral (MS) images for skin cancer lesion classification, but recent works have yielded promising results (with accuracies up to 80% [2, 3]), despite the smaller number of images (of the order of 1,000) they contain compared to large public repositories of RGB images. MS imaging, specifically, provides detailed pixel-wise information on skin chromophore absorption properties. By having a greater number of images for each lesion with varied skin information relative to each chromophore, the use of MS images could be considered as a form of non-artificial image augmentation. In this study, we aimed to train a custom CNN using a dataset of MS images of skin lesions, and then retrain the same neural network using only 3 images from the MS set (the ones closest to RGB wavelengths to simulate conventional color images) to compare classification performance on a set of unseen test images when adding spectral information rather than only using color.

2. Multispectral system and dataset

Authors typically prioritize melanoma detection, particularly distinguishing it from melanocytic nevi, which bear a similar appearance. Basal cell carcinomas (BCCs), the most common non-melanocytic skin cancers, are also addressed in lesion classification tasks. Hence, with our MS system, we obtained and processed MS images of 327 nevi (including melanocytic) and 182 malignant lesions (including melanomas and BCCs). For each lesion, a spectral cube of 8 wavelengths ranging from 414 nm to 995 nm was acquired (Figure 1), using a MS system based on multiplexed LED illumination and a 12-bit depth monochromatic camera with a resolution of 1280 x 960 pixels. The MS images of the lesions were collected at two hospitals^{2,3} and patients provided written informed consent according to the principles outlined in the 1975 Declaration of Helsinki (revised in Tokyo in 2004).

3. Data preprocessing, CNN and search for the best training strategy

The spectral images were converted into reflectance images with values ranging from 0 to 1 after being calibrated with a standard gray sample (Neutral 5, X-Rite ColorChecker®). Lesion segmentation from the surrounding healthy skin was not performed, but the images were artificially augmented using rotations and flips. Other types of data augmentation were avoided to prevent alteration of the grayscale values of the images. Reflectance cube images were resized to be square, 128 x 128 pixels, as input into

the CNN. It was found that using a higher resolution did not improve the results. A customized CNN based on VGG-16 model with three-dimensional (3D) convolutional layers (Figure 1) was trained from scratch. The dataset of images was highly imbalanced, with a ratio of 4:1 for nevi to malignant lesions. Initially, a custom function was used to generate class weights for weighting the loss during training; however, this imbalance was likely to bias the model's learning. Therefore, a balanced subset of the data was created by downsampling the dataset to 70 nevus, 70 melanoma, and 70 BCC samples. Twenty percent of the images were reserved for testing and were not seen during training. The remaining 80% were used in an 8-fold cross-validation scheme, with a proportional number of samples. It was found that the training strategy yielding the best results was retraining the models with each new fold of data. Hyperparameters' fine-tuning was carried out by following a random grid search strategy prior to the final training instances. The combination of a batch size of 4 (a larger batch size did not yield improvement), learning rates ranging from $5 \cdot 10^{-5}$ to $5 \cdot 10^{-6}$, 100 epochs, and RMSprop as optimizer was found to be optimal.

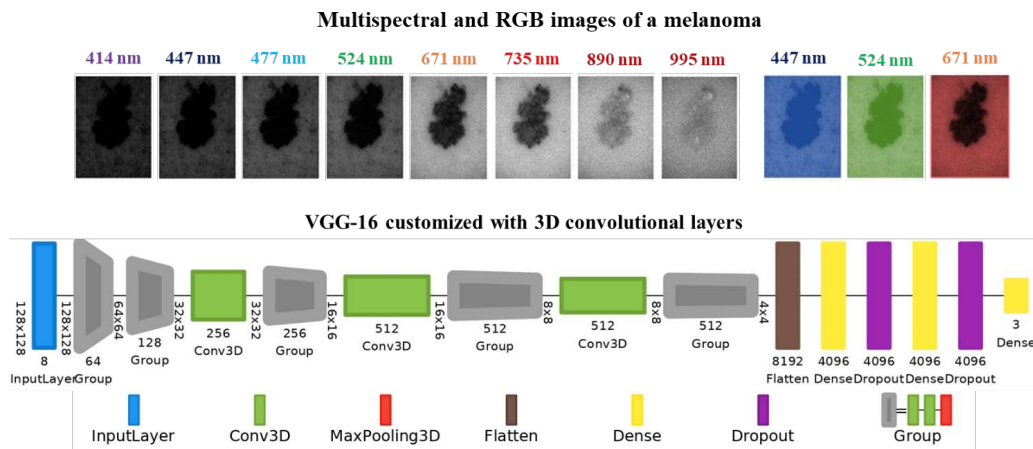


Figure 1 MS and RGB images of a melanoma and CNN.

4. Results and conclusions

To check if having an MS set of images instead of a set of RGB images improves the learning of the model, the CNN VGG-16 was trained first, with the spectral cubes of the skin lesions containing the 8 images, and then with the spectral cubes containing only 3 images corresponding to the wavelengths 477 nm, 524 nm and 671 nm. Each type of training instance was launched 5 times and the results were averaged.

It was found that the classification accuracy obtained in the first case was much higher, obtaining 71% compared to second type of training instances, in which a 47% was obtained. Therefore, we can conclude that spectral information does provide something more than just using color or morphological information, so that the training of the CNN is better.

Acknowledgments

Funded by MCIN/AEI/10.13039/501100011033 (PID2020-112527RB-I00).

References

- [1] M.F. Jojoa-Acosta, L.Y.C. Tovar, M.B. Garcia-Zapirain and W.S. Percybrooks, "Melanoma diagnosis using deep learning techniques on dermatoscopic images", *BMC Med. Im.*, **21**(1), 6 (2021)
- [2] I. Lihacova, A. Bondarenko, Y. Chizhov, D. Uteshev, D. Bliznuks, N. Kiss and A. Lihachev, "Multi-Class CNN for Classification of Multispectral and Autofluorescence Skin Lesion Clinical Images", *J. Clin. Med.*, **11**(10), 2833 (2022)
- [3] M. La Salvia, E. Torti, R. Leon, H. Fabelo, S. Ortega, F. Balea-Fernandez, B. Martinez-Vega, I. Castaño, P. Almeida, G. Carretero, J.A. Hernandez, G.M. Callico, F. Leporati, "Neural Networks-Based On-Site Dermatologic Diagnosis through Hyperspectral Epidermal Image", *Sensors*, **22**, 7139 (2022)

Manufacturing protocols for straight micromixers combining stereolithography and pulsed laser ablation

Bastián Carnero^{1,2}, Yago Radziunas-Salinas¹, Bruno K. Rodiño-Janeiro², Sylvana Varela Ballesta^{2,3} and M. Teresa Flores-Arias^{1,*}

¹*Departamento de Física Aplicada, Photonics4Life research group, Facultade de Física, iMATUS, Universidade de Santiago de Compostela, Campus Vida, E-15782 Santiago de Compostela, Spain*

²*BFlow SL, Edificio Emprendia, Santiago de Compostela, 15706, Spain*

³*Departament d'Enginyeria Mecànica, Universitat Rovira i Virgili, Tarragona, 43007, Spain*

*e-mail: maite.flores@usc.es

1. Introduction

Microfluidics is a growing multidisciplinary field that focuses on manipulating and controlling small fluid volumes, typically at microliter scales, drawing considerable attention across diverse fields like biomedicine, engineering, and chemistry. A pivotal challenge in microfluidics lies in achieving effective fluid mixing, given the low Reynolds number. Several strategies, such as employing microstructures, have been devised to improve mixing efficiency.

Traditionally, photolithography served as the primary method for structuring substrates, despite its drawbacks such as intricate and time-consuming prototyping processes and the generation of hazardous chemical waste. However, laser technologies like stereolithography (SLA) and Pulsed Laser Ablation (PLA) have emerged as reliable and user-friendly alternatives for microfluidics devices manufacturing. SLA 3D printers utilize selective photopolymerization of liquid resins to craft highly detailed 3D objects with resolutions in the hundreds of microns range. PLA employs pulsed lasers to micro-pattern 2D surfaces with resolutions in the tens of microns range.

This study integrates both SLA and PLA technologies to fabricate a complex microfluidics device: a straight micromixer. Each technology is used in its most suitable dimensional range [1].

2. Materials and Methods

2.1 3D Printer

A Formlabs Form 3B SLA printer was used to produce a substrate featuring 550 μm inward and outward square channels on its surface. Commercial Model resin from Formlabs was selected as printing resin given the precision it offers and its performance when replicating polymers.

2.2 Pulsed Laser Ablation

PLA of the bottom of the 3D printed microchannel was performed using the Santiago TeraWatt Laser (STELA) of the Laser Laboratory for Acceleration and Applications (L2A2) facility at Santiago de Compostela. This laser offers 1 mJ of energy per pulse, 35 fs of pulse duration, a fixed repetition rate of 1 kHz and 800 nm of wavelength with a bandwidth of 75 nm.

3. Results and discussion

PLA allows the creation of various micropatterns on resin surfaces. Optimal parameters for regular, homogeneous channels were identified as 90 mW, repetition rate of 1kHz, 1mm/s of platform velocity and 2 passes, resulting in channels with a width of $39.6 \pm 1.9 \mu\text{m}$ and a depth of $129.1 \pm 2.3 \mu\text{m}$. To enhance fluid flow and proper polydimethylsiloxane (PDMS) removal, wider channels were desired, achieved by ablating two or more contiguous lines with varying separations. The results showed that ablating three contiguous lines with a 35 μm separation provided the most suitable channels, with a width of $95.5 \pm 5.2 \mu\text{m}$ and a depth of $230.9 \pm 4.7 \mu\text{m}$.

Using these parameters, two manufacturing protocols were developed, with the goal of obtain various groove patterns with different orientations in the channels (that will enhance mixing). Protocol 1 is focused on micropatterning the bottom of inward channels using PLA (Fig. 1a-h), to be sealed directly with adhesive film for immediate use. In the case of 90° oriented structures (Fig. 1b,f), images revealed consistent groove formation, featuring a width of $94.3 \pm 8.3 \mu\text{m}$ and depth of $243.5 \pm 15.5 \mu\text{m}$. For 20° structures (Fig. 1c,g), narrower grooves ($86.6 \pm 4.0 \mu\text{m}$) were observed due to overlapping lines and showed a greater depth ($253.3 \pm 11.1 \mu\text{m}$). For 45° structures (Fig. 1d,h), an intermediate scenario was obtained. Protocol 2 starts with the creation of grooves on the top of outward channels (Fig. 1i-k) using PLA for subsequent replication through PDMS soft lithography (Fig. 1l-n), facilitating scalable production. For 90° orientation (Fig. 1l,l), proper groove formation ($W=123.0 \pm 4.8 \mu\text{m}$) is achieved. In this protocol, grooves in the master become ridges in the replicas and vice versa. The depth of master grooves is notably greater ($301.3 \pm 9.9 \mu\text{m}$) than that obtained in Protocol 1, since ablation on an elevated structure increases to debris release. Figures show a 3D confocal view of successful master-to-replica transfer and show similar surface roughness, demonstrating high the replication capability of PDMS.

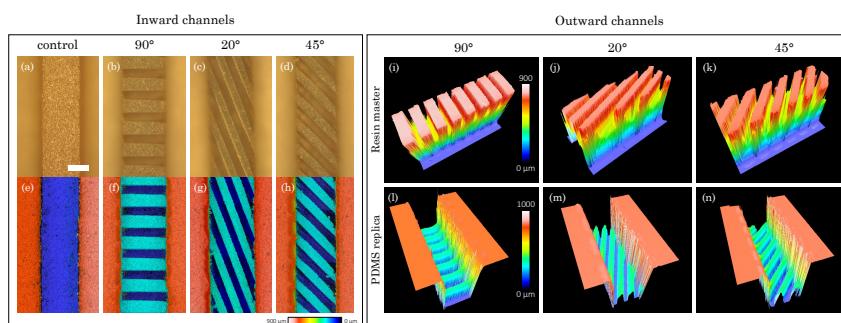


Figure 1 a-h) Optical (top) and confocal (bottom) microscope images of the micropatterned structures on the bottom of 3D printed microchannel, featuring: a), e) none, b), f) 90°, c), g) 20°, and d), h) 45° oriented grooves, respectively. Scale bar: 300 μm . Magnification: 5X. i-n) 3D Confocal view of the micropatterned structures on the top of printed microchannel (top)(i-k) and their corresponding PDMS replicas (bottom)(l-n) featuring: i), l) 90°; j), m) 20°, and k), n) 45° oriented grooves.

Flow experiments and computer fluid dynamic simulation were performed for the manufactured micromixers. Both showed that microstructures enhance mixing compared to flat channels (Fig. 1a,e), with lower angles contributing to better mixing

4. Conclusions

In conclusion, combining technologies like SLA and PLA enables the fabrication of intricate microfluidic devices like straight micromixers. Through precise parameter optimization and manufacturing protocols, efficient micropatterning of channels was achieved, enhancing their mixing performance. Micromixers were validated via flow experiments and simulations.

Acknowledgments

This work has been supported by contracts: PID2022-138322OB-100 MCIN/AEI/10.13039/501100011033/FEDER, UE and Consellería de Educación Xunta de Galicia/FEDERED431B 2023/07. B. Carnero acknowledges GAIN/Xunta de Galicia for contract 11-IN606D-2021-2604925. Y. RadziunasSalinas acknowledges Ministerio de Ciencia, Innovación y Universidades for contract FPU22/01231.

References

- [1] B. Carnero et al. "Versatile hybrid technique for passive straight micromixer manufacturing by combining pulsed laser ablation, stereolithographic 3D printing and computational fluid dynamics", Lab on a Chip, (2024)

Compact liquid-crystal anisotropic axicon for the generation of Bessel beams with tunable polarization transformation

María del Mar Sánchez-López^{1*}, Ignacio Moreno¹, Tomasz Jankowski², Nouredine Bennis², Anna Spadlo² and José Francisco Algorri³

¹*Instituto de Bioingeniería, Universidad Miguel Hernández, 03202 Elche, Spain*

²*Institute of Applied Physics, Military University of Technology, 00908 Warsaw, Poland*

³*Photonics Engineering Group, Universidad de Cantabria, 39005 Santander, Spain*

*E-mail: mar.sanchez@umh.es

1. Introduction

Bessel beams present unique line-focusing and non-diffracting properties that find applications in materials processing, optical trapping and free-space optical communications [1]. The most efficient way to generate a Bessel beam is through a conical lens or axicon. Axicons are commercially available, either as refractive or as diffractive optical components, but their performance parameters cannot be tuned. Instead, tunable axicons based on liquid-crystal technology have been demonstrated, either with liquid-crystal spatial light modulators (SLM) or with other liquid-crystal (LC) components [2]. However, in all these techniques the polarization state of the Bessel beam remains constant along propagation. In 2015, we proposed the concept of anisotropic axicon to modify the state of polarization (SOP) along propagation [3]. The method relies on having different propagation constants in the two orthogonal polarization components of the Bessel beam, such that there is an axial phase shift between these components. Such anisotropic axicon was demonstrated using a SLM to display two different diffractive axicons, each one affecting one of the two orthogonal linear polarization components and having a different period. Combining such axicons with spiral phases led to higher-order vector Bessel beams with periodically varying polarization along propagation [3]. Despite being extremely versatile, anisotropic axicons based on SLMs are bulky optical systems that require careful alignment. In this work we present a compact and efficient alternative that consists in cascading a LC tunable axicon with a refractive axicon. While the refractive axicon equally deflects all polarization components, the LC element adds a linear radial phase only to the polarization component parallel to the LC director. Therefore, an anisotropic axicon is effectively built that creates a Bessel beam exhibiting a SOP with tunable variation along propagation [4].

2. Compact anisotropic LC axicon and generation of a Bessel beam with polarization variation

The fabricated LC axicon only requires two voltage sources whose values were set to achieve a quasilinear birefringence across the device. In Fig.1(a-c) the LC device is viewed between parallel polarizers at 45° relative to the LC director for different applied V_{rms} voltages. The well-contrasted interference rings within an active area of radius $r_{max}=5$ mm, of almost constant separation, indicate that the phase profile $\phi(r)$ approximates rather well a linear radial phase, as required for an axicon. Note that this profile only affects the polarization component parallel to the LC director axis (vertical), for which it induces a very small radial wavenumber thus leading to a very small deflection angle. When this LC axicon is combined with a refractive axicon, the combination acts as an anisotropic axicon. When illuminated with linearly polarized light oriented at 45°, it generates a Bessel beam behind the axicon plane where the SOP changes upon propagation describing a trajectory in the Poincaré sphere along the meridian in the plane S2-S3. We combined the LC axicon with a commercial glass axicon (Thorlabs, model AX252-A) of 25 mm clear aperture and 0.9° deflection angle). Figure 1(d-e) shows the experimentally measured intensity of the Bessel beam center as a function of the propagation distance (z) when being analyzed by a circular polarizer. It shows the expected sinusoidal variation with z , and how the period of the polarization transformation can be tuned via the voltage values applied to the LC axicon. The Stokes parameters of the Bessel beam were also measured versus z . Figure 1(g) shows the experimental SOP trajectory for the case with voltages (3.0, 0.5) V_{rms} represented in the Poincaré sphere, which confirms the variation along the S2-S3 plane. Finally, we captured the Fourier transform of the optical field by adding a lens and looking at its back focal plane. Figure 1(h) shows the result when only the refractive axicon is used, showing the characteristic Durnin ring [1]. On the contrary, when the LC

axicon is added to create the compound axicon, the Durnin ring splits in two rings with a very small separation, each one with orthogonal linear polarization. Figures 1(j,k) show a zoomed image of the area indicated with the yellow square inset in Figs. 1(h,i), and clearly shows the double ring.

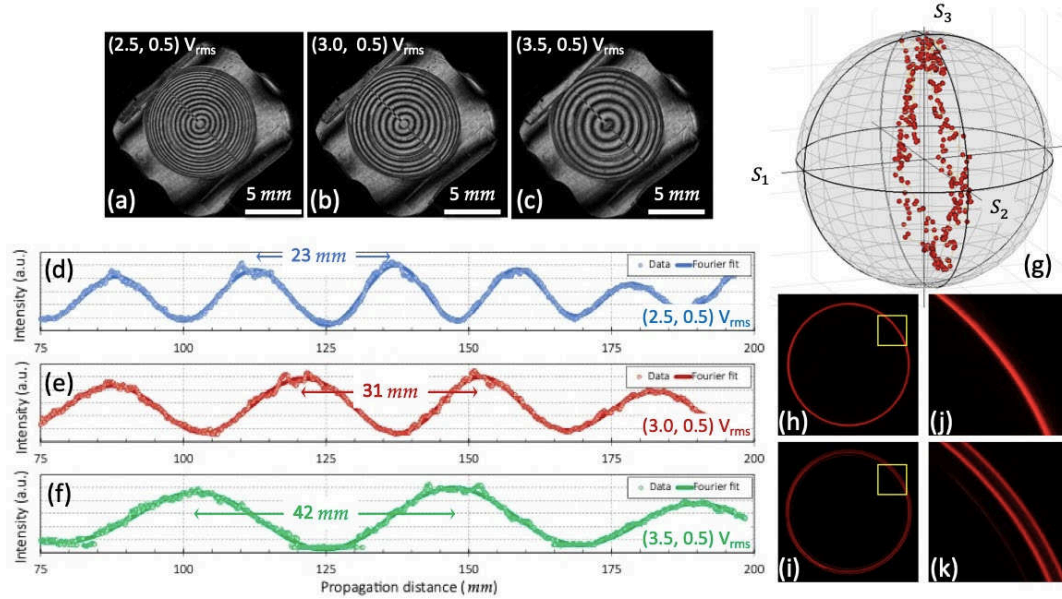


Figure 1. (a)-(c) Interference pattern for different voltages addressed to the LC axicon. (d)-(f) Intensity along propagation distance for the compound refractive-LC axicon with circular analyzer in front of the camera. The arrows indicate the theoretical periods. (g) SOP trajectory derived from the measured Stokes parameters corresponding to (3.0, 0.5) V_{rms} . (h)-(k) Polarization splitting at the Fourier plane of the axicon ring.

3. Conclusions

In summary, we have demonstrated a compact anisotropic axicon with tunable longitudinal polarization modulation of the generated Bessel beam. It consists in a refractive axicon and a liquid-crystal element of linear radial phase profile that generates the collinear superposition of two orthogonally polarized Bessel beams with different propagation constant. The measured periods of the polarization modulation are tunable through voltage and match well the theoretical model. The results prove a new, compact and very efficient way of producing Bessel beams with tunable polarization modulation along the propagation axis. This capability could find applications in axial polarimetry, optical trapping in multiple planes or axial-dependent laser microfabrication.

Acknowledgments

Funding from Ministerio de Ciencia e Innovación (ref.: PID2021-126509OB-C22) and Generalitat Valenciana (ref. CIAICO/2021/276) is acknowledged.

References

- [1] D. McGloin and K. Dholakia, “Bessel beams: diffraction in a new light”, *Contemp. Phys.* **46**, 15-28 (2005).
- [2] J. F. Algorri, V. Urruchi, N. Bennis and J. M. Sánchez-Pena, “Modal liquid crystal micro-axicon array”, *Opt. Lett.* **39**, 3476-3479 (2014).
- [3] I. Moreno, J. A. Davis, M. M. Sánchez-López, K. Badham and D. M. Cottrell, “Nondiffracting Bessel beams with polarization state that varies with propagation distance,” *Opt. Lett.* **40**, 5451-5454 (2015).
- [4] T. Jankowski, N. Bennis, A. Spadlo, J. F. Algorri, M. M. Sánchez-López and I. Moreno, “Liquid crystal anisotropic axicon for the generation of non-diffracting Bessel beams with longitudinally varying polarization”, *Opt. Laser Technol.* **170**, 110255 (2024).

Pantalla LCoS alineada verticalmente y uso de órdenes superiores en una red blazed.

G. Nájjar^{1,2,*}, F.J. Martínez-Guardiola^{1,2}, A. Pérez-Bernabeu¹, A. Moya¹, A.R. Sánchez-Montes¹, S. Gallego^{1,2}, A. Márquez^{1,2}

¹*I.U. Física Aplicada a las Ciencias y las Tecnologías, Universidad de Alicante, P.O. Box 99, E-03080, Alicante, España*

²*Dept. de Física, Ing. de Sistemas y Teoría de la Señal, Universidad de Alicante, P.O. Box 99, E-03080, Alicante, España*

*E-mail: guillem.najar@ua.es

1. Introducción

La modulación espacial de frentes de onda es una característica presente muchas aplicaciones diferentes en Óptica y Fotónica [1]. Entre las diferentes opciones para dicha modulación, las pantallas de cristal líquido sobre silicio (LCoS) se han popularizado debido a su versatilidad, su eficiencia luminosa, alta resolución espacial y su capacidad de modulación sólo de fase [2]. Sus propiedades han sido ampliamente estudiadas en la literatura [3] y han demostrado ser de mucha utilidad en aplicaciones como la óptica adaptativa [4], las pantallas holográficas [5], o los multiplexores ópticos reconfigurables (ROADM) [6], entre otras. En este artículo se analiza un dispositivo LCoS de alineamiento vertical (VA-LCoS) comercial de la firma SANTEC (modelo SLM-200).

En primer lugar, realizamos una calibración completa de la pantalla para obtener el retardo introducido por la pantalla en función del nivel de gris mostrado en la pantalla. Una vez calibrada la pantalla para distintas longitudes de onda y configuraciones de la pantalla, se analizará la eficiencia en difracción de una serie de redes blazed centrándonos en su uso para elementos ópticos difractivos multiorden.

2. Experimentos y resultados

El dispositivo utilizado en el experimento, como se ha comentado, es una pantalla VA-LCoS que trabaja en reflexión, con un revestimiento antirreflectante diseñado para trabajar con longitudes de onda entre 450nm y 1600nm. Se trata de una pantalla que utiliza cristal líquido nemático alineado homeotrópicamente con una resolución de 1920x1200 píxeles, de tamaño 8 μm y un factor de llenado del 95% y con direccionamiento analógico, lo que reduce el flicker al mínimo [6], también dispone de una profundidad de color de 10bits, lo que nos permite 1024 niveles de gris distintos. Esta pantalla nos ofrece la posibilidad de configurarla para distintas longitudes de onda de forma que ajusta su respuesta al retardo en función del nivel de gris. Como fuente de luz utilizamos un láser supercontinuo NKT VARIA, de forma que podemos seleccionar la longitud de onda a utilizar,

Para medir el retardo utilizamos el método de polarimetría lineal, en el que el dispositivo se sitúa entre dos polarizadores lineales orientados perpendicular o paralelamente entre sí a 45° con respecto a las líneas neutras del VA-LCoS, con estas dos medidas se obtiene el retardo introducido [6].

En la Fig. 1 mostramos el retardo medido frente al voltaje aplicado para dos configuraciones del LCoS distintas. La señal titulada 480 (360° @ 480 nm) corresponde al retardo obtenido cuando iluminamos la pantalla, configurada para una longitud de onda de 480nm, con un haz de 480nm. Mientras que la señal titulada 480 (360° @ 1550 nm) corresponde al rango de retardo obtenido cuando iluminamos la pantalla con una longitud de onda de 480nm, pero la pantalla está configurada para una longitud de onda del infrarrojo (1550nm). Observando como el resultado es que para la segunda configuración se obtiene una variación del retardo que sigue siendo lineal pero muy por encima de los usuales 2π radianes.

A continuación, nos interesa analizar la eficiencia de difracción para los distintos órdenes de difracción cuando se muestra una red blazed en la pantalla VA-LCoS. En este experimento, capturamos varios órdenes de difracción simultáneamente utilizando una cámara como radiómetro. La cámara que utilizamos es el modelo PCO-1600 de pco.imaging. Se trata de un sistema de cámara CCD con una resolución de 1600x1200 píxeles y un tamaño de píxel de 7,4x7,4 μm^2 .

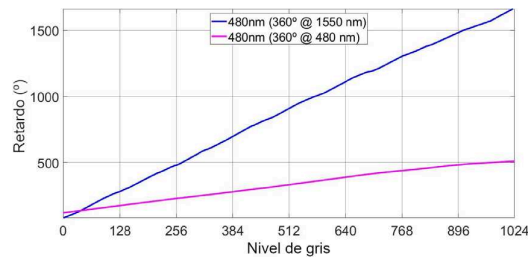


Figura 1. Retardo obtenido para las dos configuraciones de profundidad de fase y para el láser de 480.

En la figura 2, se muestran los resultados obtenidos, donde podemos ver cómo la luz se difracta hacia los órdenes superiores a medida que aumenta el retardo. Esto abre la posibilidad de utilizar órdenes superiores para transmitir información en interconexiones ópticas y la aplicación de elementos ópticos difractivos multiorden programables con pantallas VA-LCoS.

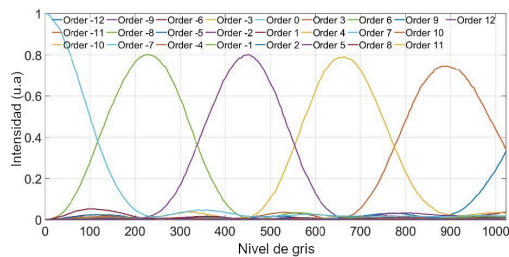


Figura 2. Eficacia de difracción para longitud de onda 480 nm y configuración (360° @ 1550 nm).

3. Conclusión

Ha quedado demostrado cómo un VA-LCoS se puede utilizar para implementar elementos ópticos difractivos con una profundidad de fase superior a 360°, y cómo el comportamiento lineal se preserva incluso si cambiamos la configuración del dispositivo para una longitud de onda diferente. Hemos mostrado algunos resultados, validando su uso para elementos ópticos difractivos multiorden.

Reconocimientos

Financiado por "Generalitat Valenciana" (España) (PROMETEO/2021/006), "Ministerio de Ciencia, Innovación y Universidades/AEI" (España) (PID2021-123124OB-I00 cofinanciado por ERDF/EU). ARS M agradece a la "Generalitat Valenciana" el contrato (GRISOLIAP/2021/106), y APB agradece al "Ministerio de Ciencia, Innovación y Universidades/AEI" el contrato (PRE22-105016).

Referencias

- [1] G. Lazarev, P.-J. Chen, J. Strauss, N. Fontaine and A. Forbes, "Beyond the display: phase-only liquid crystal on Silicon devices and their applications in photonics", *Opt. Express* 27, 16206 (2019).
- [2] S. T. Wu and D. K. Yang, *Reflective Liquid Crystal Displays* (John Wiley & Sons Inc., Chichester, (2005).
- [3] J. Frances, A. Marquez, C. Neipp, D. Puerto, S. Gallego, I. Pascual and A. Beléndez, "Polarimetric analysis of cross-talk phenomena induced by the pixelation in PA-LCoS devices", *Optics & Laser Technology* 152, 108125 (2022).
- [4] C. Schwarz, P. M. Prieto, E. J. Fernández, and P. Artal, "Binocular adaptive optics vision analyzer with full control over the complex pupil functions," *Opt. Lett.* 36(24), 4779–4781 (2011).
- [5] J. Christmas y N. Collings, "Displays Based on Dynamic Phase-Only Holography", *Appl. Sci.* 8(5), 685 (2018).
- [6] F. J. Martínez, Andrés Márquez, Sergi Gallego, Jorge Frances, Inmaculada Pascual, "Extended linear polarimeter to measure retardance and flicker: application to liquid crystal on silicon devices in two working geometries," *Opt. Eng.* 53(1) 014105 (2014).

Estudio de los parámetros críticos para el comportamiento láser de redes de Bragg inscritas en guías de onda activas

Ángel Sanz-Felipe*, Juan A. Vallés Brau

*Departamento de Física Aplicada & I3A, Facultad de Ciencias, Universidad de Zaragoza,
C/ Pedro Cerbuna 12, 50009 Zaragoza.*

*E-mail: angel_sf@unizar.es

1. Introducción

La escritura con láser de femtosegundo de redes de Bragg en guías de onda dopadas con tierras raras permite combinar el comportamiento reflectivo de las redes de Bragg con la respuesta activa de las tierras raras. Estas estructuras presentan un gran potencial para conseguir la amplificación de luz y el posible comportamiento láser en estructuras monolíticas de pequeño tamaño, habiéndose desarrollado en algunos trabajos experimentales hasta la actualidad [1]. Sin embargo, existe una alta dependencia con sus parámetros de diseño y condiciones de trabajo para conseguir tal comportamiento láser. Por ello, es fundamental un estudio teórico para encontrar los parámetros adecuados para su diseño y optimización previos a su fabricación. En este trabajo se ha implementado un método numérico para simular la propagación de luz en redes de Bragg inscritas en guías de onda activas y que ha permitido encontrar las condiciones críticas de diseño y de trabajo para obtener y optimizar la respuesta láser de estas estructuras.

2. Método numérico

Se ha desarrollado un programa de simulación numérica que calcula la propagación de la potencia óptica a lo largo de una red de Bragg de periodo uniforme inscrita en una guía de onda dopada con Er/Yb. El programa utiliza un método Runge-Kutta dividiendo la guía en secciones de un tamaño Δz suficientemente pequeño (20-30 secciones/mm). En cada sección se calcula la potencia óptica y su derivada a lo largo de la dirección de propagación de la guía, tanto para la potencia copropagante (R) como contrapropagante (L):

$$\frac{dP_{R/L}}{dz} = \left[A - \alpha + \frac{\ln(t)}{\Delta z} \right] P_{R/L} - \frac{\ln(t)}{\Delta z} P_{L/R} \quad (1)$$

El primer sumando en la derecha establece los cambios en la potencia propagada en el sentido de cálculo. El primer término en el corchete, $A = A(\sigma, \eta, z)$, es una función que incorpora el comportamiento activo del material [2]. El segundo término, α , es el coeficiente de pérdidas del material de la guía. La red de Bragg inscrita en la guía se simula con el tercer término a través del coeficiente de transmisión, t , asignado a cada sección de la red [3], de forma que el efecto de la red completa se calcula por medio de la cantidad de luz transmitida en cada sección de la guía. El carácter reflectivo de la red de Bragg obliga a incluir la porción de luz que es reflejada en cada sección y pasa a propagarse en el sentido de cálculo. De ello se encarga el segundo sumando de la derecha: un término cruzado que equivale a la porción reflejada de la potencia óptica que viajaba en sentido contrario. Así, la potencia copropagante reflejada en cada tramo de la red es incorporada a la potencia contrapropagante y viceversa, quedando mutuamente dependientes. El coeficiente de transmisión es un valor menor que uno, por lo que el signo negativo que tomará el logaritmo contribuye a la disminución o aumento de la potencia en cada caso (por transmisión o reflexión respectivamente). Esta combinación del carácter reflectivo de la red de Bragg con el carácter activo de las tierras raras dará lugar a un régimen de reflexiones múltiples autoamplificadas que, bajo las condiciones adecuadas, conducirá a su funcionamiento como láser.

El cálculo numérico de la respuesta de estas estructuras se realiza de forma iterativa. Primero se calcula la propagación de la potencia copropagante $P_R(z)$ partiendo de $P_L(z) = 0$. Los valores obtenidos se usan para calcular de vuelta la potencia contrapropagante, $P_L(z)$. Estos valores se usan para la siguiente iteración, y así sucesivamente hasta alcanzar una solución convergente. Así, el programa calcula la propagación de la potencia de la señal (en su caso), de fluorescencia y de bombeo a lo largo de la guía. Por otro lado, la reflectividad espectral de la red de Bragg es simulada como un pico de reflexión de 1 nm de ancho centrado en $\lambda = 1534$ nm, correspondiente al pico de máxima amplificación del ion Er^{3+} . En trabajos previos se ha comprobado experimentalmente la validez de estas condiciones de simulación y del método numérico [4].

3. Simulaciones y resultados

Cuando la estructura trabaja en un régimen de reflexiones autoamplificadas, la luz queda confinada y amplificada hasta alcanzar una alta potencia de emisión espontánea amplificada (ASE) en 1534 nm. Este fenómeno depende drásticamente de cuatro parámetros: la eficiencia de la red de Bragg (dada por su reflectividad pasiva), su longitud, las pérdidas del material y la potencia de bombeo ($\lambda = 980$ nm). En este trabajo se ha simulado la respuesta de estas redes de Bragg activas en función de estos cuatro parámetros dentro de rangos típicos para estos materiales, obteniendo un completo banco de resultados con el que aislar las diferentes dependencias y las condiciones críticas en que se consigue su comportamiento láser.

La Fig. 1(a) presenta la máxima señal ASE obtenida en redes de diferente longitud en función de la potencia de bombeo usada para un valor de pérdidas típico (1.30 dB/cm). La señal ASE alcanza valores en torno a 17 mW con redes entre 6 y 9 mm de longitud. Sin embargo, si el bombeo no es suficiente, esta señal se reduce drásticamente en redes largas hasta llegar a desaparecer el comportamiento láser. Por otro lado, la Fig. 1(b) muestra los valores críticos de reflectividad pasiva de la red de Bragg por encima de los cuales se consigue el comportamiento láser con 300 mW de bombeo en función de su longitud y de las pérdidas del material. Las redes más largas requieren una red de Bragg menos eficiente, lo que es más favorable para su fabricación, pero su respuesta es muy sensible a las pérdidas, parámetro de difícil control en el proceso de escritura de la red. Un diseño intermedio, en torno a 5-6 mm, permitiría encontrar un equilibrio entre las diferentes dependencias y optimizar así la respuesta láser de estas estructuras con vista a su fabricación.

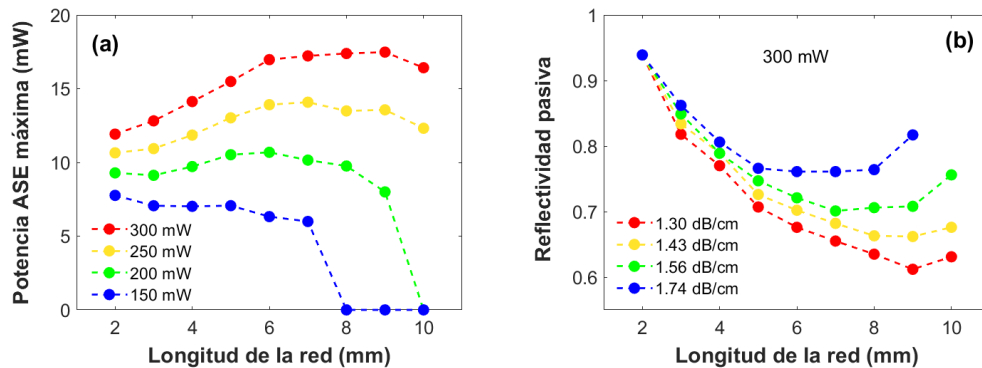


Figura 1. (a) Potencia ASE máxima generada con diferentes longitudes de red y potencias de bombeo. (b) Parámetros críticos de eficiencia de la red de Bragg, longitud y pérdidas por encima de los cuales se observa comportamiento láser.

4. Conclusiones

El método numérico desarrollado nos ha permitido simular la propagación de potencia óptica a lo largo de una red de Bragg inscrita en una guía de onda activa. El banco de simulaciones en función de los parámetros relevantes nos ha permitido detectar valores críticos del diseño y condiciones de trabajo de estas estructuras para elegir un diseño más óptimo que favorezca y optimice su respuesta láser.

Agradecimientos

Este trabajo ha sido financiado por el proyecto PID2019-108598GB-I00/AEI/10.13039/501100011033, y por el Departamento de Industria e Innovación (Gobierno de Aragón) por medio de la subvención a grupos de investigación E44-20R (cofinanciado con FEDER 2014-2020: Construyendo Europa desde Aragón).

Referencias

- [1] Y. Alon *et al.*, “Femtosecond Bragg grating inscription in an Yb-doped large-mode-area multicore fiber for high-power laser applications”, *Opt. Lett.* **45**, 4563-4566 (2020).
- [2] D. Benedicto *et al.*, “Characterization of Multicore Integrated Active Waveguides Written in an Er³⁺/Yb³⁺ Codoped Phosphate Glass”, *J. Light. Technol.* **39**, 5061-5068 (2021).
- [3] Á. Sanz-Felipe *et al.*, “Waveguide Bragg gratings fabrication and optimization as a function of the duty cycle”, in XII Reunión Española de Optoelectrónica, OPTOEL’21 (2021) 59-64.
- [4] Á. Sanz-Felipe *et al.*, “Modeling optical amplification in Er/Yb-codoped integrated Bragg gratings”, *Ceram. Int.* **49**, 41281-41287 (2023).

Análisis de la reproducción colorimétrica en dispositivos Apple

Aurora Larrosa^{1*}, Esther Perales^{1,2}, Carmen Vázquez^{1,2}, Julián Espinosa^{1,2},
Eric Kirchner³, Lan Njo³

¹Departamento de Óptica, Farmacología y Anatomía,

²IUFACyT, Universidad de Alicante, Carretera de San Vicente del Raspeig, s/n. San Vicente del Raspeig
- Alicante

³AkzoNobel Technology Group Color, Sassenheim, Holanda

*E-mail: aurora.larrosa@ua.es

1. Introducción

En los últimos años las compras online se han convertido en la forma preferida por muchos usuarios a la hora de adquirir artículos. Hoy en día, contamos con innumerables páginas de venta online para la adquisición de artículos de todo tipo y los teléfonos inteligentes y *tablets* se han convertido en un producto de consumo. Para las industrias como las de la moda, la alimentación o la automoción es esencial que los productos se muestren de manera atractiva puesto que la apariencia visual es un factor fundamental en los criterios de aceptación o rechazo del producto. Por tanto, la reproducción del color en dispositivos de visualización de datos (pantallas) es un área de máxima actualidad y de gran importancia. El espacio sRGB define una gama específica de colores que se considera reproducible por la mayoría de los dispositivos digitales, monitores, impresoras y navegadores web, sin embargo, el avance tecnológico en la fabricación de dispositivos electrónicos ha hecho que este espacio digital de representación del color, originalmente diseñado para pantallas de rayos catódicos, no sea el más adecuado en un mercado en el que predominan pantallas LCD y OLED.

Por este motivo, el objetivo de este trabajo consiste en la evaluación y análisis de la caracterización de dispositivos móviles y *tablets* de la marca comercial *Apple* (una de las empresas más grandes del mundo en el ámbito de la electrónica) para así estudiar la consistencia de la representación del color en estos dispositivos con una nueva tecnología de pantalla y conocer si los modelos existentes son válidos y adecuados.

2. Metodología

Para generar colores correctamente en una pantalla es necesaria su previa caracterización espectral y colorimétrica. Existen tres tipos de modelos para llevar a cabo esta transformación entre valores RGB y valores triestímulo XYZ: 3D Look-Up Tables (LUT) (tablas de interpolación en las que se considera que no hay independencia entre canales creadas a partir de la medida de colores con los tres canales encendidos simultáneamente), modelos numéricos (aproximan la transformación por ecuaciones polinómicas obtenidas mediante regresión a partir de un conjunto de medidas) y modelos físicos (predicen el comportamiento teniendo en cuenta la naturaleza de la propia mezcla aditiva de los colores de cada canal).

Para la caracterización de los dispositivos *Apple*, se evaluó el modelo físico más común para caracterizar un monitor [1]: el *gain-offset-gamma* (método GOG). Como todos los modelos físicos se divide en dos etapas:

1. Función de transferencia electro-óptica. Establece una relación entre los valores digitales d del dispositivo y medidas experimentales de la luminancia normalizada Y de cada canal. Para cada canal $i = R, G, B$ tendrá la siguiente forma:

$$Y_i(d_i) = \begin{cases} \beta_i \cdot d_i & \text{si } 0 \leq d_i < d_{0,i} \\ (k_{1,i} \cdot d_i + k_{2,i})^{\gamma_i} & \text{si } d_{0,i} \leq d_i \leq 1 \end{cases} \quad (1)$$

Consiste en una parte lineal hasta el valor digital frontera d_0 y una parte exponencial regida por el exponente γ . Los parámetros β , k_1 y k_2 pueden obtenerse por las condiciones de diferenciabilidad de la función y $Y(1) = 1$.

2. Matriz de transformación. Transforma las luminancias a un espacio de color independiente del dispositivo. Los elementos de la matriz son los valores triestímulo de los canales con luminancia máxima.

$$\begin{pmatrix} X \\ Y \\ Z \end{pmatrix} = \begin{pmatrix} X_{R,\max} & X_{G,\max} & X_{B,\max} \\ Y_{R,\max} & Y_{G,\max} & Y_{B,\max} \\ Z_{R,\max} & Z_{G,\max} & Z_{B,\max} \end{pmatrix} \cdot \begin{pmatrix} Y_R \\ Y_G \\ Y_B \end{pmatrix} \quad (2)$$

Para caracterizar la función de transferencia de cada canal y la matriz de transformación se midió con el espectrorradiómetro Konica Minolta CS-2000A, la cromaticidad y la luminancia de imágenes de color uniforme que emiten únicamente en uno de los canales. Los valores seleccionados para medir la reproducción tonal para el canal rojo tienen valores de $G = 0$ y $B = 0$, mientras que $R = 0, 5, 10, \dots, 50, 75, 100, 125, \dots, 200, 225, 255$. Se repitió el proceso para los canales verde y azul. Una vez obtenidos estos datos para los 11 dispositivos se calcularon los parámetros γ y d_0 ajustando la curva de (1) a las medidas.

3. Resultados y discusión

En la tabla 1 se muestran los parámetros γ ajustados de cada canal para los 11 dispositivos.

Dispositivo	γ_R	γ_G	γ_B	Dispositivo	γ_R	γ_G	γ_B
iPhone 7	2.384	2.302	2.354	iPad 2	2.315	2.307	2.299
iPhone 8	2.401	2.340	2.409	iPad 6th Generation	2.248	2.286	2.465
iPhone SE	2.402	2.336	2.438	iPad 9th Generation	2.249	2.284	2.349
iPhone 12	2.217	2.213	2.184	iPad Pro 2nd Generation	2.335	2.393	2.394
iPhone 13	2.376	2.391	2.271	iPad Air 4th Generation	2.394	2.342	2.308
iPhone XS Max	2.231	2.255	2.287				

Tabla 1 Lista de los dispositivos caracterizados y valores gamma correspondientes a cada ajuste a (1).

En total, se han calculado 33 parámetros γ todos con valores comprendidos entre 2.1 y 2.5, de los cuales 28 se encuentran por debajo del $\gamma = 2.4$ característico del sRGB [1]. Sólo encontramos 3 dispositivos en el que alguna de sus γ_i es mayor de 2.4: *iPhone 8* y *iPhone SE* para los canales rojo y azul y *iPad 6th Generation* en el azul. Tampoco se encuentran muchas gammas con valores bajos. Tan solo en el *iPhone 12* se encuentra una γ_i menor de 2.2 (en el canal azul). El resto de los parámetros γ se encuentra entre 2.2 y 2.4. Para cada canal se han calculado el γ medio y su desviación estándar: $\gamma_R = 2.32 \pm 0.07$, $\gamma_G = 2.31 \pm 0.05$ y $\gamma_B = 2.34 \pm 0.08$. Las tres se acercan a una γ de 2.3 y el canal con mayor desviación es el azul, seguido del rojo. Además, también se calcularon los errores relativos medios del ajuste de las luminancias para cada TRC y con respecto a la curva sRGB, obteniéndose un error relativo alrededor del 10%, error alto para que sea aceptable en cuanto a una reproducción de color exacta. Los dispositivos de esta marca parecen ser consistentes en cuanto a la reproducción del color en sus pantallas, con una desviación relativa máxima inferior al 1%.

4. Conclusión

En este trabajo se ha comprobado que los parámetros medios de todos los dispositivos no se corresponden con el modelo sRGB. El canal con mayor desviación estándar es el azul; esto puede deberse a las características intrínsecas de los materiales de los OLEDs azules [2]. Por tanto, para una buena reproducción del color en estos dispositivos sería necesario considerar otro modelo con parámetros más adecuados. En particular, debido a la consistencia de estos dispositivos en cuanto a la reproducción del color, se podría implementar un modelo de reproducción del color en cualquier dispositivo que mejorase el predeterminado basado en unos parámetros γ y d_0 predeterminados. Por otro lado, sería necesario conocer las coordenadas cromáticas y las luminancias máximas características de los tres canales del dispositivo, pero esta información es proporcionada en las especificaciones técnicas. De esta forma, una empresa dedicada a la venta de pinturas podría presentar a sus clientes su catálogo digitalmente, tras medir los valores triestímulo de sus pinturas o productos siguiendo el modelo determinado en este trabajo. Este procedimiento se podría repetir para otras marcas comerciales con el fin de proporcionar una herramienta válida para la reproducción del color en diferentes pantallas.

Referencias

- [1] C. Poynton, *Digital Video and HDTV: Algorithms and Interfaces, The Morgan Kaufmann Series in Computer Graphics* (Morgan Kaufmann, 2003) p. 321
- [2] D. Wang, C. Cheng, T. Tsuboi, and Q. Zhang, "Degradation Mechanisms in Blue Organic Light-Emitting Diodes," Chinese Chemical Society of Chemistry (2020).

Exploring the fluid dynamics of a carotid bifurcation model with low-coherence digital in-line sideband holography

Cristina Errea, Julia Lobera, and Francisco José Torcal-Milla*

Laser Optical Technologies Group. Aragon Institute for Engineering Research (I3A). University of Zaragoza, Zaragoza (Spain).

*E-mail: fjtorcal@unizar.es

1. Introduction

The analysis of biological models' behavior has increased in interest in recent years, aided by the growing importance of personalized medicine. Ex-vivo investigation of fluid dynamics using representative models of vascular conduits provides a valuable approach to assess vascular behavior under specific conditions without jeopardizing the patient health. To measure the fluid dynamics, several approaches can be used: particle tracking [1], endoscope holography [2], and so on. In this work, digital in-line sideband holography has been used, [3]. This holography technique takes advantage of the in-line configuration simplicity with just one illumination beam that acts as reference beam and object beam at the same time. It requires the use of an analogic filtering of the recording, that allows to eliminate the dual image inherent to in-line holography with the adequate posterior analysis procedure. Traditionally, holographic techniques have been implemented with laser sources, but the use of highly coherent sources introduces speckle noise. For fluid velocimetry in biomedical applications, the speckle noise is particularly cumbersome as it appears associated with the small imperfections inherent to the vessel model walls. This issue jeopardizes the measurement of the velocity field inside the vessel model. For this reason, we propose to use a low-coherence source, such as a LED (Light Emitting Diode). We have previously demonstrated that interference is possible with this type of sources and therefore holography is possible too, [4]. The advantage of low spatial coherence is that it reduces the volume from which the scattered light can be coherently recorded by the sensor to conform the hologram. Therefore, it can potentially reduce the speckle noise coming from the model walls. To control the object size to be recorded, we need to control the spatial coherence of the source. This has been done just by placing a tiny aperture at a certain distance from the LED. In the next section, the experimental set-up and preliminary results are explained.

2. Experimental set-up and preliminary results

Figure 1a shows the experimental set-up used along this work. The light source consists of a LED with an aspherical lens that produce a quasi-collimated beam. After the lens, an adjustable iris is placed to reduce the divergence to an adequate value and, therefore, to control the spatial coherence of the beam. A second lens is used to produce a collimated beam that illuminates the object, which consists of a model of carotid bifurcation made by carving the arteria vessels into a silicon block, Figure 1b. After the carotid bifurcation, an objective lens is placed to image the object central plane on the camera sensor. Finally, a sideband aperture is placed at the focal plane of the objective lens [3]. This aperture allows us to eliminate the twin image problem of standard in-line holography set-ups.

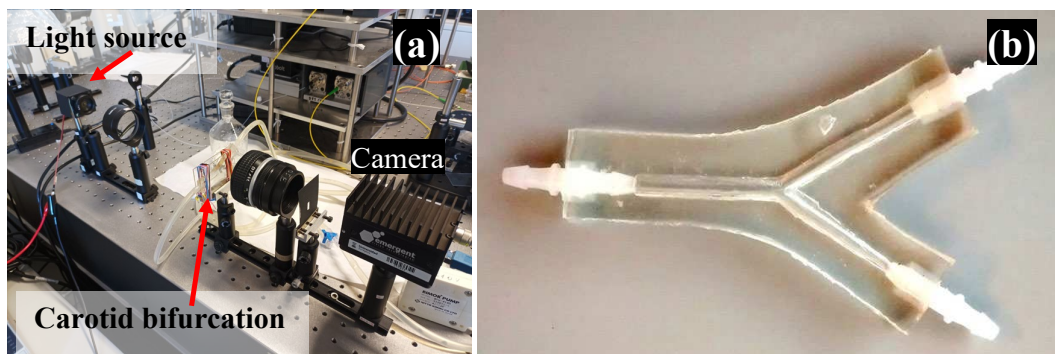


Figure 1 (a) Experimental set-up and (b) model of carotid bifurcation.

Figure 2a shows a typical hologram obtained with this configuration. Due to the low coherence of the source, the only defects that are observed are those on focus, making invisible those that would appear by using a laser source, even being out of focus. It can be also observed a non-uniform background intensity due to the shape of the emitting area of the LED.

As we have mentioned, the purpose of this work is to obtain the velocity field of the fluid inside the carotid bifurcation model by using a low-coherence light source to avoid the coherent noise inherent to imperfections in the vessel when laser sources are used for illumination. We record series of holograms and apply the particle tracking velocimetry algorithm [3] to locate the seeding particles and obtain the velocity field within the model. Figure 2b shows the in-plane velocity field for a determined time.

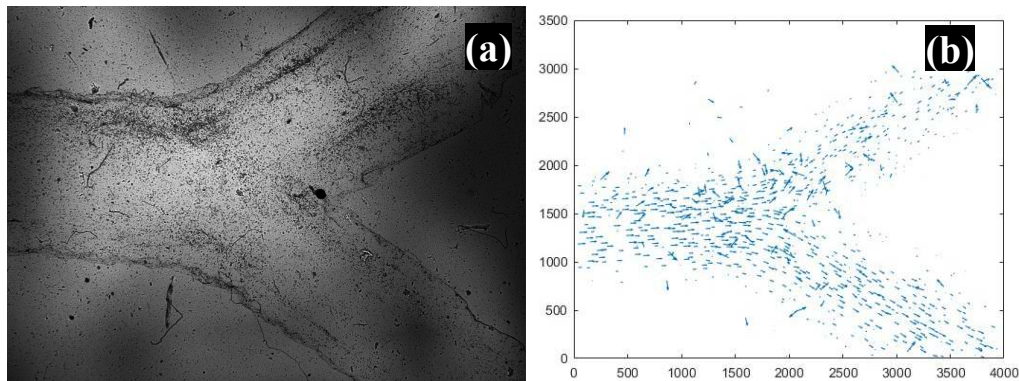


Figure 2 (a) Hologram of the carotid bifurcation model seeded with tracking particles and (b) velocity map obtained after the analysis of two consecutive holograms (axes in pixels).

3. Conclusions

In this work, a low-coherence light source is proved to be useful to obtain the 2D velocity field of a fluid in an in-line sideband holographic set-up. The selected object is a carotid bifurcation model made by carving the arteria vessels into a silicon block. We demonstrate that the use of a low-coherence source still allows the recording of a hologram. Besides, this kind of source avoids the speckle noise produced by the vessel walls imperfections that appears when a laser source is used.

Acknowledgments

This work has been partially funded by “Programa de Becas y Ayudas del Instituto de Investigación en Ingeniería de Aragón (I3A) 2023”, Laser Optical Technologies Group of the Aragón’s Government (E44_23R), and PID2020-113303GB-C22 project of the Ministerio de Ciencia, Innovación y Universidades.

References

- [1] J. Lobera, V. Palero, E. M. Roche, M. Gómez-Climente, A. M. López-Torres, N. Andrés N, M. P. Arroyo, “Multiplexed two in-line holographic recordings for flow characterization in a flexible vessel,” *Proc. SPIE* 2017;10333:103330J
- [2] L. Arevalo, V. Palero, J. Lobera, N. Andres, and M.P. Arroyo, “Combining endoscopes with PIV and digital holography for the study of vessel model mechanics”, *Meas. Science Tech.* **26**, 115701 (2015).
- [3] A.M. López, J. Lobera, N. Andrés, A. Subías, E.M. Roche, F.J. Torcal-Milla, M.P. Arroyo, J. Pallarés, and V. Palero, “Double field of view digital sideband holography as an optimized method to measure velocity fields in a large fluid volume,” *Opt. Laser Eng.* **175**, 107993 (2024).
- [4] F.J. Torcal-Milla, J. Lobera, A.M. Lopez, V. Palero, N. Andres, M.P. Arroyo, “Mach-Zehnder-based measurement of light emitting diodes temporal coherence,” *Optik* **267**, 169722 (2022).

Light Structuring Through Few-mode Optical Fibers Using Singular Value Decomposition of the Transmission Matrix

Angel Cifuentes¹, Miguel Varga¹, Gabriel Molina-Terriza^{1,2,3}

¹Centro de Física de Materiales, Paseo Manuel de Lardizabal 5, 20018 Donostia-San Sebastián, Spain

²Donostia International Physics Center, Paseo Manuel de Lardizabal 4, 20018 Donostia-San Sebastián, Spain

³IKERBASQUE, Basque Foundation for Science, María Díaz de Haro 3, 48013 Bilbao, Spain

*E-mail: angelsergio.cifuentes@ehu.eus

1. Introduction

In recent years advances computer generated holography along with spatial light modulators have led to the tailoring of light field after propagating through complex media[1] such as optical multimode fibers (MMF) [2]. Not only can experimenters now control the spatial distribution following the media but multiple literature reports have shown that the output polarization can be controlled as well [3], [4]. Among the many methods used to achieve this one of the most robust and complete consists on acquiring the transmission matrix[5], TM, of the media under study. This has led to the development of MMF based instruments applications going from sensing[6] to bioimaging [3]. While MMF have gained a wider attention these wavefront shaping techniques can have important applications when used with few-mode fibers (FMF) as well. The reduced number of modes translates into reduced computational effort while still offering the possibility of structuring light at the tip of the FMF.

In this work we show how singular value decomposition (SVD) can be used to shape a cylindrical vector (CV) beam at the output of a FMF. We initially demonstrate this by using a 1-meter long optical fiber (Thorlabs HI1060-J9), originally intended for single mode operation within a wavelength range of 910 to 1650 nm, at 810 nm the was found to guide 6 modes.

2. Methods

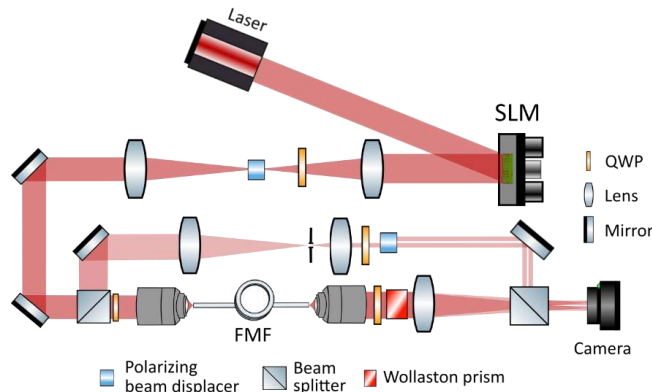


Figure 1. Experimental setup for the measurement of the TM of an optical fiber using a 810 nm single-frequency laser.

A simplified schematic representation of the experimental setup used to acquire the TM is shown in Fig. 1. To acquire the TM, we displayed in sequence a set of tightly focused spots at the fiber input facet and imaged the speckle pattern at the output tip on to a digital camera. Using a reference beam and phase shifting interferometry we are able to calculate the complex amplitude of each output speckle. This results in a TM in a cartesian basis, defined by the chosen input locations at the fiber input and pixels of our output imaging camera. By using polarization optics such as Wollaston prisms and polarizing beam displacers we are able to characterize the fiber two orthogonal polarizations, left and right handed circular for this work. Further insight into the TM measurement procedure can be found elsewhere [5], [7]

The TM can be decomposed using SVD such that $\mathbf{TM} = \mathbf{U}\mathbf{\Sigma}\mathbf{V}^*$. The number of singular values, $\sigma = \text{diag}(\mathbf{\Sigma})$, above the background noise level allowed us to determine the number of guided modes, n .

The left, $\mathbf{U} = [\mathbf{u}_1 \dots \mathbf{u}_n]$, and right, $\mathbf{V} = [\mathbf{v}_1 \dots \mathbf{v}_n]$, singular vectors form an orthonormal basis for the fiber's input and output, respectively.

3. Results and discussion

To shape a CV beam we define a desired output field, \mathbf{F}_{out} , as two overlapped single ringed Laguerre-Gaussian (LG) modes, $\mathbf{Y}_{0,l}(\mathbf{r})$, with RHCP and LHCP and opposite topological charge, i.e. $\mathbf{Y}_{LH}(\mathbf{r}) = \mathbf{Y}_{0,l}(\mathbf{r})$ and $\mathbf{Y}_{RH}(\mathbf{r}) = \mathbf{Y}_{0,-l}(\mathbf{r})$ [8]. As an initial step to approximate \mathbf{Y}_{RH} and \mathbf{Y}_{LH} we estimated the fiber's total spatial-frequency content. This was done by accumulating the amplitude of the far-field, obtained as the Fourier transform, FT, of the fiber's output basis and thresholding the far-field to obtain an aperture that captures 95% of the total power (Figure 2 a and b). An azimuthal phase is then added and by applying the inverse FT we obtain the desired field (Figure 2 c and d).

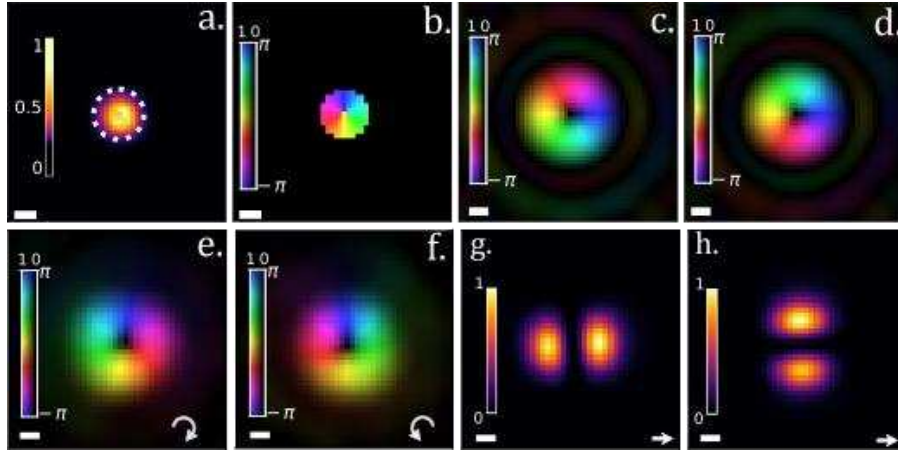


Figure 2. a. Accumulated far-field intensity for fiber I. Scale bar equals $0.1\mu^{-1}$, note that the color map is logarithmic in scale. b. Thresholded far-field with azimuthal phase corresponding to a topological charge $l=+1$. c. and d. Inverse Fourier transform of b. and its conjugate, respectively. e. and f. RHCP and LHCP field, experimentally observed, corresponding to a vector beam at the fiber tip. g. and h. intensity of the fiber output when viewed through a horizontal polarizer with g. corresponding to a radial and h. corresponding to a tangential CV beam.

We then project the desired field onto the output basis of the fiber, \mathbf{V} , and from there calculate the required fibre input and SLM hologram using \mathbf{U} . The results of this procedure can be observed in Figure 2. e and f, where we show the interferometrically measured field for both RHCP and LHCP. In figure 2 g and h we can observe a radially and tangentially polarized beam when viewed through a horizontal polarizer. While CV beams generated using FMFs have been reported [9] our approach offers a more comprehensive analysis and is not limited solely to these.

References

- [1] I. M. Vellekoop and A. Mosk, 'Focusing coherent light through opaque strongly scattering media', *Opt. Lett.*, vol. 32, no. 16, pp. 2309–2311, 2007.
- [2] A. M. Caravaca-Aguirre and R. Piestun, 'Single multimode fiber endoscope', *Opt. Express*, vol. 25, no. 3, pp. 1656–1665, 2017.
- [3] A. Cifuentes *et al.*, 'Polarization-resolved second-harmonic generation imaging through a multimode fiber', *Optica*, vol. 8, no. 8, pp. 1065–1074, 2021.
- [4] J. Trägårdh, T. Pikálek, M. Šerý, T. Meyer, J. Popp, and T. Čížmár, 'Label-free CARS microscopy through a multimode fiber endoscope', *Opt. Express*, vol. 27, no. 21, pp. 30055–30066, 2019.
- [5] S. Popoff, G. Lerosey, M. Fink, A. C. Boccara, and S. Gigan, 'Controlling light through optical disordered media: transmission matrix approach', *New J. Phys.*, vol. 13, no. 12, p. 123021, 2011.
- [6] A. Cifuentes and J. Trägårdh, 'A method for single particle tracking through a multimode fiber', *Opt. Express*, vol. 30, no. 20, pp. 36055–36064, 2022.
- [7] M. Plöschner, T. Tyc, and T. Čížmár, 'Seeing through chaos in multimode fibres', *Nat. Photonics*, vol. 9, no. 8, pp. 529–535, 2015.
- [8] L. Allen, M. W. Beijersbergen, R. Spreeuw, and J. Woerdman, 'Orbital angular momentum of light and the transformation of Laguerre-Gaussian laser modes', *Phys. Rev. A*, vol. 45, no. 11, p. 8185, 1992.
- [9] G. Volpe and D. Petrov, 'Generation of cylindrical vector beams with few-mode fibers excited by Laguerre-Gaussian beams', *Opt. Commun.*, vol. 237, no. 1–3, pp. 89–95, 2004.

Lateral-shearing interferometric microscopy for applications in biology, material sciences and semiconductors.

Roland A. Terborg¹, Sebastian Haegele¹, Rubaiya Hussain¹, Iris Cusini¹, Valerio Pruneri*^{1,2}

¹*ICFO-Institut de Ciències Fotòniques, The Barcelona Institute of Science and Technology, 08860 Castelldefels (Barcelona), Spain*

²*ICREA-Institució Catalana de Recerca i Estudis Avançats, 08010, Barcelona, Spain*

*E-mail: valerio.pruneri@icfo.eu

1. LIM technology

Optical microscopes can detect objects by means of several physical processes, such as light emission, scattering, absorption and reflection. However, for highly transparent samples, such as cells or ultra-thin materials, these mechanisms are often too weak for obtaining high contrast images. In cell imaging, some of the most common and effective solutions to this problem involve the use of fluorescent labels which can be linked to antibodies that target specific parts of the cell, although these pose a threat to living cells (cytotoxicity). For ultra-thin materials, the atomic force microscope is one of the standard tools, but this technique can damage the samples and is time-consuming.

Over the past decades, several interferometric techniques for label-free and highly sensitive imaging of cells have emerged, leveraging changes in phase to create optical contrast. The majority of the commercial phase imaging systems use a Mach-Zehnder configuration, where a light beam is split into two beams, a probe traversing the sample and a separate reference. Due to their construction, most of them are not compatible with standard microscopes and the Mach-Zehnder interferometers are highly sensitive to external perturbations like vibrations, air turbulence and temperature drifts, which in turn requires additional control systems (e.g., optical tables), increasing complexity and costs.

To overcome the previous problems, we have developed the lateral-shearing interferometric microscopy (LIM) technology [1,2,3] for industrial applications that require quantitative phase imaging with high sensitivity, high stability and high compatibility with existing inspection processes, commercial microscopes and other optical imaging systems (see Figure 1). The LIM has a noise floor as low as 0.1nm in optical path difference (OPD). Contrary to other phase imaging systems that use separated probe and reference beams, the key feature of the LIM imager is the use of a common-path setup with sheared and partially overlapping beams. This leads to very stable interferometry as the probe and reference points are close to each other (only a few microns apart), and undergo the same environmental changes, like vibration and air turbulence effects. In addition, the proposed imager can work with low-coherence light, such as a light emitting diode (LED) instead of a laser, and, moreover, its constituting optical elements are simple and robust.

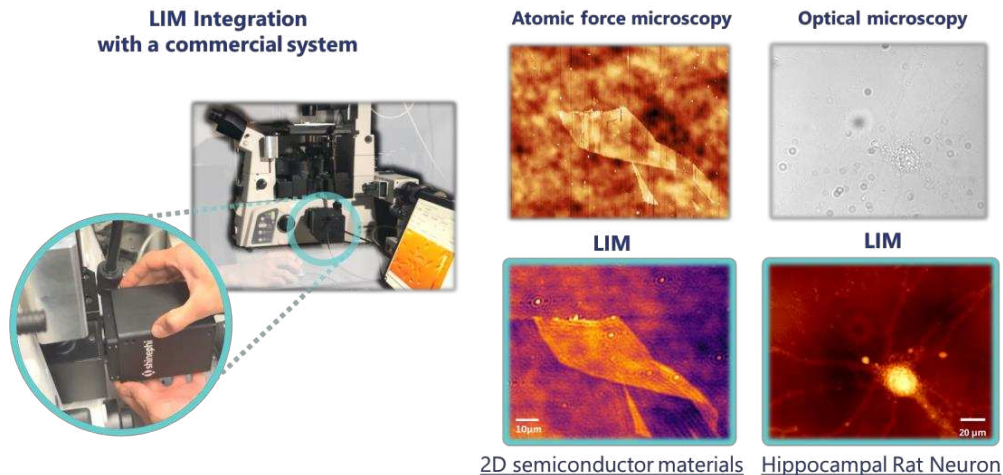


Figure 1 Integration of the LIM imager with a commercial Nikon optical microscope (left) and comparison of the LIM images with standard imaging tools (right) using samples relevant for the life sciences, material analysis and the semiconductor industry.

2. Conclusions

We present the working principle of the LIM technology, as well as some specific use cases from its wide range of applications, for example in cell imaging and optical metrology, showing that the LIM can become an important tool to boost the design and production capabilities of the life sciences, microelectronics and semiconductors industry.

Acknowledgments

This project has received funding by: The European Union’s Horizon 2020 research and innovation program under the Marie Skłodowska-Curie grant agreement No. 847517 (ENLIGHTEN) and No. 754510 (PROBIST). The European Union’s Horizon 2020 FET-Open research and innovation program under grant agreement No. 101034765 (LIM), Project MAGICAL (PID2022-137952NB-I00) funded by the MCIN/AEI/10.13039/501100011033/ FEDER, UE. Severo Ochoa CEX2019-000910-S funded by MCIN/AEI/ 10.13039/501100011033. Fundació Cellex. Fundació Mir-Puig. Generalitat de Catalunya. Centres de Recerca de Catalunya (CERCA). Agència de Gestió d’Ajuts Universitaris i de Recerca (2021 SGR 01458). PDC2023-145941-I00 funded by MCIN/AEI/10.13039/ 501100011033 and by the European Union “NextGenerationEU”/PRTR”.

References

- [1] Terborg, R. A.; Pello, J.; Mannelli, I.; Torres, J. P.; Pruneri, V. Ultrasensitive Interferometric On-Chip Microscopy of Transparent Objects. *Sci. Adv.* **2016**, *2* (6), e1600077. <https://doi.org/10.1126/sciadv.1600077>.
- [2] Haegele, S.; Corrielli, G.; Hejda, M.; Duempelmann, L.; Terborg, R. A.; Osellame, R.; Pruneri, V. Large Field-of-view Holographic Imager with Ultra-high Phase Sensitivity Using Multi-angle Illumination. *Opt. Lasers Eng.* **2023**, *161* (June 2022), 107315. <https://doi.org/10.1016/j.optlaseng.2022.107315>.
- [3] Haegele, S.; Martínez-Cercós, D.; Arrés Chillón, J.; Paulillo, B.; Terborg, R. A.; Pruneri, V. Multispectral Holographic Intensity and Phase Imaging of Semitransparent Ultrathin Films, *ACS Photonics* **2024**, *11* (5), 1873-1886. DOI: 10.1021/acsp Photonics.3c01834

Nested opto- and mechanical resonators for an all fiber, frequency encoded, mass balance proposal

Anna I. Garrigues-Navarro^{1*}, Martina Delgado-Pinar^{1,2}, Antonio Díez^{1,2}, Miguel V. Andrés^{1,2}

¹Laboratory of Fiber Optics, ICMUV, Universitat de València, Burjassot, Spain

²Department de Física Aplicada i Electromagnetisme, Universitat de València, Burjassot, Spain

*e-mail: ana.i.garrigues@uv.es

1. Introduction

This research presents the setup and characterization of an optical microbalance design, based on an optical fiber ring resonator with a nested mechanical resonant cavity. Since mechanical vibrations are sensitive to small mass changes in the vibrating medium, the nested mechanical resonant cavity will change the performance of the optical ring; in particular, it will introduce a time-dependent wavelength sweep on the optical resonances at the mechanical frequency. Thus, this design of two coupled resonators defines a frequency-out microbalance, feature that shows a high intrinsic interest. We can foresee potential biosensing applications for this design, based on the achieved experimental resolution.

2. Experimental Setup

Our optical cavity is formed by a ring resonator constructed with commercial SMF-28e fiber and it includes a directional 99:1 coupler, with the 1% output arm spliced to the free input arm, see Fig. 1 (a). A polarization controller, PC, positioned outside the cavity ensures optimal polarization alignment. We employed a narrow linewidth tunable diode laser (<100 Hz), TDL, as the light source. The detection was performed using a photodiode, PD, and oscilloscope (350 MHz bandwidth), OSC. On its part, the mechanical resonating cavity consists of a small section of the fiber ring fixed at both ends to two piezoelectric ceramics, PZT, driven by AC generator, as depicted in the inset of Fig. 1 (a). Figure 1 (b) shows the output transmittance of the optical ring, without any mechanical vibration, together with its main experimental characteristics.

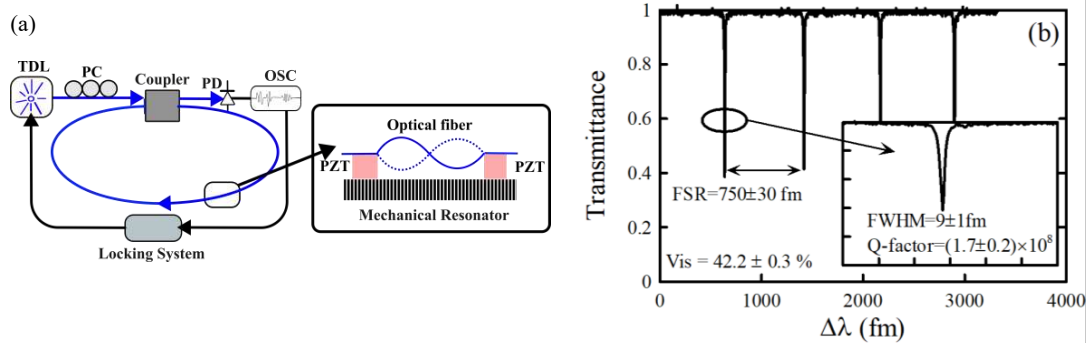


Figure 1. (a) Scheme of the experimental setup. (b) Optical characterization of the passive ring.

While the optical resonances are determined by the length of the ring and the effective index of the fundamental mode in the fiber, the mechanical resonator will support flexural standing waves at discrete frequencies in the kHz range. At first order, these resonant frequencies for a silica rod (that is, the fiber) with our boundary conditions for the extremes, f_n , are given by the expression

$$f_n \approx \frac{\pi}{4} \frac{a}{L_{ac}^2} \left[\left(n + \frac{1}{2} \right) \right]^2 \sqrt{\frac{E}{\rho}} \quad (1)$$

where E is the Young's modulus, ρ is the density, n the order of resonance, a is the fiber radius and L_{ac} is the length of the mechanical resonator.

3. Active characterization and results.

As the AC driving voltage for the piezoelectric transducers is turned on, that is, the mechanical cavity is active, the optical resonances sweep in wavelength, as far as the AC frequency fits one of the mechanical resonances, f_n . When the TDL is tuned to the slope of an optical resonance, the output transmission is amplitude modulated. A locking system was included to ensure the working point is fixed at half the notch amplitude, where the transmittance is nearly linear with wavelength shifts. The successive f_n frequencies were identified by observing the maximum amplitude modulation of the optical signal, Fig. 2 (a) shows their values in a logarithmic-axes graphic. The length of the mechanical resonator was extracted by fitting the data to Eq. 1, $L_{ac}=18.2$ mm.

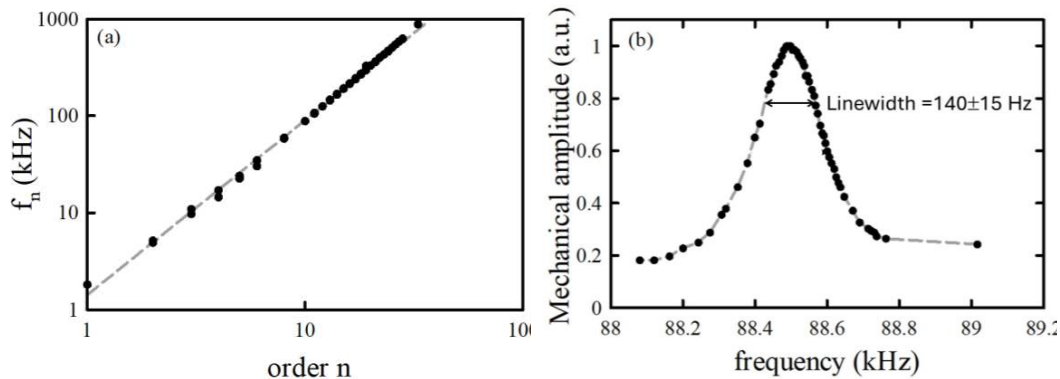


Figure 2. (a) Resonant mechanical frequencies. (b) Characterization of mechanical resonance $n = 10$.

It can be observed that, especially for resonances 3-6, two resonant frequencies are detected for the same order, slightly shifted. This is because, nevertheless the ideally cylindrical geometry of the resonator, small asymmetries lead to the splitting of the resonances. Furthermore, imperfections on the placement of the adhesive drops in the extremes of the mechanical resonators might also contribute to the splitting. The characterization of the resonance $n = 10$, the narrowest one, was done in detail, see Fig. 2(b). Its Q-factor reaches a value of 600, which is relatively high for a mechanical resonance of a macroresonator like this. Error bars of direct measurements are not observable.

4. Conclusions.

The nested cavities presented in this work provides a resolution, in terms of the minimum mechanical frequency shift that can be measured, of 7.0 Hz (5% of the linewidth of the resonance $n = 10$). From this value, we evaluated the resolution in terms of mass that this system may measure when adding a layer of, as an example, biomolecules, covering the perimeter of the fiber (we assumed that the density of such layer is that of the silica), resulting in 94 ng. The dynamic range is derived from the FSR of the optical ring, 225 μg , and the sensitivity is extracted from the linear fit of the slopes of the optical resonances, 74.8 Hz/ μg . As a summary, this work, although it is not yet at a state that can be used for practical biosensing, paves the way to transfer the technology of commercial quartz balances to Photonics.

Acknowledgements and funding

This research was funded by the Ministerio de Ciencia e Innovación and co-funded by the European Regional Development Fund, Ref. TED2021-130200B-I00, the European Commission, Ref. H2020-MSCARISE-2019-872049 and the Generalitat Valenciana, Ref. CIPROM/2022/030. A.I. Garrigues Navarro thanks OPTICA (formerly OSA) for her scholarship OPTICA Women Scholars Programme 2022 Class.

References

- [1] J. M. Seelig and I. Hoppmann, W. H., "Normal mode vibrations of systems of elastically connected parallel bars," vol. 36, no. 1, pp.93–99.
- [2] I. M. White and X. Fan, "On the performance quantification of resonant refractive index sensors," vol. 16, no. 2, p. 1020.

Experimental characterization of the Q-factor of whispering-gallery modes in non-uniform fiber resonators

J. Julian-Barriel^{1*}, M. Delgado-Pinar^{1,2}, A. Díez^{1,2} and M.V. Andrés^{1,2}

¹Laboratory of Fiber Optics, ICMUV, Universitat de València, Burjassot, Spain

²Laboratory of Fiber Optics, Departament de Física Aplicada i Electromagnetisme - ICMUV, Universitat de València, Burjassot, Spain

E-mail: juan.julian@uv.es

1. Introduction

The objective of this work is to investigate the relation between axial non-uniformity of commercial optical fibers and the quality factor (Q-factor) of optical Whispering-Gallery Modes (WGMs) excited azimuthally in the fiber. In order to do so, we measured the fiber radius profile along several centimeters, with sub-nanometric resolution, by using WGMs. This radius profile was compared with the Full Width at Half Maximum (FWHM) of the WGMs spectra excited at each axial point. This procedure was performed in two different optical fibers, a standard telecom fiber, the SMF-28e from Corning Inc., and a photosensitive fiber, the PS1250/1500 from FiberCore Ltd.

WGMs are surface waves guided in the azimuthal direction by the surface of a resonator with a circular perimeter. In our case light is guided along a silica cylinder surface (that is, the outer radius of the fiber) thanks to the refractive index difference between inner (silica) and outer (air) media. The relation between the resonant wavelength of the WGM and the radius resonator is linear [1], thus it is possible to estimate their variations as:

$$\Delta\lambda_m = \lambda_m \cdot (\Delta a/a) \quad (1)$$

Optical WGMs excited in optical fibers exhibit very narrow linewidths, hence ultra-high Q-factors. At wavelengths around 1550 nm, the Q-factor can achieve values close to 10^8 , which allows using them in many applications [2], specifically in sensing [3]. There are several factors which contribute to lower the Q-factor, such as radiation losses, material absorption, surface scattering, surface contaminants, and external losses [1]. Another effect must be considered to fully understand the real Q-factor of cylindrical resonator: the deviations from the ideal cylindrical shape. In this case the excited optical modes correspond to the modes in a cone with a small angle, which have lower Q-factors [4].

2. Experiment

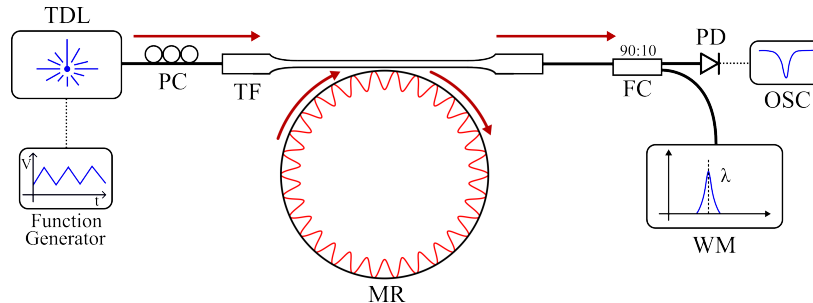


Figure 1 Scheme of the experimental setup. MR: microresonator.

The scheme of the experimental set up employed to excite and measure the WGM is shown in Fig. 1. A tunable diode laser (TDL), frequency-modulated by a function generator is employed as the light source (linewidth < 300 kHz). The signal is coupled to a tapered fiber (TF) of $3 \mu\text{m}$ waist fabricated at our laboratory. This narrow taper allows to couple light to the fiber under test (FUT) and excite the WGMs. A fiber coupler (FC) is employed to split the transmitted optical signal and to send it both to a photodetector (PD) and a wavelength-meter (WM). An oscilloscope (OSC) is employed to record the spectrum.

For each investigated FUT, one WGM resonance wavelength was measured along a 10 cm axial length. Each resonance was measured several times to ensure consistency. The radius change is calculated using Eq. 1, and the recorded profiles are shown in Fig. 2. PS1250/1500 fiber has larger radius variations, of the order of 100 nm in 10 cm. The second FUT, (SMF-28e) has a more uniform radius, with only 2 nm deviation in 10 cm. In this fiber the FWHM of the resonances does not change with the axial point where the WGM was excited. Whereas the resonances excited in PS 1250/1500 are much wider in regions with higher axial slope. The correlation between the axial radius deviation and the FWHM of the WGM is shown in Fig. 3

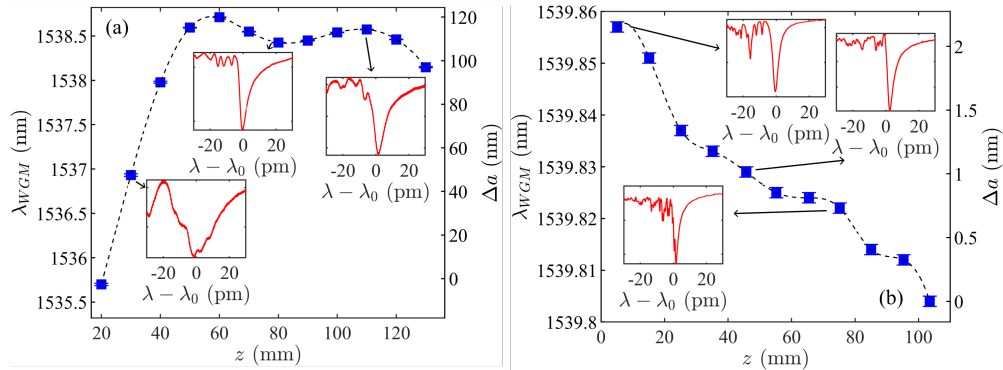


Figure 2 Axial profiles of the FUT. Right axis: estimated radius variation. Left axis: experimental resonant wavelength. (a) PS1250/1500 fiber (b) SMF-28e fiber.

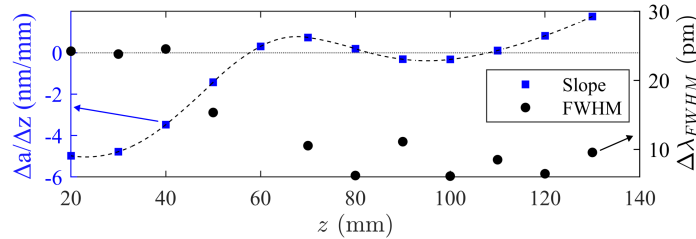


Figure 3 Left axis: axial slope of PS1250/1500 fiber. Right axis: FWHM of the measured WGM.

3. Conclusions

The results obtained for the axial radius profile of two commercial fibers show that the Q-factor of WGMs excited in the fiber cladding is related to the uniformity of the axial radius profile. In high slope areas the resonances are up to four times wider than in low slope areas. Another conclusion drawn from this work is that the uniformity of the radius of optical fibers is highly variable from one specific product to another. This does not, in general, affect their light guiding properties and specific applications, but is important when choosing a fiber for their application as microresonators.

Acknowledgments

This research was funded by the Ministerio de Ciencia e Innovación and co-funded by the European Regional Development Fund (Fondo Europeo de Desarrollo Regional, FEDER), grant number TED2021-130200B-I00 and the European Commission, grant number H2020-MSCARISE2019-872049. J. Julián-Barriel thanks the Conselleria de Educació, Universidades y Empleo for his ACIF grant.

References

- [1] X. Roselló-Mechó, "Whispering gallery modes: advanced photonic applications", Doctoral thesis, May 2019, Universitat de València.
- [2] K. J. Vahala, "Optical microcavities", *Nature*, **424**, 2003, 839-846.
- [3] J. Liao and L. Yang, "Optical whispering-gallery mode barcodes for high-precision and wide-range temperature measurements", *Light Sci. Appl.*, **10**, 2021, 32.
- [4] M. Sumetsky, "Localization of light on a cone: theoretical evidence and experimental demonstration for an optical fiber", *Opt. Lett.*, **36**, 2011, 145-1.

Multimodal sensing and perception for autonomous vehicles

Gerard deMas-Giménez^{1*}, Pablo García-Gómez², Eduardo Bernal¹, Adrià Subirana¹,
Jordi Riu¹ and Santiago Royo¹⁻²

¹*Center for Sensors, Instruments and Systems Development (UPC-CD6), Universitat Politècnica de Catalunya, Rambla de Sant Nebridi 10, 08222, Terrassa, Spain.*

²*Beamagine S.L., Carrer de Bellesguard 16, 08755, Castellbisbal, Spain.*

*E-mail: gerard.de.mas@upc.edu

1. Introduction

Autonomous driving has been a long-awaited dream since the appearance of the first car due to its potential high impact on human lives and the environment[1]. Yet, with the recent advances in artificial intelligence and the appearance of Light Detection And Ranging (LiDAR) in the market, we may not have to wait much longer.

Artificial Intelligent perception algorithms, however, need huge amounts of data in order to be reliable. Several data acquisition prototypes have been proposed and used to produce labeled autonomous driving data sets. The best known ones are nuScenes[2], KITTI[3], and Waymo Open[4]. Most of them include LiDAR technology, as well as other sensors like cameras or radars. The use of LiDAR is key to progress in the field due to the precise and real-time 3D measurement of the scene that provides.

However, state-of-the-art data sets present weaknesses from two perspectives. First, most of them use the same rotating LiDAR technology, which lacks resolution in comparison to the most novel solid-state LiDAR models. Moreover, this hinders generalization performance from neural networks, which easily get used to a single type of data distribution. Secondly, sensors like cameras and LiDARs have little tolerance to adverse weather conditions such as fog, smoke, or heavy rain. A truly autonomous vehicle has to be robust under any situation it might encounter.

Overall, producing representative real-life data sets for autonomous driving is costly and time-consuming. To tackle this issue, there have been efforts to develop reliable and representative virtual environments powered by physics engines to produce synthetic data of autonomous driving scenes, such as in the CARLA Simulator[5], or the Nvidia Omniverse[6]. These simulations ease data generation and labelling. Nevertheless, these methods cannot be used to generate synthetic data of adverse weather conditions as they differ too much from to real life acquisitions.

2. Methodology

To address this issue, this work proposes a data acquisition system for autonomous driving strongly based on data fusion and multimodal imaging, including a solid-state LiDAR, radars, and RGB, thermal, SWIR and polarimetric cameras.

Figure 1 shows the sensor configuration of the prototype for data acquisition and data set generation. The vehicle is a Dacia Duster Essential ECO-G, due to its size and reasonable price. It can be seen that the prototype uses three high-resolution RGB cameras. Two of them with a wide field of view (FoV) that reach a combined of 115°x50° of the frontal part of the vehicle. The other RGB camera has a narrower FoV and its main purpose is to focus on small and distant objects in the current trajectory of the vehicle. Additionally, the prototype has a high-resolution SWIR camera that gives us redundant information and different failure modes from the RGB cameras, to give more robustness to the system and improve detection in challenging environments. The prototype uses two automotive radars to get 3D and velocity information from its surroundings. Lastly, as its core sensor, we have an L3CAM. That is a multimodal embedded system produced by Beamagine S.L.that contains a thermal camera, a polarimetric camera sensible to visible light, and a high-resolution solid-state LiDAR to obtain robust 3D information of the scene at real-time refresh rate. In total, 10 different sensors and the combinations of their imaging modes may be used to cover the front region of the vehicle.

It can be seen that there is a complete overlap between all sensor modes in a FoV of $60^\circ \times 20^\circ$ in front of the vehicle. This sensor configuration shows high robustness due to its redundancy and resilience against adverse weather conditions and low illumination. Furthermore, the addition of non-conventional sensors such as thermal, polarimetric, or SWIR cameras in combination with radars, gives complementary information in conditions where RGB cameras and LiDARs might fail, such as fog or heavy rain.

All the sensors are controlled by an automotive-certified Nvidia Drive AGX through a ROS-based software architecture. Apart from data acquisition and visualization, the Nvidia Drive also controls the temporal synchronization of every sensor as well as all data fusion algorithms, including spatial calibration. To store the data we use an onboard QNAP NAS synchronized with the Nvidia Drive.

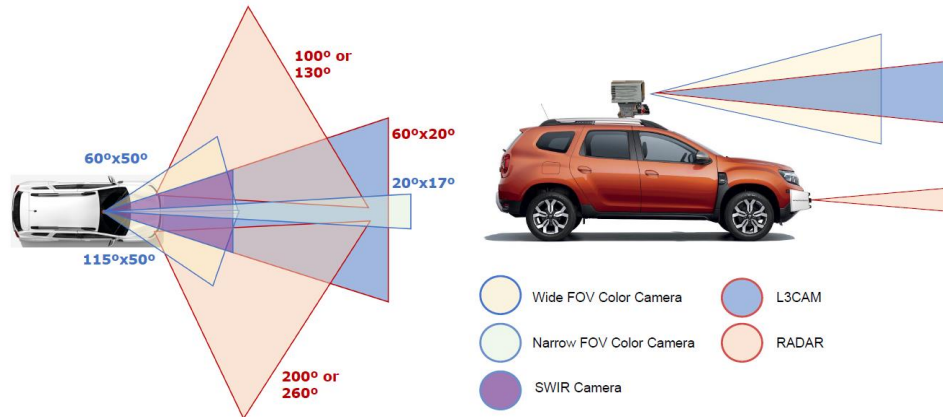


Figure 1 Sensors configuration on the onboard prototype.

3. Conclusions

This work presents a data acquisition system for autonomous driving based on multimodal imaging that is robust under adverse weather conditions. As future work, the authors intend to publish a labeled data set for autonomous driving with the acquired data from the prototype. Also, the authors are currently working on developing a digital twin of the prototype to further generate complementary synthetic data.

Acknowledgments

This work has been possible thanks to projects MISTED PID2020-119484RB-I00 and USEFUL TED2021-132338B-I00 funded by Ministerio de Ciencia e Innovación de España. This work is part of a Ph.D. Thesis with grant number 2023 FI-1 00229 co-funded by the European Union.

References

- [1] D. Parekh *et al.*, “A Review on Autonomous Vehicles: Progress, Methods and Challenges,” *Electronics*, vol. 11, no. 14, Art. no. 14, Jan. 2022, doi: 10.3390/electronics11142162.
- [2] H. Caesar *et al.*, “nuScenes: A multimodal dataset for autonomous driving.” arXiv, May 05, 2020. doi: 10.48550/arXiv.1903.11027.
- [3] A. Geiger, P. Lenz, and R. Urtasun, “Are we ready for autonomous driving? The KITTI vision benchmark suite,” in *2012 IEEE Conference on Computer Vision and Pattern Recognition*, Providence, RI: IEEE, Jun. 2012, pp. 3354–3361. doi: 10.1109/CVPR.2012.6248074.
- [4] P. Sun *et al.*, “Scalability in Perception for Autonomous Driving: Waymo Open Dataset.” arXiv, May 12, 2020. doi: 10.48550/arXiv.1912.04838.
- [5] F. Nesti, G. Rossolini, G. D’Amico, A. Biondi, and G. Buttazzo, “CARLA-GeAR: a Dataset Generator for a Systematic Evaluation of Adversarial Robustness of Vision Models.” arXiv, Jun. 09, 2022. Accessed: Oct. 04, 2023. [Online]. Available: <http://arxiv.org/abs/2206.04365>
- [6] “NVIDIA Omniverse Documentation.” Accessed: Apr. 03, 2024. [Online]. Available: <https://docs.omniverse.nvidia.com/>

The Gradient-Phase Interferometer for Precise Segment Phasing in the Primary Mirror of the ESO Extremely Large Telescope

Noel Rodrigo^{1*}, Pau Santos¹, Santiago Royo¹, Alexander Diaz², Gaizka Murga², Maialen González², Borja Vega², Afonso Teixeira², Juan Francisco Márquez², Andreas Förster³, Sebastian P. Schmid³, Samuel Lévêque³, Philippe Gitton³ and Martin Dimmler³

¹CD6, Universitat Politècnica de Catalunya, Rambla Sant Nebridi 10, E08222, Terrassa, España

²IDOM, Avenida Zarandoa 23, 48015 Bilbao, España

³European Organisation for Astronomical Research in the Southern Hemisphere, Karl-Schwarzschild-Straße 2, 85748 Garching bei München, Germany

*E-mail: noel.rodrigo@upc.edu

1. Introduction

The Extremely Large Telescope (ELT) is a revolutionary ground-based optical/infrared telescope, boasting a primary mirror (M1) with a 39-meter diameter. With its cutting-edge technology and colossal size, the ELT is poised to address numerous unsolved questions in astronomy and astrophysics. However, the segmented nature of the M1 mirror presents a significant challenge: the 798 hexagonal segments must be precisely aligned and phased to maintain the desired optical performance [1].

Accurate segment phasing is critical for minimizing wavefront errors, which degrade the image quality and thus the sensitivity of the telescope. The phasing process involves adjusting the relative piston of each pair of neighbor segments, ensuring that they collectively form a single continuous surface. Existing techniques for segment phasing are often limited by their accuracy, reliability, and time efficiency [2].

In this paper, we validate a novel interferometer concept specifically designed to optimize the segment pre-phasing process during day time for the ELT's M1 mirror. Our novel interferometer concept utilizes a gradient-phase reference beam to achieve 300 nm accuracy in piston together within a $\pm 250 \mu\text{m}$ range, reliability, and efficiency in segment alignment [3]. The innovative design proposed allows for simultaneous measurement of multiple segments, substantially reducing the overall phasing time and contributing to the ELT's operational readiness.

We begin by describing the theoretical principles underlying our novel interferometer, followed by a discussion of the interferometer's design and implementation. Finally, we compare the final prototype already built to validate the measurement method with the commercial interferometer Picoscale (SmarAct GmbH, Germany). Picoscale is an interferometer for contactless high precision displacement measurements based on an extremely compact Michelson-Interferometer.

2. The Gradient-Phase Interferometer

The novel Gradient-Phase Interferometer (GPI) has a wedge prism in the reference arm in order to create a linear gradient phase along the reference beam Eq. (1). A compensation plate is introduced in the other interferometer arm. In this way, the optical path difference (OPD) is only 0 in the center of the beam when the relative piston between the reference mirror and the target mirror is 0, Eq. (2). The GPI uses partially coherent light, which enables to measure piston from the relative position of the fringes on the image sensor, rather than by conventional fringe counting.

$$OPL_{REF}(x) = n(x) \cdot d \quad (1)$$

$$OPL_{TAR}(x) = n \cdot d + 2Piston \quad (2)$$

Such linear phase change allows the measurement of the piston between two segments as a linear

function of the displacement of the interference pattern across the detector. The measurement of relative tip and tilt are decoupled from the relative piston measurement and may be obtained simultaneously.

The relative tip between the reference and the target mirror changes the interference fringe width and thus, the envelope width of the partially coherent interferogram. On the other side, relative tip between mirrors affects the inclination of the interference fringes. Thus, the three measurements are decoupled and can be measured with a single interferogram.

In order to achieve the desired piston range, the area of the imaging sensor has been divided into different regions with a constant phase change between them, which is obtained by means of a stepped compensation plate. The thickness of each zone of the compensation plate has been carefully chosen in order to have some overlapping between consecutive zones in terms of OPD function and ensure complete coverage of the measurement range. Such OPD function can be described as $OPD(x_i) = OPD(x'_{i+1})$, where x is the axis along the gradient phase has been created and the subindex i designates the stepped compensation plate zone.

As shown in Fig. 1, a partially coherent light source transmitted by beam splitters BS1 and BS2 illuminates the area of interest of the reference mirror and is reflected back by BS2 and BS3 and transmitted by BS4 to the sensor. The light from the same light source reflected by beam splitters BS1 and BS4 and transmitted by BS3 illuminates the target mirror and is reflected back and transmitted by BS3 and BS4 to the same imaging system which captures the interference between the two beams.

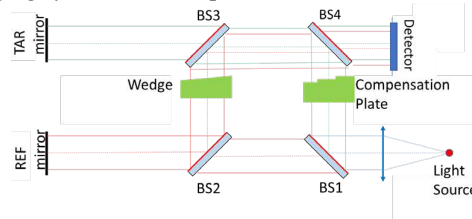


Figure 1 Schematic optical configuration of the Phase-Gradient Interferometer.

3. Results

The GPI has been compared with the Picoscale to validate the piston measurements. Target mirror was mounted on a piezoelectric and Picoscale was aligned to measure the linear displacement of the Target mirror. Simultaneous measurements have been acquired with GPI and Picoscale while modifying the relative piston between the Target and Reference mirrors in a $\pm 250 \mu\text{m}$ range, Fig. 2 (left). Linear relation between tip and fringe period have been also empirically demonstrated, Fig. 2 (right).

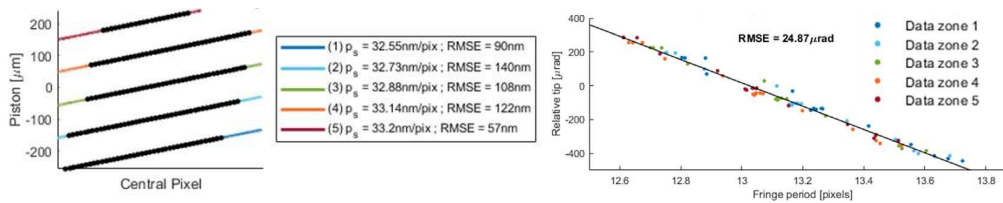


Figure 2 Linear relation between GPI central pixel and reference Piston measured with Picoscale (left). Fringe period as a function of relative tip (right).

4. Conclusions

We have validated the GPI for precise piston measurement. Moreover, results show linear relation between Picoscale and GPI with a maximum RMSE of 140 nm, thus confirming that GPI can measure relative piston for segment phasing with a precision better than 300 nm in a $\pm 250 \mu\text{m}$ range.

References

- [1] <https://elt.eso.org/>
- [2] S. Leveque, et al., "Day-time local phasing of neighbouring segments of the E-ELT primary mirror, based simultaneous multi- λ shearing interferometry", Proc. SPIE 9912, Advances in Optical and Mechanical Technologies for Telescopes and Instrumentation II, 99124G (2016).
- [3] G. Murga, et al., "The Extremely Large Telescope (ELT) M1 Local Coherencer to phase mirror segments," Proc. SPIE 12182, Ground-based and Airborne Telescopes IX, 1218206 (2022).

Quantum Communications Space Systems: INTA contributions

Alberto Álvarez-Herrero^{1*} on behalf of the INTA team

¹*Departamento de Óptica Espacial, Instituto Nacional de Técnica Aeroespacial, INTA,
Ctra de Ajalvir km4,28850 Madrid, Spain;*

*E-mail: alvarez@inta.es

1. Resumen

En los últimos años el desarrollo de tecnologías cuánticas ha experimentado un crecimiento espectacular, impulsado por el interés de la industria y los gobiernos en implementar estos sistemas en el corto y medio plazo. Algunos de los campos donde se vislumbra un gran potencial son los sensores, la computación y las comunicaciones. En este contexto, la amenaza que supone el ordenador cuántico para la criptografía clásica ha estimulado intensamente los desarrollos en comunicaciones cuánticas. En ese sentido, la implementación de una red de distribución clave cuántica (QKD, Quantum Key Distribution) en Europa, así como el desarrollo de las tecnologías requeridas para QKD se consideran objetivos estratégicos.

Una de las actividades más importantes es la iniciativa de la Comisión Europea denominada European Quantum Communications Infrastructure (EuroQCI). La EuroQCI consiste en un segmento terreno formado por redes de fibra óptica en los núcleos urbanos de las principales ciudades y un segmento espacial para las comunicaciones de larga distancia. Como parte del segmento espacial de la EuroQCI, la ESA (European Space Agency) está desarrollando SAGA (Security And cryptoGrAphic mission), que consiste en una red de satélites de comunicaciones cuánticas.

En este marco, España tiene importantes iniciativas que involucran grandes consorcios nacionales con actores industriales, académicos y nuevas empresas de base tecnológica. Por un lado, el Ministerio de Ciencia, Innovación y Universidades, a través del CDTI (Centro de Desarrollo Tecnológico e Industrial) y con fondos del PERTE Aeroespacial está financiando el desarrollo de un sistema de QKD desde órbita geoestacionaria (GEO) y también el desarrollo de un sistema desde órbita (LEO). Por otro lado, apoyado en el Plan de Recuperación, Transformación y Resiliencia y en la financiación autonómica, también ha lanzado los Planes Complementarios entre los que se incluye uno específico para comunicaciones cuánticas entre las ocho áreas estratégicas seleccionadas.

El INTA participa en estos grandes proyectos, aportando su conocimiento en Óptica Espacial, y específicamente en polarimetría, ya que habitualmente son los estados de polarización de los fotones los que se emplean para la transmisión de la clave. Además de esto, el INTA aporta su larga experiencia y su red de estaciones terrenas, así como sus conocimientos en seguridad. Esto es especialmente importante en el caso del sistema de navegación por satélite Galileo que, además, es un caso de uso futuro de sistemas QKD. Por otro lado, su programa de constelaciones de pequeños satélites, ANSER, permitirá realizar demostraciones tecnológicas de enlaces QKD entre satélites.

En este trabajo se presentarán las contribuciones a estos proyectos, haciendo especial hincapié en los desarrollos ópticos en los que se está trabajando. Estos van desde el diseño de la instrumentación óptica embarcada en satélite para la emisión y recepción de clave cuántica mediante fuentes de fotones Prepare&Measure, hasta sistemas de control de la polarización basados en cristales líquidos que evitan mecanismos abordo, lo que resulta esencial para pequeñas plataformas.

Acknowledgments

El autor quiere agradecer al equipo del INTA su gran dedicación y excelente trabajo, que presenta en esta contribución en representación del mismo.

Además, agradece el apoyo de “MADQuantum-CM”, proyecto financiado por la Comunidad de Madrid y por el Plan de Resiliencia, Transformación y Recuperación, (NextGenerationEU-European Union).

Multipoint temperature sensing with time-resolved acousto-optic interaction in optical fibers

Jean Paul Marrou Osores^{1*}, Jaime Cascante Vindas², Martina Delgado Pinar¹, Antonio Diez Cremades¹ y Miguel V. Andrés Bou¹

¹*Departamento de Física Aplicada y Electromagnetismo, ICMUV, Universidad de Valencia, C/Dr. Moliner, 50, 46100 Burjassot, Spain*

²*Escuela de Ingeniería Eléctrica, Universidad de Costa Rica, Ciudad de la Investigación, San Pedro, San José, 11501-2060 UCR, Costa Rica*

*E-mail: jean.marrou@uv.es

1. Introduction

The acousto-optic interaction in optical fibers is a phenomenon that has been widely studied and that allows the fabrication of sensors by means of the mode coupling induced by the periodic modulation of the refractive index in a specific interaction length of the fiber [1]. A particular variant of this technique is to use wave packets traveling longitudinally through the interaction zone, so that the information of interest is time resolved and easily captured with a photodetector and a conventional bandwidth oscilloscope [2]. Since time can be correlated with the axial coordinate of the interaction length through the velocity of the acoustic pulse, this technique allows axial resolution.

An example of sensing is the real-time temperature measurement, from several hot spots at once, of a longitudinal element with a length less than the interaction length of our fiber optic sensor. This publication demonstrates this possibility with an experimental setup.

2. Methodology and Results

Figure 1 shows the experimental setup used to perform the multipoint temperature measurement with acousto-optic interaction along 80 cm of SMF-28e bare optical fiber and which has been axial resolved with the help of a photodetector and oscilloscope. In this configuration an SMF-28e optical fiber has been installed between two positioners (XYZ and Z), whose input has been connected to an Agilent 8164B tunable laser (TPL) through a manual polarization controller (FPC) and its output to a MHz bandwidth oscilloscope through a New Focus 2011 variable gain photodetector (OSC2). The interaction zone consists of 80 cm of bare optical fiber, which has been connected at one end to a 2 MHz piezoelectric using a solid aluminum cone and 0-triethyl acetylacrylate-based glue. The piezoelectric is excited with sine wave packets in the range of 2.5-3.0 MHz and an amplitude less than 100 V. The "burst" function of a Hameg HMF2550 arbitrary function generator (AFG) and an AR 75A250 RF amplifier (AMP) have been used to excite the flexural acoustic wave packet.

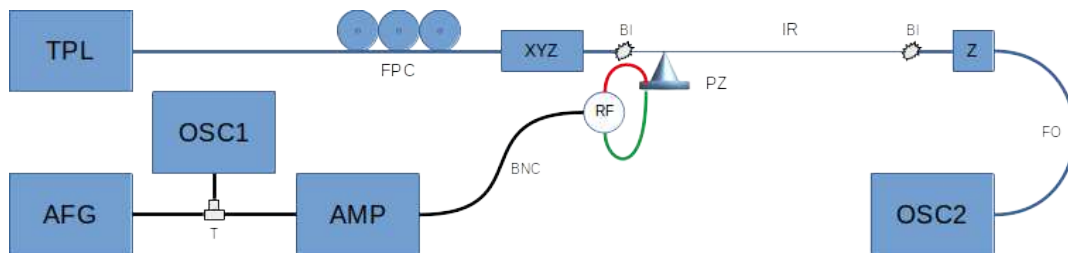


Figure 1 Experimental setup. Arbitrary Function Generator (AFG), BNC Cable (BNC), Electrical Piezoelectric (PZ), Fiber Optics (FO), Fiber Optic Interaction Region (IR), Fiber Polarization Controller (FPC), Mechanical Z Positioner (Z), Oscilloscope (OSC1), Oscilloscope with Photodetector (OSC2), RF Amplifier (AMP), Tunable Polarized Laser (TPL), RF Connector (RF), Acoustic Blocker (BI), XYZ Mechanical Stage (XYZ).

Figure 2 shows the results of the temperature measurement for a range between 24 °C and 65 °C. Fig. 2 (a) shows the spectral behavior of the resonance generated by exciting a flexural acoustic wave at a frequency of 2602.8 kHz and launching a 1550 nm broad spectrum LED into the optical fiber. We see

that the measurable range determined by the width of this resonance is limited up to 65 °C because the peak of the resonance at room temperature coincides with the valley at 65 °C. After that limit, no significant changes could be recorded. Fig. 2 (b) collects the temporal snapshots and Fig. 2 (c) plots the difference in mV, for each of the temperatures, of the point of maximum change with respect to the value at room temperature. In this case, the piezoelectric was excited with 25 cycles per packet at 2602.8 kHz and the laser was tuned at 1522.7 nm. This hot spot was generated on a 5 mm wide aluminum plate with the help of two Peltier cells and a PID controller. A quadratic response was fitted ($R^2= 0.987$).

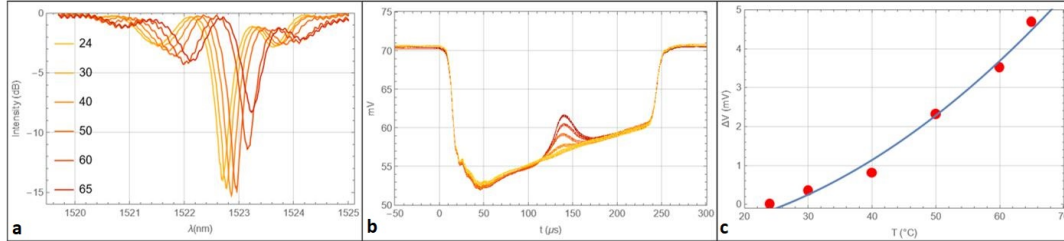


Figure 2 (a) resonance spectral tunability with temperature, (b) temporal traces of the transmittance as a function of temperature when launching acoustic packets and (c) results plotted with respect to room temperature, for a range between 24 °C and 65 °C. Line is an eye guide.

Figure 3 shows an example of qualitative temperature sensing at various points in the interaction region. This test has been performed by approaching the tip of an electric soldering iron to the surface of the bare optical fiber. In this test we can see how the time response of the recorded signal changes at the physical points where the soldering iron has been brought close. Due to the electrical frequency and the number of cycles per packet used, the spatial resolution is limited to approximately 5 cm.

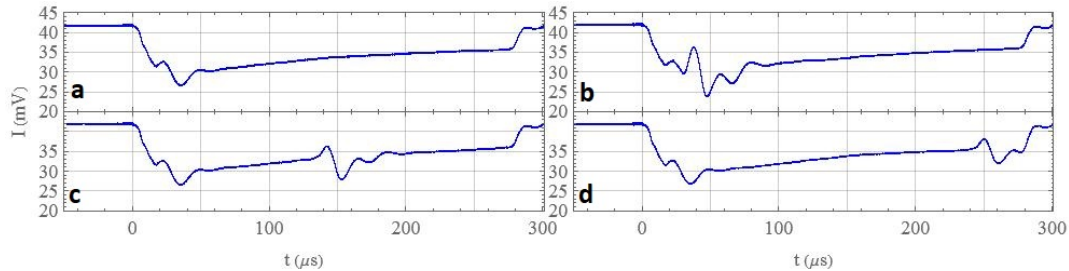


Figure 3 Multipoint temperature sensing test in the interaction length. (a) reference, (b) 10 cm, (c) 40 cm, (d) 70 cm.

3. Conclusion

In this paper we have reported an example of multipoint temperature sensing using time-resolved acousto-optic interaction in optical fibers. The range of temperatures that can be measured with this resonance ranges from 24 to 65 °C, and the axial resolution is less than 5 cm, value that can be improved further by a precise control of the acoustic packet.

Acknowledgments

This research was funded by the Ministerio de Ciencia e Innovación and co-funded by the European Regional Development Fund, Ref. TED2021-130200B-I00, the European Commission, Ref. H2020-MSCARISE-2019-872049 and the Generalitat Valenciana, Ref. CIPROM/2022/030

References

- [1] Lu, J., Shi, F., Xu, J., Meng, L., Zhang, L., Cheng, P., Zhou, X., Pang, F. and Zeng, X. "Recent progress of dynamic mode manipulation via acousto-optic interactions in few-mode fiber lasers: mechanism, device and applications". *Nanophotonics* **10(3)**, 983-1010 (2021). <https://doi.org/10.1515/nanoph-2020-0461>
- [2] E. P. Alcusa-Sáez, A. Díez, M. González-Herráez, and M. V. Andrés, "In-fiber time-resolved acousto-optics," in *Latin America Optics and Photonics Conference*, OSA Technical Digest (online) (Optica Publishing Group, 2014), paper LTu3D.1.

Measurement of optical fiber diameter changes with nanometer resolution based on forward-stimulated Brillouin scattering.

C. Álvarez-Ocampo^{1,*}, M. Delgado-Pinar^{1,2}, A. Díez^{1,2}, J. L. Cruz^{1,2}, M. V. Andrés^{1,2}

¹Laboratory of Fiber Optics, ICMUV, Burjassot, Spain

²Departament de Física Aplicada i Electromagnetisme, Universitat de València, Burjassot, Spain

*E-mail: carlos.alvarez@uv.es

1. Introduction

The physical mechanism of electrostriction can lead to strong interaction between optical and acoustic waves in dielectric waveguides. This mechanism leads to the different types of Brillouin scattering processes. In forward-stimulated Brillouin scattering (FSBS), two copropagating optical waves interact with transverse acoustic mode resonances (TAMRs). In recent years, FSBS has been proposed as a novel mechanism on which new fiber optic sensing techniques can be based [1-2]. In single-mode optical fibers, an optical beam propagating along the fiber core can stimulate the oscillation of two types of TAMRs, purely radial modes, $R_{0,m}$, and a series of torsional-radial modes, $TR_{2,m}$. Each TAMR exists at a specific frequency, which depends on the acoustic velocities in the optical fiber and its diameter. In conventional optical fibers, TAMRs with resonance frequency from a few tens of MHz to 1 GHz can be excited by FSBS, and the quality factor of such acoustic resonances is of the order of a few thousand. Any change of the mechanical properties of the fiber will produce the frequency shift of the resonances. Based on this operation principle, several sensing applications have been reported. For instance, simultaneous measurement of strain and temperature based on the dependence of the acoustic velocities on such physical magnitudes has been reported [3]. Due to the high Q-factor of TAMRs, a remarkable resolution of 0.2 °C in temperature and 25 $\mu\epsilon$ in strain was achieved.

In this paper, we present an experimental work in which we investigate the limits of FSBS to detect structural changes of the optical fiber. Specifically, we study the ability to detect and measure small diameter changes, and we analyze the resolution of the method.

2. Experimental results

Figure 1 shows the experimental setup. TAMRs were excited in the fiber by short optical pulses that were delivered into the fiber under test. The pump laser emitted linearly polarized optical pulses of 700 ps duration at 20 KHz repetition rate, with 150 mW average power at 1064 nm wavelength. A half- and two quarter-wave plates were used for polarization control of the pump. The pump beam was delivered into the FUT with a $\times 30$ aspheric lens and 3-axis stage. TAMRs were detected optically by means of a probe beam provided by a CW tunable laser emitting in the C band that was delivered into the fiber through a WDM. The polarization modulation of the probe signal caused by the oscillation of $TR_{2,m}$ acoustic modes was translated into intensity modulation with a linear polarizer.

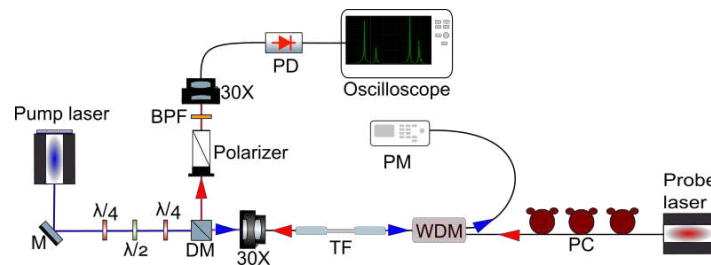


Figure 1 Experimental arrangement. BPF: bandpass filter; PM: power meter; M: mirror; PD: fast photodiode; DM: dichroic mirror; WDM: fiber optic wavelength-division multiplexer; PC: optical fiber polarization controller; TF: Fiber under test.

The fiber structure investigated consisted of a segment of 5 cm in length of conventional optical fiber (nominal diameter of 125 μm), followed by a 4 cm long segment of fiber whose diameter was reduced by

a certain amount in a controlled manner using a fusion-and-pulling processing technique. The first section was included as a reference. Different structures were prepared and tested with decreasing values of diameter of the processed fiber section. Resonant frequencies of $TR_{2,m}$ acoustic modes were studied from the FFT of the probe optical signal.

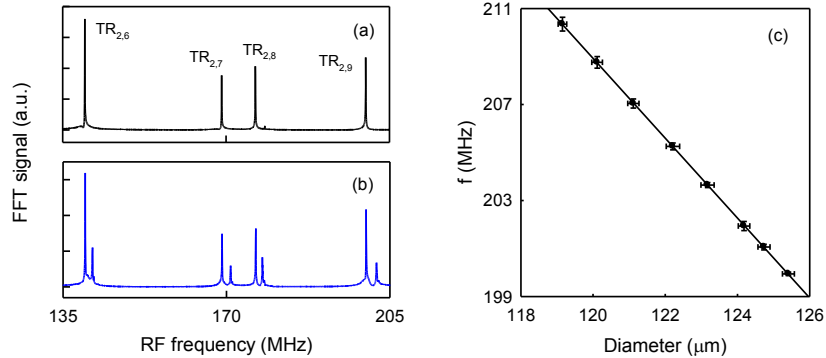


Figure 2 (a) Radio-frequency (RF) spectrum of the probe signal for (a) a section of 5 cm in length of uncoated pristine fiber (125 μm nominal diameter), and (b) a concatenated optical fiber structure composed by a section of 5 cm of pristine optical fiber followed by 4 cm of 124 μm diameter fiber. (c) Resonance frequency of $TR_{2,9}$ acoustic mode vs. fiber diameter.

Figure 2 shows part of the RF spectrum of the probe signal in two different cases. Figure 2 (a) corresponds to the spectrum when only a section of pristine fiber is tested. Different peaks corresponding to the oscillation of several $TR_{2,m}$ modes (labelled in the figure) are observed. Figure 2 (b) corresponds to a fiber structure that includes a section of pristine fiber and a section of 124 μm diameter. Here, it can be observed the splitting of each $TR_{2,m}$ mode as a result of the sensitivity of the resonance frequencies with the fiber diameter. We investigated the resonance frequency shift as a function of fiber diameter. Figure 2 (c) shows the result for the $TR_{2,9}$ acoustic resonances. Frequency increases linearly as the fiber diameter decreases; for this resonance, the slope is $-1.66 \text{ MHz}/\mu\text{m}$.

The resolution, i.e., the smallest fiber diameter change that can be detected by this method depends on the frequency shift rate, but also on the spectral bandwidth of the peak. The FWHM of the peak produced by the oscillation of the $TR_{2,9}$ was 160 kHz. If we assume that our RF analyzer can resolve a frequency shift equal to $1/10^{\text{th}}$ of the FWHM, then a fiber diameter change of $<10 \text{ nm}$ can readily be detected. Similar resolution values are achieved when considering any other resonance.

3. Conclusions

FSBS provides a powerful tool for the characterization of optical fibers. The frequency dependence of the resonant acoustic modes excited by FSBS with the fiber radius, in conjunction with the high Q-factor of these resonances, make it possible to measure diameter changes with nanometric resolution.

Acknowledgments

This research was funded by the Ministerio de Ciencia e Innovación and co-funded by the European Regional Development Fund (TED2021-130200B-I00), the European Commission (H2020-MSCA-RISE2019-872049), and the Generalitat Valenciana (CIPROM/2022/030).

References

- [1] Y. Antman, A. Clain, Y. London, and A. Zadok, "Optomechanical sensing of liquids outside standard fibers using forward stimulated Brillouin scattering", *Optica*, **3**, 510 (2016).
- [2] D. M. Chow, Z. Yang, M. A. Soto, and L. Thévenaz, "Distributed forward Brillouin sensor based on local light phase recovery", *Nat. Commun.* **9**, 2990 (2018).
- [3] L. A. Sánchez, A. Díez, J. L. Cruz, and M. V. Andrés, "Strain and temperature measurement discrimination with forward Brillouin scattering in optical fibers," *Opt. Express* **30**, 14384-14392 (2022)

Characterisation of the Double Pulse configuration for the PW class laser system VEGA-3 at CLPU

E. García-García^{1*}, M. Olivar¹, I. Hernández-Palmero¹, O. Varela¹, F. Galán¹, J.D. Pisonero¹, J. Pisonero¹, A. Vaquero¹, J.M. Hernández-Pérez¹, R. Lera¹, G. Gatti¹, M.D. Rodríguez Frías^{1,2} and C. Méndez¹

¹ Pulsed Laser Centre (CLPU), Salamanca, Spain

³ Universidad de Alcalá, E-28801, Madrid, Spain

*E-mail: egarcia@clpu.es

1. System description and stability characterisation

Laser-plasma acceleration is a well established technique for particle acceleration to the order of GeV [1]. Novel techniques tailoring the yield of energy and charge of the accelerated beam are still being developed. One of those techniques is the use of an auxiliary beam that can pre-ionize the laser bubble for a second beam that accelerates the charge and the use of a two co-linear propagating copies from the same laser has proven to be a way to reduce beam to beam fluctuations and instabilities [2,3].

VEGA is a laser amplification chain installed in the Spanish Pulsed Laser Centre (CLPU) [4]. It has three main laser lines named VEGA-1,2,3 with a peak intensity of 20 TW, 200 TW and 1 PW, respectively. All the three outputs share a common front-end which ensures good temporal coherence, great contrast at the picosecond regime and an equivalent spectrum for all the outputs that allows operating all of them below 40 fs when one of the other outputs has been configured for pulses below 30 fs. The CLPU is an user open facility that has developed several improvements on the laser chain to extend the system capabilities to the cutting edge science and user requests. One of them is the implementation of a double pulse line within the VEGA-3 amplifier as can be seen in Fig.1.

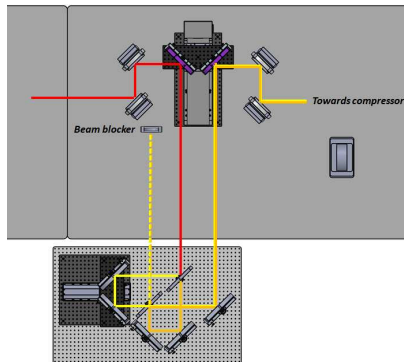


Figure 1 Double pulse installation scheme. The beam is extracted with a bypass mirror to be sent to the Mach-Zehnder interferometer before it returns to the main amplifier before the compressor.

In order to generate a double pulse line we have chosen to extract the beam from the chain after the main amplifier, and use a Mach-Zehnder interferometer approach to generate a copy of the pulse. This approach after the main amplifier ensures a safe amplification process, a good management of the dispersion by choosing equal substrate beam splitters and a delay range from 0 fs to 1 ns with different energy balances. The main drawback of this configuration is that half of the energy of the initial pulse must be blocked out. Different energy balances between the two pulses can be achieved changing the reflective/transmission characteristics of the beamsplitters. Three different beam splitters are part of the scheme with the following reflection/transmission values: 50/50, 60/40, 80/20. With these elements four different pulse-pulse energy combinations are available in the experimental room taking into account

compressor losses: 10J/2.5J, 12K/2J, 8J/3J and 7.5J/5J.

In this work we report the characterization done after the compressor to determine key parameters in the double pulse laser operation. The measures were taken with the amplifier working at its nominal values of 38 J of energy and 1 Hz of repetition time. The beam is then attenuated with a fixed value all reflective attenuator to 4 mJ before it is sent to the double pulse stage configured with the beam splitter configuration of 50/50 for the first beam splitter and 80/20 for the second.

Jitter measurements have been taken for periods longer than two hours on different days. The measures were taken by recording the spectrum of every shot for a fixed delay with two different spectrometers from Avantes AvaSpec 2048 and Ocean Insight HR4Pro each of them with a resolution below 0.5 nm. Then Fourier analysis is carried out to retrieve the instantaneous phase difference between both pulses and from there the time delay.

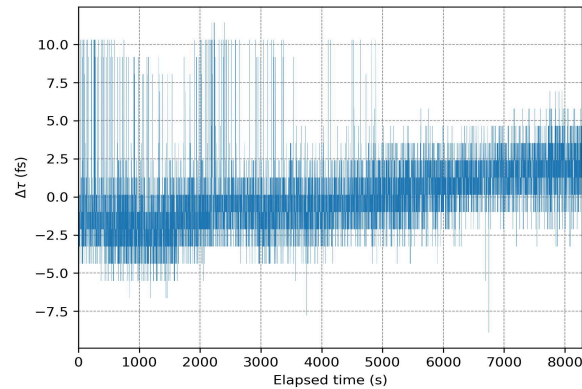


Figure 2 Time evolution of the extracted instantaneous delay between pulses for every shot. The noisy signal gives an idea of the measurement precision being on the order of a few femtoseconds. The standard deviation for the measure is 4 fs.

2. Conclusions

VEGA-3 capabilities have been extended by the addition of a double pulse scheme. This scheme has been characterized to ensure safe amplification and no degradation of the original VEGA-3 performance.

The temporal jitter between pulse replicas has been measured for the time lapse greater than two hours. We have found a clear growing tendency (Fig.2) that could be related with the warming dynamic in the system, but it is still to be determined. The jitter standard deviation is below 4 fs for the plus two hour measurement that ensures a good temporal stability between the two replica pulses for its experimental usage.

Acknowledgments

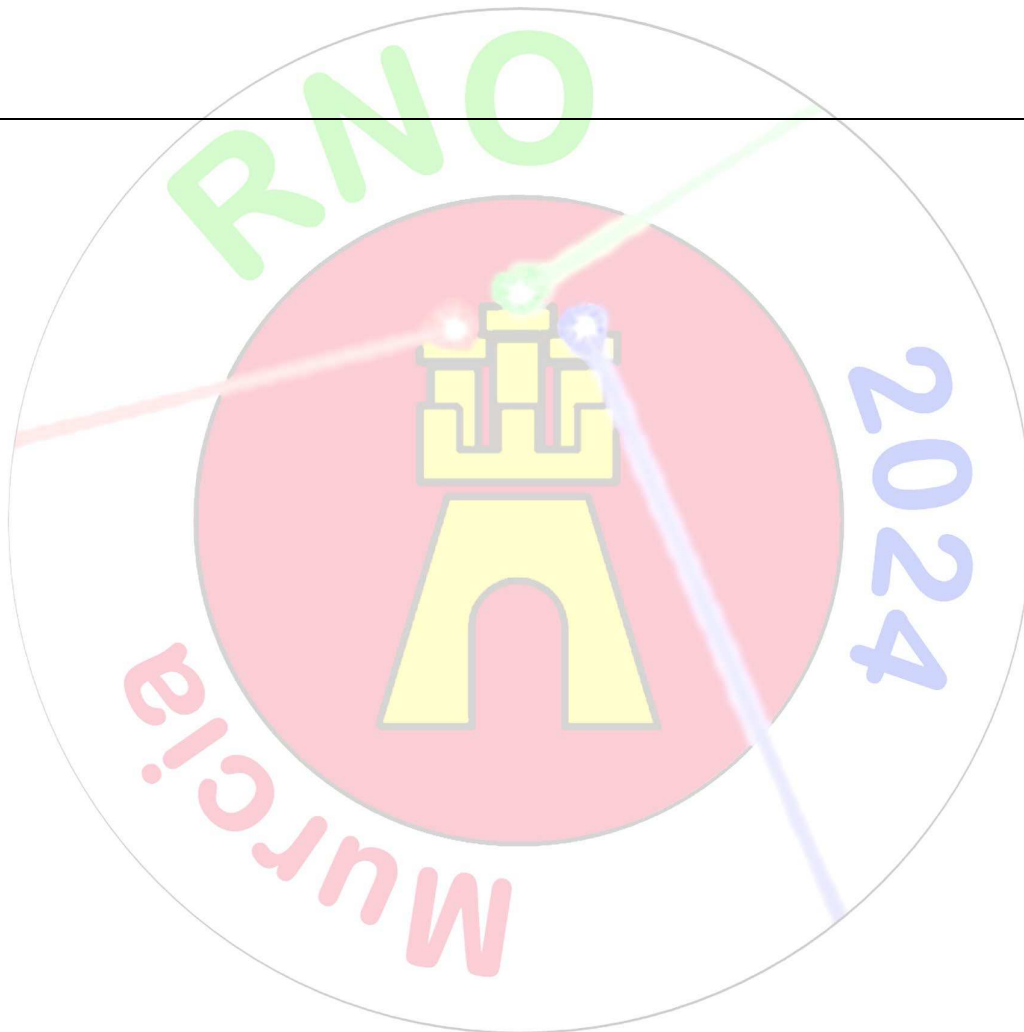
We acknowledge the Spanish MCIN through ICTS Equipment Project No. ICTS-2020-04-CLPU-17, FEDER, UE. We also acknowledge all the areas of the CLPU for their support.

References

1. T. Tajima and J. M. Dawson, "Laser Electron Accelerator," *Phys Rev Lett* **43**, 267–270 (1979).
2. Z. M. Chitgar, P. Gibbon, J. Böker, A. Lehrach, and M. Büscher, "Electron self-injection threshold for the tandem-pulse laser wakefield accelerator," *Phys. Plasmas* **27**, 023106 (2020).
3. M. Yigitoglu Keskin, W. Pring, J. A. Pérez-Hernández, R. Lera Matellanes, J. Mill, D. De Luis, N. Boudjema, O. Varela, E. García-García, C. Méndez Valverde, E. Brunetti, B. Ersfeld, S. Kumar, S. M. Wiggins, G. Gatti, L. Volpe, L. Roso, M. B. Demirköz, and D. A. Jaroszynski, "Method of producing 100 keVs ion beams from a gas jet using two intense laser pulses," in *Laser Acceleration of Electrons, Protons, and Ions VII*, C. B. Schroeder, J. Schreiber, M. S. Hur, S. S. Bulanov, and D. A. Jaroszynski, eds. (SPIE, 2023), p. 5.
4. "CLPU. Centro de Láseres Pulsados - CLPU," <https://www.clpu.es/>.

RESÚMENES/ABSTRACTS

PÓSTERS



Size and temperature characterization of levitating particles

Laura Martínez Maestro¹, Juan Ignacio Tomás Echavarría¹, Miguel Antón-Revilla²,
Dries van Oosten³, Rosa Weigand¹ and Javier Hernandez-Rueda^{1,*}

¹ Department of Optics, Faculty of Physics, Universidad Complutense de Madrid, Spain

² Department of Optics, Faculty of Optics and Optometry, Universidad Complutense de Madrid, Spain

³ Debye Institute for Nanomaterials Science, Utrecht University, the Netherlands

*E-mail: fj.hernandez.rueda@ucm.es

We present a novel experimental method designed for probing the photoluminescence and scattering phenomena arising from individual levitating particles excited by laser. Our setup synergistically integrates a quadrupole ion trap, a dark-field microscope combined with a multi-wavelength laser system and a spectroscopy apparatus. We illustrate how the scattering and photoluminescence signals can be used for determining the size and temperature of trapped particles, respectively. In this work, we focus on characterizing the size and temperature of Er/Yb-doped dielectric particles.

1. Nanoparticle Trap system.

The particle trap apparatus is based on a linear quadrupole Paul trap configuration and is built within a transparent vacuum chamber.[1] The trap uses four metallic rods, which are diagonally connected in pairs to either an oscillating high-voltage source or to a direct-current voltage. This configuration yields a time-oscillating quadrupolar electric field capable of trapping single particles. The inset in Figure 1 a) shows a picture of an array of trapped particles. The bright red spots in the picture correspond to the laser light scattered by single trapped particles along the axis of the trap.

2. In-situ dark-field microscopy for particle size characterization.

The trap is combined with a dark-field microscope that enables us to visualize the intensity of scattered light using a CCD camera. We systematically record the scattering signal as a function of the polarization angle of incident continuous-wave (cw) laser beams across three distinct wavelengths (642 nm, 785 nm and 852 nm). Figure 1 b) presents a graph of the scattered light intensity as a function of the polarization angle that results from illuminating a single Er/Yb-doped dielectric particle using a cw-laser at 852 nm. From the scattering experiments, we extract the optical visibilities at three wavelengths and compare them with calculations carried out using Mie theory. This comparison provides the size of the illuminated particles.

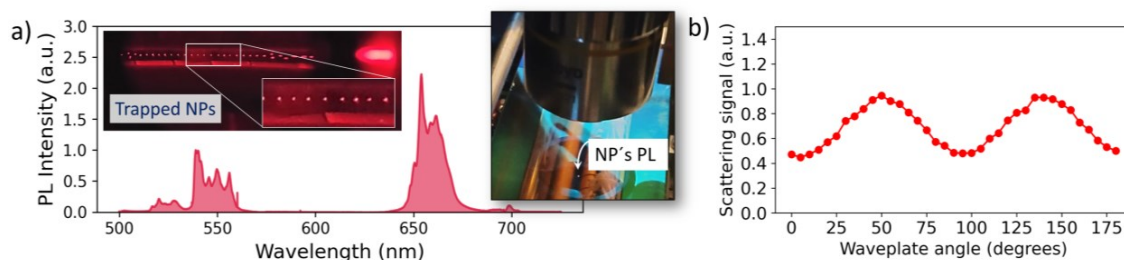


Figure 1 a) Photoluminescence of trapped Er-doped nanoparticles upon CW-laser illumination. The insets show an array of trapped particles (left) and the emitted PL signal by a single trapped particle (right). b) Scattering signal of single trapped nanoparticles as a function of the angle of a $\lambda/2$ plate. This measurement provides the size of the particle.

3. Fluorescent spectroscopy of single particles.

Our dark-field microscope allows us to guide the scattered or emitted light towards a spectrometer using a fiber-optic port. Figure 1 a) presents a photoluminescence spectrum of a single Er/Yb-doped dielectric particle excited by a cw-laser at 980 nm. This specific example allows us to infer a particle temperature of 25 °C based on the ratio of the spectral peaks at 525 nm and 546 nm [2]. The inset on the right-hand side of Fig. 1 a) illustrates a picture of the particle emitting green light.

4. Conclusions.

The experimental apparatus presented in this contribution has potential for investigating the scattering properties [3] and photoluminescence signature of single trapped nano-objects, such as quantum dots, particles with different geometries, composition and sizes as well as atomically thin materials or metamaterials.

Acknowledgments

The research presented in this conference contribution has been funded through Programa de Atracción de Talento de la Comunidad de Madrid, Modalidad 1, project number 2020-T1/IND-19951.

References

- [1] J. Hernandez-Rueda, D. van Oosten, Ultrafast laser ablation of trapped gold nanoparticles. *Optics Letters* 44 (13) pages 3294-3297 (2019).
- [2] F. Vetrone, R. Naccache, A. Zamarrón, A. Juarranz de la Fuente, F. Sanz-Rodríguez, L. Martínez Maestro, E. Martín Rodríguez, D. Jaque, J. García Sole, J. Capobianco, Temperature sensing using fluorescent nanothermometers. *ACS Nano* 4 (6), 3254-3258 (2010).
- [3] J. Hernandez-Rueda, D. van Oosten, Transient scattering effects and electron plasma dynamics during ultrafast laser ablation of water. *Optics Letters* 44 (7), 1856-1859 (2019).

Bio-inspired nanophotonics: new strategies to confine, transport and harvest light with organic matter.

Sara Núñez-Sánchez^{1*}

¹*Centro de Física das Universidades do Minho e do Porto (CF-UM-UP),*

Campus de Gualtar, PT-4710 - 057 Braga, Portugal.

**E-mail: S.Nunez-Sanchez@fisica.uminho.pt*

Nanophotonic devices are designed to confine, transport, and manipulate light at nanoscale. This manipulation is mainly constricted by the optical properties of the matter of its constituents. In the case of molecules, they have been used in photonics mainly as sources and sinks of photons in doped matter. However, photosynthetic organisms go further, and they use compact arrangements of molecules to promote an optimized transport at the nanoscale. In this work, we aim to understand how compact molecular arrangements like photosynthetic complexes can impact the optical properties of matter opening a new era for the manipulation of light by bio-inspired light-trapping strategies at the nanoscale.

Taking inspiration from the molecular composition of photosynthetic organelles, we've developed a collection of organic materials consisting of densely packed molecular aggregates within a polymeric framework. This set of organic materials exhibits tunable optical properties being the playground to create photonic structures like those found in natural systems. [1] In this contribution, I will present our last results on the design and development of two nanophotonic structures inspired by photosynthetic organelles and composed of these bio-inspired materials.

Firstly, inspired by sophisticated hierarchical photonic multilayer structures present the iridoplast of "*Begonia Pavonine*", we built an all-organic 2D photonic crystal. We did this by doping polymer layers with J-aggregates and forming a Bragg stack like the distribution of photosynthetic pigment in iridoplasts.[2] We demonstrate that the combination of the near-zero-index properties of the molecular layers with the biomimetic photonic structuring allows for enhanced absorption at wavelengths as it happens in natural systems. [3] Secondly, inspired by the molecular structure of light-harvesting complexes in "*Rhodospirillum molischianum*" bacteria, we have investigated the interactions between light and organic nanorings with dimensions like the corresponding natural nanoscale architectures. Electromagnetic simulations reveal that these J-aggregate nanorings can function as resonators, enabling the confinement of light beyond subwavelength scales and the concentration of electric fields in specific regions through polaritons. [1]

These findings pave the way for bio-inspired building components for photonics and metamaterials across the visible to infrared spectrum, all within an entirely organic platform. On the other hand, this provides a fresh perspective on nanoscale light-matter interactions in photosynthetic organelles while opening the door for the development of bio-inspired organic polaritonic platforms and structures.

Acknowledgments

This work was supported by i) the Portuguese Foundation for Science and Technology (FCT) under the contract 2022.03164.CEECIND and in the framework of the Strategic Funding UIDB/04650/2020 and ii) the European Union through the Horizon Europe research and innovation program under Grant Agreement #101129661-ADAPTATION. S.N-S acknowledges the financial support of grant TED2021-130522B-I00 funded by MCIN/AEI/10.13039/501100011033 and the "European Union NextGenerationEU/PRTR.

References

- [1] S. T. Holder, et al. "Bio-inspired building blocks for all-organic metamaterials from visible to near-infrared", *Nanophotonics* 12, 307–318 (2023)
- [2] M. A. Castillo, et al. "Enhanced Light Absorption in All-Polymer Biomimetic Photonic Structures by Near-Zero-Index Organic Matter", *Advance Functional Materials* 32, (2022)
- [3] M.Castillo, M. A. et al. "Tunable narrowband excitonic Optical Tamm states enabled by a metal-free all-organic structure", *Nanophotonics* 11, 4879-4888, (2022).

Fabricación y caracterización de celdas de cristal líquido basadas en fotoalineado de colorantes azo

Adrián Moya¹, Eva M. Calzado^{1,2*}, Emilio J. Mena^{1,3}, Víctor Navarro-Fuster², Manuel Ortuño^{1,2}, Andrés Márquez^{1,2} y Augusto Beléndez^{1,2}

¹*I.U. Física Apl. a las Ciencias y las Tecnologías, Univ. Alicante, P.O.Box 99, E-03080, Alicante, España*

²*Dept. de Física, Ing. de Sistemas y T. Señal, Univ. Alicante, P.O.Box 99, E-03080, Alicante, España*

³*Dept. de Óptica, Farmacología y Anatomía, Univ. de Alicante, P.O.Box 99, E-03080, Alicante, España*

*E-mail: evace@ua.es

1. Descripción

La investigación, caracterización y modelización de elementos ópticos basados en cristal líquido (LC Liquid Crystal) con fotoalineado es un área de gran relevancia en la actualidad debido a la versatilidad de funcionalidades que aportan los cristales líquidos en multitud de aplicaciones [1].

Las láminas de fotoalineado que encierran el cristal líquido constituyen un elemento crucial en términos de calidad óptica del producto, y en el control del alineamiento del LC en el interior de la celda. Una modulación en la orientación de las partículas LC induce un cambio en el índice de refracción, cambio que está controlado e influenciado por las capas de alineado que pueden tener diferentes patrones y/o composiciones en función de la aplicación buscada. Además, otra de las ventajas del uso de sistemas basados en LC es la capacidad de este de interactuar con campos eléctricos externos, por lo que lo convierte en un candidato excepcional para crear medios variables o con características dinámicas. La capacidad del fotoalineado de generar orientaciones espacialmente variantes del eje óptico del cristal líquido es por tanto muy importante para el diseño de elementos ópticos por fase geométrica. Para fabricar la capa de fotoalineado se utilizan diversos polímeros fotosensibles que en general pertenecen a la familia de los colorantes azo [2-4].

En este trabajo de investigación se han fabricado y caracterizado celdas de cristal líquido con capas de fotoalineado basadas en los colorantes azo comerciales Brilliant Yellow (BY) y Methyl Red (MR) con el cristal líquido comercial E7 con el objetivo de obtener una lámina retardadora, paso previo necesario para nuestras futuras investigaciones.

Para la fabricación de las celdas de LC basado en BY se prepararon disoluciones al 0,4 w% de BY en DMF. Mediante la técnica de spin-coating se depositaron películas de colorante de unos 10 nm sobre los sustratos de vidrio con capa de ITO. Una vez depositadas fueron calentadas durante media hora para eliminar restos del disolvente. Posteriormente esta película de material se iluminó con una haz de luz linealmente polarizada de longitud de onda 473nm, dentro del espectro de absorción del BY, en forma de spot de diámetro 1 cm y con una densidad de energía de 18 mW/cm² durante 20 minutos. Con ello se produce en el material una reconfiguración en sus enlaces que genera una dirección de alineamiento perpendicular a la dirección de polarización del haz incidente. Para montar la celda de LC se utilizaron dos sustratos con película de material fotoalineado separados por unos espaciadores de tamaños entre 5-20 μm. El espacio entre los dos sustratos delimitado por los espaciadores se rellenó con el LC E7 y se procedió por último al sellado de la celda.

Respecto a la fabricación de celdas de LC basadas en MR se utilizaron dos técnicas para conseguir el fotoalineado del material. En primer lugar se procedió de manera similar a la ya descrita para el BY para fabricar la capa de fotoalineado por spin coating. En este caso se prepararon disoluciones de MR al 1w% en dietil y sobre las películas depositadas se incidió con luz linealmente polarizada de longitud de onda 532nm en forma de spot de diámetro 1,5 cm y con una densidad de energía de 44 mW/cm² durante 20 minutos. Posteriormente se montó la celda siguiendo el procedimiento detallado para el BY.

La otra técnica para generar la capa de fotoalineado en el MR consistió en montar primero la celda e introducir una mezcla de LC E7 dopado al 1w% en peso de MR. Una vez fabricada la celda se iluminó el dispositivo con luz lineal a la longitud de onda de 532nm con las mismas características descritas para las películas depositadas por spin coating produciéndose el fotoalineado.

Para la caracterización de las celdas se incidió con luz linealmente polarizada a 45° a la longitud de onda de 633nm sobre la celda, recolectando la luz a la salida mediante un polarímetro (Fig. 1a, 2a). Seguidamente se aplicó campo eléctrico para comprobar si el estado de polarización de la luz a la salida de la celda cambiaba al aplicar distintos voltajes (Fig. 1b-c, 2b-c).

2. Figuras

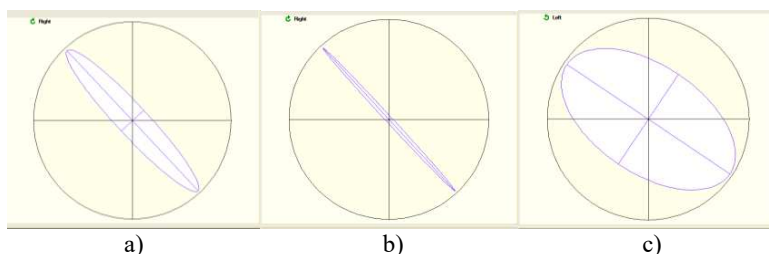


Figura 1 Estado de polarización de la celda de LC E7 con capa de fotoalineado de BY y espaciador de $10\ \mu\text{m}$ para a) 0 V b) 0,98 V c) 1,90 V.

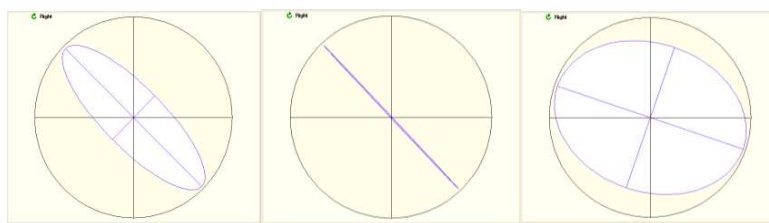


Figura 2 Estado de polarización de la celda de LC E7 con capa de fotoalineado de MR y espaciador de $10\ \mu\text{m}$ para a) 0 V b) 1,18 V c) 1,25V.

3. Conclusiones

Tras la realización de este trabajo de investigación se ha observado que todas las celdas fabricadas para ambos colorantes funcionan según lo esperado. En todos los casos las celdas actúan como una lámina retardadora en las que las líneas neutras están definidas. Además, al aplicar campo eléctrico externo a las celdas responden cambiando la polarización de la luz incidente al variar el voltaje.

Agradecimientos

Financiado por “Generalitat Valenciana” (España) (PROMETEO/2021/006), “Ministerio de Ciencia, Innovación y Universidades/AEI” (España) (PID2021-123124OB-I00 cofinanciado por ERDF/EU; y PID2019106601RB-I00).

Referencias

- [1] Oleg Yaroschchuk and Yuriy Reznikov, “Photoalignment of liquid crystals: basics and current trends”, *J. Mater Chem.* **22**, 286–300 (2012).
- [2] V. S. Milulich, AI A. Muravsky, An. A. Murauski and V. E. Agabekov, “Effect of cis/trans-Isomerisation on Photoalignment of Azo Dyes”, *Russian Journal of General Chemistry.* **85**, 571-576 (2015).
- [3] Yannanqui Li, Tao Zhan and Shin-Tson Wu, “ Flat cholesteric liquid crystal polymeric lens with low f-number”, *Optics Express.* **28**, 5875-5882 (2020).
- [4] Liang-Chen Lin, Hung-Chang Jau, Tsung-Hsien Lin and Andy Y.-G. Fuh, “ Highly efficient and polarization-independent Fresnel lens based on dye-doped liquid crystal.

Brewster quasi-Bound States in the Continuum in Silicon Nanodisk Metasurfaces

L. Hidalgo-Arteaga^{1*} and J. A. Sánchez-Gil¹

¹*Instituto de Estructura de la Materia, Consejo Superior de Investigaciones Científicas,
Serrano 121, 28006 Madrid*

*E-mail: lucia.hidalgo@iem.cfmac.csic.es

1. Abstract

In recent years, exploration of Bound States in the Continuum (BICs) has emerged as a significant focus in photonics [1]. These states, existing within the continuum of modes, possess extraordinary properties and exhibit strongly resonant behavior with infinite Q-factors. Among various configurations giving rise to electromagnetic BICs, metasurfaces have garnered widespread attention. These planar arrays with sub-wavelength periodicity restrict outgoing radiation channels, fostering the emergence of BICs, particularly symmetry-protected BICs and accidental BICs. The rich phenomenology associated with BICs has led to exploration across the electromagnetic spectrum, revealing applications in lasing, enhanced nonlinearities, electromagnetically induced transparency, sensing, and more [2].

However, relaxing certain parameters needed to obtain a BIC gives rise to quasi-BICs with large, but finite, Q-factors that can be accessed from the far field. Recently, a Brewster-like mechanism [3] involving the tilting of vertical dipole resonant meta-atoms has been demonstrated to render certain quasi-BICs inaccessible through plane wave illumination. This mechanism can be actively tuned through magneto-optic control, leading to active switching and tuning of Brewster quasi-BICs, adding an active dimension to BICs in metasurfaces [4]. Active BICs are crucial for designing advanced planar devices with tunable functionalities.

This research delves into recent advancements in photonics, with a focus on bound states in the continuum (BICs) within metasurfaces in the visible and THz spectrum of light. Using two distinct methods, the CEMD formulation [5] and the SMUTHI Python library [6], the study examines the spectral and angular tuning of BICs, uncovering phenomena such as Brewster quasi-BICs resulting from disk tilting. The potential applications of metasurface-based BICs, including sensing and low-loss photonic components, are highlighted. Therefore, this study aims to explore BICs in metasurfaces and, more specifically, investigate the possibility of tuning the spectral and angular range of the quasi-BIC by modifying the tilt of the disks.

Acknowledgments

JASG acknowledges the financial support from the grants BICPLAN6G (TED2021-131417B-I00) and LIGHTCOMPAS (PID2022-137569NB-C41), funded by MCIN/AEI/10.13039/501100011033, “ERDF A way of making Europe”, and European Union NextGenerationEU/PRTR. LHA also acknowledges the financial support from a CSIC JAEIntro contract.

References

[1] C. W. Hsu, B. Zhen, A. D. Stone, D. D. Joannopoulos, and M. Solijacic, “Bound states in the continuum,” *Nature Review Materials* **1**, 16048 (2016).

- [2] Azzam, Shaimaa I., and Alexander V. Kildishev. "Photonic Bound States in the Continuum: From Basics to Applications." *Advanced Optical Materials* **9**, no. 1 (2020).
- [3] D. R. Abujetas, Á. Barreda, F. Moreno, J.J. Sáenz, A. Litman, J.-M. Geffrin, & J.A. Sánchez-Gil "Brewster quasi bound states in the continuum in all-dielectric metasurfaces from single magnetic-dipole resonance meta-atoms," *Scientific Reports*, **9**, no. 1 (2019).
- [4] D. R. Abujetas, N. de Sousa, A. García-Martín, J.M. Llorens, J. A. Sánchez-Gil, "Active angular tuning and switching of Brewster quasi bound states in the continuum in magneto-optic metasurfaces," *Nanophotonics* **10**, 4223 (2021).
- [5] D. R. Abujetas, J. Olmos-Trigo, J. J. Sáenz, J. A. Sánchez-Gil, "Coupled electric and magnetic dipole formulation for planar arrays of particles: Resonances and bound states in the continuum for all-dielectric metasurfaces," *Phys. Rev. B* **102**, 125411 (2020); D. R. Abujetas and J. A. Sánchez-Gil, "Near-Field Excitation of Bound States in the Continuum in All-Dielectric Metasurfaces through a Coupled Electric/Magnetic Dipole Model," *Nanomaterials* **11**, 998 (2021)
- [6] Egel, Amos et al. "SMUTHI: A python package for the simulation of light scattering by multiple particles near or between planar interfaces." (2021).

Metasurface design algorithm for near-field polarization control

Angela Soria-Garcia^{1*}, Joaquin Andres-Porras¹, Luis Miguel Sanchez-Brea¹, Jesus del Hoyo¹, Veronica Pastor-Villarrubia², Mahmoud H. Elshorbagy^{2,3}, and Javier Alda²

¹Applied Optics Complutense, Optics Department, Faculty of Physics, Universidad Complutense de Madrid, Plaza de las Ciencias, 1, 28040 Madrid, Spain.

²Applied Optics Complutense, Optics Department, Faculty of Optics and Optometry, Universidad Complutense de Madrid, C/ Arcos de Jalón 118, 28037 Madrid, Spain.

³ Physics Department, Faculty of Science, Minia University, El Minia, 61519 Egypt.

*E-mail: angSORIA@ucm.es

1. Introduction

Metasurfaces are ultrathin optical structures that have gained great interest for their ability to modulate the amplitude, phase, or polarization of a light beam. In contrast to conventional optics, metasurfaces are generally composed of a set of structures whose dimensions and period are smaller than the wavelength [1]. In particular, for visible light, these structures are in the nanometer range. Several algorithms have been proposed to efficiently determine the sizes, heights, or orientations of these nanostructures so that they can be applied as meta-holograms, polarization converters, flat lenses, or optical vortex generators [2].

2. Design algorithm

In this work, we develop an algorithm that determines the metasurface structure given a target near-field polarization distribution in the image plane, which is represented by a Jones matrix. This method is based on the polar decomposition (PD) of a Jones matrix (J), which claims that any J can be expressed as the product of a retarder (unitary matrix, U) and a diattenuator (Hermitian matrix, H). Fig. 1 shows a diagram of the developed algorithm. First, we define as seed a random symmetric and unitary matrix on the metasurface plane. Then, since we are working in the near-field range, we apply the Rayleigh-Sommerfeld (RS) propagation method to each component of the Jones matrix to determine the intensity at the image plane and, there, we decompose the resulting Jones matrix into the unitary and Hermitian ones. At this point, we discard the Hermitian matrix, and we extract the global phase of the unitary one to add it to the target Jones matrix. Then, we use the inverse RS propagation method to return to the metasurface plane and, after the polar decomposition, we keep only the information provided by the unitary matrix. This procedure is repeated iteratively for a certain number of steps. Finally, we obtain the metasurface Jones matrix that generates the desired polarization distribution in the image plane.

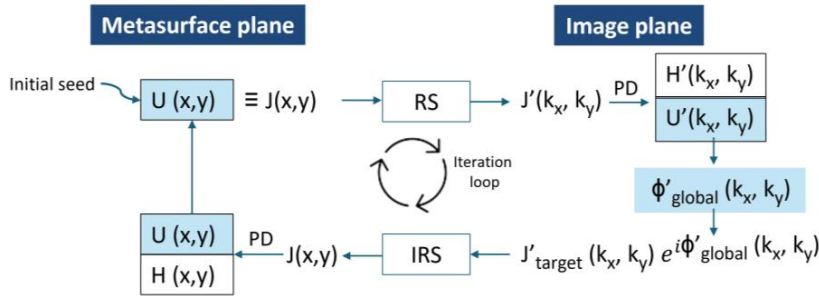


Figure 1: Design algorithm to determine the Jones matrix of a metasurface in the near-field.

Once we have the metasurface Jones matrix, we need to extrapolate it to the dimensions of each pillar of the metasurface for its further fabrication. In that way, as our metasurface Jones matrix is symmetric and unitary, we can decompose it in terms of its eigenvectors (V) and eigenvalues (Λ) matrix as

$$J_{\text{metasurface}} = V\Lambda V^T = R(\theta) \begin{bmatrix} e^{i\phi_x} & 0 \\ 0 & e^{i\phi_y} \end{bmatrix} R(-\theta) \quad (1)$$

where super index T denotes the transposed matrix. Since V is also a real unitary matrix, we can express it as an in-plane rotation by an angle θ. Moreover, as V satisfies that $V^T = V^{-1}$, its transpose corresponds to a

rotation of $-\theta$. On the other hand, Λ contains the phase shifts maps (ϕ_x and ϕ_y), where each coordinate corresponds to the phase shift generated by each pillar of the designed metasurface. These methods have been implemented using Python open-source software packages *Diffractions* and *Py_pol* [3, 4]. Finally, we use a lookup table of a certain material that associate ϕ_x and ϕ_y with the dimensions of the metasurface (such as diameter in the case of cylindrical pillars or length and width in the case of rectangular pillars). In that way, we will obtain a dimension map of the metasurface for its fabrication through e-beam lithography or nanolithography methods, among others.

3. Results

In this section, we present the Jones matrix of a metasurface designed with the proposed algorithm. Specifically, we have designed a metalens that generates two foci with linear polarizations at 45° and 135° , respectively (Fig. 2a). Therefore, when we illuminate the metalens with circular light, we will obtain both foci (Fig. 2b), whereas when the input light is 45° linearly polarized, only one focus with linear polarization at 45° will be generated, thus lacking the imaginary part (Fig. 2c).

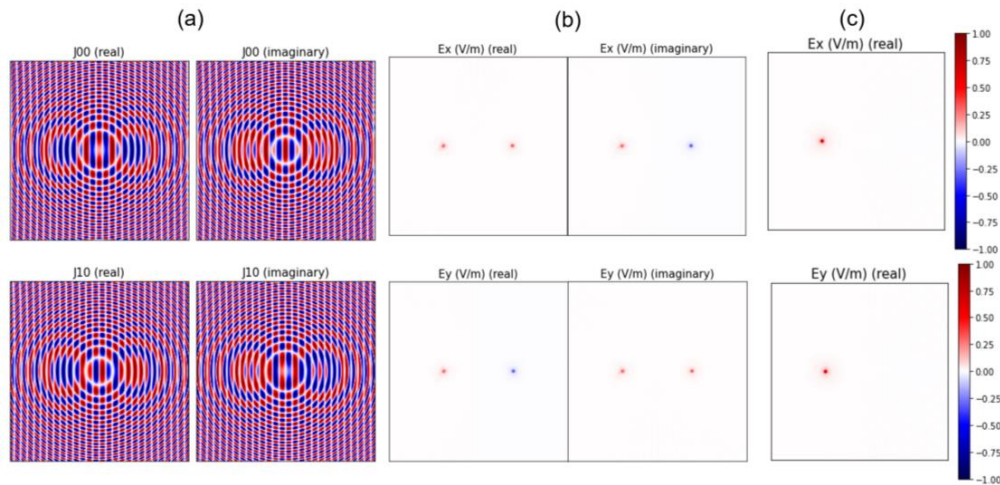


Figure 2: (a) J_{00} and J_{10} elements of the designed Jones matrix of a double focus metalens. Focal plane of the designed metalens by illuminating with (b) circular and (c) 45° linearly polarized light.

4. Conclusions

We have developed an algorithm that determines the dimensions of the building blocks of a metasurface given a target near-field polarization distribution. In fact, we have checked its performance by designing a metalens that generates two foci with different polarization states.

Acknowledgments

This work has been funded by “VDOEST” PID2022-138071OB-I00 project, funded by MCIN/AEI/10.13039/501100011033/FEDER, EU. Angela Soria-Garcia also acknowledges funding of a predoctoral fellowship from Universidad Complutense de Madrid and Banco Santander.

References

- [1] N. Yu and F. Capasso. “Flat optics with designed metasurfaces”. *Nature Mater.* **13**, 139-150 (2014).
- [2] Noah A. Rubin, et al. “Jones matrix holography with metasurfaces”. *Sci. Adv.* **7**, eabg7488, (2021).
- [3] L.M. Sanchez-Brea, “Diffractions: Python library for Diffraction and Interference Optics.” (2019). <https://diffractions.readthedocs.io/en/latest/>
- [4] J. del Hoyo, et al. “Open source library for polarimetric calculations ‘py_pol’ ”. *Proc. SPIE, Computational Optics 2021*, vol. 11875, 12-20.

Moderate-refractive-index nanoantennas for QD fluorescence enhancement

Rafael Ramos Uña*, Braulio García Cámara and Ángela I. Barreda Gómez

Department of Electronic Engineering, Carlos III University of Madrid, Avda. de la Universidad, 30, Leganés, 28911 Madrid, Spain

*E-mail: raramosu@ing.uc3m.es

Enhancing the emission of quantum emitters is crucial for the development of quantum technologies based on photons. In particular, the use of nanostructures for boosting the performance of single-photon sources has been proposed [1]. Initially, metallic nanostructures have been considered due to their ability to generate localized surface plasmons, creating hot-spots where the emission of quantum emitters experience significant enhancement [2]. Nevertheless, metallic nanostructures suffer from high losses attributed to Joule's effect. In response to that, high refractive index dielectric (HRID) nanoparticles (NPs) have emerged as an alternative, which are characterized for showing plasmon-like scattering resonances with negligible absorption in certain spectral ranges, such as visible or near-infrared. In addition, HRID nanoparticles can present magnetic response in spite of being non-magnetic materials. The interferential effects between the electric and magnetic resonances can lead to directional properties, which may increase the collection efficiency of the scattered radiation [3]. Despite these advantages, HRID nanoparticles do not enhance light emission as much as metallic structures due to the generation of weaker hot-spots. In contrast, hybrid metal-dielectric nanostructures offer enhanced functionality and efficiency compared to purely metallic or dielectric nanostructures [4,5].

Recently, moderate-refractive index (MRI) dielectric nanoparticles have been numerically and experimentally demonstrated for enhancing the emission of excitons in 2D materials [6]. These MRI materials ($n \approx 2.2$) present broadband Mie resonances allowing the enhancement of multiple excitons simultaneously.

In this work, we analyze different dimer configurations with the aim of enhancing the photoluminescence signal of a quantum dot (QD) located in the gap. Particularly, dimers of pure metallic, pure HRI dielectric, pure MRI dielectric nanoparticles, and hybrid combinations of metallic and dielectric NPs have been numerically explored. A sketch of the considered geometry is shown in Figure 1.



Figure 1. Scheme of one of the analyzed dimer configurations. In this case, the dimer corresponds to a hybrid nanostructure combining a moderate refractive index and a metallic nanoparticle.

Acknowledgments

This work was funded by the Spanish Research Agency (AEI) through the project No. PID2022-137857NA-100. A.B. thanks MICINN for the Ramos y Cajal Fellowship (grant No. RYC2021-030880-I). R.R. thanks also the Spanish Research Agency (AEI) for his predoctoral grant.

References

- [1] S. Khalid, F.P. Laussy, “Perfect single-photon sources”. *Sci Rep* 14, 2684 (2024).
- [2] Surface plasmons on metal nanoparticles: the influence of shape and physical environment *J Phys Chem C*, 111 (10), pp. 3806-3819 (2007)
- [3] J. Geffrin, B. García-Cámara, R. Gómez-Medina, et al. Magnetic and electric coherence in forward- and back-scattered electromagnetic waves by a single dielectric subwavelength sphere. *Nat Commun* 3, 1171 (2012).
- [4] A. Barreda, S. Hell, M.A. Weissflog, A. Minovich, T. Pertsch, I. Staude, “Metal, dielectric and hybrid nanoantennas for enhancing the emission of single quantum dots: A comparative study”, *J. Quant. Spectrosc. Radiat. Transf.* 276, 107900 (2021).
- [5] P.A. Dmitriev, E. Lassalle, L. Ding, Z. Pan, Darren C. J. Neo, V. Valuckas, R. Paniagua-Dominguez, et al “Hybrid Dielectric-Plasmonic Nanoantenna with Multiresonances for Subwavelength Photon Sources” *ACS Photonics* 10 (3), 582-594 (2023)
- [6] J. Fang, K. Yao, M. Wang, Z. Yu, T. Zhang, T. Jiang, S. Huang, et al “Observation of Room-Temperature Exciton-Polariton Emission from Wide-Ranging 2D Semiconductors Coupled with a Broadband Mie Resonator”, *Nano Lett.* 23 (21), 9803-9810 (2023)

Sub-nanometric stitching metrology for ALBA synchrotron X-ray mirrors

Albert Van Eeckhout^{1*}, Igors Sics¹, Dominique Heinis¹ and Josep Nicolas¹

¹*Optics Lab, ALBA Light Source Facility, Carrer de la Llum 2-26, Cerdanyola del Vallès, 08290 Barcelona, Spain*

*E-mail: aveeckhout@cells.es

1. Introduction

The ALBA synchrotron is a facility where electrons are accelerated to 99.9999986% of the speed of light to provide synchrotron light ranging from infrared to X-rays. Of this spectrum, X-rays bandwidths are predominantly used because synchrotrons are one of the few facilities where it is possible to obtain a coherent X-ray beam with high brilliance, larger than 10^{18} photons \cdot s $^{-1}\cdot$ mm $^{-2}\cdot$ mrad $^{-2}\cdot$ 10 $^{-3}\cdot$ bandwidth $^{-1}$. The generated X-rays are captured by the beamlines, which include a series of optical elements: a) monochromators, to pick the desired bandwidth, b) mirrors, to focus the light beam and increase the brilliance, and c) a set of diagnostics to properly align all the optical elements. The optics laboratory of the ALBA synchrotron is responsible for the design, specification, and characterization of the optical elements of the beamlines.

X-ray mirrors are based on the total external reflection. Since the real part of the index of refraction of X-ray mirrors, n , is very close to the unit ($n \approx 1 - 10^{-5}$), reflection only occurs at small grazing angles (typically < 10 mrad) [1]. Consequently, X-ray mirrors present lengths up to 1.5 meters and require sub-nanometer figure accuracies to obtain sub-micron focus spots [2]. This motivates the development of surface metrology techniques capable of characterizing these mirrors with uncertainties well below the nanometer.

Two types of instruments are currently used at the optics laboratory of the ALBA synchrotron for the X-ray mirrors metrology: the ALBA nanometer optical measurement (ALBA-NOM), based on angle measurements with an autocollimator [3]; and a stitching interferometry system based on a Fizeau interferometer [4]. Both systems are complementary since each offers a unique set of advantages. NOM can quickly measure a wide range of curvatures with nrad uncertainties, thanks to data-redundancy algorithms [5]. And the stitching interferometers give bidimensional data with better spatial resolution, which eases the analysis of 2D features, such as twist.

In stitching interferometry, the mirror is scanned with the interferometer by taking a set of partially overlapped sub-aperture measurements that covers the whole mirror surface. This is done because the mirror surface is larger than the aperture of the interferometer (typically ≤ 150 mm). Then, the data redundancy contained in the overlapping regions is used to join the sub-aperture measurements. We proved that this redundancy can be also used to remove some additive systematic errors, such as the reference surface, when a set of “completeness conditions” are satisfied [6].

2. Abstract

In this work, we present a 2D version of the Linear Error Elimination Procedure (LEEP), which allows determining and subtracting all the additive systematic errors of each sub-aperture measurement [4]. We discuss the main features of LEEP, including the “2D completeness conditions” required for the measurement routine. A main condition is that the scan trajectory along the surface under test must be two-dimensional, i.e. not a straight line, to allow for 2D reconstruction [4]. In addition, it must have a non-constant stitching step, to avoid periodic errors in the reconstructed surface. We also prove that LEEP has intrinsic ambiguities in curvature and twist, which can be solved by measuring the orientation of the interferometer and the measured mirror at each step.

Finally, we use the stitching interferometry system built in the optics laboratory of ALBA to measure a mirror and evaluate the effective error suppression of LEEP. As seen in Fig. 1, we can reconstruct the reference flat from the measured sub-apertures, with a repeatability of 40 picometers rms.

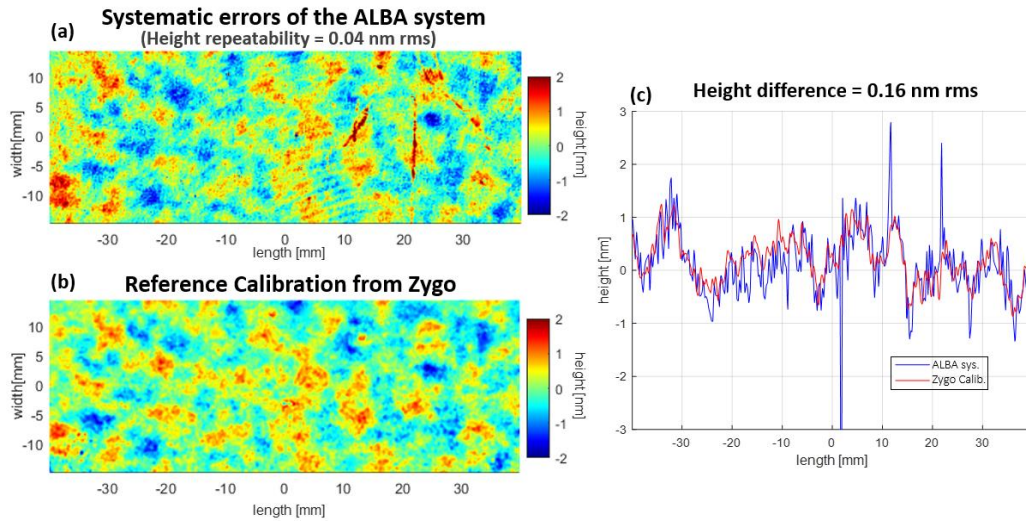


Figure 1 (a) Systematic errors obtained from stitching the measured sub-apertures with LEEP. (b) Calibration of the reference surface provided by Zygo. (c) Linear profile of the central line (width = 0 mm). The profile obtained from ALBA measurements is represented with a blue line, and the profile of the Zygo calibration is represented with a red line. These representations do not include curvatures and twist. This figure has been previously presented in ref. [4].

Acknowledgments

We acknowledge the financial support of Spanish MINECO (PID2021-562 126509OB-C21)

References

- [1] A. T. Macrander and X. Huang, "Synchrotron X-Ray Optics," *Annu Rev Mater Res* **47**, 135–152 (2017).
- [2] K. Yamauchi, K. Yamamura, H. Mimura, Y. Sano, A. Saito, M. Kanaoka, K. Endo, A. Souvorov, M. Yabashi, K. Tamasaku, T. Ishikawa, and Y. Mori, "Wave-optical analysis of submicron focus of hard x-ray beams by reflective optics," in A. K. Freund, A. T. Macrander, T. Ishikawa, and J. L. Wood, eds. (2002), p. 271.
- [3] J. Nicolas and J. C. Martínez, "Characterization of the error budget of Alba-NOM," *Nucl Instrum Methods Phys Res A* **710**, 24–30 (2013).
- [4] A. Van Eeckhout, I. Sics, L. Ribó, C. Colldelram, and J. Nicolas, "The stitching interferometry system of ALBA," in *EUV and X-Ray Optics: Synergy between Laboratory and Space VIII*, R. Hudec and L. Pina, eds. (SPIE, 2023), Vol. 12576, p. 125760E.
- [5] L. Huang, T. Wang, J. Nicolas, F. Polack, C. Zuo, K. Nakhoda, and M. Idir, "Multi-pitch self-calibration measurement using a nano-accuracy surface profiler for X-ray mirror metrology," *Opt. Express* **28**, 23060–23074 (2020).
- [6] J. Nicolas, M. L. Ng, P. Pedreira, J. Campos, and D. Cocco, "Completeness condition for unambiguous profile reconstruction by sub-aperture stitching," *Opt. Express* **26**, 27212–27220 (2018).

Analysis of the propagation features of a new type of finite-energy Airy plasmon polariton

Mireya Pando, Rosario Martínez-Herrero and Javier Hernández-Rueda*

Department of Optics, Faculty of Physics, University Complutense of Madrid, Spain

*E-mail: fj.hernandez.rueda@ucm.es

1. Theory

Airy beams have become a very active and promising research field strongly developed over the last decade due to their interesting fundamental and technological applications [1-5]. More recently a great deal of attention has been devoted to the study of Airy surface plasmons polaritons (ASPPs) as a means to manipulate light at the nanoscale, see for example reference [6] and the references therein. In this communication, we analyze the propagation characteristics of a new type of finite Airy surface plasmon polariton beams.

Our analysis starts by considering an ASPP propagating along a metal-dielectric interface, which is perpendicular to the y-axis. The metallic medium ($y < 0$) is characterized by a complex dielectric function ε_c , with $\text{Re}\varepsilon_c < 0$ and $\text{Im}\varepsilon_c > 0$, while the dielectric environment ($y > 0$) is described by a real dielectric function ε_d and satisfies $\varepsilon_d + \text{Re}\varepsilon_c < 0$. Assuming the paraxial approach and following our previous work [7], the electric field of an ASPP, $E(x, z) = e^{iyk_{dy}} E_{0d}(x, z)$, propagates along the z-axis in the dielectric medium and, for $z \geq 0$, is given by

$$E(x, z) = e^{iyk_{dy}} \left(i \frac{\partial f}{\partial x}, \frac{\varepsilon_c k_{dy}}{\varepsilon_d} f, i \frac{\partial f}{\partial z} \right) \quad (1)$$

where k_{dy} is the wavenumber along the y-axis and $f(x, z)$ is a scalar function defined as

$$f(x, z) = e^{ik_{sp}z} f_0(x, z) \quad (2)$$

with k_{sp} the wavenumber of the surface plasmon. Under the paraxial approximation, $f_0(x, z)$ satisfies the so-called paraxial equation

$$\frac{\partial^2 f_0(x, z)}{\partial x^2} + 2ik_{sp} \frac{\partial f_0(x, z)}{\partial z} = 0 \quad (3)$$

Using the angular plane-wave spectrum formalism of optical fields as done in Ref. [7], it can be proven that, for $z > 0$, a solution associated with an ASPP can be written as follows

$$f_0(x, z) = \int_{-\infty}^{\infty} e^{\frac{i u^3}{3}} F(u) e^{i|k_{sp}|ux} e^{-i \frac{zu^2 k_{sp}^*}{2}} du \quad (4)$$

where the finite energy condition is guaranteed for any function $F(u)$ fulfilling

$$\int_{-\infty}^{\infty} |F(u)|^2 du < \infty. \quad (5)$$

In this communication, we consider a new type of finite energy ASPP defined by the function $F(u)$

$$F(u) = \sqrt{\frac{p}{2\sqrt{\pi}}} H_1(up) e^{-\frac{p^2 u^2}{2}} \quad (6)$$

where H_1 is the Hermite polynomial of order 1 and p a dimensionless constant.

The experimental implementation of this kind of ASPP can be done by using procedures similar to those used in references [8] and [9].

2. Conclusions

To illustrate the propagation characteristics of the ASPP presented in the preceding section, we have considered an air-silver interface and a wavelength of 633 nm. Consequently, we use the following dielectric functions for air and silver:

$$\varepsilon_d = 1 \text{ (air); } \varepsilon_c = -18.3132 + 0.49806i \text{ (silver)}$$

The main conclusions can be summarized as follows:

- We observe the typical self-bending behavior with increasing z -values and a shift along the x -axis of the maximum intensity as the plasmon propagates toward higher z -values.
- For the current study case the ASPP keeps its shape for longer z , compared to the usual Gaussian ASPP.
- In addition, the superposition of two counter-propagating beams results in the formation of a localized hot spot on the surface, the intensity of this focal spot is greater than that obtained by superimposing two conventional Gaussian ASPPs under identical conditions.

Acknowledgments

Programa de Atracción de Talento de la Comunidad de Madrid, Modalidad 1, project 2020-T1/IND-19951. M. P. acknowledges funding via a Beca de Colaboración con Departamento number: 998142.

References

- [1] A. Forbes, M. de Oliveira, and M. R. Dennis, "Structured light," *Nat. Photonics* 15(4), 253–262 (2021).
- [2] J. Wang and Y. Liang, "Generation and detection of structured light: A review," *Front. Phys.* 9, 688284 (2021).
- [3] N. K. Efremidis, Z. Chen, M. Segev, et al., "Airy beams and accelerating waves: An overview of recent advances," *Optica* 6(5), 686–701 (2019).
- [4] R. Martínez-Herrero, A.S. Sanz, "Partially coherent airy beams: A cross-spectral-density approach" *Physical Review A*, 106(5), 053512 (2022)
- [5] A. S. Sanz, R. Martínez-Herrero, "Exploring the dynamics of finite-energy Airy beams: a trajectory analysis perspective," *Opt. Express* 32, 5592-5606 (2024)
- [6] A.E. Minovich, A.E. Klein, Neshev, et al. "Airy plasmons: non-diffracting optical surface waves" *Laser & Photonics Reviews*, 8(2), 221-232 (2014)
- [7] R. Martínez-Herrero, A. Manjavacas, "Basis for paraxial surface-plasmon-polariton packets", *Physical Review A*, 94, 6, 063829 (2016)
- [8] Y. Lumer, L. Drori, Y. Hazan, M. Segev, "Accelerating self-imaging: the Airy-Talbot effect", *Physical Review Letters*, 115, 1, 013901, (2015).
- [9] Y. Wen, Y. Chen, Y. Zhang, H. Chen, S. Yu, "Tailoring accelerating beams in phase space", *Physical Review A*, 95, 2, 023825, (2017)

Determinación de la aberración de fase con aprendizaje profundo

Victor H. Flores¹, Julio C. Estrada¹, Angela Soria-Garcia², Luis Miguel Sanchez-Brea²,
Jesús del Hoyo², Javier Vargas^{2*}

¹Centro de Investigación en Matemáticas A. C., C.P. 36023, Guanajuato, Gto., México.

²Departamento de Óptica, Universidad Complutense de Madrid, Plaza de Ciencias 1, 28040 Madrid, España

*E-mail: jvargas@ucm.es

La interferometría por desplazamiento de fase (PSI, phase-shifting interferometry) es una técnica utilizada en metrología óptica para medir la aberración de fase que presenta un frente de onda de prueba, a partir de un conjunto de interferogramas [1]. La PSI emplea una secuencia de desplazamientos de fase, normalmente aplicados mediante cambios controlados en la longitud de la trayectoria del haz de referencia, para generar múltiples interferogramas. Estos interferogramas, que difieren en un incremento de fase conocido o desconocido, permiten calcular con precisión la distribución de fase del frente de onda de prueba. Aplicando algoritmos como la transformada de Fourier con ventanas [2], mínimos cuadrados iterativos [3], análisis de componentes principales [4], o combinaciones de ellos [5], se puede extraer la información de fase de los patrones de intensidad observados en los interferogramas. Este proceso da lugar a mediciones de alta resolución de las diferencias de trayectoria óptica y de la topografía de superficies, lo que hace que la PSI sea especialmente valiosa para aplicaciones como el ensayo de lentes, la caracterización de superficies y la alineación de sistemas ópticos.

La precisión de PSI depende de varios factores, como el número de patrones utilizados, el muestreo uniforme de los desplazamientos de fase en el intervalo $[0, \pi]$ rad, el nivel de ruido en los interferogramas, la estabilidad del sistema óptico o la robustez de los algoritmos utilizados para la extracción de fase. Los últimos avances en este campo se han centrado en la mejora de la robustez de la PSI frente a las vibraciones ambientales y en el desarrollo de algoritmos adaptativos que puedan manejar cambios dinámicos en el sistema óptico utilizado [6], incluso mediante el procesamiento de un único patrón de franjas. Esto ha ampliado las aplicaciones prácticas de la PSI, convirtiéndola en una herramienta indispensable para medidas óptica de precisión en entornos industriales y en investigación. Sin embargo, un paso que sigue siendo complejo y muy vulnerable a errores es el proceso de desenrollamiento de la fase envuelta obtenida a partir de los patrones de PSI (*phase-unwrapping*). En este trabajo, introducimos un enfoque basado en redes neuronales para extraer directamente los coeficientes de Zernike que caracterizan a la fase moduladora mediante el procesamiento de un único patrón de franjas. De esta forma, se consigue evitar el proceso de desenrollamiento de fase y también posibles errores en la demodulación de la fase causados por las posibles vibraciones ambientales que pudieran afectar al sistema óptico. Nuestro modelo combina un *autoencoder* con una red adicional totalmente conectada [7]. El *autoencoder* está diseñado para aprender una representación compacta de los patrones de franjas dentro de un espacio latente de características, lo que facilita la posterior estimación precisa de los coeficientes de Zernike. Seguidamente, la red totalmente conectada procesa esta representación de características y mapea el espacio latente aprendido a otro espacio de características. Este nuevo espacio representa la descomposición de Zernike de la fase moduladora, ofreciendo un marco físicamente interpretable. Nuestro modelo ha sido entrenado con patrones de franja simulados que han sido obtenidos asignando coeficientes aleatorios a los seis primeros polinomios de Zernike. De esta forma hemos generado un conjunto de 10,000 patrones. En primera fila de la Fig. 1 mostramos ejemplos de los patrones de franjas sintéticos utilizados en el entrenamiento y en la segunda fila los patrones correspondientes generados por el *autoencoder*, lo que muestra la capacidad de la red para aprender una representación compacta de los interferogramas. En la Fig. 2 mostramos ejemplos de la fase absoluta conocida (primera fila) y de los patrones de franjas correspondientes (segunda fila). En las filas tercera y cuarta de la Fig. 2, se muestran las fases absolutas reconstruidas y el coseno de estas fases obtenidas. La Fig. 2 muestra como el modelo propuesto es capaz de reconstruir con precisión la fase moduladora absoluta a partir de un único patrón de franjas complejo y sin necesidad de ningún paso de desenrollamiento de fase. Se observa que el mapa de fase absoluta reconstruido puede mostrar una inversión de signo, lo cual es totalmente irrelevante.

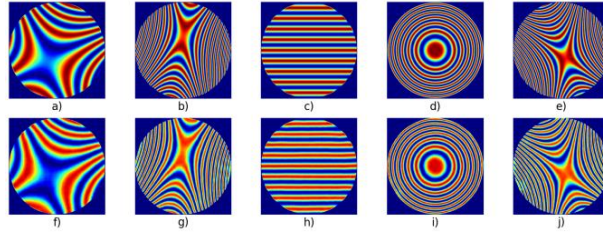


Figura 1 Ejemplos de patrones de franjas simulados (fila superior) y generados (fila inferior) por el autocodificador.

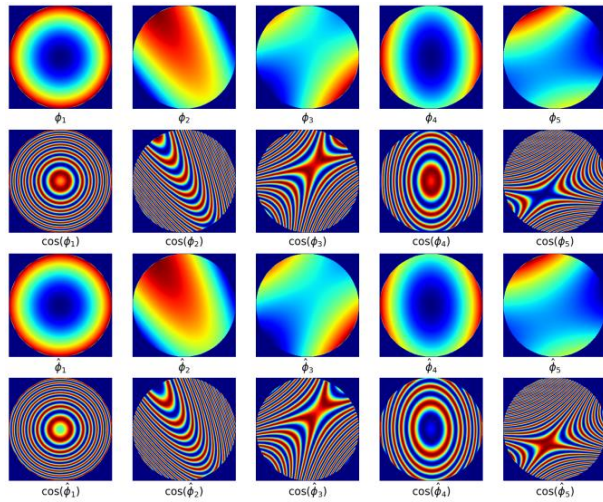


Figura 2. Comparación entre los casos simulados (dos primeras filas superiores) y reconstruidos por el modelo de aprendizaje profundo propuesto (filas inferiores) de diferentes fases absolutas y patrones de franja.

Como conclusión, hemos demostrado que el modelo propuesto puede reconstruir con precisión el mapa de fase absoluta a partir de interferogramas simulados sin necesidad de técnicas de desenvoltura.

Agradecimientos

Agradecemos el apoyo financiero del Ministerio de Ciencia e Innovación español, subvención PID2022-137548OB-I00 financiada por MCIN/AEI/10.13039/501100011033/ y por FEDER “A way of making Europe”. Victor H. Flores agradece al Consejo Nacional de Humanidades, Ciencias y Tecnologías (Conahcyt) por la beca postdoctoral concedida y Ángela Soria-García agradece la financiación de una beca predoctoral de la Universidad Complutense de Madrid y del Banco Santander.

Referencias

- [1] D. Malacara, M. Servín, and Z. Malacara, *Interferogram Analysis for Optical Testing* (Dekker, 1998).
- [2] Q. Kemao, “Two-dimensional windowed Fourier transform for fringe pattern analysis: Principles, applications and implementations”, *Opt. Lasers Eng.* **45**, 304-317 (2007).
- [3] Z. Y. Wang and B. T. Han, “Advanced iterative algorithm for phase extraction of randomly phase-shifted interferograms”, *Opt. Lett.* **29**, 1671 (2004).
- [4] J. Vargas, J.A. Quiroga and T. Belenguer, “Phase-shifting interferometry based on principal component analysis”, *Opt. Lett.* **36**, 1326 (2011).
- [5] J. Vargas, C.O.S. Sorzano, J.C. Estrada and J.M. Carazo, “Generalization of the Principal Component Analysis algorithm for interferometry”, *Opt. Commun.* **286**, 130-134 (2013).
- [6] J. Vargas, S. Wang, J.A. Gómez-Pedrero and J.C. Estrada, “Robust weighted principal components analysis demodulation algorithm for phase-shifting interferometry”, *Opt. Express* **29**(11), 16534-16546 (2021).
- [7] D. Bank, N. Koenigstein and R. Giryes, “Autoencoders” arXiv:2003.05991v2 (2020)

Haces no uniforme y totalmente polarizados invariantes en propagación para polarimetría Mueller

Juan Carlos G. de Sande¹, Juan Carlos Suárez-Bermejo^{2*}, Massimo Santarsiero³ y Gemma Piquero⁴

¹ ETSIS de Telecomunicación, Universidad Politécnica de Madrid, Campus Sur, Madrid-28031

² Dpto. de Materiales, Universidad Politécnica de Madrid, Avda. de la Memoria, 28040-Madrid

³ Dipartimento di Ingegneria Industriale, Elettronica e Meccanica, Roma Tre., Rome 00146, Italy

⁴ Dpto. de Óptica, Universidad Complutense de Madrid, Plaza de las Ciencias s/n 28040-Madrid

E-mail: juancarlos.suarez@upm.es

Los haces no uniformemente y totalmente polarizados (NUTP) se caracterizan por la variación de la polarización a lo largo de la sección transversal (véase, por ejemplo, [1-7]). Los primeros estudios sobre estos haces exploraron su generación mediante métodos interferométricos o láseres de semiconductores, lo que estimuló el desarrollo de técnicas para sintetizar campos con diversos patrones de polarización en las secciones transversales, así como la necesidad de modelos para caracterizar estos haces. Con el paso del tiempo, se han introducido diferentes tipos de haces NUTP, incluyendo los haces radial, azimutal, y espiralmente polarizados, además de la utilización de moduladores espaciales de luz (SLM) para su generación [7]. La introducción de los haces NUTP ha encontrado aplicaciones en diversos campos, como las pinzas ópticas, la manipulación de partículas, la microscopía y la polarimetría, entre otros. En la literatura se han publicado numerosos trabajos sobre este tema (véase, por ejemplo, [6] y las referencias asociadas). Una aplicación específica de estos haces es su uso en la polarimetría Mueller de muestras transparentes y homogéneas [8-11].

Es importante destacar que los haces NUTP, en general, experimentan cambios en su distribución de polarización a medida que se propagan libremente o a través de sistemas ópticos ABCD. En aplicaciones como la polarimetría Mueller, especialmente al analizar muestras pequeñas o con propiedades ópticas no uniformes, es necesario enfocar el haz de entrada en la región de interés, lo que podría requerir sistemas ópticos y potencialmente afectar a la polarización. Por lo tanto, resulta útil contar con haces que conserven su perfil de polarización durante la propagación en el espacio libre, a excepción de un factor de escala transversal, asegurando así la observación del mismo patrón de polarización independientemente de la distancia a la muestra.

En esta contribución se estudia un tipo de haces NUTP totalmente coherentes e invariantes en la propagación paraxial [11]. Estos haces se generan como la superposición de dos campos uniformes y totalmente polarizados con polarizaciones ortogonales. La forma más común de describir estos haces es mediante la superposición de modos Hermite-Gauss o Laguerre-Gauss, que son invariantes en propagación. La anomalía de fase o fase de Gouy es el único factor que causa cambios en la forma de estos haces durante la propagación.

Como caso particular de los haces NUTP generados de esta manera e invariantes en la propagación, nos centramos en los haces Full Poincaré (FPB), que incluyen todos los estados de polarización posibles en su sección transversal. Estos haces han recibido una atención especial en los últimos años [12-14], y se han propuesto e implementado diversos métodos para su generación, utilizándose por ejemplo en aplicaciones de polarimetría Mueller [10]. Dado que se necesitan, al menos, cuatro estados de polarización linealmente independientes para caracterizar completamente la matriz de Mueller de una muestra en técnicas polarimétricas, los FPBs pueden ser útiles como generadores de estados de polarización en paralelo.

Estos tipos de haces NUTP invariantes poseen propiedades interesantes; por ejemplo, si un haz tiene un perfil de polarización invariante durante la propagación, esta propiedad se mantiene para

cualquier otro haz obtenido del primero mediante la introducción de un elemento óptico lineal, determinista y homogéneo en su trayectoria. Esto se debe a que cualquier elemento óptico de este tipo puede describirse mediante una matriz de Jones constante. Además, la propiedad de invariancia de forma se conserva no solo en la propagación libre, sino también para cualquier operador escalar lineal, incluida la propagación del haz a través de sistemas ópticos isótropos caracterizados por una matriz de transformación ABCD. Como caso especial, cuando la condición de invariancia solo se requiere en el campo lejano, se pueden obtener una variedad de campos invariantes mediante procedimientos analíticos simples.

En este trabajo se presentan diversos ejemplos de este tipo de haces, así como una propuesta de síntesis experimental y su aplicación en polarimetría. En el contexto de la polarimetría, se calcula no solo el mapa de polarización transversal, sino también las coordenadas de los puntos donde deben realizarse las medidas para reducir los errores en la determinación de la matriz de Mueller de la muestra.

Agradecimientos

Este trabajo ha sido financiado por el Ministerio de Economía y Competitividad bajo el proyecto PID2019 104268GB-C21.

References

- [1] R. Chipman, W. Lam, G. Young, *Polarized Light and Optical Systems* en *Optical Sciences and Applications of Light* (CRC Press, 2018).
- [2] T. Erdogan, O. King, G W Wicks, D. G. Hall, E. Anderson, M. J. Books, “Concentric-Circle-Grating, Surface-Emitting Semiconductor Lasers”, *Appl. Phys. Lett.* **60**, 1921-1923 (1992).
- [3] G. Piquero, J. M. Movilla, P. M. Mejías, R. Martínez-Herrero, “Degree of polarization of non-uniformly partially polarized beams: a proposal”, *Opt. Quantum. Electron.* **31**, 223-226 (1999).
- [4] Q. Zhan, “Cylindrical vector beams: from mathematical concepts to applications”, *Adv. Opt. Photon.* **1**, 1–57 (2009).
- [5] J.A Davis. I. Moreno, K. Badham, M.M. Sánchez-López, D. M. Cottrell, “Nondiffracting vector beams where the charge and the polarization state vary with propagation distance,” *Opt. Lett.* **41**, 2270-2273 (2016).
- [6] G. Piquero, R. Martínez-Herrero, J. C. G. de Sande, M. Santarsiero, “Synthesis and characterization of non-uniformly totally polarized light beams: tutorial,” *J. Opt. Soc. Am. A*, **37**, 591-605 (2020).
- [7] P. García-Martínez, D. Marco, J. L. Martínez-Fuentes, M. del Mar Sánchez-López, I. Moreno, “Efficient on-axis SLM engineering of optical vector modes”, *Optics and Lasers in Engineering*, **125**, 105859-105868 (2020).
- [8] R.M.A. Azzam, “Stokes-vector and Mueller-matrix polarimetry”, *J. Opt. Soc. Am., A* **33**, 1396–1408 (2016).
- [9] J.C.G. de Sande, G. Piquero, M. Santarsiero, “Polarimetry with azimuthally polarized light”, *Opt. Commun.* **410**, 961-965 (2018).
- [10] J. C. Suárez-Bermejo, J.C.G. de Sande, M. Santarsiero, G. Piquero, “Mueller matrix polarimetry using full Poincaré beams”, *Opt. Laser Eng.*, **122**, 134-141 (2019).
- [11] J.C.G. de Sande, G. Piquero, J.C. Suárez-Bermejo, M. Santarsiero, “Mueller Matrix Polarimetry with Invariant Polarization Pattern Beams”, *Photonics* **8**, 491-506 (2021).
- [12] A. Beckley A, T. Brown, M Alonso, “Full Poincaré beams”, *Opt. Express.* **18**, 10777-10785 (2010).
- [13] E. Galvez, S. Khadka, W. Schubert y S. Nomoto, “Poincaré-beam patterns produced by nonseparable superpositions of Laguerre–Gauss and polarization modes of light”, *Appl. Opt.* **51**, 2925-2934 (2012).
- [14] G. Piquero, L. Monroy, M. Santarsiero, M. Alonzo, J.C.G de Sande, “Synthesis of full Poincaré beams by means of uniaxial crystals”, *Journal of Optics* **20**, 065602, 8 pp. (2018).

Towards optimized volume holograms for augmented and virtual reality near-eye displays

Adrià Cobos^{1,2}, Dorian Treptow¹, Fernando Díaz-Doutón²

¹*Inmersia Computers S.L, C/Roger de Llúria, 49, 08009, Barcelona, Spain*

²*Centre for Sensors, Instruments and Systems Development (CD6), Universitat Politècnica de Catalunya (UPC), Rambla Sant Nebridi, 10, 08222, Terrassa, Spain.*

*E-mail: adria.cobos@upc.edu

1. Introduction

Augmented and virtual reality (AR and VR) technologies have the potential to revolutionize how we interact with the world, even surpassing the impact of smartphones. The market is rapidly expanding and is expected to skyrocket in the coming years as it becomes more widely adopted by consumers. However, this would only be possible if compact, portable, comfortable, efficient, and immersive AR and VR devices were available. Such features are basically determined by the Near-Eye Display (NED) component, which consists of the overall optical system of the device. Although NEDs have experienced great technical advances in the last years, no device allowing the above-mentioned characteristics at once has yet being implemented. In these regards, traditional NED design strategies based on refractive elements face the challenge of achieving a reduction in size while keeping good optical performance. To overcome this limitation, diffractive optics may offer a solution: light can be efficiently diffracted with only a thin layer of the order of micrometres, making them suitable for lightweight and thin NEDs [1].

Diffractive approaches include the implementation of holographic optical elements (HOEs), such as those based on thin or thick holograms, to name few. In particular, thick holograms, also called volume holograms, possess properties of great interest for AR NEDs: they exhibit a high degree of angular and spectral selectivity, enabling a see-through view, while allowing the implementation of multiple optical functions thanks to their wavefront reconstruction capability. Note that these elements require a holographic recording process. Although being strong contenders, volume holograms may suffer from low efficiency and aberrations if that process is not optimized. In these regards, a proprietary simulation software developed to address these issues and drive this optimization process is presented in this work.

2. Developed simulation software

Kogelnik's coupled wave theory is the most widely used model to analyze the diffraction behavior of volume holograms [2], due its relatively easy implementation, compared to rigorous coupled wave analysis (RCWA). However, as being an approximated model, its accuracy has been demonstrated to diminish for far off-Bragg conditions. To circumvent this issue, Uchida's phase shift correction approach was introduced to correct the diffracted direction when dealing within off-Bragg conditions [3], which has been demonstrated in the literature to impressively follow the real diffracted direction at each point [4].

Current research highlights the design of AR hologram-based optical combiners using Kogelnik's theory, even with said limitations. Additionally, broadly used commercial software (like *OpticStudio*, Ansys Inc.) feature even more limiting features. In these regards, we have implemented a novel proprietary simulation software (in *Matlab*, Mathworks Inc.) faced towards the design of volume hologram-based optical combiners for AR and VR NED devices, able to reliably predict the performance of the HOE. The software simulates 2D holograms through recording and reconstruction processes, mimicking real-life lab procedures. Recording involves defining hologram characteristics like material, shape, and size of the substrate, and the optical characteristics of the interfering beams (spectrum, arrangement, ...). The hologram reconstruction process simulation, by illuminating the hologram with an arbitrary probe beam, was also implemented. The key differentiation of the developed software lies in Uchida's method implementation rather than Kogelnik's approach, and the introduction of features lacking in the state-of-the-art software implementations, such as multiple-ray efficiency, and compensation for shrinkage and wavelength shifts, among others.

3. Results and conclusions

The aimed reconstruction configuration that helped to validate the software capabilities consisted on a retinal display geometry: all diffracted light coming from a punctual source is focused onto a single point located at user's pupil plane, and then is projected onwards into the retina. Fig. 1 top showcases an example of a pre-compensated RGB recording process (left), with the pre-knowledge of the reconstruction wavelength shift and shrinkage, allowing for a latter aimed collinear reconstruction amongst three RGB channels (right). The outcomes of this simulation have been tested experimentally (implementing the corresponding recording and reproduction setups), featuring the expected reconstruction performance, as exemplified in Fig. 1 downside: each color channel is diffracted efficiently and is collinear with the other two. Additionally, the developed software helped in the analysis and optimization of other multiple parameters of the holographic process (HOE material, reconstruction sources spectra, tolerancing, etc.).

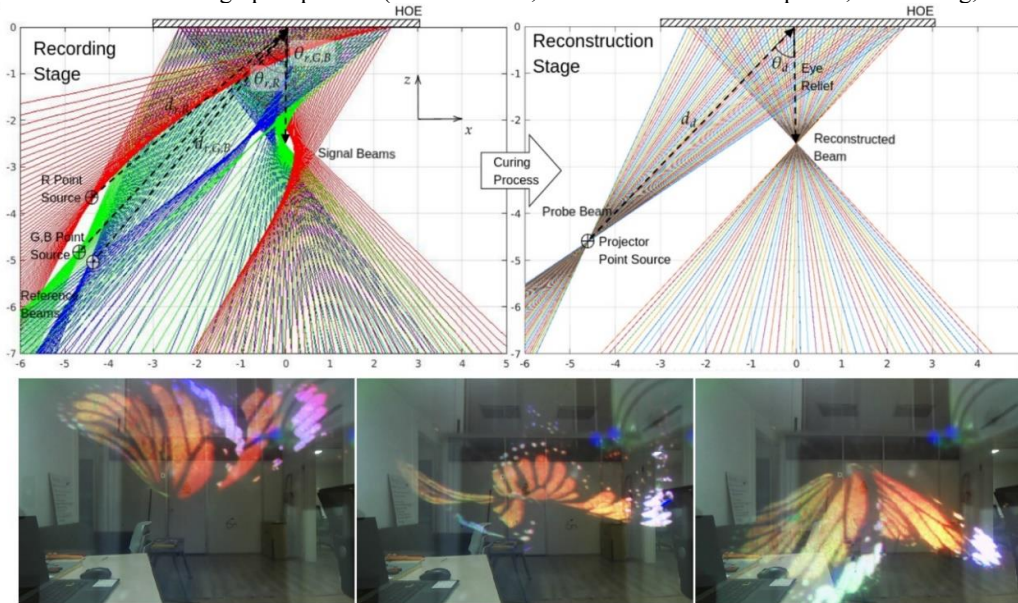


Figure 1: (Top) example of RGB pre-compensation for shrinkage and wavelength shift in recording (left) and reconstruction stages (right), in a retinal display geometry. Axis units in cm. (Down) 3 images from the experimental reconstruction results of the simulated geometry using a RGB laser display source, for a see-through view.

The implications of this software extend beyond current conventional simulation software capabilities: it provides design freedom and novel feature tools for system design and development, solving critical gaps in holographic simulation for high performance volume holograms and allowing the implementation of complex specific recording optics. Currently, 3D holographic simulation software based on RCWA is in development process to enhance precision and rigorousness.

Acknowledgments

With the support of the Industrial Doctorates Plan of the Department of Research and Universities of the Government of Catalonia.

References

- [1] J. Xiong, E. L. Hsiang, Z. He, T. Zhan, and S. T. Wu, "Augmented reality and virtual reality displays: emerging technologies and future perspectives", *Light Sci Appl.* **10**, 216 (2021).
- [2] H. Kogelnik, "Coupled Wave Theory for Thick Hologram Gratings", *Bell Syst. Tech. J.* **48**, 2909-2947 (1969).
- [3] N. Uchida, "Calculation of diffraction efficiency in hologram gratings attenuated along the direction perpendicular to the grating vector", *J. Opt. Soc. Am.* **63**, 280-287 (1973).
- [4] M. Prijatelj, J. Klepp, Y. Tomita, and M. Fally, "Far-off-Bragg reconstruction of volume holographic gratings: A comparison of experiment and theories", *Phys. Rev. A* **87**, 063810 (2013).

Automatic characterization of morphological structures and their orientation in biomedical images

Adela Ayala[†], Guillermo Orenes-Miñana[†], Iryna Standret, Juan M. Bueno, and Enrique J. Fernandez^{*}

*Laboratorio de Óptica, Instituto Universitario de Investigación en Óptica y Nanofísica,
Universidad de Murcia, Campus de Espinardo (Ed. 34), 30100 Murcia, Spain*

[†]These authors contributed equally to the work

^{*}E-mail: enriquej@um.es

1. Introduction

Characterizing morphological structures and determining their orientation in biomedical images are fundamental tasks in both basic research and clinical practice [1]. In particular, multiphoton microscopy provides invaluable insights into the intricate structures and processes occurring within living organisms.

Analyzing and understanding the complex morphology and orientation of anatomical features or cellular structures within these images present significant challenges. Firstly, biomedical images often exhibit complex and heterogeneous morphology, making automated analysis and interpretation difficult. Additionally, inherent noise, artifacts, and variations in imaging modalities further complicate the accurate extraction of morphological features and orientation information. In this work we present a novel and straight forward computational technique for image analysis and orientation estimation, characterizing its strengths and limitations. Some examples of application of the technique over images from biological samples are also shown.

2. Methods

The method for the automatic characterization of the structure and orientation was based on the calculation of the gradient of the images' intensity I at every location (x,y) following the equation:

$$\nabla I = \frac{\partial I}{\partial x} \hat{x} + \frac{\partial I}{\partial y} \hat{y}. \quad (1)$$

The vector gradient provides information about the orientation and magnitude of the increase of intensity at every considered point. The Probability Density Function (PDF) as a function of the orientation θ of the set of gradient vectors G was calculated to estimate the parameters which characterized the image. A threshold in the module of the gradient vector at every pixel to be accounted in the PDF was introduced to tune the precision and sensibility of the method. Orientation θ was restrained to angles belonging to the first and second quadrant. The PDF was estimated through the calculation of the normalized frequency histogram of the set G for a given bin size. The PDF was fitted to a linear combination of Gaussian functions in the general form:

$$PDF(G) = \sum_i^K \frac{a_i}{\sigma_i \sqrt{2\pi}} \exp\left(-\frac{1}{2} \frac{(\theta - \theta_i)^2}{\sigma_i^2}\right) + D. \quad (2)$$

The subindex i indicated the presence of i -structures, each at orientation θ_i . The parameters a_i and σ_i provided information of the relative dominance of each structure in terms of visibility and area over the image. The parameter D was a pedestal in the set of Gaussian functions which could be related to the background of the image relative to the visibility of the structures.

A set of phantom images were generated to test the method. Those incorporated patches of structures following sinusoidal intensity functions at selected orientations. The relative area of the structures' patches, background, and noise could be incorporated. All the analysis and phantoms were generated by using MatLab (The MathWorks, Inc, Natick, MA).

3. Results

Figure 1 shows an example of a phantom of 1024×1024 pixels² with regions of the same spatial frequency at 2 orientations covering 1/3 and 1/4 regions of the image, with no background and 5% noise level. In the right side of the Fig. 1 it is presented the corresponding PDF with black dots and the best curve fitting to series of Gaussian functions. From the parameters of the fitting there was obtained a set of data characterizing the phantom. From the relative height of the Gaussian functions, the relative size of the patches (i.e. the area associated to each zone) was obtained. From the width of each Gaussian function the spatial frequency of the sinusoidal fringes relative to the resolution of the image it was computed. The pedestal of the curve, presented as parameter D in the method section, yielded in this case the noise of the image.

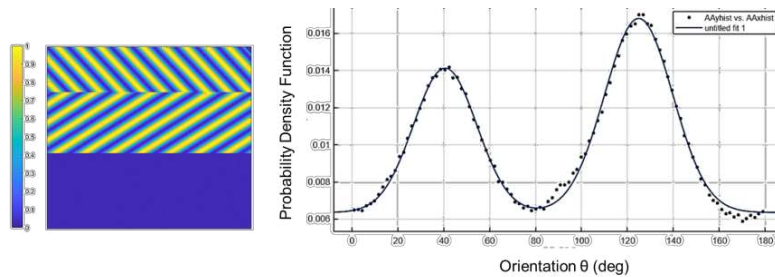


Figure 1 Phantom and associated PDF with fitting to Gaussian functions combination.

The method demonstrated to be robust when it was applied to images from biological samples, as it is shown in Figure 2. In particular, images from avian corneal punches obtained by multiphoton microscopy were analyzed and successfully characterized in terms of the main orientation of their collagen fibers.

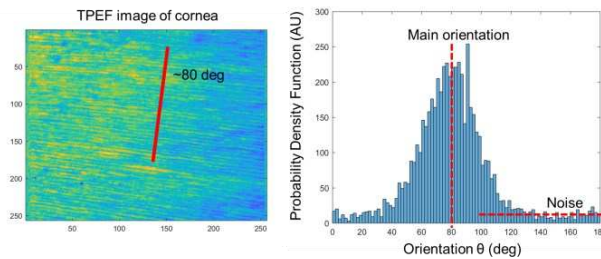


Figure 2 Multiphoton image of a chicken cornea and associated PDF showing the orientation and the noise level.

4. Conclusions

A new method based on the statistical analysis of the intensity gradient of the images has been successfully developed and tested. The PDF of the orientation of the gradient was fitted to series of parametrized Gaussian functions. The generation of phantom allowed charactering mathematically the parameters of the fitting describing the properties of the phantom. The use of this new method with images from biological samples of medical interest is robust, and it opens the door to its application where the accurate characterization of morphological structures is crucial for disease diagnosis, treatment planning, and monitoring of disease progression.

Acknowledgments

Supported by grant PID2020-113919RBI00/AEI/10.13039/501100011033.

References

- [1] F. J. Ávila and J. M. Bueno, "Analysis and quantification of collagen organization with the structure tensor in second harmonic microscopy images of ocular tissues," *Appl. Opt.* 54(33), 9848-9854 (2015).

Topographical characterization of an intraocular lens. A preliminary study based on in-line digital holography.

Rosa Vila-Andres^{1*}, Anabel Martínez-Espert¹, José J. Esteve-Taboada¹ and Vicente Micó¹

¹*Departamento de Óptica y Optometría y Ciencias de la Visión, Universitat de València, Burjassot, Spain*

*E-mail: rosa.vila@uv.es

1. Introduction

The aim of this work was to obtain the topography of a commercial diffractive IOL using digital in-line holography. Multifocal intraocular lenses (MIOLs) are increasingly used to replace the crystalline lens in the treatment of cataracts or presbyopia. The optical performance of the diffractive MIOLs is determined by the design of its diffractive profile. Some studies have inspected IOLs topographies with interferometric techniques [1,2]. Nevertheless, the transparency and morphological profile of diffractive MIOLs make them a potentially suitable sample to be inspected by holography under the Gabor regime.

In-line Gabor holography, firstly introduced by Gabor in 1948 [3], is a technique based on the interference of a reference beam coming from a non-diffracted coherent source of light and an object beam created from the diffraction of the reference beam passing through a weak-diffractive sample, thus creating a hologram which can be recorded by a photographic plate (or digital sensor in more actual configurations) as depicted in Figure 1. Due to the holographic principle, optical phase data from the sample ($\Delta\phi$) can be successfully retrieved, being related to the geometrical thickness steps on the objects (ΔL) and/or the difference between the refractive indexes of samples and their involving medium (Δn) as $\Delta\phi = 2\pi \Delta n \Delta L / \lambda$.

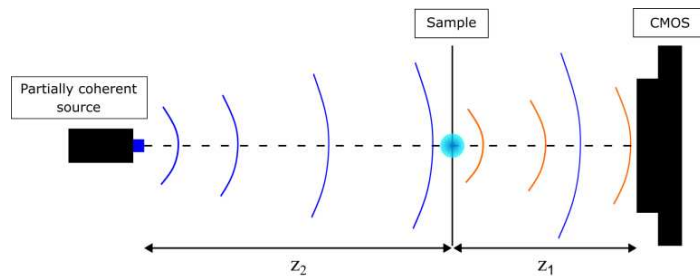


Figure 1: Schematic diagram of a general digital in-line holographic configuration.

2. Methods

Sample: The commercially available MIOL used in this study was the Acriva Trinova IOL (VSY Biotechnology, TheNetherlands) of 17 D power. This lens is trifocal and features an aspheric design with a sinusoidal diffractive profile, with 11 concentric rings. Its optical zone diameter measures 6.0 mm, and it has a refractive index of 1.462 [4,5]. For a proper conservation of its structure, the measured lens was placed inside a cuvette filled with saline solution.

Experimental assembly and image processing: A divergent and partially coherent source of light (450 nm of wavelength) was located at 87 mm from the cuvette. Next, a CMOS was located 5mm after the cuvette. For this configuration, a single hologram was recorded and back propagated to the sample plane using the angular spectrum method approach. Then, optical phase maps were reconstructed using a Gerchberg-Saxton algorithm based on 600 iterations, whose result was directly translated to height steps according to the previous equation. Finally, in order to validate our results, we generated the MIOL profile in MatLab using the equation proposed in Ref. [6]. Subsequently, we compared our experimental data with the numerical profile and with the experimental results of Vega et al. [5], who obtained the MIOL profile by confocal microscopy.

3. Results

Figure 2(A) shows the height map of the AcrivaTrinova IOL obtained with the digital in-line holographic system. Figure 2(B) shows the locally reconstructed topography of the measured MIOL, where it becomes notable that all the recorded rings for the measured area were successfully reconstructed with a similar height. For the same measured region, an average radial profile of complete first four rings was obtained and an average height of $0.78 \pm 0.14 \mu\text{m}$ was computed from the 2nd to the 4th noise-free rings, perfectly matching the theoretical value of $0.84 \mu\text{m}$ and the previously measured values by Vega et al. of $0.78 \pm 0.10 \mu\text{m}$ [5].

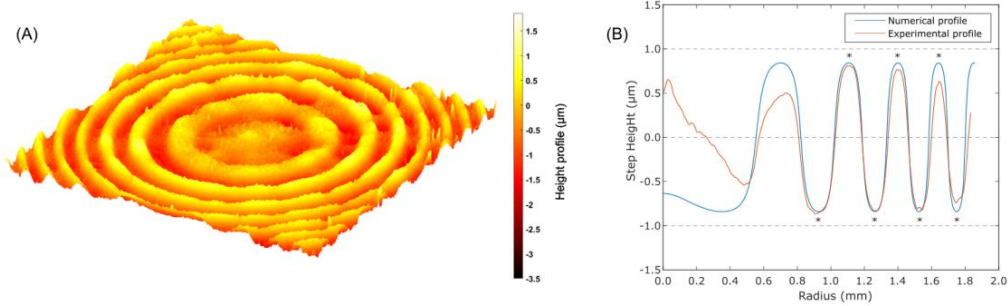


Figure 2: (A) Measured height map of the Acriva Trinova IOL. (B) Theoretical vs experimental profile of the Acriva Trinova IOL with the considered height steps for height computation marked with asterisks.

4. Conclusions

These preliminary findings show a potential suitability of digital in-line holography in the quality control inspection of MIOLs. These methods would introduce a compact and low-cost approach in comparison with previously established techniques.

Acknowledgments

R. V-A., V. M. and J. E-T. acknowledge the financial support by the Grant PID2020-120056GB-C21 from MCIN/AEI/10.13039/501100011033, by the Spanish Ministerio de Ciencia, Innovación and R. V-A. acknowledge the financial support by the Spanish Ministerio de Universidades FPU21/05151.

A. M-E. acknowledges the financial support from Universitat de València (programa Atracció de Talent 2021).

References

- [1] D. Gatinel, C. Pagnouille, Y. Houbrechts and L. Gobin L. “Design and qualification of a diffractive trifocal optical profile for intraocular lenses”. *J Cataract Refract Surg.* 37(11), (2011).
- [2] Q Wu, X Wang, L Liu and J Mo. “Inspection of Intraocular Lens with Dual-Side View Optical Coherence Tomography”. *IEEE Photonics J*, 13(3), (2021).
- [3] D Gabor. “A New Microscopic Principle”. *Nature*, 161, 777-778 (1948).
- [4] VSY Biotechnology, Product Downloads, Available online (accessed on 30 April 2024): <https://www.vsybiotechnology.com/detail/ophthalmology/healthcare-professionals/our-products/downloads>
- [5] F. Vega, M. Valentino, F. Rigato and MS Millán. “Optical design and performance of a trifocal sinusoidal diffractive intraocular lens”, *Biomed Opt Express.* 12(6), 3338-3351 (2021).
- [6] S.T.S Holmström, I Çim, and H. Urey, “An ophthalmic multifocal diffractive lens,” *European Patent Specification 3435143B1*

Puesta a punto de un sistema para holografía pulsante en régimen lineal

Emilio J. Mena^{1,3*}, Joan J. Sirvent-Verdú¹, Adriana R. Sánchez-Montes¹, Guillem Nájjar^{1,2}, Mariela L. Álvarez^{1,2}, Sergi Gallego^{1,2}, Andrés Márquez^{1,2}

¹*I.U. Física Aplicada a las Ciencias y las Tecnologías, Universidad de Alicante, P.O. Box 99, E-03080, Alicante, España*

²*Dept. de Física, Ing. de Sistemas y Teoría de la Señal, Universidad de Alicante, P.O. Box 99, E-03080, Alicante, España*

³*Dept. de Óptica, Farmacología y Anatomía, Universidad de Alicante, P.O. Box 99, E-03080, Alicante, España*

*E-mail: emilio.mena@ua.es

1. Materiales holográficos con láseres pulsante y continuo

La holografía ha experimentado un notable avance en las últimas décadas, ofreciendo innovadoras aplicaciones en diversas áreas como la óptica y la fotónica [1, 2]. Además, en el ámbito de la ciencia y la tecnología, ha transformado el almacenamiento de información, las técnicas y dispositivos de visualización (displays) y el procesado y transmisión de información [3, 4]. En los últimos años la holografía también ha estado presente en el desarrollo de metasuperficies [5, 6], lo que ha revolucionado el rango de aplicaciones de la Nanofísica. La idea de hacer holografía pulsante reside en la necesidad de acortar el tiempo de registro, lo que puede ser muy beneficioso a la hora de realizar hologramas de objetos en movimiento o de procesos ultrarrápidos necesarios para el almacenaje holográfico [7, 8].

En este trabajo se ha desarrollado y se ha puesto a punto un sistema experimental en el cual, mediante espejos abatibles, se puede incorporar un láser de emisión continua o un láser pulsante de nanosegundo (láser pulsante Nd:YAG con tasa de repetición de 10 Hz, duración de pulso de 6 ns y energía por pulso de 150 mJ), el cual, gracias a un *seeder*, se consigue obtener un haz coherente. De esta forma, al registrar con una longitud de onda de $\lambda = 532 \text{ nm}$ y, conocido el ángulo de incidencia θ por la ley de Bragg Eq. (1), se pretende alinear el montaje para obtener redes de volumen de, aproximadamente, $\frac{1}{\Lambda} = 1500 \text{ líneas/mm}$.

$$\sin \theta = \frac{\lambda}{2\Lambda} \quad (1)$$

Con este montaje, formado por un sistema afocal tipo telescopio de Galileo, un *beam splitter* y diversos espejos, se consigue expandir y colimar el haz, que es dividido en dos, obteniendo el haz de referencia y el objeto (Fig. 1). Estos inciden sobre el material fotosensible registrándose las franjas de interferencia que forman y, por tanto, generándose la red de volumen.

Una vez el sistema experimental está montado, se pretende optimizar la composición de un fotopolímero sensible al verde de alto rendimiento basado en polivinil-alcohol/acrilamida (PVA/AA). El proceso consistirá en registrar primero con el láser continuo, para después hacerlo con el pulsante coherente y analizar y comparar los procesos fotoquímicos y de difusión que se producen al variar tanto la energía por pulso como el número de pulsos y la separación temporal entre los mismos. De esta forma se podrá estudiar los efectos de registro en régimen lineal que consisten en la absorción a un fotón.

Cabe destacar que las medidas a realizar son la intensidad transmitida y difractada en función del tiempo de exposición y la respuesta angular una vez finalizado el proceso de registro. Para llevar a cabo estos procesos se utiliza un haz rojo de $\lambda = 633 \text{ nm}$, ya que a esta longitud de onda el colorante utilizado para crear el fotopolímero no es sensible.

2. Conclusiones

Con este trabajo se presenta la puesta a punto de un sistema para poder realizar holografía con un innovador láser pulsante coherente que nos permitirá estudiar cómo se comporta el material de registro al

variar parámetros como la energía por pulso, el número de pulsos o la separación temporal entre los mismos. Además, con este montaje también se podrá trabajar la holografía con procesos multifotón, en los que se produce absorción a dos fotones.

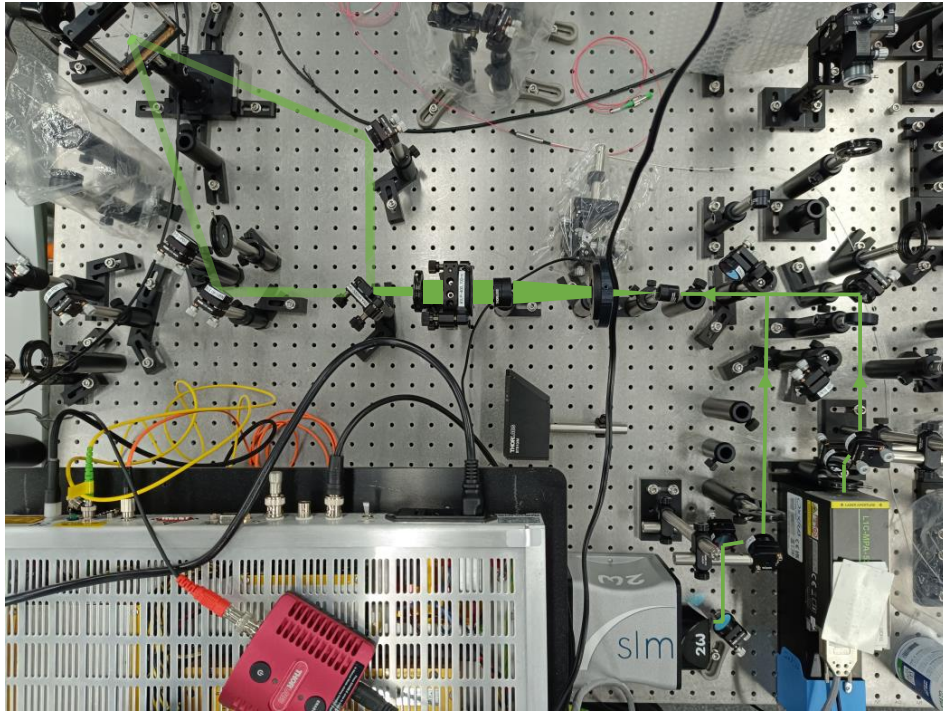


Figura 1 Sistema experimental en el cual, mediante un espejo abatible, se puede incorporar el láser pulsante o el continuo

Agradecimientos

Financiado por “Generalitat Valenciana” (España) (PROMETEO/2021/006), “Ministerio de Ciencia, Innovación y Universidades/AEI” (España) (PID2021-123124OB-I00 cofinanciado por ERDF/EU; y PID2019106601RB-I00). ARS-M agradece a la “Generalitat Valenciana” el contrato (GRISOLIAP/2021/106) y JJS-V agradece al “Ministerio de Ciencia, Innovación y Universidades/AEI” el contrato (FPU22/04316).

Referencias

- [1] P. Hariharan, *Optical Holography: Principles, techniques and applications*, 2nd ed. (Cambridge University Press, New York, USA, 1996).
- [2] R. K. Kostuk, *Holography: Principles and Applications* (CRC Press, Boca Raton, Florida, USA, 2019).
- [3] J. T. Sheridan, R. K. Kostuk, et al., “Roadmap on holography”, *J. Opt.*, vol. 22, p. 123002, 2020.
- [4] B. Javidi and T. Fournel, *Information Optics and Photonics* (Springer, New York, 2010).
- [5] C. Li, T. Wieduwilt, F.J. Wendisch, A. Márquez, et al., “Metafiber transforming arbitrarily structured light”, *Nat Commun*14, 7222 (2023).
- [6] A. Márquez, C. Li, A. Beléndez, S. Maier, H. Ren, “Information multiplexing from optical holography to multi-channel metaholography”, *Nanophotonics*, vol. 12, no. 24, pp. 4415-4440 (2023).
- [7] Y. Zhao, J. Zhong, Y. Ye, Z. Luo, J. Li, Z. Li, and J. Zhu, "Sensitive polyvinyl alcohol/acrylamide based photopolymer for single pulse holographic recording", *Mater. Lett.* 138, 284–286 (2015).
- [8] F.J. Martínez, R. Fernández, A. Márquez, S. Gallego, M. L. Álvarez, I. Pascual, and A. Beléndez, “Exploring binary and ternary modulations on a PA-LCoS device for holographic data storage in a PVA/AA photopolymer”, *Opt. Express* 23, 20459-20479 (2015).

Generación de vórtices ópticos en infrarrojo mediante elementos ópticos holográficos

Álvaro Paredes¹, Julia Marín Sáez^{2*}, Victoria Collados¹ and Jesús Atencia¹

¹*Departamento de Física Aplicada, Facultad de Ciencias, Instituto de Investigación en Ingeniería de Aragón, Universidad de Zaragoza, Pedro Cerbuna, 12, 50009 Zaragoza*

²*Departamento de Física Aplicada, Escuela Politécnica Superior, Universidad de Zaragoza, Ctra de Cuarte s/n, 22071 Huesca*

*E-mail: jmarinsaez@unizar.es

1. Introducción

Un vórtice óptico es una onda caracterizada por tener una fase helicoidal, dada por

$$\phi = m\theta \quad (1)$$

donde θ es la componente azimutal y m es un número entero que se denomina carga topológica. Los vórtices ópticos se emplean en numerosas aplicaciones (pinzas ópticas, interferometría, comunicaciones[1] ...). En este último campo interesan vórtices con longitudes de onda comprendidas dentro de la ventana de comunicaciones, es decir, en torno a los 1550 nm.

Entre los diversos métodos de obtención de vórtices ópticos destaca la utilización de un modulador espacial de luz (SLM). Un SLM es un dispositivo de cristal líquido que permite la implementación de máscaras de fase. Para generar un vórtice a partir de una onda plana se puede implementar en el SLM una máscara de fase espiral como la expresada en (1), o bien la fase de la interferencia calculada entre dos ondas planas, una de las cuales porta un vórtice, lo que da lugar a una red de fase con dislocación. Se pueden obtener vórtices ópticos con distinta carga topológica con un mismo SLM modificando adecuadamente la máscara de fase[2].

Sin embargo, los SLM son elementos caros, con un umbral de daño bajo y no permiten el desarrollo de sistemas compactos. Una solución para obtener un vórtice en infrarrojo es registrar un elemento óptico holográfico (EOH) en un material fotosensible, generando una modulación espacial de su índice de refracción mediante la interferencia de una onda plana y una onda portadora de vórtice generado por un SLM [3].

Los EOHs pueden registrarse en materiales fotosensibles con espesores del orden de la decena de micras, sobre soporte de vidrio o plástico, con lo cual son elementos económicos, compactos y fáciles de implementar en un sistema de comunicaciones ópticas.

2. Metodología

El material fotosensible en el cual se han registrado los EOHs es el fotopolímero comercial Bayfol HX200, caracterizado previamente para su uso en NIR[4]. En dicho estudio se encontró que su modulación de índice depende de la frecuencia espacial (a mayor frecuencia espacial, mayor modulación), además de la intensidad y exposición de registro. El valor máximo de modulación de índice proporcionado por el material alcanza 0.03 según el fabricante.

Para reconstruir a 1550 nm eficientemente es necesario haber registrado en el EOH la máxima modulación de índice posible, teniendo en cuenta que el registro debe hacerse con longitud de onda visible, ya que es el rango espectral al cual es sensible. Según [4], se elige una exposición de 16 mJ/cm² y ángulo entre haces a 532 nm tal que el periodo espacial es 1 μ m. Con esto la modulación máxima de índice esperada es 0.024, lo que daría una eficiencia teórica del 47% en 1550 nm.

3. Resultados

Se han registrado EOHs con vórtices generados por el SLM con diversas cargas topológicas. La eficiencia obtenida para 1534 nm es del 30% aproximadamente, algo menor que la esperada. Ello puede ser debido a la complejidad para medir la eficiencia a dicha longitud de onda. En la Fig. 1 se muestra el vórtice con carga topológica $m = 2$ obtenido al reconstruir el EOH con longitud de onda 1534 nm y su interferencia con una onda plana.

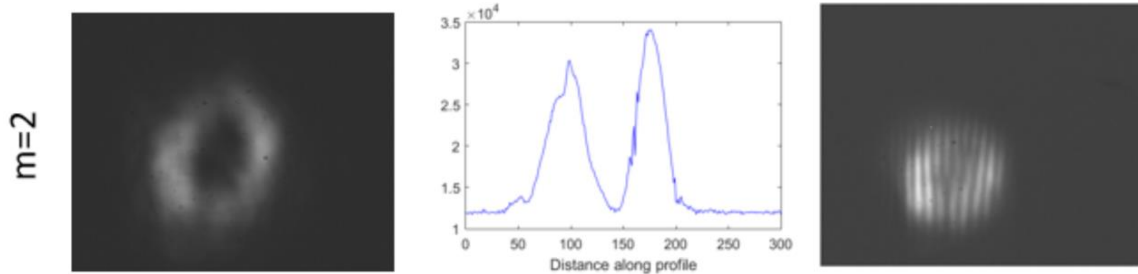


Figure 1 Vórtice de carga $m = 2$ obtenido en la reconstrucción del EOH con longitud de onda 1534 nm.

4. Conclusiones

Se han registrado EOH con un vórtice óptico generado con un SLM a 532 nm, diseñado para obtener eficiencia máxima a 1534 nm. Se ha obtenido una eficiencia del 30% aproximadamente para 1534 nm, lo cual evidencia la viabilidad del método, si bien sería necesario un material de registro con modulación de índice mayor para obtener mayor eficiencia.

Agradecimientos

Trabajo financiado por el Ministerio de Ciencia e Innovación y la Agencia Estatal de Investigación (PID2019-108598GB-I00), y por el Departamento de Industria e Innovación del Gobierno de Aragón (Grupo TOL, E44-23R).

Referencias

- [1] A. E. Willner, H. Song, K. Zou, H. Zhou, and X. Su, “Orbital Angular Momentum Beams for High-Capacity Communications,” *J. Light. Technol.* **41**, 1918–1933 (2023).
- [2] Z. Zhang, Z. You, and D. Chu, “Fundamentals of phase-only liquid crystal on silicon (LCOS) devices,” *Light Sci. Appl.* **3**, e213–e213 (2014).
- [3] J. Atencia, M.-V. Collados, M. Quintanilla, J. Marín-Sáez, and Í. J. Sola, “Holographic optical element to generate achromatic vortices,” *Opt. Express* **21**, 21056 (2013).
- [4] J. Marín-Sáez, J. Atencia, D. Chemisana, and M.-V. Collados, “Characterization of volume holographic optical elements recorded in Bayfol HX photopolymer for solar photovoltaic applications,” *Opt. Express* **24**, p. A720 (2016).

Propiedades cromáticas de las lentes sectoriales

Sara Fernández-Núñez^{1*}, José Antonio Gómez-Pedrero¹, Luis Miguel Sánchez-Brea¹,
y Francisco José Torcal-Milla²

¹Departamento de Óptica, Universidad Complutense, Plaza de Ciencias 1, 28040, Madrid

²Departamento de Física Aplicada, Universidad de Zaragoza, C/ Pedro Cerbuna, 12, 50009, Zaragoza

*E-mail: sarafn@ucm.es

1. Introducción

Las lentes sectoriales son un tipo de lentes difractivas que se forman por un mosaico de sectores angulares, siendo la fase de cada sector la correspondiente a una lente monofocal con una focal comprendida en el intervalo

$$\left[\bar{f} - \frac{\Delta f}{2}, \bar{f} + \frac{\Delta f}{2} \right], \quad (1)$$

Presentan la propiedad de tener un foco extendido [1]. Aunque la distribución más sencilla de las focales de los sectores individuales es la distribución lineal entre los valores extremos del intervalo definido por la ecuación (1), es posible demostrar, que las distribuciones no lineales definidas por una función cuadrática o cúbica [1] permiten mejores resultados en términos de ausencia de artefactos difractivos y magnitud de la profundidad de foco de la lente. Aunque las lentes sectoriales están definidas como placas zonales de Fresnel [1], es posible extender este diseño a lentes de fase o, incluso, a kinoformas.

En este trabajo nos hemos centrado en el análisis de las propiedades cromáticas de las lentes sectoriales. En primer lugar, hemos realizado un análisis por simulación numérica utilizando el método de Bluestein [2] o Chirp Z-transform (CZP) que permite el cálculo numérico de la transformada de Fourier con un muestreo distinto en el dominio espacial que en dominio de frecuencias. Posteriormente, hemos llevado a cabo un experimento, utilizando un modulador espacial de luz en un sistema óptico con tres fuentes láser con longitudes de onda cercanas a las líneas espectrales de Fraunhofer F, C y d.

2. Simulación numérica

En la Figs. 1a) y 1b) mostramos, respectivamente, una placa zonal de Fresnel con 380 mm de focal (calculada para una longitud de onda de 518 nm) y una lente sectorial con la misma focal.

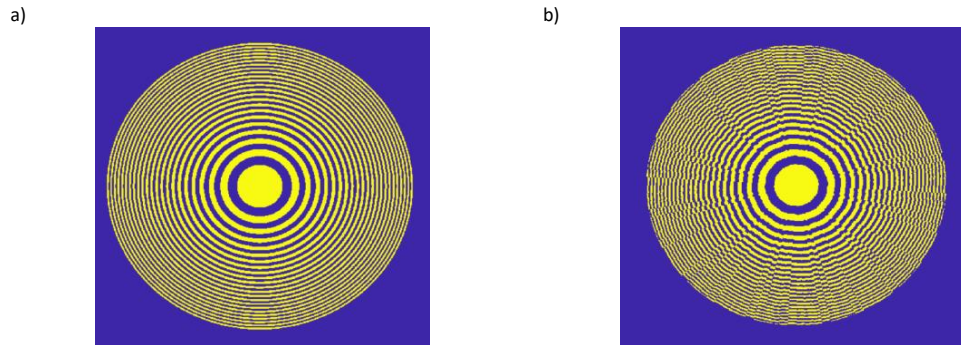


Figure 1 a) Placa zonal de Fresnel convencional calculada para una longitud focal principal de 380 mm para una longitud de onda de 518 nm. b) Placa sectorial calculada con los mismos parámetros.

Por su parte, la Fig. 2, muestra la intensidad en el centro del haz, a lo largo del eje Z, de un haz láser centrado en las longitudes de onda de 656 nm (rojo), 518 nm (verde) y 488 nm (azul), respectivamente, tras atravesar las placas zonales mostradas en la Fig. 1 y propagarse entre las distancias $z=280$ mm y $z = 420$ mm, medidos desde el plano de la placa zonal. La intensidad de la Fig. 2 ha sido calculada numéricamente usando el algoritmo de propagación CZT [2]. Podemos ver que, desde el punto de vista cromático, las lentes sectoriales tienen un comportamiento parecido a la placa zonal de Fresnel, pero conservando la propiedad de foco extendido en las tres longitudes de onda consideradas.

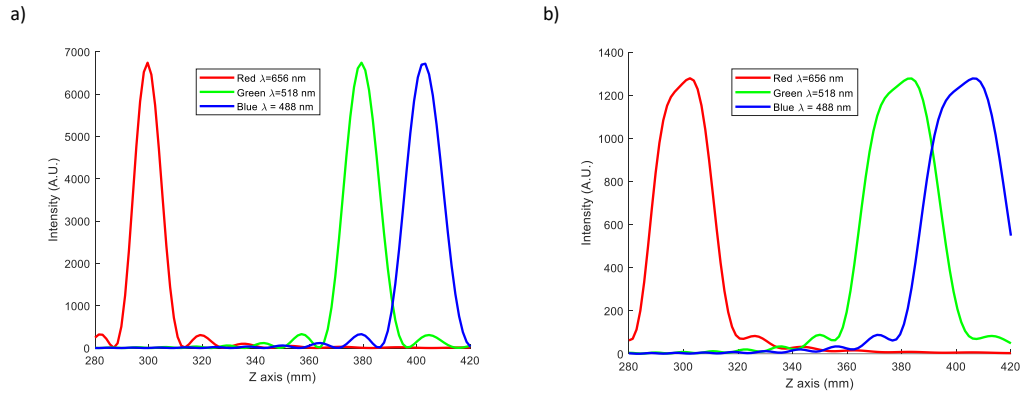


Figure 2 a) Simulación del valor máximo de intensidad frente a la coordenada z de un haz rojo (656 nm), verde (518 nm) y azul (488 nm) tras atravesar la placa zonal de Fresnel convencional representada en la Fig1.a), b) gráfico de intensidad máxima vs z calculada en las mismas condiciones, pero correspondiente a la lente sectorial de la Fig1.b).

3. Resultados experimentales

Para comprobar los resultados de las simulaciones hemos utilizado un dispositivo experimental basado en un modulador espacial de luz (SLM) iluminado por tres fuentes cuyas longitudes de onda son 656 nm (láser rojo), 518 nm (láser verde) y 488 nm (láser azul). Como se puede observar en la Figura 3, los perfiles de intensidad en el centro del haz al propagarse a lo largo del eje Z muestran, en líneas, generales el comportamiento predicho en las simulaciones de la Fig. 2

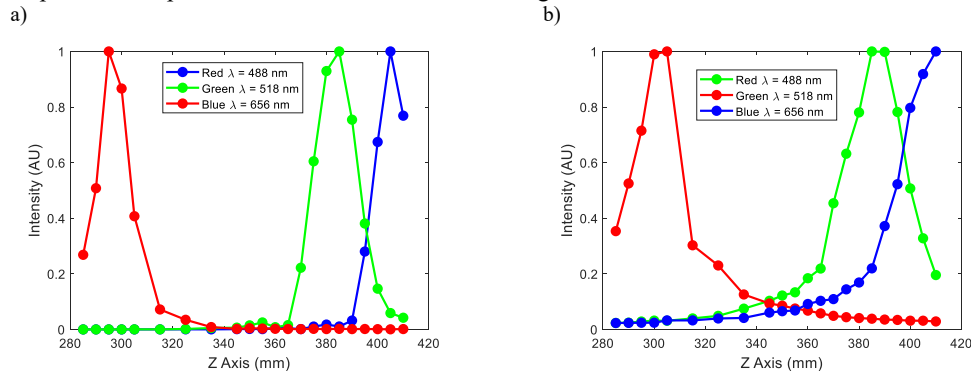


Figure 3 a) Medida experimental del valor máximo de intensidad frente a la coordenada z de un haz rojo (656 nm), verde (518 nm) y azul (488 nm) tras difractarse en la placa zonal de Fresnel convencional representada en la Fig1.a), b) gráfico de intensidad máxima vs z calculada en las mismas condiciones, pero correspondiente a la lente sectorial de la Fig1.b).

4. Conclusiones

En este trabajo hemos estudiado mediante simulación numérica y medidas experimentales el comportamiento cromático de una placa zonal de rango extendido (lente sectorial) comparando dicho diseño con una placa zonal estándar.

Agradecimientos

Agencia Estatal de Investigación y Fondo Europeo de Desarrollo Regional, proyectos PID2021-122486OA-I00 y PID2022/138071OB/100.

Referencias

- [1] F.J. Torcal-Milla, et al, "Sector-based Fresnel zone plate with extended depth of focus", *Opt. Las. Tech.* **154**, 108294 (2022).
- [2] Y. Hu, et al, "Efficient full-path optical calculation of scalar and vector diffraction using the Bluestein method", *Light Sci. App.*, **9**, 119 (2020).

Developing holographic couplers for see-through application without prisms

J.J. Sirvent-Verdú^{1*}, J. C. Bravo^{1,2}, J. Colomina-Martínez², E.J. Mena², C. Neipp^{1,2}, S. Gallego^{1,2}, A. Beléndez^{1,2}

¹*Departamento de Física, Ingeniería de Sistemas y Teoría de la Señal, Universidad de Alicante. Carretera de San Vicente del Raspeig s/n (03690).*

²*Instituto Universitario de Física Aplicada a las Ciencias y las Tecnologías Universidad de Alicante. Carretera de San Vicente del Raspeig s/n (03690)*

*E-mail: jj.sirvent@ua.es

1. Introduction

Augmented reality, 3D Image, and Mixed Reality have become some of the most demanding technologies nowadays, in which many high-tech companies are heavily investing, such as Sony, Apple, Bosch, Essilor, etc. For this see-through application, holography can play a fundamental role. Indeed, a holographic optical element (HOE) can be either used as a mirror to redirect the image on the user's eyes or as a coupler in a waveguide combiner [1], where the design needs to achieve both the in- and out-coupling of an image produced by a projector, usually located on the temple of the glasses, with two complementary holograms.

In this latter case, it is important to note that the image is to be guided by the Total Internal Reflection (TIR) principle along the glass, which would imply extremely oblique recording angles in the hologram fabrication. One way to achieve this goal is the use of prisms and index matching systems, which is a complex and precise optical set-up [2], but it is not suitable to fabricate these elements massively. Our group was the pioneer to propose an alternative solution to record these elements [3], based on using a different recording wavelength. Then, this process can be done without prisms and index matching systems.

Photopolymers are the selected holographic recording medium to fabricate these couplers, which have become an important and versatile solution for many applications, mainly related to holography: the flexibility to change their chemical composition, the low cost, together with their optical properties (low scattering, wavelength sensitivity, etc.). In addition, the possibility to incorporate nanoparticles opens a new range of possibilities, even to obtain tunable holograms [2,4].

In this work we present an overview of our advances in the fabrication of holographic couplers for see-through based on photopolymers, analyzing different aspects such as different geometries in transmission and reflection, different photopolymer compositions, shrinkage effects and noise gratings.

2. Experimental Set-up

A two-beam holographic set-up is used, as depicted in [5], where the interference of two plane waves, given by the corresponding 532 nm - wave vectors \mathbf{k}_o and \mathbf{k}_r , is used to expose the photopolymer film, where the HOE is recorded. Therefore, the grating vector \mathbf{K} , or its grating spacing Λ and its slant angle φ , is given by the recombination of both beams with Eq. (1), which ultimately describes its diffraction properties,

$$\mathbf{k}_o - \mathbf{k}_r = \mathbf{K} = \boldsymbol{\rho} - \boldsymbol{\sigma}. \quad (1)$$

Regarding the see-through application, two conditions need to be accomplished: first, that the diffracted beam is propagating under TIR; second, that the Bragg condition is fulfilled at near-normal incidence. Geometries in Table 1 yield both features for designed wavelengths of 633 nm and 473 nm. Its corresponding wave vectors, when a different reconstruction wavelength is used, are $\boldsymbol{\rho}$ and $\boldsymbol{\sigma}$, whose angles of propagation are known as the Bragg and diffracted beam angles, as in [6].

Intended operating wavelength	Recording scheme	Recording angles in air ($\pm 0.1^\circ$)	Spatial frequency (± 20 lines/mm)	Slant angle ($\pm 0.3^\circ$)	Bragg angle in the material ($\pm 0.3^\circ$)	Diffracted beam angle ($\pm 0.3^\circ$)
633 nm	Transmission	4.8, 69.2	1710	-69.2	-0.3	41.9
473 nm	Reflection	30, 60	5600	27.3	-1.0	55.5

Table 1 Recording geometries for different operating wavelengths

To allow the coupling function of the incoming beam into the waveguide, two complementary gratings need to be placed within the same substrate. If the transmission scheme is used, both HOEs are placed on the front surface of the glass, contrary to the reflection case, where they need to be located on the back surface, as Fig. 1(c) illustrates. Through a reversion of the sign of the recording angles, the same effect in the Bragg condition is produced. Hence, the guided diffracted beam from the in-coupler HOE can be diffracted again, being reflected from the opposite surface of the waveguide in the out-coupler grating.

3. Results

In this section, we present the experimental validation of the see-through capability of the recorded HOEs in a waveguide combiner, using Bayfol HX-200 from Covestro as the holographic recording material. Fig. 1(a) and Fig. 1(b) correspond for the transmission (633 nm) and reflection (473 nm) schemes in Table 1.

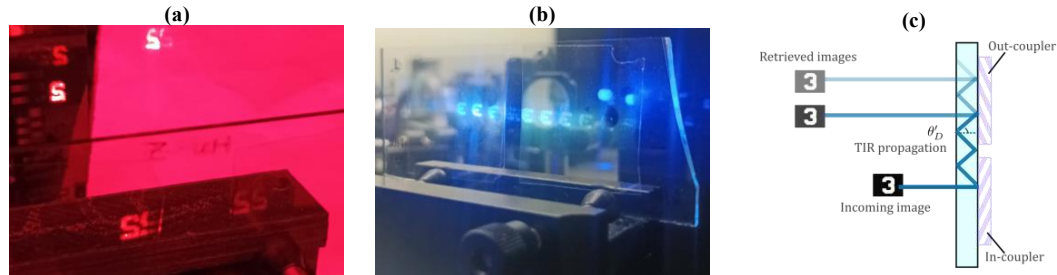


Figure 1 TIR propagation in a waveguide combiner with holographic couplers for the 633-transmission (a) and 473-reflection (b) schemes in Table 1. For the latter case, the schematic of the waveguide in- and out-coupling is presented (c).

The diffracted counterpart of the reconstruction beam, when fulfilling the Bragg condition, is trapped within the glass thanks to the TIR propagation. By placing alongside a complementary grating, as in Fig. 1(c), an image can be retrieved, which is superimposed on the real surrounding environment.

4. Conclusions

In this work, we have validated the manufacturing of holographic couplers recorded in photopolymers for a see-through application. Using a recording wavelength different from the one intended for the reconstruction step, we have proposed different geometries without the use of prisms and index matching systems, both for transmission and reflection schemes. Moreover, we adduce experimental evidence that by combining two complementary HOEs within the same substrate, an image can be retrieved while maintain the see-through capability of the system.

Acknowledgments

This work was funded by the “Generalitat Valenciana” (Spain) (PROMETEO/2021/006), “Ministerio de Ciencia, Innovación y Universidades/AEI” (Spain) (PID2021-123124OB-I00 cofunded by “ERDF/EU” and PID2019-106601RB-I00). JJS-V thanks the “Ministerio de Ciencia, Innovación y Universidades/AEI” for the grant FPU22/04316.

References

1. J. Xiong, K. Yin, K. Li, and S.-T. Wu, "Holographic optical elements for augmented reality: Principles, present status, and future perspectives," *Adv. Photonics Res.* **2**(1), 2000049 (2021).
2. M. Miki, R. Ohira, and Y. Tomita, "Optical Properties of Electrically Tunable Two-Dimensional Photonic Lattice Structures Formed in a Holographic Polymer-Dispersed Liquid Crystal Film: Analysis and Experiment," *Materials* **7**(5), 3677–3698 (2014).
3. R. Fernández, S. Bleda, S. Gallego, C. Neipp, A. Márquez, Y. Tomita, I. Pascual, and A. Beléndez, "Holographic waveguides in photopolymers," *Opt. Express* **27**(2), 827–840 (2019).
4. S. Gallego, D. Puerto, M. Morales-Vidal, M. G. Ramirez, S. I. Taleb, A. Hernández, M. Ortuño, and C. Neipp, "Tunable Waveguides Couplers Based on HPDLC for See-Through Applications," *Polymers* **13**(11), (2021).
5. J. J. Sirvent-Verdú, J. C. Bravo, J. Colomina-Martínez, C. Neipp, D. Puerto, A. Márquez, and S. Gallego, "See-through display based on commercial photopolymer: Optimization and shrinkage effects," *Heliyon* **9**(6), e16646 (2023).
6. H. Kogelnik, "Coupled Wave Theory for Thick Hologram Gratings," *The Bell System Technical Journal* **48**, (1969).

Calibration of a focus tunable lens under the effect of gravity

Elisabet Pérez-Cabré*, Fátima Cuéllar, Laura Clavé and María Sagrario Millán

Departament d'Òptica i Optometria, Universitat Politècnica de Catalunya, Terrassa (Barcelona)

*E-mail: elisabet.perez@upc.edu

1. Introduction and motivation

Focus tunable lenses refer to refractive mediums capable of dynamically and continuously adjusting their focal length without physically shifting the lens plane. They have proved to be useful components in optical systems by reducing complexity, size, weight, response time and power consumption. They have been integrated in numerous applications such as robotic and machine vision-based devices, augmented-reality systems or advance optical instrumentation in general [1]. Calibration is an essential prerequisite enabling the use of a given component to its maximal capacity. In this work, we use the EL-16-40-TC-VIS-5D tunable lens developed by Optotune (Switzerland). This lens features a core containing an optical fluid sealed with an elastic polymer membrane. An electromagnetic actuator applies pressure to the container, altering the curvature of the lens. Control over the optical power is achieved by adjusting the electrical current flowing through the actuator's coil [2].

In this work, we conduct an analysis of the EL-16-40-TC-VIS-5D lens under the effect of gravity, specifically comparing its performance when the optical axis is oriented vertically (with the lens in a horizontal position) versus the optical axis oriented horizontally (with the lens in a vertical position). A calibration procedure is employed to achieve a corrected linear behaviour in terms of the optical power provided by the tunable lens in both vertical and horizontal conditions.

2. Focus tunable lens calibration

The EL-16-40-TC-VIS-5D tunable lens from Optotune (Fig. 1a) has a 16mm clear aperture and a focal power range spanning from -2 to +3 D (diopters). With a fast response time of 5ms and high repeatability typically within ± 0.05 D, the lens features a refractive index $n_D=1.30$ and an Abbe number $\nu=100$, as specified by the manufacturer datasheet. Notably, when the lens operates with a vertical optical axis (without the effect of gravity), its wavefront error at 0.0 D is less than 0.25λ at 532nm, while the RMS is below 0.50λ when the optical axis is horizontal (with the effect of gravity).

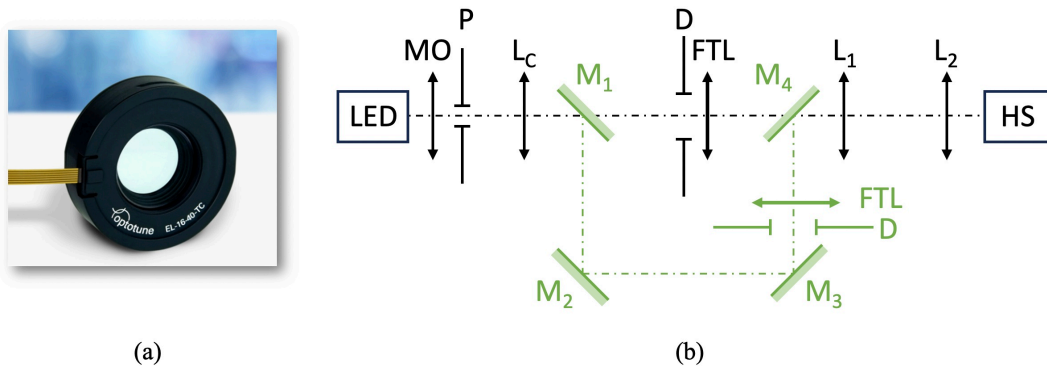


Figure 1 (a) Optotune focus tunable lens. (b) Calibration setup: description of the components in the text.

The calibration setup (Fig. 1b) comprises a 530nm emitting LED serving as the light source. A microscope objective (MO) focuses the light onto a 200-micron pinhole (P), followed by a collimating lens (L_C) to ensure uniform illumination of the tunable lens (FTL). The optical arrangement facilitates sequential evaluation of the lens behaviour with and without the effect of gravity, corresponding to the vertical and horizontal orientations, respectively. In the vertical position, the optical axis of the setup remains horizontal. An iris diaphragm (D), just in front of the tunable lens, controls the illuminated aperture of the lens. Two additional lenses (L_1 , L_2) permit to adjust the beam diameter to match the area

of the Hartman-Shack (HS) sensor. For horizontal positioning, a double periscope modifies the light path accordingly (green path). In both configurations, the tunable lens is located at the same distance from the HS sensor, which in turn is conjugated with the lens plane.

Before introducing the tunable lens into the setup, the incident wavefront on the HS sensor is recorded and used as a reference. Any subsequent variation is attributed to the lens's effect. The defocus Zernike coefficient is related to the optical power introduced by the lens. Using the provided software and electronic controller of the lens, we vary its focal power from -2 to +3D. Two different experiments were conducted: a gradual variation of the focal power from minimum to maximum power in 0.2D steps (0.1D within the -1.0 to +1.0 region), and larger jumps of the optical power from positive to negative values until reaching 0.0 D. A typical sequence for this second experiment was: +3.0D → -2.0D → +2.8D → -1.8D → +2.6D → -1.6D... and so on.

Both experiments were initially conducted with the lens in horizontal position (vertical optical axis) and repeated across multiple days. The same procedure was then carried out with the lens in vertical position (horizontal optical axis), with measurements taken after varying intervals, ranging from hours to weeks. The last measure with the lens in vertical position was carried out after four weeks from the first measurement. The collected data enable determination of the mean optical power achieved by the lens and its associated statistical error. Figure 2 displays the results, demonstrating an excellent linear behaviour, particularly when the lens was used in a horizontal orientation (Fig. 2a). Finally, a calibration lookup table was built to linearize and optimize the lens response in accordance with the expected optical power, for both cases, when the lens was used in horizontal position and for a vertical orientation (Fig.2b).

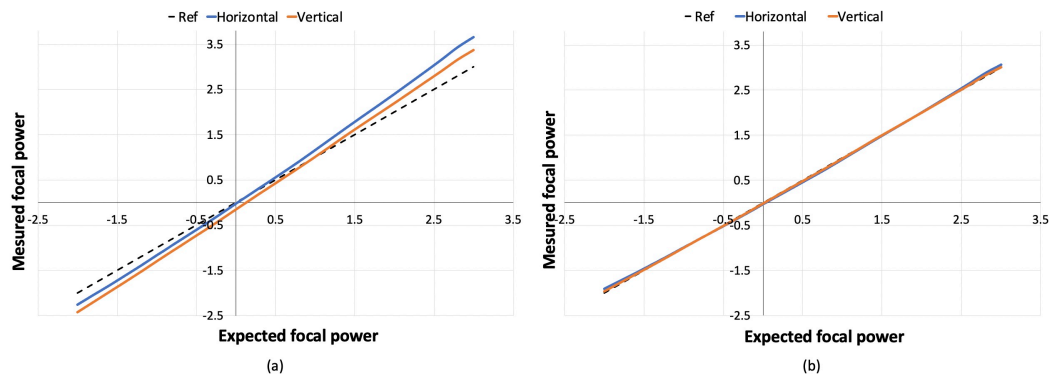


Figure 2 Measured focal power for both, horizontal and vertical orientations of the lens: (a) initial output signal of the lens, (b) optimized output signal after calibration.

3. Conclusions

The EL-16-40-TC-VIS-5D model of focus tunable lenses from Optotune with a variation of 5D in optical power exhibits a remarkable behaviour in terms of reproducing specific focal lengths, even when employed in vertical orientation despite the influence of the gravitational force.

Acknowledgments

Authors thank the Agencia Estatal de Investigación for financial support (PID2020-114582RB-I00/AEI/ 10.13039/501100011033).

References

- [1] Chen, L., Ghilardi, M., Busfield, J. J. C., & Carpi, F., "Electrically Tunable Lenses: A Review", *Frontiers in Robotics and AI*, 8, 678046 (2021).
- [2] <https://www.optotune.com/> (2023).

Spatio-temporal characterization of ultrashort light pulses by structured compressed sampling with a single-pixel detector

Mitzi Ordóñez-Pérez^{1*}, Pedro J. Clemente-Pesudo^{1,2}, Erick Ipus¹, Gladys Minguez-Vega¹, and Enrique Tajahuerce¹

¹IGROC-UJI, Institute of New Imaging Technologies (INIT), Universitat Jaume I, 12071, Castelló, Spain.

²Servei Central d'Instrumentació Científica (SCIC), Universitat Jaume I, Castelló, Spain.

1. Abstract

We propose a novel approach employing structured sampling and a single-pixel detector to measure, simultaneously, the spatial profile and the spatially resolved temporal profile of a femtosecond laser beam with an autocorrelation method. The experimental system integrates a digital mirror device (DMD) into a conventional autocorrelation setup. An experimental comparison with a raster scanning method illustrates the advantages of this setup, achieving comparable accuracy with reduced energy levels. This study introduces a promising technique for the precise characterization of ultrafast laser pulses, with potential applications in various fields that demand accurate spatial and temporal measurements as material processing or imaging applications.

2. Introduction

Recent advancements in radiation-matter interaction have prompted innovative fields of optics research, particularly in ultrafast optics. Ultrashort laser pulses have gained significant importance due to their unique properties [1], finding applications in diverse scientific fields like high-resolution biomedical imaging[2], nonlinear optics, and materials microprocessing [3]. Understanding and controlling both spatial and temporal dimensions of these pulses is fundamental for their effective application. The proposed research aims to enhance the characterization of ultrashort pulses, providing insights into their temporal and intensity attributes at each spatial point. Femtosecond laser waveforms are complex and require thorough spatiotemporal characterization for scientific and technological applications. Conventional pulse measurement devices like autocorrelators, the frequency-resolved optical gating (FROG), and the spectral phase interferometry for direct electric-field reconstruction (SPIDER), focus on temporal characteristics but overlook spatial variations. This limitation becomes apparent with wide-spectrum ultrashort pulses and the spatiotemporal coupling from diffraction in wide field devices, necessitating complete spatio-temporal characterization.

For the spatial characterization, the Single-pixel imaging techniques are an excellent tool, utilizing spatial light modulators (SLM) and bucket detectors, scan objects and reconstruct images with high efficiency and multidimensional capability [4]. This method offers advantages such as improved light efficiency and tolerance to scattering. Computational imaging with single-pixel cameras simplifies detection and facilitates measurement of multiple light parameters [5], expanding applications into infrared and terahertz wavelengths [6]. Single-pixel detectors excel in timing resolution compared to ferroelectric liquid-crystal spatial light modulators.

This research proposes using spatial light modulators Digital Mirror Devices (DMD) and smart sampling techniques to characterize the temporal profile of ultrashort light pulses with spatial resolution. By adapting strategies from single-pixel imaging, the study aims to extend the dimensionality of ultrafast laser beam characterization. Temporal resolution will be addressed through fringe-resolved autocorrelation, employing Walsh Hadamard sampling to encode spatial information with temporal details.

3. Results

In a preliminary experimental setup, a pulsed beam with a specific spatiotemporal structure undergoes characterization through the simultaneous operation of an interferometric autocorrelator, providing temporal information, and a single pixel camera setup, providing spatial information. The pulsed beam is directed into a Michelson-type interferometer, where it is duplicated using a beam splitter. One interferometer arm features a movable arm, while the other has a rigid arm. Both replicas of the light beam strike on a nonlinear crystal, generating a second harmonic signal due to the temporal delay from one beam compared to the other. Hadamard

basis functions on the DMD encode this new light beam after the nonlinear crystal, and the signal is integrated into a detector. This process enables the retrieval of an autocorrelation trace for each element of the Hadamard basis, from which the complete pulse structure is reconstructed to measure the temporal shape of the ultrashort laser beam with spatial resolution. Computational image reconstruction techniques allow us to determine the correlation signal intensity at each spatial coordinate, facilitating the extraction of the temporal pulse length at each point, and providing the spatiotemporal information of the initial pulse.

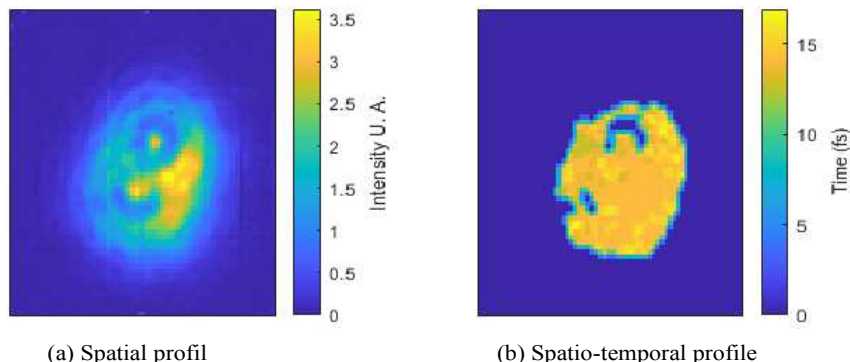


Figure 1: Reconstructions of the spatial and spatio-temporal profiles of a pulsed light beam obtained from preliminary experimental results.

This retrieval of an autocorrelation trace for each Hadamard basis element, as in the simulation, leads to the reconstruction of the complete pulse structure, containing the temporal shape of the ultrashort laser beam with spatial resolution. The technique was experimentally verified as shown in Figure 1. In addition, we reconstructed the image with a reduced number of measurements by applying compression algorithms, demonstrating that it is possible to perform the measurement in a shorter time.

4. Results

We have proposed a novel technique based on the integration of a DMD and computational imaging techniques in an autocorrelator to obtain the spatiotemporal characterization of a laser pulse. We have verified the idea with both computer simulations and preliminary experiments. For the experiments, we used a femtosecond oscillator with an average pulse width of 15 fs. We successfully recovered the spatial profile and temporal length of the pulse at each point, showing how well the data recovery process works. For our configuration, the measurement of the spatiotemporal distribution with a raster scanning technique is difficult in positions where the intensity is low. However, the proposed method stands out as superior, increasing the area where the pulse is well characterized while keeping the accuracy level the same.

5. References

- [1] Diels, J., [*Ultrashort Laser Pulse Phenomena*] (1 2006).
- [2] Thomas, J. and Rudolph, W., “Biological microscopy with ultrashort laser pulses,” *Tunable Laser Applications* **150**, 245 (2008).
- [3] Račiukaitis, G., “Ultra-short pulse lasers for microfabrication: a review,” *IEEE Journal of Selected Topics in Quantum Electronics* **27**(6), 1–12 (2021).
- [4] Jauregui-Sánchez, Y., Clemente, P., Láncis, J., and Tajahuerce, E., “Single-pixel imaging with fourier filtering: application to vision through scattering media,” *Optics Letters* **44**, 679 (1 2019).
- [5] Rutkauskas, M., Srivastava, A., Arbuckle, D., Altman, Y., and Reid, D. T., “Spectral shaping of mid-infrared laser pulses with a digital micromirror device,” in [*Optical Sensors and Sensing Congress*], *Optical Sensors and Sensing Congress*, SM1B.4, Optica Publishing Group (2020).
- [6] Farina, A., Betcke, M. M., Di Sieno, L., Bassi, A., Ducros, N., Pifferi, A., Valentini, G., Arridge, S., and D’Andrea, C., “Multiple-view diffuse optical tomography system based on time-domain compressive measurements,” *Optics Letters* **42**, 2822 (7 2017).

30 años de Óptica espacial en el INTA: una historia de éxito.

Tomas Belenguer Dávila*, Alberto Álvarez Herrero*, Luis Miguel González Fernández*

INTA

Carretera de Ajalvir Km, 4.5

28850 Torrejón de Ardoz

Madrid, España

Resumen (Abstract):

Durante más de tres décadas, el INTA, a través de su laboratorio pionero en instrumentación espacial (LINES), que ha evolucionado hacia el Departamento de Óptica Espacial, ha desempeñado un papel destacado en las principales misiones espaciales a nivel nacional. Desde la histórica misión Integral, dedicada al estudio de los rayos gamma, hasta la innovadora misión Plato, centrada en la investigación de tránsitos planetarios y oscilaciones estelares (PLANetary Transits and Oscillations of stars), se traza un recorrido exhaustivo por el desarrollo de la óptica espacial en las misiones cósmicas. Además, se analizan las contribuciones y desafíos que el diseño óptico debe abordar para adaptarse a la instrumentación que requieren las complejas misiones actuales, que van desde la exploración planetaria (ExoMars 2026) hasta la exploración solar (Solar Orbiter, IMaX, TuMag) y la exploración terrestre (programa ANSER, CINCLUS, MORERA).

Análisis numérico de lentes difractivas cilíndricas basadas en series de Fourier

Angela Soria-García¹, Francisco Jose Torcal-Milla^{1,2}, Joaquín Andres-Porras¹,
Jesús del Hoyo¹, Jose Antonio Gomez-Pedrero¹, Luis Miguel Sanchez-Brea^{1,*}

¹ Grupo Complutense de Óptica Aplicada, Departamento de Óptica, Facultad de Física y Facultad de Óptica y Optometría, Universidad Complutense de Madrid, Madrid (España)

² Grupo de Tecnologías Ópticas Láser. Instituto de Investigación en Ingeniería de Aragón (I3A), Departamento de Física Aplicada, Universidad de Zaragoza, Zaragoza (España)

*E-mail: optbrea@ucm.es

1. Introducción

Las lentes difractivas angulares permiten obtener una gran profundidad de foco manteniendo una cintura del haz estrecha. Entre los diseños más recientes, se han desarrollado lentes difractivas angulares con foco extendido basadas en la modulación angular mediante serie de Fourier [1]. Se pueden optimizar los coeficientes de Fourier para producir profundidad de foco extendida o multifoco, lo cual es útil en numerosas áreas como la óptica visual, la concentración solar, la litografía, etc. [2, 3]. Por otro lado, las lentes cilíndricas se utilizan en aplicaciones como la corrección del astigmatismo, el conformado de haces láser, la espectroscopia óptica, la holografía, la microscopía, etc. En este trabajo se define y analiza numéricamente una lente difractiva cilíndrica binaria cuyos bordes siguen un patrón definido por una serie de Fourier.

2. Definición de la lente y análisis numérico

Sea una lente cilíndrica difractiva binaria, cuyos bordes no son rectos sino ondulados. La transmitancia de la lente se define como la binarización entre los niveles de fase 0 y π de la función

$$t(x, y) = \exp\left(\frac{-ikx^2}{2g(y)}\right), \quad (1)$$

donde $k=2\pi/\lambda$, la focal depende de la posición y de forma periódica según

$$g(y) = f' + \frac{\Delta f}{2} \sum_{l=1}^{\infty} a_l \cos\left(\frac{2\pi l}{p} y\right), \quad (2)$$

f' es la distancia focal de diseño, Δf la profundidad de foco deseada, p el periodo de la corrugación, l el orden de los coeficientes de Fourier y a_l los coeficientes de Fourier.

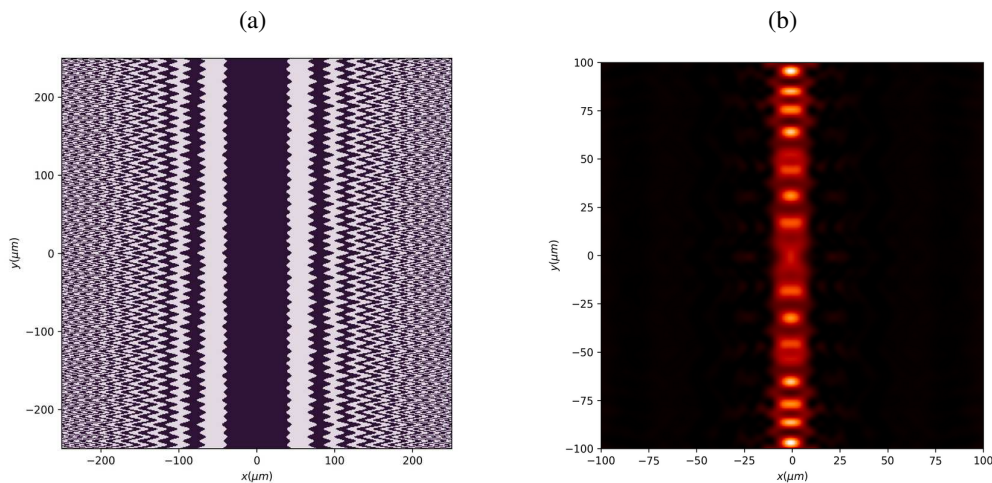


Figura 1 a) Ejemplo de lente difractiva cilíndrica con brodes que siguen una serie de Fourier, con $\lambda = 632,8$ nm, $f' = 5$ mm, $\Delta f=0,5$ mm, $p=5$ μ m, y órdenes de Fourier $l=1, \dots, 4$, $a_l = 1, 1, 0,5, 2,5$. b) Intensidad XY en el plano focal de la lente, $z=f'$.

En la Fig. 1a se muestra un ejemplo de la lente propuesta. Para definir dicha lente y determinar la distribución de intensidad alrededor del plano focal, hemos utilizado el paquete de Python, de código abierto, Diffractio [4]. En la Fig. 1b se muestra la distribución de intensidad obtenida en la zona focal f' cuando la lente es iluminada con una onda plana. En el caso mostrado, los coeficientes de Fourier de la lente propuesta no están optimizados, por lo que la distribución de intensidad en el foco (línea focal) no es del todo homogénea. Además, en la Fig. 2 se muestra la distribución de intensidad XZ para $y=0$ y para un rango en z alrededor del foco. La Fig. 2a muestra el foco para una lente cilíndrica convencional con la distancia focal de diseño y la Fig. 2b muestra la intensidad correspondiente para la lente de la Fig. 1b. Se observa una fuerte elongación del foco, a costa de un ligero ensanchamiento. En este caso, la distribución de intensidad alrededor del foco no es uniforme, y aparece cierta luz espuria. Para obtener una distribución de luz más uniforme y estrecha alrededor del foco los coeficientes de Fourier se pueden optimizar mediante el algoritmo Particle Swarm Optimization [5].

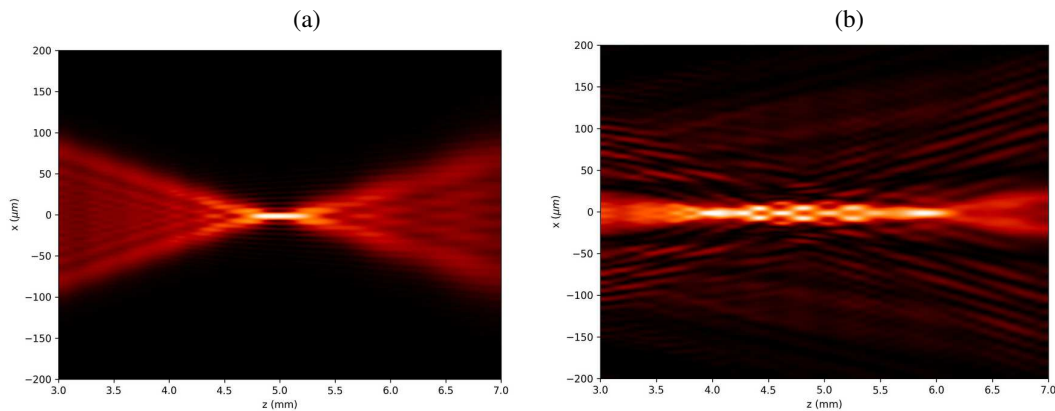


Figura 2 Distribución de intensidad alrededor de la zona focal $z = f'$ para (a) lente cilíndrica binaria convencional, (b) lente de Fourier de la Fig. 1b.

3. Conclusiones

En este trabajo demostramos que la lente cilíndrica basada en series de Fourier permite producir una línea focal con profundidad de foco extendida alrededor de la distancia focal de diseño.

Agradecimientos

Este trabajo ha sido financiado por el proyecto “VDOEST” PID2022-138071OB-I00, del MCIN/AEI/10.13039/501100011033/FEDER, EU. Angela Soria-Garcia también agradece la financiación de una beca predoctoral de la Universidad Complutense de Madrid y el Banco Santander.

Referencias

- [1] A. Soria-Garcia, et al. “Fourier series diffractive lens with extended depth of focus”, *Opt. Laser Tech.* **164**, 109491 (2023).
- [2] M.A. Nanavaty, “Evolving generation of new Extended Depth of Focus intraocular lenses,” *Eye* **2024**, 1-3 (2024).
- [3] J. Liu, *et al.*, “Spectrum-integral Talbot effect for UV photolithography with extended DOF,” *IEEE Photon. Technol. Lett.* **27**, 2201-2204 (2015).
- [4] L.M. Sanchez-Brea et al, “Diffractio: an open-source library for diffraction and interference calculations” *Proc. SPIE. Strasbourg (France) 2024.* <https://pypi.org/project/diffractio/>.
- [5] L.J.V. Miranda, “PySwarms: A research toolkit for particle swarm optimization in Python”, *J. Open Source Softw.* **3**(21) 433 (2018).

Py_pol + Diffractio: herramienta numérica para el estudio vectorial de la propagación de la luz

Jesús del Hoyo^{1*}, Luis Miguel Sanchez-Brea¹, Angela Soria-García¹,
Joaquin Andres-Porras¹, Mahmoud H. Elshorbagy^{2,3}, Veronica Pastor-Villarrubia²,
Javier Alda², Francisco Jose Torcal-Milla⁴

¹*Applied Optics Complutense, Optics Department, Faculty of Physics, Universidad Complutense de Madrid, Plaza de las Ciencias, 1, 28040 Madrid, Spain.*

²*Applied Optics Complutense, Optics Department, Faculty of Optics and Optometry, Universidad Complutense de Madrid, C/ Arcos de Jalón 118, 28037 Madrid, Spain.*

³*Physics Department, Faculty of Science, Minia University, El Minia, 61519 Egypt.*

⁴*Grupo de Tecnologías Ópticas Láser. Instituto de Investigación en Ingeniería de Aragón (I3A), Departamento de Física Aplicada, Universidad de Zaragoza, Zaragoza (España)*

*E-mail: jhoyo@ucm.es

Diffractio [1] es una librería Python de código abierto diseñada para la óptica difractiva e interferencial. En un primer momento se desarrolló con un enfoque escalar, con diversos algoritmos de propagación plano a plano, tales como la aproximación de campo lejano (FFT) y de campo cercano: Rayleigh-Sommerfeld (RS), Chirped Z-transform (CZT), y paso a paso: Beam Propagation Method (BPM) y Wave Propagation Method (WPM). Posteriormente, Diffractio se amplió para incluir capacidades vectoriales, abordando la propagación vectorial y el análisis de polarización mediante diversos métodos: Transformada rápida de Fourier vectorial (VFFT) [2], Vector Rayleigh-Sommerfeld (VRS) [3], Vector Chirped Z-Transform (VCZT) [4], y Fast Polarized Wave Propagation Method (FPWPM) [5]. Además, estos algoritmos son adaptables a varias dimensiones: X, XY, XZ y XYZ, lo que garantiza un cálculo rápido con requisitos de almacenamiento mínimos.

Diffractio también incluye módulos para la generación de máscaras y fuentes de luz. Por ello, la librería está estructurada en torno a tres módulos principales: El módulo **Fields** que incluye los algoritmos de propagación, el análisis y almacenamiento de datos y la visualización. El módulo **Sources** incluye las fuentes de luz, mientras que el módulo **Masks** comprende máscaras de amplitud y fase, elementos ópticos, y elementos ópticos difractivos. Este conjunto de funcionalidades hace a Diffractio una herramienta para la simulación óptica en docencia, ciencia e ingeniería. Para el caso vectorial, las máscaras incluyen elementos polarizadores dependientes de la posición, definidos a través de matrices de Jones:

$$\mathbf{J}(x, y) = \begin{bmatrix} J_{00}(x, y) & J_{01}(x, y) \\ J_{10}(x, y) & J_{11}(x, y) \end{bmatrix}. \quad (1)$$

Para ello, Diffractio funciona de forma conjunta con nuestro paquete de código abierto Py-Pol [6] que permite la realización de cálculos de polarización tanto en el formalismo de Jones como en el de Stokes-Mueller. [7]. Py_pol contiene cuatro módulos principales: **Jones_vector**, **Jones_matrix**, **Stokes** y **Mueller** para representar los diferentes elementos ópticos (Jones_matrix y Mueller) y ondas electromagnéticas (Jones_vector y Stokes). Permite pasar fácilmente de un formalismo a otro. Incorpora métodos de cálculo de parámetros como, por ejemplo, el acimut, ángulo de elipticidad, grado de despolarización (ondas), o retardancia, polarizancia, cálculo de autoestados (elementos ópticos). Tiene métodos para hacer comprobaciones como, por ejemplo, determinar si un elemento óptico es un retardador o puede despolarizar. También incorpora algoritmos más complejos, como el filtrado de errores para obtener vectores y matrices físicamente realizables. Adicionalmente, incorpora herramientas de representación de elipses de polarización y estados en la esfera de Poincaré. Finalmente, todos los objetos pueden ser multidimensionales, para incorporar en un mismo objeto información espacial (que permite la combinación con Diffractio), temporal o espectral. De esa manera, se reducen los requisitos computacionales para realizar cálculos complejos.

Una vez ejecutada la propagación de los haces vectoriales a través de máscaras (escalares o vectoriales) con Diffractio, el campo final se puede estudiar con Py-pol, ya que admite el análisis de los diversos parámetros vectoriales (retardancia, polarizancia, depolarización, cálculo de acimuts, etc.). En la Figura 1

se muestra un ejemplo de propagación vectorial de un haz de Gauss con polarización en espiral que atraviesa una lente de Fresnel polarizada (niveles binarios definidos como polarizador lineal horizontal y vertical respectivamente) con astigmatismo (focales de la lente: 20 y 21 mm, respectivamente). La fuente y la máscara están definidas a través de sus propiedades polarimétricas (vectores y matrices de Jones XY) mientras que la propagación se realiza mediante el algoritmo VRS [3].

La librería *Diffractio* está disponible en los repositorios Python Package Index (PyPI) y Github, en <https://pypi.org/project/diffractio/> y <https://github.com/optbrea/diffractio>, respectivamente. Además, hay disponible una completa documentación en línea, <https://diffractio.readthedocs.io/en/latest/>, que ilustra el funcionamiento de la biblioteca y su aplicación práctica en óptica física con numerosos ejemplos. De igual forma, la librería *Py-pol* está disponible en los repositorios Python Package Index (PyPI) y Bitbucket, en <https://pypi.org/project/py-pol/> y https://bitbucket.org/optbrea/py_pol/src/master/, respectivamente. La documentación en línea se encuentra en <https://py-pol.readthedocs.io/en/master/>.

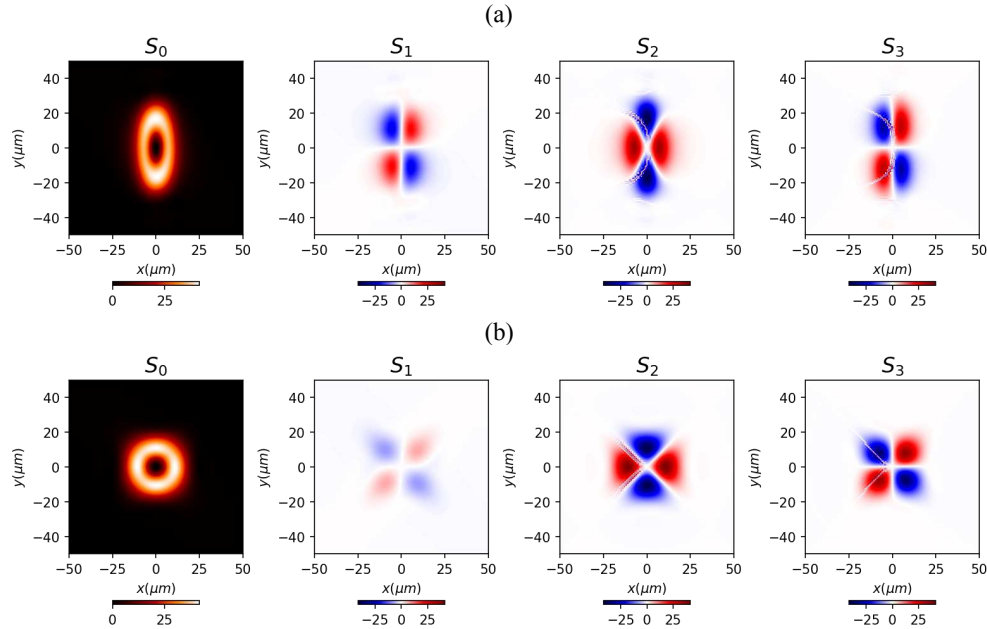


Figura 1 Ejemplo de haz de Gauss con polarización en espiral que atraviesa una lente de Fresnel polarizada con astigmatismo y se propaga mediante el algoritmo VRS. (a) Parámetros de Stokes del haz en el primer foco. (b) Parámetros de Stokes del haz en el plano de mínima confusión.

Agradecimientos

Este trabajo ha sido financiado por el proyecto “VDOEST” PID2022-138071OB-I00, del MCIN/AEI/10.13039/501100011033/FEDER, EU. Angela Soria-Garcia también agradece la financiación de una beca predoctoral de la Universidad Complutense de Madrid y el Banco Santander.

Referencias

- [1] L.M. Sanchez-Brea et al, “Diffractio: an open-source library for diffraction and interference calculations” Proc. SPIE. Strasbourg (France) 2024.
- [2] Jahn, K. and Bokor, N., “Intensity control of the focal spot by vectorial beam shaping,” Optics Communications 283(24), 4859–4865 (2010). 2.3
- [3] Ye, H., et al., “Creation of a longitudinally polarized subwavelength hotspot with an ultra-thin planar lens: Vectorial Rayleigh-Sommerfeld method,” Laser Physics Letters 10(6) (2013).
- [4] Hu, Y., et al., “Efficient full-path optical calculation of scalar and vector diffraction using the Bluestein method,” Light: Science and Applications 9 (2020)
- [5] Wende, M., et al. “Fast algorithm for the simulation of 3D-printed microoptics based on the vector wave propagation method,” Optics Express 30(22), 40161 (2022).
- [6] J. del Hoyo, et al. “Open source library for polarimetric calculations “py_pol”, Proc. SPIE, Computational Optics 2021, vol. 11875, 12-20.
- [7] J.J. Gil and R. Ossikovski. “Polarized light and the Mueller matrix approach”, volume 1. CRC press, 2017.

Reconstruction-less autofocus for single-pixel microscopy.

Samuel I. Zapata-Valencia^{1*}, Heberley Tobon-Maya¹, Lindsey Willstatter¹, Stefano Bonora², Andrea Farina³, Jesus Lancis¹, Enrique Tajahuerce¹

¹ *Institute of New Imaging Technologies (INIT), Universitat Jaume I, E12071 Castelló.*

² *CNR-Institute of Photonics and Nanotechnology, via Trasea 7, 35131 Padova, Italy*

³ *Politecnico di Milano, Dipartimento di Fisica, Piazza L. da Vinci 32, 20133 Milano, Italy*

*E-mail: szapata@uji.es

Abstract

This work presents an autofocusing technique for Single-pixel Microscopy (SPM) that eliminates the need for reconstructing the complete visualized object during the focusing process and its numerical validations. In SPM, a set of structured patterns is projected over a micro-sized sample, usually codified on a digital micromirror device (DMD). The correct focusing of these over the sample plane determines the quality of the recovered image. The focusing process of the structured patterns requires an exhausting procedure for validating the sample position, usually by reconstructing the complete image in a batch, expending time and computational efforts [1,2]. This communication presents a focusing method for Hadamard-based SPM, minimizing the number of measurements required for the focusing process by projecting only those Hadamard patterns most impacted by an out-of-focus sample. A cost is utilized to determine the focus plane by implementing a gradient descent algorithm. The proposed method is validated by getting the image of an USAF test target in focus by introducing a controlled numerical phase with a focus tunable lens.

1. Single-pixel microscopy

Single-Pixel Microscopy (SPM) is a technique where a micro-sized sample is scanned through sequential projection of a demagnified set of structured patterns, usually codified on a digital micromirror device (DMD). A bucket detector collects the intensities produced by projecting those patterns over the sample, and the image is retrieved after some computational effort [3]. The most remarkable feature is that the detector does not need a pixelated structure, so it can operate where pixelated sensors are neither cheap nor fast or even, in the worst case, where array detectors are unavailable [1]. These are some reasons to choose the Hadamard basis for implementing the masks in SPM. The functions of the said basis are orthogonal with binary values of +1 or -1, thus allowing to take advantage of the full refresh rate of the DMD. Hadamard matrices are orthogonal and symmetric, so the inverse problem of image reconstruction can be performed without matrix inversion. Also, a fast digital transform is available for the Hadamard basis.

One essential point for SPI is that the Hadamard masks are properly projected onto the sample. Any mismatch between the actual patterns launched over the sample and their digital twins employed to solve the inverse problem results in the degradation of the quality of the reconstruction. It means that perfect focusing of the structured patterns to capture a clear image is mandatory. Although focusing cannot be considered a problem in applications of SPM that use visible light for imaging, this is not the case for infrared imaging. Here, the focusing process requires an exhausting procedure for validating the perfect overlapping between the masks and the sample position, usually by reconstructing the complete image in a batch, expending time and computational resources.

2. Reconstruction-less autofocus method.

In this method, the enhancement of the focusing process on SPM is achieved by reducing the number of projected patterns and avoiding the complete reconstruction of the imaged sample during the focusing process. The patterns, selected at a patch in the 25% of the highest sampled frequencies for the Hadamard basis, are projected over the sample. The corresponding intensity coefficient for each projected pattern is integrated into a bucket detector. A cost function was designed using the value of those selected Hadamard coefficients such that increasing the coefficients decreases the cost function value. A displacement between the sample and the pattern projection is introduced according to the cost function output. An iterative measuring of those coefficients using a gradient descent algorithm for minimizing the cost function is

performed without reconstructing the complete image for determining the best projection of the patterns over the sample.

3. Experimental validations.

A commercial inverted microscope was modified for the experimental validation of this method. A 4F system was introduced to project the image of the DMD into the field diaphragm of the microscope. The aperture plane of the 4F system was used to place a focus tunable lens to introduce a controlled defocus phase into the system for correcting the defocusing of the sample as is shown in Fig 1. Finally, the light reflected by the sample was collected into a bucket detector at the imaging port of the microscope.

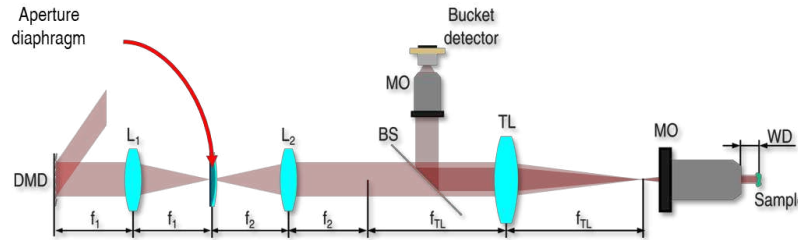


Figure 1 Single-pixel microscope setup.

The defocused USAF test target shown in Fig 2.a. was used to validate the proposed method. A 25% of the patterns of the Hadamard basis numerically projected over the sample. The gradient descent algorithm optimized the sum of the recorded intensities to determine the best focus plane after 9 iterations. A graph with the performance of the method for determining the focusing plane is shown in Fig. 2. (b). A focused USAF test target after applying the proposed method is shown in Figure 2. (c).

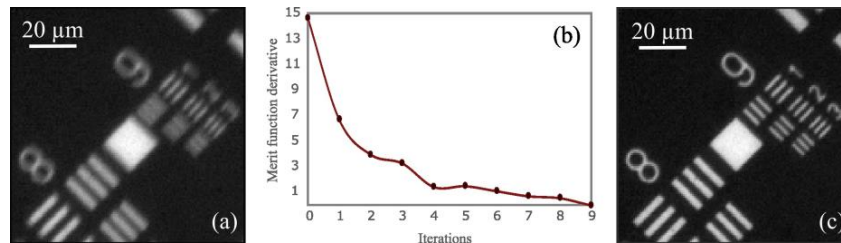


Figure 2 Experimental validation of the method. (a) Defocused image. (b) Performance for determining the best focus plane. (c) Focused image after applying the proposed method.

An autofocus technique for SPM was presented, avoiding reconstructing the image information to determine the best location of the projected patterns over the sample and reducing the number of measurements during the focusing process. In this method, the selected patterns were projected over the sample, and a bucket detector recovered their intensity twin coefficients. A cost function was built to optimize the value of the twin coefficient of each selected pattern, and an iterative gradient descent algorithm was implemented to determine the best focus location for the projected patterns over the sample without retrieving the complete image in each iteration. This technique was validated by the focusing correction of a USAF test target using 25% of the total Hadamard patterns; the samples were observed to be well-focused, indicating the effectiveness of the technique.

References

- [1] Z. Deng, S. Qi, Z. Zhang, and J. Zhong, "Autofocus Fourier single-pixel microscopy," *Opt Lett* **48**, 6076 (2023).
- [2] S. Qi, Z. Deng, P. Qi, J. Liao, Z. Zhang, G. Zheng, and J. Zhong, "Image-free active autofocusing with dual modulation and its application to Fourier single-pixel imaging," *Opt Lett* **48**, 1970 (2023).
- [3] M. F. Duarte, M. A. Davenport, D. Takbar, J. N. Laska, T. Sun, K. F. Kelly, and R. G. Baraniuk, "Single-pixel imaging via compressive sampling: Building simpler, smaller, and less-expensive digital cameras," *IEEE Signal Process Mag* **25**, 83–91 (2008).

Photon statistics and coherence properties of light sources for random illumination microscopy

Sergio Pelegrín, Jorge Carrasco, Juan M. Bueno and Enrique J. Fernandez*

*Laboratorio de Óptica, Instituto Universitario de Investigación en Óptica y Nanofísica,
Universidad de Murcia, Campus de Espinardo (Ed. 34), 30100 Murcia, Spain*

*E-mail: enriquej@um.es

1. Introduction

The semi-classical model for the detection of photons is a physical description of the interaction between light and matter in such a way that the incoming electromagnetic field is treated completely classically, while quantization is considered in the detection of the photons. The basis of photon detection statistics is given by Mandel's formula, which describes the probability of observing K photon events in a given time window [1].

The light sources exhibit different Probability Density Functions (PDFs) for the detected photons. For instance: single mode CW lasers exhibit a Poisson distribution, while thermal light sources obey to a Bose-Einstein distribution, as it is presented in Eq. 1.

$$PDF(K) = \frac{\langle K \rangle^K}{(\langle K \rangle + 1)^{K+1}}. \quad (1)$$

Because of their incoherent nature and statistical properties, thermal sources are very advantageous for many imaging techniques. An important drawback of these sources is the low number of emitted photons, particularly when they are compared with laser sources. This is critical for certain imaging techniques, for instance in multiphoton microscopy, where enormous flux of photons is required, so pulsed lasers are typically employed to illuminate the sample. A pseudo-thermal light source is an emitter whose coherence and statistical properties follows those of a thermal source, but it has been generated out of a laser. In the pseudo-thermal source the flux of photons could be significantly higher as compared with the true thermal source. In this work, different chaotic light sources are generated by manipulating pseudo-thermal emitters. Moreover, their coherence and statistical properties are characterized and modelled.

2. Methods

Figure 1 shows the experimental setup used for the characterization of the light sources. The main components were a solid-state laser (Coherent OBIS 660 LX) emitting at 660 nm, a neutral density filter to regulate the intensity, a diaphragm to reduce the beam size, and a diffuser (Thorlabs DG10-1500-A) mounted on a rotating stage.

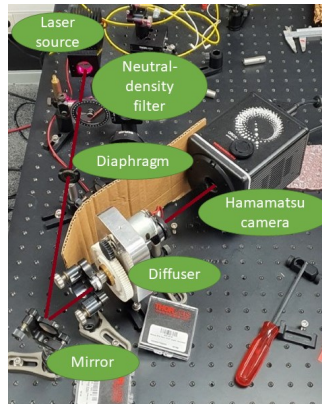


Figure 1 Experimental setup.

Sets of 100k images for each source were recorded using a camera (Orca-Quest, Hamamatsu, Japan). The camera incorporated a CMOS sensor (9.4 Mpixels) allowing individual photons to be detected in each pixel (4.6 μm lateral size). A region of interest of 128 x 128 pixels was selected on the sensor, with a

16-bit digital output, 7.2- μ s exposure time, and a sampling rate between consecutive frames of 0.5 ms. To measure the coherence properties, the second-degree spatial coherence function was experimentally obtained. Image processing and data analysis was performed using Matlab (The MathWorks, Inc, Natick, MA), with laboratory routines specifically designed for the tasks. In the experiment several sources were characterized and modelled: a CW laser a LED source and pseudo-thermal light sources generated through the use of both a combination of biprisms and an axicon.

3. Results

Figure 2 shows the experimental PDFs of photon detection (as histograms), corresponding to several light sources studied in this work together with their proposed distribution models (red lines). For the LED source, panel (a), the PDF was fitted to a Gaussian distribution, with a correlation coefficient $R^2 > 0.99$. For the generated pseudo-thermal source, panel (b), the PDF was fitted to a Bose-Einstein distribution, $R^2 > 0.99$. After manipulating the emission of the pseudo-thermal source by means of a biprism, panel (c), it was obtained that the photon statistic still followed a Bose-Einstein distribution with $R^2 > 0.99$, but the expected value was significantly higher. Replacing the biprism by an axicon, panel (d), the PDF changed to a function with even increased mean value, not following a Bose-Einstein function in this case. Several models were proposed for this last source, although the figure presents an Erlang distribution with $R^2 = 0.93$.

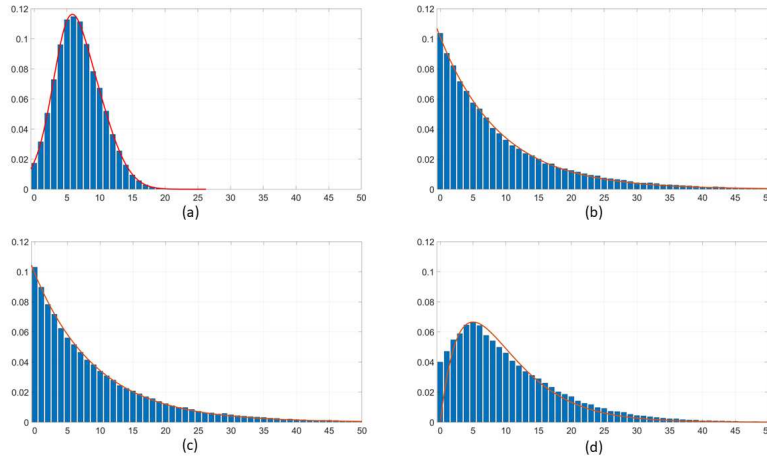


Figure 2 PDFs of photo detection events for different light sources.

The spatial second degree of coherence was obtained in any case, showing how the number of photons contained on the coherence volume could be manipulated and eventually augmented.

4. Conclusions

New light sources based on pseudo-thermal statistics have been presented by using combinations of biprisms and an axicon. An experimental characterization of such sources in terms of statistics and coherence has been accomplished, demonstrating the benefit in the number of available photons. This increase could be applied to imaging techniques suffering from low efficiency, where the need of pulsed laser is mandatory, such as multiphoton microscopy.

Acknowledgments

V. Bernardo, Hamamatsu Photonics France, is acknowledged for his valuable help with the camera employed in this study. Supported by grant PID2020-113919RBI00/AEI/10.13039/501100011033.

References

- [1] L. Mandel, "Fluctuations of Photon Beams and their Correlations," Proc. Phys. Soc. 72, 1037 (1958).
- [2] J. W. Goodman, Statistical Optics, Wiley, New York, (1985).

Measuring polarization distributions for three wavelengths simultaneously with a color polarimetric camera

Manal Altaweel¹, Irene Estévez¹, Iván Montes¹, Ángel Lizana¹, and Juan Campos^{1*}

¹ Grup d'Òptica, Departament de Física, Universitat Autònoma de Barcelona, Bellaterra, 08193, Spain

*E-mail: juan.campos@uab.cat

1. Introduction

Polarimetric color cameras represent a cutting-edge technology enabling measurement of polarization across natural scenes. Our research aims to enhance the resolution of polarization measurements at multiple discrete wavelengths simultaneously. However, a significant challenge arises from spectral overlap among the color filters, where, for instance, the green filter may partially transmit red and blue channels. To ensure accurate measurements and mitigate color cross-talk, the application of demosaicing algorithms becomes imperative [2]. Moreover, achieving improved resolution necessitates the implementation of interpolation techniques [1]. This study addresses these challenges, proposing novel strategies to enhance the capabilities of polarimetric color cameras for precise and high-resolution polarization measurement across diverse natural environments.

2. Interpolation and demosaicing results

Color polarimetric cameras feature structured superpixels, each equipped with color filters and four polarizers oriented differently. This setup enables the simultaneous sampling of both polarization orientation and color in every macro-pixel of the camera. However, achieving functions for each color and polarization across all pixels necessitates interpolation techniques. By effectively interpolating data, we ensure comprehensive coverage of polarization orientations and colors throughout the entire image, thus enhancing the resolution and fidelity of polarimetric imaging.

In this work we have studied an interpolation method based on the Fourier Transform of the captured image. Different orders appear with different phases that can be separated to obtain the values of the polarization channels. This interpolation is the optimal one for band limited functions as can be seen in Figure 1. The errors increase for non band limited functions.

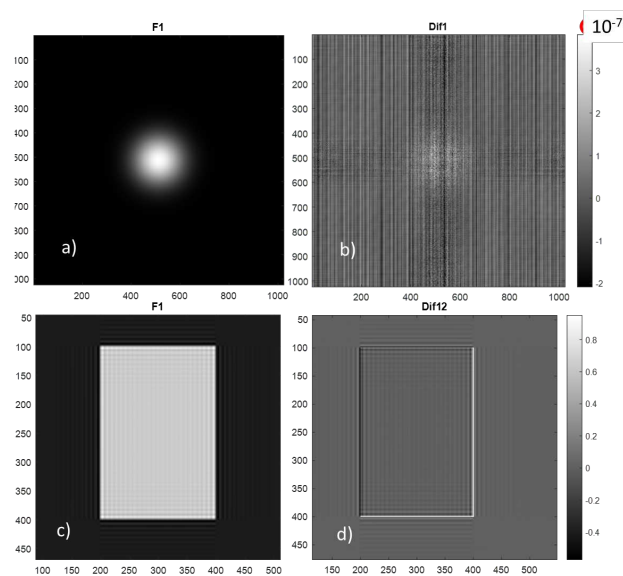


Figure 1 a) and c) reconstructed functions, b) and d) reconstruction errors. a) and b) band limited functions; c) and d) non band limited functions

We want to measure the polarization distribution for three wavelengths simultaneously (470, 554, and 630 nm), situation that, as color polarization cameras are novel technology, is not reported in literature. Each color filter has an intensity transmission different from zero for the three wavelengths, thus the color information is mixed. By measuring the filter transmissions for each wavelength, it is possible to build a linear system to separate the information for each color. As an example, in Fig. 2, the polarization retrieving for a spatially heterogeneous polarization image (linear polarization azimuthally varying, first row, and the degree of polarization radially varying, second row) is provided, for the red channel case. The reconstructed images, absolute errors and error differences between corrected and non-corrected images are provided as different columns in Fig. 2.

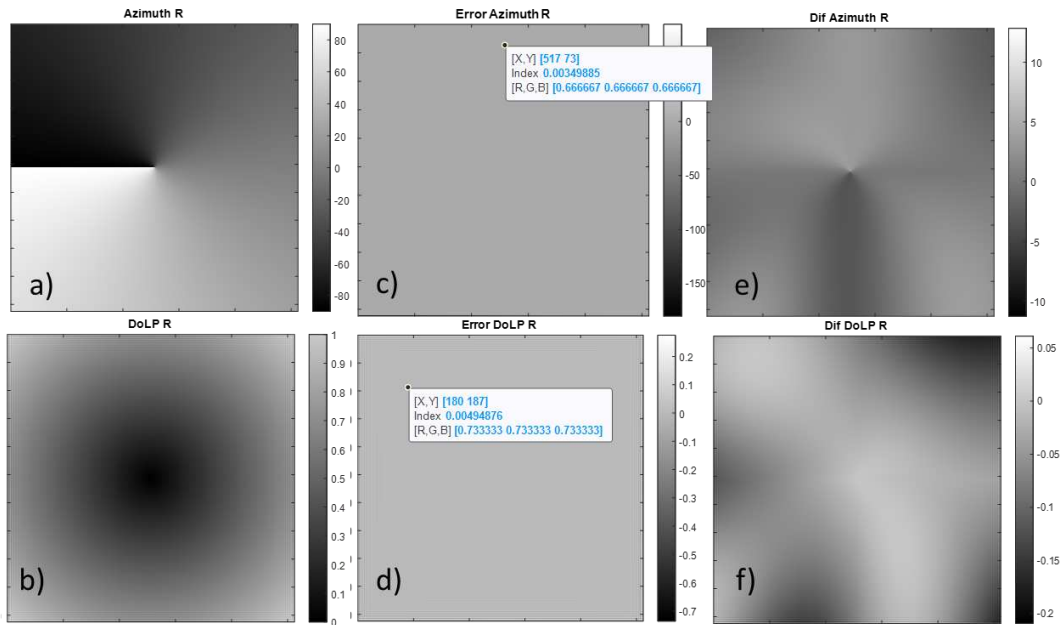


Figure 2. a) and b) reconstructed Azimuth (top) and Degree of Linear Polarization (bottom) in the red channel with the crosstalk corrected; c) and d) the corresponding errors; e) and f) differences between the reconstruction with and without cross-talk correction.

3. Conclusions

We have developed the expressions for the sampled functions when using the color polarizer sensor based on the Fourier Transform (FT) method. Each order of the FT of the sampled image is written as a linear combination of the FT of each function, and an interpolation method has been developed.

The problem of the crosstalk between the three color channels is formulated and successfully resolved as a linear equation system.

Simulation results show that the errors of the method are very low, particularly in scenarios where the functions are nearly band-limited.

Acknowledgments

We acknowledge funding support from Ministerio de Ciencia e Innovación and Fondos FEDER (PID2021-562 126509OB-C21 and PDC2022-133332-C21), Generalitat de Catalunya (2021SGR00138) and Beatriu de Pinós Fellowship (2021-BP-00206).

References

- [1].J. S Tyo., C. F LaCasse., M. Ratliff B. Opt. Lett. 34, (20) 3187–3189 (2009),
- [2].R. Dumoulin, P.J. Lapray, J.B. Thomas and I. Farup, 16th International Conference on Signal-Image Technology & Internet-Based Systems (SITIS), 275-280, (2022)

Optical quality check in afocal systems: from the workshop to the clinic.

María Pilar Urizar^{1*}, Gonzalo Guerrero¹, Lucía Martín¹, Irene Sisó-Fuertes¹,
Enrique Gamba¹ and Carlos Dorronsoro¹

¹2EyesVision, Madrid, Spain

*E-mail: purizar@2eyesvision.com

1. Introduction

SimVis Gekko is the first see-through and binocular head-mounted visual simulator of presbyopic corrections. It allows ophthalmologic patients to try on different intraocular lenses and provide feedback about the new visual experience, before surgical implantation [1, 2]. The working principle is based on the temporal multiplexing of tunable lenses (TLs) [3]. Each of the two optical modules of the SimVis Gekko projects a TL onto the pupil plane of the patient's eye, using a twisted miniaturized afocal 4-f system. Each optical module is an active afocal system that induces periodic defocus variations in optical power at 50 Hz, generating a multifocal image on the retina of the observer that is perceived as static.

During the assembly and adjustment of the active afocal systems, as well as the revision of the SimVis Gekko headset, it is essential to implement a rigorous optical quality control process to ensure a correct binocular image quality [4]. The first step is the calibration of the active TL, including dynamic effects, in combination with the afocal projection system. This allows to correctly project any optical power profile, matching the optical quality of real intraocular lens models. Additionally, it is necessary to avoid potential misalignments of the optical elements of the optical modules to prevent undesirable effects (distortion, magnification or prismatic shift) as well as incorrect stereoscopic fusion of the binocular images. At 2EyesVision, each calibration test is performed in a different dedicated optical bench.

In this work we present the development of a compact device, named SimVis Dock, an optical quality station capable of performing on site, in the ophthalmology clinics, all the quality checks needed to ensure the correct optical performance of the SimVis Gekko, and its active afocal binocular systems in particular. It combines all the optical evaluations mentioned in an automatic procedure.

2. Methods

The proposed optical quality station comprises two optical channels, each of which is composed of a display, a projection system with a motorized collimating lens, a prism at the projected image, and a camera to record the projected image of the display (Figure 1). The optical quality station performs an autocalibration and, sequentially, three different optical tests to analyze the quality of the SimVis Gekko binocular afocal system: static power check, dynamic power check and binocularity. All these tests are based on image generation and image processing and are automatically performed without the need to manipulate the quality check station or the SimVis Gekko.

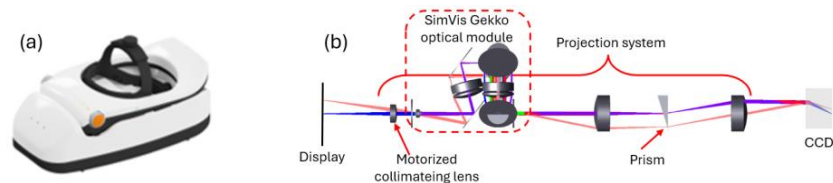


Figure 1 (a) Image of the SimVis Dock quality check station with the SimVis Gekko being tested. (b) Schematic diagram of the optical design of one optical channel of the SimVis Dock with the optical module of the SimVis Gekko on it.

The autocalibration process double-checks the alignment and the optical power adjustment of the optical quality station itself. A checkerboard image is generated at the display and imaged through the projection system of the station that axially adjusts the motorized collimating lens to define the far vision (0-Diopters) configuration. Subsequently, a near vision configuration is defined by calculating the position of the collimating lens at 3 Diopters (D).

After the autocalibration, the first quality check performed is a static power check. During this test, the afocal SimVis Gekko system is placed in the quality check station and the checkerboard stimulus is imaged for different electrical signals in the TLs of the SimVis Gekko active optical modules. This process is conducted for the two positions of the motorized collimating lens, 0 D and 3 D, thus analyzing the optical power of the TL as a function of its electrical signal. The second quality test is a dynamic power check to analyze the temporal multiplexing performance of the TL. A low-cost focimeter [6] is

implemented, whereby the axial displacement of a slit image along the optical axis of the TL when changing its optical power is transformed into a lateral displacement when the slit is observed through a prism [7], and captured in a low-cost camera. Setting the collimating lens of the station at 0 D, a generic trifocal lens is simulated with the SimVis Gekko, and the slit lateral displacements are registered with a 0.2-ms resolution. The third quality test is a binocularity check to ensure a good binocular vision experience. In this case, a crosshair is shown in the display and the position of the image through both optical channels of the SimVis Gekko are compared.

3. Results

All the calibration processes performed by the quality check station were carried out in two different sets of SimVis Gekko units. In the first set, all units had passed all the quality checks in all the dedicated production quality check optical benches. In the second set, the units were misaligned or had failed the binocularity and optical quality tests.

The static power check at the quality check station was measured for each SimVis Gekko units 25 times at different days and times. The results were in good agreement with the baseline data from the production bench with a variability of 0.3 D in both SimVis Gekko units, slightly bigger than the manufacturing tolerance. The analysis of the data showed that the variation of the TL temperature among the tests was affecting the variability of these results. Future developments will incorporate recent research results on this topic [7] and will enable the monitorization and compensation of the temperature effects on the optical power performance of the TL. The results of the dynamic power check at the quality check station were also in good agreement with the ideal simulation of a trifocal lens. The optical power measured at each foci presented a slight variability (± 0.2 D), due to temperature changes, again, and to instabilities in the image processing algorithm, now solved. The fast temporal steps of 6 ms at each foci of the trifocal lens simulated were also well reconstructed. The first results of the binocularity test at the quality check station presented a significant difference with respect to the production bench result.

The alignment requirements between the optical modules of the SimVis Gekko and the optical channels of the quality check station was critical, requiring careful positioning and preventing from having quick and easy tests. Magnetic sensors did not provide enough positioning accuracy. In the future, the relative alignment of both optical systems will be redesigned to increase positioning tolerance.

The results obtained with the optical quality station (misalignments or miscalibrations) were comparable with the results obtained from the dedicated optical benches used in the production line.

4. Conclusions

We presented a unique compact optical quality station (SimVis Dock) for an active afocal binocular system (SimVis Gekko). The station can perform, in ophthalmology clinics, three important quality checks to ensure a good performance of the optical modules of the SimVis Gekko (tunable lens calibration and dynamic behavior, and binocular alignment). We compared the results of the optical quality check station with the baseline data from the quality production benches, showing good agreement between them, although the binocularity test still needs to be improved.

Acknowledgments

Ministerio de Ciencia e Innovación, Ayudas a proyectos de colaboración publico-privada (CPP2021-008388) to CD; Torres Quevedo (PTQ2021-011963) to ISF.

References

- [1] Vinas, M., Aissati, S., Romero, M., Benedi-Garcia, C., Garzon, N., Poyales, F., ... & Marcos, S. (2019). Pre-operative simulation of post-operative multifocal vision. *Biomedical optics express*.
- [2] Barcala, X., Zaytouny, A., Rego-Lorca, D., Sanchez-Quiros, J., Sanchez-Jean, R., Martinez-de-la-Casa, J. M., & Marcos, S. (2023). Visual simulations of presbyopic corrections through cataract opacification. *Journal of Cataract & Refractive Surgery*.
- [3] Dorronsoro, C., Radhakrishnan, A., Alonso-Sanz, J. R., Pascual, D., Velasco-Ocana, M., Perez-Merino, P., & Marcos, S. (2016). Portable simultaneous vision device to simulate multifocal corrections. *Optica*
- [4] Barcala, X., Gamba, E., Sawides, L., Martinez-Ibarburu, I., Rodriguez-Lopez, V., & Dorronsoro, C. (2021, September). Optical quality evaluation for active afocal systems. *Optical Design and Engineering VIII*. SPIE.
- [5] Dorronsoro, C., Barcala X., Gamba, E., Akondi V., Sawides, L., Marrakchi Y., Rodriguez-Lopez, et al. (2019). Tunable lenses: dynamic characterization and fine-tuned control for high-speed applications. *Optics Express*
- [6] Lopez-De-Haro, A., Barcala X., Martinez-Ibarburu I. Marrakchi Y., Gamba, E., Rodriguez-Lopez, V., Sawides, L. & Dorronsoro C. (2022, September). Closed-loop experimental optimization of tunable lenses. *Applied Optics*.
- [7] Marrakchi, Y., Barcala X., Gamba, E., Martinez-Ibarburu I., Dorronsoro C & Sawides, L. (2023,). Experimental characterization, modelling and compensation of temperature effects in optotunable lenses. *Scientific Reports*

Herramientas de inteligencia artificial generativa aplicadas a la docencia en Fotónica

Gemma Piquero*, Óscar Martínez-Matos, Javier Hernández-Rueda
y Laura Martínez Maestro

Departamento de Óptica, Facultad de Ciencias Físicas, UCM, Madrid

**E-mail: piquero@ucm.es*

En la actualidad, las nuevas herramientas de Inteligencia Artificial Generativas (IAg), como ChatGPT, son un reto en el contexto docente, pero a la vez una oportunidad tanto para el profesorado como para el estudiantado, que pueden sacar máximo provecho de ellas. El lanzamiento de ChatGPT el 30 de noviembre de 2022 ha revolucionado el mundo de la educación, acelerando una nueva ola de innovación [1]. Varios estudios muestran que los estudiantes de ciencias, ingeniería, matemáticas y ciencias naturales utilizan con frecuencia herramientas basadas en inteligencia artificial [2].

En este trabajo se presentan resultados preliminares de un Proyecto de Innovación Educativa cuyos objetivos son el análisis y validación del uso de este tipo de herramientas de IAg en la asignatura de “Fotónica”, de cuarto curso del Grado en Física en la UCM. La actividad propuesta en este proyecto se ha llevado a cabo de manera preliminar en el curso 2023/24 con los estudiantes matriculados en la asignatura Fotónica del Grado en Física. Esta experiencia previa, pero mejorada y ampliada, se extenderá al curso 2024/25. En esta contribución se presentan los resultados más relevantes.

La actividad realizada se centra en el uso de ChatGPT en una de las tareas englobadas dentro de la evaluación continua de la asignatura de Fotónica. Más concretamente, se propone a los estudiantes utilizar ChatGPT de forma crítica para realizar un trabajo sobre las aplicaciones de fotodetectores en diversas áreas de la ciencia. Los trabajos se realizan en grupos de 4-5 estudiantes que eligen un área concreta de aplicación de los fotodetectores. Todos los trabajos de los integrantes del mismo grupo versan sobre el mismo tema pero cada miembro del grupo utiliza diferentes “prompts” (instrucciones suministradas o diálogos mantenidos con ChatGPT). Esta actividad de evaluación continua, enfocada de esta forma, permite al estudiantado por un lado profundizar en el contenido de la materia, y por otro lado incentiva su actitud crítica en relación al uso de las IAg, ya que deben analizar todos los trabajos de su grupo y compararlos. Esta actividad contribuirá a una mejora en la obtención de las competencias detalladas en el plan de estudios de la asignatura, como por ejemplo: “Trabajo en equipo”, “Conocimientos de informática relativos al ámbito de estudio”, “Razonamiento crítico”, “Capacidad de gestión de la información”, etc.

Además de los trabajos sobre el tema de fotodetectores, se ha realizado una encuesta a los estudiantes de la asignatura de Fotónica sobre la utilización de ChatGPT, obteniéndose conclusiones muy interesantes. Por ejemplo, destaca que ya usan habitualmente ChatGPT, que fundamentalmente suelen usar esta herramienta para programar o que buscan la información en Wikipedia para comparar y no en bases de datos más fiables.

El interés de la propuesta radica en que promueve el desarrollo de competencias digitales entre los estudiantes con un enfoque en la actitud crítica ante la información obtenida de ellas. Estas competencias son fundamentales en el contexto actual, donde la tecnología desempeña un papel cada vez más importante en la educación y en el mercado laboral. Aunque se ha aplicado de forma concreta en la asignatura de Fotónica, se puede extender a otras asignaturas del Grado en Física, a otros Grados e incluso a la enseñanza en Secundaria y Bachillerato.

Agradecimientos

Los autores agradecen a los estudiantes matriculados durante este curso en la asignatura de “Fotónica”, de cuarto curso del Grado en Física en la UCM, su participación en esta propuesta.

Referencias

[1] E Koh and S Doroudi, (Taylor & Francis, 2023), Vol. 9, pp. 109.

[2] J von Garrel and J Mayer, Humanities and Social Sciences Communications 10 (1), 799 (2023).

Prácticas de Óptica Física expuestas en Reels

Julián Espinosa^{1,2*}, Carmen Vázquez^{1,2}, David Mas^{1,2}, Aurora Larrosa¹, Elisabet Chorro³, Esther Perales^{1,2}, Jorge Pérez^{1,2}, Consuelo Hernández^{1,2}, Begoña Domenech^{1,2}, Néstor Tejedor¹

¹*Departamento de Óptica, Farmacología y Anatomía,*

²*IUFACyT, Universidad de Alicante, Carretera de San Vicente del Raspeig, s/n. San Vicente del Raspeig - Alicante*

³*Departamento de Tecnologías de la Información y la Comunicación aplicadas a la Educación, UNIR, Avenida de la Paz 137, Logroño - La Rioja*

*E-mail: julian.espinosa@ua.es

1. Introducción

Las redes sociales en Internet sirven como canales de comunicación, fuentes de información y medios de entretenimiento. Esto, unido a su popularidad entre los jóvenes, supone una oportunidad para aprovechar su influencia y mejorar la enseñanza universitaria [1]. Entre las actividades exigidas en los Grados científicos, las prácticas de laboratorio desempeñan un papel fundamental al cultivar habilidades técnicas, fomentar el pensamiento crítico, promover la resolución de problemas y desarrollar el trabajo en equipo. Normalmente, la evaluación de estas actividades se realiza sobre informes escritos o exposiciones orales en las que los estudiantes plasman sus resultados y conclusiones, aunque a menudo deriva en una inclinación hacia la mera presentación formal de datos y descuida otros aspectos. En este contexto, se plantea la exploración del uso de videos cortos, específicamente a través de la función Reels de la red social Instagram, para presentar las prácticas de laboratorio, de forma que se ponga un mayor énfasis en la aplicación práctica de los conocimientos adquiridos, así como en su análisis y presentación.

2. Método

Se ha propuesto la exposición de 6 prácticas de laboratorio de Óptica Física mediante Reels de Instagram a estudiantes de 3º del Grado de Física de la Universidad de Alicante, agrupados en parejas. A cada pareja se le ha asignado una práctica sobre la que debían realizar un video corto de 90 segundos y publicarlo como Reel en Instagram. Esos videos se han republicado en la cuenta del laboratorio @laboratoriodeopticafisica [2]. La evaluación del Reel se plantea de forma que el 50% consiste en la valoración del profesorado atendiendo al contenido y presentación, y el resto depende de las estadísticas sociales obtenidas en un periodo de 15 días. Los Reels republicados se han clasificado en tres terciles atendiendo a dichas métricas y se puntúan según su posición. Además, se ha encuestado la opinión al alumnado para valorar su satisfacción con la actividad, el grado de colaboración y participación y el nivel y eficacia del aprendizaje percibido.

3. Resultados y discusión

La figura 1 muestra los resultados de las encuestas de opinión con escala Likert sobre diferentes aspectos. En general, están satisfechos con la experiencia (61%). Un 53% considera que sirve para entender mejor los conceptos y recordar más detalles (62%). Además, el 88% valorara positivamente el aporte a su aprendizaje de los Reels de los compañeros. Destaca que la mayoría de los estudiantes (79%) no considera que realizar el Reel les haya supuesto un mayor esfuerzo que una exposición tradicional, y el 94% afirma que no ha empleado demasiado tiempo en visionar los de otros. Sin embargo, no hay una gran diferencia respecto a la opinión sobre extender o no esta experiencia a otras asignaturas (53% a favor vs. 47% en contra). Por último, muestran una disposición a favor del trabajo en grupo, considerando un 67% que aprenden más y mostrando conformidad con el reparto de trabajo un 92%.

Se han contabilizado como métricas sociales el número de reproducciones y de “me gusta” de cada Reel. En la figura 2 se representan los resultados de estas métricas para cada uno de los usuarios y para el Reel que explica a los estudiantes la propuesta de exposición de prácticas publicado en nuestra cuenta (LAB). La clasificación en terciles viene delimitada por 390 y 457 en cuanto al número de reproducciones y por 14 y 17 respecto al número de “me gusta”. Destacan 4 Reels muy por encima de los umbrales de

primer tercil (>900 reproducciones y >80 “me gusta”).



Figura 1. Resultados de la encuesta con escala Likert de opinión (1: Completamente en desacuerdo o insatisfecho. 4: Completamente de acuerdo o muy satisfecho)

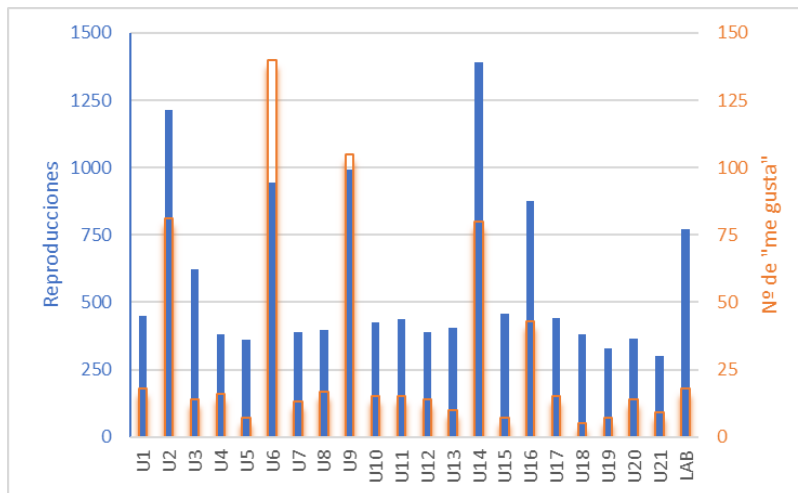


Figura 2. Métricas sociales (reproducciones en azul y número de “me gusta” en naranja) de los Reels publicados por los estudiantes (usuarios U1 a U21). El usuario LAB indica las métricas del Reel del usuario @laboratoriodeoptica fisica explicando la propuesta.

4. Conclusiones

Este trabajo constituye una innovación en la enseñanza de las prácticas de laboratorio al incorporar el uso de redes sociales, lo que amplía la participación, estimula el desarrollo de habilidades de comunicación científica y permite una evaluación integral del proceso de aprendizaje. No obstante, es esencial continuar refinando esta metodología para asegurar su eficacia y la equidad en la evaluación.

Agradecimientos

Programa de Redes de investigación en docencia universitaria 2023. Código 5938. Universidad de Alicante.

Referencias

- [1] Irwandani et al., “Effectiveness of Physics Learning Media Course assisted by Instagram on Student’s Creative Thinking Skill,” in *Journal of Physics: Conf. Series* (2020), vol 1467, 012006.
- [2] @laboratoriodeoptica fisica. Instagram, 30 Abril, 2024, <https://is.gd/lz8vwD>

Actividades de divulgación científica del Grupo de Investigación de Óptica de Castellón (GROC·UJI)

Francis Cortes, Sergio Fernández, Erick Ipus, Armin Lenz, Luis Ordoñez, Mitzi Ordoñez, Heberley Tobón, Samuel Zapata, Carlos Doñate, Vicente Durán, Daniel Torrent, Omel Mendoza, Lluís Martínez*, Gladys Mínguez, Enrique Tajahuerce, Jesús Lancis, Vicent Climent

Departament de Física – Instituto de Nuevas Tecnologías de la Imagen (INIT), Universitat Jaume I, Castelló de la Plana, España

*E-mail: lluis.matinez@uji.es

1. Divulgación científica

La comunicación y difusión de los resultados de investigación, y la divulgación de la ciencia y el conocimiento en general, es hoy en día una más de las tareas del personal investigador. La Unión Europea, en su apuesta por la ciencia por y para la sociedad, anima a establecer canales de información y diálogo entre las investigadoras e investigadores y el resto de la sociedad, para alcanzar una comunicación activa y participativa entre la comunidad científica y la ciudadanía. Con la mirada puesta en este objetivo, presentamos en esta comunicación las actividades de divulgación científica del Grupo de Investigación de Óptica de Castelló (Grup de Recerca d'Òptica de Castelló, GROC·UJI), de la Universitat Jaume I, que cuentan con el protagonismo principal de los doctorandos y las doctorandas del grupo, miembros de los Student Chapters de SPIE y OPTICA del GROC·UJI (Optics Castelló, OCAS).

2. Programa anual de actividades de divulgación científica.

Cada año, el GROC·UJI participa en diferentes actividades de divulgación, muchas de ellas parte del programa anual de la Unidad de Divulgación Científica y Ciencia Ciudadana del Vicerrectorado de Innovación, Transferencia y divulgación Científica de la Universitat Jaume I.

Las actividades del Día Internacional de la Niña y la Mujer en la Ciencia (semana del 11 de febrero), con actividades como charlas y talleres por parte de investigadoras del grupo en centros educativos de Castelló y su entorno, pretenden visibilizar el papel de la mujer en la ciencia, trabajar por la igualdad de oportunidades rompiendo la brecha de género, fomentar las vocaciones científicas en niñas y jóvenes, y concienciar de la importancia de la perspectiva de género en la investigación [1].

Firujiciència es la feria de la ciencia de la Universitat Jaume I, donde estudiantado de todos los niveles preuniversitarios (desde Infantil a Bachillerato), universitarios (de Grado a Máster), y personal investigador (en formación y senior) realiza talleres y demostraciones de ciencia para todo el público asistente. Es una muy atractiva oportunidad de divulgación a todo tipo de público, con un foco muy importante en estudiantado de Infantil, Primaria y Secundaria. El GROC·UJI participa con talleres que suelen mostrar las principales propiedades de la luz a través de una serie de experiencias prácticas sobre polarización, difracción, color, fluorescencia, refracción, etc [2].

El Día Internacional de la Luz, y las actividades programadas alrededor de la conmemoración del 16 de mayo, suponen otra de las actividades principales de divulgación del grupo. En 2023, estaba impulsada también por el Departamento de Sistemas Industriales y Diseño, por la Escuela Superior de Tecnología y Ciencias Experimentales, por el Instituto de Nuevas Tecnologías de la Imagen (INIT), y se contó con las conferencias «Contaminación lumínica: ¿por qué la llamamos contaminación?», impartida por el investigador Salvador X. Bará (Universidade de Santiago de Compostela), y «Cartografía nocturna (la contaminación lumínica vista desde el cielo)», impartida por el investigador Alejandro Sánchez de Miguel (Universidad Complutense de Madrid) [3]. Además, posteriormente, como otros años, se realizaron demostraciones experimentales de óptica para poner de manifiesto la naturaleza y propiedades de la luz. Cada año se convoca el Concurso de Fotografía Digital «Día Internacional de la Luz», sobre fenómenos ópticos. En 2024, la Universitat Jaume I se convierte en la sede de referencia a nivel estatal de la celebración del Día Internacional de la Luz, y además de conferencias, demostraciones, y el concurso de fotografía, el programa [4] incluye una carrera y un taller de cianotipia, en el marco del Festival de Fotografía Imaginaria, y un par de charlas en el marco de la iniciativa ciudadana Pint of Science.



Figura 1 Demostraciones de óptica en SCIENCE GTS 2023

La Noche Europea de las Investigadoras e Investigadores se celebra el último viernes de septiembre, con el objetivo de acercar la ciencia a la ciudadanía mediante múltiples actividades dirigidas a personas de todas las edades. En 2023, la Universitat Jaume I se sumó a varias universidades y entidades en la Noche Europea de las Investigadoras e Investigadores, dentro del consorcio SCIENCE GTS. Los talleres del GROC·UJI en la Noche Europea ponen de manifiesto que la luz se utiliza en el día a día en muchas de nuestras actividades cotidianas. Con el taller, se pudo descubrir diferentes aspectos y fenómenos relacionados con la óptica, y entender el funcionamiento de dispositivos que están al alcance de todos [5].

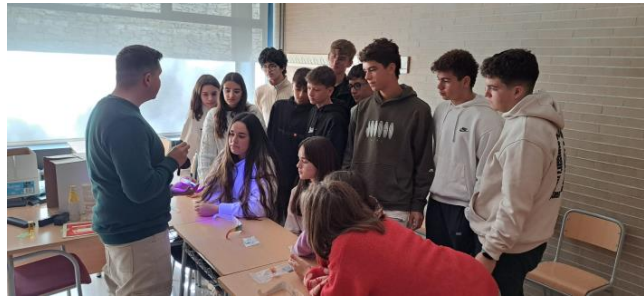


Figura 2 Programa «Conecta con la Ciencia»

Cada otoño, el programa «Conecta con la Ciencia» desarrolla talleres científicos y charlas en las Sedes de la Universidad en el territorio, dirigidos al estudiantado de Secundaria. El taller de Óptica pretende acercar la ciencia a los más jóvenes, demostrando distintas propiedades físicas, conceptos relacionados con la óptica y explicar el funcionamiento del ojo humano.

Además de estas cinco citas del calendario anual de divulgación, el Student Chapter OCAS también organiza otras actividades, como en febrero de 2023 el evento de divulgación científica «A la llum de València», desarrollado conjuntamente con los capítulos de estudiantes Photonets UV (Universitat de València) y Physics League (Universidad de Valladolid), además de la participación del Instituto de Física Corpuscular de Valencia, con un espectáculo de teatro interactivo abierto al público en general y una feria científica en el Jardín Botánico de la Universitat de València, con diversas demostraciones presentadas por miembros de los distintos capítulos estudiantiles.

3. Conclusiones

El GROC·UJI participa cada año en diferentes actividades de divulgación, con el impulso de su Student Chapter de SPIE y OPTICA (OCAS), para divulgar la ciencia y el conocimiento en el entorno de la Universitat Jaume I

Referencias

- [1] <https://www.uji.es/investigacio/base/cultura-cientifica/pc4/acc-divulga/11-feb/base/actual>
- [2] <http://www.firujciencia.uji.es>
- [3] <https://www.uji.es/com/investigacio/arxiu/noticies/2023/5/dia-internacional-llum/>
- [4] <https://www.uji.es/investigacio/base/cultura-cientifica/pc4/base/dil/>
- [5] <https://www.uji.es/com/investigacio/arxiu/noticies/2023/9/science-gts/>

Galileo and Saturn's rings in the lab: an experience for undergraduates and Master's students

Antonio Marzoa^{1,2*} and Santiago Vallmitjana³

¹*Department of Precision Engineering, SENER Aeroespacial, S.A., C/ Creu Casas i Sicart, 86-87, 08290, Cerdanyola del Vallès, Barcelona, Spain*

²*Department de Física, Universitat Politècnica de Catalunya, C/ d'Esteve Terradas, 7, 088660, Castelldefels, Barcelona, Spain*

³*Departament de Física Aplicada, Universitat de Barcelona, C/ de Martí i Franqués, 1-11, 08028, Barcelona, Spain*

*E-mail: antonio.marzoa@upc.edu

1. Introduction

In many General Optics courses, the study of Geometrical Optics and optical instruments is carried out from a purely theoretical and problem-solving approximation, and aberrations and resolution are subjects that are treated solely from a theoretical point-of-view, with few practical or realistic examples. In addition, when undergraduates and master students deal with optical instruments in the laboratory usually there is not enough time (or there is a lack of material) to perform a deeper analysis in the real problems that arise when designing a real instrument, particularly when dealing with topics such as resolution and magnification, that sometimes are misunderstood by the students.

Additionally, when introducing concepts and discoveries in theoretical classes, a quite common tool is to use historical examples are used to illustrate the development of such concept of a particular research field. However, sometimes this historical example is used just as an anecdote, and it is not addressed in its own historical context.

For those reasons, several academic years ago and in the framework of the Photonics Master's degree, a workshop to introduce details of aberrations, resolution and magnification in optical telescopes was developed [1], [2].

As an example on how to improve the introduction of historical examples in class, the case of Saturn's rings observations by Galileo Galilei [3], [4] is used in combination with the experimental workshop above-described [2]. This communication describes the workshop and presents the results of the experience obtained by the students during different courses.

2. Galileo and Saturn

In 1610, Galileo Galilei (1564 - 1642) reported the early observations of Saturn's rings [3]. However, he did not get to the correct explanation on what was what he was observing around the planet, and he noted that Saturn presented some "ears" or star companions.

It was not until March 1655, when the young Dutch astronomer, Christiaan Huygens (1629–1695), used his telescope [5], which presented better optical quality than Galileo's and was able to magnify the image of distant objects up to 50 times, that the mystery of Saturn's "ears" was solved: the planet presented rings that encircle its equator, and depending on the relative position of the rings plane and the Earth, the rings were clearer.

The limitations that Galileo found with his instruments prevented him from correctly understanding his discovery. This is a clear example of how the limitations of scientific instruments dictate the advance of Science in any era, and was used in the workshop to both motivate the students and to discuss with them the details of Galileo's discovery.

3. Description of the laboratory practice

In the laboratory workshop described in this communication, students first design a telescope that they will later build in an optical bench. The telescope must have the same characteristics of Galileo's, which are giving to them as input data. To do the design, they use a ray-tracing Java application from the JavaOptics Course [6] from the University of Barcelona.

In parallel to this simulation, students are introduced to Galileo's pioneering observations, and they must compare their design with Galileo's (recreating his design in the Java application). Additionally,

they are encouraged to perform a simulation of the images produced by Galileo's telescope by programming their own code in MATLAB® or Python, or by using defocusing and blurring filters with commercial photography programs such as Photoshop® on a reference image of Saturn.

After that, students move to the optical bench and build a telescope similar to Galileo's (see Figure 1). Finally, they use their system to observe a reference image of Saturn placed at a certain distance from them (see Figure 1).

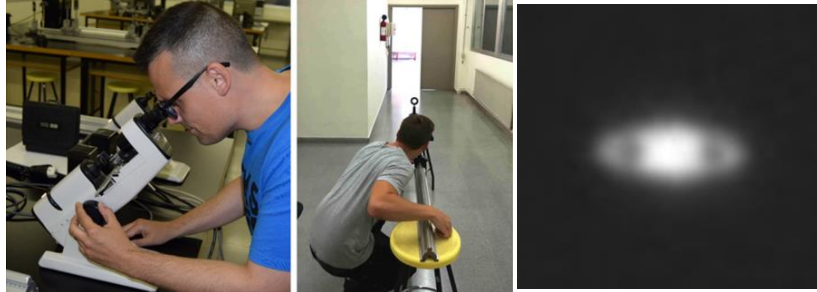


Figure 1 Students preparing their telescope in the laboratory (left and center), and Saturn's image obtained by them (right).

To quantify the resolution capabilities of the system that they have constructed, Saturn's image is replaced by a resolution test chart. Later on, the students use a diaphragm and equivalent corrected optical components to see how they affect to both the resolution and to the quality of the final image.

Details of the practise and results obtained by the students will be given in the poster of this communication at the conference.

4. Conclusions

An experimental workshop in optical resolution for telescopes, inspired by the limitations of Galileo's telescopes in his early observations of Saturn rings, has been presented. The discussion of the results obtained by the students and the implications of this experience on the formation of optics and photonics are also presented in the poster.

The authors strongly believe that both the experimental implementation and the comparison with historical examples can have a great impact on a student's personal learning experience.

Acknowledgments

Authors want to express their gratitude to the students that have participated in the workshop during all its past editions, and to their colleagues from the Optics area of the Applied Physics Department of University of Barcelona for their support and the educational resources they have developed during the last decades.

References

- [1] A. Marzoa and S. Vallmitjana, "Understanding resolution with Galileo's telescopes," in *Educ. and Training in Opt. & Photonics Conf.* (2021).
- [2] A. Marzoa and S. Vallmitjana, "Dealing with telescope magnification and resolution: recreating Galileo's observations in the lab", *Optical Engineering*, **63**(7) (2024).
- [3] A. Marzoa, "Galileo y las orejas de Saturno: la importancia de la resolución," *Astronomía* 275, 30–37 (2022).
- [4] E. A. Partridge and H. C. Whitaker, "Galileo's work on Saturn's rings," *Pop. Astron.* 3, 408–414 (1987).
- [5] C. Huygens, *Systema Saturnium, sive de causis mirandorum Saturni phaenomenon, et comite ejus planeta novo*, Adrian Vlacq, The Hague (1659).
- [6] A. Carnicer et al., "An on-line applet-based optics course for undergraduate students," *Proc. SPIE* 4829, 23–24 (2004).

Topological modes in planar structures containing Halide Perovskites semiconductors

Heitor da Silva^{1*}, Isaac Suarez¹, Juan P. Martínez-Pastor¹ and Albert Ferrando¹

¹*Institute of Material Science, University of València, C/ Catedràtic José Beltrán, 2. 46980 Paterna - Spain*

*E-mail: heitor.silva@uv.es

In recent years, halide perovskite materials have attracted significant attention due to their remarkable optoelectronic properties, leading to the development of various devices, including solar cells, lasers, and photodetectors [1]. Exploring novel photonic architectures incorporating this family of semiconductors presents an intriguing strategy for creating more efficient devices. This study proposes the integration of halide perovskite thin films into planar multilayer structures capable of confining and propagating topological modes. These modes represent unique distributions of the electromagnetic field confined within the boundary of an optical system and exist only under specific combinations of refractive indices and geometrical parameters.

In this work, we propose planar topological structures consisting of alternating layers of high and low refractive indices, as illustrated in Figure 1. By employing a transfer matrix method in conjunction with an effective refractive index method [2,3], we design this nontrivial architecture to concentrate light on edge states that overlap with the halide perovskite thin film (see Figure 1). Through a comprehensive theoretical analysis, which includes deriving reflectance and transmittance curves, as well as determining effective refractive indices and power distribution of propagating modes, we assess the enhancement of fundamental properties (such as light absorption and emission) of the halide perovskite thin film. Additionally, we establish practical applications for the resulting device.

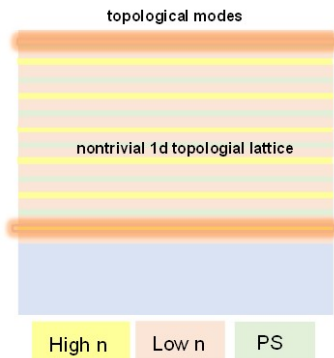


Figure 1. Topological structure.

References

- [1] A. K. Jena, A. Kulkarni and T. Miyasaka, “Halide Perovskite Photovoltaics: Background, Status, and Future Prospects”, *Chem. Rev.* 2019, 119, 5, 3036–3103 (2019).
- [2] G. Lifante Pedrola, *Beam propagation method for design of optical waveguide devices* (John Wiley & Sons, UK, 2015).
- [3] C. R. Pollock and M. Lipson, *Integrated Photonics* (Springer New York, NY, 2003)

Finite element 3D modeling of photonic open microcavities with 2D perovskites:

S. de Maria-Garcia^{1,3}, L. Sanchis¹, S. Gorji¹, W.L. Smith⁴, A. Ferrando^{1,2},
M.A. Garcia-March³, G Muñoz-Matutano^{1*}

1 Instituto de Ciencia de Materiales, Universidad de Valencia, P.O. Box 22085, 4607, Valencia, Spain;

2 Department d'Optica, Universitat de València, Dr. Moliner, 50, E-46100 Burjassot (València), Spain;

3 Instituto Universitario de Matemática Pura y Aplicada, Universitat Politècnica de València, 46022 València, Spain;

4 Imperial College London;

**E-mail: guillermo.MunozMatutano@mq.edu.au*

1. Abstract

We present a study in Comsol of symmetric and asymmetric fiber based optical micro-cavity with which we are able to study both Laguerre-Gaussian and Hermite-Gaussian modes. These cavities are formed by two mirror bragg with layers of different refractive indices, as well as different shapes in the 2D and 3D case. With this model we can change the different parameters to achieve the desired optical modes at the required frequencies so that we put 2D materials such as perovskite to interact and study exciton-polariton condensates, which have one of the richest realizations of a light-based quantum fluid [1].

2. Figures and tables

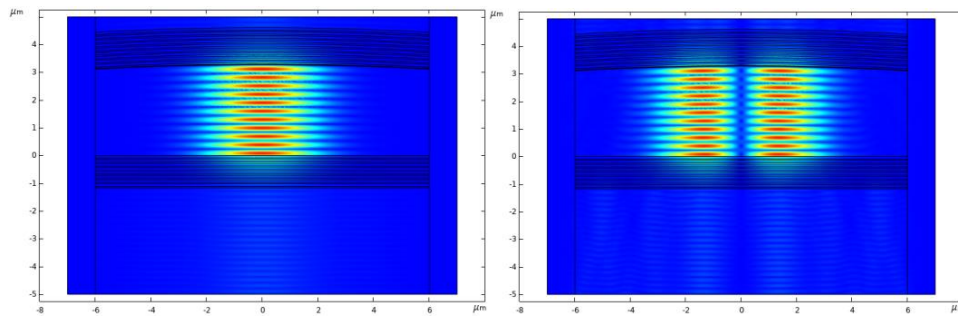


Figure 1 First and second modes in the 2D cavity simulation.

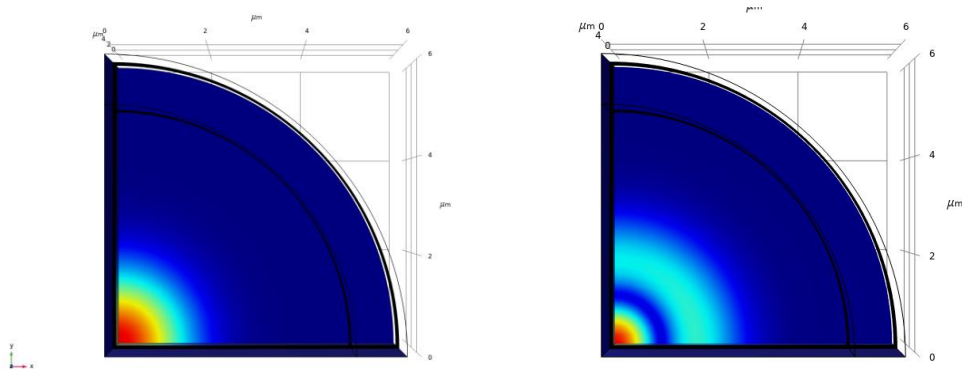


Figure 2 First and second modes in the 3D cavity simulation.

Acknowledgments

This study forms part of the Advanced Materials programme and was supported by MCIN with funding from European Union NextGenerationEU (PRTR-C17.I1) and by Generalitat Valenciana, with Ref. 20220883 (PerovsQuTe). G. Muñoz Matutano thanks the Ramón y Cajal programme (contract RYC2020-030099-I), QuantERA II Cofund 2021 PCI2022- 133004, Projects of MCIN with funding from European Union NextGenerationEU (PRTR-C17.I1) and by Generalitat Valenciana COMCUANTICA/007 (QuanTwin), and Red Temática RED2022-134391-T

References

- [1] I. Carusotto “Quantum fluids of light”, Rev Mod Phys 85, 299 (2013).

Abrupt transition to coherent emission in a semiconductor laser with optical feedback

María Duque Gijón^{*}, Cristina Masoller¹ and Jordi Tiana-Alsina²

¹ Departament de Física, Universitat Politècnica de Catalunya, Rambla Sant Nebridi 22, 08222 Terrassa, Spain

² Department de Física Aplicada, Facultat de Física, Universitat de Barcelona, Martí i Franques 1, 08028 Barcelona, Spain

*E-mail: maria.duque.gijon@upc.edu

1. Abstract

Semiconductor lasers are very sensitive to optical feedback. Optical feedback is well known to reduce the laser threshold, but the characteristics on the transition from low-coherence radiation (dominated by spontaneous emission) below threshold to high-coherence radiation (dominated by stimulated emission) above threshold have not yet been investigated. Here, we study experimentally how the coherence of the light emerges during the turn-on of a semiconductor laser (AlGaInP MQW - Thorlabs HL6501MG, 653 nm when $T=18$ °C and 41.95 mA) when it is and not optically fed back by a mirror. With a speckle technique, we show that the transition into coherence varies from smooth to abrupt as the amount of light fed back to the laser increases.

Speckle is a granular, noisy spatial structure produced by the interference of coherent waves. When laser light propagates through a scattering medium, usable information can be obtained from the analysis of the speckle pattern. We demonstrate that the effect of optical feedback in the coherence of the light emitted during the turn-on is unveiled by the amount of speckle generated.

The experimental setup is shown in Fig. 1 (details can be found in [1]). The insets show examples of speckle images recorded below and above threshold. Figure 1(a) shows the LI curve for different feedback strengths, from which the threshold of the laser can be extracted for each feedback scenario. We note that shape of the LI curve is the same with and without feedback, and the only evident effect of the feedback is the lowering of the threshold current.

For different pump current and feedback strength, we recorded several speckle images (with a CMOS camera (IDS UI-1222LE-M) of pixel size 5.3 μm with a resolution of 1280×1024 ($h \times v$) pixels) from which the speckle contrast, SC, was calculated in a circle of radius 200 pixels in the center of the image, after subtracting the background. The SC is the ratio between the standard deviation of the values of the pixels, and the average value, $SC = \sigma_I / \langle I \rangle$, that allows us to quantify the coherence of the light. Figure 1(b) shows the SC for different feedback strengths and pump currents conditions. Here we see that, the stronger the feedback, the more abrupt is the increase of the coherence of the laser light when the laser turns on. To shed light on the physics behind the abrupt increase in coherence revealed by the SC, simulations using different types of single-mode and multi-mode models were planned [2].

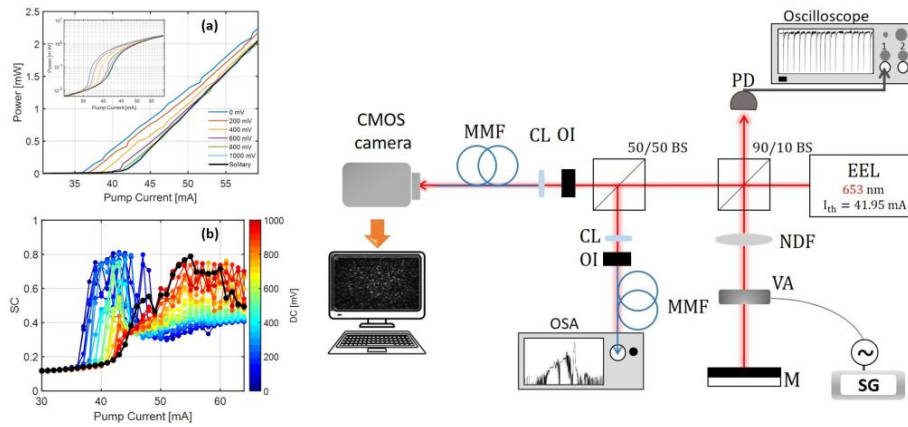


Figure 1. Right: LI curve (a) and SC (b) vs. pump current for different feedback strengths. The color code indicates the voltage in the Variable Attenuator. Left: Experimental setup. A: Manual Attenuator, VA: Variable Attenuator, MMF: Multi-Mode Fiber, BS: Beam Splitter, OI: Optical Isolator, OSA: Optical Spectrum Analyzer.

Acknowledgements

Ministerio de Ciencia, Innovación y Universidades (PID2021-123994NB-C21); Institució Catalana de Recerca i Estudis Avançats (Academia); Agencia de Gestió d’Ajuts Universitaris i de Recerca (AGAUR, FI scholarship).

References

- [1] M. Duque-Gijón, C. Masoller, and J. Tiana-Alsina, “Abrupt transition from low-coherence to high-coherence radiation in a semiconductor laser with optical feedback,” *Opt. Express* 31, 3857–3864 (2023).
- [2] M. Duque-Gijón, C. Masoller, and J. Tiana-Alsina, “Experimental study of spatial and temporal coherence in a laser diode with optical feedback,” *Opt. Express* 31, 21954–21961 (2023)

Fabricación de dispositivos fotónicos funcionales mediante escritura directa con láseres de femtosegundo

Carolina Romero^{1,2*}, Víctor Arroyo^{1,2}, Nuria Sevilla-Sierra^{1,2}, Ignacio Lopez-Quintas^{1,2}
and Javier R. Vázquez de Aldana^{1,2}

¹Grupo de Investigación en Aplicaciones del Láser y Fotónica, Universidad de Salamanca (USAL),
Pl. La Merced SN 37008 Salamanca, Spain

²Unidad de Excelencia en Luz y Materia Estructurada (LUMES), Universidad de Salamanca, Spain

*E-mail: cromero@usal.es

1. Introducción

En los últimos años la inscripción directa con láseres de femtosegundo (fs-DLW de sus siglas en inglés) se ha establecido como una técnica fiable para la inscripción de dispositivos tipo guía de ondas en materiales dieléctricos transparentes [1]. Las guías de onda son elementos esenciales para el desarrollo de dispositivos fotónicos integrados. El método de fabricación mediante pulsos láser ultracortos ofrece varias ventajas con respecto a otros métodos tradicionales como, por ejemplo, la litografía. Se trata de un método de fabricación en un solo paso, sin la necesidad de uso de máscaras, ni de un procesado posterior, tampoco se requiere que la fabricación se realice en un ambiente controlado en sala limpia. Además, el proceso óptico no lineal de absorción multi-fotónica, que tiene lugar cuando este tipo de pulsos se focalizan fuertemente dentro del material, hace que se trate de una técnica universal, que puede ser aplicada a cualquier dieléctrico transparente, tenga éste estructura cristalina o no. Sin embargo, la mayor ventaja que ofrece el fs-DLW, y que permite ampliar todavía más, si cabe, su rango de aplicación, es el hecho de que permite la escritura de estructuras tridimensionales de forma sencilla.

Por otro lado, en la búsqueda de obtener dispositivos fotónicos que sean funcionales es interesante aprovechar las propiedades de ciertos cristales de uso rutinario en óptica, como son su amplio rango de transparencia, el comportamiento anisótropo, sus altos coeficientes no lineales y/o electroópticos, etc. La idea es extraer el máximo potencial de los materiales cristalinos inscribiendo en ellos diversas estructuras, fabricadas por fs-DLW, que podrán formar parte de sensores o dispositivos *lab-on-a-chip*. En este trabajo presentamos nuestros últimos desarrollos en diferentes materiales cristalinos, en particular: LiNbO₃, YAG y BBO.

2. Materiales y métodos

Además, de las características ya mencionadas, la técnica de fs-DLW es muy versátil y podemos fabricar guías de onda tanto rectas como con estrechamiento Fig.1 a) y b), que se pueden inscribir en el interior así como cerca de la superficie del material, también se pueden combinar distintas estrategias, por ejemplo, dentro de la propia guía se puede incluir un micro estructurado, Fig.1 d), o se pueden añadir estructuras en superficie, a posteriori, mediante ablación ultrarrápida Fig. 1 c), que faciliten la extracción de luz por onda evanescente.

En el caso del LiNbO₃ nos hemos centrado en la fabricación de dispositivos con aplicación directa en astrofotónica, para ello, hemos desarrollado diversas estructuras funcionales que puedan formar parte de elementos de detección miniaturizados, como pueden ser los espectrómetros por Transformada de Fourier [2]. Mediante diferentes estrategias de fotoinscripción, abordando diversas geometrías en la modificación del índice de refracción (sección hexagonal, guías de doble línea, guías *depressed cladding*, etc), se obtiene un control modal de la luz guiada. Hemos combinado estas estructuras de guiado con canales realizados por ablación ultrarrápida en la parte superior de la muestra de manera que parte de la luz confinada en la guía pueda ser extraída y detectada Fig. 1 c).

Otra parte de nuestros esfuerzos están siendo orientados al desarrollo de sensores ópticos integrados, para ello hemos utilizado principalmente cristales de YAG. En este material hemos fabricado estructuras en superficie, de manera que éstas puedan interactuar con el ambiente mediante onda evanescente y detectar pequeños cambios [3]. Realizamos previamente un diseño adecuado de la guía, en función de la longitud de onda de guiado, para que la estructura, que va cambiando sus dimensiones a lo largo del material, se comporte de forma monomodal. Conforme se va propagando la luz en el dispositivo el modo

aumenta longitudinalmente, con lo que aumentamos la superficie de interacción con el ambiente, a la vez que se produce un estrechamiento en la dimensión transversal (Fig. 1 a) y b)).

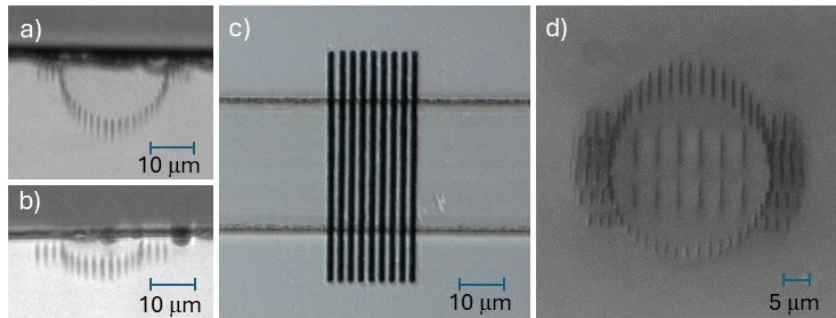


Figura 1 Imágenes de microscopio óptico de diversas estructuras fabricadas mediante fs-DLW. Paneles a) y b) secciones de entrada y salida, respectivamente, de una guía en superficie tipo *depressed cladding* en YAG. c) Detalle de estructuras lineales transversales fabricadas por ablación ultrarrápida sobre una guía en superficie en LiNbO₃ d) Sección de entrada de una guía interna con modificación de índice tipo *depressed cladding* con micro-estructuras en el interior en KTP.

Para finalizar, presentamos nuestros avances en el estudio de una serie de dispositivos fotónicos no lineales, que hemos fabricado principalmente en KTP, donde hemos modificado de forma precisa y controlada las propiedades ópticas de la susceptibilidad de segundo orden $\chi^{(2)}$. Contamos en nuestro laboratorio con un sistema de microscopía de segundo armónico de elaboración propia [4], que nos permite analizar las estructuras creadas. Hemos comprobado que en ciertas condiciones la señal de segundo armónico se puede ver amplificada y esto puede tener una aplicación directa en determinadas situaciones donde la señal generada en el material no modificado pudiera ser baja.

3. Conclusiones

En este trabajo presentamos nuestros resultados más recientes en relación con la fabricación mediante fs-DLW de estructuras tipo guía de onda en materiales dieléctricos transparentes, con un enfoque claro en mejorar y controlar ciertos aspectos de la propagación y/o la extracción de la luz. La fotoinscripción mediante fs-DLW es una técnica establecida que permite la integración de diferentes tipos de dispositivos fotónicos, y que abre una ruta muy prometedora para crear dispositivos funcionales totalmente integrados y miniaturizados con características mejoradas.

Agradecimientos

Agradecemos el apoyo del Ministerio de Ciencia, Innovación y Universidades a través del proyecto PID2020-119818GB-I00.

Referencias

- [1] L. Li, W. Kong, F. Chen, "Femtosecond laser-inscribed optical waveguides in dielectric crystals: a concise review and recent advances", *Adv. Photon* **4**, 024002 (2022).
- [2] M.J. Grotevent, S. Yakunin, D. Bachmann, et al. "Integrated photodetectors for compact Fourier-transform waveguide spectrometers", *Nat. Photon.* **17**, 59–64 (2023).
- [3] J. Lapointe, A. Grégoire, J.P., Bérubé, R. Vallée, "Enhancing Evanescent Wave Coupling of Near-Surface Waveguides with Plasmonic Nanoparticles", *Sensors* **23**, 3945 (2023).
- [4] N. Sevilla-Sierra, J. R. Vázquez de Aldana, C. Romero, X. Mateos, and I. Lopez-Quintas, "Unveiling second harmonic generation from femtosecond-laser microstructured Nd:YAG crystal," *Opt. Express* **32**, 16845-16854 (2024).

PW-class laser spatio-temporal characterization

Cristian Barbero^{1,*}, Enrique García-García^{1,2,3}, Cruz Méndez^{2,3}, M. D. Rodríguez-Frías^{2,4}, Miguel López-Ripa¹, Íñigo J. Sola^{1,3} and Benjamín Alonso^{1,3}

¹Grupo de Investigación en Aplicaciones del Láser y Fotónica (ALF), Universidad de Salamanca, 37008, Salamanca, Spain

²Centro de Láseres Pulsados (CLPU), Salamanca, Spain

³Unidad de Excelencia en Luz y Materia Estructuradas (LUMES), Universidad de Salamanca, Spain

⁴Universidad de Alcalá, E-28801, Madrid, Spain

*E-mail: cristianbp@usal.es

1. Introduction

High-power ultrashort pulsed lasers are used daily to accelerate particles and to study some fundamental physics such as laboratory astronomy [1], just to name one example. Those experiments rely on the proper handling of temporal and spatial properties of the pulse to concentrate the energy as close as possible to the lambda-cube regime [2]. In this regime, a direct pulse measurement is not possible because the extreme electric fields would destroy the measurement device. Some indirect measurements of high intensity pulses have been proposed by studying the fluctuations of the quantum vacuum at focus, but the practical application is still not implemented. Standard techniques to characterize these high intensity pulses rely on independent measurements of energy, temporal duration, phase or spatial profile and wavefront, using an attenuated pulse and assuming linear processes.

During the last decade numerous techniques have been developed to fully characterize the electric field, i.e., spatio-temporal characterization, across the beam aperture. To date, a standard procedure to perform such characterization has not yet been established and all the devices have some highlights and drawbacks. In this contribution we apply the recently reported technique Bulk-Lateral Shearing Interferometry (BLASHI) [4] to the characterization of the laser beam VEGA-3, the petawatt laser system installed at the Spanish Centre for Pulsed Laser (CLPU). Thus, the spatio-temporal (and, equivalently, spatio-spectral) structure of the beam can be studied for eventual corrections.

2. Experimental procedure and results

In the BLASHI technique, a beam copy is created, temporally delayed and spatially sheared, in a bulk material, namely, a walk-off crystal (Fig. 1). Both replicas interfere on spatial and spectral domains, encoding, along with a reference pulse measurement, the information regarding the beam spatio-spectral and spatio-temporal structure. The measurements were performed for VEGA-3 laser pulses (30 J, 1 Hz, 30 fs), after passing through an ultrashort pulse compressor, and a down-size telescope to adjust the beam size to the measurement device. The beam was also attenuated 10000 times using all reflective high-quality optics without compromising the spatial and temporal properties.

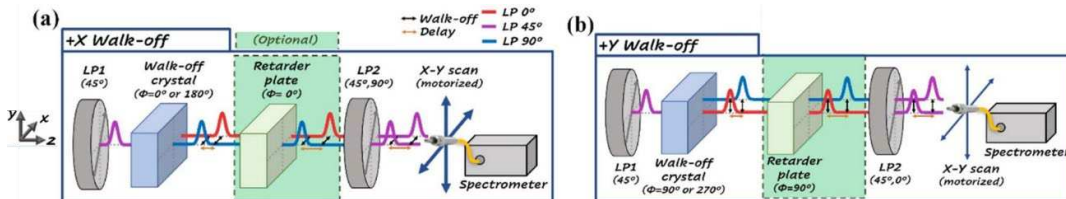


Figure 1 Schematic of the BLASHI device. The input pulse, linearly polarized at 45°, is sent to the walk-off crystal that generates the sheared and delayed pulse copy. An optional retarder plate can adjust the temporal delay. Then, both pulse replicas are projected to a common polarization direction, and the interference signal is gathered in a spectrometer that is swept in space. The shear is induced in the horizontal (a) and vertical (b) plane, depending on the walk-off crystal orientation. The measured trace encodes the gradient of the spectral phase. Image from ref [3].

The retrieval (Fig. 2) reveals the dependence of the spatio-spectral and spatio-temporal intensity and phase for different wavelengths and time slices. This measurement shows a close to linear spatial phase shift in the left side of the x-axis that could be related to pulse front tilt not completely corrected at the compressor. The spectral domain measurement shows a stable spatial profile at different wavelengths while the phase shifts below π in the central part of the spectrum. The temporal domain is set to represent the peak intensity position and the lateral positions where slightly below the full width at half maximum.

This is a key diagnostic to know, correct, and control the beam structure for the posterior experiments. The accommodation of the beam dimensions to the setup aperture and the limited statistics due to the low repetition rate are currently the main measurement issues being further to be addressed.

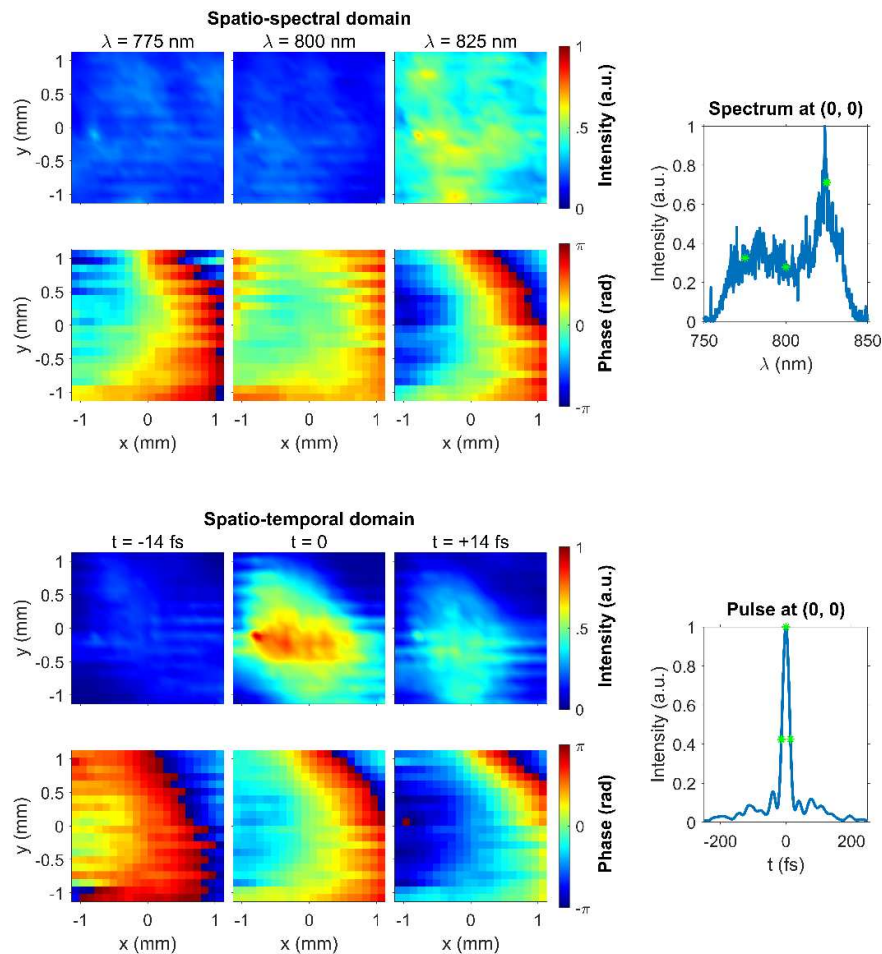


Figure 2 Retrieved VEGA-3 spatial intensity and phase for three spectral and temporal snapshots (green dots in the spectrum and pulse profile). The evolution between the chosen snapshots is smooth, so with this information one can have an idea of the full evolution.

3. Conclusions

In the present contribution, BLASHI technique for spatio-temporal characterization of ultrafast pulsed laser beams has been applied to VEGA-3, a PW-class laser. The results show the capability of extracting the spatio-temporal (or, alternatively, spatio-spectral) beam structure, supplying a precious knowledge of the laser characteristics for its application in high-intensity experiments.

Acknowledgments

Junta de Castilla y León and fondos FEDER (SA136-P20), MINECO (EQC2018-004117-P), and Ministerio de Ciencia e Innovación (PID2020-119818GB-I00). C. B. acknowledges Junta de Castilla y León and Fondo Social Europeo Plus for the PhD contract.

References

- [1] Z. Li, Y. Leng, y R. Li, "Further Development of the Short-Pulse Petawatt Laser: Trends, Technologies, and Bottlenecks", *Laser Photonics Rev.* **17**, 2100705 (2023).
- [2] J. W. Yoon et al., "Realization of laser intensity over 1023 W/cm²", *Optica* **8**, 630–635 (2021).
- [3] M. López-Ripa, Í. J. Sola, and B. Alonso, "Bulk lateral shearing interferometry for spatiotemporal study of time-varying ultrashort optical vortices", *Photonics Res.* **10**, 922–931 (2022).

Conversión de imágenes del infrarrojo medio en un cristal de CPLN

H. Maestre*, M. Cuenca, A. E. Ortega, A. J. Torregrosa, J. Capmany

¹Instituto de Investigación en Ingeniería de Elche I3E, Universidad Miguel Hernández, Avda. de la Universidad s/n, 03202 Elche (Alicante).

*E-mail: hmaestre@umh.es

1. Introducción

Debido las limitaciones de los sensores de imagen en el infrarrojo que dificultan la obtención simultánea de video de alta velocidad con buena resolución, y con una buena relación S/N sin recurrir al costoso enfriamiento criogénico [1], resulta de interés poder trasladar en tiempo real, imágenes en el infrarrojo a la banda espectral de detección del silicio, donde existen actualmente sensores de imagen CCD o CMOS que combinan las anteriores características, operando sin necesidad de refrigeración, y de bajo coste. La óptica no lineal, proporciona una herramienta muy útil para ello, basada en realizar un proceso de suma de frecuencia en un cristal no lineal [2], entre la imagen infrarroja original y un haz láser intenso de bombeo. Es teóricamente posible alcanzar una eficiencia cuántica $QE \sim 1$ optimizando condiciones. Sin embargo, factores como la aceptación angular en el ajuste de fase que se requiere en el cristal no lineal para que el proceso resulte eficiente, limita la resolución espacial que se obtiene en la imagen convertida. Mediante el empleo de un cristal ferroeléctrico similar al niobato de litio periódicamente polarizado (PPLN), al que se añade un chirp lineal en la estructura de dominios (Chirped-poling Lithium Niobate, CPLN), es posible incrementar dicha resolución, relaciona directamente con el campo angular convertido. Es además posible, si el diseño del chirp alcanza un cuasi-ajuste de fase denominado adiabático [3], compatibilizar una buena eficiencia y una elevada resolución.

Presentamos aquí resultados preliminares de una conversión de imagen de longitud de onda alrededor de $3,9 \mu\text{m}$ en infrarrojo medio a otra imagen alrededor de 840 nm y su visualización en una cámara CMOS de silicio empleando un cristal CPLN con chirp lineal.

2. Montaje experimental y resultados

La figura 1 muestra el esquema experimental empleado. Como fuente de iluminación, se emplea un láser de diodo de cascada cuántica de 10 mW en onda continua, con emisión máxima a $3,9 \mu\text{m}$ y anchura espectral total de 5 nm a mitad de máximo. La onda de bombeo la proporciona un láser de diseño propio, que emite un haz gaussiano a 1064 nm , capaz de operar tanto en onda continua como en modo pulsado Q-Switch mediante reconfiguración. El cristal no lineal, de dimensiones $1 \times 5 \times 10 \text{ mm}^3$, contiene un chirp lineal que abarca periodos de 19 a 24 micras.

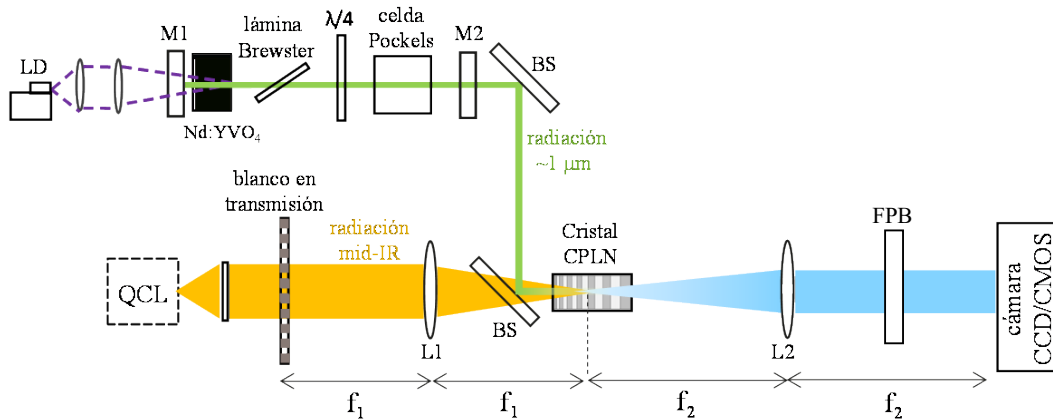


Figura 1. Representación esquemática del sistema de conversión empleado. LD: diodo láser 808 nm, M1: espejo de entrada de cavidad láser HR@1064 nm y AR@808 nm, M2: espejo de salida de la cavidad láser PR=50%@1064 nm, BS: Combinadores de haz, QCL: Láser de cascada cuántica de $3,9 \mu\text{m}$, L1: lente de entrada del sistema $4f$ de 50 mm de focal, L2: lente de salida del sistema $4f$ de 100 mm de focal, FPB: filtro pasobanda a 840 nm .

El sistema de conversión se implementó alrededor de un sistema 4-f de Fourier formado por dos lentes convergentes (L1 y L2) de focales $f_1 = 5$ cm and $f_2 = 10$ cm con el centro del cristal situado en el plano de Fourier. En la Figura 2 se muestran las imágenes captadas en una cámara CMOS estándar, realizadas en paso único externo, empleando un haz de bombeo a 1064 nm tanto en onda continua como en modo pulsado. Como blanco, iluminado en modo transmisión, se han empleado una rendija de anchura variable (figura 2, a-c), y un blanco con patrones de barras horizontales y verticales (USAF 1951, figura 2, e,f). La óptica empleada muestra cierto grado de aberración esférica en nuestras condiciones experimentales, debido a la difícil colimación, previa a su focalización sobre el CPLN, del láser de cascada cuántica, que no presenta un patrón de emisión de buenas características espaciales. El haz de bombeo empleado tiene un diámetro de 1,2 mm a $1/e^2$, desbordando ligeramente la apertura de 1 mm del cristal CPLN. El chirp introducido en el cristal permite al sistema operar sin estabilización térmica en un rango apreciable de temperatura ambiente.

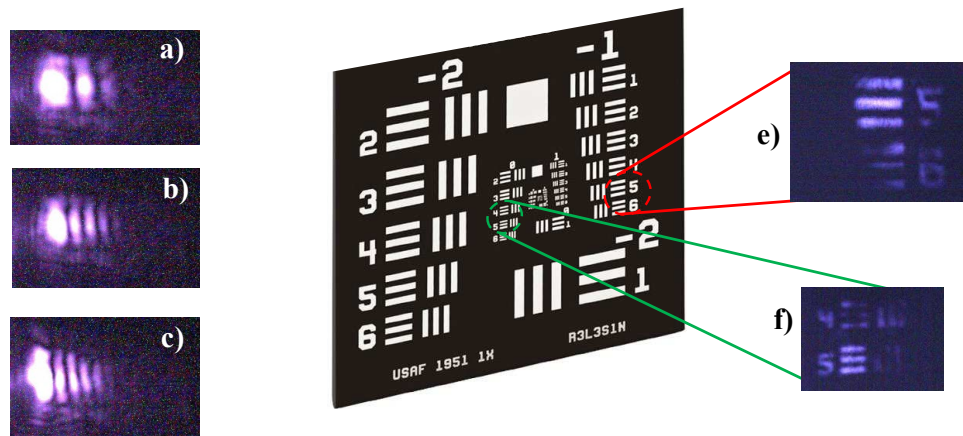


Figura 2. a, b y c) Imágenes convertidas visualizadas en la cámara CMOS empleando como blanco el patrón de difracción de una rendija de anchura variable. d) y e) imágenes de un blanco USAF 1951 a) grupo -1, elementos 5 y 6, b) grupo 0, elementos 4 y 5.

3. Conclusiones

Presentamos resultados preliminares de conversión de imagen en tiempo real del infrarrojo medio a la banda de detección de un sensor de imagen de silicio mediante el empleo de un cristal de CPLN con chirp diseñado para alcanzar el régimen adiabático en un proceso de suma de frecuencias. Estos resultados nos permiten seleccionar parámetros de diseño adecuados con los que evolucionar y optimizar el sistema para la demostración del primer sistema de visión activa por tiempo de vuelo (range-gated) en el infrarrojo medio. En la reunión se presentará y discutirá en mayor detalle las condiciones para obtener elevada eficiencia y buena resolución sin aberración, empleando una fuente de iluminación infrarroja de mejores características.

Agradecimientos

El presente trabajo ha sido financiado por los siguientes proyectos: CIAICO 2021/326 (Generalitat Valenciana), PID2020-117658RB-I00 del MICIU/AEI/ 10.13039/501100011033 y FEDER (European Union Next Generation EU/PRTR).

Referencias

- [1] A. Rogalski, P. Martyniuk, M. Kopytko “Challenges of small-pixel infrared detectors: a review”, Rep. Prog. Phys. 79, 046501, 1-42, (2016) “
- [2] J. E. Midwinter, “Parametric Infrared Image Converters,” IEEE J. Quantum Electron. 4(11), 716–720 (1968).
- [3] H. Suchowski, B. D. Bruner, A. Arie, and Y. Silberberg, “Broadband frequency conversion,” Opt. Photonics News 21(10), 36–41 (2010).

High efficiency upconversion of IR eye-safe images

J. Capmany^{1*}, A. J. Torregrosa¹, X. Hachair²

¹*Instituto de Investigación en Ingeniería de Elche I3E, Universidad Miguel Hernández, Avda. de la Universidad s/n, 03202 Elche (Alicante).*

²*Nexvision S.A.S, Parc SWEN Sud – Bât. D2 Hall D4, 1 Bd de l’Océan – Imp. Paradou
13 009 Marseille France*

*E-mail: jcapmany@umh.es

1. Introduction

Nonlinear upconversion of infrared images to the detection band of silicon-based Focal Plane Array detectors is a useful resource to overcome some performance and cost limitations of existing image sensors in the infrared in terms of speed, resolution, and high signal-to-noise ratios with uncooled operation [1]. Even though any of the former figures of actual IR image sensors can be improved individually, they cannot be improved simultaneously to achieve the present performance of CCD or CMOS image sensors. For instance, speed and S/N ratio can be improved through pixel grouping (like binning), but at the expense of resolution, and S/N itself can be also improved by strong cooling which increases cost. The eye-safe region around 1550 nm is of particular interest for laser-illuminated active night vision including range-gating. Once a high conversion efficiency with good resolution is achieved, the performance of active systems is transparent to the upconversion step and it can perform similar to actual active systems in the near infrared at around 850-900 nm that have a lower threshold for human eye damage. However, night vision systems rely on the use of an image intensifier tube or an EMCCD (electron-multiplying charge coupled device)

Nonlinear image upconversion is usually based on sum-frequency mixing (SFM) an IR image with an intense pump beam in a nonlinear crystal [2]. There is a compromise between conversion efficiency and resolution. Typically, the upconversion imaging systems reported have a conversion efficiency around 20-50% in power. Here, we show 98 % power conversion efficiency corresponding to a quantum efficiency $QE = 0.4$. This relatively high QE allows to sacrifice some conversion efficiency to improve resolution.

2. Experimental configuration and results.

A USAF 1951 resolution target is illuminated using two different 1550 nm sources. One is a 10 mW continuous wave DFB diode laser, and the other one is a Q-Switched laser delivering 50 ns pulses at 5 KHz. The target images are externally mixed with a dichroic mirror in a PPLN crystal with a pump beam at 1064 nm providing real time upconverted images of the target at 631 nm. The images are detected with a silicon CMOS colour camera.

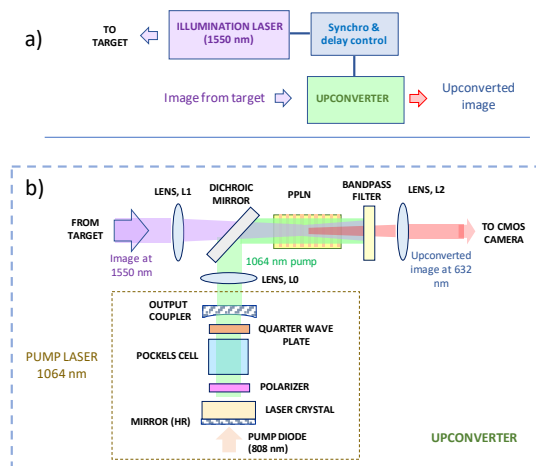


Figure 1. Schematic representation of the upconverting system. a) General operation scheme. b) Upconverter.

Weak continuous wave IR images at 1.5 mW illumination could be upconverted in the system. The PPLN crystal is 5 mm long with a domain period of 11.8 μm and a $3 \times 1 \text{ mm}^2$ cross sectional area operating at room temperature. In both cases, we have used an intense pump laser beam at 1064 nm provided by a self-made Q-Switched laser delivering 140 μJ pulses of 3.5 ns duration at a pulse repetition rate of 5 KHz, with a peak power of 40 KW in a 300 μm radius at $1/e^2$ intensity gaussian beam.

The image upconversion system is built around a 4-f Fourier processor system formed by two positive lenses of focal lengths $L1 = 2.5 \text{ cm}$ and $L2 = 5.0 \text{ cm}$, with the pump beam acting as a soft aperture in the Fourier plane where the middle of the PPLN crystal is located. The resolution limit in this case is 12 lp/mm for a target located in the object focal plane of lens L1. In case of pulsed illumination, we use a digital delay generator to synchronize the pump pulse and the illumination pulse inside the PPLN crystal.

In SFM, the instantaneous conversion efficiency depends only on the pump laser intensity. By scaling up the pump pulse energy and enlarging the pump beam size up to the thickness of the PPLN crystal, we expect to come very close to $QE = 1$, and to improve resolution to the typical values of 50-60 lp/mm in image intensifiers for night vision using a shorter focal around 1 cm in L1. Figure 2 shows upconverted images from the target illuminated in continuous wave and in pulsed mode, and an oscilloscope trace for measurement of the QE using the infrared detected power of a 1550 nm continuous wave signal with the pump beam pulses switched off (upper trace) and on (lower trace).



Figure 2. a) Upconverted image in CW. b) Upconverted image in synchronized pulse mode. c) Quantum Efficiency $QE = 0.4$, representing a 98% power conversion efficiency.

3. Conclusion

We show an efficient upconversion system for eye-safe illumination of targets useful for illumination assisted night vision and range-gated systems in the eye-safe region, where standard image intensifiers or EMCCD cameras cannot operate due to their spectral response limitation to the near infrared around 850-900 nm. The results presented achieve good practical characteristics, although there is room for improvement up to theoretical limits in QE and resolution.

Acknowledgments

This work has been funded by the following projects: PID2020-117658RB-I00 del MICIU/AEI/10.13039/501100011033 and FEDER (European Union Next Generation EU/PRTR).

References

- [1] A. Rogalski, P. Martyniuk, M. Kopytko "Challenges of small-pixel infrared detectors: a review", Rep. Prog. Phys. 79, 046501, 1-42, (2016).
- [2] J. E. Midwinter, "Parametric Infrared Image Converters," IEEE J. Quantum Electron. 4(11), 716-720 (1968).

Experimental study of just noticeable Gaussian noise differences in synthetic flat image patches of different luminance

Luis Miguel Calvo¹, Pedro Latorre-Carmona², Rafael Huertas³ and Samuel Morillas^{4*}

¹*Telefónica Innovación Digital, Valladolid*

²*Departamento de Ingeniería Informática, Universidad de Burgos, Avda. Cantabria s/n, 09006, Burgos, Spain*

³*Departamento de Óptica, Facultad de Ciencias, Avenida de la Fuente Nueva s/n, 18071, Granada Spain*

⁴*Instituto Universitario de Matemática Pura y Aplicada, Universitat Politècnica de València, Camino de Vera s/n 46022 Valencia*

*E-mail:smorillas@mat.upv.es

1. Introduction

Digital color images are inherently susceptible to noise, which arises from various physical and technological limitations. Noise manifests as unwanted variations in pixel components intensity, disrupting the intended color and affecting image quality. Understanding how noise affects visual quality and modeling its perception are crucial aspects of digital image processing when digital images are intended for human consumption.

Among the different sources of noise affecting digital images [1], in this study, we are interested in the most common source of camera noise: the sensor thermal noise that is usually modelled as white gaussian noise, where each image pixel channel is added a random value from a zero-mean Gaussian distribution of a given standard deviation that characterizes noise intensity. The presence of Gaussian noise can affect the perceptual image quality in different ways. Image quality is intended to be improved by digital image processing methods like image filtering by reducing the amount of noise in the image [2]. So, it is interesting to study how different noise intensities are perceived. In this work we focus on this problem. We assume that a good indicator for this perception is the determination of just noticeable differences (JNDs) between noise intensity. We also assume that there is a dependency between the JNDs, the noise intensity and the background luminance, so we will study the JNDs related to different noise intensity levels and background luminance. The psychophysical study done is explained in Section 2. Results are discussed in Section 3 and some conclusions and lines of future work are given.

2. Psychophysical study

We approach the determination of JNDs by using a two-alternative forced choice methodology. We used 4 gray image patches defined in the $L^*a^*b^*$ space with $a^*=b^*=0$ and $L = 20, 40, 60, \text{ and } 80$. Each image patch was added 4 levels of Gaussian noise in the linear RGB space (IRGB) space equal to [0.01, 0.02, 0.03, 0.04]. These 16 images will constitute the reference images for which we will compute the corresponding JNDs. For this, each of the 16 images is compared with another 10 images with increased image intensity in a two-alternative forced choice experiment. Properly characterized displays were used and the experiment was carried out in a dark room. Observers were given 5 minutes time to adapt to illumination conditions. 68 observes took place in the experiment. They were asked to select what image of each pair shown was perceived as having a higher noise intensity. The 160 image pairs were assessed 6 times in a random order for each observer. Position of each pair in left or right was also randomized. To avoid a too long experiment, it was split into two sessions. Averaged successful detection rates were computed for each of the 10 images that were compared against each of the 16 reference images. These 10 detection rates were fitted to a psychometric function following an accumulated normal distribution shape and the noise intensity corresponding to 75% detection rate was determined as the JND in each case. Figure 1 shows the fitted psychometric curves along with the JNDs found.

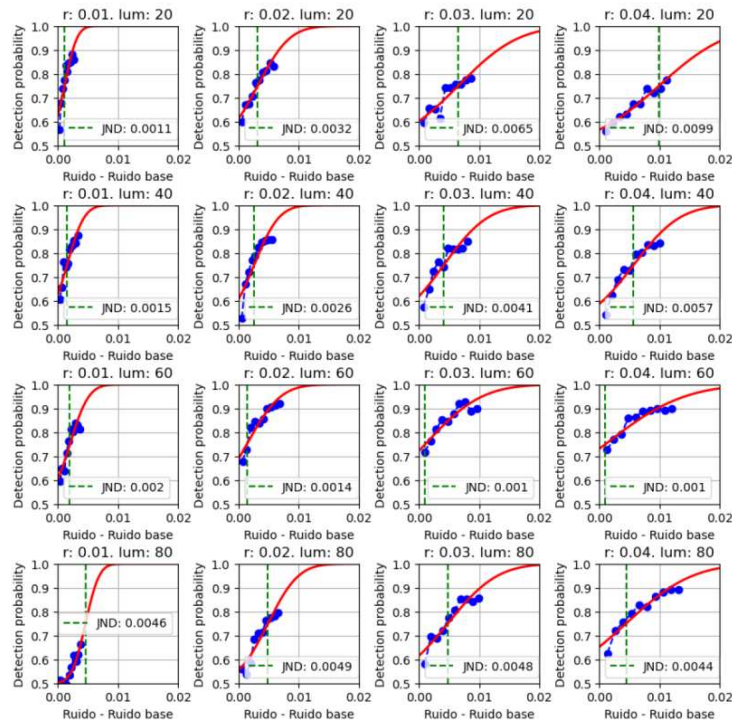


Figure 1 Fitted psychometric curves and JNDs found. Averaged successful detection rate is shown vs. the noise intensity difference between reference image and test image for each pair.

3. Results discussion, conclusions and future work

From Figure 1 we can see that there is a dependency on the JNDs computed related to both reference image noise intensity and background luminance. Following the Weber Law, the higher the noise intensity in the reference image, the higher the JND. The relation between JNDs and background luminance is less evident. For low noise, it seems to be a direct relation between luminance and JND, suggesting that higher luminance is able to mask low intensity noise. However, this is not observed for medium to high noise. In these cases, not only higher luminance is unable to mask the noise but also it is observed that noise conspicuity is higher for medium luminance. This may be related to observers adapting to average luminance and so increasing their sensitivity to differences observed close to that medium luminance. Given these interesting results, we conclude that it would be worth to study in the future analogous JNDs but in the presence of varying spatial texture instead of background luminance to find out up to what extent background texture can mask image noise.

Acknowledgments

This research was funded by Generalitat Valenciana under grant CIAICO/2022-051 IMaLeVICS and Spanish Ministry of Science under grant PID2022-140189OB-C21.

References

- [1] R.D. Gow, D. Renshaw, K. Findlater, L. Grant, S.J. Leod, J. Hart, R.L. Nicol, A comprehensive tool for modelling CMOS Image-Sensor-Noise performance, *IEEE Transactions on Electron Devices* (2007) 54 6 pp. 1321-1329
- [2] K.N. Plataniotis, A.N. Venetsanopoulos, *Color Image Processing and Applications*, Springer-Verlag, (2000) 355 pp 1-45, 51-100, 109-157.
- [3] Peter G. Engeldrum, *Psychometric scaling: A toolkit for imaging systems development*, Imcotek Press, ISBN 0967870607, 2000.

Do alcohol consumption and the presence of interocular differences affect driving performance?

Francesco Martino^{1*}, José Juan Castro Torres¹, Miriam Casares López¹, Pilar Granados-Delgado¹, Luis Jiménez del Barco and Rosario G. Anera¹

¹Laboratory of Vision Sciences and Applications (LabVisGra.), University of Granada, Department of Optics, Avenida de Fuentenueva, s/n 18071 Granada, Spain.

*E-mail: francesco@ugr.es

1. Introduction

According to the World Health Organization, alcohol is the most widely consumed psychoactive substance in the world [1] and plays an important role as a central nervous system depressant [2] that impairs both the ability and aptitude to drive, increasing the risk of being involved in a traffic accident. Those who drive under the influence (DUI) of alcohol make many more driving errors, drive faster, have poorer decision making and increased reaction times [3]. Alcohol consumption also impairs binocular visual performance [3]. Other factors that influence this performance are for example interocular differences. An important phenomenon known as intraocular scattering may be responsible for the increase of these interocular differences that can be induced in case of monovision technique or in unilateral ocular pathologies such as cataracts. With this in mind, it is of interest to study how different degrees of interocular differences (simulated by filters) affect vision and especially driving performance under moderate alcohol consumption condition equivalent to a BrAC (Breath Alcohol Content) of 0.40 mg/l (equal to a Blood Alcohol Content, BAC of 0.08%).

2. Methods

Twenty young subjects (9 females and 11 males) with a mean age of 26.3 ± 2.9 years participated in this study. The inclusion criteria for this study were as follows: a binocular best-corrected logMAR visual acuity of 0.0 or better, normal distance and near stereopsis (≤ 40 arcsec), no pathologies or pharmacological treatment that could affect visual performance, no contraindication to alcohol consumption, a minimum of 24 hours without previous alcohol consumption, and being a social drinker with a score less than or equal to 8 on the Alcohol Use Disorders Identification Test (AUDIT). All participants were required to have held a driver's license for at least two years and to drive a minimum of 2,000 km per year. A Bangerter foil of 0.8 (BF_0.8) and a fog filter, Black Pro Mist 2 (BPM2, Tiffen, Hauppauge, NY, USA), were used to induce different levels of monocular deterioration, as in other works [4]. Each participants consumed the corresponding dose of alcohol (67% orange juice and 33% vodka) within a time period of 30-40 minutes. The mean BrAC obtained in this research for all participants was 0.40 ± 0.04 mg/l measured with the Alcotest 6810 (Dräger Safety AG& Co. Lubeck, Germany), which corresponds to the legal limit for driving in many countries [1]. At the visual level, visual acuity, contrast sensitivity function for different spatial frequencies (logSC), distance stereoacuity and visual disturbance index (VDI) were measured. Interocular differences were calculated for two ocular parameters: the objective scatter index, OSI, and the logarithm of the straylight, log(s). To assess driving performance, a driving simulator (Simax Driving Simulator) was used. The following variables were measured in the different scenarios (highway, mountain road and city): mean speed, distances traveled invading the shoulder, the opposite and total lane, standard deviation of the lateral position of the vehicle (SDLP), reaction time and number of collisions. Three global indices were obtained: the overall visual performance score (OVPS), the overall driving performance score (ODPS), and the overall interocular differences score (OIDS). Under all filter conditions, participants completed two sessions: one without alcohol consumption (baseline) and one after alcohol consumption (aAC).

3. Results and discussion

In terms of visual performance (including visual acuity, VDI and distance stereoacuity), there was a tendency for a deterioration after alcohol consumption and filter conditions. For spatial frequencies ranging from 3 to 18 cpd, contrast sensitivity significant impaired under alcohol consumption ($p=0.007$)

and filter conditions ($p < 0.001$). Furthermore, for 6 cpd, an important interaction ($p = 0.044$) effect between alcohol and the filter was determined suggesting that the addition of the filter exacerbate the subjects' condition when they are exposed to alcohol. In relation to driving performance, all measured variables deteriorated under moderate alcohol consumption and filter (by reaction time, SDLP and number of collisions) conditions ($p < 0.05$). However, no interaction effect between alcohol consumption and filter condition was found in driving performance, indicating that adding the filter does not further deteriorate subjects when they are under the influence of alcohol, but regardless of the filters used, there was an impairment after alcohol consumption of both visual function and driving performance. In both experimental conditions (baseline and aAC), interocular differences between the two ocular parameters (OSI and $\log(s)$) increased significantly ($p < 0.05$) and gradually, from the baseline to the BF_0.8 on the dominant eye. For all filter conditions, comparing the baseline and after alcohol consumption, no change was found for interocular differences in $\log(s)$ and OSI. On the other hand, a significant correlation was found between OVPS and ODPS ($\rho = -0.617$, $p < 0.001$) as well as between OIDS and ODPS ($\rho = 0.193$, $p = 0.032$) (Figure 1). As a result, a better driving performance is associated with reduced interocular differences in ocular parameters and less impairment in binocular visual performance.

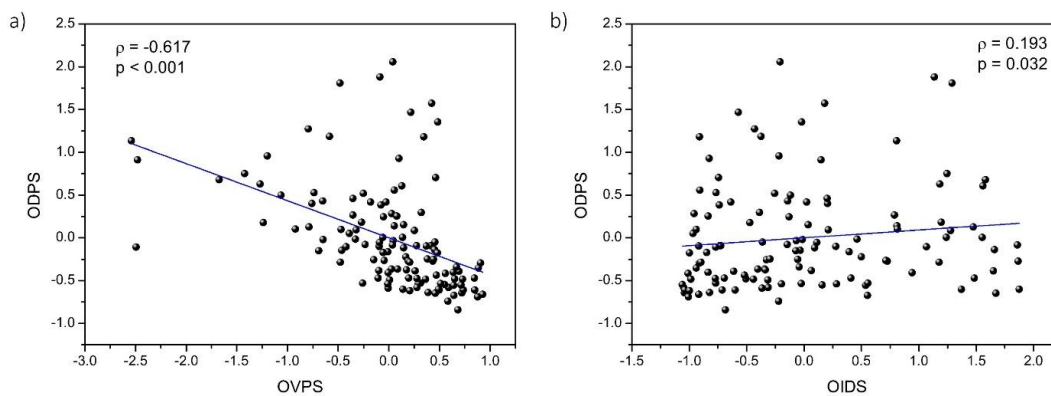


Figure 1. The overall driving performance score (ODPS) as a function of (a) the overall visual performance score (OVPS), and (b) the overall interocular differences score (OIDS), under the two experimental and filter conditions.

4. Conclusion

Alcohol consumption and filter conditions significantly affect driving performance. Reduced visual and driving performance are directly related to higher interocular differences caused by intraocular scattering. Our findings contribute to the understanding of the importance of limiting interocular differences, which can be common among presbyopes corrected using the monovision technique, as well as in cases of cataract surgery on one eye. More, these interocular differences can have a negative impact on driving performance and road safety, particularly when combined with moderate alcohol consumption.

Acknowledgements

Grants A-FQM-532-UGR20, funded by FEDER/Junta de Andalucía and PID2020-115184RB-I00, funded by MCIN/ AEI/10.13039/50110001103.

References

- [1] V. Poznyak and D. Rekve. “Global Status Report on Alcohol and Health”, World Health Organization, Geneva (2018).
- [2] S. A. Khan and B. Timney, “Alcohol slows interhemispheric transmission, increases the flash-lag effect, and prolongs masking: Evidence for a slowing of neural processing and transmission”, *Vision Res.* **47**(13), 1821-1832 (2007).
- [3] F. Martino et al. Deterioration of binocular vision after alcohol intake influences driving performance. *Sci Rep.* **11**(1), 8904-8904 (2021).
- [4] J. J. Castro et al, “Visual performance after the deterioration of retinal image quality: induced forward scattering using Bangerter foils and fog filters”, *Biomed Opt Express.* **12**(5): 2902–2918 (2021).

Frequency analysis of interocular corneal astigmatism symmetry in a large sample

Raquel Salvador-Roger^{1*}, César Albarrán-Diego¹, Nuria Garzón², María García Montero², Gonzalo Muñoz^{3,4}, Vicente Micó¹ and José J. Esteve-Taboada¹

¹Department of Optics, Optometry and Vision Sciences. Universitat de València. 46100 Burjassot, Spain.

²Department of Optometry and Vision, Universidad Complutense de Madrid. 28037 Madrid, Spain.

³Marqués de Sotelo Ophthalmological Clinic. 46002 Valencia, Spain

⁴Baviera Castellón Ophthalmological Clinic. 12003 Castelló de la Plana, Spain.

*E-mail: raquel.salvador@uv.es

1. Introduction

The human body shows mirror symmetry (MS). [1] This phenomenon is described when one half of an object or shape is a reflection of the other half, as if it were mirrored across a line. Regarding symmetry in terms of astigmatism, previous studies have attempted to characterize its interocular symmetry. [2,3] Nevertheless, these works only considered the axis of astigmatism when drawing their conclusions, which implies that they address both components of astigmatism, magnitude and axis, as independent variables, which are not. Moreover, there was no agreement concerning the influence of other biological parameters as age, sex or refractive error when talking about MS.

2. Objective

The main objective of this work was to perform an in-depth descriptive and frequency analysis of interocular corneal MS in terms of magnitude and axis using power vectors, and to study its dependence on age, sex, and refraction in a large sample.

3. Methodology

The data were collected from 2974 healthy Caucasian subjects (63 ± 13 years; 62% females) who had undergone ocular evaluation at an ophthalmological center. Written consent was obtained from all participants for ocular evaluation, and we followed the guidelines outlined in the Declaration of Helsinki. Participants aged between 20 and 79 were included, except those who met any of the following exclusion criteria: presence of ocular disease, history of ocular surgery, use of contact lenses within one week prior to data collection, or incomplete data for one or both eyes. Non-cycloplegic refractive measurements were obtained with subjective refraction trial frame and trial lenses. Power from main meridians of corneal surface were obtained using an IOL Master 700 (Carl Zeiss Meditec, Germany). Results from subjective refraction and keratometry were converted into power vectors notation, according to Thibos et al. [4] To examine the interocular corneal MS, the power vectors relationship between the right eye (OD) and left eye (OS) had to correspond to the following equations:

$$J_0^{OD} - J_0^{OS} = \pm 0.25 \text{ D} \quad (1)$$

$$J_{45}^{OD} + J_{45}^{OS} = \pm 0.25 \text{ D} \quad (2)$$

Theoretically, perfect mirror symmetry would be found when the subtraction between OD and OS corneal astigmatism components were 0. Nevertheless, a difference of ± 0.25 D was set as a limit of tolerance. The main point of this conversion was to provide symmetry as a dichotomous variable. If this criterion was met, symmetry was described as 1, otherwise, a 0 was assessed.

Descriptive analysis for the variables under study were performed for each age, sex, and sphero-equivalent (SE) group. The sample was divided into six age groups according to the age: 20-29, 30-39, 40-49, 50-59, 60-69 and 70-79 years old. Concerning the sex, the sample was divided into males and females, and, regarding the SE, groups were classified as: emmetropia (between -0.5 D and +0.5 D), myopia (< -0.5 D) and hyperopia ($> +0.5$ D).

4. Results and discussion

Fig. 1 shows the prevalence of MS for each division of the sample. Prevalence of MS according to certain combinations of variables is shown in Fig. 2. Prevalence varies between 0.68 to 0.78 depending on the

classification of the sample. When the prevalence comes from a two-by-two comparison, the highest difference is found when studying age related to SE. However, this disparity of prevalence could be related to the difference of the sample size, since there is a high percentage of the sample over 60 years old.

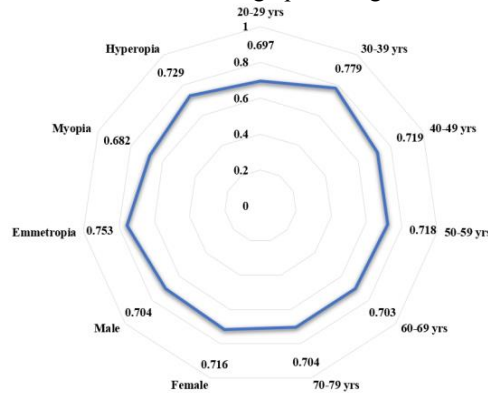


Figure 2 Prevalence of mirror symmetry according to different classifications.

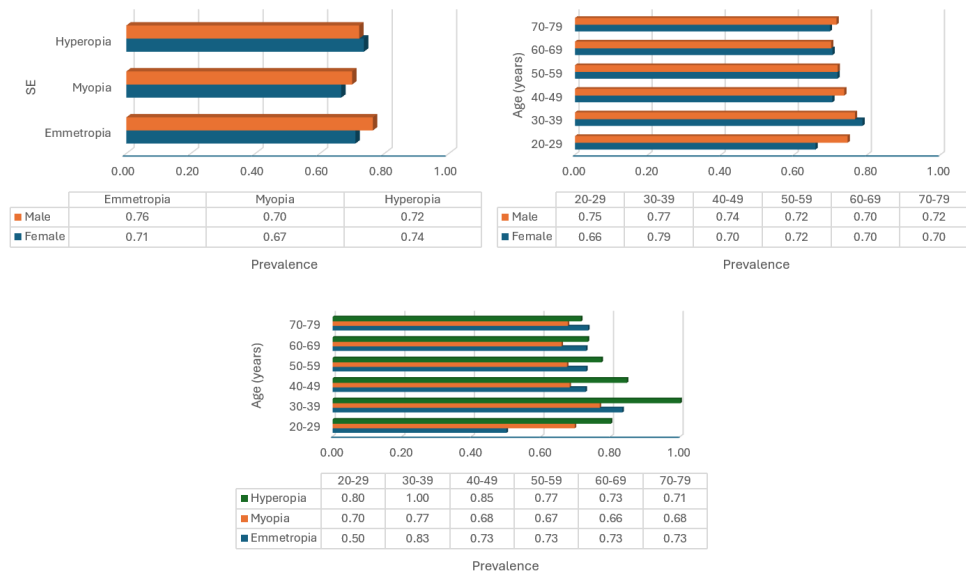


Figure 1 Two-by-two prevalence of mirror symmetry.

5. Conclusions

This model provides a prevalence of MS around 70.9% of the total sample. This fact implies that corneal astigmatism presents MS when considering magnitude and orientation and coincides with the results presented by previous research. [2,3] No important differences can be found when dividing the sample according to age, sex, or SE. Future research could focus on the statistical significance of our results.

Acknowledgments

Authors acknowledge the grant FPU (FPU20/05624) from the Spanish Ministerio de Universidades to RSR.

References

- [1] Corballis MC. "Bilaterally Symmetrical: To Be or Not to Be?", *Symmetry*. 12, 326 (2020)
- [2] Asharlou A et al. "Comprehensive profile of bilateral astigmatism: rule similarity and symmetry patterns of the axes in the fellow eyes", *Ophthalmic Physiol Opt*. 37, 33-41 (2017).
- [3] Mahmood F et al. "Rule similarity and axis symmetry patterns in young patients with bilateral astigmatism". *J Pak Med Assoc*. 72, 42-46 (2022).
- [4] Thibos LN et al. "Power vectors: An application of Fourier analysis to the description and statistical analysis of refractive error", *Optom Vis Sci*. 74, 367-375 (1997).

Objective Assessment of Fusional Vergence Amplitude: Feasibility and Impact of Vision Therapy

Cristina Rovira-Gay*, Clara Mestre, Marc Argiles, Luís Pérez-Mañá and Jaume Pujol

*Centre for Sensors, Instruments, and Systems Development (CD6). Universitat Politècnica de Catalunya
Rambla Sant Neblidi 10, 08222 Terrassa, Barcelona, Spain.*

*E-mail: cristina.rovira@upc.edu

1. Introduction

The fusional vergence test is a crucial diagnostic tool in optometric clinical practice for assessing binocular function and diagnosing binocular vision dysfunctions[1]. Base-in prisms are used to elicit divergence, and measure negative fusional vergence (NFV) amplitudes, while base-out prisms are employed to elicit convergence and measure positive fusional vergence (PFV) amplitudes. The fusional vergence test consists in gradually increasing the vergence demand until fusion is disrupted, identifying the "break point". Then, the vergence demand is reduced until fusion is restored and the patient reports single vision. The prism power at this point is the "recovery point"[2].

The fusional vergence evaluation can be done in clinics using two tests: the step vergence test, performed using a prism bar to induce disparity, or the smooth vergence test, using rotatory Risley prisms[3]. Both tests are subjective, as results rely on the patient's responses and/or examiner's criteria, their repeatability is poor, and cannot be used interchangeably due to their low level of agreement[4]. The subjectivity of these tests is an important clinical limitation that can be solved using eye-tracking systems[4]. Objective recordings of vergence eye movements offer a more detailed characterization of the fusional vergence test. In addition, they allow to monitor objectively and accurately the effects of vision therapy protocols, which is not possible with conventional clinical methods.

The goal of this study was to analyze the agreement between an objective method using an eye-tracker and the smooth vergence test to evaluate NFV and PFV amplitudes at near. After the implementation of this new test, this approach was used to objectively evaluate the changes in PFV and NFV break point in binocularly and accommodative normal individuals after performing 12 weeks of a classic vision therapy protocol.

2. Methods

First, the agreement between the smooth vergence test and the objective method to measure fusional vergence amplitudes was evaluated in 49 young adults (23±3 years). Then, a total of 32 young adults (24±4 years) were randomly classified into an experimental group (N=16), who did 12 sessions of 45-min sessions of office-based binocular vision therapy for 12 weeks, or a control group (N=16), who did 12 sessions of 15-min sessions of office-based therapy based on eye movements exercises in the frontal plane for 12 weeks. Participants' fusional vergences were measured objectively before starting the vision therapy and at the end of the protocol. To do so, the fusional vergence test was implemented in an haploscopic system that included an EyeLink 1000 Plus (SR Research Ltd.) to measure eye movements at a sampling rate of 500 Hz (Figure 1a). The visual stimulus was a column of 0.20 LogMAR letters.

Fusional convergence and divergence movements were driven by changing the stimuli position synchronously in the two screens from the baseline position (0 prism dioptres, PD) to a demand of 45 PD of convergence and divergence at 1 PD/s to mimic the stimulation with the rotatory Risley prisms. After reaching the maximum vergence demand, stimulus disparity was decreased at the same velocity until the baseline position (Figure 1b). Each fusional vergence sign was tested three times, with a brief break in between to minimize the potential for fatigue. Each repetition took 90 s.

To determine the agreement between tests, PFV and NFV amplitudes were measured at near (40 cm) with the smooth subjective test, as typically done in clinics, and with the smooth objective test. The fixation target used for both tests was a column of 0.20 LogMAR letters.

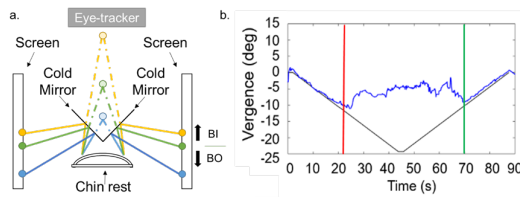


Figure 1 a. Schematic representation of the haploscopic system used in the study. The three circles in each screen represent three different stimulus positions. **b.** Example of vergence movements measured during a negative fusional vergence amplitude measure (in blue). The vergence demand driven by the stimuli is shown in black. The red and green vertical lines represent the time of the objective break and recovery points determined objectively with a custom algorithm [4].

3. Results

A better agreement between tests was found for the measurement of NFV than for PFV. Despite being statistically significant, differences between tests to measure NFV were not clinically significant. The mean \pm SD of the differences in the NFV break and recovery points was -1.74 ± 3.35 PD ($p < 0.001$) and -1.97 ± 2.60 PD ($p = 0.008$), respectively. The means of the PFV break and recovery points were 0.31 ± 6.44 PD, ($p < 0.001$) and -2.84 ± 7.01 PD, ($p < 0.001$), respectively.

Before starting the vision therapy protocol, the two groups did not show statistically significant differences in NFV ($p = 0.578$) and in PFV ($p = 0.650$). Considering the results obtained before and after the 12 weeks of therapy for the experimental group and for the control group, there was no significant effect of vision therapy on NFV and PFV amplitudes ($p = 0.338$ and $p = 0.070$, respectively). (Table 1).

	Control Group		Experimental Group	
	Baseline evaluation	Follow-up evaluation	Baseline evaluation	Follow-up evaluation
NFV break point (PD)	13.06 \pm 4.01	12.58 \pm 4.17	13.80 \pm 4.22	14.74 \pm 3.27
PFV break point (PD)	35.84 \pm 10.70	36.60 \pm 12.91	38.57 \pm 8.80	45.00 \pm 0.00

Table 1 Mean \pm standard deviation of Negative Fusional Vergence (NFV) and Positive Fusional Vergence (PFV) amplitudes measured with the objective test before (baseline evaluation) and after 12 weeks (follow-up evaluation) of vision therapy. Prism diopters: PD.

4. Conclusions

This study offers a new perspective on the potential for evaluating fusional vergence amplitudes in individuals with normal binocular vision. However, the objective and the subjective tests cannot be used interchangeably due to their relatively poor agreement. Moreover, the objective method used in this study seems to be useful to monitor the potential effects of vision therapy on binocular vision, although the change in fusional vergence amplitudes over time in both the control group and the experimental group did not reach statistical significance. Clinicians may consider these results in future therapeutic interventions to train vergence skills in individuals with typical binocular vision. This could be relevant in areas such as vergence training in sports vision, or in cases of ocular symptomatology related to digital eye strain syndrome without any other binocular dysfunctions.

Acknowledgments

This publication is part of the project PID2020-112527RB-I00 and TED2021-130409B-C54, funded by MCIN/AEI/10.13039/501100011033 and the European Union through the "NextGenerationEU"/PRTR.

References

- [1.] M. M. Scheiman and B. Wick, *Clinical Management of Binocular Vision. Heterophoric, Accommodative, and Eye Movement Disorders* (Lippincott Williams & Wilkins, 2014).
- [2.] I. P. Howard, "Vergence eye movements," in *Perceiving in Depth: Volume 1 Basic Mechanisms* (Oxford University Press, 2012), pp. 475–548.
- [3.] C. C. Lança and F. J. Rowe, "Measurement of fusional vergence: a systematic review," *Strabismus* **27**(2), 88–113 (2019).
- [4.] C. Rovira-Gay, C. Mestre, M. Argiles, V. Vinuela-Navarro, and J. Pujol, "Feasibility of measuring fusional vergence amplitudes objectively," *PLOS ONE* **18**(5), e0284552 (2023).

Smartglasses for see-through visual correction using economical Spatial Light Modulators

Víctor Vázquez, Alba M. Paniagua-Díaz, Pablo Artal

Laboratorio de Óptica, Centro de Investigación en Óptica y Nanofísica (CIOyN), Universidad de Murcia, Campus de Espinardo (Ed. 34), 30010 Murcia, Spain.

*E-mail: victor.vazquezl@um.es

1. Introduction

In the last decades, the concept of Adaptive Optics has been expanded to the optics and ophthalmology fields [1], developing key techniques for the correction of refractive errors, like myopia, hyperopia, astigmatism and more complex optical aberrations. This allows the personalization of visual correction in a more precise way, adapting it to the unique characteristics of the eye of every patient.

Making use of these techniques, the development of smartglasses capable of modifying their properties is being carried out, demonstrating its potential for defocus correction using economical Spatial Light Modulators (SLM), opening the path to more complex high order aberration correction.

In this work we development and calibrate a smartglasses prototype, with which we'll be able to realize the defocus correction of a see-through image distorted by trial lenses of different power.

2. Methods

2.1 Experimental configuration

Figure 1 shows the setup used to modulate light making use of an SLM consisting of a double pass through the two halves of a VA-LCoS device for an efficient phase modulation [2, 3]. The light goes through a 45° polarizer before entering the system, coinciding with the optical axis of the SLM. The red line in Fig.1a represents the light path. The SLM (13) is optically conjugated with the entrance pupil of the system (4) and the eye's pupil (16), by means of two 4f systems (formed by lenses 6-7 and 14-15). The red dashed lines represent an extra 4f system in a different axis, where the two halves of the modulator are optically conjugated for phase summation [2]. For the systems tests, we placed a camera in the eye's position (Fig.1c). The image reaching the camera is distorted by internal aberrations of the system.

2.2 Correction tests

Using a screen placed at the entrance of the system, a test image is displayed. It is defocused using trial lenses placed at the first conjugated plane, and then it is corrected by the SLM.

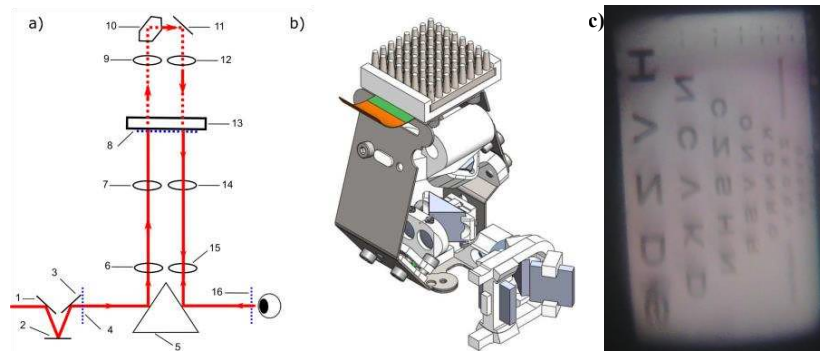


Figure 1. a) Optical setup for the phase-modulation testing with a VA-LCoS device. The conjugated planes are depicted by the dashed blue line. b) 3D design of the device. c) Test image displayed by the screen.

3. Results

The obtained results are satisfactory, we demonstrate the potential of this economical device for the phase modulation and correction of see-through images. However, there is also a considerable loss of contrast, intensity and sharpness that can be due to the multiple reflections and aberrations that occur inside the system in this design.

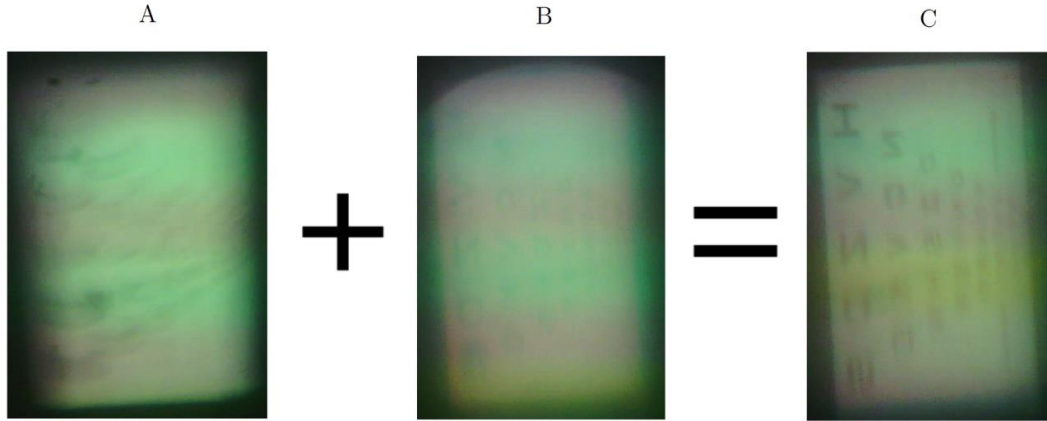


Figure 2. The first image is the test image blurred by a 4D trial lens, the second image represents the test image blurred by a -4D generated by the SLM, and the third image is the combination of both effects, where defocus is cancelled, thus performing the correction.

4. Conclusions

We demonstrate the capability of an economical SLM, arranged in a double pass through the two halves of a vertically-aligned liquid crystal on silicon device as SLM, to correct defocus through different trial lenses, opening new possibilities for wearable and affordable smartglasses based on phase modulation devices for the correction of low and high order ocular aberrations.

This system has some limitations as well. A different optical design should be performed in order to minimize the internal aberrations of the system, the blocking of undesired reflections and the loss of intensity inside the optical path.

References

- [1] Marcos, S., Werner, J. S., Burns, S. A., Merigan, W. H., Artal, P., Atchison, D. A., ... & Sincich, L. C. (2017). Vision science and adaptive optics, the state of the field. *Vision research*, 132, 3-33.
- [2] Arias, A., Paniagua-Diaz, A. M., Prieto, P. M., Roca, J., & Artal, P. (2020). Phase-only modulation with two vertical aligned liquid crystal devices. *Optics Express*, 28(23), 34180-34189.
- [3] Paniagua-Diaz, A. M., Mompeán, J., & Artal, P. (2022). Vertical-aligned liquid crystal devices for ocular wavefront correction and simulation. *Optical Engineering*, 61(12), 121806-121806.

Diseño multi-tórico para corregir el astigmatismo ocular regular con mayor tolerancia a la rotación

Diana Gargallo^{1*}, Anabel Martínez-Espert¹, Sara Perchés¹, Victoria Collados¹, Laura Remón Martín¹ y Jorge Ares¹

¹Departamento de física aplicada, Facultad de Ciencias, Universidad de Zaragoza, Zaragoza.

²Departamento de Óptica y Optometría y Ciencias de la Visión, Universitat de València, Burjassot.

*E-mail: dgargallo@unizar.es

1. Introducción

Las ametropías regulares, tales como la miopía, la hipermetropía y el astigmatismo regular, pueden ser eficazmente corregidas mediante el uso de lentes esfero-cilíndricas (S-C) convencionales, siempre y cuando se logre una alineación adecuada entre el eje de la lente y el error refractivo del ojo. Sin embargo, alcanzar una alineación estable del eje con lentes S-C, especialmente en el caso de lentes de contacto, sigue siendo un desafío en la actualidad. Las lentes de contacto requieren cierto movimiento en el ojo, lo que puede resultar en un desalineamiento del eje corrector y por consiguiente, una degradación de la calidad visual [1]. Las soluciones actuales, como el uso primas balastrados o la estabilización dinámica, introducen complejidades adicionales y pueden ocasionar incomodidad al portador. Además, estas soluciones no garantizan una alineación perfecta, pudiendo observarse desalineaciones de hasta 7° [2].

Este trabajo introduce un diseño óptico multi-zonal novedoso para lentes de contacto [3] caracterizado por la presencia de regiones anulares concéntricas con distintas potencias S-C. Al variar las orientaciones de los ejes cilíndricos entre estas regiones, el objetivo es asegurar que al menos una zona se alinee correctamente a pesar de los movimientos de la lente. Este enfoque innovador promete una calidad visual superior al aumentar la tolerancia a las desalineaciones angulares, superando las limitaciones asociadas a las lentes tóricas o cilíndricas convencionales.

2. Metodología

La Figura 1 ilustra el nuevo elemento trizonal multi-tórico (TMT) propuesto (Fig. 1(b)) en comparación con una lente S-C convencional (Fig. 1(a)). Para este estudio, el diseño se configuró con una zona central de radio de 1.40 mm, una zona en media periferia con un radio de 1.87 mm y una zona periférica con un radio de 2.25 mm. En términos de potencia S-C, la zona central presenta la prescripción nominal de S-C alineada (S-C_N0), la zona en media periferia presenta la misma potencia S-C con una posición rotada en sentido horario (CW) de -5.00° para el eje del cilindro (S-C_CW5), y la zona más periférica tiene una posición rotada en sentido antihorario (CCW) de +5.00° (S-C_CCW5).

Para evaluar dicho elemento, se realizó un estudio clínico de doble ciego que incluyó 16 ojos, utilizando el simulador visual de óptica adaptativa (VAO, Voptica SL, Murcia, España). Se midió la Agudeza Visual (AV) LogMAR colocando simultáneamente la compensación refractiva de cada paciente, la ametropía astigmática inducida (-3.50 D × 180°) y el diseño convencional o multi-tórico sin rotar y rotado tanto en sentido horario como en sentido antihorario ciertos grados.

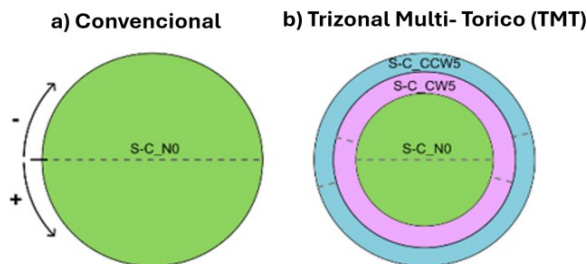


Figura 1. (a) Diseño esféricocilíndrico convencional (S-C). (b) Diseño multitórico trizonal (TMT). La línea punteada indica la dirección del eje del cilindro negativo.

3. Resultados

La Tabla 1 resume la AV media y la desviación estándar (SD) con cada elemento y rotación (se consideró el promedio entre rotaciones de sentido horario y antihorario ya que no se encontraron diferencias estadísticamente significativas entre ambas direcciones). Los resultados muestran que si la lente está correctamente alineada con el eje de la compensación S-C del paciente, la AV es mejor con el diseño tórico convencional en comparación con el diseño TMT (diferencia estadísticamente significativa, $p < 0.05$). Sin embargo, una vez que rota, la AV promedio con el diseño convencional disminuyó de -0.07 en el eje a $+0.13$ con 7.50° de rotación. En contraste, para el diseño TMT, la AV media pasa de $+0.01$ en el eje a $+0.07$ con un error de rotación de 7.50° .

Rot	Visual Acuity (logMAR)	
	Torico convencional	TMT
En eje	-0.07 ± 0.07	$+0.01 \pm 0.07$
$ 2.50^\circ $	-0.02 ± 0.04	$+0.00 \pm 0.05$
$ 5.00^\circ $	$+0.05 \pm 0.05$	$+0.02 \pm 0.05$
$ 7.50^\circ $	$+0.13 \pm 0.05$	$+0.07 \pm 0.06$

Table 1. Agudeza visual (media \pm SD) para todos los diseños y rotaciones. Rot: Rotación. TMT: Trizonal Multi-tórico.

4. Conclusiones

En conclusión, este estudio clínico ha demostrado que los nuevos diseños multi-tóricos proporcionan una calidad de imagen aceptable y estable en comparación con el diseño convencional cuando existe una rotación de la lente de hasta 7.50° . Considerando estos hallazgos, los diseños multi-tóricos propuestos parecen constituir una alternativa interesante para abordar el astigmatismo regular, mostrando una mayor tolerancia ante posibles errores de desalineación rotacional.

Agradecimientos

Gobierno de Aragón (E44-23R); Ministerio de Ciencia, Innovación y Universidades (PID2020-114311RA-I00).

Referencias

- [1] S. A. Read, S. J. Vincent, and M. J. Collins, "The visual and functional impacts of astigmatism and its clinical management," *Ophthalmic Physiol. Opt.*, vol. 34, no. 3, pp. 267–294, 2014
- [2] Young G, Hunt C, Covey M., Clinical evaluation of factors influencing toric soft contact lens fit. *Optom Vis Sci* 2002;79:11–9.
- [3] Diana Gargallo, Anabel Martínez-Espert, Sara Perches, M. Victoria Collados, Laura Remón Martín, and Jorge Ares, "Multi-toric optical element to compensate ocular astigmatism with increased tolerance under rotation," *Opt. Lett.* 49, 2289-2292 (2024)

Análisis comparativo de la medición de la curvatura corneal entre diferentes instrumentos

Esther Perales^{1,2*}, Eduardo Lajarín¹, Aurora Larrosa¹, Julián Espinosa^{1,2}

¹Departamento de Óptica, Anatomía y Farmacología, Universidad de Alicante.

²IUFACyT, Universidad de Alicante, Carretera de San Vicente del Raspeig, s/n. San Vicente del Raspeig - Alicante

*E-mail: esther.perales@ua.es

1. Introducción

La medición de la curvatura corneal es necesaria en muchos aspectos de la optometría y la oftalmología, ya sea para la adaptación de lentes de contacto, cirugías refractivas como implantación de lentes intraoculares o el diagnóstico de algunas patologías, como el síndrome de Marfan (SMF) [1, 2]. Tradicionalmente esta medida se hacía con queratómetros manuales que con el tiempo dieron paso a los auto-queratómetros y topógrafos basados en los anillos de Plácido. Más tarde, aparecieron en el mercado otros instrumentos basados en la cámara de Scheimpflug o modificaciones de los topógrafos basados en los anillos de Plácido como sería el caso del topógrafo de cono estrecho. Así, actualmente, el espesor corneal y la curvatura y astigmatismo corneal pueden medirse con diferentes dispositivos. En particular, el instrumento denominado *Pentacam* ha sido ampliamente utilizado en clínica y su precisión ha sido verificada. Este instrumento está basado en una cámara Scheimpflug giratoria de alta resolución para proporcionar escaneos transversales de imágenes que evalúan los parámetros corneales. Sin embargo, no todas las clínicas o gabinetes optométricos cuentan con este equipo, habiendo otros instrumentos basados en tecnología distinta y por tanto que proporcionen diferentes medidas de los radios de curvatura de la córnea. El objetivo de este trabajo es evaluar la concordancia entre la medida del radio de curvatura entre 4 instrumentos diferentes: un queratómetro de Hemholtz, la multiplataforma Visionix VX 650, el topógrafo de Medmont y el Pentacam.

2. Materiales y métodos

En este estudio 31 sujetos han sido incluidos. Se han descartado sujetos con patologías corneales conocidas, que se hayan realizado algún tipo de cirugía refractiva o que hayan sido portadores de lentes de contacto en los días anteriores a las medidas. Todos los sujetos han sido medidos, de ambos ojos, con los cuatro instrumentos que se pretenden comparar en el estudio por el mismo examinador. Los sujetos estaban previamente informados siguiendo las recomendaciones del comité de ética de la Universidad de Alicante y la ley de protección de datos.

Una vez medido el radio de curvatura de todos los sujetos, se procedió a un análisis estadístico para conocer si existían diferencias significativas entre instrumentos. De manera aleatoria, se seleccionó uno de los ojos de cada sujeto para el análisis estadístico, y sólo se consideró para este análisis el radio horizontal, puesto que se asume que ambos radios están correlacionados. Todo el análisis estadístico se realizó con el programa MATLAB®. A continuación, se comprobó si los datos experimentales seguían una distribución normal. Este estudio se realizó mediante la gráfica de probabilidad normal, de forma que si los datos siguen una distribución lineal nos indica que los datos siguen una distribución normal. Además, el análisis de la distribución normal también se realizó de forma más analítica mediante el test Lilliefors. Una vez comprobada la normalidad de los datos experimentales, se realizó un análisis de varianza (ANOVA) de dos factores: tipo de instrumento y sujeto para comprobar si las medidas del radio de curvatura eran significativamente diferentes.

3. Resultados y discusión

En primer lugar, se comprobó que los datos experimentales siguen una distribución normal tal como se ha comentado anteriormente. A continuación, se realizó el ANOVA.

En la tabla 1 se muestran los resultados del ANOVA realizado. Teniendo en cuenta, los p-values obtenidos puede decirse que tienen efecto sujeto e instrumento, pero no hay evidencia de una interacción sujeto-instrumento (p_value = 0.0669). Que el sujeto tenga un efecto en la medida del radio de curvatura es lo esperado, puesto que la curvatura corneal depende del sujeto. Sin embargo, que el instrumento tenga

un efecto en la medida de la curvatura corneal implica que existen diferencias significativas entre instrumentos y, por tanto, las medidas no serían comparables o intercambiables entre dispositivos.

Tabla 1. Resultados del análisis estadístico ANOVA

TABLA ANOVA					
Fuente	ss	df	MS	F	Prob > F
Instrumento	0.2108	3	0.07027	19.22	0
Sujeto	21.6816	30	0.72272	197.66	0
Interacción	0.4233	90	0.0047	1.29	0.06699
Error	0.9068	248	0.00366		
Total	23.2225	371			

En la Figura 1, se muestra la comparación múltiple de los valores medios de los radios de curvatura con la desviación estándar correspondiente para los 4 instrumentos evaluados (1: queratómetro de Helmholtz; 2: Visionix; 3: topógrafo de Medmont; 4: Pentacam). De forma predeterminada, el valor medio del grupo 1 se resalta y el intervalo de comparación está en azul. Debido a que los intervalos de comparación para los otros tres grupos no se cruzan con los intervalos para el grupo 1 se resaltan en rojo. Esta falta de intersección indica que estos valores medios son diferentes del valor medio del grupo 1. Por tanto, las medidas realizadas con el queratómetro convencional serían las más diferentes estadísticamente al resto de instrumentos. Por otro lado, también se puede observar que no existen diferencias significativas entre el Visionix y el topógrafo de Medmont, o entre el Pentacam y el topógrafo de Medmont, mientras que las medidas entre el Visionix y el Pentacam no son intercambiables. Si asumimos que el Pentacam es el “gold standard” el único instrumento comparable a este instrumento en cuanto a la medida de la curvatura corneal sería el topógrafo de Medmont.

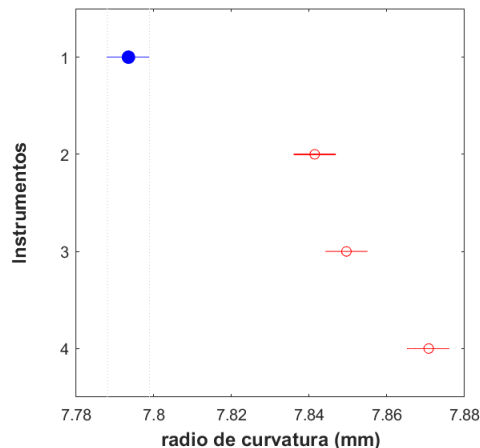


Figura 1. Comparación múltiple de los valores medios de los radios de curvatura con la desviación estándar correspondiente para los 4 instrumentos evaluados (1: queratómetro de Helmholtz; 2: Visionix; 3: topógrafo de Medmont; 4: Pentacam).

4. Conclusiones

Mediante un análisis comparativo de la medición de la curvatura corneal entre diferentes instrumentos se ha comprobado que existen diferencias significativas en las medidas entre los 4 instrumentos evaluados y por tanto, las medidas no son intercambiables entre dispositivos. Si se asume que el Pentacam es el “gold standard” el único instrumento comparable a este instrumento en cuanto a la medida de la curvatura corneal sería el topógrafo de Medmont.

Referencias

- [1] G. M. Jin, B. Xiao, Y. J., Zhou, Y. Y., Wang, X. Li, & D. Y. Zheng, (2020). Agreement of corneal curvature and central corneal thickness obtained from a swept-source OCT and Pentacam in ectopia lentis patients. *International Journal of Ophthalmology*, 13(8), 1244.
- [2] Chen J, Jing Q, Tang Y, Qian D, Lu Y, Jiang Y. Corneal curvature, astigmatism, and aberrations in Marfan syndrome with lens subluxation: evaluation by pentacam HR system. *Scientific Reports*, 8(1), 4079. 2018;8(1):4079.

The influence of disability glare and surround contrast on temporal contrast sensitivity

Pilar Casado^{1*}, Victoria Collados¹, Francisco Avila¹ and Jorge Ares¹

¹*Applied Physic, University of Zaragoza, Calle Pedro Cerbuna, Zaragoza, Spain*

*E-mail: pilarcasado@unizar.es

1. Introduction

In an optical system, straylight relates to light redirected by the process of light scattering. The human eye is not exempt from this phenomenon: when light passes through the ocular media, it is scattered, causing a veil of light that is superimposed on the retinal image, decreasing its spatial contrast. The negative effect of straylight on vision is known as disability glare [1].

Although straylight is known to produce a loss in spatial contrast sensitivity [2], little is known about its effects on the temporal abilities of the visual system. One of the tests used to assess temporal abilities is the measurement of temporal contrast sensitivity (TCS). However, this test has been shown to have a significant dependence on the stimulus parameters used for its measurement, including stimulus size, luminance, eccentricity, and stimulus surround [3]. In a previous study, we demonstrated how the TCS increased linearly with the luminance of the surround for a temporal frequency of 4 Hz and quadratically for a frequency of 20 Hz. Furthermore, the dependence of the TCS on the contrast between the stimulus and its surround (C_{ss}) was found to be linear for both frequencies [4].

Therefore, the aim of this work is to assess whether the previously found dependence between TCS and C_{ss} remains for different levels of disability glare.

2. Methods

This preliminary study was conducted on only two subjects. The system used for the measurement, shown in Figure 1, allows displaying a visual stimulus while the subject's eye is illuminated. The glare source is a white light source with an annular shape and a central circular occluder. For the measurement of the TCS, defined as the inverse of the threshold temporal contrast, a stimulus consisting of a red fixation point and two semicircles was used. During stimulus presentation, one of the circles remains static while the other flickers between two luminance levels. Both the luminance of the static semicircle and the average luminance of the flickering semicircle were 138 nt. The field of view subtended by the stimulus through the optical system was 3.2° and that of the occluder 6° , so the appearance of the stimulus and source through the system is as Figure 1b shows.

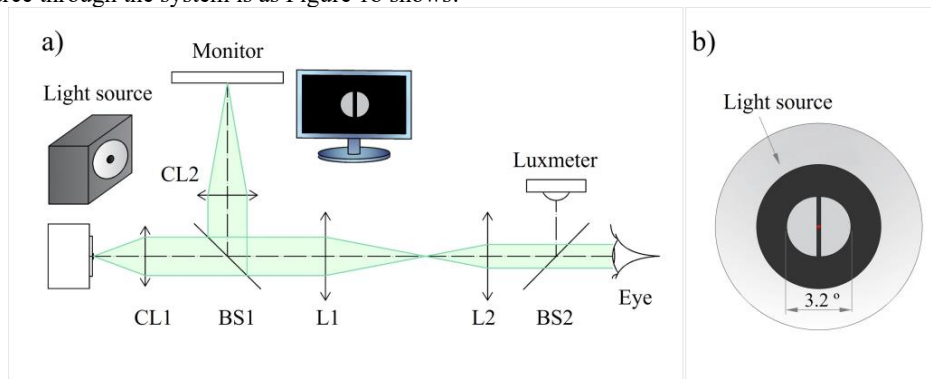


Figure 1 Fig. 1. a) Schematic of the optical system. b) Stimulus appearance through the optical system.

A 2-Alternative Forced Choice task and a QUEST algorithm [5] programmed in Matlab R2017a with the Psychtoolbox package (PTB-3) were used to measure the TCS [6]. The procedure was performed for three illuminance levels at the corneal plane (0, 50, and 200 lx) and for different C_{ss} : 1, 0.75, 0.5, 0.25, 0.1, -0.1, and -0.25. Additionally, it was carried out for two temporal frequencies: 4 and 20 Hz.

3. Results

Figure 2 shows the average TCS results obtained for the frequency of 4 Hz and 20 Hz. For an illuminance level of 0 lx, TCS increases as C_{ss} decreases, as we have observed in previous results [4]. However, TCS decreases again for negative contrasts, where the surround is brighter than the stimulus. Moreover, the TCS values for 0.25 and 0.1 are similar to those of -0.25 and -0.1. For an illuminance level of 50 lx, akin to 0 lx, the TCS increases as the C_{ss} decreases, but less noticeably. It should be noted that, for high contrasts (1 and 0.75), an increase in TCS is found for 50 lx compared to the values obtained for 0 lx. In the case of higher disability glare, 200 lx, the TCS remains nearly constant regardless of the change in C_{ss} .

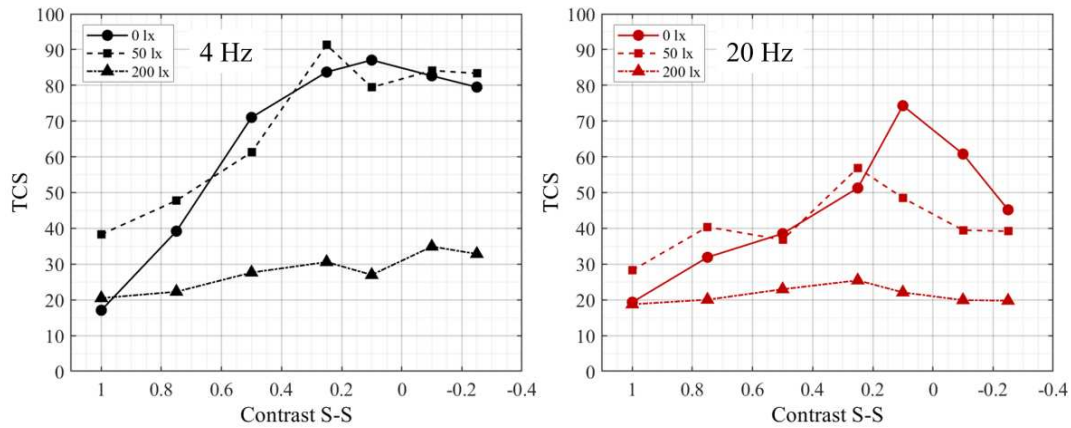


Figure 2 TCS as a function of the C_{ss} for different illuminance levels for a temporal frequency of 4 Hz (left), and 20 Hz (right).

4. Conclusions

We present a preliminary study that assesses the effect of different levels of disability glare on the dependence of the TCS on the contrast between the stimulus and the surround. Our results show that the TCS depends solely on the C_{ss} and not on the luminance of the surround, contrary to what we thought when we conducted the aforementioned study. For an illuminance level of 50 lx, it was found that, when the C_{ss} is high, the TCS is greater than the value obtained without the glare source. Moreover, for high disability glare conditions, the dependence between TCS and C_{ss} is no longer present, remaining at a low value.

Acknowledgments

This research was supported by Ministerio de Ciencia, Innovación y Universidades (Grant PID2020-114311RA-I00), and Gobierno de Aragón (Grant E44- 20R). P.C. was supported by Gobierno de Aragón.

References

- [1] T.J. Van den Berg, L. Franssen, B. Kruijt and J.E. Coppens. "History of ocular straylight measurement: A review". *Z Med Phys* **23**, 6 – 20 (2013).
- [2] T. J. T. P. van den Berg, L. Franssen, and J. E. Coppens, "Ocular media clarity and straylight," in *Encyclopedia of the Eye* (Elsevier/Academic Press, 2010).
- [3] U. Keeseey. "Variables determining flicker sensitivity in small fields". *J Opt Soc Am* **60** (3), 390-398. (1970).
- [4] P. Casado, V. Collados, F. Ávila and J. Ares. "The effect of stimulus background luminance on temporal contrast sensitivity", in Eleventh meeting on Visual & Physiological Optics (2023).
- [5] A.B. Watson, D.G. Pelli. "QUEST: a Bayesian adaptive psychometric method". *Percept Psychophys* **33**(2), 113-120 (1983).
- [6] M. Kleiner, D.H. Brainard, D. Pelli, A. Ingling, R. Murray, C. Broussard. "What's new in Psychtoolbox-3". *Perception* **36**, 1-6 (2007).

A bibliometric analysis of vision science

Mikel Aldaba

*Centre for Sensors, Instruments and Systems Development, Universitat Politècnica de Catalunya,
Terrassa, Catalunya, Spain.*

*E-mail: mikel.aldaba@upc.edu

1. Introduction.

Research in the field of vision science has a long tradition in Spain, with notable contributions such as studies on night myopia [1] or the development of the double-pass technique [2]. Over the time, reviews have been conducted to understand its historical evolution [3]. However, to describe the current state of research in the field, there is not enough perspective, necessitating the use of other tools such as bibliometric analysis [4]. The objective of this study is to conduct a bibliometric analysis of research in vision science in Spain spanning the last few decades.

2. Material and Methods

Authors contributing to the Vision Science Symposium at the National Optics Meeting (RNO), editions of 2018 and 2021, and the Biophotonics Eye Research 2023 were identified. Each author's ORCID code was retrieved. A query was conducted in the Web of Science database to obtain the contributions of all the authors, and complete bibliographic data were exported. Results were filtered to include only scientific articles written in English and Spanish. Additionally, a manual filtering of authors not working in the field of vision science was performed. To study the most relevant contributions from the obtained database, a second database was created containing the top 10% of most cited publications for each year. Furthermore, for comparative purposes, two databases of 1.000 randomly selected scientific articles published in the Web of Science categories of optics and ophthalmology for the same time period were generated. Bibliometric analysis was conducted using the Web of Science Analysis tool, Biblioshiny [5], and Vosviewer [6].

3. Results

A total of 132 authors were identified in the Web of Science query, resulting in a total of 1.817 contributions (187 for the database of 10% top publications) between 1981 and 2023. Table 1 summarizes the most relevant data from the four databases used: Vision Science (VisSci), top 10% of Vision Science (VisSci_10%), Optics, and Ophthalmology (Ophth).

	VisSci	VisSci_10%	Optics	Ophth
Sources (Journals)	271	57	99	97
Most relevant source	BOEx	JOSA-A	Optik	IOVS
Annual production	42.25	4.79	21.55	21.51
Annual Growth Rate (%)	8.07	6.51	4.25	3.65
Average citations per doc	23.33	88.11	15.91	23.54
Single-authored docs (%)	1.98	2.67	9.39	4.64
Co-Authors per Doc	6.55	14.7	4.57	4.65
International co-authorships (%)	30.99	36.9	33.87	17.62
Annual Citation per year	1.45	5.75	1.12	1.47
h-index	88	80	51	77

Table 1 Bibliometric results.

Figure 1 displays the trend topics over time based on the keywords defined by the authors, while Figure 2 illustrates the collaboration network from the co-authorship analysis of the articles.

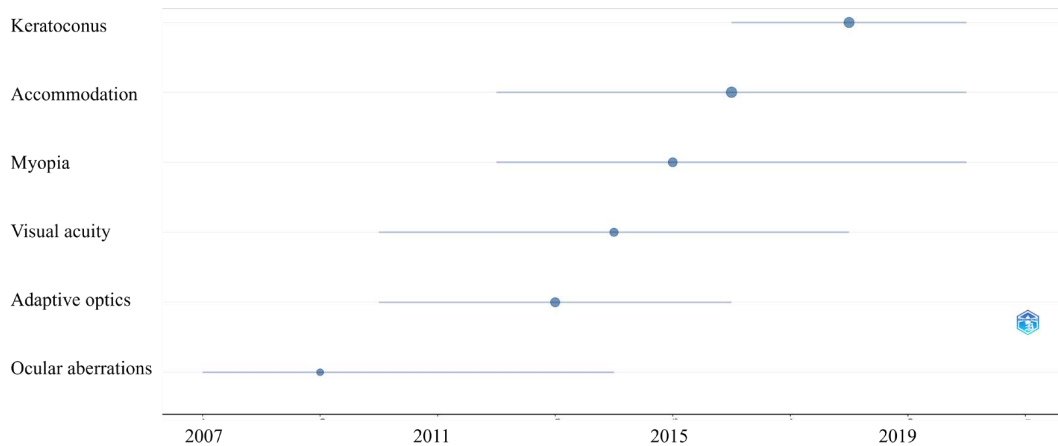


Figure 1 Trend topics over time based on keywords defined by authors.

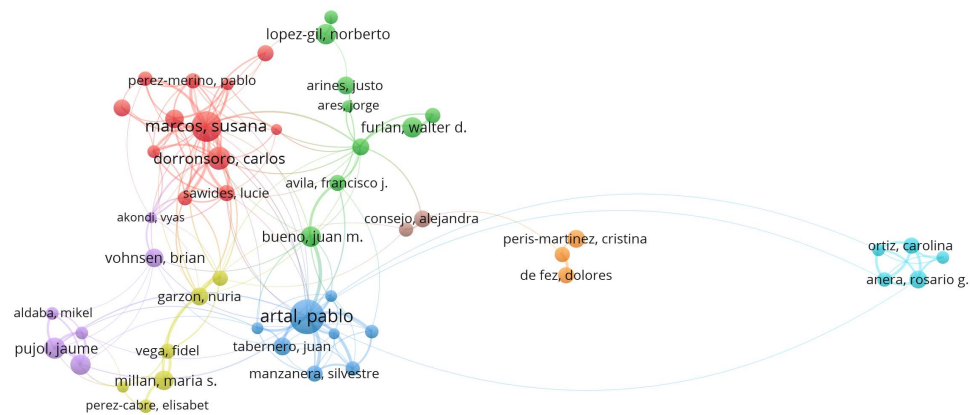


Figure 2 Collaboration network derived from co-authorship analysis.

4. Conclusions

The field of vision science is still active in Spain, with approximately one hundred researchers divided into about ten nodes. Research topics have evolved over time, and currently seem closer to ophthalmology than to optics. In comparison with these two fields, the performance of publications in the field of vision science is equal if not better, despite being a much smaller field of knowledge.

References

- [1] J. M. Otero, L. Plaza, and F. Salaverri, "Absolute thresholds and night myopia". *JOSA*, 39(2), 167-172 (1949).
- [2] J. Santamaría, P. Artal and J. Bescós, "Determination of the point-spread function of human eyes using a hybrid optical-digital method" *JOSA A*, 4(6), 1109-1114 (1987).
- [3] S. Marcos, P. Artal, J. Santamaría, M. Aguilar and L. Plaza, "Investigación en Optica Fisiologica en España" *Opt. Pura Apl.* 39 (3) 189-197 (2006).
- [4] A. Ninkov, J. R. Frank, and L. A. Maggio, "Bibliometrics: methods for studying academic publishing" *Perspectives on medical education*, 11(3), 173-176 (2022).
- [5] M. Aria, and C. Cuccurullo, "bibliometrix: An R-tool for comprehensive science mapping analysis", *Journal of Informetrics*, 11(4), pp 959-975, (2017).
- [6] N. Van Eck, and L. Waltman, "Software survey: VOSviewer, a computer program for bibliometric mapping", *Scientometrics*, 84(2), 523-538 (2010)

Effect of monocular diffusion or defocus on stereo acuity

Espinosa E.¹, Farcas I.A.^{1,2}, Tabernero J.^{1,2}, Benito A.^{1*}

¹ Laboratorio de Óptica, Universidad de Murcia, campus de Espinardo (Murcia).

² Departamento de Electromagnetismo y Electrónica, Universidad de Murcia, campus de Espinardo (Murcia).

*Email: abenito@um.es

1. Introduction and Methods

The minimum perceptible binocular angular difference, or stereoacuity, was measured in seconds of arc (StrAV; ") in a group of Optometry students (n=30; 53% female) using an autostereoscopic 3D tablet (*Commander 3D*; Freevi Corp., Las Vegas) running the ASTEROID v1.0 stereotest (Fig. 1). This test, utilizing a forced-choice method, allows for precise estimation without the additional use of lenses or filters. Baseline values were obtained for emmetropes (n=4; 13%), and for ametropes wearing their correction (92% wore glasses). The dominant eye was then penalized either with a Bangerter filter (density 0.4) or using a +1.25D stick-on reading lens (*Sticktite*, Optxeurope, Mantova). For each condition, StrAV was measured three times, with the subject's mean of the two best values considered as the result. Another measurement was performed using a +2 D trial case lens in a subgroup (n=12). Normalization was assessed by means of a Shapiro-Wilk test, and differences among filters and groups were analyzed by means of Student's t-test.



Figure 1. ASTEROID v1.0 stereotest software.[1]

2. Results

Baseline StrAV (42.1 ± 29.6 ") was worsened with both the +1.25D lens (93.5 ± 77.4 "; $p < 0.001$) and the diffuser filter (235 ± 294.7 "; $p < 0.001$). However, a few subjects (n=6) showed little variation in StrAV while using the addition ($\delta\text{StrAV} = 7.2 \pm 14.3$ "; $p = 0.11$), so measurements were repeated with a +2D lens, which worsened it ($\delta\text{StrAV} = 60.3 \pm 41.2$ "; $p = 0.002$). This test was in turn repeated in a control group (n=6), with similar baseline StrAV ($p = 0.12$), but which did suffer a significant drop in StrAV with the

1.25D lens ($\delta\text{StrAV}=131.8\pm 14.3$ "; $p=0.001$), although they did not show differences on average when penalized with the +2D lens ($p=0.50$).

3. Conclusions

Monocular penalization on stereoacuity with the Bangerter filter was greater than when using a +1.25D lens. In fact, some subjects' stereoacuity was barely penalized with this relatively low addition; this effect was achieved when increasing the addition to +2D.

References:

[1] Read JCA, Wong ZY, Yek X, Wong YX, Bachtoula O, Llamas-Cornejo I, Serrano-Pedraza I. ASTEROID stereotest v1.0: lower stereo thresholds using smaller, denser and faster dots. *Ophthalmic Physiol Opt.* 2020 Nov;40(6):815-827. doi: 10.1111/opo.12737.

Digital reading performance in junior students

Farcas I.A.^{1,2*}, Gil P.^{1,2}, Tabernero J.^{1,2} and Benito A.²

¹ Departamento de Electromagnetismo y Electrónica, Universidad de Murcia, campus de Espinardo (Murcia).

² Laboratorio de Óptica, Universidad de Murcia, campus de Espinardo (Murcia).

*E-mail: jalexandra.farcas@um.es

1. Introduction and Methods

Common visual tests do not consider visual performance while carrying out usual daily tasks, such as digital reading, which could be affected by visual disturbances that are usually not evaluated. Reading performance was measured in two groups of junior students: a group of University of Murcia students (UMU; n=66; 65% women; age=23.2±3.7 years) and another group of high school students between 12 and 16 years old (n=160; 54.5% women; age=13.9±1.2 years). Eye positions and movements were recorded by means of an eye tracker (Gazepoint, Vancouver, Canada) while subjects read two digital texts projected on a LED monitor, with letter sizes corresponding to a 0.6 decimal visual acuity at 60 centimeters. The eye tracking device uses infrared pupillometry to measure, among other parameters, the total reading time, the number of fixations, the average and variance of the time the eye stops in each fixation, the number of progressions (saccadic movements following the text) and regressions (saccadic movements going back), and the average length of the saccade [1]. University students were considered as a single category. High school students were classified according to their grade (from 1^oESO being 7th grade, to 4^o ESO being 10th grade), and average marks of the previous course were also obtained. Exclusion criteria included having a decimal visual acuity equal to or above 0.9 in both eyes, having no history of severe ocular pathology or surgery, as well as having no reading difficulties such as dyslexia. Subjects were measured using their refractive correction. The Kolmogorov-Smirnov test was used to test for normal distribution. Variables with a non-normal distribution were normalized by taking the logarithm. Student's t-test, one-way ANOVA, and Pearson correlation were used for normally distributed data, while the Mann-Whitney U test, Kruskal-Wallis test, and Spearman's rho were used otherwise. For each subject (n), a *reading performance value* (RPV) was calculated as in Eq. (1) by considering three normalized reading values: distance (in pixels) of the saccadic movements, number of progressions and number of regressions.

$$RPV = 2x \frac{Sacadic_n}{Sacadic_{max}} - \frac{Progressions_n}{Progressions_{max}} - \frac{Regressions_n}{Regressions_{max}} \quad (1)$$

2. Results

High school students' marks showed no significant differences with none of the variables analyzed. High school girls have slightly higher marks than boys, although the differences were not significant (p=0.08). When including university students (n=226), correlation analysis showed a moderate relationship between age and time spent (rho=-0.54; p<0.001), as well as between progressions, regressions, and saccadic distance (r; p>0.001). A comparison between high school grades and the university sample is shown in Table 1. Time, progressions, and regressions tend to decrease with increasing course level, while saccadic distance (p=0.117) and RPV tend to increase.

	7 th grade	8 th grade	9 th grade	10 th grade	UMU	p-value
Time	96.6±43.1	80.0±18.2	75.7±11.6	70.3±8.8	64.4±9.5	p<0.001
Progressions	122.6±34.3	122.0±41.8	118.3±29.7	113.4±37	103.0±29.1	0,023
Regressions	32.0±16.6	28.2±24.8	25.5±17.7	23.8±18.1	17.0±12.4	p<0.001
Saccadic distance	62.7±11.5	63.5±12.3	65.6±15.4	67.9±14.8	69.0±14.9	0,117
RPV	-0.18±0.31	-0.08±0.37	-0.05±0.34	0.02±0.39	0.13±0.33	0,001

Table 1. Average values (±SD) according to grade. One-way ANOVA test significance level is also shown.

There was no difference in time spent reading the texts between girls and boys ($p=0.14$), although girls tend to make fewer progressions ($p=0.001$), fewer regressions ($p=0.001$), and have larger saccades ($p<0.001$). In terms of RPV, girls tend to perform better (0.07 ± 0.36) than boys (-0.10 ± 0.35 ; $p<0.001$).

RPV was separated into three different categories: subjects showing a less mature behavior ($RPV<-0.15$), with higher movement rate and shorter saccades, subjects with an average behavior ($RPV<|0.15|$), and more mature reading behavior ($RPV>+0.15$), showing with fewer eye movements and larger saccades. A chi-square test for grade ($p=0.003$) and for sex ($p<0.001$) confirms that RPV tends to increase with age, being significantly higher in girls compared to boys. This difference was also observed when high school and university students were considered separately.

Conclusions

Results from grade (which includes age and education) and sex show that improvement in digital reading involves spending less time, reducing the number of ocular movements both in the direction of the text and in backward movements, while increasing the length of saccades. This behavior was found to be related to age and gender, particularly among girls.

Acknowledgments

Authors want to deeply thank Rafael Franco-Florenciano, Julia Gómez, Claudia Martínez and Paula Sánchez, along with the rest of the staff and students from the San Juan de la Cruz high school in Caravaca de la Cruz (Murcia, Spain), for their outstanding help.

References:

[1] Gil P, Farcas A, Benito A, Tabernero J. Functional visual tests to evaluate the effect of small astigmatism correction with toric contact lenses. *Biomed Opt Express*. 2023 May 22;14(6):2811-2820. doi: 10.1364/BOE.487410.

Análisis de la deformación de Lentes de Contacto Blandas sobre Superficies Esclero-Corneales Artificiales

Diana Gargallo^{1*}, Nerea Tolón¹, Jorge Ares¹, Ruth J.Macedo-de-Araújo² y Jose Manuel González-Méijome²

¹*Departamento de Física Aplicada, Facultad de Ciencias, Universidad de Zaragoza, Zaragoza.*

²*Clinical & Experimental Optometry Research Lab, Center of Physics (Optometry), School of Sciences, University of Minho, Braga, Portugal.*

*E-mail: dgargallo@unizar.es

1. Introducción

Las lentes de contacto fabricadas en materiales rígidos son capaces de compensar imperfecciones ópticas de la córnea mediante la “lente lágrima” que se forma entre su superficie posterior y la superficie corneal anterior [1]. No obstante, cuando se busca una experiencia cómoda desde los momentos iniciales de la adaptación, es necesario utilizar materiales blandos de hidrogel, hidrogel de silicona o similares para la fabricación de las lentes de contacto. Estas lentes de contacto blandas (LCB) cambian su forma para moldearse a la superficie ocular durante su porte, por lo que resultan más confortables y además suelen requerir un menor grado de especialización por parte de los profesionales que las adaptan. Sin embargo, el moldeo implica que el comportamiento óptico sea diferente dependiendo de la geometría de la superficie que la porte.

Se han realizado estudios que presentan un análisis teórico de dicha deformación [2,3]. No obstante son escasos, incompletos y de resultados inconcluyentes los trabajos que estudian la deformación que sufren las LCB durante el porte [4,5]. En estos estudios existe una incertidumbre al realizar las medidas sobre el ojo humano como soporte debido a los movimientos oculares, irregularidades de la lágrima, movimientos de la lente bajo la acción de los párpados. Asimismo, todos estos estudios comparten un denominador común en cuanto al cambio refractivo, ya que se centran exclusivamente en el cambio de la esfera paraxial esperada en visión central, sin abordar, por ejemplo, otros aspectos como la refracción periférica o la aberración de alto orden.

Algunos investigadores han demostrado con éxito la aplicación de dispositivos de Tomografía de Coherencia Óptica (OCT) para medir in vitro la superficie topográfica y el grosor central de lentes intraoculares y de contacto, mostrando una sensibilidad suficiente para discriminar cambios después del uso de LCB [6]. Desafortunadamente, los dispositivos de OCT comercializados para el examen ocular in vivo no pueden utilizarse fácilmente para medir LC in vitro por que no están diseñados específicamente para poder posicionar las lentes.

Por ello, el propósito de este trabajo es proponer y validar una metodología para cuantificar, mediante OCT, uno de los factores que afecta a la calidad óptica de una LCB, desviándola de las expectativas del diseñador. Este efecto se debe a la deformación que sufre al adaptarse a la superficie portadora. Para abordar las limitaciones actuales, 1) se diseñaron y fabricaron Superficies Esclero-Corneales (SECs) con diferentes geometrías para servir como plataforma donde adaptar las LCBs, y 2) se diseñó y fabricó un adaptador específico para orientar el haz del OCT hacia la zona de interés.

2. Metodología

Por un lado, se propone investigar el moldeo de flexión de las LCBs sobre SEC sintéticas con formas conocidas. El diseño de las SEC consta de dos superficies: una base escleral y una superficie corneal, ambas fabricadas en resina mediante impresión 3D utilizando tecnología de barrido láser, específicamente con la impresora *MOAI*. Posterior a la impresión, se caracterizaron las SECs con el topógrafo clínico, *Eye Surface Profiler* (Eaglet-Eye, Países Bajos) basado en perfilometría de Fourier.

Por otro lado, se elaboró un adaptador de OCT (Figura 1) fabricado con impresora 3D de modelado por deposición fundida comercial. Este adaptador incorpora espejos inclinados para redirigir el haz hacia la LCB y recoger y redirigir el haz retrodispersado hacia la entrada de la pupila del OCT.

Con las SECs y el adaptador, se realizaron mediciones perfilométricas de las LCB utilizando el OCT CASIA 2 (Tomey, Japan), que tiene una resolución axial de 10 μm . Este dispositivo puede obtener escaneos con un alcance de exploración lateral de 16 mm y un alcance axial de 12 mm, lo que permite mapear completamente el perfil de ambas superficies y bordes de la LCB.

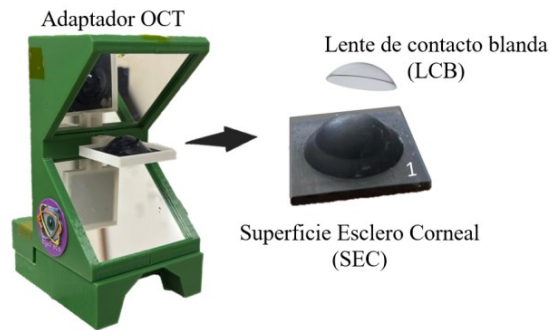


Figure 1 Adaptador OCT (izquierda) y SEC (derecha).

3. Resultados

En la Figura 2 se muestra el B-scan de una LCB de la marca *Acuvue* (Johnson and Johnson Vision Care, Ireland) con una potencia de +1.00 dioptrías, moldeada sobre una SEC esférica utilizando OCT CASIA 2. Este escaneo proporciona una visualización detallada del moldeo que ha sufrido la LCB, permitiendo una evaluación posterior mediante procesamiento de imagen.

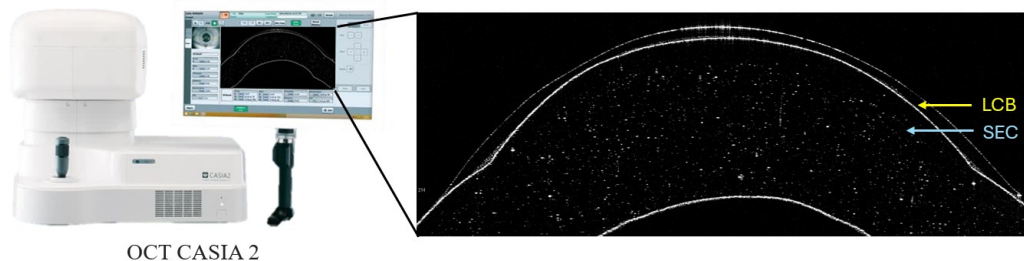


Figure 2 B-scan de LCB moldeada sobre una SEC. LCB: Lente de contacto Blanda; SEC: Superficie Esclero Corneal.

4. Conclusiones

A través del diseño y fabricación de SECs con diferentes geometrías, así como la creación de un adaptador específico, se ha establecido una metodología innovadora que permitirá medidas perflométricas completas de las LCBS a través de la OCT CASIA 2, cuantificando así la deformación experimentada. Estos avances representan un paso significativo hacia la comprensión detallada del moldeo de las LCB, lo que a su vez abre nuevas vías para cuantificar aspectos como la refracción periférica o la aberración de alto orden en diferentes superficies esclero-corneales “in vivo” y optimizar los diseños de las lentes hidrofílicas.

Agradecimientos

Ministerio de Ciencia, Innovación y Universidades (Subvención PID2020-114311RA-I00).

Referencias

- [1] Griffiths M, Zahner K, Collins M, Carney L. Masking of irregular corneal topography with contact lenses. *CLAO J* 1998; 24:76–81.
- [2] Young G, Hall L, Sulley A, Osborn-Lorenz K, Wolffsohn JS. Inter-relationship of Soft Contact Lens Diameter, Base Curve Radius, and Fit. *Optom Vis Sci.* 2017;94(4):458-465.
- [3] Sulley A, Osborn Lorenz K, Wolffsohn JS, Young G. Theoretical fitting characteristics of typical soft contact lens designs. *Cont Lens Anterior Eye.* 2017;40(4):248-252. doi:10.1016/j.clae.2017.04.001
- [4] Plainis S, Charman WN. On-eye power characteristics of soft contact lenses. *Optom Vis Sci.* 1998;75(1):44-54. doi:10.1097/00006324-199801000-0002
- [5] Abass A, Stuart S, Lopes BT, et al. Simulated optical performance of soft contact lenses on the eye. *PLoS One.* 2019;14(5):e0216484. Published 2019 May 14. doi:10.1371/journal.pone.0216484
- [6] Karnowski K, Grulkowski I, Mohan N, Cox I, Wojtkowski M. Quantitative optical inspection of contact lenses immersed in wet cell using swept source OCT. *Opt Lett.* 2014;39(16):4727-4730.

Analysis of the optical performance of intraocular lenses using profilometry

Celia García^{1*}, Juan J. Miret¹, Vicente J. Camps¹, Maria T. Caballero¹ and Juan M. Gonzalez-Leal²

¹*Group of Optics and Visual Perception. Department of Optics, Pharmacology and Anatomy, University of Alicante, 03690 San Vicente del Raspeig (Alicante) Spain*

²*Department of Condensed Matter Physics. Faculty of Sciences. University of Cadiz. 11510 - Puerto Real (Cádiz) Spain*

*E-mail: c.garcia@ua.es

1. Introduction

In recent years, various novel intraocular lens (IOLs) models have been developed for the treatment of cataract and presbyopic patients. Lens surface manufacturing control has become a key factor in ensuring the best optical and clinical characteristics of these intraocular lens. The MTF and the MTF through-focus curve are one of the most used optical parameters to characterize IOLs. Usually, these curves can be obtained from optical bench measurements according to ISO standard recommendations or from commercial devices [1][2]. The aim of this study was to develop a new methodology, based on surface profilometer measurements to assess the optical behaviour of Intraocular Lenses (IOLs) from the calculation of the MTF through-object curve.

2. Methodology

To test the feasibility of using profilometers to extract information about IOL surfaces design, a monofocal IOL that provided some depth of focus (Eyhance) was used in this study. The surface topography of the IOL was measured by using a multimode optical profilometer (Zeta Instruments, model Z 300). The three-dimensional (3D) image of the surface along the diameter of the lens was obtained by confocal grid structured illumination. The smoothed profile was performed using routines and algorithms written in Matlab (MATLAB, The MathWorks, Natick, MA) [3].

After a smoothing process of the raw data, an Application Programming Interface (API) to link Zemax with Matlab was used. Subsequently, the entire simulation process, including ray tracing and results analysis, was carried out. The MTF through-object curve was obtained by calculating the MTF value for 50 cycles/mm, in image space and changing the object vergence. Calculations were conducted for two model eyes (aberrated and not aberrated cornea).

3. Results

From smoothed profile, two options of best-fit surface were proposed: a sphere and an asphere surfaces. In the Fig. 1 is represented the difference (Δz) between heights of the best-fit surface and the smooth profile along the IOLs diameter (Y-axis) for the Eyhance IOL. From the figure it is concluded that the posterior surface of these IOL was spherical and anterior surface did not fit to any of our reference surfaces, indicating a higher order aspheric surface design.

In relation to the MTF through-object, the results obtained with this methodology are comparable with previously published methodologies. Although the shape of MTF through-focus and through-object were similar, the MTF through-object was narrower providing further near and intermediate points distances and lower depth of focus around far peak. The optical behaviour of IOLs depended on the eye model. A decrease of the SA produced a hypermetropic shift of the far focus between +0.3 D and +0.4 D.

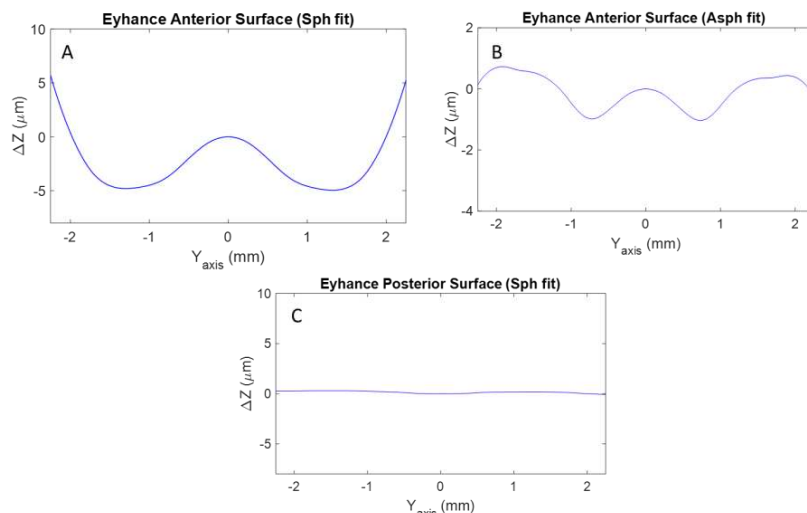


Figure 1. Subtraction lines obtained after the removal of the best-fit sphere (A) or asphere (B) of the anterior surface and best-fit sphere (C) of posterior surface from the smooth profiles of the Eyhance IOL[3].

4. Conclusions

The results of this study confirmed that the new possibility of fitting an aspherical surface as reference allows a more accurate deduction of the design of the lens surfaces and its optical properties. This methodology based on profilometer measurements proved to be comparable with other methodologies for assessing the optical quality of IOLs. By means of this methodology, the MTF through-object, based on the vergency object change, was proposed to analyze the optical behavior of IOLs. Variations in corneal aberrations led to significant shifts in IOL behavior, manifesting in alterations to the shape of the MTF through-object.

Acknowledgments

This work was supported by the “Generalitat Valenciana” of Spain (project AICO/2021/130).

References

- [1] Y. Lee, G. Łabuz, H. Son, T. M. Yildirim, R. Khoramnia and G. U. Auffarth, "Assessment of the image quality of extended depth-of-focus intraocular lens models in polychromatic light," *J Cataract Refract Surg*, vol. 46, (1), 108-115, 2020.
- [2] Camps, V. J. et al. In vitro aberrometric assessment of a multifocal intraocular lens and two extended depth of focus IOLs. *J. Ophthalmol.* 2017, 7095734 (2017).
- [3] Miret, J.J., Camps, V.J., García, C. et al. Analysis and comparison of monofocal, extended depth of focus and trifocal intraocular lens profiles. *Sci Rep* 12, 8654 (2022).

The influence of visual deterioration induced with Bangerter foils on fine motor skills

Miriam Casares López^{1*}, Pilar Granados Delgado¹, José Juan Castro Torres¹, Rosario González Añera¹

¹Department of Optics, Faculty of Sciences, University of Granada, Avenida Fuentenueva s/n, 18071 Granada, Spain

*E-mail: clmiriam@ugr.es

1. Background

Finger dexterity is defined as the ability to make rapid, skillful, controlled, manipulative movements of small objects [1]. Visual performance and visuomotor coordination are key aspects of manual dexterity, particularly when it involves the fingers. In this sense, an association between some visual functions (such as stereoacuity and fusion amplitudes) and manual tasks involving grasping has been found [2]. However, normal vision may be altered by certain conditions that increase intraocular light scattering, thus negatively affecting retinal image quality and contrast [3]. Such is the case of people whose vision is impaired due to cataracts, who may experience some difficulties when performing high visually demanding tasks that require fine visuomotor coordination. Bangerter foils, which are usually employed in ocular penalization in children undergoing amblyopia therapy, are also used to simulate visual degradation [4]. Thus, the aim of this study was to assess the influence of impaired visual performance, induced by means of Bangerter foils, on fine motor skills.

2. Methods

A total of 33 participants (20 females and 13 males) took part in the study, with ages ranging from 21 to 40 years (mean age 25.2 ± 4.7 years). The study was approved by the Human Research Ethics Committee of the University of Granada (1256/CEIH/2020). All participants underwent two experimental sessions at random: a session in normal conditions (Baseline), and a second one wearing a Bangerter foil to simulate a visual impairment equivalent to a visual acuity of 0.8 (decimal notation) (BF_{0.8}). The sensory dominant eye was selected and assessed. Visual performance was assessed in monocular viewing conditions by means of: 1) visual acuity (VA) at near (50 cm) using OptoTab VA screening test, 2) contrast sensitivity with and without glare with the device Takagi glare tester CGT-1000, and 3) optical quality using the double-pass system Optical Quality Analysis System (OQAS II), which provides the objective scatter index (OSI).

Manual dexterity was tested in monocular conditions (dominant eye) at 50 cm using the standardized tests Grooved Pegboard, O'Connor Tweezer Dexterity Test, and Purdue Pegboard, which includes two subtests: 1) inserting pegs with the dominant hand, and 2) forming assemblies. The variables obtained were the time taken to complete the task or the number of pegs/assemblies inserted. On the other hand, two non-standardized tests simulating everyday tasks were designed: water pouring and needle threading. The variable obtained in this case was the time taken to complete the task and, in the case of the water pouring task, the water spilled was also considered. The deterioration of both visual performance and manual dexterity was calculated as the difference between results in baseline condition and under BF_{0.8} condition. For some variables (VA, number of peg/assemblies inserted) results were multiplied by -1 so that more negative values indicate a higher deterioration.

3. Results

Near VA was significantly deteriorated under BF_{0.8} condition ($Z=5.019$; $p<0.001$), and the same was observed for contrast sensitivity with and without glare ($t=-11.598$; $p<0.001$ and $Z=-4.637$; $p<0.001$ respectively) and for OSI ($t=-26.935$; $p<0.001$). With respect to manual dexterity, results showed a decrease of the number of pegs ($Z=-1.586$; $p=0.113$) and assemblies ($t=1.796$; $p=0.085$) inserted in the Purdue pegboard and an increase in the time required to complete the O'Connor test and the Grooved Pegboard ($t=-3.277$; $p=0.001$ and $t=-2.328$; $p=0.013$ respectively). For the needle threading task, more time was needed to complete the task ($Z=-4.923$; $p<0.001$), and in the water pouring task, the time taken to perform the task increased ($t=-1.418$; $p>0.05$) and more water was spilled out ($Z=-0.697$; $p=0.486$). Thus,

a deterioration was observed in manual dexterity, but differences were only significant for the Grooved Pegboard and O'Connor test, as well as for the needle threading task. When analyzing the association between the visual deterioration and the performance of fine motor skills, we found a significant association between the deterioration of contrast sensitivity with glare and the increased time in Grooved Pegboard (Fig. 1). Likewise, an association was observed between near VA and the time needed to complete the needle threading task (Fig. 1). This indicates that participants whose contrast sensitivity and VA were more impaired by Bangerter foil 0.8 needed more time to complete the manual dexterity task. No significant correlations were observed between manual dexterity and the OSI.

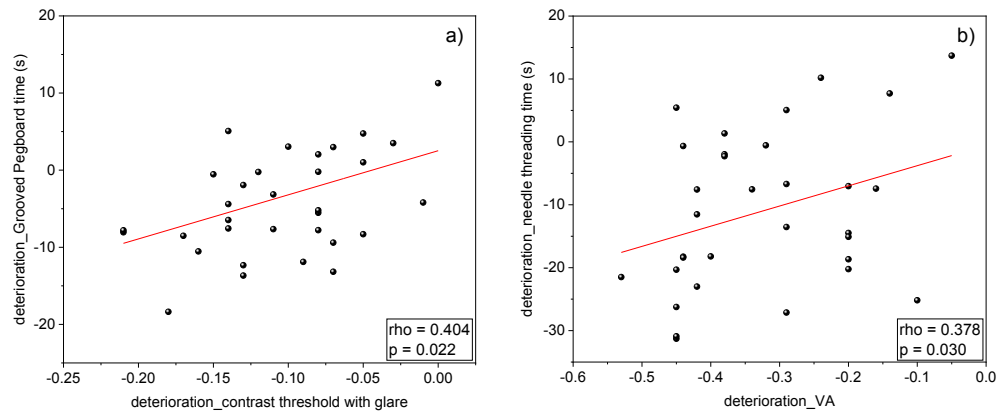


Figure 1 Correlations between the deterioration on the performance of fine motor skills and the deterioration of visual function: contrast sensitivity with glare (a) and near visual acuity (b).

4. Conclusions

The performance of fine motor skills in monocular viewing conditions was negatively affected by visual impairment. Particularly, reduced visual acuity and contrast sensitivity in the presence of glare, were associated to a higher time to complete fine motor tasks. Although our results show that visual performance is important for the performance of fine motor skills, it would be interesting to evaluate the influence of these visual functions in binocular viewing conditions, as well as the impact of different degrees of visual impairment.

Acknowledgments

Grants A-FQM-532-UGR20, funded by FEDER, and PID2020-115184RB-I00, funded by MCIN/AEI/10.13039/501100011033.

References

- [1] E. A. Fleishman and G. D. Ellison, "A Factor-analysis of fine manipulative tests". *J. Appl. Psychol.* **46**(2), 96-105 (1962).
- [2] M. E. Piano and A.R. O'Connor, "The effect of degrading binocular single vision on fine visuomotor skill task performance". *Invest. Ophthalmol. Vis. Sci.* **54**(13), 8204-13 (2013).
- [3] J. J. Castro-Torres, F. Martino, M. Casares-López, S. Ortiz-Peregrina, and C. Ortiz, "Visual performance after the deterioration of retinal image quality: induced forward scattering using Bangerter foils and fog filters". *Biomed. Opt. Express* **12**, 2902-2918 (2021).
- [4] N. V. Odell, D. A. Leske, S. R. Hatt, W. E. Adams and J. M. Holmes, "The effect of Bangerter filters on optotype acuity, Vernier acuity, and contrast sensitivity". *J. AAPOS* **12**(6), 555-559 (2008).

Accurate estimation of the relative magnification of the retinal images under different corrections

Mario Egea, Juan M. Bueno, and Enrique J. Fernandez*

*Laboratorio de Óptica, Instituto Universitario de Investigación en Óptica y Nanofísica,
Universidad de Murcia, Campus de Espinardo (Ed. 34), 30100 Murcia, Spain*

*E-mail: enriquej@um.es

1. Introduction

In individuals with refractive errors such as myopia, hyperopia, or astigmatism, the optics of the eye fail to properly focus light onto the retina, resulting in blurred vision. Corrective lenses, such as glasses or contact lenses, are prescribed to compensate for these errors. However, when corrective lenses are introduced, they alter the path of light entering the eye, causing a change in the apparent size of objects viewed through them. Relative magnification refers to the perceived size difference between an object viewed through different ophthalmic corrections. It is sometimes normalized to the perceived size of an ideal emmetropic eye. The relative magnification might have practical implications, especially in cases where precise perception of size is important. It can also affect depth perception and spatial awareness, particularly in tasks that require judging distances accurately, such as driving or sports. The apparent size of the retinal images is of particular importance for those suffering from aniseikonia. This term used in Optometry and Ophthalmology to describe a condition where there is a noticeable difference in the perceived size or shape of images between contralateral eyes. This perceptual difference occurs because of the optics of the eye, refractive errors, or differences in prescription between both eyes.

The relative magnification is typically calculated by geometrical optics, using paraxial simple eye models [1]. However, in certain cases, where a more precise calculation is required, exact eye models might fail, for instance in the presence of corneal irregularities or, in general, higher order aberrations. It is then advantageous to develop a method which might incorporate individual aberrations, or at least non-paraxial eye models, for the estimation of the relative magnification. In this work, we present a straightforward method to obtain the position of the retinal images based on optical simulation with the potential of incorporating sophisticated eye models, including customized models.

2. Methods

The simulations employed modified versions of the Liou-Brennan eye model [2]. Starting from the emmetropic version of the eye model, to generate pure axial ametropia only the vitreous' thickness was altered. In the case of absolute refractive ametropia, solely the radius of curvature of the anterior cornea was changed. For setting a given value of ametropia, the eye model was optimized, in either modality axial or refractive, until the image of the on-axis remote point was conjugated with the eye's model retina. The simulations were performed with Zemax OpticStudio (ANSYS Inc, USA). Two types of visual corrections were analyzed: spectacles and contact lenses (CL). For modelling the glasses, it was used a thin lens of index between 1.5 and 1.7 placed at 15 mm of the anterior cornea whose radii of curvature were varied to compensate for the ametropia accordingly. In the case of CL a general model used consisting of a lens of 1.25 mm central thickness, made of a material of 1.46 refractive index, with the posterior surface matching that of the anterior cornea. The radius of the anterior surface of the CL was modified to compensate for the ametropia.

The Point Spread Function (PSF) was obtained from the simulation program at different eccentricities in the form of an intensity image. The estimated position of the PSF was calculated as the weighted center of mass (CM) of the intensity pattern I at every pixel (i, j) , according to Eq. 1:

$$\overline{CM}_{PSF} = \frac{\sum_{i=1}^M \sum_{j=1}^N I_{ij} \vec{\rho}_{ij}}{\sum_{i=1}^M \sum_{j=1}^N I_{ij}}. \quad (1)$$

3. Results

Figure 1 shows the PSFs obtained for a myopic eye of 10 D of refraction, both axial and refractive, corrected with spectacles or CLs for a far distance point object situated at 15 deg of eccentricity through a pupil of 4 mm diameter.

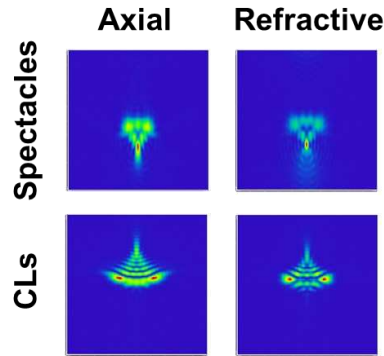


Figure 1 PSFs of a corrected myopic eye model.

The associated CM of every PSF was obtained to calculate the relative magnification as the ratio between positions of the retinal images. Figure 2 presents the results in terms of VA obtained for a 10 D myopic eye when both types of corrections are considered for a real object in front of the eye subtending 5°. The blue and red color stand for axial and refractive myopia, respectively.

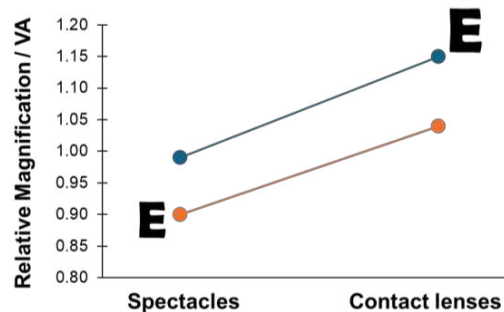


Figure 2 Estimated VA for a 10 D myopic eye model.

4. Conclusions

The calculation of the CM of the PSF from eccentric point objects has been presented by using an optical design program. The method provided information about the size of the retinal images, which can be computed to discern the VA, or the relative magnification across different corrections. Changes as large as 20% in the retinal image's size were found depending on the nature of the ametropia and its type of correction. The method is not constrained to spectacles or CL, but it could be equally applied to intraocular lenses, refractive surgery, or in subjects with significant high order aberrations. It could be also used in the calculation of the most efficient solution to ameliorate vision in those suffering from aniseikonia.

Acknowledgments

Supported by grant PID2020-113919RBI00/AEI/10.13039/501100011033.

References

- [1] Optics of the Human Eye. David A. Atchison & George Smith. 2nd Edition. Caps. 1, 7, 10, 18.
- [2] H.-L. Liou and N. A. Brennan, "Anatomically accurate, finite model eye for optical modeling," J. Opt. Soc. Am. A 14, 1684-1695 (1997).

Evaluation of the influence of headrest use and Plusoptix photorefractor holding setup on its precision

Justo Arines^{1,2}, PhD; Sofia Rendo-González¹, MSc; Nery Garcia-Porta^{1,2}, PhD

¹Applied Physics Department, Optics and Optometry Faculty. University of Santiago de Compostela, 15782 Spain.

²Institute of Materials (iMATUS) of the University of Santiago de Compostela. Spain

*E-mail: nerly.garcia.porta@usc.es

1. Introduction

Uncorrected refractive errors and strabismus are among the most common risk factors for amblyopia, but they are difficult to measure in young children [1]. Photorefractive has emerged as a useful and easy to use technique in patients with poor collaboration [2 – 3]. Plusoptix is one of the most commonly used photorefractors [4]. Handheld Plusoptix photorefractors are portable, allowing making measurements with subjects in different positions, and without the need of resting their face in a headrest. They have a child-friendly smiley face as vision target and offer the possibility of making a sound just before taking the measurement to grab the attention of babies and infants. Plusoptix make the measurements automatically, and clinicians can obtain the values of both eyes with just one measurement. Among the parameters assessed by the device are refractive errors and head tilt. Considering that a previous study reported differences larger than 0.50 DS in spherical equivalent value when comparing non cycloplegic Plusoptix photorefractive with the gold standard technique, cycloplegic retinoscopy [5], we run a study to assess if the accuracy of Plusoptix A12R in measuring the refractive error and the head tilt can be influenced by the stability of the device and/or the stability of the patient (head tilt). Our hypothesis is that the precision of the measurements is limited by holding the instrument and the instability of the head tilt of the subjects. We present as an example of the analysis, our results on the magnitude of blur and head tilt.



Figure 1 Plusoptix in use.

2. Material and methods

12 young adults with a mean age of $27,6 \pm 6,3$ years old (range: 21-40 years old) were included in this study. 9 (75%) subjects were male and 3 (25%) females. Each subject was screened with Plusoptix A12 (Nuremberg, Germany). The Plusoptix photoscreener was placed in front of the subject at a distance of 1 meter under soft light with a corneal illuminance of 44lx. The examination was performed on both eyes at the same time, without cycloplegic drops, taking automatic measurements using 6 different methods, explained below: 1) Plusoptix free & head free; 2) Level Plusoptix & free head; 3) Level Plusoptix hold on a tripod & head free; 4) Plusoptix free & head on headrest; 5) Level Plusoptix & head on headrest; 6) Level Plusoptix hold on a tripod & head on headrest. For each of the methods the subject was instructed to: a) look at the smiling face and b) to look at the nose of the face. Measurements were taken three times with each method. Mean value and standard deviation of intrasubject measurements were then calculated. Improvement of intersubject mean value and standard deviation were calculated to compare the different

methods. All measurements were performed by the same optometrist following a random order. Ethics approval was granted by the University of Santiago de Compostela Bioethics Committee (Spain). Among all the parameters provided by the Plusoptix instrument, we present in this work data of blur and head tilt. The blur was computed from the power vectors obtained from the objective refraction provided by the instrument, as the modulus of the power vector. The head tilt is a value provided by the Plusoptix.

3. Results

Figure 2 a) presents the mean value and standard deviation (as error bars) of the intersubject standard deviation of the Blur of the left eye, and of the Head tilt. We observe that the blur does not depend on the measurement method, being the mean value and the standard deviation obtained in all cases very similar. Contrary, we found differences in the magnitude and standard deviation of the measurements of the head tilt, being smaller as we increase the control on the tilt of the device and limit the movement of the head of the subjects' head. We did not find differences caused by asking subjects to look at the face or to the nose of the smiley face of the Plusoptix.

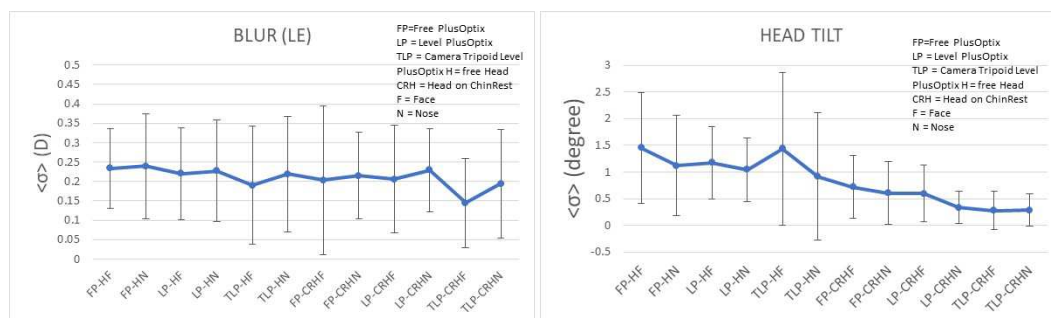


Figure 2 Mean value and standard deviation (as error bars) of the intrasubject standard deviation of the Blur of the left eye, and Head tilt.

4. Conclusions

We studied the performance of the Handheld Plusoptix photorefractors. The results showed that controlling the position of the Plusoptix and the subject's head is important to increase the precision of the instrument when determining head tilt. By contrast, blur measurements were not affected by the stability of the Plusoptix or the subjects' head movement. Analysis of the other parameters provided by the instrument will also be presented.

Acknowledgments

This work was supported by Ministerio de Ciencia e Innovación and FEDER, grant No. PID2020-115909RB-I00, and by Consellería de Cultura, Educación e Ordenación Universitaria, Xunta de Galicia grant No. ED431B 2023/07. Nery Garcia-Porta is supported financially by a Maria Zambrano contract at USC under the grants call for the requalification of the Spanish university system 2021-2023, funded by the European Union—NextGenerationEU

References

1. Yekta A, et al. Global Prevalence and Causes of Visual Impairment and Blindness in Children: A Systematic Review and Meta-Analysis. *Journal of current ophthalmology*, **34**(1), 1-15 (2022).
2. Silverstein E, McElhinny ER. Traditional and instrument-based vision screening in third-grade students. *Journal of AAPOS: the official publication of the American Association for Pediatric Ophthalmology and Strabismus*, **24**(4), 232.e1-232.e6 (2020).
3. Sanchez I, Ortiz-Toquero S, Martin R, et al. Advantages, limitations, and diagnostic accuracy of photoscreeners in early detection of amblyopia: a review. *Clinical ophthalmology*, **10**, 1365-1373 (2016).
4. Arnold R, Silbert D, Modjesky H. Instrument Referral Criteria for Plusoptix, SPOT and 2WIN Targeting 2021 AAPOS Guidelines. *Clinical ophthalmology*, **16**, 489-505 (2022).
5. Ayse YK, Onder U, Suheyla K. Accuracy of Plusoptix S04 in children and teens. *Canadian journal of ophthalmology. Journal canadien d'ophtalmologie*, **46**(2), 153-157 (2011).

Caracterización termo-óptica de materiales urbanos para fachadas, cubiertas y pavimentos

Leticia Herrera^{1-2*}, Gloria Pérez¹, Manuel Rodríguez Marín², Israel Montero¹, Arturo Martínez⁴, Fernando Martín-Consuegra¹, Carmen Alonso¹, Borja Frutos¹.

¹*Instituto de Ciencias de la Construcción Eduardo Torroja (IETCC), CSIC, Serrano Galvache 4, 28033 Madrid,*

²*Departamento de Ingeniería Mecánica. Universidad de Salamanca, Patio de Escuelas, 1, 37008 Salamanca.*

⁴*Construcción y Tecnología Arquitectónicas, Universidad Politécnica de Madrid (UPM), Av. Juan de Herrera 4, 28008 Madrid*

*E-mail: leticia.herrera@ietcc.csic.es

1. Introducción

Las crecientes olas de calor a nivel mundial generan problemas relacionados con la salud y el confort térmico de las personas, sobre todo en regiones con veranos cálidos. En este contexto, las envolventes de los edificios son las principales mediadoras entre las condiciones climáticas y el ambiente interior de los recintos. Generalmente, las propuestas para optimizar el desempeño térmico de las envolventes se fundamentan en el aumento del aislamiento térmico de las fachadas y cubiertas y no se presta atención a las propiedades termo-ópticas (reflectancia, transmitancia y emitancia) de los materiales de acabado exterior, soslayando el modo en que los cerramientos gestionan la radiación solar. Por otro lado, las propiedades termo-ópticas (TO) de las envolventes de los edificios y los pavimentos del espacio público alteran las temperaturas en los entornos urbanos, siendo un factor preponderante para el aumento de temperaturas de las ciudades [1]. El conocimiento de las propiedades TO de los materiales disponibles para el acabado urbano permite prever el desempeño de los materiales en la gestión solar mediante herramientas de simulación energética, y ofrecer opciones de diseño más precisas y menos azarosas para reducir la generación de espacios térmicamente inconfortables. Pese a esto, son escasas las bases de datos abiertas donde se incluyan datos experimentales de estas propiedades y habitualmente se utilizan valores genéricos poco precisos en las simulaciones. Se recoge en este trabajo una muestra de los avances en la caracterización TO de materiales comerciales de aplicación en fachadas, cubiertas y pavimentos para obtener diseños más fiables para mejorar la habitabilidad y la sostenibilidad de las áreas urbanas.

2. Metodología

Se han recopilado alrededor de 1000 muestras de materiales opacos de acabado urbano, gracias a la participación de 39 empresas fabricantes. Mediante un análisis previo, se han categorizado las muestras de acuerdo con su aplicación: fachadas, cubiertas y pavimentos. En cada aplicación se han dividido las muestras por el tipo de material que las compone (cerámico, base cemento, base orgánico, etc.) y el tipo de producto (ladrillo, adoquín, placa, mortero, etc.). Se ha iniciado la medida de los parámetros TO de las muestras. Por un lado, se ha medido la reflectancia total mediante un espectrofotómetro de fibra óptica que consta de una esfera integradora de 50 mm de la marca Ocean Insight y dos espectrómetros de Stellarnet (Dwarf-Star para el rango espectral de 900-1700 nm y Black Comet para 200-1080nm). Se utiliza una lámpara halógena de alta potencia HL-2000 de Ocean Insight y fibras ópticas con un diámetro de 600 μm . De estas mediciones se obtienen los parámetros de reflectancia solar y visible descritos en la norma UNE-EN 410:2011 y las coordenadas de color CIE Lab (iluminante D65 y observador de 10°). Por otro lado, se ha medido la emitancia hemisférica direccional (con ángulos de incidencia de 20° y 60°) y total (HTE), mediante el equipo portátil ET-100 de la marca Surface Optics Corporation.

3. Resultados

La Tabla 1 muestra como ejemplo un conjunto de muestras de ladrillo de aplicación en fachadas. Se han numerado 8 de ellas que representan la gama de acabados disponibles. La Tabla 1 recoge los valores de reflectancia solar (RS), visible (RV) y coordenadas de color (L^* , a^* y b^*) de esas 8 muestras. Se observa que la RV varía de 0,056 para la muestra 5 hasta 0,860 para la muestra 1 de color blanco y la RS

varía desde 0,140 para la muestra 5 de color negro, hasta 0,867 para la muestra 1. Estas dos muestras también presentan los valores extremos de la coordenada L^* de 27,676 y 96,472 respectivamente. En cuanto a las coordenadas de color a^* y b^* toman valores de 0 a 4 para las muestras 1, 4 y 5, de colores neutros, y valores mayores y positivos para el resto, como corresponde a sus colores amarillentos y rojizos. La emitancia hemisférica total depende de múltiples factores como el acabado del material y de la composición del mismo y debido a que tienen una composición similar (cerámica) las 8 muestras presentan una variación menor de entre 0,811 y 0,859.



Figura 1 Muestras de ladrillo para fachadas, empresa Malpesa.

Los resultados muestran una amplia variación en la fracción de radiación incidente reflejada por cada superficie, lo que proporciona una oportunidad de elección del material de acabado más adecuado para optimizar la gestión de la radiación solar en cada diseño.

Tabla 1 Parámetros termo-ópticos experimentales de muestras seleccionadas (numeradas en Figura 1).

Muestra	Ref. visible	Ref. solar	L^*	a^*	b^*	HTE
1	0,860	0,867	96,472	-0,146	3,959	0,852
2	0,496	0,579	76,838	5,788	20,059	0,848
3	0,268	0,385	58,344	5,919	13,895	0,840
4	0,157	0,199	46,238	1,801	-3,082	0,811
5	0,056	0,140	27,676	1,319	-2,486	0,833
6	0,162	0,249	43,104	18,986	15,304	0,850
7	0,154	0,175	44,806	8,125	8,631	0,855
8	0,350	0,445	64,600	11,982	21,978	0,846

4. Conclusiones

El estudio pretende dar a conocer la gama de respuestas termo-ópticas de los materiales de acabado urbano. Se han mostrado a modo de ejemplo los parámetros experimentales de un conjunto de ladrillos para acabado exterior de fachadas, que presentan una amplia variación de valores de reflectancia solar y visible y coordenadas de color CIELab y valores más próximos entre sí de la emitancia hemisférica total. Estos valores, junto con el resto de muestras de materiales urbanos recopiladas, brindarán una base de datos para su uso en herramientas de simulación energética que permitan estudios comparativos confiables entre materiales y en la generación de pronósticos térmicos y energéticos. Concretamente, se utilizarán para correlacionar las propiedades ópticas de los materiales de acabado con la demanda energética y el ambiente térmico de un caso de estudio en la ciudad de Madrid.

Acknowledgments

Este trabajo se ha realizado en el marco del Proyecto PID2020-114873RB-C31, mateMAD, financiado por MCIN/ AEI /10.13039/501100011033.

References

[1] Santamouris, M. Energy Build. 2020, 207, 109482.

Polarization based Monte-Carlo simulation for correlating inherent nanoparticles features with its depolarizing response

Yuxuan Mao^{1*}, Albert Van Eeckhout², Irene Estévez¹, Juan Campos¹ and Angel Lizana¹

¹*Optics Group, Department of Physics, Autonomous University of Barcelona, Bellaterra 08193, Spain*

²*ALBA Synchrotron Light Source, Cerdanyola del Valles 08290, Spain*

E-mail: Yuxuan.Mao@autonoma.cat

1. Introduction

Polarimetric methods have proved their potential in many biomedical imaging applications, leading to larger contrast of certain structures, or even revealing hidden features, as an effective image enhancement method as early detection or classification of tissue or certain pathologies^[1]. Importantly, to accurately describe the depolarizing characteristics of the sample, different useful polarimetric observables have been developed. However, even knowing that depolarizing response is originated by some inherent characteristics (as polarimetric anisotropies of constituent units, density, spatial distribution and disorder), it is difficult to implement simple optical models connecting macroscopic depolarizing response with inherent depolarizing properties. Under this scenario, in this paper we use a polarized-Monte Carlo simulation method^[2] of single-layer mixed concentration particles to calculate some depolarizing observables, this allowing to connect microscopic (model) and macroscopic (depolarizing metrics) scales.

2. Simulation method and results

The implemented polarized-Monte Carlo method^[2] calculates the Mueller matrix (MM) of simulated samples by considering different control parameters as the concentration of particles in the material (ρ), the scatter sphere radius (r), the refractive index of the material (n), the illuminating light wavelength (λ), the light source pattern and the beam diameter (D). From obtained MM, a representative set of representative depolarizing observables (Depolarization factor FD^[3], Depolarization index PD^[3], first and second Lorentz depolarization indices L1 and L2^[4], the three Indices of Polarimetric Purity (IPP) P_1, P_2, P_3 ^[5], Polarizance P, Diattenuation D, Components of Purity PD^[6] are calculated. Unlike other Monte Carlo simulations previously provided in literature, this model considers: 1) the pattern and radius of the illuminating light beam; and 2) the mixing distribution of particles, which fits the actual imaging results better.

As a representative example of obtained results, here we provide the simulations associated to silver nanoparticles with a size from 10 to 100 nm at different concentrations. In Fig. 1 we provide the results obtained under transmission situation, in terms of the IPP parameters as a function of concentration, as providing largest sensitivity for concentration determination in the evaluated range among studied metrics. As a supplement, two non-depolarizing channels, P and D, are also included in Fig. 1 for further discussion. First, we observe that compared with depolarizing channels (IPP), non-depolarizing channels, P (green dashed line) and D (blue line), show lower sensitivity to particle concentration. Therefore, although some dichroic dependence with concentration is expected (considering an increasing number of reflection-refraction with concentration and corresponding Fresnel coefficients effect) depolarizing behavior of the sample seems to be much more sensitive to this parameter (note that IPP variation almost cover its feasible range within [0,1]). Among the P_1 (red line), P_2 (orange curve) and P_3 (yellow curve), the larger dependence with concentration is obtained for P_3 channel, naturally satisfying the following conditions: $P_3 \geq P_2 \geq P_1$. The same conclusion is supported in Ref [7] about the relationship between depolarization and isotropic effect.

Moreover, we want to highlight that other control parameters of interest, may be better determined with different observables in different application scenarios. As an example, Lorentz

depolarizing parameters L1, L2 show potential for distinguishing different particle types due to its differential mean response.

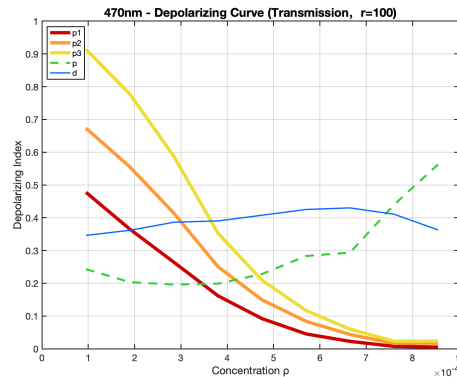


Figure 1 Depolarization parameters as a function of particle's concentration ρ . Provided simulated data is obtained for transmission configuration, wavelength $\lambda = 470\text{nm}$, and radius $r=100\text{nm}$.

Conclusions

In this paper we studied the potential of depolarizing metrics derived from MM simulated by polarized Monte Carlo method, to determine inherent characteristics of regular-shaped micro and nano particle aggregates as well as properties such as particle concentration and radius. Provided simulated results pave the way for further studies of depolarizing observables in the context of samples characterization and highlight the interest of the Indices of Polarimetric Purity (IPP) parameters to determine particles concentration or radius.

Acknowledgments

Financial support from the China Scholarship Council and Ministerio de Ciencia e Innovación and Fondos FEDER (PID2021-562 126509OB-C21 and PDC2022-133332-C21), Generalitat de Catalunya (2021SGR00138) and Beatriu de Pinós Fellowship (2021-BP-00206).

References

- [1] He, Chao, et al. "Polarisation optics for biomedical and clinical applications: a review." *Light: Science & Applications* 10.1 (2021): 194.
- [2] Ramella-Roman, Jessica C., Scott A. Prahl, and Steve L. Jacques. "Three Monte Carlo programs of polarized light transport into scattering media: part I." *Optics Express* 13.12 (2005): 4420-4438.
- [3] Gil, José Jorge, and Eusebio Bernabeu. "Depolarization and polarization indices of an optical system." *Optica Acta: International Journal of Optics* 33.2 (1986): 185-189.
- [4] Ossikovski, Razvigor. "Alternative depolarization criteria for Mueller matrices." *JOSA A* 27.4 (2010): 808-814.
- [5] San José, Ignacio, and José J. Gil. "Invariant indices of polarimetric purity: generalized indices of purity for $n \times n$ covariance matrices." *Optics communications* 284.1 (2011): 38-47.
- [6] Van Eeckhout, Albert, et al. "Unraveling the physical information of depolarizers." *Optics express* 29.23 (2021): 38811-38823.
- [7] Canabal-Carbia, Mónica, et al. "Connecting the microscopic depolarizing origin of samples with macroscopic measures of the Indices of Polarimetric Purity." *Optics and Lasers in Engineering* 172 (2024): 107830.

Combination of the Indices of Polarimetric Purity and the Polarizance- Reflection- Transformation observables for modelling depolarizing responses of samples.

Dekui Li*, Ivan Montes, Mónica Canabal, Irene Estévez, Juan Campos and Angel Lizana

Optics Group, Departamento of Physics, Universitat Autònoma de Barcelona, Bellaterra 08193, Spain

*E-mail: 1718083@uab.cat

1. Introduction

A widespread number of samples in nature usually present depolarizing behaviors when interacting with incident polarized light. Recently, it has been demonstrated that depolarizing analysis is crucial to enhance the visualization of samples consisting of multiple structures presenting different spatial depolarizing responses. Theoretically, the Mueller matrix (MM) encodes the polarimetric features of samples and is able to completely describe depolarization of samples. However, the 16 raw elements in MMs are complicated to be interpreted and cannot provide an intuitive link to the optical properties and structure of the samples. For this reason, a full field of study deals with MM decompositions and analysis, deriving a series of polarimetric observables with physical interpretation. Importantly, those observables are interdependent and can be combined to construct related polarization spaces, which highlight useful polarization information for related tasks. In this paper, we show how by combining selected spaces, further physical analysis of depolarizing samples can be achieved, this paving the way to advanced data processing for polarimetric imaging.

2. Theoretical fundamentals

The so-called Indices of Polarimetric Purity (IPP) parameters describe the polarimetric randomness introduced by samples to incident light, showing a better performance than other referential depolarization metrics. The IPP consist of three polarimetric indices namely P_1 , P_2 , and P_3 , respectively, which are calculated from the eigenvalues of the so-called coherency matrix according to Ref. [x]. The IPP are interdependent and are used to form the Purity space shown in Fig. 1(a). Recently, it has been reported that the IPP parameters provide information of two different sources of depolarization induced by samples [1]. In this sense, whereas P_1 and P_2 parameters encompass information of anisotropic depolarization, the P_3 metric essentially provides the isotropic depolarization content of samples, with the limit cases of $P_3=1$ for samples without showing isotropic depolarization behavior and $P_3=0$ for samples whose depolarizing response is fully governed by isotropic depolarization (ideal depolarizers).

In addition to Purity space, a recent collection of other three observables, more focused on physical characteristics of samples, have been used to implement the so-called Polarizance- Reflection- Transformation (PRT) space [2] shown in Fig. 1(b). In particular, this space consists of three polarimetric observables directly related to elements in MMs. For instance, the diagonal elements (m_{11} , m_{22} , m_{33}) intuitively characterize the direct reflectivity or transmittance of the Stokes elements (Q , U , V) for the reflection or transmission scenario respectively (hereafter the reflectivity is used). Thus, they are extracted to measure the direct reflectivity of different Stokes elements, and then the overall reflectivity of Stokes elements is defined as [2]:

$$R = \sqrt{\sum_{i=1}^3 m_{ii}^2} / \sqrt{3} \quad (1)$$

Besides, the rest elements (m_{12} , m_{13} , m_{21} , m_{23} , m_{31} , m_{32}) characterize the mutual transformations between the Stokes elements (Q , U , V) from the incident beam to emergent beam. The overall transformation between the Stokes elements is defined as [2]:

$$T = \sqrt{m_{12}^2 + m_{13}^2 + m_{21}^2 + m_{23}^2 + m_{31}^2 + m_{32}^2} / \sqrt{3} \quad (2)$$

Both R and T have contributions from the birefringent properties of the sample. Besides, the polarimetric P_P derived from D , and P is able to characterize the dichroism of samples.

$$P_P = \sqrt{m_{01}^2 + m_{02}^2 + m_{03}^2 + m_{10}^2 + m_{20}^2 + m_{30}^2} / \sqrt{2} \quad (3)$$

In addition, by properly combining these three polarization observables, fundamental information of samples, as their dichroism, retardation and depolarization, can be retrieved.

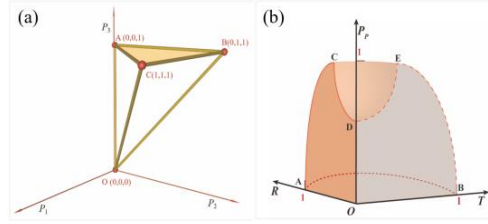


Fig. 1. Polarization representation spaces. (a) The Purity space. (b) The PRT space.

3. Results and discussions

The depolarizers simulated in this paper for case of study are based on two different inherent origins: (1) diattenuator-based depolarizers, consisting of the incoherent addition of different linear diattenuators; and (2) retarder-based depolarizers, consisting of the incoherent addition of different retarders. To control the generated samples, the model includes some parameters, such as the diattenuation D and the polarizers orientation dispersion σ , for diattenuator-based depolarizer case, and the retardance δ and the retarders orientation dispersion σ , for retarder-based case. As an example of some obtained results, in Fig. 2 a collection of diattenuator-based depolarizers with different σ are represented in the Purity and PRT spaces.

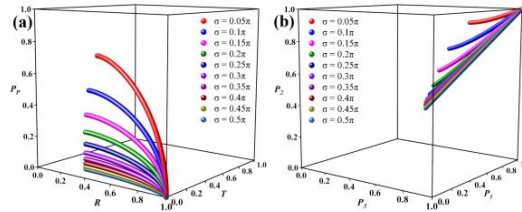


Fig. 2. Representation of the simulated diattenuator-based depolarizers with varying σ : (a) PRT space (b) Purity space.

From obtained results, we have notice that both the PRT and purity spaces present a notable discrimination capability to distinguish depolarizers responses according to different constituent elements deviation, as shown for instance in Fig. 2 for the diattenuator-based case (in this example, specially for the PRT space, see Fig. 2(a)). Note that extrapolating this result to real samples could be useful to identify disorganization of structural elements in samples, which in turn, can be connected with different human pathologies as certain types of cancer. Therefore, the use of depolarizing spaces in certain applications can be useful in sample identification and analysis.

4. Conclusions

In this paper, the PRT and Purity spaces are combined to explore and identify retarder-based and diattenuator-based depolarizers, which belongs to the anisotropic depolarizers class [1]. The distributions of samples with varying parameters are explored and discussed in such two spaces. The PRT space is capable of magnifying the discrepancies of samples with varying parameters, which means that the PRT space can distinguish between samples even when the discrepancies between them are slight. However, there will be some points of ambiguity regarding retarder-based depolarizers in the PRT space, but these samples can be distinguished by the Purity space. Some particular example was here revised for the diattenuator-based depolarizers case. The results of the current study point in the direction that combining IPP and PTR spaces leads to further information of the physical properties of depolarizing samples related to their polarimetric response. Under this scenario, the use of these spaces could play a major role in applications such as biological tissue identification and pathology detection.

Acknowledgments

We acknowledge funding support from China Scholarship Council (202306690024), Ministerio de Ciencia e Innovación and Fondos FEDER (PID2021-562 126509OB-C21 and PDC2022-133332-C21), Generalitat de Catalunya (2021SGR00138) and Beatriu de Pinós Fellowship (2021-BP-00206).

References

- [1] Monica Carbia et al., “Connecting the microscopic depolarizing origin of samples with macroscopic measures of the Indices of Polarimetric Purity,” *Opt Lasers Eng* (2024); 172: 107830.
- [2] Dekui Li et al., “Polarizance-Reflection-Transformation representation space for sensing and distinguishing pure systems,” *IEEE Sensors Journal* DOI:10.1109/JSEN.2024.3377183

Introduction to meteor spectroscopy within the UMA/SMA Fireball and Meteor Detection Network

Alicia M^a Lozano Fernández^{1*}, Vicent Peris Baixauli¹, Alberto Castellón Serrano² y M^a
Rosa López-Ramírez³

¹*Astronomical Observatory of the University of Valencia, Research Institute Building Catedrático José Beltrán, 1, 96980 Paterna, Valencia*

²*Department of Algebra, Geometry and Topology, University of Málaga, Campus de Teatinos sn, 29071 Málaga*

³*Department of Physical Chemistry, University of Málaga, Campus de Teatinos sn, 29071 Málaga*

*E-mail: lozano8@alumni.uv.es

Spectroscopy is an important aspect of meteor studies as it enables the chemical composition of incoming meteoroids to be determined. For this purpose, the Fireball and Meteor Detection Network of the University of Malaga (UMA) and the Malaga Astronomical Society (SMA) is distributed in thirteen locations throughout Spain. Currently the network has fourteen stations in operation and another four are in the progress of being installed. In addition, this network has the possibility to use the allsky cameras of the Global BOOTES Network (IAA/CSIC). In all of them, the necessary software for instrumentation control, image processing and meteor identification has been developed by SMA members and is freely available to the network participants. [1]

Meteors are particles that interact with our atmosphere, and they do not materialize on the earth's surface so we can only know their composition and nature using these detection techniques during the short period of time that the luminous phenomenon lasts. Typical spectra show the emission lines of metals such as calcium (Ca), sodium (Na) or magnesium (Mg). [2,3]



Figure 1 Fireball and Meteor Detection Network of the University of Malaga (UMA) and the Malaga Astronomical Society (SMA) distribution in Spain.

In this work, we will try to obtain and analyze the emission spectra of several meteors captured from the station located at the El Torcal Observatory (OAT). In this camera (Figure 2) a 200 lines/mm grating (Star Analyser 200) has been placed between a Sigma 4,5 mm fisheye objective Lens and a ZWO AIS 1600MM camera with a monochrome CMOS sensor, usually indicated for planetary and deep sky imaging thanks to its high sensitivity. To calibrate the detection system, various test have been carried out using high-pressure tubes of different gas tubes as emission sources (Vernier "Spectrum Carousel power supply). Hydrogen, helium or argon are used as reference to adjust the diffraction grating to the instrument assembly. In these tests, the emission spectra of these elements have been successfully obtained and some factors have been optimized to improve static detection. On the other hand, in order to measure the spectral profiles we have developed a JavaScript script in the PixInsight software development platform. This script performs the wavelength calibration by finding the calibration line

positions to subpixel precision using surface splines. Then, it extracts the spectral profile of the meteors to a numeric table. [4]

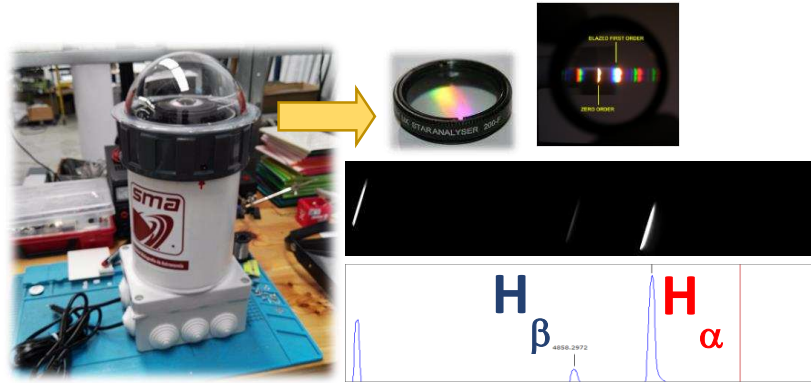


Figure 2 Camera and 200 lines/mm grating (Star Analyser 200). The calibration H emission spectrum is included.

Our spectroscope design allows us to detect stars, planet and meteor spectra. In Figure 3, you can observe one of the detected meteor and the assigned spectra.

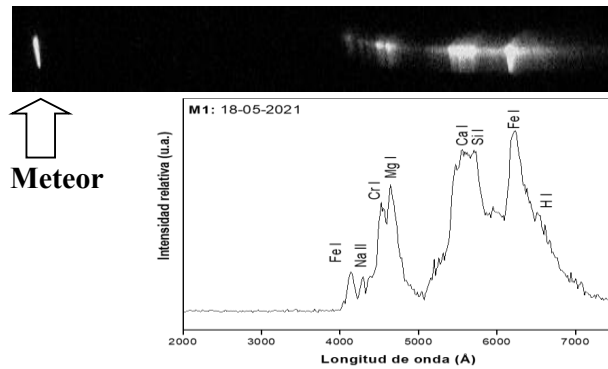


Figure 3 Emission spectrum image of a meteor and corresponding extracted spectrum with the proposed assignment.

Conclusions

In this first approach to astronomical spectroscopy within the UMA/SMA Meteor and Bolide Detection Camera Network, we can confirm that the stellar spectra of a great variety of objects as well as the spectra of meteors have been successfully recorded. We have verified that both the setup and each of the devices have been correctly arranged inside the camera and the diffraction grating used (SA-200) has enough resolution to be able to separate the main spectral lines of the detected meteors. Future meteor detections will provide a database with a more comprehensive spectral analysis.

Acknowledgments

We would like to thanks to the UMA/SMA Fireball and Meteor Detection Network for providing the spectral data of the meteors.

References

- [1] More information about the Network: <http://meteoros.astromalaga.es>
- [2] J. Borovicka, E.P. Majden, "A Perseid meteor spectrum", J. Royal Astronomical Society of Canada, 92, 153-156 (1998).
- [3] E.P. Majden, "Meteor spectroscopy with inexpensive holographic gratings", J. Royal Astronomical Society of Canada, 92: 91-92 (1998).
- [4] More information about the PixInsight software development platform: <https://pixinsight.com>

Efecto de la tonalidad de los pigmentos de absorción en la percepción del *graininess*

Esther Perales^{1*}, Néstor Tejedor-Sierra¹, Aurora Larrosa¹, Esther Perales¹, Julián Espinosa¹, Jorge Pérez¹ y Alejandro Ferrero²

¹*Departamento de Óptica, Anatomía y Farmacología, Universidad de Alicante, San Vicente del Raspeig, Alicante, España.*

²*Grupo de Investigación en Medidas de Radiación Óptica, Instituto de Óptica Daza de Valdés, Consejo Superior de Investigaciones Científicas, Madrid, España*

*E-mail: esther.perales@ua.es

1. Introducción

La adición de los pigmentos denominados de efecto especial en superficies produce cambios objetivos de sus propiedades de reflexión y uniformidad [1]. Como consecuencia, pueden ser apreciados cambios de la homogeneidad espacial de la superficie, lo que se conoce como textura visual. Existen dos efectos o tipos de textura visual asociados a estos pigmentos, en particular, el denominado *graininess* se percibe bajo una configuración geométrica difusa de la radiación incidente, y su evaluación visual es descrita como una texturización granulada y uniforme de la superficie, o patrón claro-oscuro.

Dado que estos pigmentos permiten dotar de una apariencia atractiva a los productos en los que son aplicados, su uso se ha extendido a las industrias de la automoción, cosmética, revestimientos, tintas, etc. Esto hace necesario evaluar este tipo de texturas visuales, es decir, conocer los factores que pueden afectar a la percepción de estos efectos de textura para proporcionar datos experimentales que ayuden a la definición de una escala de medida objetiva, trazable y reproducible ya que actualmente no existe ninguna normativa a nivel internacional que defina una escala de medida de estas texturas. Por esta razón, desde la Comisión Internacional de Iluminación (CIE) se está trabajando en la definición de escalas de medida para estos dos atributos de textura. Para conseguir una buena escala de medida, además de la caracterización objetiva [2, 3], es necesario realizar evaluaciones visuales que validen las medidas instrumentales. Por tanto, en este trabajo se estudió el impacto del cambio en la tonalidad del pigmento de absorción (fondo) en la percepción del efecto de *graininess* mediante un experimento psicofísico.

2. Materiales y métodos

Para este trabajo, fueron seleccionadas 9 muestras, dividiéndolas en tres grupos en función del tono del pigmento de absorción, pudiendo ser visualmente identificadas como rojo, verde y azul. Dentro de cada grupo, se controlan los parámetros estructurales que producen los efectos de textura para proporcionar, en este caso, tres niveles específicos de *graininess*. Se utilizaron pigmentos metálicos tipo *silver dollar* de diferente tamaño de partícula (desde $D_{50} = 11 \mu\text{m}$ hasta $34 \mu\text{m}$). Además, la relación entre el pigmento de absorción y el pigmento metálico fue constante (1:9) para poder analizar exclusivamente el efecto del tono. Para el experimento visual se utilizó la cabina de iluminación Verivide que controla las condiciones de observación con iluminación difusa. La distribución espectral de la fuente de luz simula la del iluminante D65, con una temperatura de color de 6439 K, y con un índice de reproducción cromática, Ra, de 95 unidades. La iluminancia en el plano de la muestra es de 1415 lx. El experimento se realizó en una sala oscura, y el observador tuvo que adaptarse a la oscuridad durante tres minutos. Todos los observadores participantes tenían buena agudeza visual con su compensación óptica y visión cromática normal evaluada con el test de Ishihara.

Las muestras fueron colocadas delante del sujeto empleando combinaciones en grupos de 3, efectuando un total de 84 combinaciones. Para cada combinación mostrada, se le preguntó al observador tomando como referencia la muestra situada en el centro, cuál de las dos muestras (izquierda o derecha) presentaba mayor similitud con respecto a la muestra central centrándose únicamente en el *graininess* y no en el color de las muestras. Para controlar posibles errores inducidos por el observador durante la prueba, se realizaron 3 repeticiones de cada serie de combinaciones. Una vez recogidas las respuestas de 15 observadores, se procesaron mediante el escalado multidimensional. En primer lugar, se analizó la variabilidad asociada a los observadores en el experimento visual. El análisis se centró en la intra-variabilidad (mismo observador, distintas repeticiones) y la inter-variabilidad (respuestas de distintos

observadores) para validar los resultados del experimento psicofísico siguiendo la ecuación 1. A continuación, se analizaron las dimensiones obtenidas con el objetivo de analizar la influencia del tono del pigmento de absorción en la percepción del *graininess*.

$$CV = 100 * \frac{std}{max - min} \quad (1)$$

3. Resultados y discusión

Como ya se ha dicho, en primer lugar se se analizó la variabilidad asociada a los observadores. La variabilidad asociada a la respuesta individual de los observadores fue del 6 %, y la variabilidad entre observadores fue del 9 %. Estos valores de variabilidad son similares a los obtenidos en otros experimentos visuales realizados con el mismo procedimiento y objetivo, y son valores bajos, lo que nos permite validar el experimento visual. En la figura 1 se representa el *graininess* visual obtenido en función del tamaño de pigmento. Como puede verse en la figura, el *graininess* visual es mayor cuanto mayor es el tamaño de pigmento, como era esperable, con una tendencia lineal ($r^2 = 0.9496$). No obstante, para el tamaño de pigmento intermedio, el *graininess* visual es similar a la del tamaño de pigmento pequeño para el pigmento verde y azul. Si se analizan los datos instrumentales obtenidos con el instrumento *BYK-mac i*, se observa que a pesar de haber una relación lineal entre ambas magnitudes ($r^2 = 0.9594$) se observa que mientras que hay una mayor variabilidad en el *graininess* instrumental, el observador no percibe esa variabilidad. En cuanto al tono del pigmento de absorción, puede decirse que el tono no influye para tamaños de pigmento pequeño y grande, sin embargo, para el fondo rojo, puede verse que el *graininess* percibido es ligeramente superior, a pesar que las muestras han sido diseñadas de la misma forma con la única variación del pigmento de absorción.

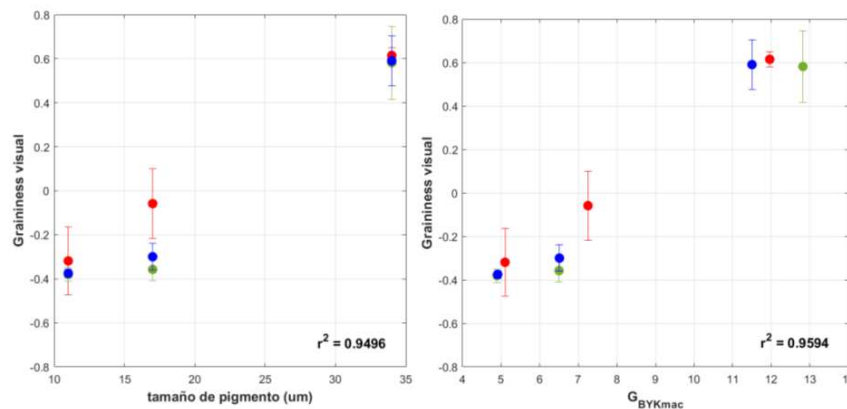


Figura 1: *Graininess* visual en función del tamaño de pigmento metálico (izquierda) y en función del *graininess* instrumental medido con el instrumento *BYK-mac i* (derecha).

4. Conclusiones

Se ha evaluado la sensación de *graininess* visual para tres tamaños de pigmento metálico y tres tonalidades de pigmento de absorción. El tono del fondo de las muestras evaluadas no parece tener un impacto en la sensación de *graininess* visual, excepto para el tamaño intermedio evaluado. Por tanto, es necesario evaluar en profundidad dicho efecto para tamaños de pigmento similares.

Referencias

- [1] G. A. Klein, *Industrial Color Physics*, vol. 154 (Springer, 2010).
- [2] A. Ferrero, J.L. Velázquez, E. Perales, J. Campos, & F. M. Verdú (2018). Definition of a measurement scale of graininess from reflectance and visual measurements. *Optics express*, 26(23), 30116-30127.
- [3] A. Ferrero., E. Perales, N. Basic, M. Pastuschek, G. Porrovecchio, A. Schirmacher, ... & P. Blattner (2021). "Preliminary measurement scales for sparkle and graininess". *Optics Express*, 29(5), 7589-7600.

Single-step Calibration of Liquid-Cristal Spatial Light Modulators with Fresnel Zone Plates

L. Ordóñez, E. Ipus, O. Mendoza-Yero*

GROC-UJI, Institute of New Imaging Technologies (INIT), Universitat Jaume I, 12071, Castelló, Spain

*E-mail: omendoza@uji.es

1. Introduction

Phase-only Spatial Light Modulators are dynamic and versatile devices capable of modulating the amplitude, phase and state of polarization of light, offering a wide range of applications across various fields including linear/nonlinear microscopy, material processing, spatial and temporal beam shaping, wavefront sensors, adaptive optics, and pulse shaping [1]. In this context, the develop of methods for accurate and fast LC-SLM calibration becomes into a key point to achieve the best performance these useful optical devices. In general, conventional calibration methods are carried out by using optical setups with multiple optical components that implies complex alignment procedures and/or multiple measurements. In this study, we propose a direct calibration method that significantly reduces the measurement time, which is especially suitable for real-time and multi-wavelength applications.

Among the different calibration methods reported in the literature, three innovative approaches stand out. Firstly, phase interference calibration method based on Billet-split Fresnel zone plates (FZPs) which is highlighted for its robustness to environmental factors and versatility across multi-wavelength scenarios [2]. Secondly, a time-efficient regional calibration method is emphasized. It requires a single nonholographic intensity measurement per grayscale command input without the need for additional optical elements [3]. In addition, a calibration method based on 1-D phase retrieval algorithm should be mentioned for its stability and anti-noise capabilities, with validation of its efficacy in mitigating crosstalk errors inherent in LC-SLMs [4].

The proposed calibration method uses a single-phase mask composed of an array of binary-phase FZPs, encoding each the gray level value ranged from 0 to 255. The method basically relies on the measurement of the focal irradiance of the FZPs by using a conventional image sensor (IS). The corresponding optical setup has few optical components (the LC-SLM, a spatial filtered, 4f system, and the IS). The integration of multiple foci into a single-phase mask notably enhances its robustness to temporal fluctuations of light. Additionally, since it only requires a single recorded image to obtain the complete calibration curve, implementing multi-wavelength calibrations can be easily achieved. The introduced method can be regarded as a generalization of a previous one [5] that deals with the analysis of the diffraction efficiency of sequentially binary phase Fresnel lenses. So, theoretical model used to support the method [5] also holds for the present one. From a practical point of view, experimental results show the effectiveness of the proposed method, validating this direct calibration technique and expanding its applicability to multi-wavelength calibration and real-time analysis.

2. Experimental setup

In Figure 1, we show the optical setup, which employs a femtosecond laser oscillator as the light source. The spectrum of the light is filtered by a bandpass spectral filter (SF) centered at 800 ± 10 nm. After the SF, the light is sent to the LC-SLM by using a mirror (M) and a 50:50 beam splitter (BS). Then, the light reflected by the LC-SLM passes through a 4-f system imaging system composed by two refractive lenses with the same focal length. This system images the screen of the LC-SLM onto the camera image sensor (IS) at the output plane. To measure the irradiance of the FZPs spots, the IS is placed at the focal distance of the FZPs.

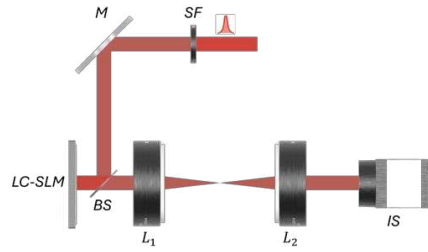


Figure 1 Single-step calibration experimental setup.

3. Results

The experimental results are illustrated in Figure 2. The FZPs are displayed on the LC-SLM. Fig. 2(a) depicts the image captured by the camera, allowing for the visualization of the FZP array. Moreover, gray values encoded in each FZP follow a sequential order from 0 at the top-left corner to 255 at the bottom-right corner. Placing the camera at the focal length of the FZPs allows the irradiance spots to be recorded, as shown in Fig. 2(b). Then, irradiance measurement is performed for each FZP. Normalized irradiance values taken from each FZP are used to correlate gray levels and phase values, enabling the generation of the phase calibration function, as shown in Fig. 2(c).

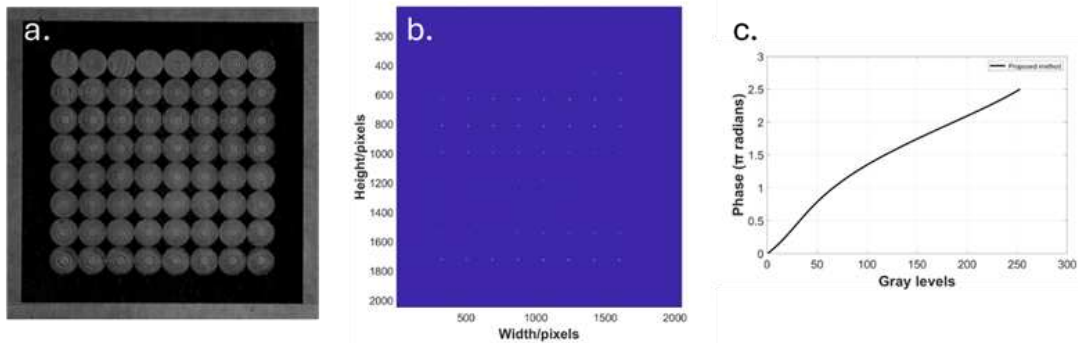


Figure 2 Experimental results. (a) Multiple FZPs captured at the focal plane of the 4-f imaging system. (b) Corresponding focal spots at the focal plane of the FZPs. (c) Obtained calibration curve from the processed data.

4. Conclusion

The proposed direct calibration method for LC-SLM significantly reduces the time expended for acquisition data with respect to conventional calibration methods, enabling potential real-time applications of LC-SLM under complex scenarios such as multi-spectral illumination or variable incident angles of light. Utilizing minimal optical components, it is possible to implement the proposed calibration method into different optical setups. Moreover, the proposed method demonstrates robustness to experimental light fluctuations and is poorly dependent on the zero-order light coming from the SLM.

References

- [1] Yang, Yiqian, Andrew Forbes, and Liangcai Cao. "A review of liquid crystal spatial light modulators: devices and applications." *Opto-Electronic Science* 2.8 (2023): 230026-1.
- [2] Wang, Chi, Jian Shan, and Junyong Zhang. "Absolutely interferometric calibration of phase liquid crystal spatial light modulators using honeycomb gratings composited with Billet-split Fresnel zone plates." *Applied Optics* 63.4 (2024): 1105-1109.
- [3] Nam, Kibum, and Jung-Hoon Park. "Reference-free in situ rapid regional calibration of phase-only spatial light modulators." *Optics Letters* 49.3 (2024): 522-525.
- [4] Zhou, Yifu, et al. "Calibration method of liquid-crystal spatial light modulator based on a 1-D phase retrieval algorithm." *IEEE Photonics Journal* 15.2 (2023): 1-11.
- [5] Mendoza-Yero, Omel, et al. "Diffraction-based phase calibration of spatial light modulators with binary phase Fresnel lenses." *Journal of Display Technology* 12.10 (2016): 1027-1032.

SENER Aeroespacial, S.A. Optics and Optomechanical projects

Antonio Marzoa^{1*}, Carlos Miravet², Jorge Mujica³, Gonzalo Taubman³, Albert Tomàs¹, Ferran Grañena¹, Oriol Casamor¹ and Isabel Soto³

¹*Department of Precision Engineering, SENER Aeroespacial, S.A., C/ Creu Casas i Sicart, 86-87, 08290, Cerdanyola del Vallès, Barcelona, Spain*

²*Avionics and Advanced Systems Division, SENER Aeroespacial, S.A., C/ de Severo Ochoa, 4, 28760, Tres Cantos, Madrid, Spain*

³*Electro-Mechanical Systems Division, SENER Aeroespacial, S.A., Zugatzarte Etorb., 56, 48930, Getxo, Bizkaia, Spain*

*E-mail: antonio.marzoa@aeroespacial.sener

1. Introduction

SENER Aeroespacial, S.A., is a Spanish engineering company integrated in SENER's group, which was founded in 1956.

Since 1967, SENER Aeroespacial, S.A., has supplied equipment, systems integration, and engineering services to international markets in the fields of Space, Astronomy and Science, Aeronautics, Vehicles and Defence [1]. In many of these fields, the development of an ad hoc optical or optomechanical system is required, and SENER's capabilities and know-how allowed their engineers to find and built proper solutions for many different projects, covering from wide angle optical design to imaging spectrometers development, through design, development and manufacturing of large optomechanical and mechatronics systems for terrestrial telescopes, among other engineering projects.

In this contribution, several of the past and on-going projects of SENER's engineers in the fields of Optics and Optomechanics in the Space, Astronomy and Science markets are presented.

2. Optics instrumentation for Space Missions

SENER Aeroespacial, S.A., is a pioneer engineering company in the design of satellite technology and equipment for space exploration. The company has worked for decades with the main space agencies in the world —ESA, NASA, JAXA— and major companies in the sector, always with the highest level of reliability. SENER's portfolio in optical instrumentation for satellites and space missions includes:

- **Scanning mechanisms:** such as Sentinel-3 Scan flip mirror for Jena-Optronik, and the scan mechanism for Meteosat Third Generation (MTG) Scan [2].
- **Refocusing mechanisms:** mechanical positioning mechanisms such as the one for Gaia's astrometric mission [3] and for Euclid's satellite secondary mirrors (M2).
- **Shutter mechanisms:** shutter mechanisms for different space missions [4].
- **Calibration systems.**
- **Filter wheels:** such as the components for Hubble's Space Telescope (HST) Faint Object Camera (FOC) and OSIRIS and Janus filters.
- **Optical baffles:** systems to prevent the stray-light reflection onto the optical tubes of different instruments.
- **Optical benches:** to hold scientific instrumentation in proper and stable positions to receive the light beam from entrance telescopes, as in the case of HERSCHEL's Optical Bench.
- **Optical mounting and alignment.**
- **Optical payloads:** SEOSAT INGENIO primary payload design and development and CARAMUEL'S QKD optical payload design [5], among other projects.

3. Astronomy and Science markets

SENER's optical technology is present in some of the largest and most important telescopes in the scientific industry, from the HST to the Gran Telescopio de Canarias (GTC) in the Canary Islands. SENER has achieved a worldwide reputation in the design, testing and placement of mirror cells with diameters up to 4 meters [6], a job requiring extremely high levels of precision. An example of such projects are the M2, M3 and M5 cells for the European Southern Observatory (ESO) Extremely Large Telescope (ELT) [7].

Additionally, SENER stand out for participation in other relevant scientific developing disruptive technologies for big scientific infrastructures [8], [9].

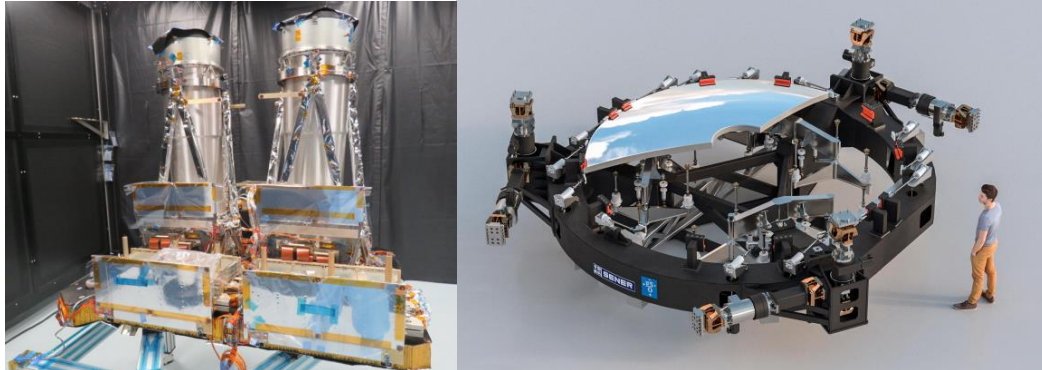


Figure 1 Examples of SENER's optics and optomechanics projects: SEOSAT's payload (left) and design of ELT's M2 cell (right).

Acknowledgments

Authors acknowledge all their colleagues from SENER that has participated in the different projects that will be summarized and presented in this poster communication.

References

- [1] [SENER Aeroespacial, S.A.](#)
- [2] C. Compostizo, A. Gonzalez-Elias, and A. Sacristán, "METEOSAT Third Generation (MTG) Scan Assembly Qualification Testing", Proc., '18th Euro. Space Mechanisms & Tribology Symp (ESMATS-18), Munich, Germany (2019).
- [3] E. Urgoiti, A. Ramirez, and P. Coste, "GAIA M2M Positioning Mechanism", Proc. '11th Euro. Space Mechanisms & Tribology Symp (ESMATS-11), Lucerne, Switzerland (2005).
- [4] J. A. Andión, and R. López, "Shutter mechanism for the PLEIADES High resolution instrument", Proc. '12th Euro. Space Mechanisms & Tribology Symp. (ESMATS-12)', Liverpool, UK (2007).
- [5] A. Alvarez-Herrero, T. Belenguer, L. Pascual, A. Álvaro, C. Miravet, P. Campo, A. Tomás, L. F. Rodríguez, M. Reyes, E. Sánchez de Gregorio, F. Cuervo, P. Pintó, "Conceptual optical design for CARAMUEL payload: a quantum key distribution system from a GEO satellite," Proc. SPIE 12633, Photonics for Quantum 2023, 126330B (2023).
- [6] A. Tomàs, M. Crusellas, E. Escalera, M. Redondo, J. M. Casalta, A. Nieto, A. González, A. Mato, N. Vega, M. Soler, J. Cozar-Castellano, J. M. Gonzalez-Cava, M. Núñez Cagigal, J. Sánchez-Capuchino, M. Barreto, "The preliminary design of the M1 assembly for the European Solar Telescope," Proc. SPIE 12188, Advances in Optical and Mechanical Technologies for Telescopes and Instrumentation V, 1218810 (2022).
- [7] A. Tomàs, J. A. Andion, M. Canchado, J. M. Casalta, O. Casamor, O. Ramos, M. Redondo, F. Grañena, G. Olivella, M. Mueller, Y. Lammen, J. F. Pirard, P. Zuluaga, "The design and development of the M2, M3 and M5 cells for the European Extremely Large Telescope," Proc. SPIE 12188, Advances in Optical and Mechanical Technologies for Telescopes and Instrumentation V, 121880K (2022).
- [8] A. Tomàs, Fernando del Campo, A. Nieto, M. Canchado, R. González, J. M. Casalta, Patrick Caillier, Lluís Cavaller, "The design of the M1 segments manipulator for the Extremely Large Telescope," Proc. SPIE 12188, Advances in Optical and Mechanical Technologies for Telescopes and Instrumentation V, 121880H (2022).
- [9] A. Marzoa, A. Tomàs, J. M. Casalta, J. Solis, J. Gonzalo, "A laser cleaning system for astronomical mirrors," Proc. SPIE 12186, Observatory Operations: Strategies, Processes, and Systems IX, 1218619 (2022).

Single-arm interferometer for the calibration of liquid crystal spatial light modulators

Erick Ipus, L. Ordóñez, O. Mendoza-Yero*

GROC-UJI, Institute of New Imaging Technologies (INIT), Universitat Jaume I, 12071, Castelló, Spain

*E-mail: omendoza@uji.es

1. Introduction

Liquid crystal spatial light modulators (LC-SLM) are highly dynamic and versatile devices, capable of modulating the amplitude, phase, and state of polarization of light. Their versatility finds use in a wide range of applications, including linear/nonlinear microscopy, material processing, spatial and temporal beam shaping, wavefront sensing, adaptive optics, and pulse shaping [1]. However, to get the optimal performance, the LC-SLMs require a precise calibration. The phase calibration process consists of finding a match between a phase retardance and a grayscale from 0 to 255. There are many calibration methods that can be classified into three main groups: interferometric [2,3], diffractive [4] and polarimetric methods [5].

Interferometric calibration methods traditionally offer a promising approach by utilizing the principles of interference to characterize and calibrate the optical response of LC-SLMs. Some reported methods use a phase lens for phase-shifting radial shearing interferometry [2]. Its principal advantage is the high vibration insensitivity and robustness to irradiance fluctuations due to misalignment. Other methods employ honeycomb gratings combined with Billet-split Fresnel zone plates [6], enabling high-accuracy calibration even in disturbed environments.

The proposed interferometric calibration method uses a grating-like phase mask to get the global calibration of the LC-SLMs by means of single irradiance measurement. The phase mask is made up of a fringe array of consecutively gray levels, but a black fringe inserted between each gray values. The interference occurs due the spatial filtering of the first diffraction order of the grating in the Fourier plane of a 4-f system. At the output plane of the relay system, the interference of the fringes is obtained, allowing the measurement of the irradiance pattern. The used phase mask can be applied for both local and global calibration of the SLM. Furthermore, the use of a single mask allows a more compact optical setup increasing the robustness to temporal light fluctuations and enabling implementation over multiple wavelengths. From a practical point of view, experimental results demonstrate the effectiveness of the proposed method, validating the calibration technique.

2. Experimental setup

In Fig. 1(a) the scheme of the proposed calibration method is shown. The light source is a femtosecond laser oscillator that emits a broadband pulsed laser beam. The spectral content of this pulse laser is first tuned with a spatial filter to get a centered quasi-monochromatic light at 800 ± 5 nm. Then, the beam illuminates the LC-SLM (Pluto-NIR-II, spatial resolution 1920×1080 pixels, $8 \mu\text{m}$ pixel pitch), where the mask is codified. The mask consists of a set of gray values fringes interspersed with black ones, see Fig. 1b.

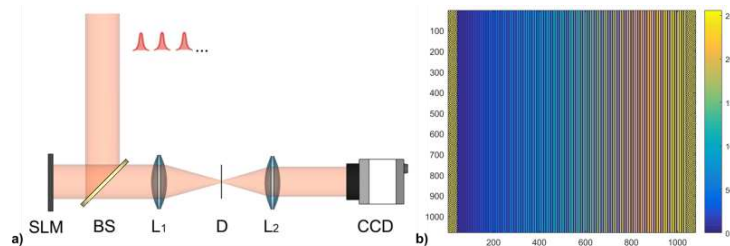


Figure 1 . a) Interferometric single-shot calibration experimental setup. b) Fringe mask that encodes gray levels used to calibrate the LC-SLM.

Finally, the display of the LC-SLM is optically conjugated with the CCD's screen by the above-mentioned relay system composed of the lenses L1 and L2. The sensor records the interference pattern

generated at the output plane of the imaging system. The recorded image is digitally processed to obtain a global calibration curve. This procedure was repeated for different incident wavelengths, 762 nm, 800 nm y 859 nm.

3. Results

The experimental results for the three different wavelengths are shown in Fig. 2. From the recorded images, the intensity was measured for each row of the image. The mean intensity value obtained for each wavelength is plot in Fig. 2(a). With knowledge of the spatial distribution of the fringes over the sensor, is possible to link the intensity values with the gray levels encoded in the mask. The normalized irradiance as a function of the grayscale is plot in Fig. 2(b).

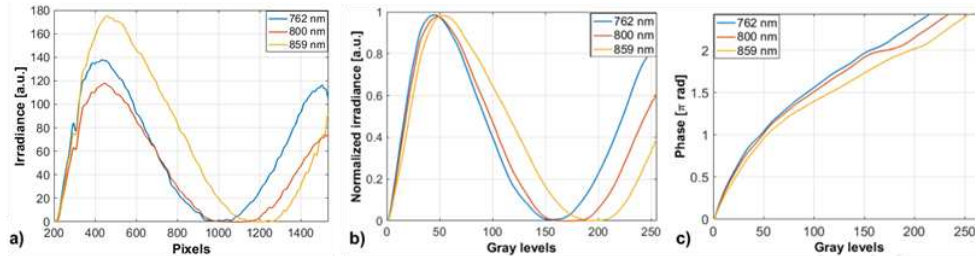


Figure 2 Experimental results for each wavelength used. (a) Pixel values taken from the images recorded. (b) Irradiance integrated as a function of the gray levels. (c) Phase calibration curve obtained from the proposed method.

From the results of Fig. 2b is possible to determine the phase calibration curve for the SLM, i.e., the dependence of the phase values with the gray levels. The phase calibration function is shown in Fig. 2(c). In these curves we can see that phase range of the SLM is extended from 0 to 2.5π approximately.

4. Conclusion

We proposed a direct and fast global phase calibration method based on a single irradiance measurement of the interferometric patterns generated by the superposition of dark fringes and gray levels fringes. Phase calibration curves were obtained for different wavelengths. We think that the proposed method can be useful in a wide range of applications including to multi-wavelength calibration and real-time analysis.

References

- [1] Yang, Yiqian, Andrew Forbes, and Liangcai Cao. "A review of liquid crystal spatial light modulators: devices and applications." *Opto-Electronic Science* 2.8 (2023): 230026-1.
- [2] Luke A. DeMars, Marta Mikula-Zdańkowska, Konstantinos Falaggis, and Rosario Porras-Aguilar, "Single-shot phase calibration of a spatial light modulator using geometric phase interferometry," *Appl. Opt.* 59, D125-D130 (2020).
- [3] Ferreira, Flávio P., and Michael S. Belsley. "Direct calibration of a spatial light modulator by lateral shearing interferometry." *Optics express* 18.8, 7899-7904 (2010).
- [4] O. Mendoza-Yero, G. Minguez-Vega, L. Martinez-Leon, M. Carbonell-Leal, M. Fernandez-Alonso, C. Donate-Buendia, J. Perez-Vizcaino, and J. Lancis, "Diffraction-based phase calibration of spatial light modulators with binary phase Fresnel lenses," *J. Disp. Technol.* 12, 1027–1032 (2016).
- [5] F. J. Martínez, A. Márquez, S. Gallego, M. Ortuño, J. Francés, A. Beléndez, and I. Pascual, "Averaged Stokes polarimetry applied to evaluate retardance and flicker in PA-LCoS devices," *Opt. Express* 22, 15064–15074 (2014).
- [6] Chi Wang, Jian Shan, and Junyong Zhang, "Absolutely interferometric calibration of phase liquid crystal spatial light modulators using honeycomb gratings composited with Billet-split Fresnel zone plates," *Appl. Opt.* 63, 1105-1109 (2024)

Set-up of a Hartmann Test for the characterization of large-area deformable mirrors

Sara Giménez-Aragón^{1*}, Santiago Royo¹

¹Center for Sensors, Instruments and Systems Development (UPC-CD6), Universitat Politècnica de Catalunya, Rambla de Sant Nebridi 10, 08222, Terrassa, Spain.

*E-mail: sara.gimenez@upc.edu

1. Introduction

The demand for high-quality optical surfaces is escalating across various sectors, from advanced astronomical telescopes to precise diagnosis of ocular diseases. Ensuring surface quality requires reliable, efficient, and rapid optical characterization techniques.

Optical characterization techniques play a pivotal role in identifying manufacturing errors or aberrations by comparing surfaces to predetermined design parameters. These techniques typically fall into two categories: interferometric tests, which use wavelength as a reference, and classical non-interferometric tests, which analyze the optical path by tracing light rays [1]. The choice of characterization technique depends on individual requirements (usually, on the resolution and dynamic range required), but it must consistently deliver accurate outcomes and generate easily interpretable data.

The Hartmann and Shack-Hartmann (SH) tests are widely implemented non-interferometric optical characterization techniques due to their simplicity, versatility, and ability to measure wavefront aberrations for optical systems with aberrations covering a large dynamic range, without requiring complex setups or coherence, as demanded in interferometric techniques. Additionally, the Hartmann-based methods are cost-effective and easier to implement in various optical systems and environments [2].

The SH wavefront sensor is an evolution of the Hartmann test, originally used for determining wavefront deformation from telescope mirrors. In the Hartmann Test, a screen with an array of holes near the entrance or exit pupil of the system under test is used. Reflected light passes through these holes, creating a spot diagram on a detector. By comparing this pattern with a reference, transverse aberrations (TA) are measured, sampling the local slope of the wavefront surface $W(x,y)$ and thus the determination of aberrations and surface shape.

$$\frac{\partial W(x,y)}{\partial x} = -\frac{TA_x}{r} \quad \text{and} \quad \frac{\partial W(x,y)}{\partial y} = -\frac{TA_y}{r} \quad (1)$$

where r is the distance from the mirror's pupil to the detector [3].

Conversely, the SH test employs an array of lenslets instead of discrete apertures. Each lenslet forms a small spot from the incoming wavefront, and by measuring the displacement of these spots, the wavefront shape is reconstructed. However, the SH sensor is not suitable for highly aberrated or curved wavefronts due to its limited dynamic range and (typically) small entrance pupil, leading to saturation and inaccuracies beyond certain thresholds. Additionally, its spatial resolution may struggle with rapid changes in curvature or steep gradients if the lenslet size is too large relative to these features.

In our pursuit of optimizing deformable mirrors (DMs) of large diameter (larger than 100 mm), conventional SH measurements are inappropriate for full surface measurements. Not only did they fail to cover the entire mirror surface, but their performance was constrained by the requirement for relatively flat wavefronts. Hence, the motivation behind developing a Hartmann test for our deformable mirrors was born.

2. Methodology

The implementation of the Hartmann Test involved constructing a comprehensive experimental setup, alongside with dedicated post-processing software. A crucial component was the Hartmann screen, meticulously crafted to cover initially diameters up to 200 mm – but which may be easily scaled –. Comprising 121 3 mm-diameter holes arranged in a 25x13 grid, as shown in Fig.1a, the screen facilitates precise positioning of the spots in the Hartmanngrams (i.e., the spot patterns) and local measurements of

TA. Once the screen was built, it was mounted with a base acting as the mirror holder, as depicted in Fig. 1b. To ensure a robust and well-aligned experimental setup, a guide was constructed to facilitate the smooth sliding of the mirror coupled to the Hartmann screen, maintaining alignment with the emitting source and detector. The emitting source employed was a He-Ne laser emitting at $0.635 \mu\text{m}$. Subsequently, a 50-50 Beam Splitter (BS) divided the incoming beam into two paths: one blocked and the other directed towards the Hartmann screen coupled to the mirror. The reflected beam then traveled back, reaching the BS, where it was redirected towards the CCD detector of a camera for further analysis. The complete experimental setup is depicted in Fig. 1c.

Upon gathering Hartmanngrams, a post-processing software is being developed using Python, due to a lack of reliable, readily available open-source software. Therefore, this work aims to elucidate the computational processing of Hartmanngrams. The algorithm progressed through Acquisition, Segmentation, Centroid Detection, Slope Measurements, and culminated in Wavefront Reconstruction. Central to this process was the precision of centroid measurements, as inaccuracies could propagate errors throughout surface evaluation. The statistical weighted average or center of mass algorithm emerged as the preferred method for centroid measurement [4]. Once the centroids were detected, local slopes were calculated using the expression from Eq (1). From this point, the aberrated wavefront can be reconstructed using the Zernike modal basis.

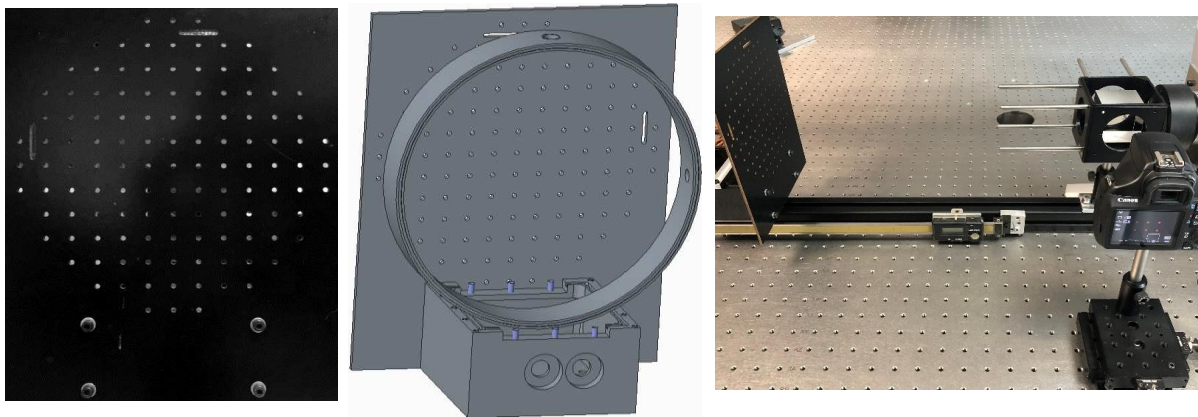


Figure 1 (a) Hartmann screen built. (b) Design of Hartmann screen coupled to mirror holder. (c) Complete experimental setup for the Hartmann Test.

3. Conclusions

This work offers a detailed experimental setup and software guide for the Hartmann Test, providing a straightforward, robust method to improve optical surface characterization, with wider applications beyond deformable mirrors. Future endeavors include studying noise implications and assessing the precision and accuracy of the computational package.

Acknowledgments

This work has been possible thanks to projects MISTED PID2020-119484RB-I00 and USEFUL TED2021-132338B-I00 funded by Ministerio de Ciencia e Innovación de España. This work has also been supported by SLIMOp Space.

References

- [1] M. Bass and V. N. Mahajan, *Handbook of optics*, 3rd ed. New York: McGraw-Hill, 2010.
- [2] D. Malacara, Ed., *Optical shop testing*, 3rd ed. in Wiley series in pure and applied optics. Hoboken, N.J: John Wiley, 2007.
- [3] D. Malacara-Hernández and D. Malacara-Doblado, “What is a Hartmann test?,” *Appl. Opt.*, vol. 54, no. 9, p. 2296, Mar. 2015, doi: 10.1364/AO.54.002296.
- [4] S.-H. Baik, S.-K. Park, C.-J. Kim, and B. Cha, “A center detection algorithm for Shack–Hartmann wavefront sensor,” *Opt. Laser Technol.*, vol. 39, no. 2, pp. 262–267, Mar. 2007, doi: 10.1016/j.optlastec.2005.08.005.

Portable multispectral imaging for eye fundus evaluation

Marina Bou^{1*}, Meritxell Vilaseca¹, and Francisco J. Burgos¹

¹ Centre for Sensors, Instruments and Systems Development, Universitat Politècnica de Catalunya, Rambla Sant Nebridi 10, Terrassa 08222 (Barcelona), Spain

*E-mail: marina.bou@upc.edu

1. Introduction

Fundus imaging is regularly used in clinical practice to diagnose several eye fundus diseases since it offers a very detailed visualization of the fundus and its structures. Fundus cameras allow non-invasive and fast examination of the fundus, providing accurate information on the progression of diseases. These systems acquire images through three channels (R, G and B) providing only colorimetric information because they are limited to the visible (VIS) range. As a consequence, some alterations may go unnoticed or be perceived as healthy structures due to metamerism (i.e., they produce the same R, G and B signals as other structures, despite having different spectral properties) [1]. Moreover, fundus structures located at deeper layers are difficult to observe with these cameras, since light is strongly absorbed and scattered by the previous tissues. Multispectral (MS) imaging systems have been used to overcome these limitations obtaining images through more than three channels and beyond the VIS, e.g., in the near-infrared (NIR) [2,3], where light penetrates deeper. These systems provide accurate spectral information, which is very useful when differentiating between healthy and diseased structures since the reflected light depends on the chemical composition of the tissue. Additionally, the use of portable fundus cameras is increasing due to the potential of smartphones in terms of computing power, image resolution and ease of use [4]. However, all of the commercial portable fundus cameras work only in the VIS range; therefore, they are affected by metamerism and can only explore the most superficial layers of the fundus. In order to overcome these limitations, the goal of this work was to build and characterize two portable fundus cameras and compare their performance to improve fundus examination. One is based on a smartphone for color imaging, while the other employs MS technology in the VIS-NIR range.

2. Methods and materials

The developed prototype (Figure 1) has been built as an ensemble of a color and a MS fundus camera. The illumination system is composed by a set of seven fiber-coupled LEDs: one broad-band LED (470 - 850 nm) is used to obtain color images, and six narrow-band LEDs (peaks within 400 - 900 nm) illuminate the fundus sequentially for MS imaging. All the LEDs are coupled to a custom-made optical fiber with seven inputs and one output. The fiber is connected to a PanOptic™ ophthalmoscope (Hill-Rom Holdings, Inc.), which provides uniform illumination over the fundus and collects the reflected light. Color fundus images are acquired with a smartphone through a purpose-built application that controls the LEDs and the camera. On the other hand, a CMOS camera UI-1480SE-M-GL (Imaging Development Systems GmbH) is used to capture MS images; for this, a separate software has been implemented in Matlab R2022b. At this initial stage, the imaging devices are interchanged for the acquisition of color and MS images, being attached to the PanOptic™ ophthalmoscope with the help of mechanical supports.

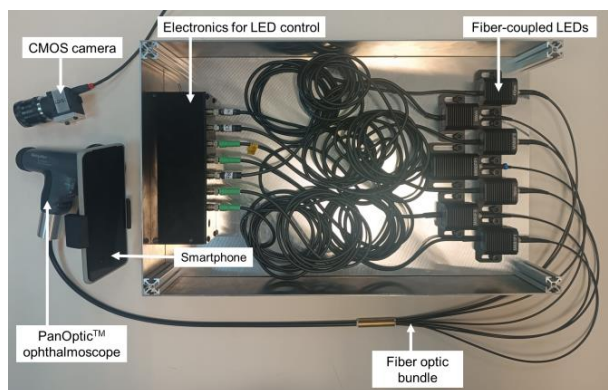


Figure 1 Prototype of the portable fundus cameras.

An artificial eye OEMI-7 (Ocular Instruments Inc.) was used to simulate a real environment while conducting laboratory tests. Each component has been characterized and tested individually and as a part of each fundus camera to ensure its performance in terms of spectral range, field of view, acquisition time, etc.

3. Results and future work

The different components of each fundus camera have been evaluated and adjusted to meet the specified requirements. The spectral emission of the LEDs was measured through the spectrometer CAS140D171U1A (Instrument Systems, GmbH) (Figure 2 left). The transmittance of the PanOptic™ ophthalmoscope was also studied with the same spectrometer and the integrating sphere ISP80. After an exhaustive analysis of all its components (Figure 2 right), a filter of the original illumination system was removed since it blocked wavelengths beyond 700 nm. During preliminary tests, the smartphone's camera showed good performance when illuminating the fundus with the white LED, and the CMOS camera showed good response in the VIS-NIR range. Currently, all the components of both color and MS fundus cameras are being fine-tuned to obtain optimized fundus images in the shortest possible time. The use of the smartphone for MS imaging was discarded because the acquisition of the whole set of images was too long due to the internal processes of the device that could not be avoided. In general terms, a single acquisition for the six spectral channels took around 5s, which is unacceptable for fundus imaging because images must be acquired very quickly before pupil constriction occurs, since the light reflected by the retina is very low.

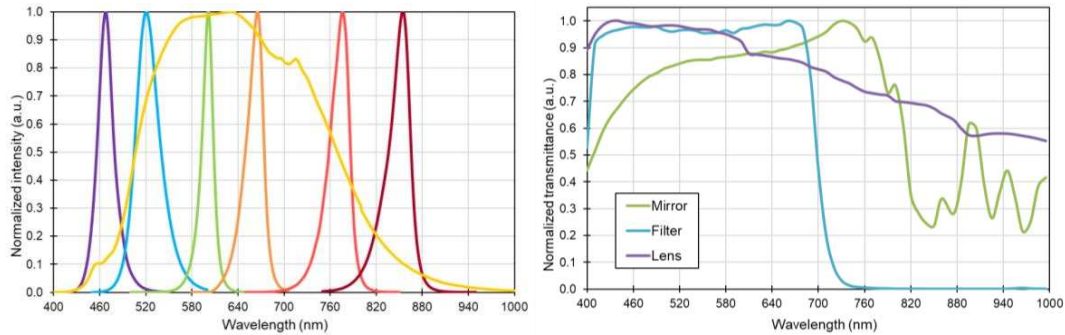


Figure 2 Normalized spectral emission of the LEDs (left). Spectral transmittance of the main optical components of the PanOptic™ ophthalmoscope (right).

Acknowledgments

This publication is part of the project PID2020-112527RB-I00, funded by MCIN/AEI/10.13039/501100011033. The first author gratefully acknowledges the Universitat Politècnica de Catalunya and Banco Santander for the financial support of her predoctoral grant FPI-UPC.

References

- [1] F. J. Burgos-Fernández, T. Alterini, F. Díaz-Doutón, L. González, C. Mateo, C. Mestre, J. Pujol, and M. Vilaseca, "Reflectance evaluation of eye fundus structures with a visible and near-infrared multispectral camera," *Biomed. Opt. Express* **13**(6), 3504–3519 (2022).
- [2] T. Alterini, F. Díaz-Doutón, F. J. Burgos-Fernández, L. González, C. Mateo, and M. Vilaseca, "Fast visible and extended near-infrared multispectral fundus camera," *J. Biomed. Opt.* **24**(09), 096007-1-096007-7 (2019).
- [3] C. Zimmer, D. Kahn, R. Clayton, P. Dugel, and B. Freund, "Multiple-wavelength imaging of the retina and choroid.," *Retina Today* **9**(7), 94–99 (2014).
- [4] R. E. Hacısoftaoglu, M. Karakaya, and A. B. Sallam, "Deep learning frameworks for diabetic retinopathy detection with smartphone-based retinal imaging systems," *Pattern Recognit. Lett.* **135**, 409–417 (2020).

SEDOPTICA-MOF: programas para visibilizar a las investigadoras

María-Baralida Tomás^{1*}, Rosa Ana Pérez-Herrera², Ana I. Gómez-Varela³, Beatriz Santamaria Fernández⁴, Alba de las Heras⁵, Pilar Granados-Delgado⁶, Anna I. Garrigues-Navarro⁷, Martina Delgado-Pinar⁷ y Verónica González-Fernández⁸

¹Instituto Universitario de Física Aplicada a las Ciencias y las Tecnologías, Universidad de Alicante

²Departamento de Ingeniería Eléctrica, Electrónica y de Comunicación, Universidad Pública de Navarra

³Departamento de Física Aplicada, Instituto de Materiales, Universidad de Santiago de Compostela

⁴Departamento de Ingeniería Mecánica, Química y Diseño Industrial, Universidad Politécnica de Madrid

⁵Departamento de Física Aplicada, Universidad de Salamanca

⁶Departamento de Óptica, Universidad de Granada

⁷Departamento de Física Aplicada, Universitat de València

⁸Departamento de Óptica, Universidad Complutense de Madrid

*E-mail: maria.baralida@ua.es

1. Introducción

La desigualdad de género existe en toda la sociedad y las comunidades científicas no son una excepción. La proporción de mujeres en los más altos cargos de gestión es muy inferior a su participación en los campos de trabajo, las investigadoras más jóvenes tienen contratos precarios en mayor proporción que sus compañeros y durante más tiempo, lo que repercute en el abandono de la profesión, y en la carrera investigadora las mujeres tienen un mayor número de obstáculos [1]. Para luchar contra estas desigualdades y visibilizar el trabajo de las investigadoras en las áreas de óptica y fotónica en España, en el Área de Mujer en Óptica y Fotónica de SEDOPTICA hemos desarrollado diferentes actividades que exponemos a continuación.

2. Cuenta con ellas

El programa *Cuenta con ellas* consiste en una base de datos de científicas en óptica y fotónica con reseñas cortas de las investigadoras. En ella pueden encontrarse de manera sencilla expertas por nombre o temática que pueda ayudar en la organización de eventos paritarios en caso de tener dificultades a la hora de encontrar científicas en un determinado campo. Esta base de datos está en continua actualización, por lo que animamos a todas las asistentes a la RNO 2024 a mandar su reseña para su publicación en nuestra web [2]. En la Figura 1 se pueden observar algunas de las investigadoras presentes en nuestra base de datos y esperamos que el número de científicas aumente mucho más.



Figura 1. Algunas investigadoras en óptica y fotónica en la base de datos *Cuenta con ellas* de nuestra página web [2].

Para visibilizar un poco más a estas investigadoras, se han realizado calendarios en los años 2023 y 2024 en los que cada mes se resalta una científica de la base de datos *Cuenta con ellas* mostrando su foto y una pequeña reseña.

3. Conoce a las investigadoras

El programa *Conoce a las investigadoras* pretende dar a conocer la labor investigadora llevada a cabo por mujeres españolas y extranjeras en cualquier fase de su carrera profesional. Consiste en la publicación mensual de una entrevista a una investigadora recogiendo las experiencias profesionales y personales de la científica, así como su experiencia en el tema de la igualdad de género a lo largo de su carrera científica. La mayoría de entrevistas publicadas son en formato escrito, aunque también hay entrevistas en vídeo publicadas en el canal de YouTube de SEDOPTICA [3].

Aprovechando la celebración de la Reunión Nacional de Óptica se ha publicado y entregado a los asistentes a la RNO 2024 un libro impreso con las entrevistas realizadas desde el inicio del programa en 2019 hasta 2021 aunque estas mismas entrevistas y las realizadas a partir de 2022 y hasta la actualidad se pueden visitar en nuestra página web [4].

4. Hablan las socias

El ciclo de conferencias *Hablan las socias* comenzó a desarrollarse en mayo de 2023 y consiste en visibilizar a las socias de SEDOPTICA mediante la realización de una charla de aproximadamente 1 hora sobre su campo de investigación. Estas conferencias se realizan cada dos meses colaborando en cada caso con un comité distinto de SEDOPTICA. Las charlas realizadas hasta ahora se pueden visualizar en el canal de YouTube de SEDOPTICA [3] a través de los códigos QR mostrados en la Tabla 1.







Comité colaborador	Nombre de la charla	QR para visualizar la charla
Color	Ayudas visuales para daltónicos	
Espectroscopía	Simulando hielos astrofísicos en el laboratorio	
Optoelectrónica	¿Qué podemos aprender sobre nuestro planeta utilizando cables de fibra óptica submarino?	
Óptica Cuántica y Óptica No Lineal	De las estrellas al átomo: ¿qué puede hacer la espectroscopía por los astrónomos?	
Divulgación, Enseñanza e Historia de la Óptica	Mujeres que iluminan la ciencia: una mirada a la historia femenina de la óptica y la fotónica	
Ciencias de la Visión	Corrección visual de cataratas basada en gafas inteligentes	

Tabla 1. Códigos QR para poder ver las charlas del ciclo de conferencias *Hablan las socias* realizadas hasta ahora.

Agradecimientos

Agradecemos a todas las personas que han colaborado en las diferentes actividades organizadas por SEDOPTICA-MOF o que nos han apoyado de un modo u otro.

Referencias

- [1] M.J. Yzuel and A. Peinado, “Women in Science: Physics and Optics”, ETOP 2013 Proceedings, paper EFE1.
- [2] <https://areamujersedoptica.wordpress.com/cuenta-con-ellas/>
- [3] <https://www.youtube.com/@SEDOPTICA>
- [4] <https://areamujersedoptica.wordpress.com/conoce-a-las-investigadoras/>

Design and construction of an underwater LiDAR system for multimodal imaging.

Aleix.R BOBI-OLMO^{1*}, Eduardo BERNAL¹, Pablo GARCÍA-GOMEZ², Enrique MARTÍNEZ², Jordi RIU² and Santiago ROYO¹⁻²

¹*Center for Sensors, Instruments and Systems Development (UPC-CD6), Universitat Politècnica de Catalunya, Rambla de Sant Nebridi 10, 08222, Terrassa, Spain.*

²*Beamagine S.L., Carrer de Bellesguard 16, 08755, Castellbisbal, Spain.*

*E-mail: aleix.ramon.bobi@upc.edu

1. Introduction

Due to the complexity of operating vehicles underwater, the majority of the oceans and seas have not been properly mapped [1]. This is yet to be solved, despite the fact that the topography of the marine scene, as well as salinity and temperature data, are of interest to several sciences and sectors. The majority of solutions rely on sonar or stereo imaging, which compromises either resolution or range. In the case of sonar, resolution is limited by its wavelength [2], with an additional depth limitation because most vessels transporting sonar devices cannot cross shallow waters. Range in stereo imaging typically underperforms if operating in an environment with textureless surfaces or low light levels.

An interesting alternative would be the use of a LiDAR solution, combining the real-time acquisition of 3D data, with higher resolution than the sonar, and larger ranges than conventional RGB underwater (UW) cameras, covering an intermediate range of solutions and enabling multimodal imaging. However, underwater applications differentiate it from conventional LiDAR systems and several aspects must be highlighted. The first and most significant problem is connected to the environmentally harsh conditions encountered at sea beyond the underwater operation itself, such as high pressures at depth, turbulence, turbidity, battery/energy supply challenges, and data transmission issues. Furthermore, the substantial absorption at those wavelengths prevents the GPS/GNSS signal from being detected underwater. Optically, a key aspect is the fact that we have a very narrow transmission window, which also affects the optical design. Usually, LiDAR uses IR lasers, at wavelengths from NIR to MWIR, but in a marine environment, IR wavelengths have high extinction coefficients and the transmission window is centered around the green part of the visible spectrum. Most UW-LiDAR systems use 532 nm lasers, thanks to its high transmission and adaptability to different kinds of oceanic waters, and the fact that can be generated easily using the second harmonic generation process (SHG). However, some UW LiDAR systems employ different wavelengths to boost transmission in more particular ocean circumstances, while others use multiple wavelengths to discern between coral species.

Despite its promise, underwater LiDAR remains relatively unexplored, with only a handful of commercially available systems offered exclusively through high-cost rental agreements. The aim of this project is the development of a moderate cost LiDAR unit which it can be further exploited for many tasks, including subsea structure inspection for sea platforms and infrastructures, mapping the coral reefs, fish detection [3] analyzing archeological sites [4], mine detection and others. One of the most interesting tasks for a UW LiDAR is the inspection of metal infrastructures at sea or complex scenes at sea, which are typically difficult to handle using radar imaging due to echoes. Additionally, underwater LiDAR systems offer the advantage of requiring smaller vessels compared to sonar systems, further enhancing their versatility and applicability in various marine environments.

A typical UW LiDAR would then consist of a scanner, a receiver, the hardware associated with it, some computing power, the hardware required for the estimation of pose and position determination, as well as the exterior infrastructure required for this purpose. As a cornerstone, the laser and its optics, and, if required, the SHG unit depending on the wavelength. With the radiometric model generated, we can estimate the range of use for our LiDAR. With this, we are able to determine that a 1 kW peak power 532nm commercial laser will operate in ranges of 30 to 40 meters for clear ocean waters and 10 to 20 meters for normal coastal seas.



Figure 1 Left figure: typical marine scene with a school of fishes. Right figure: a high sea infrastructure.

2. Conclusions

The application of underwater LiDAR technology is poised to revolutionize the mapping and inspection of diverse underwater environments, enhancing our ability to detect and characterize various elements within marine scenes, including underwater infrastructures and potentially undiscovered features. This advancement holds significant promise across multiple sectors including industry, defense, and academia, offering transformative benefits that are likely to catalyze a surge in related research and the development of more sophisticated underwater LiDAR systems.

Acknowledgments

This work has been possible thanks to projects MISTED PID2020-119484RB-I00 and USEFUL TED2021-132338B-I00 funded by Ministerio de Ciencia e Innovación de España. This work is part of a Ph.D. Thesis with grant number 2024 FI-1 00222 given by the Joan Oró from the Secretaria d'Universitats i Recerca from the department of Recerca i Universitats of Generalitat de Catalunya.

References

- [1] "How much of the ocean has been explored?: Ocean Exploration Facts: NOAA Office of Ocean Exploration and Research." Accessed: Dec. 21, 2023. [Online]. Available: <https://oceanexplorer.noaa.gov/facts/explored.html>
- [2] J. Dillon and R. Charron, "Resolution Measurement for Synthetic Aperture Sonar," in *OCEANS 2019 MTS/IEEE SEATTLE*, Seattle, WA, USA: IEEE, Oct. 2019, pp. 1–6. doi: 10.23919/OCEANS40490.2019.8962823.
- [3] E. Dubrovinskaya, F. Dagleish, B. Ouyang and P. Casari, "Underwater LiDAR Signal Processing for Enhanced Detection and Localization of Marine Life," *2018 OCEANS - MTS/IEEE Kobe Techno-Oceans (OTO)*, Kobe, Japan, 2018, pp. 1-8, doi: 10.1109/OCEANSKOB.2018.8559113.
- [4] J. W. C. Hale, D. S. Davis, and M. C. Sanger, "Evaluating the Archaeological Efficacy of Bathymetric LiDAR across Oceanographic Contexts: A Case Study from Apalachee Bay, Florida," *Heritage*, vol. 6, no. 2, Art. no. 2, Feb. 2023, doi: 10.3390/heritage6020051.

Raman study of different species of lichens after space and Mars like conditions

LOPEZ-RAMIREZ, M.R.^{1*}, MARTINEZ-FRÍAS, J.³, G^a SANCHO, L.⁴, BAQUÉ, M.⁵,
DE VERA, J.P.⁶, DE LA TORRE NOETZEL, R.²

¹UMA, Dpto. Química Física, Málaga, Spain

²INTA, National Institute for Aerospace Technology, Dpm. Earth Observation and Space Sciences, Madrid, Spain

³IGEO-CSIC, Univ. Complutense Madrid, Madrid, Spain

⁴UCM, Univ. Complutense Madrid, Dpm. Plant Sciences II, Madrid, Spain

⁵DLR, German Aerospace Center, Institute of Planetary Research, Planetary Laboratories, Berlin, Germany

⁶DLR, Space Operations and Astronaut Training, MUSC, Cologne, Germany

*E-mail: mrlopez@uma.es

Astrobiology experiments try to answer fundamental questions related to the survival capacity of biological organisms in space, the effects of the space environment on unprotected biological and chemical material and the results of degradation of organic molecules that will support the interpretation of missions, such as Rosetta, Curiosity, Mars2020 and ExoMars.

In this sense, we need results from experiments under space and Mars conditions to enable the development of appropriate predictions about the stability of organisms and their constituent organic parts. The extremophile lichens *Circinaria gyrosa*, *Xanthoparmelia hueana* and *Umbilicaria krepelhuberi* are the selected species within the BIOMEX (Biology and Mars Experiment) and BIOMARSS (BIOindicadores en MARTE y Espacio) that have been exposed to space and simulated Mars-like conditions in planetary chambers and we have studied and identified possible degradation process in different layers and biomarkers [1,2].

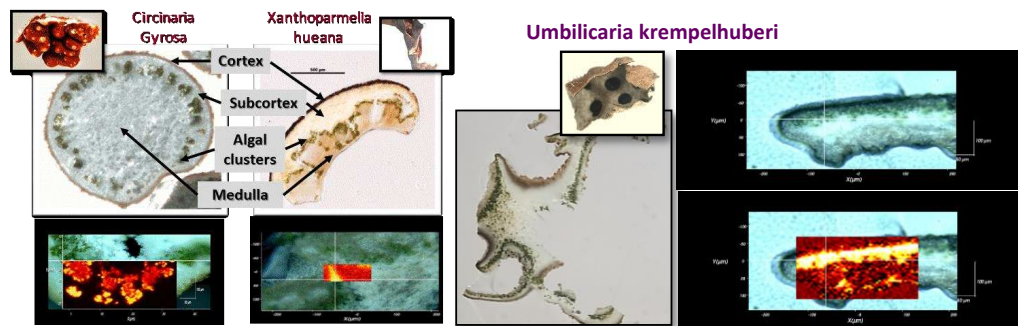


Figure 1 Original lichen species of *Circinaria gyrosa*, *Xanthoparmelia hueana* and *Umbilicaria krepelhuberi* and their thin sections. The Raman images show the algal cluster of each lichens filtered by 1524 cm^{-1} $\nu(\text{C}=\text{C})$ carotene band.

Raman spectroscopy has been able to detect characteristic compounds of these lichens as β -carotene, found as an accessory pigment of the photosynthetic apparatus of the algal symbiont, and calcium oxalate monohydrate, $\text{Ca}_2(\text{C}_2\text{O}_4)\times\text{H}_2\text{O}$, referred to as whewellite in mineralogical context. The conclusions of this work will be important to understand what are the effects to consider when biological systems are exposed to space or Mars-like conditions and to expand our knowledge of how life survives in most extreme conditions that is a prerequisite in future planetary exploration projects.

Acknowledgment

Support for this work was provided by the Spanish Ministry of Economy, Industry and Competitiveness (MINECO), by the project BIOindicadores en MARTE y Espacio (BIOMARSS) (PID2019-109448RB-I00) and by INTA.

References

- [1] U. Böttger, J. Meessen, J. Martinez-Frias, H.-W. Hübers, F. Rull, F. J. Sánchez, R. de la Torre, J.- P. de Vera. 2013. Raman Spectroscopic Analysis of the Calcium Oxalate Producing Extremotolerant Lichen *Circinaria gyrosa*. *International Journal of Astrobiology* 00 (2013) 1–14.
- [2] M.R. Lopez Ramirez, L.G Sancho, J. P. de Vera, M. Baqué, U. Böttcher, E. Rabbow, J. Martínez-Frías, R. de la Torre Noetzel. *Spectrochimica Acta, Part A*. 261 (2021) 120046.

Theoretical and experimental analyses of a radially polarized beam: Further implications on uniaxial retarder characterization

Mercedes Contreras, Óscar del Barco and Juan M. Bueno

Laboratorio de Óptica, Universidad de Murcia, 30100 Murcia, Spain

E-mail: bueno@um.es

1. Introduction

Polarization phenomena are related to the transversality of the electromagnetic waves, where an oscillating electric field and a magnetic field are mutually perpendicular. Whereas the vibration direction of the light coming from a non-coherent source are uncorrelated, the electric field vector of a polarized light oscillates describing a specific pattern. In this sense, polarized light beams usually present homogeneous states such as linear, circular or elliptical ones [1]. However, spatially variant polarization [2], especially radial and azimuthal polarized beams, have become popular in recent years due to their successful applications in different research fields, in particular imaging microscopy [3]. These polarization states, known as vector beams, are axially symmetric and can be generated via different active and passive methods [4].

From a mathematical point of view, homogeneous polarized beams can be described using the Jones matrix formalism [5], which offers a straightforward expression for totally polarized states, as well as a description of optical elements (retarders, polarizers, ...).

The aim of this work is to describe the theoretical basis of a radial polarized beam through the Jones formalism. In addition, different experiments have been conducted to further explore and analyze the intensity patterns and validate different polarization effects occurring when using radial polarization.

2. Theoretical formalism, experimental setup and procedure

The polarization state of each radially distributed section (along an angle φ) of a vector beam can be described by a Jones vector given by:

$$J_{rad} = \begin{pmatrix} \cos\varphi \\ \sin\varphi \end{pmatrix}. \quad (1)$$

Considering the Jones formalism, the matrices for a linear polarizer (with axis α) and a retardation plate (δ , retardation; θ , slow axis orientation) are expressed as:

$$MJ_{pol}^{\alpha} = \begin{pmatrix} \cos^2\alpha & \sin\alpha\cos\alpha \\ \sin\alpha\cos\alpha & \sin^2\alpha \end{pmatrix} ; \quad MJ_{\delta}^{\theta} = \begin{pmatrix} \cos\frac{\delta}{2} + i\sin\frac{\delta}{2}\cos(2\theta) & i\sin\frac{\delta}{2}\sin(2\theta) \\ i\sin\frac{\delta}{2}\sin(2\theta) & \cos\frac{\delta}{2} - i\sin\frac{\delta}{2}\cos(2\theta) \end{pmatrix} \quad (2)$$

Via these expressions, an alternative method to calculate the unknown retarder parameters (δ , θ) will be developed, based on solving a system of two equations. Moreover, this formalism will be also used to theoretically demonstrate that the intensity of a radially polarized beam passing a retardation plate is independent of the intrinsic retarder parameters.

The latter demonstration will be confirmed via an experimental setup built for this purpose, where a 635-nm laser diode, a collimation (pinhole+lens) set and a vertical linear polarizer are used. The light beam passes an S-waveplate [3,6] which turns linear into radial polarized light. Another rotating linear polarizer placed behind the S-waveplate serves as analyzer. Finally, a detector and/or a camera are used as recording devices.

The bow-tie intensity pattern associated to a radial polarized beam will be recorded and analyzed for different orientations of the analyzer. The spatially-resolved beam intensity will be also measured. Differences will be modelled and correlated to the results predicted by the Malus' law.

For the second part of the experiment, a retardation plate (used as unknown) was included into the setup. The newly generated intensity pattern was studied. Then, the intensity was assessed at different locations across the beam profile for different orientations of the slow axis of the retarder, θ . Results will be compared to the theoretical calculations previously performed.

3. Results

As an example, Figure 1 shows the experimentally recorded intensity patterns for a radial polarized beam. These correspond to the transmission analyzer axis oriented along the horizontal (left) and vertical (right) directions. As expected, the typical “bow-tie” for two perpendicular directions appears [2,3,6].

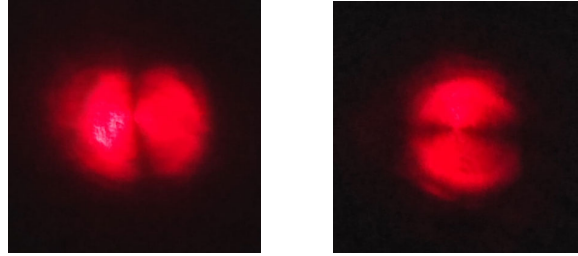


Figure 1 Bow-tie intensity pattern obtained with the analyzer’s transmission axis at 0° (left) and 90° (right).

When using the Jones formalism to model the experiment setup including the retarder plate used as unknown, the pair of equations obtained to compute the retardation plate parameters are:

$$\begin{cases} I_1 = x^2 + y^2 - x^2y^2 \\ 4I_2 = 4 - 3x^2 - 4y^2 + 4xy \end{cases} \quad (3)$$

where $x \equiv \cos\left(\frac{\delta}{2}\right)$ and $y \equiv \cos(2\theta)$. I_1 and I_2 correspond to the intensities measured for two different configurations of the analyzer.

It has been also tested, both theoretical and experimentally, that the intensity of a radial polarized beam passing a retardation waveplate keeps constant not only for any combination (δ, θ) , but also for any azimuthal direction φ in the plane perpendicular to the beam propagation.

4. Conclusions

In the present study, the Jones matrix formalism has been used to describe a radial polarized beam and the changes occurring when passing certain polarization elements. Using a simple experimental setup, the changes in the intensity patterns have been recorded and analyzed. Theory and experiments agree to each other.

Acknowledgments

Supported by grant PID2020-113919RBI00/AEI/10.13039/501100011033.

References

- [1] J. Casas, *Óptica* (Librería General, Zaragoza, 2008).
- [2] I. Moreno, J. Albero, J. A. Davis, D. M Cottrell, and J. B. Cushing, “Polarization manipulation of radially polarized beams,” *Optical Engineering* **51**(12), 128003 (2012).
- [3] R. M. Martínez-Ojeda, C. Hernández-García, and J. M. Bueno, “Enhancement of second harmonic microscopy images in collagen-based thick samples using radially polarized laser beams,” *Opt. Communications* **499**, 127273 (2021).
- [4] Q. Zhan, “Cylindrical vector beams: from mathematical concepts to applications,” *Adv. Opt. Photon.* **1**, 1-57 (2009).
- [5] R. C. Jones, “A new calculus for the treatment of optical systems I. Description and discussion of the calculus,” *J. Opt. Soc. Am.* **31**(7), 448-503 (1941).
- [6] B. Alonso, I. Lopez-Quintas, W. Holgado, R. Drevinskas, P. G. Kazansky, C. Hernández-García, and I. J. Sola, “Complete spatiotemporal and polarization characterization of ultrafast vector beams,” *Comm. Physics* **3**(1), 151 (2020).

Stimulated teleportation of high-dimensional spatial states with a nonlinear spatial detector

Adam Vallés,^{1,*} Bereneice Sephton,² Isaac Nape,² Mitchell A. Cox,³ Fabian Steinlechner,⁴ Thomas Konrad,⁵ Juan P. Torres,¹ Filippus S. Roux,⁶ and Andrew Forbes²

¹ ICFO - Institut de Ciències Fotoniques, The Barcelona Institute of Science and Technology, Castelldefels (Barcelona) 08860, Spain

² School of Physics, University of the Witwatersrand, Private Bag 3, Wits 2050, South Africa

³ School of Electrical and Information Engineering, University of the Witwatersrand, Johannesburg, South Africa

⁴ Fraunhofer Institute for Applied Optics and Precision Engineering, Albert-Einstein-Str. 7, 07745 Jena, Germany

⁵ School of Chemistry and Physics, University of KwaZulu-Natal, Durban, South Africa

⁶ National Metrology Institute of South Africa, Meiring Naud'e Road, Brummeria, Pretoria 0040, South Africa

*E-mail: adam.valles@icfo.eu

1. Main text

Quantum teleportation plays an important part in the progress of quantum information and the development of quantum technologies, making it an active area of research since the seminal paper was published in 1993 [1]. While being demonstrated in both: the continuous and discrete variable regimes, as well as with multiple degrees of freedom in a single photon, high-dimensional teleportation has not been experimentally achieved beyond 3 dimensions [2]. Here we experimentally demonstrate discrete-variable stimulated teleportation using the spatial degree of freedom, whereby the restrictive linear Bell-measurement is replaced with a non-linear approach [3], being able to perform amplitude and phase projections to any arbitrary spatial mode [4]. This scheme is illustrated in the setup of Fig. 1, in which we are able to establish a teleportation setup where the channel supports at least $\ell = 15$ orbital angular momentum (OAM) modes. The balance of channel capacity with noise is shown in the upper-right inset. Using a probe of purity and dimension [5] we use a traditional measure and estimate a channel fidelity which decreases with channel dimension, but is always well above the upper bound of the achievable fidelity for classical teleportation. We also illustrate the potential of the teleportation channel by testing all possible outcomes from the mutually unbiased basis (MUBs) considering four-dimensional states. The results are shown in the bottom-right inset of Fig. 1. We encoded each superposition (one at a time) in SLM_A and projected photon B in each of the four states. The strong diagonal with little cross-talk confirms teleportation across all states.

With this, our experiment is shown to be fundamentally different from previous linear implementations as it does not rely on ancillary photons to increase the dimensionality. Both linear teleportation and our nonlinear stimulated teleportation scheme require an entangled photon pair as a quantum resource, but linear optical approaches for qudit teleportation require ancillary photons in a manner that the experimental configuration is hard-coded for a particular channel's dimensionality, e.g., the present state-of-the-art ($d = 3$). The nonlinear approach we demonstrate uses the same experimental configuration, and only one entangled pair, for teleportation across multiple dimensions and across many spatial bases. In our stimulated teleportation process, we exploit a bright coherent state produced by a laser as the input source in order to enhance the up-conversion efficiency of the nonlinear crystal, but with the outcomes still conditioned on biphoton coincidences. However, these limiting factors might be alleviated by using artificial nonlinear media such as metasurfaces and metamaterials [6], and can in principle reach unity in future platforms.

So, while the need for *ancillary* photons is fundamental to linear optical solutions, the need for additional photons in the nonlinear case is a technological need because of present low efficiency. In contrast, the existing linear optical teleportation roadmap has the intrinsic efficiency limit that scales exponentially with dimension, e.g. $\gamma^{(d-1)/2}$ if SPDC is used to create the required photons, hence a much higher penalty for source inefficiency. As an example, if materials forming the non-linear platforms for creation and detection reach 10% efficiency then for $d = 15$ our approach would have an efficiency of 0.1²

$= 10^{-2}$ considering we also use SPDC to create the unknown input state, while with the linear case it is 10^{-7} ; 100 dimensions again returns 10^{-2} for our approach (crucially, it does not depend on d) but now 10^{-49} for the linear case.

Our latest results [7] open the way to implementing stimulated teleportation in a useful way with an encouraging paradigm allowing versatile and high-capacity optical quantum communication protocols for on-demand states.

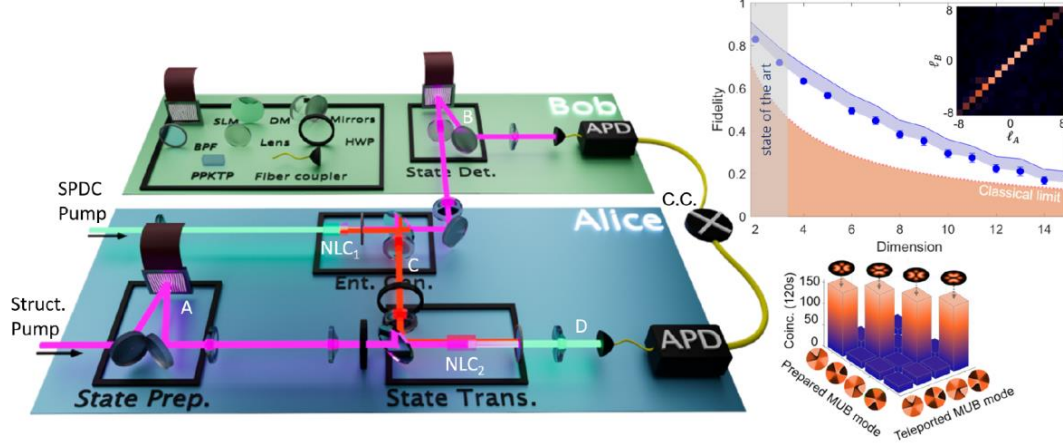


Figure 1 Experimental teleportation system. Two entangled photons, B and C, are produced from a nonlinear crystal (NLC₁) configured for collinear non-degenerate spontaneous parametric downconversion (SPDC). Photon C is sent to interact in NLC₂ with the state to be teleported (photon A), as prepared by Alice using a spatial light modulator (SLM_A), while Bob measures the teleported photon B with a spatial light modulator (SLM_B). Projection of the upconverted photon D then gives the unitary rotation on which to perform on the signal such that the unknown state can be retrieved and successful teleportation achieved. Insets show the experimental fidelities (points) for teleportation channel dimensions up to the maximum achievable channel capacity of $K = 15 \pm 1$, all well above the classical limit (dashed line). The smaller inset within shows the measured OAM modal spectrum of the optimised teleportation channel. The lower inset shows the measurements for the teleportation of a 4-dimensional state, constructed from the states $\ell = \{\pm 1, \pm 3\}$ OAM states.

References

- [1] Charles H Bennett, Gilles Brassard, Claude Crépeau, Richard Jozsa, Asher Peres, and William KWootters. “Teleporting an unknown quantum state via dual classical and einstein-podolsky-rosen channels,” *Phys. Rev. Lett.*, 70:1895, 1993.
- [2] Yi-Han Luo, Han-Sen Zhong, Manuel Erhard, Xi-Lin Wang, Li-Chao Peng, Mario Krenn, et al. “Quantum teleportation in high dimensions.” *Phys. Rev. Lett.*, 123(7):070505, 2019.
- [3] SN Molotkov. “Quantum teleportation of a single-photon wave packet.” *Physics Letters A*, 245(5):339–344, 1998.
- [4] Berenice Sephton, Adam Vallés, Fabian Steinlechner, Thomas Konrad, Juan P. Torres, Filippus S. Roux, and Andrew Forbes. “Spatial mode detection by frequency upconversion.” *Opt. Lett.*, 44(3):586–589, 2019.
- [5] Isaac Nape, Valeria Rodríguez-Fajardo, Feng Zhu, Hsiao-Chih Huang, Jonathan Leach, and Andrew Forbes. “Measuring dimensionality and purity of high-dimensional entangled states.” *Nature Communications*, 12(1):1–8, 2021.
- [6] Yuri Kivshar. All-dielectric meta-optics and non-linear nanophotonics. *National Science Review*, 5(2):144–158, 2018.
- [7] Berenice Sephton, Adam Vallés, Isaac Nape, Mitchell A Cox, Fabian Steinlechner, Thomas Konrad, Juan P Torres, Filippus S Roux, and Andrew Forbes. “Quantum transport of high-dimensional spatial information with a nonlinear detector.” *Nature Communications*, 14(1):8243, 2023.

Sedes de las Reuniones de los Comités de SEDOPTICA	
Viernes, 05/07 (12:00-13:00 h)	
<i>Ciencias de la Visión</i>	C2/04
<i>Color</i>	F0/17
<i>Mujer, Óptica y Fotónica</i>	F0/18
<i>Nanofotónica</i>	F0/19
<i>Óptica Cuántica y No Lineal</i>	B2/07
<i>Técnicas de la Imagen</i>	C2/06
<i>Divulgación, Enseñanza e Historia</i>	F0/20
<i>Red Temática FASLIGHT</i>	B2/09

Premios RNO 2024



Premios RNO 2024

Socio de Honor SEDOPTICA Edición 2022

Ramón Vilaseca

1er Premio Joven Investigador Postdoctoral

-Liquid crystals Mueller matrix imaging polarimeters tolerances to experimental errors.

Iván Montes-González

Accésit - Modalidad Investigador Postdoctoral

-Lateral-shearing interferometric microscopy for applications in biology, material sciences and semiconductors.

Roland A. Terborg

1er Premio Joven Investigador Predoctoral

-Femtosecond laser ablation in 3D-printed biopolymeric scaffolds to increase cell adhesion for bone tissue regeneration purposes.

Yago Radziunas-Salinas

Accésit 1 - Modalidad Investigador Predoctoral

-Generation of extreme-ultraviolet high-topological charge spatiotemporal optical vortices.

Rodrigo Martín-Hernández

Accésit 2 - Modalidad Investigador Predoctoral

-Investigating the perception of complex natural stimuli in polychromatic conditions using Adaptive Optics.

Elena Moreno

Premios SPIE-SEDOPTICA

-Image quality of an enhanced monofocal intraocular lens with corneal astigmatism.

Fátima Cuéllar

-Parallelized laser-scanned super-resolution depletion microscopy

Nick Toledo-García

Premios Justiniano Casas (Comité de Técnicas de la Imagen – 9ª edición)

-Polarimetric methods for the image enhancement in biological applications.

Albert van Eeekhout

-Percepción del emborronamiento estático y dinámico para el desarrollo de instrumentación clínica en optometría y oftalmología.

Víctor Rodríguez López

Premios Ramón Corbalán (Comité de Óptica Cuántica y no Lineal – 2ª ed.)

-Prehistoria de la Óptica Cuántica, *Rev. Española de Física* 37, 21 (2023).

Eugenio Roldán (*Premio a la Divulgación y Educación Científica en Óptica*)

-Time-resolved imaging techniques applied to femtosecond laser material processing, *Óptica Pura y Aplicada* 54, 1 (2021).

Mario García Lechuga (*Premio a la Divulgación de una Tesis Doctoral*)

-Instrucciones para atrapar la luz.

Laia Serradesanferm (*Premio a Contribuciones Breves de Divulgación*)

-Efecto Schwinger, o cómo crear materia de la nada con un láser.

María Rodríguez Domínguez (*Premio a Contribuciones Breves de Divulgación*)



Epílogo

Cerrar un *Libro de Resúmenes* como éste en el que todos somos autores es una responsabilidad que debo asumir como Presidente del Comité Organizador de la XIV RNO. He de confesar que me he sentido orgulloso de teneros en Murcia. Es fácil (y gratis) hacer estimaciones, pero sin duda es mucho más gratificante ver que esos números se han quedado cortos, muy cortos.

En algunas de las intervenciones que hice durante el evento ya lo hice constar. Todo lo (bueno) acontecido en la Capital del Segura ha sido fruto del esfuerzo del equipo que he tenido a mi alrededor y al que siempre estaré agradecido. A ellos he de añadir toda la ayuda recibida por parte de SEDOPTICA con nuestro Presidente Luis Plaja a la cabeza y el apoyo económico de nuestros *sponsors*. No me puedo olvidar de la Universidad de Murcia sin cuyos recursos humanos e infraestructura todo hubiese sido mucho más complicado (¡y caro!). Y cómo no, recordaros que sin vuestras contribuciones “este tinglao” no hubiese tenido lugar.

Como los más veteranos ya sabemos, es un hecho demostrado que tras asistir a un congreso sea de la índole que sea, a la larga (y por mucho que nos duela) lo único que perdura en nuestra memoria es la parte social en la que la interacción en ambientes menos rigurosos da más frutos de los que a veces se podría pensar. Espero que en esta ocasión también haya sido así, porque por suerte, para la parte científica ya queda este documento que aquí se cierra y podremos consultar a partir de ahora a nuestro antojo.

Estoy más que seguro de que al contrario del tema de *The Doors* allá por el 1967, esto no será “*the end, beautiful friend, the end*”, sino un punto y seguido, que nos permitirá coincidir dentro de 3 años para seguir disfrutando de (y con) esta comunidad científica de la que tod@s formamos parte.

¡Un fuerte abrazo!

Juan M. Bueno
Universidad de Murcia

(Va) Por el que hizo la primera foto y por el que dio nombre al **fotón**.
Por el que inventó la cámara, por el que descubrió a **Camarón**.
Por todos esos miopes con dioptrías a **mogollón**.
También va por los présbitas, a los que la vista se les **cansó**,
aunque eso es cosas de abuelos. Vamos... ¡digo **yo!**
Por los que trabajan sin descanso en temas de **polarización**,
bien sea con matrices de Mueller o por qué no, con las de **Jones**.
Por aquellos que se obsesionan con los patrones de **difracción**.
Por las transformadas de Fourier y las interferencias de un **Michelson**.
Por la longitud de onda que va asociada a un **electrón**.
Por los mili, los micro, los nano, los pico, los femto y los **ato(N)**.
Por el láser, los LEDs, la bombilla y los tubos de **Xenón**.
Por los que sueñan con que su sistema tenga **super-resolución**.
Birrefringencia es un término ruso, recuerdo que alguien **afirmó**,
decir eso es simple y llanamente, una total **aberración**.
Quítale todos los Zernikes y dime listico, ¿qué te **salió?**
Un sistema perfecto (que sabemos no existe) él mismo **respondió**.
No hacen falta alforjas para este viaje, amigo mío ¡por **Dios!**
Por cada científico brillante que el Nobel **ganó**,
Por los que hacemos ciencia modesta, día a día, con **pasión**.
Por los que todavía dan vueltas al chiste que el martes alguien **contó**,
en el que entra un veterinario a la consulta del **doctor**.
¡Qué malo que era! Las quejas... al **organizador**.
Porque acabar esta rima me está costando un **montón**,
Ufff, esto suena a Sabina cantando... “Lo nuestro **duró**”.
Bueno, si no es por la música, al menos que sea por la **voz**.
Va por cada uno de vosotros, que a Murcia se **acercó**.
Va por todos los que disfrutamos de nuestra querida **R.N.O.**

